

**Analysis of the Chemical Composition of Atmospheric and Chamber
Generated Aerosol Using Mass Spectrometry**

Thesis by
Shane Murphy

In Partial Fulfillment of the Requirements
for the Degree of
Doctor of Philosophy



California Institute of Technology

Pasadena, California

2009

(Defended May 28, 2009)

© 2009

Shane Murphy

All Rights Reserved

To My Parents

Acknowledgements

I remember when I first arrived at Caltech during the visiting weekend for prospective students. I was a very unsure over which graduate school to attend and what to study, but then I met John Seinfeld and Rick Flagan. John and Rick showed me around their labs personally and instilled a great sense of excitement in me for studying aerosols, clouds, and all things atmospheric. I would never have guessed that two huge names in science would be so kind and personable. Ever since that moment, my adventure at Caltech has been an excellent one. There have certainly been high points and low points and a fair amount of stress related to field campaigns, but in the end, I could not have asked for a better experience.

The field campaigns are probably the part of my graduate career that I will remember most. Under John and Rick's guidance I have been fortunate enough to fly in research aircraft all over the country. Spending months in airports and flying near coal-fired power plants and refineries may not sound too fun, but it is amazing how exciting it can be when you are completely immersed in the science. I am also extremely grateful to John and Rick for trusting me to be independent during these field campaigns. I cannot express how much I have learned by being allowed to find my own way some of the time.

Of course I never would have found my way if it was not for the help and guidance of many people over the years. I started my graduate career on the roof lab where Roya, Tomtor, Sally, Jason, and Jesse showed me how to do good laboratory science. I am especially indebted to Roya who was the one who brought me into the wonderful world of aerosol mass spectrometry. She was also the kind and patient person who was there holding my hand during my first field campaign. I spent many hours in

the roof with Sally and Jesse running experiments and also having some fun from time to time. Jesse taught me a lot about how to think about atmospheric chemistry, and for that I am extremely grateful.

There have been a lot of people who have been by my side during the five field projects that I was a part of. Armin and I went through the most together and his determination pushed me through a lot of hard times. He taught me a lot about how to persevere in tough situations. I formed a special bond with Kerri Pratt during our long months in Colorado being the only two graduate students on the ICE-L field project. I am eternally indebted to John Jayne and Jose Jimenez for answering untold telephone calls at ridiculous hours when the AMS was acting up again. Without the programming aid and advice of Pete DeCarlo and Joel Kimmel, the data for this thesis would never have been created. Tracey, Tomtor, Bill, Harmony, Scott, and Andrew have been wonderful companions and mentors in the field. Fred Brechtel and Haf Jonsson were always there when no one else could figure “it” out, whatever it may have been. They are two of the most talented experimentalists I know and definitely two of the kindest people. I am eternally grateful to Nave, Mike, Roy, Greg, and Chris for making sure I never had to use the safety training that they gave me and for making sure that I was able to do science with such a beastly instrument on such a small plane.

I have also been fortunate enough during my time at Caltech and in the field to work closely with several influential professors and principal investigators. Paul Wennberg has always provided insightful advice and has been kind enough to be a member of my thesis committee along with Haf Jonsson. I have learned a lot about how to do science and how to be a good advisor from Thanos Nenes, Patrick Chuang, and

Graham Feingold. It has been a lot of fun working with the members of their groups too. I was fortunate enough to meet Cynthia Twohy, Dave Rogers and Paul DeMott during my last field campaign and I look forward to doing more science with them in the future.

I have had the unique opportunity during my graduate career to be a part of a very unique group known as the AMS users, or just the “users”. This group has become a model for me of how science should work. I have never met a group of scientists who are more eager to share and collaborate than this one. A big bonus is that they are great people too. I will not soon forget the many adventures I’ve had with Eben, Achim, Tim, Ed, and many other “users”.

It has been a lot of fun in the last few years of my graduate career to share some of what I have learned with some of the newer members of the lab and to learn from them. I have been very impressed with Puneet and Jill, who will take over the reins of the AMS when I leave. I’ve had many good conversations with Arthur and I have no doubt the chamber is in good hands.

During the parts of my thesis where I could not be in the field or lab but had to write papers or proposals instead, the many days of sitting in front of a computer have been made infinitely easier by the friendship and entertainment of Daven, Philip, Zach, Jean, Anne and Havala. Jason Surratt has been with me since the beginning and having long conversations about our futures has been a godsend here at the end. I have also truly enjoyed getting to know Beth both scientifically and personally.

I also wish to acknowledge Mike Vondrus for machining many things for me over the years and for being a wonderful human being; Ann Hilgenfeldt, Yvette Grant, Sara Moore, and Marcy Fowler for making all the last minute requests and travel happen;

Kathy Bubash for keeping me on track with all the paperwork that I forgot to do; Tuyen Dang for all her assistance with my fellowship; and Suresh Guptha for always managing to fix whatever I had broken on my computer.

I would not have been able to do all of this work without the funding support of NASA, NOAA, and the Office of Naval research. I am especially indebted to NASA for providing me with the NASA Earth and Space Sciences Fellowship during the last two years.

I have made many great friends during my time at Caltech, whom I wish to acknowledge here. Without them, I probably would have lost it well before I made it to this point: Mark and Andrea for going on all the adventures that no one else would, John and Catherine for always being up for anything, Daven and Elena for reminding me that there is always time for dance and coffee, Morgan for reminding me that height doesn't matter in surfing, Philip for many good conversations, and Mike Vicic for talking about anything and everything with me. I have also been fortunate enough to be on two excellent intrumural soccer and basketball teams that have given me a good excuse to go have fun.

Finally I wish to express my extreme gratitude to my family. My parents have always been extremely supportive and I could not have done any of this without them. My sister has been a great confidant, having gone through the rigors of graduate school herself. Last, but most definitely not least, is the person who is by far the best thing that has happened to me at Caltech, my fiancée Karen. It is impossible to write how much she has meant to me over the last few years, but fortunately I don't have to because I have the rest of my life to tell her.

Abstract

This thesis presents results demonstrating the use of particulate composition measurements to determine the mechanisms of aerosol formation in both chamber and field studies. Aerosol composition measurements are also used to theoretically estimate the water-uptake behavior and ability to nucleate cloud droplets of atmospheric aerosol; these estimates are compared with in-situ airborne measurements. Common to all studies presented is the use of online aerosol mass spectrometry, a technique with high time resolution and minimal artifacts.

Chemical mechanisms involved in particle formation from the photooxidation of isoprene were explored in chamber studies using both online and offline mass spectrometry. The yield of aerosol and the nature of oligomers formed was found to depend on the NO_x concentration. Peroxides were found to be important under low- NO_x conditions while under high- NO_x conditions the majority of the particulate mass was found to derive from reaction products of methacrolein.

Particle formation from photooxidation of aliphatic amines was shown to be a feasible route of secondary organic aerosol formation in the atmosphere. Chamber studies at low relative humidity demonstrated that particle formation is primarily the result of acid-base reactions between amines and nitric or sulfuric acid, though diverse oxidized organic compounds are also formed. Thermodynamic calculations show that certain amines can compete with ammonia to form aminium salts at atmospherically relevant concentrations. An airborne field study near a major bovine source in the San Joaquin Valley, CA, gave evidence of particulate amine formation in the atmosphere.

The composition of particulate emissions from ships was studied during a joint shipboard and airborne field project in the Eastern Pacific. Particulate emissions were found to contain significantly higher levels of organic material than accounted for in current inventories. Observed hydrophobic organic material is concentrated in smaller particles and acts to suppress hygroscopic growth and activity of ship-exhaust particles as cloud condensation nuclei.

Ongoing research involves quantifying the impact of reactions within cloud droplets on the organic composition of aerosols. A recently completed field campaign investigated the role of particle chemistry in determining if aerosols can act as ice crystal nuclei.

Table of Contents

Dedication.....	iii
Acknowledgements	iv
Abstract.....	viii
List of Tables	xviii
List of Figures	XX
1 Introduction.....	1
1.1 Background and Motivation	2
1.2 Organization of Thesis.....	3
1.3 References.....	7
2 Chemical Composition of Secondary Organic Aerosol Formed from the Photooxidation of Isoprene.....	9
2.1 Abstract.....	10
2.2 Introduction.....	11
2.3 Experimental Section	13
2.3.1 Chamber Experiments.....	13
2.3.2 Filter Extractions.....	14
2.3.3 Liquid Chromatography / Electrospray Ionization – Mass Spectrometry	15
2.3.4 ESI – Ion Trap Mass Spectrometry.....	17
2.3.5 Matrix Assisted Laser Desorption Ionization -Time of flight Mass Spectrometer	18
2.3.6 High Resolution ESI-MS	18

2.3.7 Aerodyne Time of Flight Aerosol Mass Spectrometer	19
2.3.8 Gas Chromatography / Mass Spectrometry	20
2.3.9 Gas Chromatography – Flame Ionization Detection	21
2.3.10 Total Aerosol Peroxide Analysis	22
2.3.11 Particle-Into-Liquid Sampler Coupled to Ion Chromatography	23
2.4 Results	24
2.4.1 High-NO _x Condition	24
2.4.2 Low-NO _x Condition	31
2.5 Discussion	37
2.5.1 Gas-Phase Chemistry	37
2.5.2 High-NO _x SOA	39
2.5.2.1 Importance of MACR Oxidation	39
2.5.2.2 Oligomers	40
2.5.2.3 Organic Nitrates	41
2.5.2.4 2-MG as Monomeric Units	41
2.5.2.5 Mono-Acetate and Mono-Formate Oligomers	42
2.5.2.6 Heterogeneous Esterification Reactions	43
2.5.2.7 Additional Routes for SOA Formation	48
2.5.3 Low-NO _x SOA	51
2.5.3.1 Hydroperoxides: Key Component to SOA Formation	51
2.5.3.2 Oligomerization	52
2.5.3.3 Acid Catalysis	53
2.5.3.4 Formation Mechanism of Low-NO _x SOA products Observed by GC/MS54	

2.5.3.5 Evolution of SOA Composition.....	56
2.5.3.6 Tracer Compounds for Isoprene Oxidation in the Remote Atmosphere ..	57
2.6 Conclusions.....	58
2.7 Acknowledgements.....	60
2.8 References.....	61

3 Secondary Aerosol Formation from Atmospheric Reactions of Aliphatic

Amines	90
3.1 Abstract.....	91
3.2 Introduction.....	92
3.3 Experimental.....	94
3.3.1 PILS-IC	95
3.3.2 Aerodyne cToF-AMS	97
3.3.3 Effective density	98
3.3.4 Oxidation experiments.....	100
3.4 Atmospheric reaction pathways of amines	101
3.5 Salt aerosol formation from acid-base reactions of amines	103
3.5.2 Atmospheric formation of aminium nitrate salts: theory.....	104
3.5.3 Atmospheric formation of aminium nitrate salts; experimental	106
3.5.4 Aminium sulfate salts	109
3.6 Aerosol formation from photooxidation and ozonolysis of amines.....	110
3.6.1 Experimental protocol.....	115
3.6.2 Trimethylamine (TMA) photooxidation	116

3.6.3 Trimethylamine (TMA) ozonolysis	119
3.6.4 Methylamine (MA) photooxidation.....	121
3.6.5 Methylamine (MA) ozonolysis	122
3.6.6 Triethylamine (TEA) photooxidation	123
3.6.7 Triethylamine (TEA) ozonolysis	125
3.6.8 Diethylamine (DEA) photooxidation.....	126
3.6.9 Ethylamine (EA) photooxidation.....	127
3.6.10 Ethanolamine (MEA) photooxidation and ozonolysis.....	127
3.6.11 Photooxidation in the absence of NO _x	128
3.6.12 Effect of oxidation conditions on particle chemistry	128
3.6.13 Effective density shifts.....	129
3.7 Implications.....	129
3.8 Thermodynamic data for amine systems	131
3.9 Acknowledgements.....	133
3.10 References.....	133

4 Comprehensive Airborne Characterization of Aerosol from a Major

Bovine Source.....	162
4.1 Abstract.....	163
4.2 Introduction.....	164
4.3 Experimental Methods	167
4.3.1 Aerosol Chemical Composition (Aerodyne C-ToF-AMS).....	167
4.3.2 Aerosol Chemical Composition (PILS).....	169

4.3.3 Aerosol Hygroscopicity and Refractive Index (DASH-SP)	172
4.3.4 Cloud Condensation Nuclei Counter (CCNc).....	173
4.3.5 Size Distributions and Particle Number Concentration	174
4.3.6 Flight Strategy.....	174
4.4 Results.....	175
4.4.1 Meteorology.....	175
4.4.2 Particle Number Concentrations and Size Distributions	176
4.4.3 Submicrometer Aerosol Chemical Composition	178
4.4.3.1 Total Aerosol Mass and Major Components	178
4.4.3.2 Inorganic Aerosol.....	179
4.4.3.3 Organic Aerosol	180
4.4.4 Aerosol Mixing State.....	182
4.4.5 Refractive Index.....	182
4.4.6 Hygroscopic Properties of the Aerosol.....	183
4.4.6.1 Subsaturated Water Uptake.....	183
4.4.6.2 CCN	184
4.5 Discussion.....	186
4.5.1 Enhancements in Mass Production and Water Uptake in the Plume Aerosol	187
4.5.2 Amines as an Atmospheric Base.....	188
4.5.2.1 Is Nitric Acid or Ammonia the Limiting Reactant?.....	188
4.5.2.2 Sources and Character of Amines.....	190
4.5.2.3 Total Amine Mass Calculations.....	191
4.5.3 Degree of Oxidation and Volatility in the Aerosol.....	193

4.5.4 Factors Influencing Aerosol Number/Mass Concentrations.....	195
4.5.5 Estimated Subsaturated Hygroscopic Growth Factors for the Organic Fraction	196
4.5.6 Relationship Between Sub- and Supersaturated Water Uptake.....	199
4.5.7 Parameterization for Sub- and Supersaturated Water Uptake	200
4.6 Conclusions.....	202
4.7 Appendix.....	204
4.8 Acknowledgements.....	206
4.9 References.....	206
5 Comprehensive Simultaneous Shipboard and Airborne Characterization of Exhaust from a Modern Container Ship at Sea	244
5.1 Abstract.....	245
5.2 Introduction.....	246
5.3 Methods.....	248
5.3.1. Container Ship	248
5.3.2 Shipboard Platform Measurements.....	248
5.3.3 Aircraft-Based Measurements	249
5.3.3.1 Aerosol Number and Volume	250
5.3.3.2 Aerosol Mass, Chemistry, and Absorption	251
5.3.3.3 Aerosol Hygroscopic Growth and Cloud Condensation Nuclei Activity.....	252
5.3.4 Theory for Predicting Subsaturated Hygroscopic Growth.....	253
5.3.5 Theory for Cloud Condensation Nuclei (CCN) Closure.....	253
5.4 Results.....	256

5.4.1 Flight Tracks and Meteorology.....	256
5.4.2 In-Stack Composition	258
5.4.3 Particle Number, Volume, and Mass in the Airborne Exhaust Plume.....	260
5.4.4 Airborne Particulate Composition	262
5.4.5 Aerosol Hygroscopicity	264
5.4.6 CCN Activity	266
5.5 Discussion	268
5.5.1 Comparison of Ship and Airborne Data.....	268
5.5.2 Plume Dilution and Aging	272
5.5.3 Hygroscopic Growth.....	273
5.5.4 CCN Closure.....	275
5.6 Implications.....	276
5.7 Acknowledgments.....	278
5.8 Supporting Information.....	278
5.8.1 Shipboard Platform Test Methods	279
5.8.1.1 Measurement of Stack Gases	279
5.8.1.2 Measurement of Particulate Matter (PM) mass and Ions.....	279
5.8.1.3 Measurement of Particle-Phase Elemental and Organic Carbon.....	279
5.8.1.4 Measurement of Size-Resolved Particulate Composition.....	280
5.8.1.5 Measurement of Carbonyls	280
5.8.1.6 C ₁₀ to C ₃₀ Hydrocarbons, Including Naphthalene and PAHs	281
5.8.1.7 1,3 Butadiene; Benzene; Toluene; Ethylbenzene and Xylenes	281
5.8 Literature Cited	283

6 Conclusions and Future Studies	307
6.1 Conclusions.....	308
6.2 Future Studies	312
6.2.1 Tracing Organic Aerosol Production from Cloud Processing Reactions	312
6.2.2 Determining the Chemical Characteristics of Ice Nuclei	313
6.3 References.....	316
Appendices	
Appendix A Secondary Organic Aerosol Formation from Isoprene	
Photooxidation	318
Appendix B Apportionment of primary and secondary organic aerosols in Southern California during the 2005 study of organic aerosols in riverside (SOAR-1)	329
Appendix C Aerosol hygroscopicity in the marine atmosphere: A closure study using high-time-resolution, multiple-rh DASH-SP and size-resolved C-ToF-AMS data	339

List of Tables

Table 2.1 High-NO _x chamber experiments conducted.....	64
Table 2.2 Quantified SOA products (in ng/m ³) from high-NO _x chamber experiments....	65
Table 2.3 Low-NO _x chamber experiments conducted.....	66
Table 2.4 Low-NO _x isoprene SOA products elucidated by GC/MS	67
Table 3.1 Summary of structures of amines studied and estimated global emissions from animal husbandry.....	142
Table 3.2 Initial conditions of all experiments conducted.....	143
Table 3.3 Theoretically calculated dissociation constants for different nitrate systems. $K_{P,298}$ for ammonium nitrate = $7.14E-7 \text{ Pa}^2$	144
Table 3.4 Estimated percent mass yields ^a of non-salt aerosol during ozonolysis and photooxidation. All yields have an uncertainty of ~25% of their magnitude.....	145
Table 3.5 Thermodynamic data for various amine nitrate systems. Amines and nitric acid are in the gas phase and nitrates are solid.....	146
Table 4.1 Summary of in-plume and out-of-plume measurements of composition and particle number and mass concentration.....	217
Table 4.2 DASH-SP hygroscopicity and dry particle refractive index data.....	218
Table 4.3 Summary of CCN data for flights A and B.....	219
Table 4.4 Summary of κ values for the total aerosol and the organic component of the aerosol.....	220
Table 5.1 Selected Heavy Fuel Oil Properties.....	288
Table 5.2 Gaseous stack emission factors in g (kWhr) ⁻¹ by chemical class.....	289

Table 5.3 Particulate Stack Emission Factors.....	290
Table 5.4 Summary of absorption coefficient and non-refractory dry particulate composition in the ship exhaust plume at various plume ages.....	291
Table 5.5 Gas and particulate emission factors in g (kg fuel)^{-1} from this and previous studies of emissions from ships burning heavy fuel oil.....	292

List of Figures

Figure 1.1. Estimated radiative forcing of climate in 2005 relative to pre-industrial times.....	8
Figure 2.1. ESI-ITMS negative mode spectra collected via direct infusion analyses. (a) 500 ppb isoprene, high-NO _x , seeded; (b) 500 ppb MACR, high-NO _x , seeded.....	68
Figure 2.2. MALDI positive mode spectrum obtained with a graphite matrix for a 500 ppb isoprene, high-NO _x , dry seeded experiment.....	69
Figure 2.3. LC/MS TIC of filter extracts from 500 ppb, high-NO _x , nucleation (a) Isoprene, and (b) MACR experiments. (c), (d), and (e) LC/MS EICs of organic nitrate species common to both MACR and isoprene high-NO _x samples.....	70
Figure 2.4. (a) Mass spectrum for the largest chromatographic peak from Figure 2.3d (b) Upfront CID mass spectrum for the same chromatographic peak	71
Figure 2.5. TOF-AMS spectra collected at low vaporizer temperatures for: (a) 50 ppb isoprene, 250 ppb NO _x , H ₂ O ₂ , no seed, (b) 500 ppb MACR, 800 ppb NO _x , H ₂ O ₂ , with seed, and (c) 500 ppb isoprene, HONO, no seed.....	72
Figure 2.6. (a) TIC of a high-NO _x isoprene nucleation experiment collected using GC/MS; (b) EI mass spectrum for the 2-MG residue; (c) EI mass spectrum for a linear dimer made up of two 2-MG residues.....	73
Figure 2.7. MALDI positive mode spectrum obtained with a graphite matrix for a 500 ppb isoprene, low-NO _x , acid seeded experiment	74
Figure 2.8. TOF-AMS spectra for a 500 ppb isoprene low-NO _x experiment. (a) Low temperature vaporizer (~ 150°C); (b) high temperature vaporizer (~ 600°C).....	75

Figure 2.9. Time evolution plots produced from the TOF-AMS instrument for selected fragment ions and the total organic mass observed from a typical low-NO _x experiment.....	76
Figure 2.10. (a) GC/MS TIC of isoprene low-NO _x SOA; (b) averaged EI spectrum for the dimeric products eluting between 58.8 and 59.2 min and fragmentation scheme; (c) averaged CI(CH ₄) spectrum for the latter products.....	77
Figure 2.11. Reaction mechanism of isoprene oxidation under low- and high-NO _x conditions.....	78
Figure 2.12. ESI-ITMS negative mode product ion spectra from a high-NO _x isoprene SOA sample. (a) MS ² spectrum for an isolated <i>m/z</i> 323 ion; (b) MS ³ spectrum for an isolated <i>m/z</i> 323 ion.....	79
Figure 2.13. ESI-ITMS negative mode product ion mass spectra for high-NO _x SOA. (a) Product ion mass spectrum for a <i>mono</i> -acetate dimer (<i>m/z</i> 161); (b) Product ion mass spectrum for a <i>mono</i> -formate trimer (<i>m/z</i> 249).....	80
Figure 2.14. Proposed charge-directed nucleophilic reaction occurring during collisional activation in (-)ESI-ITMS.....	81
Figure 2.15. (a) GC/MS EIC (= <i>m/z</i> 219) for high-NO _x isoprene nucleation sample treated only with TMS derivatization; (b) duplicate sample, but treated by hydrolysis/ethylation followed by TMS derivatization. (c) EI mass spectrum for ethyl ester of 2-MG acid; (d) EI mass spectrum for ethyl ester of linear 2-MG acid dimer	82
Figure 2.16. Proposed mechanism for SOA formation from isoprene photooxidation under high-NO _x conditions.....	83

Figure 2.17. Proposed gas-phase formation mechanism for a C ₄ hydroxydialdehyde monomer.....	84
Figure 2.18. Low-NO _x SOA formation pathways as elucidated by GC/MS.....	85
Figure 2.19. (a) GC/MS EIC for a PM _{2.5} aerosol sample collected in Rondônia, Brazil; (b) averaged EI mass spectrum for the TMS derivatives of the isomeric hemiacetal dimers.....	86
Figure 2.20. EI mass spectra for low-NO _x SOA products. (a), (b), and (c) mass spectra of isomeric C ₅ alkene triols; (d) and (e) mass spectra of diastereoisomeric 2-methyltetrol performate derivatives. (f) and (g) mass spectra of diastereoisomeric 2-methyltetrols.....	89
Figure 3.1. Calculation of the effective density. (A) Triethylammonium nitrate (TEAN); (B) the same distributions shown in (A) after photooxidation	147
Figure 3.2. Mass spectra for the nitrate salts of the amines studied.....	148
Figure 3.3. Time series from exp. 19 in Table 3.2 of the cToF-AMS (bottom) and the PILS-IC (top).....	149
Figure 3.4. Time Series of data from the DMA (Panel A), PILS-IC (Panel B), and cToF-AMS (Panel C) showing rapid replacement of ammonium sulfate by methylammonium sulfate.....	150
Figure 3.5. Mechanisms of amine oxidation by: (A) OH in the presence of NO _x , (B) Ozone, in the absence of NO _x , and (C) OH in the absence of NO _x	152
Figure 3.6. Photooxidation of trimethylamine. Panel (A) NO _x and ozone; panel (B) particle volume; panel (C) ionic species measured by the PILS-IC; panels (D) and (E) fragment ions from the cToF-AMS.....	153

Figure 3.7. Aerosol mass spectra from the cToF-AMS during different stages of trimethylamine photooxidation and ozonolysis.....	154
Figure 3.8. Ozonolysis of trimethylamine. Panel (A) ozone concentration; panel (B) DMA volume; panel (C) formate concentration; panel (D) ions measured by the PILS-IC.....	155
Figure 3.9. Methylamine photooxidation. Panel (A) Ozone and NO _x concentrations; panel (B) time series for the DMA; panel (C) time series for the PILS-IC; panel (D) fragment ions from the cToF-AMS.....	156
Figure 3.10. Photooxidation of 500 ppb triethylamine. Panel (A) Ozone and NO _x concentrations; panel (B) time series for the DMA; panel (C) time series for the PILS-IC; panel (D) fragment ions from the cToF-AMS.....	157
Figure 3.11. Ozonolysis of triethylamine. Panel (A) Ozone concentrations; panel (B) time series for the DMA; panel (C) time series for the PILS-IC; panel (D) fragment ions from the cToF-AMS.....	158
Figure 3.12. Photooxidation of diethylamine. The volume trace from the DMA (bottom panel), and the prominent peaks in the cToF-AMS spectra (Panels A-C).....	159
Figure 3.13. Photooxidation of 100 ppb of ethanolamine. Panel (A) Ozone and NO _x concentrations; panel (B) time series for the DMA; panel (C) time series for the PILS-IC; panel (D) fragment ions from the cToF-AMS.....	160
Figure 3.14. cToF-AMS spectra of aerosol generated from TEA oxidation under various conditions.....	161
Figure 4.1. A) Complete flight tracks for the two flights in the San Joaquin Valley of California. B/C) Detailed tracks for flights A and B (12 and 30 July 2007).....	221

Figure 4.2. Time series of particle number concentration and meteorological data for flight A. (Upper panel) Time series of particle number concentration and meteorological data for flight A. (Lower panel) Time series of aerosol size distribution.....	222
Figure 4.3. Time series of particle number concentration and meteorological data for flight B. (Upper panel) Time series of particle number concentration and meteorological data for flight B. (Lower panel) Time series of aerosol size distribution.....	223
Figure 4.4. Vertical profiles of particle number concentration and meteorological data for flights A (upper panel) and B (lower panel).....	224
Figure 4.5. HYSPLIT five-day backward trajectory analysis for flights A and B.....	225
Figure 4.6. Time series of PILS water-soluble aerosol composition and C-ToF-AMS composition for flights A and B.....	226
Figure 4.7. Spatial distribution of various aerosol species (diethylamine, ethylamine, ammonium, nitrate, excess nitrate and organic) during flight A.....	227
Figure 4.8. Spatial distribution of various aerosol species (ethylamine, ammonium, nitrate, excess nitrate and organic) during flight B.....	228
Figure 4.9. Vertical distribution of total submicrometer particulate mass and species concentrations from both the PILS and C-ToF-AMS, for flights A and B.....	229
Figure 4.10. Aerosol mass spectra from the C-ToF-AMS in the background aerosol and in the plume at various downwind distances from the feedlot for flight B.....	230
Figure 4.11. A comparison of the plume organic mass spectra versus the background aerosol organic mass spectra for flights A and B.....	231
Figure 4.12. Speciated size distributions as determined by the C-ToF-AMS for flights A and B.....	232
Figure 4.13. Growth factor data from flight A at RHs of 74% and 92%.....	233
Figure 4.14. Growth factor data from flight B at RHs of 74% (A), 85% (B) and	

92% (C).....	234
Figure 4.15. Relationship between the hygroscopic growth factor at 92% RH and mass fractions of nitrate and organics during flight B.....	235
Figure 4.16. Time series of activated fraction of aerosol (CCN/CN), and total CCN concentration during flights A and B.....	236
Figure 4.17. Normalized CCN activation ratio, $(CCN/CN)_{\text{measured}}:(CCN/CN)_{\text{ammonium sulfate}}$, as a function of hygroscopic growth factors for flight B.....	237
Figure 4.18.. The relationship between the m/z 57:44 ratio, the organic mass fraction, the CCN fraction with less droplet growth than ammonium sulfate ($D_i < D_{AS}$), and the hygroscopic growth factor at RH = 92%.....	238
Figure 4.19. Spatial distribution of the calculated organic growth factors, using the ZSR mixing rule, for flights A and B.....	239
Figure 4.20. Critical supersaturation versus delta T calibration for ammonium sulfate aerosol.....	240
Figure 4.21. Critical supersaturation versus delta T calibration for ammonium sulfate aerosol.....	241
Figure 4.22. Growth kinetics plots for ammonium sulfate aerosol (500 cm ³ /min).....	242
Figure 4.23. Growth kinetics plots for aerosol ammonium sulfate aerosol (1000 cm ³ /min).....	243
Figure 5.1. Photograph taken of the container ship.....	293
Figure 5.2. Flight track of the CIRPAS Twin Otter during the ship exhaust plume study.....	294

Figure 5.3. Size-resolved particulate chemical composition obtained through the MOUDI/filter setup in the ship's stack.....	295
Figure 5.4. TEM image of particles collected with the in-stack thermophoretic sampler.....	296
Figure 5.5. Time series of the aerosol number concentration measurements.....	297
Figure 5.6. Time series of all instruments measuring aerosol mass or volume during the first in-plume approach to the ship.....	298
Figure 5.7. Top Panel: particle number and volume distributions at different plume ages Middle Panel: chemically resolved mass distribution during the first in-plume approach to the ship. Bottom Panel: organic:sulfate mass ratio in the ship exhaust plume.....	299
Figure 5.8. Reference AMS organic mass spectrum from a diesel bus chase study, C-ToF-AMS organic mass spectra from the ship exhaust plume and background aerosol in the marine boundary layer.....	300
Figure 5.9. Hygroscopic growth factors for particles measured by the DASH-SP and predicted using a volume-weighted mixing rule.....	301
Figure 5.10. CCN droplet closure within the exhaust plume. Top Panel: Results obtained using bulk (size-averaged) chemistry. Bottom Panel: Results obtained when size-resolved chemistry is used in the calculations.....	302
Figure 5.11. Growth kinetics plot for aerosol in and out of the ship exhaust plume.....	303
Figure 5.12. Flow diagram of the sampling system used on-board the container ship.....	304

Figure 5.13. Vertical profiles of relative humidity and potential temperature during the study.....	305
Figure 5.14. NOAA Hysplit three-day back trajectory for the air mass present during the study.....	306
Figure 6.1. C-ToF-AMS data from Research Flight 3 of the ICE-L field campaign showing enhanced organic and chloride in mixed phase and ice clouds.....	317

Chapter 1

Introduction

Introduction

1.1 Background and Motivation

Atmospheric aerosols (airborne particulate matter) have significant impacts on climate, visibility, and human health and aerosol composition is critically important for all of these impacts. Composition is relevant to human health because the chemistry of a particle determines its toxicity. Visibility is affected because composition controls hygroscopicity, which determines the size and optical properties of a particle. Aerosols affect climate in two principal ways: 1) directly, by scattering and absorbing incoming solar radiation and 2) indirectly, by affecting the radiative properties and lifetime of clouds. Composition influences the direct effect for the same reasons that it impacts visibility, while its role in the indirect effect stems from the fact that the ability of an aerosol to act as a cloud condensation nuclei (CCN) is determined by both its size and chemical makeup. Figure 1.1, from the 2007 International Panel on Climate Change assessment report, shows that the magnitude of the cooling from direct and indirect effects of aerosols may equal or exceed the warming generated by greenhouse gases. Perhaps more importantly, the uncertainty in the magnitude of the direct and indirect radiative effects of aerosols dwarfs the uncertainty associated with warming caused by greenhouse gases (IPCC, 2007).

Aerosols can be emitted directly from a source or they can form in the atmosphere when gas-phase precursors are reacted and become nonvolatile enough to condense. These two mechanisms are known as primary and secondary aerosol formation respectively. There are anthropogenic and biogenic sources of both primary and secondary aerosol. While the inorganic composition of atmospheric aerosols has

been studied for many years, only recently has the development of new instrumentation allowed for quantitative measurement of the organic fraction of atmospheric aerosol. It is now understood that organic aerosols represent a significant fraction of the submicron aerosol mass throughout the world (Zhang et al., 2007), and that a large fraction of the organic aerosol is secondary. While results from a wide variety of instruments are presented in this thesis, particular emphasis is given to results obtained using an Aerodyne compact Time of Flight Aerosol Mass Spectrometer (C-ToF-AMS). The development of this online aerosol mass spectrometer has provided increased sensitivity and time-resolution necessary to make quantitative airborne measurements of ambient organic aerosol both at low loadings and in highly concentrated, but spatially narrow plumes emanating from point sources. To obtain the results presented in this thesis, it was necessary to carry out the first-ever airborne deployment of a C-ToF-AMS instrument.

1.2 Organization of Thesis

This thesis presents results on the sources and impacts of atmospherically relevant aerosol, particularly organic aerosol. Emphasis is placed on the use of compositional measurements as a tool to determine the sources of atmospheric aerosol, the mechanisms by which it is formed, and the impact of aerosol on human health and climate. Chapters 2 and 3 describe laboratory-based experiments in large (22 m³) environmental chambers. These experiments explore the mechanisms that allow gas-phase compounds, specifically isoprene and amines, which were previously thought too volatile to condense, to form aerosol. Chapters 4 and 5 describe airborne field

experiments where the physical and chemical characteristics of aerosol from globally and regionally important sources are quantified. Relationships between the aerosol observed during the field and chamber studies are also discussed. The final chapter summarizes the results of the previous chapters and presents areas of ongoing research at the frontiers of aerosol-cloud interactions.

Chapter 2 presents a detailed analysis of the chemical composition of aerosol formed from the oxidation of isoprene. Isoprene has long been known to be the most abundant gas-phase volatile organic compound (VOC) on Earth, but until recently it was not thought to contribute to aerosol formation because the products of its gas-phase oxidation were too volatile (Appendix A gives details on the aerosol yield from isoprene). Chapter 2 demonstrates that the majority of aerosol formed from isoprene photooxidation under high-NO_x conditions is derived from further oxidation of the first generation product methacrolein. The significant differences in the chemical composition of aerosol formed under high and low-NO_x conditions are explored and the importance of oligomers and peroxides is discussed. Comparisons between online and offline mass spectroscopic techniques are used to confirm that the observed aerosol-phase products are not artifacts.

The potential for alkylamines to form aerosol is explored in Chapter 3 through a series of laboratory chamber experiments and thermodynamic calculations. Aerosol formation from reaction of amines with OH, ozone, and nitric acid is investigated and aminium nitrate salt formation is found to be a dominant aerosol formation pathway. Significant non-salt organic aerosol is also observed during the oxidation of certain amine precursors. Thermodynamic calculations show that a small subset of the amines studied

is capable of forming ammonium nitrate salts under atmospheric conditions where the gas-phase ammonia concentrations are typically significantly higher than those of amines.

Chapter 4 presents results from flights near a major bovine source in the San Joaquin Valley of California. Agricultural emissions are a significant source of particulate pollution and this study characterizes the chemical and physical characteristics of aerosol emitted from this globally important source. The mass of ammonium nitrate species, observed in the chamber experiments of Chapter 3, is also quantified. The sub- and supersaturated water uptake behavior of aerosol from the source is described and a relationship between these two regimes of hygroscopic growth is found.

Aerosol emissions from a modern container ship are described in Chapter 5. The study presented represents the first-ever simultaneous shipboard and airborne measurements of container ship emissions. Particulate emissions from the ship are found to contain significantly more organic than estimated from previous field campaigns. This additional organic mass is found to impact global emission factors of organic particulates from shipping and the activity of ship emissions as cloud condensation nuclei.

Chapter 6 summarizes the results of the thesis and describes current research efforts at the frontier of aerosol-cloud interaction. The current research efforts focus on the potential of reactions within cloud droplets to form organic aerosol and the impact of chemical composition on the ability of aerosol to act as ice crystal nuclei (IN).

Appendix A gives details on the aerosol yields from the photooxidation of isoprene under a wide range of conditions. Appendix B presents a thorough analysis of the nature of organic aerosol in the Los Angeles Region. Appendix C presents a

comparison of theoretically predicted (based on compositional inputs) and measured hygroscopic particle growth in a marine environment.

1.3 References

1. Intergovernmental Panel on Climate Change (IPCC) (2007). *Climate Change 2007*, Cambridge, UK: Cambridge Univ. Press, Cambridge and New York.

2. Zhang, Q., J.L. Jimenez, et al., “Ubiquity and Dominance of Oxygenated Species in Organic Aerosols in Anthropogenically—Influenced Northern Hemisphere Mid-latitudes” *Geophysical Research Letters*, 34, L13801, 2007.

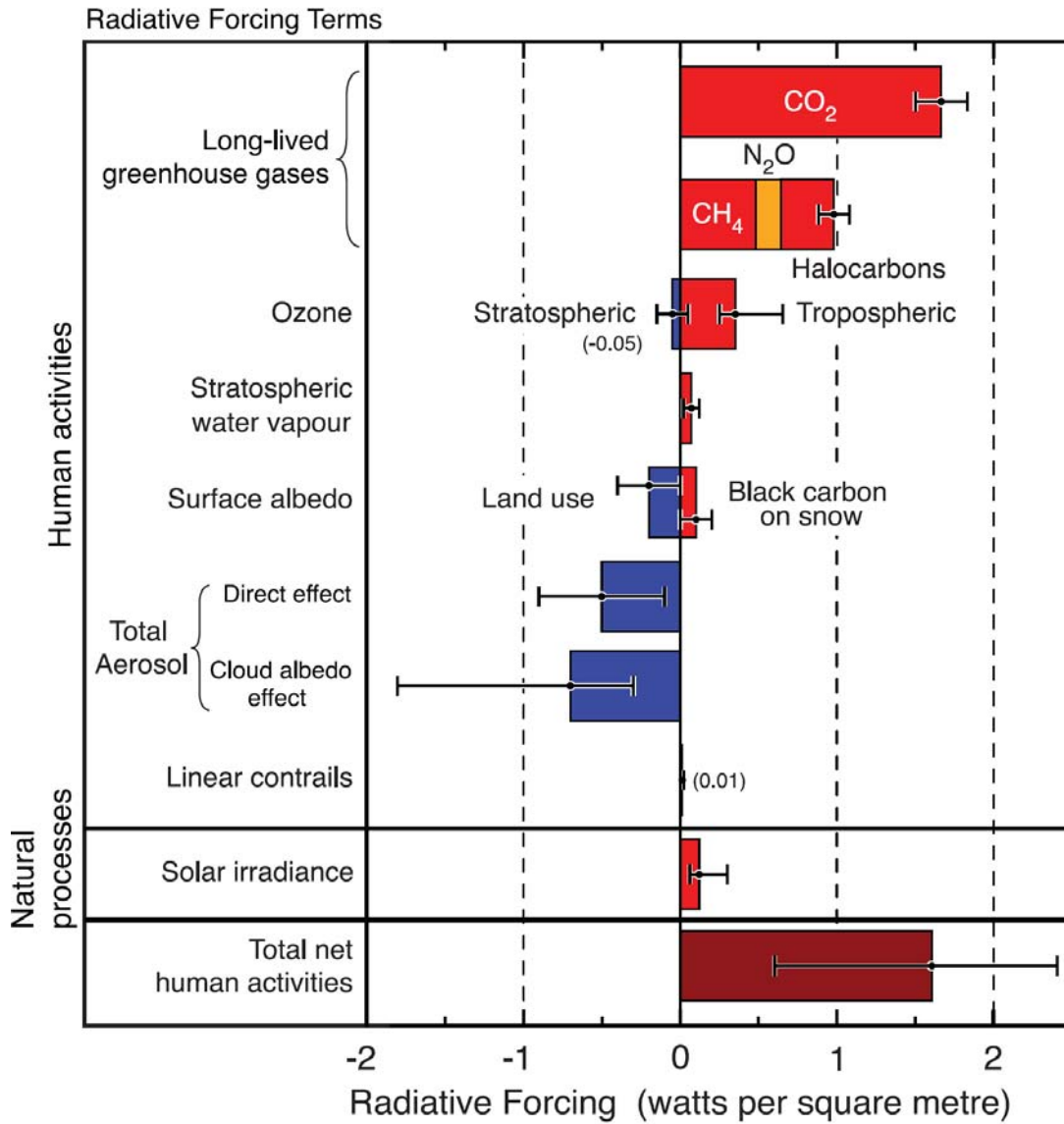


Figure 1.1: Estimated radiative forcing of climate in 2005 relative to pre-industrial times.

Chapter 2

Chemical Composition of Secondary Organic Aerosol Formed from the Photooxidation of Isoprene*

*This chapter is reproduced by permission from “Chemical Composition of Secondary Organic Aerosol Formed from the Photooxidation of Isoprene” by Jason D. Surratt, Shane M. Murphy, Jesse H. Kroll, Nga L. Ng, Lea Hildebrandt, Armin Sorooshian, Rafal Szmigielski, Reinhilde Vermeylen, Willy Maenhaut, Magda Claeys, Richard C. Flagan, and John H. Seinfeld, *Journal of Physical Chemistry A*, 110 (31), 9665-9690, 2006. Copyright 2006 American Chemical Society

2.1 Abstract

Recent work in our laboratory has shown that the photooxidation of isoprene (2-methyl-1,3-butadiene, C_5H_8) leads to the formation of secondary organic aerosol (SOA). In the current study, the chemical composition of SOA from the photooxidation of isoprene over the full range of NO_x conditions is investigated through a series of controlled laboratory chamber experiments. SOA composition is studied using a wide range of experimental techniques: electrospray ionization – mass spectrometry, matrix-assisted laser desorption ionization – mass spectrometry, high-resolution mass spectrometry, online aerosol mass spectrometry, gas chromatography / mass spectrometry, and an iodometric-spectroscopic method. Oligomerization was observed to be an important SOA formation pathway in all cases; however, the nature of the oligomers depends strongly on the NO_x level, with acidic products formed under high- NO_x conditions only. We present, to our knowledge, the first evidence of particle-phase esterification reactions in SOA, where the further oxidation of the isoprene oxidation product methacrolein under high- NO_x conditions produces polyesters involving 2-methylglyceric acid as a key monomeric unit. These oligomers comprise ~ 22–34% of the high- NO_x SOA mass. Under low- NO_x conditions, organic peroxides contribute significantly to the low- NO_x SOA mass (~ 61% when SOA forms by nucleation and ~ 25–30% in the presence of seed particles). The contribution of organic peroxides in the SOA decreases with time, indicating photochemical aging. Hemiacetal dimers are found to form from C_5 alkene triols and 2-methyltetrols under low- NO_x conditions; these compounds are also found in aerosol collected from the Amazonian rainforest, demonstrating the atmospheric relevance of these low- NO_x chamber experiments.

2.2 Introduction

Secondary organic aerosol (SOA) is formed in the troposphere from the oxidation of volatile organic compounds (VOCs), where the resultant low vapor pressure oxidation products partition between the gas and aerosol phases. Recent laboratory experiments have established that SOA formation can also result from the heterogeneous reactions between particle associated substances and relatively volatile species resulting in the formation of high molecular weight (MW) products via oligomerization (polymerization).¹⁻⁵ Until recently, the formation of SOA from the photooxidation of isoprene, the atmosphere's most abundant non-methane hydrocarbon, was considered insignificant.^{6,7} This was largely due to the known volatility of first-generation gas-phase oxidation products, such as methacrolein (MACR), methyl vinyl ketone (MVK), and formaldehyde, from isoprene oxidation in the presence of NO_x, and a previous chamber study that concluded that isoprene oxidation does not lead to SOA formation.⁸ Recent field observations of certain organic aerosol compounds, diastereoisomeric 2-methyltetrols (2-methylerythritol and 2-methylthreitol) and 2-methylglyceric acid, attributable to isoprene oxidation, and the experimental observation that isoprene under highly acidic conditions can lead to the formation of polymeric, humic-like substances through heterogeneous reactions, re-opened the issue of SOA formation from isoprene.^{7,9-13} Subsequent to their ambient identification, Edney et al.¹⁴ and Böge et al.¹⁵ detected 2-methyltetrols in SOA formed from laboratory chamber studies of isoprene.

Recent work in our laboratory has shown that SOA formation from isoprene oxidation can be significant.^{16,17} Extensive experiments were carried out under both low- and high-NO_x conditions using either nitrous acid (HONO) or hydrogen peroxide (H₂O₂)

as the OH radical source. Photooxidation experiments were also conducted using isoprene first-generation gas-phase oxidation products as the VOC precursor. While no aerosol growth was observed from MVK oxidation, SOA formation was observed from MACR at high-NO_x conditions. High molecular-weight (MW) species were observed to form from isoprene oxidation under both low- and high-NO_x conditions.¹⁷ Moreover, SOA yields were observed to exhibit a dependence on the NO_x level. This dependence appears to be attributed to differences in organic peroxy radical (RO₂) chemistry. At high [NO] (i.e., high-NO_x conditions), RO₂ radicals react mainly with NO to produce small alkoxy radicals (RO) that likely fragment into smaller organics, which are expected to be too volatile to partition appreciably to the aerosol phase, or form organic nitrate species (RONO₂). In the absence of NO_x (i.e., low-NO_x conditions), RO₂ radicals instead react with HO₂ radicals (present in the chamber experiments in large quantities from the OH + H₂O₂ reaction) to form organic hydroperoxides, which have been experimentally shown to be important SOA components from other VOC precursors.^{18,19} Hydroperoxides have been suggested to be involved in polymerization in the aerosol phase via reactions with aldehydes to form peroxyhemiacetals.^{18,19}

Although it is now established that OH-initiated oxidation of isoprene leads to SOA, detailed understanding of the chemical reaction pathways leading to the production of isoprene SOA is lacking. Results from chamber studies have elucidated the importance of the further oxidation of MACR as a primary route for SOA formation from isoprene under high-NO_x conditions. Known RO₂ chemistry at low-NO_x conditions leads to the initial gas-phase oxidation products, likely hydroxyhydroperoxides, of isoprene, which upon further oxidation leads to SOA production. Nonetheless, detailed evaluation

of the mechanism of SOA formation from the oxidation of isoprene has not yet been carried out.

In the present work, a suite of offline analytical techniques is used in conjunction with online aerosol mass spectrometry to investigate the detailed chemical composition of SOA from isoprene oxidation. SOA is produced from the photooxidation of isoprene under varying NO_x conditions and is collected onto filters for offline chemical analyses. Offline mass spectrometry (MS) techniques are used to detect organic species from aerosol filter samples, including oligomeric components of isoprene SOA (as detected in prior studies only by online time of flight aerosol mass spectrometry (TOF-AMS) measurements). Tandem MS and gas chromatography (GC)/MS derivatization techniques are employed to structurally elucidate oligomeric components. Organic peroxides are detected and quantified from low- NO_x isoprene SOA using a conventional iodometric-spectroscopic method. Tracer compounds for isoprene oxidation in the ambient atmosphere, as found in the Amazonian rainforest, are detected here for the first time in the low- NO_x chamber experiments. The low- NO_x conditions are most relevant to understanding SOA formation in highly vegetated, remote regions.⁷ In some cases, such as the southeastern US, where atmospheric transport of pollutants from urban areas can influence SOA formation²⁰, conditions closer to those of the high- NO_x experiments may be applicable.

2.3 Experimental Section

2.3.1 Chamber Experiments

Experiments were carried out in Caltech's dual indoor 28 m³ Teflon smog chambers.^{21,22} Experimental protocols are similar to those described previously,^{16,17} so

will be described only briefly here. Most experiments were carried out with hydrogen peroxide (H_2O_2) as the hydroxyl radical (OH) precursor; in some cases, HONO was used instead to demonstrate that the particular OH source has no effect on the outcome of the experiments. For some experiments, ammonium sulfate seed particles were introduced into the chamber (at volume concentrations of 20–30 $\mu\text{m}^3/\text{cm}^3$) by atomization of a 0.015 M ammonium sulfate solution. A known concentration of isoprene (or any other precursor, such as MACR) was then introduced by sending air over a measured volume of the pure compound (Aldrich, 99.8%) into the chamber. For H_2O_2 /high- NO_x experiments, NO was also introduced into the chamber from a gas mixture (500 ppm gas cylinder in N_2 , Scott Specialty Gases). In low- NO_x experiments, NO was not added and NO_x concentrations were < 1 ppb. When the isoprene (monitored by gas chromatography – flame ionization detection (GC-FID)), NO_x , and seed concentrations became constant inside the chamber, irradiation by UV lights (centered at 354 nm) was started, initiating the reaction.

SOA volume growth ($\mu\text{m}^3/\text{cm}^3$) was monitored with a differential mobility analyzer (DMA). For quantification of SOA products collected on filter samples, the DMA volumes were used for each experiment to determine the total SOA mass collected. Filter sampling commenced when the particle growth had terminated, i.e., when the aerosol volume had reached its maximum value. Depending on the total volume concentration of aerosol in the chamber, the filter sampling time was 2 to 4 h, which typically resulted in 3–7 m^3 of total chamber air sampled.

2.3.2 Filter Extractions

Collected Teflon filters (PALL Life Sciences, 47-mm diameter, 1.0- μm pore size, teflo membrane) were extracted in 5 mL of HPLC-grade methanol by 40 min of sonication. The filters were then removed from the methanol sample extracts and archived at -20°C . Each extract was blown dry under a gentle N_2 stream (without added heat) and then reconstituted with 1 mL of a 50:50 (v/v) solvent mixture of HPLC-grade methanol and 0.1% aqueous acetic acid solution. The reconstituted extracts were then stored at -20°C until analysis was performed. In most cases, filter extracts were chemically analyzed within 1–2 days after filter extraction. Lab control filters were extracted and treated in the same manner as samples. Aliquots of each of these filter extracts were analyzed by the four mass spectrometry techniques to follow.

In order to ensure that H_2O_2 was not condensing onto filter media and introducing artifacts in the chemical analyses, several blank filters were collected under dark conditions from the chamber containing typical experimental well-mixed concentrations of isoprene, NO , and ammonium sulfate seed aerosol, sampled for the same duration ($\sim 2\text{--}4$ h) as a sample filter. No significant chemical artifacts or contaminants were observed in the analytical techniques from these blank filters, consistent with the lack of observed aerosol growth under dark conditions.

2.3.3 Liquid Chromatography / Electrospray Ionization – Mass Spectrometry (LC/ESI-MS)

A Hewlett-Packard 1100 Series HPLC instrument, coupled with a single quadrupole mass analyzer and equipped with an electrospray ionization (ESI) source, was used to identify and quantify relatively polar, acidic SOA components. Data were

collected in both positive (+) and negative (-) ionization modes; the quantitative analysis presented here is limited to the negative ionization mode. An Agilent Eclipse C₁₈ column (3.0 x 250 mm) was used to separate the organic species before detection. The eluents used were 0.1% aqueous acetic acid (A) and methanol (B). In the 40-min gradient elution program used, the concentration of eluent B increased from 5% to 90% in 35 min, and then decreased to 5% in 5 min. The total flow rate of the eluent used in the LC/MS analysis was 0.8 mL min⁻¹. Optimum electrospray conditions were found using a 60 psig nebulizing pressure, 3.5 kV capillary voltage, 13 L min⁻¹ drying gas flowrate, and a 330°C drying gas temperature. During the full scan mode of analysis, the cone voltage was set at 60 V, avoiding fragmentation of most species and allowing their detection as deprotonated molecules ([M - H]⁻). During the upfront collision-induced dissociation (CID) mode of analysis, the cone voltage was set to 110 V, resulting in partial fragmentation of the [M - H]⁻ ions. By comparing these two sets of MS data (upfront CID mode to the full scan mode of analysis) and by examining the fragmentation patterns of the species, some structural information on the analyzed species was obtained. This was particularly useful in confirming results from other MS/MS techniques used and for the identification of oligomeric components.

Using a set of six acidic species (*meso*-erythritol, citramalic acid, 2-hydroxy-3-methylbutyric acid, pimelic acid, pinic acid, and suberic acid monomethyl ester) as surrogate standards, this method was also used to quantify the amount of polar acidic species. Filter extraction efficiency was established by standard additions of these surrogate standards to blank filters. On average, the extraction efficiency for each standard was ~ 60% with an estimated error bar of ~ ±15% over the concentration range

used to generate the LC/MS calibration curves. This average extraction efficiency was included in the calculations to quantify identified isoprene SOA products.

As we will note shortly, to investigate the probable importance of a C₄ hydroxy dialdehyde species formed under high-NO_x conditions, selected sample extracts were derivatized using the Girard Reagent P (1-(carboxymethyl)pyridium chloride hydrazide, MW=187) to increase sensitivity for aldehydic species in the (+)LC/MS mode. The Girard Reagent P (GirP) reacts with aldehydes and ketones to form water-soluble hydrazones with a permanently charged pyridine moiety, and water is eliminated in this reaction.²³ The organic unit that adds to aldehydes and ketones has a mass of 152 Da. A series of aldehyde standards, glyoxal (MW=58), succinic semialdehyde (MW=102), and glutaraldehyde (MW=100), were derivatized using the GirP and analyzed with (+)LC/MS. These small polar aldehyde standards typically go undetected using (+)ESI techniques such as in LC/MS; however, upon derivatization they were detected as the singly charged $[M - H_2O + 152(\text{GirP})]^+$ ions (glyoxal was also detected as doubly charged $[M - 2H_2O + 152(\text{GirP})]^{2+}$ ion), where M is the MW of the aldehyde species. These compounds eluted between 1 to 2 min from the LC column, including a derivatized compound corresponding to the proposed C₄ hydroxy dialdehyde species (MW = 102 and $[M - H_2O + 152(\text{GirP})]^+ = 236$).

2.3.4 ESI – Ion Trap Mass Spectrometry (ESI-ITMS)

Aliquots of the filter extracts were also analyzed by a ThermoElectron LCQ ion trap mass spectrometer equipped with an ESI source, via direct infusion. This instrument does not provide chromatographic separation, precluding quantification. Instead, the

instrument was used for the qualitative detection of product species. In addition, specific ions of interest were isolated from the rest of the sample ion matrix and further fragmented to produce product ion mass spectra, aiding in structural elucidation.

Data were collected in both positive and negative ionization modes. As the same species were detected in both modes ($[M - H]^-$ and $[M + Na]^+$ ions), we only present here the data collected under negative ionization; the data collected under positive ionization serve as confirmation of the negative ionization data.

2.3.5 Matrix Assisted Laser Desorption Ionization -Time of flight Mass Spectrometer (MALDI-TOFMS)

Another aliquot of the filter extract was analyzed on an Applied Biosystems Voyager-DE Pro MALDI-TOFMS instrument. After 6 μ L of each extract had been dried on the steel target plate, the plate was gently brushed with graphite particles, which served as the matrix. The samples were analyzed in the linear mode, in both positive and negative ionization modes. 400-500 laser shots were summed to obtain a representative mass spectrum of each sample. This method was mainly used to assess the molecular weight (MW) range of the aerosol, to detect oligomeric signatures, and to confirm the MWs of species identified by the ESI techniques.

2.3.6 High Resolution ESI-MS

Extracts were also analyzed by a Waters LCT Premier Electrospray time-of-flight mass spectrometer with W geometry in the Department of Chemistry at the University of California, Irvine, operated in the negative ionization mode. Samples were analyzed by flow injection. The calibration was carried out using sodium formate clusters with co-

injection of fmoc-amino acids of appropriate mass spiked into the analytical sample for lock-mass corrections to obtain accurate mass for the oligomeric ions with m/z 266, 323, 365, 368, 467, and 470. These ions were only detected in the high-NO_x experiments and elemental compositions were determined with reasonable accuracy (within +/- 5 ppm), and were consistent with other analytical observations (such as ESI-MS/MS and GC/MS derivatization data).

2.3.7 Aerodyne Time of Flight Aerosol Mass Spectrometer (TOF-AMS)

During most chamber experiments, real-time particle mass spectra were collected continuously by an Aerodyne Time of Flight Aerosol Mass Spectrometer (TOF-AMS), and averaged spectra were saved every 5 min. The design and capabilities of the TOF-AMS instrument are described in detail elsewhere.²⁴ Briefly, chamber air enters the instrument through a 100- μ m critical orifice at a flowrate of 1.4 cc/s. Particles with a vacuum aerodynamic diameter between 50 and 800 nm are efficiently focused by an aerodynamic lens, passed through a chopper, and then impacted onto a tungsten vaporizer. The chopper can be operated in three modes: (1) completely blocking the beam to gather background mass spectra; (2) out of the beam's path to collect ensemble average mass spectra over all particle sizes; (3) chopping the beam to create size-resolved mass spectra. The vaporizer is typically run at $\sim 550^{\circ}\text{C}$ to ensure complete volatilization of the SOA and the inorganic seed; during several runs the vaporizer temperature was lowered to $\sim 160^{\circ}\text{C}$ to reduce thermally induced fragmentation of oligomers. Once vaporized, molecules undergo electron ionization at 70 eV and are orthogonally pulsed every 19 μ s into the time of flight mass analyzer.

2.3.8 Gas Chromatography / Mass Spectrometry (GC/MS)

Extracts of selected filters were analyzed for polar organic compounds by GC/MS using a method that was adapted from that reported by Pashynska et al.²⁵ The sample workup consisted of extraction of all or half of the filter with methanol under ultrasonic agitation and derivatization of carboxyl and hydroxyl functions into trimethylsilyl (TMS) derivatives. The extract was divided into two parts; one part was trimethylsilylated while the other part was stored in a refrigerator at 4°C for eventual further analysis. GC/MS analyses were performed with a system comprising a TRACE GC2000 gas chromatograph, which was coupled to a Polaris Q ion trap mass spectrometer equipped with an external ionization source (ThermoElectron, San Jose, CA, USA). A Heliflex[®] AT[™]-5MS fused-silica capillary column (5% phenyl, 95% methylpolysiloxane, 0.25 µm film thickness, 30 m × 0.25 mm i.d.) preceded by a deactivated fused-silica precolumn (2 m × 0.25 mm i.d.) (Alltech, Deerfield, IL, USA) was used to separate the derivatized extracts. Helium was used as carrier gas at a flow rate of 1.2 mL min⁻¹. The temperature program was as follows: isothermal hold at 50°C for 5 min, temperature ramp of 3°C min⁻¹ up to 200°C, isothermal hold at 200°C for 2 min, temperature ramp of 30°C min⁻¹ up to 310°C; and isothermal hold at 310°C for 2 min. The analyses were performed in the full scan mode (mass range: m/z 50 – 800), and were first carried out in the electron ionization (EI) mode and subsequently in the chemical ionization (CI) mode. The ion source was operated at an electron energy of 70 eV and temperatures of 200°C and 140°C in the EI and CI modes, respectively. The temperatures of the GC injector and the GC/MS transfer line were 250°C and 280°C, respectively. For chemical ionization,

methane was introduced as reagent gas at a flow rate of 1.8 mL min⁻¹. We present here mainly the data collected in the EI mode; the data collected in the CI mode are used if insufficient MW information is obtained in the EI mode.

Selected extracts were also subjected to a hydrolysis/ethylation and/or a methoximation procedure prior to trimethylsilylation. The purpose of the hydrolysis/ethylation procedure was to confirm the presence of ester linkages, while that of the methoximation procedure was to evaluate the presence of aldehyde/keto groups, in oligomeric SOA. The hydrolysis/ethylation procedure involved reaction of the extract residues with 40 µL of analytical-grade ethanol and 8 µL of trimethylchlorosilane (Supelco, Bellafonte, PA, USA) for 1 h at 60°C. Details about the methoximation procedure can be found in Wang et al.¹²

2.3.9 Gas Chromatography – Flame Ionization Detection (GC-FID)

Quantitative determination of the 2-methyltetrols (i.e., 2-methylthreitol and 2-methylerythritol), the C₅ alkene triols [i.e., 2-methyl-1,3,4-trihydroxy-1-butene (*cis* and *trans*) and 3-methyl-2,3,4-trihydroxy-1-butene] and 2-methylglyceric acid, in selected filters, was performed by GC-FID with a GC 8000 Top instrument (Carlo Erba, Milan, Italy). The sample workup was the same as that for GC/MS analysis except that filter parts were spiked with a known amount of erythritol (Sigma, St. Louis, MO, USA) as an internal recovery standard; it was assumed that the GC-FID responses of the trimethylsilyl derivatives of the analytes and the internal recovery standard were similar. The GC column and conditions were comparable with those used for GC/MS; the column was a CP-Sil 8 CB capillary column (5% diphenyl, 95% methylpolysiloxane, 0.25 µm

film thickness, 30 m × 0.25 mm i.d.) (Chrompack, Middelburg, The Netherlands) and the temperature program was as follows: isothermal hold at 45°C for 3 min, temperature ramp of 20°C min⁻¹ up to 100°C, isothermal hold at 100°C for 10 min, temperature ramp of 5°C min⁻¹ up to 315°C; and isothermal hold at 315°C for 20 min. Measurement of the 2-methyltetrols in the low-NO_x SOA samples was performed after the unstable products tentatively characterized as 2-methyltetrol performate derivatives had decayed to 2-methyltetrols, i.e., after leaving the reaction mixture for two days at room temperature.

2.3.10 Total Aerosol Peroxide Analysis

The total amount of peroxides in the low-NO_x isoprene SOA was quantified using an iodometric-spectrophotometric method adapted from that used by Docherty et al.¹⁸ to analyze peroxides formed by α -pinene-ozonolysis. The method employed here differed only in the choice of extraction solvent: we used a 50:50 (v/v) mixture of methanol and ethyl acetate, rather than pure ethyl acetate. Calibration and measurements were performed at 470 nm on a Hewlett-Packard 8452A diode array spectrophotometer. A standard calibration curve was obtained from a series of benzoyl peroxide solutions. Benzoyl peroxide was the standard used for quantification of organic peroxides formed from low-NO_x experiments, as its MW is close to the average MW determined from the mass spectrometry techniques, in particular the MALDI-TOFMS measurements. The molar absorptivity determined from the standard curve was ~ 852, in excellent agreement with that determined by Docherty et al. and with the value of 845 determined with the original method development paper.^{18,26} As a confirmation that the technique was reproducible, we extracted and analyzed in the same fashion, three α -pinene-ozonolysis

filters collected from our laboratory chambers. We measured ~ 49% of the SOA mass, produced from α -pinene ozonolysis, to be organic peroxides, in excellent agreement to that of Docherty et al.'s measurement of ~ 47% for the same system. A few high-NO_x isoprene filter samples were also analyzed by this method, but resulted in the detection of no organic peroxides (below detection limits of this technique).

2.3.11 Particle-Into-Liquid Sampler Coupled to Ion Chromatography (PILS/IC)

The PILS/IC (particle-into-liquid sampler coupled to ion chromatography) is a quantitative technique for measuring water-soluble ions in aerosol particles. The PILS developed and used in this study²⁷ is based on the prototype design²⁸ with key modifications, including integration of a liquid sample fraction collector and real-time control of the steam injection tip temperature. Chamber air is sampled through a 1-micrometer cut-size impactor and a set of three denuders (URG and Sunset Laboratories) to remove inorganic and organic gases that may bias aerosol measurements. Sample air mixes with steam in a condensation chamber where rapid adiabatic mixing produces a high water supersaturation. Droplets grow sufficiently large to be collected by inertial impaction before being delivered to vials held on a rotating carousel. The contents of the vials are subsequently analyzed off-line using a dual IC system (ICS-2000 with 25 μ L sample loop, Dionex, Inc.) for simultaneous anion and cation analysis. The background levels of individual species (Na⁺, NH₄⁺, K⁺, Mg²⁺, Ca²⁺, SO₄²⁻, Cl⁻, NO₂⁻, NO₃⁻, oxalate, acetate, formate, methacrylate, pyruvate) concentrations for analyzed filter samples, presented as the average concentration plus three times the standard deviation (σ), are less than 0.28 μ g m⁻³.

2.4 Results

As noted, experiments were conducted at high- and low-NO_x conditions. High-NO_x conditions were achieved through the addition of substantial NO_x (~ 800 to 900 ppb NO_x) to the reaction chamber, leading to isoprene:NO_x molar ratios of ~ 0.56 to 0.63. Under low-NO_x conditions no NO_x is added to the chamber, where NO_x mixing ratios of < 1 ppb (small amounts of NO_x likely desorb from chamber walls) were observed. The low-NO_x condition simulates a remote (NO_x-free) atmosphere; for example, at typical isoprene and NO_x mixing ratios observed in the Amazonian rainforest (~ 4 to 10 ppb and 0.02 to 0.08 ppb, respectively),^{7,29} the isoprene:NO_x ratios that result are ~ 50 to 500, comparable to the isoprene:NO_x ratio of the present experiments (~ 500).

2.4.1 High-NO_x Condition

Table 2.1 lists nine high-NO_x chamber experiments that were conducted to generate SOA for aerosol filter sampling. All experiments were conducted with 500 ppb of isoprene or MACR in order to produce sufficient aerosol mass for all offline analytical measurements. In most of the experiments conducted, H₂O₂ served as the OH radical precursor; in this manner, initial oxidation of isoprene is dominated by OH. It is estimated that ~ 3–5 ppm of H₂O₂ was used in each of these experiments based upon isoprene decay during irradiation.¹⁷ All of these experiments were conducted at low relative humidity (RH < 5%) in order to limit the uptake of H₂O₂ into the particle phase. In the high-NO_x experiments using H₂O₂ as an OH source, ~ 800 to 900 ppb of NO was injected into the chamber. With the HONO source, lower initial NO concentrations were achieved, as the source of NO was HONO photolysis and a NO_x side-product from the HONO synthesis. Nucleation (seed-free) and ammonium sulfate seeded experiments

were also conducted in order to examine if the presence of seed aerosol has an effect on the chemistry observed. In Experiment 6, acidified ammonium sulfate seed (0.015 M $(\text{NH}_4)_2\text{SO}_4 + 0.015 \text{ M H}_2\text{SO}_4$) was used to investigate the possible effect of acid catalysis on oligomerization reactions, which has been previously observed to occur for other VOC precursors, such as α -pinene and 1,3,5-trimethylbenzene.^{1,3-5,30} No discernable increase in SOA mass is observed for this acid-seeded experiment (Experiment 6) when comparing to its corresponding dry-seeded and nucleation (seed-free) experiments (Experiments 5 and 9).

To illustrate the overall chemical composition typically observed under high- NO_x conditions, shown in Figure 2.1a is a first-order (-)ESI-IT mass spectrum obtained via direct infusion analysis of an isoprene SOA sample collected from Experiment 1. Prior work in our laboratory has shown that most organics detected in the negative ion mode occur as the deprotonated molecules ($[\text{M} - \text{H}]^-$ ions),^{2,3,20} making (-)ESI sensitive for the detection of polar acidic species. As can be seen in Figure 2.1a, many such species are detected. Observable 102 Da differences between many of the $[\text{M} - \text{H}]^-$ ions and the detection of high-MW species (up to MW ~ 470) indicate the presence of oligomeric species with more than the 5 carbons of the parent isoprene. Organic nitrate species are detected in this spectrum as even-mass $[\text{M} - \text{H}]^-$ ions (m/z 266, 368, and 470).

Figure 2.1b shows, by comparison, a first-order (-)ESI-IT spectrum, also obtained via direct infusion analysis, for a MACR high- NO_x sample (Experiment 3). Many of the ions detected correspond exactly to those observed from isoprene oxidation (Figure 2.1a). It should be noted that when the MACR, H_2O_2 , and dry ammonium sulfate seed aerosol are well-mixed in the chamber under dark conditions, no aerosol growth is observed,

confirming that photooxidation is required to produce SOA. The SOA components formed in this MACR experiment (as shown in Figure 2.1b) extend out to higher MWs than those of isoprene, which is likely a result of the amount of MACR precursor available in this experiment and also owing to the removal of one oxidation step (the oxidation of isoprene).

SOA products detected in Figures 2.1a and 2.1b are confirmed by additional mass spectrometry techniques. Figure 2.2 shows a mass spectrum collected using the MALDI-TOFMS instrument in the positive ion mode for a high-NO_x, seeded isoprene photooxidation experiment (Experiment 9). SOA components observed here are detected mainly as the sodiated molecules ($[M + Na]^+$ ions), which is consistent with our experiences in analyzing polymeric standards, such as aqueous glyoxal, with a graphite matrix. In Figure 2.2, only species that correspond to ions detected in the (-)ESI-IT spectra are highlighted. For example, for the $[M - H]^-$ ion series detected in (-)ESI-IT spectra at m/z 161, 263, 365, and 467, a corresponding $[M + Na]^+$ ion series is detected at m/z 185, 287, 389, and 491, respectively, using MALDI-TOFMS. It should be noted that the (+)-ESI-IT spectra also detected the same ions ($[M + Na]^+$) as those of the MALDI technique, confirming that the species observed in Figures 2.1 and 2.2 are not a result of ionization artifacts specific to individual techniques.

The LC/MS results obtained in the negative ionization mode are used to quantify the SOA components common to all high-NO_x isoprene SOA (as detected in Figures 2.1 and 2.2). Figures 2.3a and 2.3b show total ion chromatograms (TICs) for an isoprene photooxidation experiment (Experiment 2) and a MACR photooxidation experiment (Experiment 4), respectively, both carried out at high NO_x in the absence of seed aerosol.

These TICs show that many of the SOA products formed in each system are the same since the retention times (RTs) are comparable and the m/z values of the molecular ion species ($[M - H]^-$) associated with each chromatographic peak are the same. Shown in Figure 2.3c-e are extracted ion chromatograms (EICs) for three organic nitrate species ($[M - H]^-$ at m/z 266, 368, and 470) common to both isoprene and MACR high- NO_x photooxidation experiments. For each chamber experiment, EICs were used instead of TICs for the quantification of each $[M - H]^-$ ion detected in order to deconvolute any coeluting species. Figure 2.4a shows a mass spectrum recorded for the largest chromatographic peak (RT = 15.7 min) from the EIC of m/z 368 (Figure 2.3d). The m/z 759 ion that is also detected in this mass spectrum is a cluster ion corresponding to $[2M + \text{Na} - 2H]^-$; such cluster ions are commonly observed in (-)LC/ESI-MS conditions. In Figure 2.4b is a resultant upfront CID mass spectrum taken for this same chromatographic peak, showing many product ions from the dissociation of m/z 368. The product ion m/z 305 corresponds to a neutral loss of 63 Da, which is likely nitric acid (HNO_3). Another product ion m/z 291 corresponds to neutral loss of 77 Da, likely from the combined losses of a methyl (CH_3) radical and a nitrate (NO_3) radical (or CH_3ONO_2). The neutral loss of 102 Da results in the product ion m/z 266; these types of product ions are used to aid in the structural elucidation of SOA components, and will be discussed subsequently. Owing to the lack of available authentic oligomeric standards, quantification was carried out by using a series of calibration curves generated from surrogate standards (listed in the Experimental section) covering the wide range of RTs for all detected species. Each surrogate standard contained a carboxylic acid group, the likely site of ionization for detected SOA components, except for the meso-erythritol

standard. Due to the initial high percentage of aqueous buffer present in the LC/MS gradient, we were able to detect small polar organics, such as 2-methylglyceric acid. In order to quantify this compound, the polyol meso-erythritol, detected as the $[M - H + \text{acetic acid}]^-$ ion, was used. Unlike meso-erythritol, 2-methyltetrols (and other polyols) were not detected using the (-)LC/MS technique. All surrogate standards were within $\sim \pm 1.5$ min of the RTs of the detected SOA components. Table 2.2 shows the LC/MS quantification results for high-NO_x SOA. Four types of oligomers are quantified here. For ease of comparison, experiments corresponding to the same VOC and OH precursor type are grouped together under the same column heading.

SOA components observed thus far are not artifacts formed on filters and are observed over varying isoprene concentrations, as confirmed by online particle mass spectrometry. Figure 2.5 shows mass spectra collected from three high-NO_x chamber experiments using the Aerodyne TOF-AMS instrument. In these experiments, the TOF-AMS instrument was operated at $\sim 160^\circ\text{C}$ to lessen the degree of thermal fragmentation of the high-MW SOA components. Figure 2.5a shows a TOF-AMS spectrum collected for a 50 ppb isoprene, high-NO_x nucleation experiment (not included in Table 2.1 due to insufficient aerosol mass for offline chemical analysis techniques). Even at these isoprene concentrations, high-MW species are detected in the SOA produced. Differences of 102 Da are noted in this spectrum, again indicating the presence of oligomers. The oligomers present here confirm the species detected by the (-)ESI and (+) MALDI techniques (Figures 2.1 and 2.2, respectively), where the observed TOF-AMS ions result from a loss of a hydroxyl (OH) radical from the molecular ion (i.e., α -cleavage of a hydroxyl radical from a carboxylic acid group). ESI detects these

oligomers as the $[M - H]^-$ ion and MALDI as the $[M + Na]^+$ ion, so ions measured in the TOF-AMS instrument are lower by 16 and 40 units, respectively. For example, ions of m/z 145, 187, 247, and 289 measured by the TOF-AMS instrument (Figure 2.5), correspond to m/z 161, 203, 263, and 305, respectively, using (-)ESI (Figure 2.1). Four different series of oligomers are highlighted in this spectrum, where ions of the same oligomeric series are indicated in a common color. Figure 2.5b corresponds to a MACR high- NO_x , dry seeded experiment, in which a filter sample was collected (Experiment 3), showing the same oligomeric signature to that of the low concentration (50 ppb) isoprene experiment. Figure 2.5c corresponds to an isoprene high- NO_x , HONO experiment (Experiment 8). Again, many ions at the same m/z values are detected, as those of Figures 2.5a and 2.5b, suggesting the chemical components of the SOA are the same in these samples. Though probably present, oligomeric compounds formed under conditions similar to those of Figure 2.5c were not detected in the original study of SOA formation from this laboratory,¹⁶ as a less sensitive quadrupole AMS was used; such high-MW species were reported in a subsequent study using the TOF-AMS.¹⁷ These online chemical results confirm that the 102 Da differences observed in the offline analytical techniques (ESI and MALDI) are not a result of sample workup or ionization artifacts. Also, these online chemical results suggest that seeded versus nucleation experiments do not lead to significant differences in the chemistry observed, in agreement with the ESI analyses. The OH precursor (HONO or H_2O_2) also does not have a substantial effect on the chemistry observed (i.e., similar products formed, however, abundances may vary), an observation that is also consistent with the offline mass spectrometry analyses.

PILS/IC measurements were carried out for Experiments 1 (nucleation) and 2 (dry seeded). In both experiments the acetate anion was the most abundant organic anion detected ($14.72 \mu\text{g}/\text{m}^3$ in Experiment 1 and $23.47 \mu\text{g}/\text{m}^3$ in Experiment 2) followed by the formate anion ($1.18 \mu\text{g}/\text{m}^3$ in Experiment 1 and $2.90 \mu\text{g}/\text{m}^3$ in Experiment 2). It should be noted that these two ions elute off the IC column immediately after sample injection, and there is a possibility that other early-eluting monocarboxylic acid species co-eluted with these two species leading to an overestimate of their mass. In addition, the extent to which the acetate and formate levels quantified here represent decay products from oligomers detected in the particle phase is uncertain. It is likely that a significant fraction of this mass results from the decomposition of oligomers at the sample collection conditions (high water concentrations and temperatures) in the PILS instrument and possibly by the use of potassium hydroxide (KOH) as the eluent for anion analyses in the IC instrument.

GC/MS with TMS derivatization (restricted to carboxyl and hydroxyl groups) was employed to determine the functional groups present within SOA components formed under high- NO_x conditions. Figure 2.6a shows a GC/MS TIC of a high- NO_x isoprene nucleation experiment (Experiment 5). 2-methylglyceric acid (2-MG), detected previously in ambient and laboratory filter samples,^{10,11,13,14} was found to elute from the GC column at 29.08 min. The corresponding EI mass spectrum for this peak is shown in Figure 2.6b. The chemical structure of trimethylsilylated 2-MG, along with its respective MS fragmentation, is also shown in this mass spectrum. Using GC-FID to quantify the amount of 2-MG present in this same sample, it was found that $3.8 \mu\text{g}/\text{m}^3$ was formed, which accounted for $\sim 3.7\%$ of the SOA mass. This was consistent with LC/MS

measurements of 2-MG from other high-NO_x isoprene nucleation experiments (such as 2.7% of the SOA mass for Experiment 1). A *di*-ester peak was observed to elute from the GC column at 51.59 min. The corresponding EI mass spectrum for this chromatographic peak is shown in Figure 2.6c along with its proposed chemical structure and MS fragmentation pattern.

2.4.2 Low-NO_x Condition

Table 2.3 lists nine low-NO_x chamber experiments. All experiments were conducted with H₂O₂ as the OH radical precursor with no added NO_x. Ozone formation is attributed mainly to residual NO_x emitted by the chamber walls; these O₃ concentrations observed likely have negligible effect on the gas-phase chemistry due to the slow reactivity of O₃ towards isoprene. Experiments were conducted with 50% of the light banks in the chamber except for Experiments 10 and 11, in which 100% of the light banks were used and resulted in the higher temperatures observed. All experiments were conducted with 500 ppb of isoprene except for Experiment 17, in which 100 ppb of isoprene was used. Nucleation (seed-free) and seeded (ammonium sulfate and acidified ammonium sulfate) experiments were conducted in order to examine if the presence of seed aerosol has an effect on the chemistry observed. Assuming a density $\sim 1.25 \text{ g/cm}^3$ (derived from the comparison of DMA aerosol volume and TOF-AMS aerosol mass measurements), acid seeded (0.015 M (NH₄)₂SO₄ + 0.015 M H₂SO₄) experiments formed the largest amounts of SOA mass ($\sim 259 \text{ }\mu\text{g/m}^3$ for Experiment 14) compared to the corresponding nucleation ($\sim 72.5 \text{ }\mu\text{g/m}^3$ for Experiment 12) and ammonium sulfate seeded experiments ($\sim 72.8 \text{ }\mu\text{g/m}^3$ for Experiment 15). Lower mixing ratios of isoprene

(Experiment 17) in the presence of acid seed also resulted in larger amounts of SOA when compared to the nucleation and ammonium sulfate seeded experiments.

No particle-phase organics were detected using (-) and (+)ESI techniques. Analysis of filter sample extracts using these techniques were nearly identical to the blank and control filters. This shows that SOA components at low-NO_x conditions are not acidic in nature like those of the high-NO_x SOA. Due to the expected presence of hydroperoxides and polyols, other analytical techniques, such as the iodometric-spectrophotometric method and GC/MS with TMS derivatization, were employed to understand the chemical nature of low-NO_x SOA. The peroxide aerosol mass concentration was measured for all experiments except for Experiments 12, 13, and 16. The iodometric-spectrophotometric method measures the total peroxide content (sum of ROOH, ROOR, and H₂O₂) of the aerosol, but because no peroxides were measured from filters collected from air mixtures containing isoprene, H₂O₂, and seed aerosol, it is assumed that the peroxides measured are organic peroxides. The nucleation experiments (Experiments 10 and 18a) had the highest contribution of peroxides (~ 61% on average) to the SOA mass observed. Dry ammonium sulfate (Experiments 11 and 15) and acidified ammonium sulfate seeded experiments (Experiments 14 and 17) led to comparable contributions of organic peroxides to the overall SOA mass (~ 25 and 30%, respectively). Quality control tests were conducted by the addition of ammonium sulfate to standard solutions of benzoyl peroxide to test if the seed had an effect on the UV-Vis measurement of total peroxides. The amount of ammonium sulfate added to the benzoyl peroxide standards was determined by the ratio of SOA volume growth to the typical ammonium sulfate seed volume employed (~ 3:1) as determined from the DMA. Little

difference was observed ($\sim 0.6\%$), showing that ammonium sulfate seed has a negligible effect on the measurement of peroxide content from seeded experiments. In most cases, the RHs were $< 9\%$ except during Experiment 15 (RH = 25%) and Experiment 18b (late sampling, RH = 13%). Even for these higher RH experiments, no large differences were observed in the fraction of peroxides formed compared to the lower RH experiments. As observed previously¹⁷, the SOA mass was found to decrease rapidly in nucleation experiments after reaching peak growth, and as a result, the peroxide content of the SOA was measured at different times in Experiment 18. The iodometric-spectrophotometric measurement made at the peak growth in the aerosol volume, as determined from the DMA, for Experiment 18, showed that the peroxides accounted for $\sim 59\%$ of the total SOA mass. Twelve hours later, once the aerosol volume decay reached its constant value, the peroxide contribution to the SOA mass is found to have dropped to 26%.

Figure 2.7 shows a (+)MALDI mass spectrum for a low- NO_x acid-seed experiment (Experiment 14). The m/z range (49 – 620) of ion species observed was not significantly different from (+)MALDI results obtained for nonacid-seeded experiments. The abundances of these ions were higher for the acid experiments, but quantification of these species is not possible due to uncertainties in the ionization efficiencies. In the absence of seed MALDI signal was low or non-existent, likely due to very low ionization efficiencies in the absence of a sulfate matrix. Quantification is also difficult with MALDI because of inconsistencies and inhomogeneities of sample preparation and lack of understanding of sample matrix effects.³¹ It is clear, however, that oligomerization occurs in low- NO_x SOA. Common 14, 16, and 18 Da differences are observed between many peaks throughout this spectrum. Structural elucidation of these peaks in Figure 2.7

was not possible using the (+)MALDI technique owing to the inability of performing MS/MS experiments on selected ions from the sample matrix.

Figure 2.8 shows two TOF-AMS mass spectra for a 500 ppb, low-NO_x nucleation experiment (Experiment 12) in the m/z range of 200 – 450. These mass spectra also indicate the existence of oligomeric components for low-NO_x SOA. The mass spectrum in Figure 2.8a was collected at a low vaporizer temperature (~ 150°C) while that in Figure 2.8b was collected at a higher temperature (~ 600°C). The presence of more higher-mass peaks at high vaporizer temperatures (Figure 2.8b) may indicate that the low-NO_x oligomers are heterogeneous, with some series of oligomers being easily volatilized below 200°C while others are not volatile at these temperatures.

The chemical composition of the SOA formed under low-NO_x conditions was found to change over the course of the experiment. The evolution of selected ions and of the total organic mass measured by the TOF-AMS instrument is shown in Figure 2.9. All ion signal intensities shown here are divided by the signal intensity of sulfate to correct for loss of particle mass to the chamber walls. Figure 2.9a shows the evolution of two prominent high-mass fragment ions m/z 247 and 327. These high-mass fragment ions increase in abundance with time, with the increase in m/z 327 being more significant. This increase is observed for all high-mass ($m/z > 200$) fragment ions. Figure 2.9b shows the change in the intensity of the fragment ion m/z 91, which is proposed to serve as a tracer ion for peroxides formed under low-NO_x conditions, where the proposed formula for this fragment ion is C₃H₇O₃, and the structure for one of its isomers is shown in Figure 2.9b. This peroxide tracer ion reaches its maximum signal after seven hours have elapsed in the experiment. Over the next six hours this ion decreases to a lower constant

value; such a loss cannot be attributed to wall loss processes since the m/z 91 signal has already been normalized to the sulfate signal. Figure 2.9c shows the time evolution of the organic mass from Experiment 13. The organic mass also slightly decreases after reaching its peak value; however, the decrease observed for the organic mass is much lower than that of the peroxide tracer ion (m/z 91).

PILS/IC data were collected for some low-NO_x experiments. Aerosol mass concentrations of acetate were much lower than in the high-NO_x case. For example, for Experiment 12, acetate anion accounted for only 1.67 $\mu\text{g}/\text{m}^3$, \sim 14–22 times lower than that of high-NO_x levels. Formate anion was detected at comparable mass concentrations to that of the high-NO_x experiments (\sim 1.51 $\mu\text{g}/\text{m}^3$). Again, it should be noted that these two ions elute off the IC column immediately after sample injection and there is a possibility that other early-eluting monocarboxylic acid species co-eluted with these two species, leading to an overestimate of their mass. No other organic anions were detected at significant levels from these low-NO_x experiments.

Figure 2.10a shows a GC/MS TIC of a low-NO_x, dry ammonium sulfate seeded experiment (Experiment 13). The chromatographic peaks at RTs = 31.21, 32.25, and 32.61 min correspond to isomeric C₅ alkene triol species (*cis*-2-methyl-1,3,4-trihydroxy-1-butene, 3-methyl-2,3,4-trihydroxy-1-butene, *trans*-2-methyl-1,3,4-trihydroxy-1-butene, respectively), which have been previously measured in ambient aerosol from the Amazonian rainforest and Finnish boreal forests.^{11,12} This is the first detection of these species in a controlled laboratory chamber experiment. The chromatographic peaks at RTs 38.22 and 38.97 min correspond to the 2-methyltetrols (2-methylthreitol and 2-methylerythritol, respectively), which also have been detected in ambient aerosol

studies,^{7,10,11,13} as well as in one previous photooxidation chamber study.¹⁴ The C₅ alkene triols and 2-methyltetrols have received much attention in prior studies; the corresponding mass spectra for their respective chromatographic peaks can be found in Figure 2.20. GC-FID measurements were made to quantify the 2-methyltetrols and C₅ alkene triols for a low-NO_x dry seeded experiment (Experiment 13-peaks in Figure 2.10a) and a low-NO_x acid seeded experiment (Experiment 14). It was found that the 2-methyltetrols and C₅ alkene triols accounted for 3.91% and 0.60% of the SOA mass, respectively, for the dry seeded experiment (Experiment 13), and decreased to 0.46% and 0.06% of the SOA mass, respectively, for the acid seeded experiment (Experiment 14). The insert shown in Figure 2.10a is the *m/z* 219 EIC for six isomeric dimers (MW = 254) eluting between 58.8 and 59.2 min. The corresponding averaged EI mass spectrum for these chromatographic peaks is shown in Figure 2.10b. The general chemical structure of the trimethylsilylated dimer, along with its respective MS fragmentation, is also shown in this mass spectrum. The fragmentation pattern shown here indicates that the dimer forms by the reaction of a C₅ alkene triol (indicated by the *m/z* 335 fragment ion) with a 2-methyltetrol (indicated by the *m/z* 219 fragment ion) to form the hemiacetal dimer shown. To confirm the MW of the isomeric hemiacetal dimers eluting between 58.8 and 59.2 min, an averaged CI(CH₄) mass spectrum was also collected and is shown in Figure 2.10c. The MW of the trimethylsilylated dimer (derivatized MW = 686) is confirmed by the [M + H - CH₄]⁺ ion at *m/z* 671. The SOA products that elute at 34.91 and 35.47 min were tentatively characterized as diastereoisomeric 2-methyltetrol performate derivatives, which are unstable and upon reaction in the trimethylsilylation reagent mixture are converted into 2-methyltetrols. Their corresponding EI mass spectra can also be found in

Figure 2.20. It should be noted that the peaks labeled *1, *2, and *3 in the GC/MS TIC (Figure 2.10a) were also present in the laboratory controls and were identified as palmitic acid, stearic acid and palmitoyl monoglyceride, respectively. Table 2.4 summarizes all low-NO_x SOA components elucidated by GC/MS.

2.5 Discussion

2.5.1 Gas-Phase Chemistry

Gas-phase oxidation of isoprene is dominated by the reaction with OH.^{16,17} Under high-NO_x conditions, O₃ and NO₃ radicals play only a minor role in the initial oxidation of isoprene as they form only once [NO] approaches zero, by which time most of the isoprene is consumed. Under low-NO_x conditions, O₃ and NO₃ radicals also contribute negligibly to isoprene oxidation. Figure 2.11 shows the initial gas-phase reactions that occur under both low- and high-NO_x conditions. In both cases, the initial oxidation of isoprene occurs by reaction with OH, followed by the immediate addition of O₂ to form eight possible isomeric isoprene hydroxyperoxy (RO₂) radicals (for simplicity, only three are shown).

Under high-NO_x conditions, the isoprene hydroxyperoxy radicals react predominantly with NO; however, they may also react with NO₂ to form peroxy nitrates (ROONO₂, not shown in Figure 2.11), but these are likely unimportant to the formation of isoprene SOA due to their thermal instability. RO₂ + NO reactions result in the formation of either hydroxynitrates or hydroxyalkoxy (RO) radicals. Our observations of organic nitrates in high-NO_x SOA as observed in Figure 2.1 ([M - H]⁻ ions with even *m/z* values) indicate that these hydroxynitrates are likely SOA precursors. Two of the

hydroxyalkoxy radicals decompose into MVK and MACR, where their yields are 32–44% and 22–28%, respectively.³²⁻³⁵ The remaining hydroxyalkoxy radical forms a 1,4-hydroxycarbonyl, which may isomerize and dehydrate to form 3-methylfuran.³⁶ SOA formation has been observed from the photooxidation of MACR and 3-methylfuran, indicating that these are SOA precursors (indicated by black boxes in Figure 2.11).¹⁷ However, 3-methylfuran is not expected to contribute greatly to the SOA formed by isoprene oxidation because of its low gas-phase product yield (< 2-5%).³³⁻³⁵ The higher gas-phase product yields observed for MACR suggest it is the most important SOA precursor from isoprene oxidation under high-NO_x conditions; this is consistent with the similarities of the chemical products observed in isoprene and MACR SOA (Figure 2.1 and Table 2.2). Even though MVK typically has the highest gas-phase product yield observed, it is not a contributor to SOA formation under high-NO_x conditions, as negligible amounts of aerosol was produced from the high-NO_x photooxidation of 500 ppb MVK. Other products of isoprene oxidation under high-NO_x conditions (not shown in Figure 2.11) include C₅ hydroxycarbonyls, C₄ hydroxycarbonyls, and C₅ carbonyls; these may contribute to SOA formation but experimental evidence is currently lacking.

Under low-NO_x conditions, the isoprene hydroxyperoxy radicals react predominantly with HO₂. These reactions result in the formation of hydroxy hydroperoxides, which are highlighted in dotted boxes to indicate that these species are possible SOA precursors. Under similar reaction conditions, Miyoshi et al.³² observed by IR spectroscopy that hydroperoxides are major gas-phase products from isoprene oxidation under NO_x-free conditions. Aerosol formation was also observed; however, the composition of the resultant aerosol was not investigated.

In contrast to Kroll et al.¹⁶, under the present conditions there may be some contribution (~ 10–30%) of RO₂ + RO₂ reactions under low-NO_x conditions owing to the higher [isoprene]₀/[H₂O₂] ratios used in the current study.³² For simplicity, only the RO₂ + RO₂ reactions that lead to hydroxyalkoxy radicals are shown in Figure 2.11. As in the high-NO_x case, these hydroxyalkoxy radicals will likely form MVK, MACR, and hydroxycarbonyls. The RO₂ + RO₂ reactions not shown can lead to the formation of diols and other isomeric hydroxycarbonyls. As will be discussed subsequently, the diols that result from RO₂ + RO₂ reactions (not shown) may form SOA as well.¹⁵

2.5.2 High-NO_x SOA

2.5.2.1 Importance of MACR Oxidation

MACR oxidation under high-NO_x conditions produces significant amounts of SOA (Experiments 3 and 4). When comparing the SOA products from isoprene and MACR oxidation at high-NO_x conditions, many of the same products are observed (Figure 2.1). Tandem MS data obtained for selected ions common to both isoprene and MACR samples, like the *m/z* 368 ion shown in Figure 2.4, produced similar product ion spectra, further indicating that these species are indeed the same. This observation is consistent with our previous proton transfer reaction-mass spectrometry (PTR-MS) studies of isoprene oxidation, which demonstrate a strong correlation between the amount of SOA formed and MACR reacted in the gas phase.^{37,38} In these studies, aerosol growth continued well after isoprene was fully consumed, indicating the likely importance of second- (or later-) generation gas-phase products and/or heterogeneous (particle-phase) reactions. It should be noted that when the MACR, H₂O₂, and dry ammonium sulfate

seed aerosol are well mixed in the chamber before irradiation begins, no aerosol growth is observed. This rules out the possibility of reactive uptake of MACR into the particle phase; instead the oxidation of MACR is a necessary step in SOA formation from the photooxidation of isoprene.

2.5.2.2 Oligomers

Oligomerization occurs in SOA formed under high-NO_x conditions, where both offline and online mass spectrometry techniques (Figures 2.1, 2.2, and 2.5) measure species with much higher MWs than that of the parent isoprene, with characteristic 102 Da differences. Tandem MS techniques, such as upfront CID on the LC/MS instrument, confirm that oligomers are indeed formed from a common 102 Da monomeric unit. For example, when isolating the *m/z* 368 ion from the rest of the sample matrix and further fragmenting it to generate a product ion spectrum, two successive neutral losses of 102 Da were observed at *m/z* 266 and 164 (Figure 2.4b). Two isomeric compounds with *m/z* 266 in Figure 2.3c were found to elute off the LC column at ~ 2.5–3 min earlier than the compound with *m/z* 368 studied here. The fact that the compounds with *m/z* 266 ions elute off the LC column at earlier RTs, and that *m/z* 266 is a product ion of *m/z* 368, strongly suggests that these two ions are characteristic of the same oligomeric series. The compounds characterized by *m/z* 368 and 266 are likely a trimer and dimer, respectively. The other series of oligomers quantified in Table 2.2 also had 102 Da differences observed and similar LC/MS behaviors, with ions with lower mass eluting from the LC column at earlier RTs.

2.5.2.3 Organic Nitrates

Organic nitrates, detected as even-mass $[M - H]^-$ ions in (-)ESI spectra, were measured in all high-NO_x experiments. All organic nitrates detected in high-NO_x SOA samples had similar product ion spectra as m/z 368 (Figure 2.4b), with neutral losses of 63 (HNO₃), 77 (CH₃ radical + NO₃ radical, possibly CH₃NO₃), and 102 Da, suggesting that all even-mass $[M - H]^-$ ions are oligomeric organic nitrate species. Unlike the (-)ESI techniques (Figure 2.1 and 2.3), the GC/MS technique did not allow for the detection of organic nitrate species, likely a result of their instability at the high temperature of the GC injector and/or derivatization techniques used during sample workup. Organic nitrates also were not clearly detected in the MALDI-TOFMS (Figure 2.2) and the TOF-AMS (Figure 2.5) instruments. This is likely a result of the harsh ionization techniques employed by these instruments. Even with (-)ESI, these organic nitrates were not completely stable, as shown in Figure 2.4a for the m/z 368 ion. Organic nitrates found in the high-NO_x SOA likely form from the further oxidation of the hydroxynitrate species found in the gas phase from RO₂ + NO reactions.

2.5.2.4 2-MG as Monomeric Units

As shown in Table 2.2, other varieties of oligomers were observed as well. From further use of tandem MS techniques, it was found that one of these series of oligomers likely involved 2-MG (2-methylglyceric acid), a recently discovered SOA tracer compound for isoprene oxidation in the ambient atmosphere,^{10,13,14} as an important monomer. Confirmation of the 2-MG monomer in high-NO_x SOA was provided by GC/MS with TMS derivatization (Figures 2.6a and 2.6b). Because monomeric 2-MG is

small and polar, it was not effectively retained by the LC reverse phase column (RT ~ 1.3 min) and was detected in its deprotonated form at m/z 119. Figure 2.12 shows product ion spectra obtained with (-)ESI-ITMS for Experiment 9. In Figure 2.12a, the m/z 323 ion is isolated in the ion trap from the rest of the ion matrix and is collisionally activated to produce the MS² spectrum shown here. The m/z 221 ion is the base peak in this spectrum, and the m/z 119 ion also detected as the result of further fragmentation of the m/z 221 product ion. The fact that the m/z 119 ion was detected as a product ion in the MS² and MS³ spectra shown in Figure 2.12, strongly suggests that 2-MG is a monomer in this oligomeric series. It is important to note that m/z 119 was also a fragment ion produced in the upfront CID spectrum for the m/z 368 ion in Figure 2.4b. It was found that m/z 119 was a common product ion to each oligomeric series, suggesting the importance of 2-MG in oligomerization reactions.

2.5.2.5 Mono-Acetate and Mono-Formate Oligomers

The PILS/IC measurements of high levels of particulate acetate and formate anions in both the seeded (Experiment 1) and nucleation (Experiment 2) experiments, coupled with the high volatilities of their acid forms produced in the gas phase from the oxidation of isoprene, suggests that these compounds resulted from the decomposition of oligomeric SOA. The formation of *mono*-acetate and *mono*-formate oligomers was observed by tandem (-)ESI-MS measurements. Figure 2.13 shows two product ion spectra for a *mono*-acetate dimer ($[M - H]^-$ at m/z 161) and *mono*-formate trimer ($[M - H]^-$ at m/z 249), respectively. The observation of a neutral loss of 42 Da (ketene, H₂C=C=O) and a dominant product ion m/z 59 (acetate anion) in the MS² spectrum of the

m/z 161 ion (Figure 2.13a), provides strong evidence for acetylation. In the MS² spectrum of the m/z 249 ion (Figure 2.13b), the major product ion m/z 147 results from the common neutral loss of 102 Da. The product ion m/z 221 results from a neutral loss of 28 Da (CO), a rearrangement reaction which is characteristic of formates. The product ion m/z 119 (deprotonated 2-MG) resulting from the combined neutral losses of 102 and 28 Da is also observed. *Mono*-acetate oligomers were also detected by the GC/MS TMS derivatization method; the details of these findings will be discussed in a forthcoming GC/MS complementary paper.

2.5.2.6 Heterogeneous Esterification Reactions

Oligomer species containing the m/z 119, 221, and 323 ions as detected by the (–)ESI techniques were also observed by GC/MS as their respective TMS derivatives as shown Figure 2.6a. As in previous measurements of 2-MG,¹⁴ the EI mass spectrum shown in Figure 2.6b confirms the formation of monomeric 2-MG in high-NO_x isoprene SOA. The dimer detected at m/z 221 by (–)ESI techniques (as shown in Figure 2.12b) involving 2-MG as an important monomer, is detected at 51.59 min in Figure 2.6a. The chemical structure of this species likely contains 1 carboxyl and 3 hydroxyl groups, as shown in Figure 2.6c. The formation of an ester linkage is also denoted in this structure, which is the expected site of oligomerization. The ions m/z 583 ($[M + TMS]^+$) and m/z 495 ($[M - CH_3]^+$) confirm that the MW of this dimer species is 222 (which is also in agreement with the ESI results). The ion m/z 467 ($[M - (CH_3 + CO)]^+$) is consistent with a terminal trimethylsilylated carboxylic group, while the ion m/z 480 ($[M - CH_2O]^+$) is explained by a rearrangement of a trimethylsilyl group and points to a terminal

trimethylsilylated hydroxymethyl group. The elemental composition ($C_8H_{14}O_7$) of the structure shown in Figure 2.6c was also confirmed by high-resolution ESI-TOFMS measurements. These results strongly suggest that particle-phase esterification reactions occurred between 2-MG molecules, where a hydroxyl group of one 2-MG molecule reacted with a carboxylic acid group of another one. The products that result from this reaction would be the ester compound shown in Figure 2.6c and a water molecule. The neutral loss of 102 Da, likely corresponding to dehydrated 2-MG or a 2-MG residue in the form of a lactone (i.e., 2-hydroxy-2-methylpropiolactone), observed from the ESI-MS/MS techniques can be explained by the charge-directed nucleophilic reaction shown in Figure 2.14. To our knowledge, this is the first evidence of particle-phase esterification reactions in SOA. It should be noted that the mass spectra, not shown here, for the chromatographic peaks in Figure 2.6a at 60.01 and 60.31 min, correspond to branched and linear 2-MG acid trimers (corresponding to MW = 324), respectively. A detailed discussion of the EI mass spectral behavior of the TMS derivatives of 2-MG, 2-MG dimer and trimers will be presented in a complimentary GC/MS study.

Figure 2.15a and 2.15b compares the GC/MS EICs, using the m/z 219 ion as the base peak, for a filter sample from Experiment 5 treated with trimethylsilylation only to that of a filter sample (also from Experiment 5) treated by hydrolysis/ethylation + trimethylsilylation, respectively, to show further confirmation of polyesters formed via esterification reactions between 2-MG molecules. When treating SOA from the same chamber experiment with the hydrolysis/ethylation procedure, a noticeable decrease in 2-MG and 2-MG oligomers is observed. For example, the peaks at 29.08, 51.59, and 60.31 min (Figure 2.15a) observed after trimethylsilylation appear as smaller peaks upon the

hydrolysis/ethylation experiment, as shown in the second chromatogram (Figure 2.15b). This decrease is a result of the formation of ethyl esters of 2-MG and of linear dimer (RTs = 27.42 and 50.48 min, respectively). The mass spectra confirming the formation of these ethyl ester species are shown in Figures 2.15c and 2.15d, respectively. The m/z 365 and 277 ions in Figure 2.15c confirm the MW of the ethyl ester of 2-MG to be 148, where its formation is the resultant of polyesters decomposing into this derivatized monomer. The detection of m/z 539 and 451 in Figure 2.15d confirm the MW of the ethyl ester of the linear 2-MG dimer, likely a result of the incomplete decomposition of larger polyesters (i.e., trimers, tetramers, pentamers, etc.) in high-NO_x SOA.

Figure 2.16 shows the overall proposed reaction mechanism for SOA formation from the photooxidation of isoprene under high-NO_x conditions. This figure denotes important initial gas- phase and particle-phase reactions that lead to the observed SOA products. As was discussed earlier, further gas-phase oxidation of MACR is required in order to form SOA from isoprene under high-NO_x conditions. Oligomeric organic nitrates, such as the m/z 368 ion, are comprised of an organic nitrate monomer, which is detected as the deprotonated m/z 164 product ion (Figure 2.4b); therefore, it is possible that one gas-phase product of MACR oxidation is its hydroxynitrate form, as shown in Figure 2.16. Through further oxidation of the aldehyde group in this hydroxynitrate species, it is expected that the acid form of this species results in the particle phase, thus being available for esterification reactions with 2-MG (Reaction 2 in Figure 2.16). To our knowledge, no organic nitrates have been measured in the gas phase from MACR oxidation (though nitrate formation has been inferred from OH-methacrolein reaction kinetics³⁹); however, the detection of organic nitrates in the particle phase suggests that

this is possibly a minor channel for SOA formation. On the other hand, the formation of 2-MG from the oxidation of MACR is still uncertain, due to the unknown intermediates leading to its formation. Recently, it was proposed that 2-MG forms from the reaction of methacrylic acid or MACR with H_2O_2 in the liquid aerosol phase under acidic conditions.¹³ No aerosol growth was observed for MACR, H_2O_2 , and dry ammonium sulfate seed aerosol under dark conditions, however, it is possible that other products such as formic and acetic acid, as well as oxidants formed during isoprene photooxidation, may promote the reactive uptake of MACR into the aerosol phase. Further measurements of MACR oxidation products are needed in order to better understand the formation of 2-MG, which might occur in either the particle or gas phase.

From our detailed analytical measurements discussed above, the importance of 2-MG to particle-phase reactions in high- NO_x SOA is now well established. 2-MG monomers can react intermolecularly via esterification to produce 2-MG oligomers (Reaction 1), or react with *mono*-nitrate monomers to produce *mono*-nitrate oligomers (Reaction 2), or react with acetic or formic acid to produce *mono*-acetate and *mono*-formate oligomers, respectively (Reactions 3 and 4). These proposed esterification reactions are equilibrium reactions, and as a result, the addition of an acid or removal of water could promote the formation of these esters. As stated earlier, the high- NO_x experiments were conducted at very low relative humidities ($\text{RH} < 5\%$); therefore, this condition could allow for the ester formation we observe. We also observe high concentrations of organic acids (2-methylglyceric, acetic, and formic acid) at the high- NO_x condition, which could provide the acidity needed to drive these reactions. It has been shown⁴⁰ that heterogeneous esterification of polyols by vapor-phase treatment with

acetic acid and trifluoroacetic anhydride (used as an alternative to the sulfuric acid catalyst) will occur at room temperature without the use of liquids. Thus it is reasonable to infer that esterification reactions may occur under the dry, room temperature conditions of our chamber experiments. It should be noted that there is also evidence from the TOF-AMS that supports this reaction mechanism. The ratio of the TOF-AMS ion signals associated with the 2-MG dimer (m/z 205) to that of the 2-MG monomer (m/z 103) increases during the course of the high- NO_x experiments; therefore, providing additional confirmation of our proposed reaction mechanism in Figure 2.16. These results from the TOF-AMS, however, are not quantitative due to the majority of these molecules being fragmented (thermally or by the electron impact ionization) to smaller ions.

In comparison to MACR oxidation, the further oxidation of MVK likely does not produce SOA under high- NO_x conditions due to its ketone moiety. The lack of an aldehydic hydrogen precludes the formation of acidic products (like that of 2-MG from MACR oxidation), which are necessary components needed for the particle-phase esterification reactions (Figure 2.16). One of the most abundant gas-phase products produced from MVK oxidation under the high- NO_x condition is methylglyoxal. It was shown in a prior chamber study by Kroll et al.⁴¹ that methylglyoxal does not reactively uptake onto inorganic seed aerosol; therefore, this could explain the lack of SOA growth from the further oxidation of MVK.

For the isoprene/ H_2O_2 experiments, except for Experiment 6, the most abundant oligomer series was the *mono*-nitrate oligomers (Table 2.2). The *mono*-nitrate oligomers accounted for ~ 8–13% of the SOA mass formed in these experiments. As for the

isoprene/H₂O₂ experiments, the *mono*-nitrate oligomers were the most abundant oligomers for the MACR/H₂O₂ experiments (~ 35% of SOA mass for seeded experiment vs ~ 20% for nucleation experiment). Even though most of the chemical products are the same in the H₂O₂ and HONO experiments, the abundances of these products are different. In contrast to the H₂O₂ experiments, the 2-MG oligomers are the most abundant oligomers for the HONO experiments. These differences could be due to different NO_x levels. SOA mass closure was observed to be the highest for the MACR/H₂O₂/seeded experiment (~ 57% of SOA identified) and the isoprene/H₂O₂/seeded experiments (22–34% identified). It is important to stress that the organic aerosol mass loadings formed in these isoprene high-NO_x chamber experiments (~ 50 – 200 μg m⁻³) are much higher than those found in ambient aerosol where isoprene emissions are the highest (~ 5 μg m⁻³). The amount of organic aerosol mass controls the gas-particle partitioning of semi-volatile species produced from the oxidation of hydrocarbons, as more organic aerosol mass allows for more uptake of these species; therefore, the mass closure results presented apply only to the aerosol mass loadings produced in this current study and are not absolute for the isoprene system. The key insight from our analysis is the detection of these various oligomeric products formed from particle-phase esterification reactions.

2.5.2.7 Additional Routes for SOA Formation

As shown in Table 2.2, the polyester products from oligomerization of 2-MG and related components account only for a portion (22–34%) of the SOA formed from isoprene oxidation under high-NO_x conditions. This lack of mass closure could result

from the LC/MS technique underestimating the amount of polyesters, possibly related to the use of a C₁₈ reverse phase column and the unavailability of authentic standards. The C₁₈ reverse phase column could have degraded the oligomers into smaller units as they pass through the column, or very large oligomers could have permanently been retained onto the reverse phase material, and hence were not detected. Negative bias associated with filter sampling, such as evaporative losses during sampling or storage, could also be a source of incomplete mass closure. The presence of acetic acid in eluent mixture used for the LC/MS runs could also have caused an underestimation of the oligomers formed due to the possibility of acid-catalyzed hydrolysis during ESI, a process that would lead to a decrease in the detection of oligomeric compounds. Besides possible errors associated with quantifying esterification products identified by the LC/MS technique, the possibility still exists that other unidentified second- (or later-) generation gas- or particle-phase products from isoprene oxidation contribute to SOA formation, and as a result, would increase the mass closure significantly.

Glyoxal, a C₂ dialdehyde, has been recently shown to be reactively taken up into particulate matter,^{41,42} however, not at the low RHs employed in this study (RH < 5%). Theoretically, it has been shown that this reactive uptake of glyoxal results from thermodynamically favorable hydration and oligomerization.^{43,44} When first interpreting the MS data from the ESI and MALDI techniques, it was considered that a dialdehyde species possibly corresponded to the 102 Da neutral losses observed from the oligomeric components. Figure 2.17 shows a proposed gas-phase reaction scheme for the formation of a C₄ hydroxy dialdehyde species (MW=102) from the further oxidation of MACR. In contrast to glyoxal, dissolution may not be required for this proposed dialdehyde species

to form SOA; therefore other heterogeneous processes may occur. The detailed analysis of the GC/MS derivatization and the ESI tandem MS results, however, provides strong chemical evidence for the formation of polyesters, where the neutral loss of 102 Da is explained by the dehydrated lactone form of 2-MG (Figure 2.14). In addition, a GC/MS derivatization analysis made for MACR high-NO_x SOA (Experiment 3) that included a methoximation step prior to trimethylsilylation to reveal aldehyde functions in the formed oligomers was negative.

To investigate further the probable importance of a C₄ hydroxy dialdehyde species and its respective hemiacetal oligomers, selected sample extracts were derivatized using the Girard Reagent P to increase sensitivity for aldehydic species in the (+)ESI mode. A high-NO_x isoprene and MACR sample were treated with this derivatizing agent, and as a result, the detection of the *m/z* 236, 206, and 192 ions resulted for both samples, which likely corresponds to the detection of the proposed C₄ dialdehyde, glyoxal, and methylglyoxal, respectively. However, the proposed hemiacetal oligomers that would be produced from this C₄ dialdehyde were not detected, consistent with observations made in the methoximation GC/MS experiment. It is possible that the detection of the proposed C₄ dialdehyde resulted from the decomposition of oligomers during the derivatization step of the sample workup procedure (which is equivalent for the detection of glyoxal and methylglyoxal in the particle phase). As a confirmation that the observed ions were derivatized species of the proposed C₄ dialdehyde, glyoxal, and methylglyoxal, upfront CID LC/MS analysis was used to detect common neutral mass losses and fragment ions associated with derivatized aldehydes and ketones. The common neutral losses and fragment ions associated with the GirP derivatization detected were similar to

those found by Lai et al.,²³ providing further evidence of the detection of these small aldehyde species in high-NO_x isoprene and MACR SOA. The detection of these small dicarbonyls provides some evidence that aldehydes may account for a fraction of the unquantified (unidentified) SOA mass (Table 2.2) produced from isoprene oxidation under high-NO_x conditions. The mechanism (reactive uptake and/or oligomerization) and the degree in which these aldehydes form SOA, however, remains unclear and bears further study.

2.5.3 Low-NO_x SOA

2.5.3.1 Hydroperoxides: Key Component to SOA Formation

As discussed previously, in the absence of NO_x, the RO₂ radical chemistry is dominated by RO₂ + HO₂ reactions, owing to the large amounts of HO₂ formed from the OH + H₂O₂ reactions.¹⁷ RO₂ + RO₂ reactions are expected to be less substantial (10–30% contribution) due to the high HO₂/RO₂ ratios in these experiments, and as a result, hydroperoxides are expected to be the dominant gas-phase products. Due to their expected low volatilities, hydroperoxide species can partition to the aerosol phase and likely form high-MW species via peroxyhemiacetal formation with aldehydic species.^{18,19} Hydroperoxides resulting from the oxidation of aromatic and biogenic VOCs have been observed and calculated to be important contributors to the overall SOA mass.^{18,45,46} Indeed, as shown in Table 2.3, organic peroxides (i.e., hydroperoxides or ROOR) also are a significant component (~ 61% of the SOA mass for nucleation experiments and ~ 25% and 30% of the SOA mass for dry seeded and acid seeded experiments, respectively) of the low-NO_x isoprene SOA. The large discrepancy in peroxide content observed between

nucleation (seed-free) and seeded experiments is currently not understood. As discussed in the results section, there is no evidence of interference from ammonium sulfate on the peroxide content measurement. Owing to the neutral nature of the hydroperoxides (and ROOR) measured by the iodometric-spectrophotometric method, no tandem ESI-MS measurements could be made to structurally elucidate this fraction. Thus, it is difficult to explain the differences in the peroxide content observed between nucleation and seeded experiments. It is possible that in the seeded cases the hydroperoxide species are heterogeneously converted into neutral species other than peroxidic compounds, such as polyols. Further studies should be conducted to investigate the role of inorganic seed on the amount of peroxides formed in the aerosol phase. As noted in the high-NO_x case, the mass closure results presented here apply only to the aerosol mass loadings produced in this current study and can not be concluded as absolute for the isoprene system at low-NO_x conditions.

2.5.3.2 Oligomerization

Oligomers were found to form under low-NO_x conditions, as shown in the (+)MALDI (Figure 2.7), GC/MS with TMS derivatization (Figure 2.10), and TOF-AMS (Figures 2.8 and 2.9) data. In contrast to high-NO_x conditions, no distinct pattern or obvious monomeric unit, like the 102 Da differences observed in the high-NO_x oligomeric SOA (Figures 2.1, 2.2, and 2.5), was observed in the low-NO_x oligomers. The oligomers formed in the low-NO_x case are not acidic in nature like in the high-NO_x case. Structural elucidation of these oligomers is limited, as these neutral products are not ionizable using ESI-MS. MALDI (Figure 2.7) was able to provide some indication of

the MW ranges of the oligomeric SOA, but structural elucidation was not possible. The large mass contribution of organic peroxides to the low-NO_x SOA (Table 2.3) provides some insight into the oligomerization reactions occurring. It is possible that some fraction of the oligomeric SOA is formed by peroxyhemiacetals, which result from heterogeneous reactions of hydroperoxides and aldehydes.

Due to the neutral nature of the oligomeric SOA produced under low-NO_x conditions, only the GC/MS derivatization technique provides structural elucidation of the oligomers formed owing to the presence of polyols. Hemiacetal formation reactions between C₅ alkene triols (Table 2.4) and 2-methyltetrols (Table 2.4) were found to occur using this technique (Figure 2.10b). The reaction involves a terminal hydroxyl group of a 2-methyltetrol, which serves as a nucleophile, reacting with the tautomeric keto form of one C₅ alkene triol (Table 2.4) to form the hemiacetal dimer shown in Figure 2.10b. As was observed by the GC/MS *m/z* 219 EIC, six isomeric forms of this hemiacetal dimer could be partially resolved. However, further elucidation of higher-order hemiacetal (acetal) oligomers could not be conducted owing to their likely thermal decomposition in the GC injector of the GC/MS instrument, their high MW preventing their elution from the GC column, and lack of ionization when using ESI-MS techniques. As for the confirmation of peroxyhemiacetal oligomers, analytical techniques need to be developed in order to further elucidate the neutral higher-order hemiacetal (acetal) oligomers likely present in low-NO_x SOA.

2.5.3.3 Acid Catalysis

The SOA mass for the acid seed experiment (Experiment 17) is significantly larger (~ 3.6 times) than that of the dry seeded/nucleation experiments (Experiments 15/12), in contrast to high- NO_x conditions, in which acid seed had no such observable effect. Note that the SOA mass concentration was virtually identical in experiments using dry (nonacid) seed aerosol and in those in the absence of seed aerosol, where particle formation takes place by nucleation (Experiments 12, 13, and 15). GC-FID measurements made for selected low- NO_x experiments also provide evidence for acid-catalyzed particle-phase reactions. The C_5 alkene triols and 2-methyltetrols decreased in their contributions to the overall SOA mass when acid seed was present. For example, the 2-methyltetrols and C_5 alkene triols contributed $\sim 3.91\%$ and 0.6% , respectively, to the SOA mass for Experiment 13 (non-acid case), where as in Experiment 14 (acid case), the 2-methyltetrols and C_5 alkene triols were found to decrease to $\sim 0.46\%$ and 0.06% , respectively, of the SOA mass. This result is in contrast to that observed by Edney et al.¹⁴ in which isoprene tracer compounds were observed to increase in concentration, and is possibly due to the differing isoprene: NO_x ratios employed. In conjunction with the above GC-FID results, the fact that C_5 alkene triols and 2-methyltetrols were found to form hemiacetal dimers (and likely higher order oligomers) suggests that the presence of acidified aerosol catalyzes hemiacetal (and likely acetal) oligomer formation under low- NO_x conditions. The same may be the case for peroxyhemiacetal formation reactions.

2.5.3.4 Formation Mechanism of Low- NO_x SOA products Observed by GC/MS

The detection of organic peroxides in the particle phase (Table 2.3) by the iodometric-spectrophotometric method, provides strong evidence that the hydroperoxides

that result from the gas phase $\text{RO}_2 + \text{HO}_2$ reactions are sufficiently polar (nonvolatile) to partition to the aerosol phase, thereby elucidating one major reaction pathway leading to SOA formation under low- NO_x conditions. The detection of 2-methyltetrols, C_5 alkene triols, 2-methyltetrol performate derivatives, and hemiacetal dimers (Table 2.4) suggests that the RO_2 radicals that form from the initial oxidation (OH/O_2) of isoprene follow some other route. The formation of 2-methyltetrols has been explained by self- and cross-reactions of the RO_2 radicals formed from the initial oxidation (OH/O_2) of isoprene, leading to intermediate 1,2-diols, which may undergo a second cycle of oxidation (OH/O_2) reactions followed by self- and cross-reactions of the RO_2 radicals.⁷

The detection of C_5 alkene triols in ambient aerosol may indicate the importance of intermediate epoxydiol derivatives of isoprene, which may also be intermediates in the formation of 2-methyltetrols.^{11,12} Wang et al.¹² hypothesized from MS evidence that these epoxydiol intermediates could be trapped in the aerosol phase and subsequently converted into C_5 alkene triols and 2-methyltetrols through acid-catalyzed reactions. Acid-catalyzed reactions of epoxydiols may be a formation pathway for 2-methyltetrols and C_5 alkene triols, but these monomers may also form from other pathways.

Shown in Figure 2.18 is a proposed mechanism for the formation of key SOA components from the oxidation of isoprene under low- NO_x conditions. As suggested by Böge et al.¹⁵, 2-methyltetrols may form by several possible pathways. The formation of the 2-methyltetrols through two cycles of oxidation (OH/O_2) reactions followed by self- and cross-reactions of the RO_2 radicals is only briefly included in this figure. It is possible that epoxydiols may form from rearrangements of hydroxyhydroperoxides or hydroxyperoxy radicals. Once formed, these epoxydiols could be taken up into the

particulate phase, and through hydrolysis form 2-methyltetrols. In addition, an alternative pathway leading to the formation of 2-methyltetrols has been reported in a recent study by Böge et al.¹⁵ That study proposed that intermediates in the formation of 2-methyltetrols (i.e., 2-methyl-3-butene-1,2-diol and 2-methyl-2-vinyloxirane) are converted to 2-methyltetrols through reaction with hydrogen peroxide on acidic particles. The latter pathway is also included in the scheme in Figure 2.18. Further gas and particle-phase studies are needed in order to fully elucidate the pathways leading to the formation of 2-methyltetrols, the C₅ alkene triols and related dimeric products.

2.5.3.5 Evolution of SOA Composition

As in Kroll et al.¹⁷, a rapid decay of the SOA mass was observed after the initial SOA growth reached its maximum for all low-NO_x nucleation experiments. This loss is not attributable to wall removal processes since the particles shrink in size rather than reduce in number (as measured by the DMA). The loss of SOA mass was observed to stop immediately after chamber lights were turned off, and to resume once the lights were turned back on, indicating a photochemical effect.

Indeed, when comparing the peroxide measurements made at (or around) the initial SOA growth maximum to some later experimental time after SOA mass decay, it was found that the organic peroxide content of the aerosol significantly decreased (~ 59% to 26% of SOA mass, respectively for Experiment 18). This observation provides strong evidence that organic peroxides decompose in the particle phase due to photolysis and/or subsequent particle-phase reactions, or they are driven out of the particle as a result of gas-phase compounds being reacted away, shifting the equilibrium back to the gas phase.

TOF-AMS measurements also confirmed that the peroxide content of low-NO_x SOA decreases with time as shown in Figure 2.9b. This decrease in peroxide content as a function of time also coincided with high-mass fragment ions ($m/z > 200$) increasing in their abundance (in Figure 2.9a only m/z 247 and 327 are shown), suggesting the possibility that peroxide decomposition causes oligomerization reactions. These oligomerization reactions likely lead to hemiacetals (as elucidated by GC/MS).

2.5.3.6 Tracer Compounds for Isoprene Oxidation in the Remote Atmosphere

The low-NO_x chamber experiments conducted in this study confirm that 2-methyltetrols indeed serve as tracer compounds for isoprene oxidation in the ambient atmosphere, especially in remote regions such as the Amazonian rainforest. The detection of C₅ alkene triols and hemiacetal dimers in the present low-NO_x experiments corresponds well to their observation in ambient aerosol collected from the Amazonian rainforest¹² and Finnish boreal forests (note that hemiacetal dimers in aerosol collected from the Finnish boreal forests is not yet confirmed).¹¹ From these field studies, C₅ alkene triols were postulated to form by acid-catalyzed ring opening reactions of epoxydiol derivatives of isoprene in low RH environments. However, hemiacetal dimers were not recognized in ambient samples; this current study elucidates their formation under low-NO_x conditions. Once it was realized that hemiacetal dimers form from C₅ alkene triols and 2-methyltetrols, we referred back to data collected from the Amazonian rainforest.⁴⁷ When investigating the GC/MS data carefully, it was found that the hemiacetal dimers were indeed detected, suggesting the atmospheric relevance of these low-NO_x chamber experiments. Shown in Figure 2.19 is a GC/MS EIC of an Amazonian fine aerosol

sample (i.e., PM_{2.5}; particulate matter with an aerodynamic diameter < 2.5 μm) collected during the wet season (low-NO_x conditions) using multiple ions, i.e., *m/z* 231 (to show the C₅ alkene triols), *m/z* 219 (to show 2-methyltetrols as well as the dimers) and *m/z* 335 (characteristic of the dimers). An averaged EI mass spectrum for the hemiacetal dimers is also included in this figure to further confirm their presence in ambient aerosol.

2.6 Conclusions

The composition of SOA from the photooxidation of isoprene under both high- and low-NO_x conditions has been thoroughly investigated through a series of controlled laboratory chamber experiments. It is found that the chemical nature of the resultant SOA is significantly different in the two NO_x regimes. Under high-NO_x conditions, the SOA components are acidic and form upon the further oxidation of MACR. SOA components formed under low-NO_x conditions, by contrast, are not acidic, with primary species identified being polyols and organic peroxides. Based on SOA growth, acid-catalysis seems to play a larger role under low-NO_x conditions. Organic peroxides (likely dominated by hydroperoxides) contribute significantly to the low-NO_x SOA mass (~ 61% for nucleation experiments and ~ 25% and 30% for dry seeded and acid seeded experiments, respectively). However, differences in the organic peroxide contribution and the rate of loss in SOA mass for nucleation (seed-free) and seeded experiments are not well understood and require further investigation. The chemical composition changes with time in the low-NO_x case, showing evidence of chemical aging.

Oligomerization is an important SOA formation pathway for both low- and high-NO_x conditions, as oligomers were observed in both cases. The nature of the oligomers,

however, is distinctly different in each NO_x regime. Under high- NO_x conditions, the oligomers have clear monomeric units, with observable 102 Da differences using both online and offline mass spectrometry techniques. Using tandem ESI-MS techniques and GC/MS with trimethylsilylation, it is found that polyesters account for these high- NO_x oligomers, with 2-MG as the key monomeric unit. These polyesters account only for a fraction ($\sim 22\text{--}34\%$) of the SOA mass formed from isoprene oxidation. This lack of mass closure could result from an underestimate of the amount of polyesters formed or additional, unidentified MACR or isoprene oxidation products that contribute to the SOA mass. One key unresolved question is the path by which 2-MG is formed, which at present is not understood. Further gas- and particle-phase studies on isoprene oxidation under high- NO_x conditions are needed in order to elucidate the 2-MG formation pathway.

Previously detected tracer compounds for isoprene oxidation in the ambient atmosphere were detected in the low- NO_x experiments. C_5 alkene triols and hemiacetal dimers are reported here for the first time in a controlled laboratory experiment, suggesting that the oxidative conditions used in these experiments are relevant to remote regions. The GC/MS results suggest that hemiacetal dimers formed in these low- NO_x chamber experiments result from the reactions of 2-methyltetrols and C_5 alkene triols (a reaction that is likely relevant to the real atmosphere). Besides the formation of hemiacetal (acetal) oligomers in low- NO_x SOA, it is speculated that peroxyhemiacetal oligomers could also form, due to the large amounts of peroxides measured in the particle phase. The formation of low- NO_x oligomers may correlate to the decomposition of peroxides with experimental time, providing some insight into the mechanism of oligomerization. Additional analytical techniques need to be developed in order to

elucidate the neutral/unstable products found in SOA produced from the photooxidation of isoprene.

2.7 Acknowledgements

Research at Caltech was funded by the U.S. Environmental Protection Agency to Achieve Results (STAR) Program grant number RD-83107501-0, managed by EPA's Office of Research and Development (ORD), National Center for Environmental Research (NCER), and by the U.S. Department of Energy, Biological, and Environmental Research Program DE-FG02-05ER63983; this work has not been subjected to the EPA's required peer and policy review and therefore does not necessarily reflect the views of the Agency and no official endorsement should be inferred. Jason Surratt was supported in part by the United States Environmental Protection Agency (EPA) under the Science to Achieve Results (STAR) Graduate Fellowship Program. Research at the Universities of Antwerp and Ghent was supported by the Belgian Federal Science Policy Office through the BIOSOL project (contract SD/AT/02A) and a visiting postdoctoral fellowship to Rafal Szmigielski, and by the Research Foundation – Flanders (FWO). We would like to thank John Greaves at the University of California, Irvine for the accurate mass measurements on the ESI-TOF instrument. We would like to also thank Paul Ziemann at the University of California, Riverside for his useful communications regarding peroxide measurements in SOA.

2.8 References

- (1) Iinuma, Y.; Böge, O.; Gnauk, T.; Herrmann, H. *Atmos. Environ.* **2004**, *38*, 761.
- (2) Gao, S.; Keywood, M.; Ng, N.; Surratt, J. D.; Varutbangkul, V.; Bahreini, R.; Flagan, R. C.; Seinfeld, J. H. *J. Phys. Chem. A* **2004**, *108*, 10147.
- (3) Gao, S.; Ng, N.; Keywood, M.; Varutbangkul, V.; Bahreini, R.; Nenes, A.; He, J.; Yoo, K.; Beauchamp, J.; Hodyss, R.; Flagan, R.; Seinfeld, J. *Environ. Sci. Technol.* **2004**, *38*, 6582.
- (4) Tolocka, M.; Jang, M.; Ginter, J.; Cox, F.; Kamens, R.; Johnston, M. *Environ. Sci. Technol.* **2004**, *38*, 1428.
- (5) Kalberer, M.; Paulsen, D.; Sax, M.; Steinbacher, M.; Dommen, J.; Prevot, A.; Fisseha, R.; Weingartner, E.; Frankevich, V.; Zenobi, R.; Baltensperger, U. *Science* **2004**, *303*, 1659.
- (6) Kanakidou, M.; Seinfeld, J.; Pandis, S.; Barnes, I.; Dentener, F.; Facchini, M.; Van Dingenen, R.; Ervens, B.; Nenes, A.; Nielsen, C.; Swietlicki, E.; Putaud, J.; Balkanski, Y.; Fuzzi, S.; Horth, J.; Moortgat, G.; Winterhalter, R.; Myhre, C.; Tsigaridis, K.; Vignati, E.; Stephanou, E.; Wilson, J. *Atmos. Chem. Phys.* **2005**, *5*, 1053.
- (7) Claeys, M.; Graham, B.; Vas, G.; Wang, W.; Vermeylen, R.; Pashynska, V.; Cafmeyer, J.; Guyon, P.; Andreae, M. O.; Artaxo, P.; Maenhaut, W. *Science* **2004**, *303*, 1173.
- (8) Pandis, S.; Paulson, S.; Seinfeld, J. H.; Flagan, R. C. *Atmos. Environ.* **1991**, *25*, 997.
- (9) Limbeck, A.; Kulmala, M.; Puxbaum, H. *Geophys. Res. Lett.* **2003**, *30*.
- (10) Ion, A. C.; Vermeylen, R.; Kourtchev, I.; Cafmeyer, J.; Chi, X.; Gelencsér, A.; Maenhaut, W.; Claeys, M. *Atmos. Chem. Phys.* **2005**, *5*, 1805.
- (11) Kourtchev, I.; Ruuskanen, T.; Maenhaut, W.; Kulmala, M.; Claeys, M. *Atmos. Chem. Phys.* **2005**, *5*, 2761.
- (12) Wang, W.; Kourtchev, I.; Graham, B.; Cafmeyer, J.; Maenhaut, W.; Claeys, M. *Rapid Commun. Mass Spectrom.* **2005**, *19*, 1343.
- (13) Claeys, M.; Wang, W.; Ion, A.; Kourtchev, I.; Gelencsér, A.; Maenhaut, W. *Atmos. Environ.* **2004**, *38*, 4093.
- (14) Edney, E. O.; Kleindienst, T. E.; Jaoui, M.; Lewandowski, M.; Offenberg, J.H.; Wang, W.; Claeys, M. *Atmos. Environ.* **2005**, *39*, 5281.

- (15) Böge, O.; Miao, Y.; Plewka, A.; Herrmann, H. *Atmos. Environ.* **2006**, *40*, 2501.
- (16) Kroll, J.; Ng, N. L.; Murphy, S. M.; Flagan, R. C.; Seinfeld, J. H. *Geophys. Res. Lett.* **2005**, *32*.
- (17) Kroll, J. H.; Ng, N. L.; Murphy, S. M.; Flagan, R. C.; Seinfeld, J. H. *Environ. Sci. Technol.* **2006**, *40*, 1869.
- (18) Docherty, K.; Wu, W.; Lim, Y.; Ziemann, P. *Environ. Sci. Technol.* **2005**, *39*, 4049.
- (19) Johnson, D.; Jenkin, M. E.; Wirtz, K.; Martin-Reviejo, M. *Environ. Chem.* **2004**, *1*, 150.
- (20) Gao, S.; Surratt, J. D.; Knipping, E. M.; Edgerton, E. S.; Shahgholi, M.; Seinfeld, J. H. *J. Geophys. Res.* **2006**, *in press*.
- (21) Cocker, D.; Flagan, R. C.; Seinfeld, J. H. *Environ. Sci. Technol.* **2001**, *35*, 2594.
- (22) Keywood, M.; Varutbangkul, V.; Bahreini, R.; Flagan, R.; Seinfeld, J. *Environ. Sci. Technol.* **2004**, *38*, 4157.
- (23) Lai, C.; Tsai, C.; Tsai, F.; Lee, C.; Lin, W. *Rapid Commun. Mass Spectrom.* **2001**, *15*, 2145.
- (24) Drewnick, F.; Hings, S.; DeCarlo, P.; Jayne, J.; Gonin, M.; Fuhrer, K.; Weimer, S.; Jimenez, J.; Demerjian, K.; Borrmann, S.; Worsnop, D. *Aerosol Sci. Technol.* **2005**, *39*, 637.
- (25) Pashynska, V.; Vermeylen, R.; Vas, G.; Maenhaut, W.; Claeys, M. *J. Mass Spectrom.* **2002**, *37*, 1249.
- (26) Banerjee, D.; Budke, C. *Anal. Chem.* **1964**, *36*, 792.
- (27) Sorooshian, A.; Brechtel, F. J.; Ma, Y.; Weber, R. J.; Corless, A.; Flagan, R. C.; Seinfeld, J. H. *Aerosol Sci. Technol.* **2006**, *in press*.
- (28) Weber, R.; Orsini, D.; Daun, Y.; Lee, Y.; Klotz, P.; Brechtel, F. *Aerosol Sci. Technol.* **2001**, *35*, 718.
- (29) Seinfeld, J. H.; Pandis, S. N. *Atmospheric Chemistry and Physics: From Air Pollution to Climate Change*; Wiley: New York, 1998.
- (30) Iinuma, Y.; Böge, O.; Miao, Y.; Sierau, B.; Gnauk, T.; Herrmann, H. *Faraday*

Discuss. **2005**, 130, 279.

(31) Knochenmuss, R.; Zenobi, R. *Chem. Rev.* **2003**, 103, 441.

(32) Miyoshi, A.; Hatakeyama, S.; Washida, N. *J. Geophys. Res.* **1994**, 99, 18779.

(33) Tuazon, E.; Atkinson, R. *Int. J. Chem. Kinet.* **1990**, 22, 1221.

(34) Paulson, S.; Flagan, R. C.; Seinfeld, J. H. *Int. J. Chem. Kinet.* **1992**, 24, 79.

(35) Sprengnether, M.; Demerjian, K.; Donahue, N.; Anderson, J. *J. Geophys. Res.* **2002**, 107.

(36) Baker, J.; Arey, J.; Atkinson, R. *Environ. Sci. Technol.* **2005**, 39, 4091.

(37) Ng, N. L.; Kroll, J. H.; Keywood, M. D.; Bahreini, R.; Varutbangkul, V.; Lee, A.; Goldstein, A. H.; Flagan, R. C.; Seinfeld, J. H. *Environ. Sci. Technol.* **2006**, 40, 2283.

(38) Lee, A.; Goldstein, A. H.; Ng, N. L.; Kroll, J. H.; Varutbangkul, V.; Flagan, R. C.; Seinfeld, J. H. *J. Geophys. Res.* **2006**, 111.

(39) Chuong, B.; Stevens, P. S. *Int. J. Chem. Kinet.* **2004**, 36, 12.

(40) Yuan, H.; Nishiyama, Y.; Kuga, S. *Cellulose* **2005**, 12, 543.

(41) Kroll, J. H.; Ng, N. L.; Murphy, S. M.; Varutbangkul, V.; Flagan, R. C.; Seinfeld, J. H. *J. Geophys. Res.* **2005**, 110.

(42) Liggió, J.; Li, S.; McLaren, R. *Environ. Sci. Technol.* **2005**, 39, 1532.

(43) Barsanti, K.; Pankow, J. *Atmos. Environ.* **2005**, 39, 6597.

(44) Tong, C.; Blanco, M.; Goddard III, W. A.; Seinfeld, J. H. *Environ. Sci. Technol.* **2006**, 40, 2333.

(45) Johnson, D.; Jenkin, M. E.; Wirtz, K.; Martin-Reviejo, M. *Environ. Chem.* **2005**, 2, 35.

(46) Bonn, B.; von Kuhlmann, R.; Lawrence, M. *Geophys. Res. Lett.* **2004**, 31.

(47) Decesari, S.; Fuzzi, S.; Facchini, M.; Mircea, M.; Emblico, L.; Cavalli, F.; Maenhaut, W.; Chi, X.; Schkolnik, G.; Falkovich, A.; Rudich, Y.; Claeys, M.; Pashynska, V.; Vas, G.; Kourtev, I.; Vermeylen, R.; Hoffer, A.; Andreae, M. O.; Tagliavini, E.; Moretti, F.; Artaxo, P. *Atmos. Chem. Phys.* **2006**, 6, 375.

Table 2.1. High-NO_x chamber experiments conducted

expt. no.	VOC ^a	OH precursor ^b	seeded ^c / nucleation	initial [NO] ppb	initial [NO ₂] ppb	initial [NO _x] ppb	[O ₃] ^d ppb	T _i °C ^d	total SOA mass concentration ^{d,e,f} μg/m ³
1	Isoprene	H ₂ O ₂	nucleation	827	34	860	498	28.5	74
2	Isoprene	H ₂ O ₂	dry AS	759	112	869	525	28.3	73
3	MACR	H ₂ O ₂	dry AS	791	60	850	540	25.2	181
4	MACR	H ₂ O ₂	nucleation	898	30	926	519	25.0	197
5	Isoprene	H ₂ O ₂	nucleation	805	87	891	294	24.3	104
6	Isoprene	H ₂ O ₂	AAS	825	80	904	450	24.6	111
7 ^g	Isoprene	HONO	dry AS	50	333	382	132	20.1	68
8 ^g	Isoprene	HONO	nucleation	89	279	366	134	21.4	73
9	Isoprene	H ₂ O ₂	dry AS	891	74	963	325	24.9	95

^aAll VOC gas phase mixing ratios were 500 ppb. MACR = methacrolein.

^bH₂O₂ and HONO are not measured directly, but from isoprene decay during irradiation we estimate ~ 3 ppm of H₂O₂, and [HONO] is unlikely greater than measured [NO₂].

^cAS = ammonium sulfate seed, AAS = acidic ammonium sulfate seed

^dAveraged over the course of the filter sampling.

^eSubtraction of seed aerosol taken into account when necessary. SOA volume derived from DMA wall loss uncorrected measurements for use in mass closure from filter sample analyses.

^fAssuming a SOA density of 1.35 g/cm³. This value is derived from comparison of DMA aerosol volume and AMS aerosol mass measurements.

^g10% of light bank used and hence lower temperature observed. Also lower amounts of initial NO due to HONO as precursor.

Table 2.2. Quantified SOA products (in ng/m³) from high-NO_x chamber experiments

	[M-H] ⁻ ion	surrogate standard used for quantification ^a	isoprene/High NO _x /H ₂ O ₂				MACR/High NO _x /H ₂ O ₂		isoprene/HONO	
			expt. 1	expt. 2	expt. 6	expt. 9	expt. 3	expt. 4	expt. 7	expt. 8
<i>mono</i> - nitrate oligomers	266	pimelic acid	1970	4170	3890	3910	9360	3860	1470	830
	368	pinic acid	1350	2450	3700	4440	20600	10100	830	750
	470	pinic acid	2330	2930	2300	2640	28900	16700		210
	572	pinic acid	^b				2960	6810		
	674	suberic acid monomethyl ester					670	710		
	776	suberic acid monomethyl ester					220	450		
	878	suberic acid monomethyl ester					210			
total mass from <i>mono</i> -nitrate oligomers (μg/m ³)			5.65	9.55	9.89	11.0	62.7	38.8	2.30	1.79
% contribution to the total SOA mass			8	13	9	12	35	20	3	2
2-MG ^c oligomers	119	meso-erythritol	2050	3170	9680	4500	1240	460	4170	11600
	221	citramalic acid	1170	2590	2330	2110	3840	1720	550	1000
	323	2-hydroxy-3-methylbutyric acid	630	970	430	470	2740	1320	70	160
	425	pimelic acid		280	290	260	1650	680		130
	527	pimelic acid					720	480		
total mass from 2-MG oligomers (μg/m ³)			3.85	7.01	12.7	7.34	10.2	4.66	4.79	12.9
% contribution to the total SOA mass			5	10	11	8	6	2	7	18
<i>mono</i> - acetate oligomers	161	citramalic acid		40	100		90		110	70
	263	2-hydroxy-3-methylbutyric acid	680	1720	600	670	4070	1300	360	160
	365	pimelic acid	770	1890	820	1240	4830	1760	250	290
	467	pinic acid	340	450	180	420	3750	1310		130
	569	pinic acid		790			8600	2960		
671	suberic acid monomethyl ester					450	360			
total mass from <i>mono</i> -acetate oligomers (μg/m ³)			1.79	4.89	1.70	2.33	21.8	7.69	0.72	0.65
% contribution to the total SOA mass			2	7	2	2	12	4	1	1
<i>mono</i> - formate oligomers	147	meso-erythritol	200	380	11300		200			1370
	249	2-hydroxy-3-methylbutyric acid	460	1340		40	1970	810	60	
	351	2-hydroxy-3-methylbutyric acid	370	1000		60	2880	1390	30	
	453	pimelic acid	290	380			1800	710		
total mass from <i>mono</i> -formate oligomers (μg/m ³)			1.32	3.10	11.3	0.10	6.85	2.91	0.09	1.37
% contribution to the total SOA mass			2	4	10	0.1	4	1	0.1	2
total mass identified (μg/m ³)			12.6	24.6	35.6	20.8	102	54.1	7.90	16.7
% of SOA identified			17	34	32	22	56	27	12	23

^a Surrogate standards used covered the range of retention times for detected [M-H]⁻ ions. All standards used were within +/- 1.5 minutes of retention times for sample [M-H]⁻ ions.

^b A blank cell indicates the corresponding species was below detection limit.

^c 2-MG = 2-methylglyceric acid

Table 2.3. Low-NO_x chamber experiments conducted

expt. no. ^{a,b}	seeded ^c / nucleation	[O ₃] ^d ppb	T, °C ^d	total SOA mass concentration ^{d,e,f} μg/m ³	peroxide aerosol mass concentration μg/m ³	% contribution of peroxides to the SOA mass concentration observed
10 ^g	nucleation	32	29.1	186	116	62
11 ^g	dry AS	36	28.7	282	97	34
12	nucleation	b.d.l.	23.7	73	<i>h</i>	<i>h</i>
13	dry AS	12	24.1	69	<i>h</i>	<i>h</i>
14	AAS	b.d.l.	23.8	259	67	26
15	dry AS	11	23.9	73	19	25
16 ⁱ	dry AS	2	25.6	24	<i>h</i>	<i>h</i>
17	AAS	b.d.l.	23.6	93	23	24
18a	nucleation	7	26.2	55	32	59
18b ^j	nucleation	37	27.0	22	6	26

^a All VOC gas phase mixing ratios were 500 ppb, except for Experiment 17 (100 ppb)

^b H₂O₂ was the OH precursor used for each low NO_x isoprene experiment. H₂O₂ is not measured directly, but from isoprene decay during irradiation we estimate ~ 3 ppm of H₂O₂.

^c AS = ammonium sulfate seed, AAS = acidic ammonium sulfate seed.

^d Averaged over the course of filter sampling.

^e Subtraction of seed aerosol taken into account when necessary. SOA volume derived from DMA wall loss uncorrected measurements for use in mass closure from filter sample analyses.

^f Assuming a SOA density of 1.25 g/cm³. This value is derived from comparison of DMA aerosol volume and AMS aerosol mass measurements.

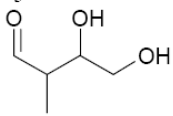
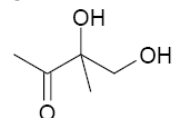
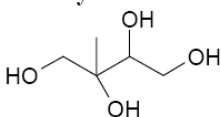
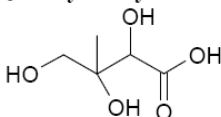
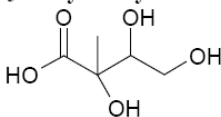
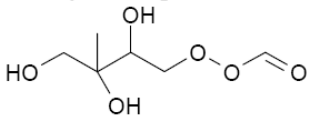
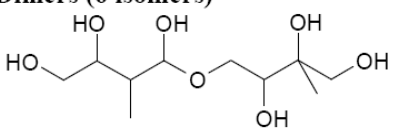
^g 100% of light bank used and hence higher temperatures in chamber observed during sampling.

^h No peroxide measurement made for this sample.

ⁱ Half of the typical [H₂O₂] used ~ 1.5 ppm

^j Late sampling, after peak growth, during the rapid decay of the aerosol mass/volume typical of low NO_x experiments.

Table 2.4. Low-NO_x isoprene SOA products elucidated by GC/MS

Compound / Structure	MW (MW TMS- derivative)	Elemental composition	Detection in Ambient Atmospheres
C₅ alkene triols / ald form 	118 (334)	C ₅ H ₁₀ O ₃	[Wang et al., 2005] ¹² [Kourtchev et al., 2005] ¹¹
C₅ alkene triols / keto form 	118 (334)	C ₅ H ₁₀ O ₃	[Wang et al., 2005] ¹² [Kourtchev et al., 2005] ¹¹
2-methyltetrols  <i>threo + erythro</i>	136 (424)	C ₅ H ₁₂ O ₄	[Claeys et al., 2004] ⁷ [Edney et al., 2005] ¹⁴ [Böge et al., 2006] ¹⁵ [Ion et al., 2005] ¹⁰ [Kourtchev et al., 2005] ¹¹
C₅ trihydroxy monocarboxylic acid  <i>threo + erythro</i> (minor compounds)	150 (438)	C ₅ H ₁₀ O ₅	Not yet detected in ambient aerosol
C₅ trihydroxy monocarboxylic acid  <i>threo + erythro</i> (minor compounds)	150 (438)	C ₅ H ₁₀ O ₅	Not yet detected in ambient aerosol
2-methyltetrol performate derivatives  (unstable products)	180 (396)	C ₆ H ₁₂ O ₆	Not yet detected in ambient aerosol
Dimers (6 isomers)  (minor compounds)	254 (686)	C ₁₀ H ₂₂ O ₇	Detected in ambient aerosol for the first time in this study

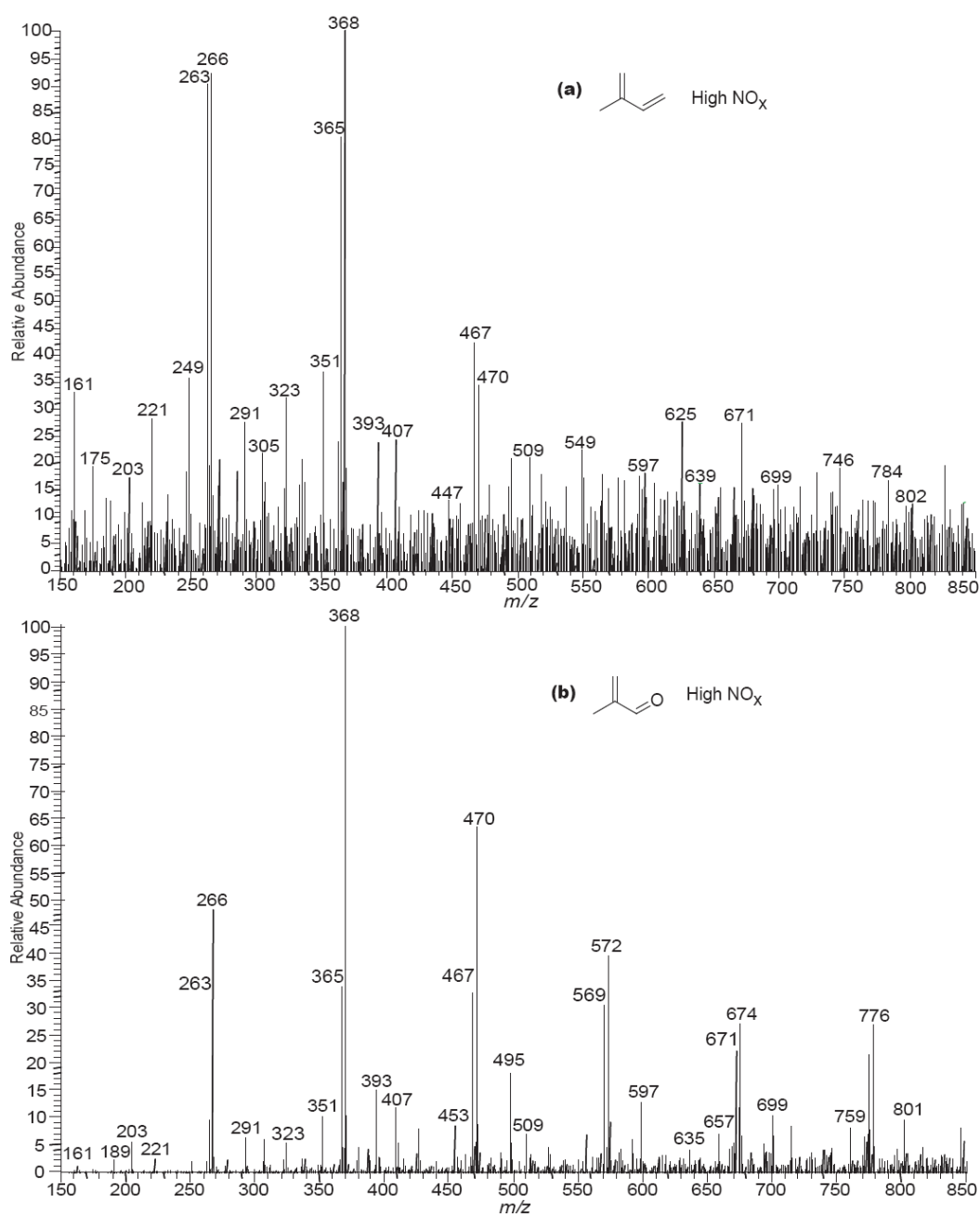


Figure 2.1. ESI-ITMS negative mode spectra collected via direct infusion analyses. (a) Spectrum of a filter extract obtained from a 500 ppb isoprene, high- NO_x , seeded experiment. (b) Spectrum of a filter extract obtained from a 500 ppb MACR, high- NO_x , seeded experiment. These mass spectra show that MACR oxidation produces many of the same SOA products as that of isoprene oxidation under high- NO_x conditions. Common 102 Da differences between ions in both spectra are observed indicating the presence of oligomers.

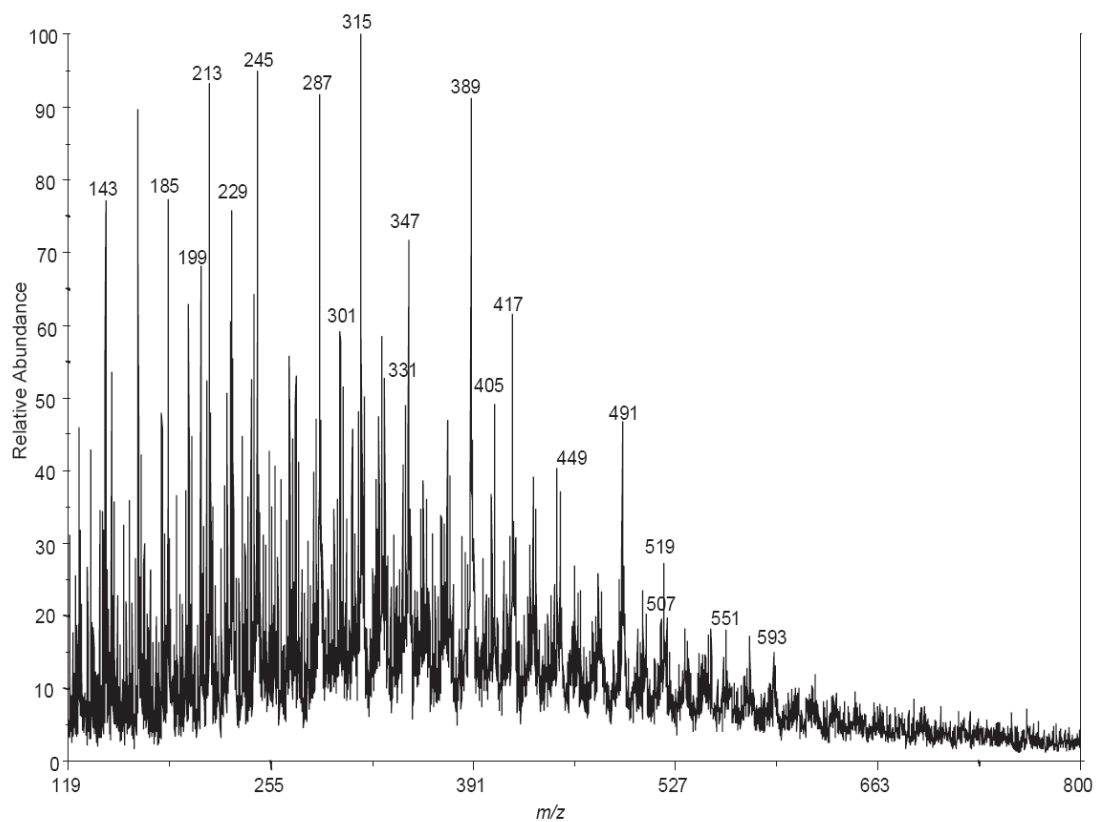


Figure 2.2. MALDI positive mode spectrum obtained with a graphite matrix for a 500 ppb isoprene, high-NO_x, dry seeded experiment (Experiment 9). Highlighted Na⁺ adduct ions confirm the existence of the species detected by ESI.

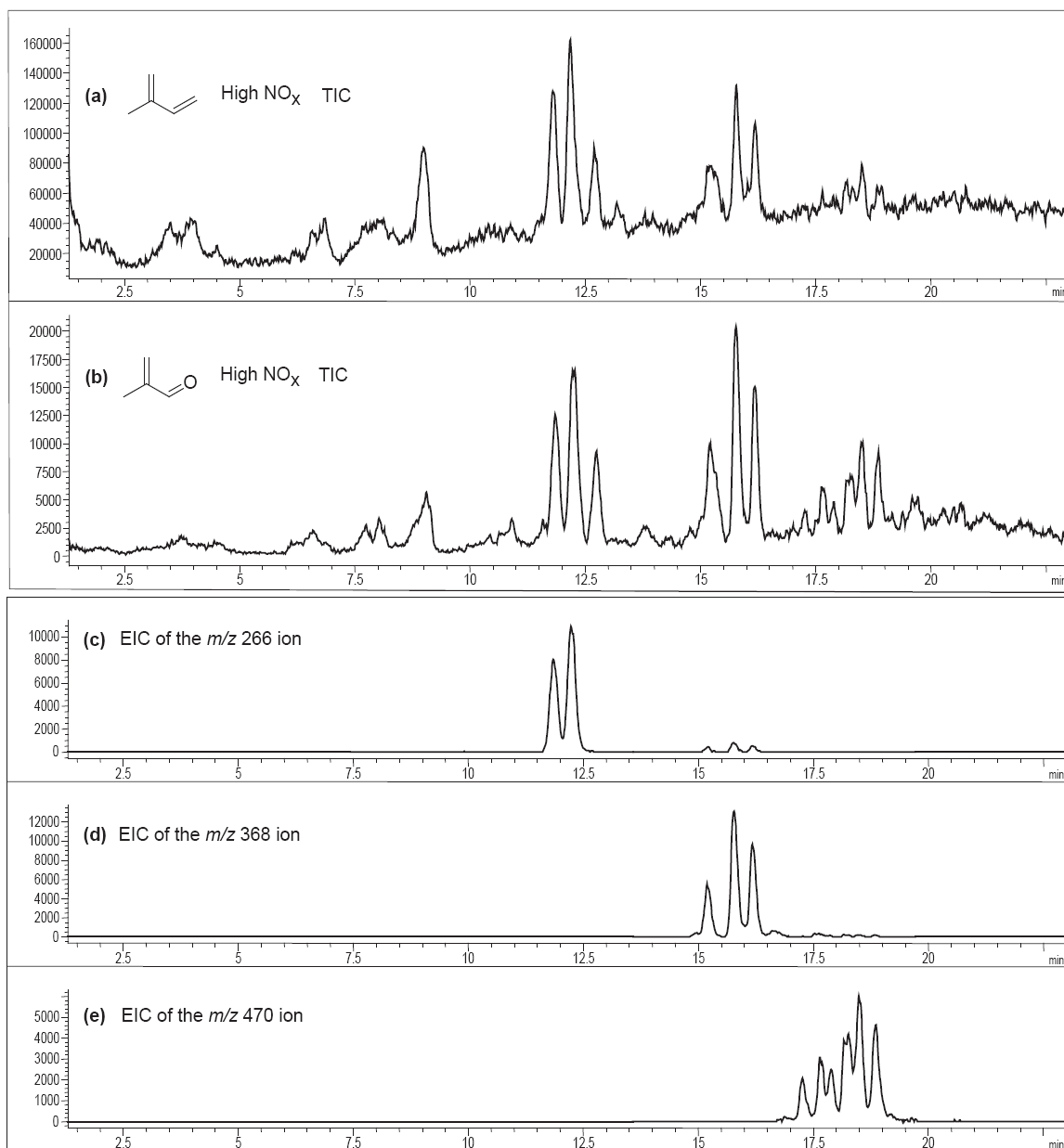


Figure 2.3. (a) LC/MS TIC of a filter extract from a 500 ppb isoprene, high-NO_x, nucleation experiment. (b) LC/MS TIC of a filter extract from a 500 ppb MACR, high-NO_x, nucleation experiment. The similar retention times and mass spectra associated with each chromatographic peak in these two TICs indicate that MACR is an important SOA precursor from isoprene oxidation under high-NO_x conditions. (c), (d), and (e) are LC/MS EICs of organic nitrate species common to both MACR and isoprene high-NO_x samples. These organic nitrate ions are a part of the same oligomeric series confirmed by MS/MS analyses.

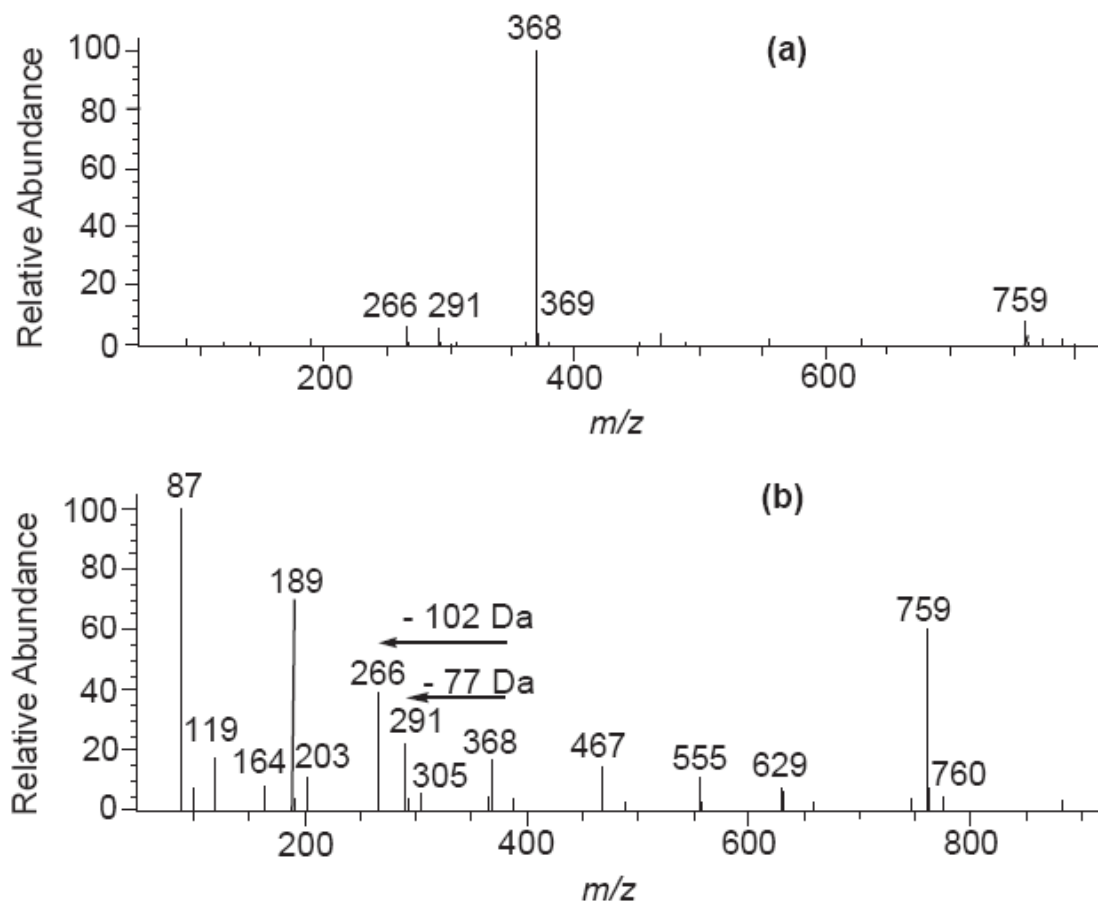


Figure 2.4. (a) Mass spectrum for the largest chromatographic peak (RT = 15.7 min) from Figure 2.3d (EIC of m/z 368 ion). (b) Upfront CID mass spectrum for the same chromatographic peak in Figure 3d (EIC of m/z 368 ion). The neutral losses observed in the upfront CID mass spectrum are associated with a trimeric organic nitrate species. This fragmentation pattern of m/z 368 is consistent with ion trap MS/MS results. The product ion m/z 266 corresponds to a neutral loss of 102 Da (common to all MS techniques), the product ion m/z 291 corresponds to a neutral loss of 77 Da (likely CH_3 radical and NO_3 radical, CH_3NO_3), the product ion m/z 305 corresponds to a neutral loss of 63 Da (likely HNO_3), the product ion m/z 203 corresponds to a neutral loss of 165 Da, and the product ion m/z 164 corresponds to a neutral loss of 204 Da (two losses of common monomer).

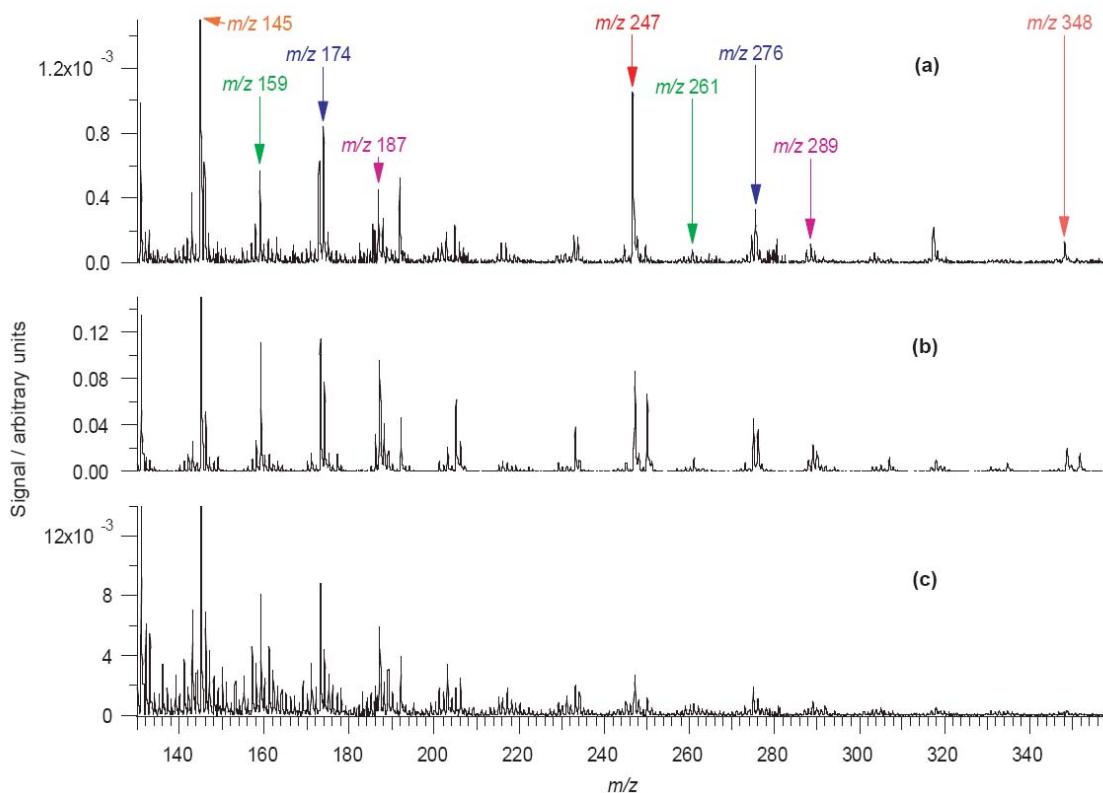


Figure 2.5. TOF-AMS spectra collected at low vaporizer temperatures for the following high- NO_x chamber experiments: (a) 50 ppb isoprene, 250 ppb NO_x , H_2O_2 as the OH precursor, no seed; (b) 500 ppb MACR, 800 ppb NO_x , H_2O_2 as the OH precursor, with seed; and (c) 500 ppb isoprene, HONO as the OH precursor, no seed. These spectra indicate that the OH precursor does not have a substantial effect on the chemistry observed, that MACR is an important SOA precursor from isoprene oxidation, and that the 102 Da differences observed in the offline mass spectrometry data are not a result of sample workup or ionization artifacts.

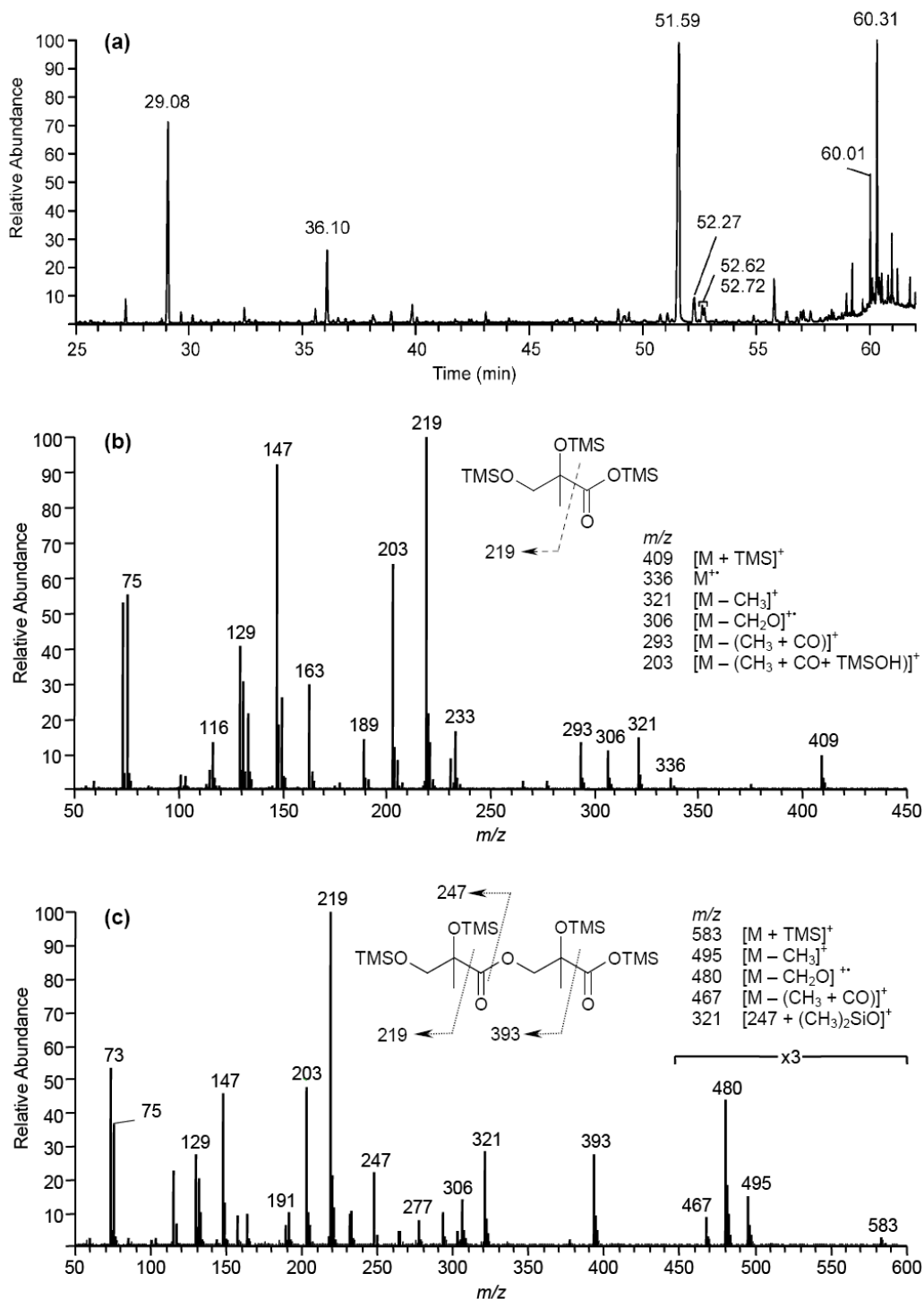


Figure 2.6. (a) TIC of a high- NO_x isoprene nucleation experiment (Experiment 5) collected using GC/MS in the EI mode. (b) EI mass spectrum for the 2-MG residue (RT = 29.08 min). (c) EI mass spectrum for a linear dimer made up of two 2-MG residues (RT = 51.59 min). These two mass spectra confirm that 2-MG is present in high- NO_x SOA and that it is involved in particle-phase esterification reactions resulting in polyesters (as shown by the dimer structure above).

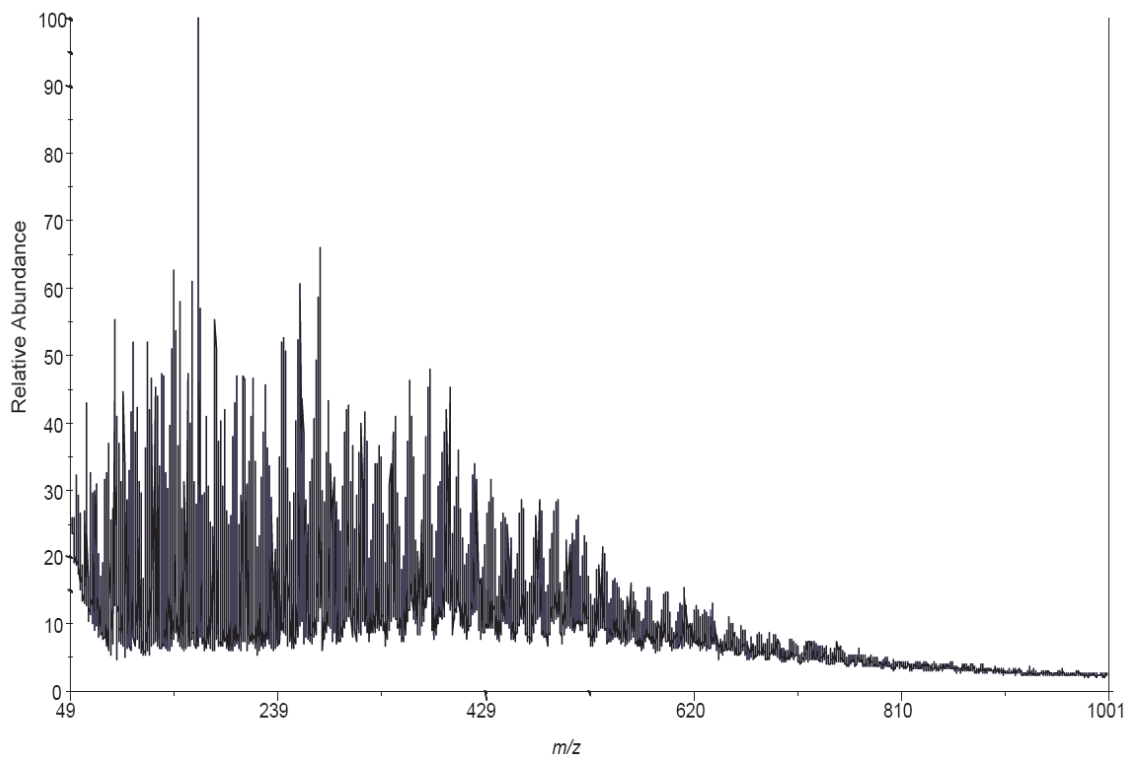


Figure 2.7. MALDI positive mode spectrum obtained with a graphite matrix for a 500 ppb isoprene, low-NO_x, acid seeded experiment (Experiment 14). High-molecular mass species formed up to ~ 620 Da.

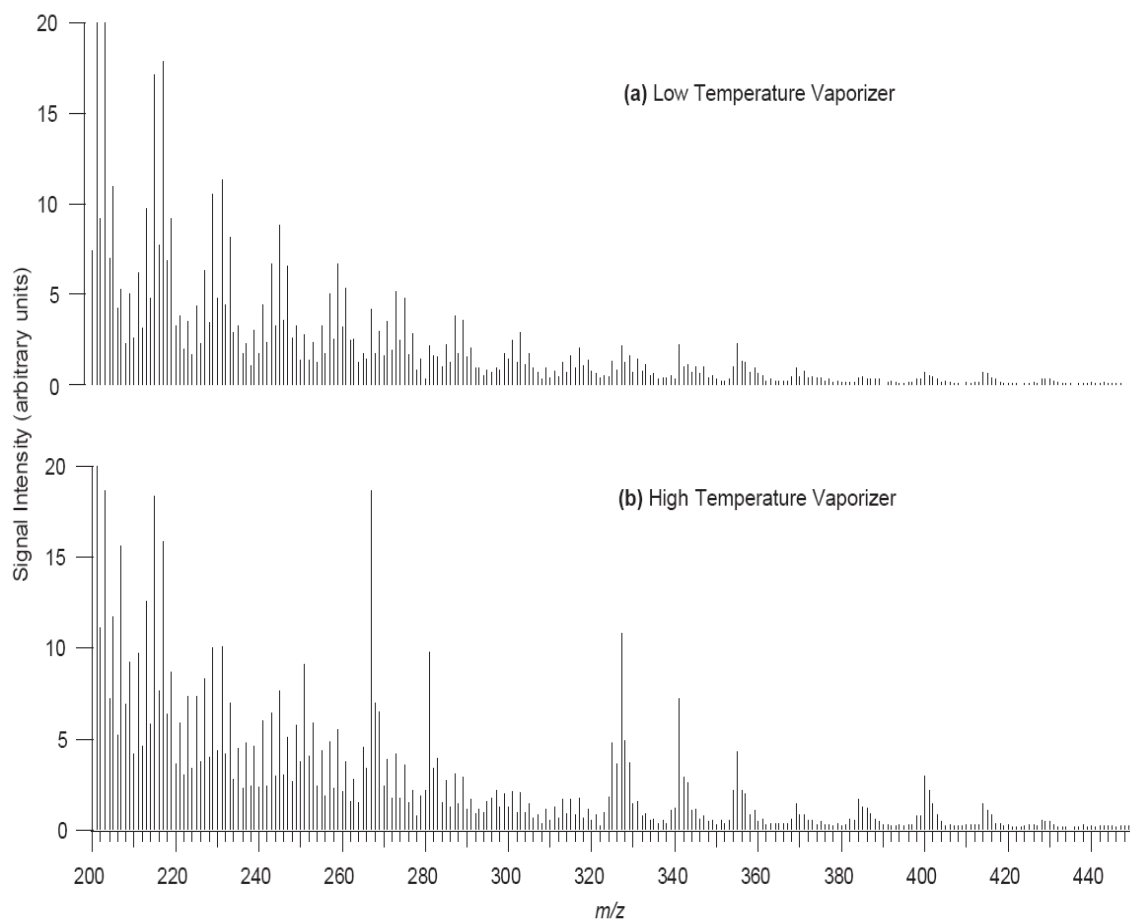


Figure 2.8. TOF-AMS spectra for a 500 ppb isoprene low- NO_x experiment (Experiment 12). (a) Mass spectrum obtained with a low temperature vaporizer ($\sim 150^\circ\text{C}$). (b) Mass spectrum obtained with a high temperature vaporizer ($\sim 600^\circ\text{C}$). The spectrum is richer at higher temperature with some prominent peaks at higher m/z , indicating that the high-MW oligomers that are not easily volatilized at $< 200^\circ\text{C}$.

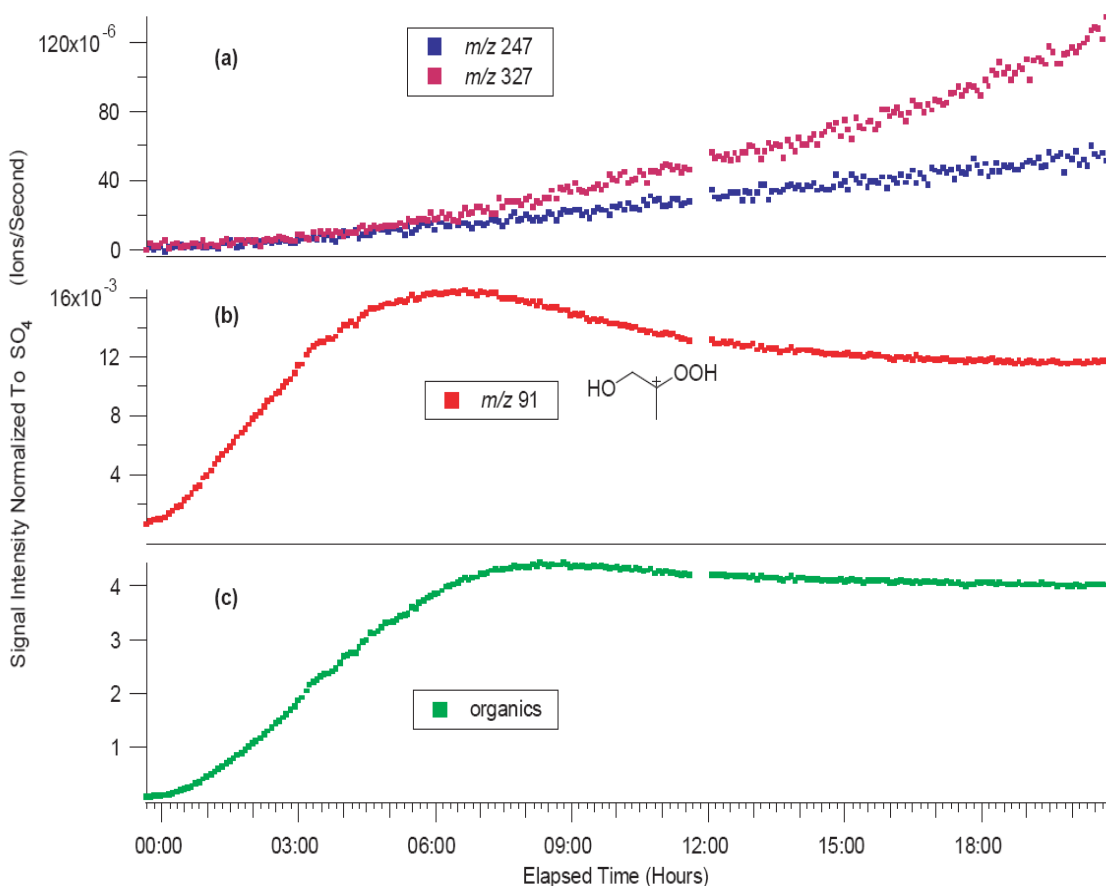


Figure 2.9. Time evolution plots produced from the TOF-AMS instrument for selected fragment ions and the total organic mass observed from a typical low-NO_x experiment (Experiment 13). All ion signal intensities are divided by the signal intensity of sulfate. Because sulfate concentration is a tracer for wall loss (neither created nor removed during the run), the ratio of ion signal to sulfate signal should give an indication of the behavior without wall loss. (a) Time evolution plot for high-mass fragment ions *m/z* 247 and 327. (b) Time evolution plot for the proposed peroxide fragment ion *m/z* 91 (C₃H₇O₃), where the structure of one isomer is shown. (c) Time evolution plot for the total organic mass. These plots indicate that the chemical composition changes with experimental time, where the decomposition of organic peroxides correlates to oligomerization within low-NO_x SOA. The missing data points (11:30 to 12:00 hours) in these plots are due to the vaporizer in the TOF-AMS instrument being turned off.

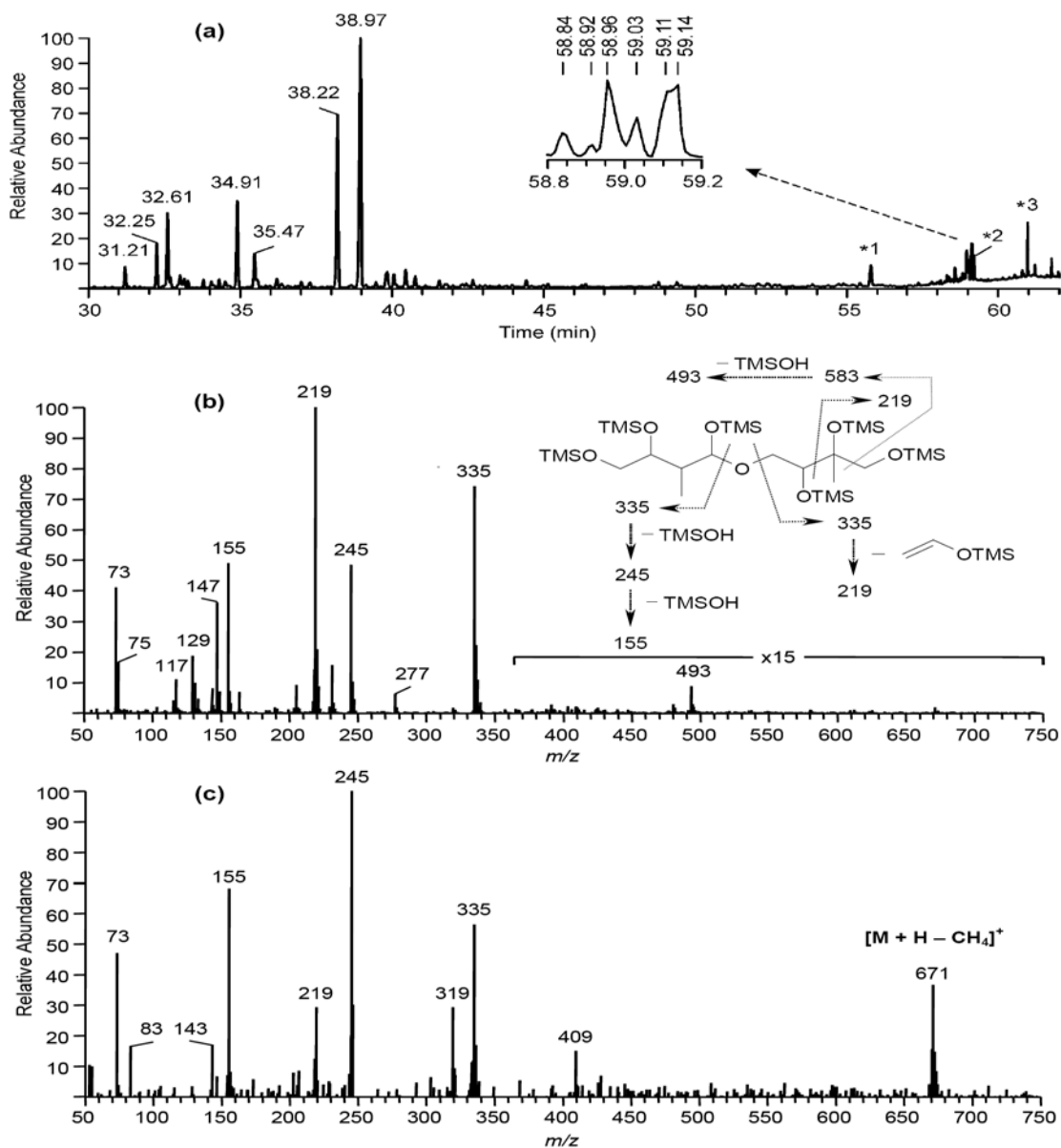


Figure 2.10. (a) GC/MS TIC of isoprene low-NO_x SOA. The insert shows the *m/z* 219 EIC for the dimeric products eluting between 58.8 and 59.2 min. Peak identifications: RTs 31.21, 32.25 and 32.61 min: C₅ alkene triols; RTs 34.91 and 35.47 min: unstable products tentatively characterized as 2-methyltetrol performate derivatives; RTs 38.22 and 38.97 min: 2-methyltetrols (2-methylthreitol and 2-methylerythritol, respectively). The EI spectra for the latter seven compounds are provided in Fig.2.20. The peaks labeled *1, *2 and *3 were also present in the laboratory controls and were identified as palmitic acid, stearic acid and palmitoyl monoglyceride, respectively. (b) averaged EI spectrum for the dimeric products eluting between 58.8 and 59.2 min and fragmentation scheme; and (c) averaged CI(CH₄) spectrum for the latter products.

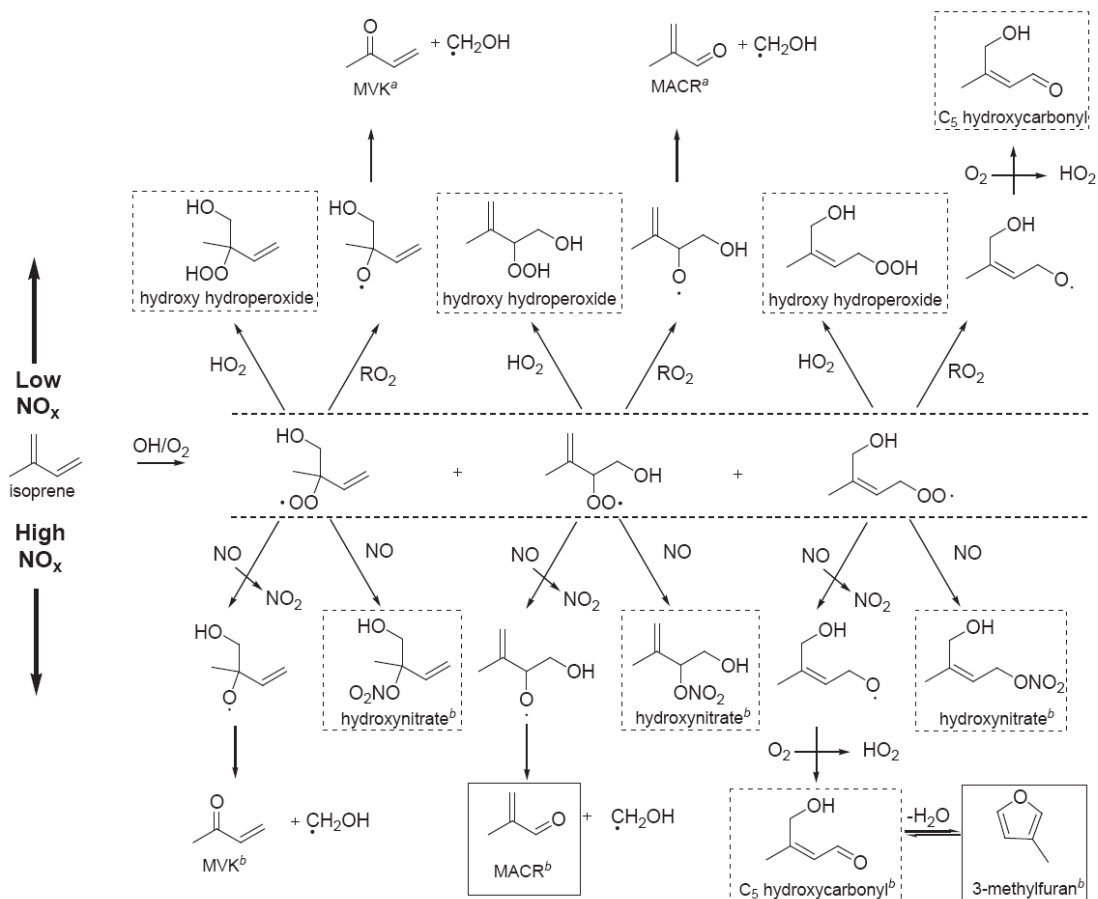


Figure 2.11. Reaction mechanism of isoprene oxidation under low- and high- NO_x conditions. Dotted boxes indicate possible SOA precursors, whereas black boxes indicate known SOA precursors. For simplicity, only three of the eight initial isoprene hydroxyperoxy (RO_2) radicals are shown. $\text{RO}_2 + \text{RO}_2$ reactions leading to diols and other hydroxycarbonyls have been omitted for simplicity.

^a Miyoshi et al.³¹ showed that $[\text{isoprene}]_0/[\text{H}_2\text{O}_2]$ determines molar yields of MVK, MACR, and formaldehyde under low- NO_x conditions.

^b Kroll et al.¹⁶ summarized molar yields of gas-phase products from isoprene oxidation under high- NO_x conditions reported in the literature.

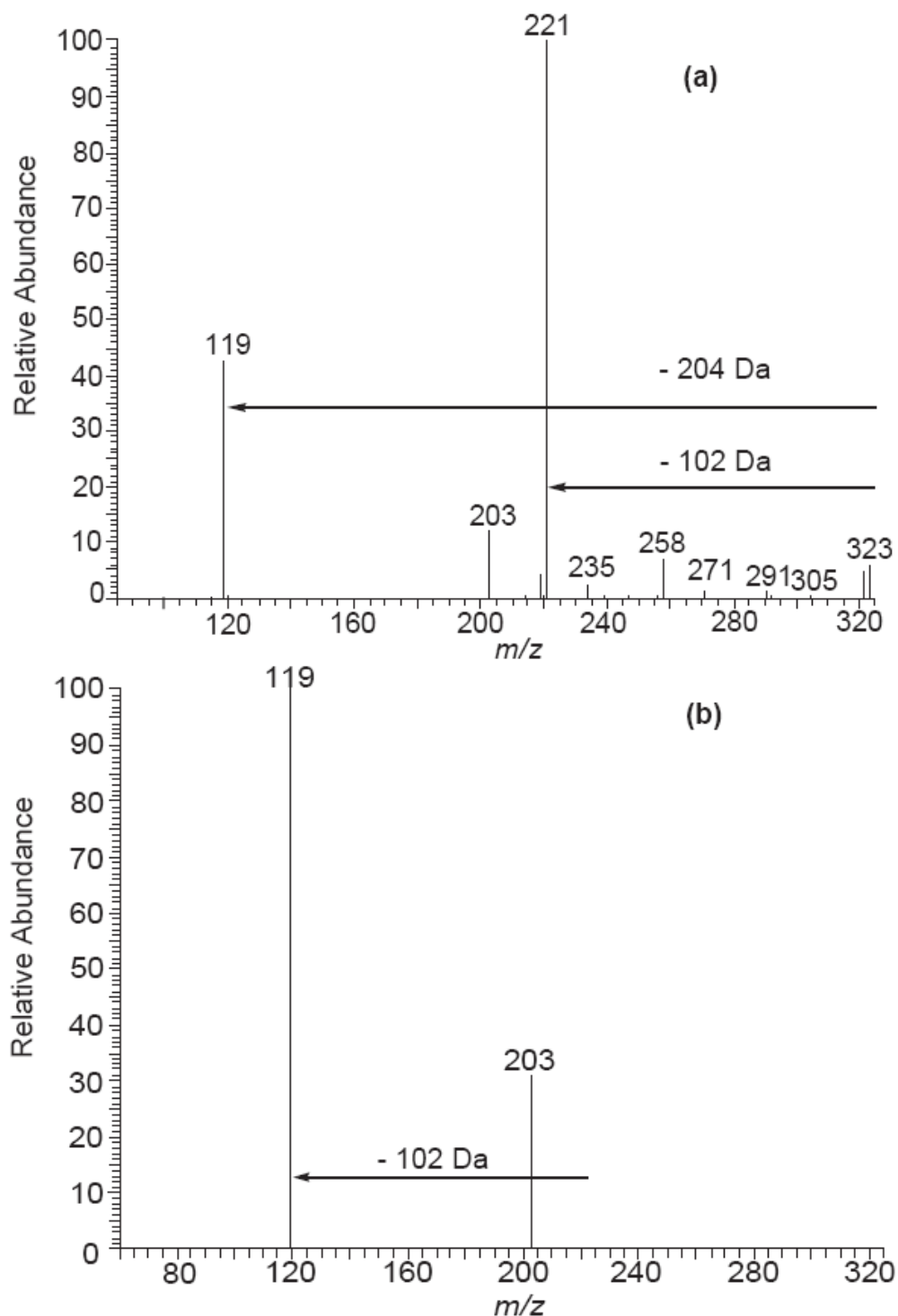


Figure 2.12. ESI-ITMS negative mode product ion spectra from a high- NO_x isoprene SOA sample (Experiment 9). (a) MS^2 spectrum for an isolated m/z 323 ion. Two neutral losses of 102 Da are observed as shown by the product ions m/z 221 and 119. (b) MS^3 spectrum for an isolated m/z 323 ion generated from the further fragmentation of the dominant daughter ion ($= m/z$ 221) in the MS^2 spectrum. These spectra indicate that 2-MG ($[M - H]^-$ ion $= m/z$ 119) is a monomer for the oligomeric m/z 323 ion.

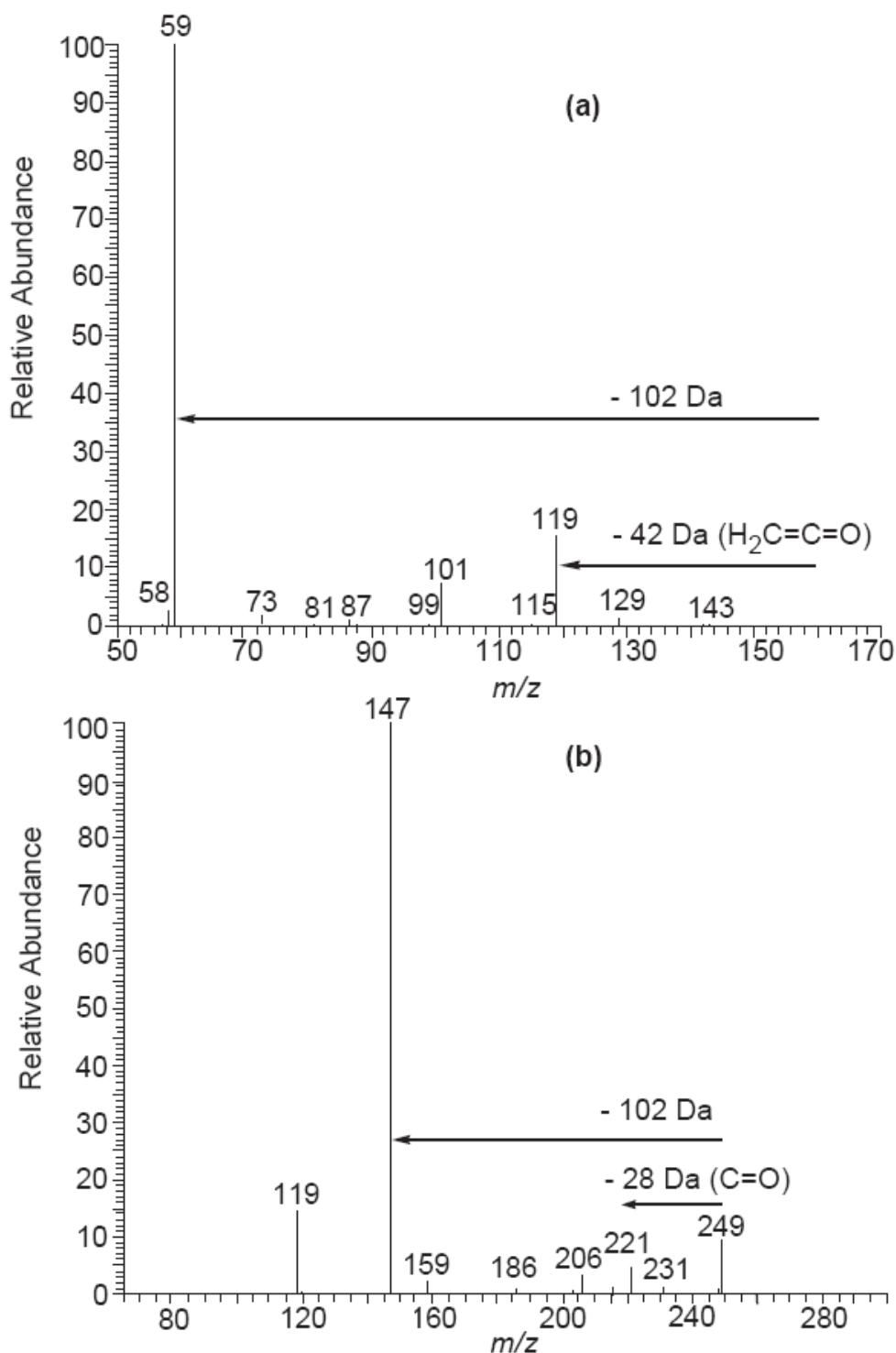


Figure 2.13. ESI-ITMS negative mode product ion mass spectra providing evidence for *mono*-acetate and *mono*-formate oligomers in high- NO_x SOA. (a) Product ion mass spectrum for a *mono*-acetate dimer (m/z 161). (b) Product ion mass spectrum for a *mono*-formate trimer (m/z 249).

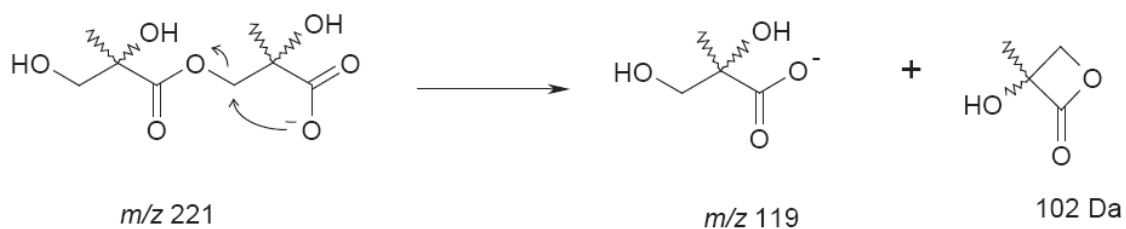


Figure 2.14. Proposed charge-directed nucleophilic reaction occurring during collisional activation in (-)ESI-ITMS, explaining the observation of 102 Da (2-hydroxy-2-methylpropiolactone) losses from oligomeric high-NO_x SOA.

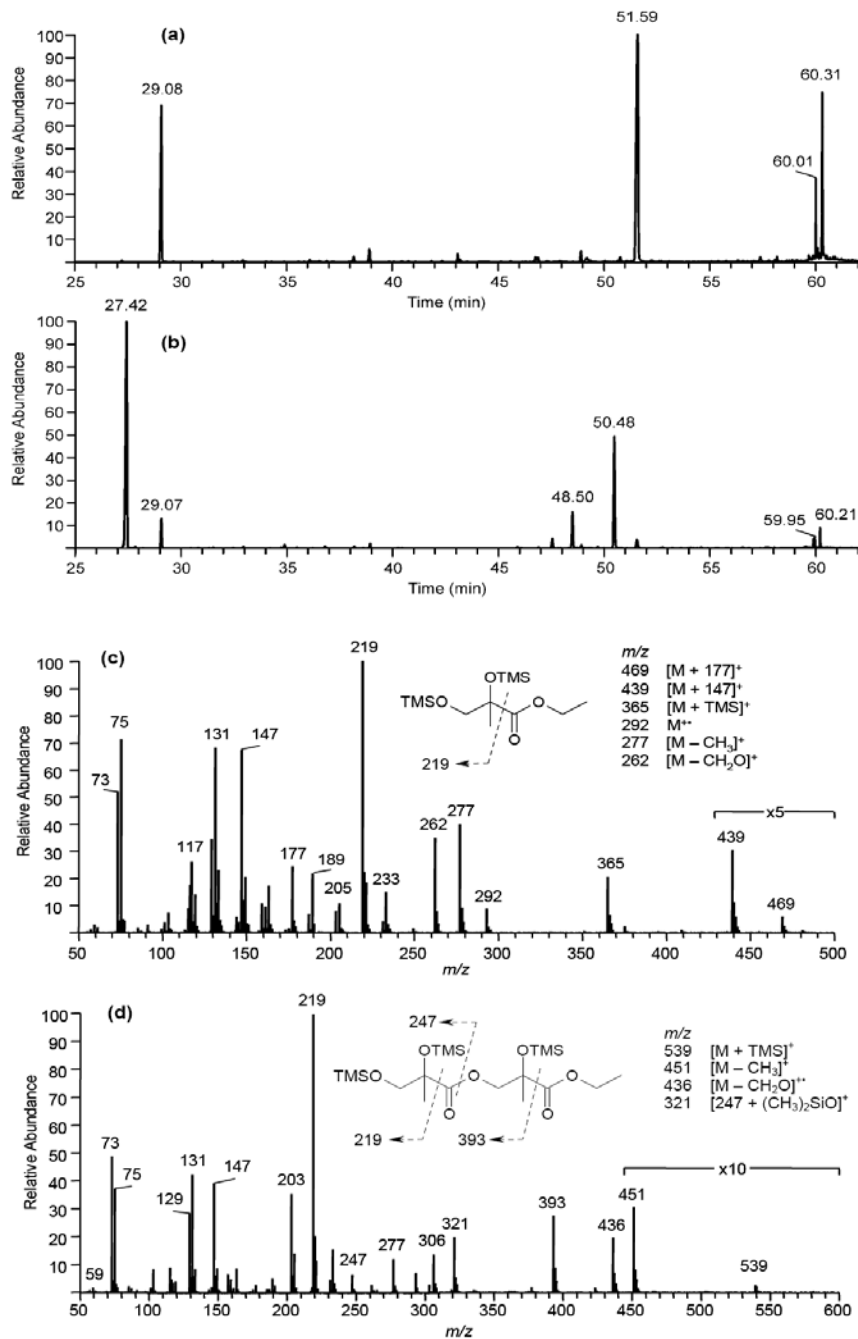


Figure 2.15. (a) GC/MS EIC ($= m/z$ 219) for high- NO_x isoprene nucleation sample (Experiment 5) treated only with TMS derivatization. (b) GC/MS EIC ($= m/z$ 219) for a duplicate sample of the same experiment (Experiment 5) in part a, but treated this time by hydrolysis/ethylation followed by TMS derivatization. (c) EI mass spectrum for ethyl ester of 2-MG acid detected in part b (RT = 27.42 min). (d) EI mass spectrum for ethyl ester of linear 2-MG acid dimer detected in part b (RT = 50.48 min). The hydrolysis/ethylation followed by TMS derivatization results presented here confirm the existence of polyesters in high- NO_x SOA.

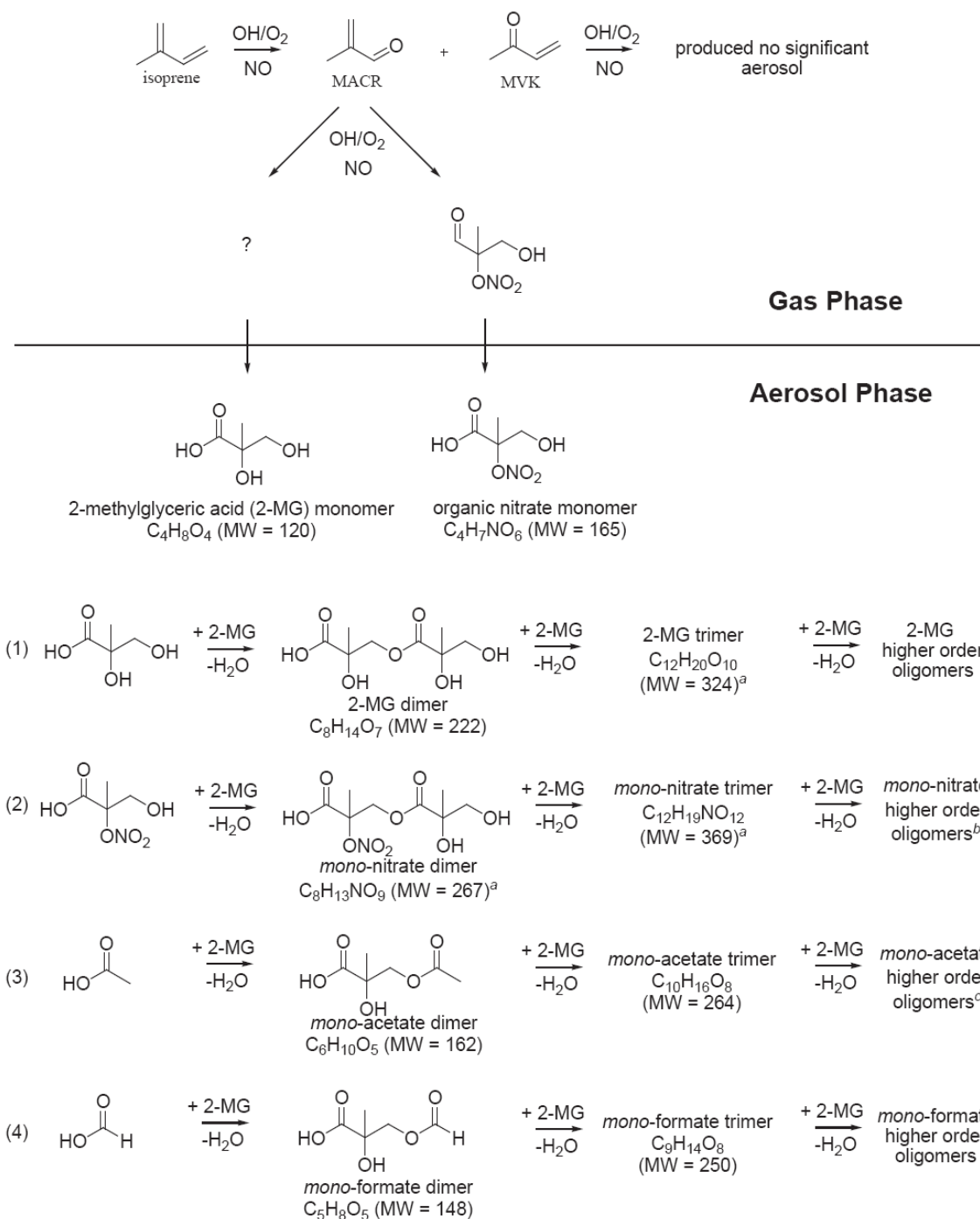


Figure 2.16. Proposed mechanism for SOA formation from isoprene photooxidation under high- NO_x conditions. Symbol used: ?, further study needed in order to understand the formation (in gas/particle phase) of 2-MG.

^a Elemental compositions confirmed by high-resolution ESI-MS.

^b Elemental composition of *mono-nitrate* tetramer (MW = 471) confirmed by high-resolution ESI-MS.

^c Elemental compositions of *mono-acetate* tetramer and pentamer (MW = 366 and 468, respectively) confirmed by high-resolution ESI-MS.

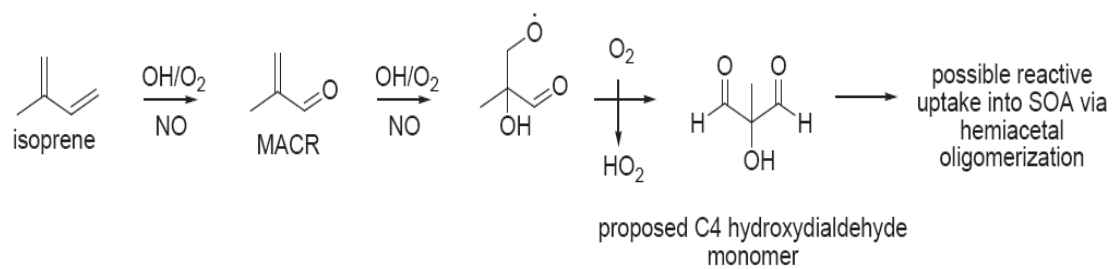


Figure 2.17. Proposed gas-phase formation mechanism for a C₄ hydroxydialdehyde monomer, possibly accounting for a fraction of the unidentified SOA mass in high-NO_x experiments.

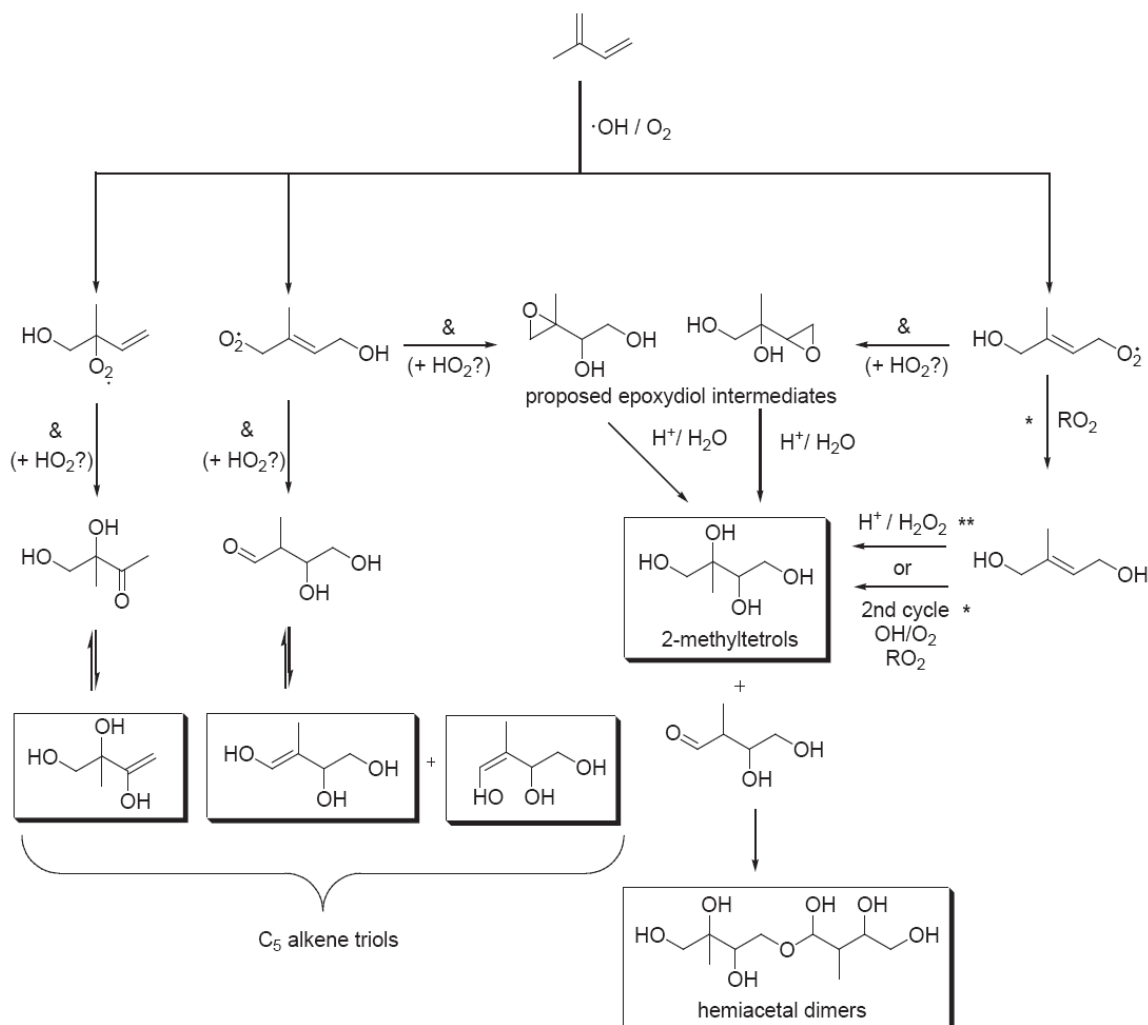


Figure 2.18. Low- NO_x SOA formation pathways as elucidated by GC/MS. Boxes indicate products detected in low- NO_x SOA. Symbols used: &, further study needed for the formations of the hypothetical carbonyl diol and epoxydiol intermediates which may result from the rearrangements of RO_2 radicals and/or hydroperoxides; *, for details about this pathway leading to 2-methyltetrols and also holding for isomeric products, see reference 7; **, for details about this alternative pathway, see reference 14. 2-methyltetrol performate derivatives (shown in Table 2.4) were omitted for simplicity; however, these could serve as precursors for 2-methyltetrols if in the presence of acid and water.

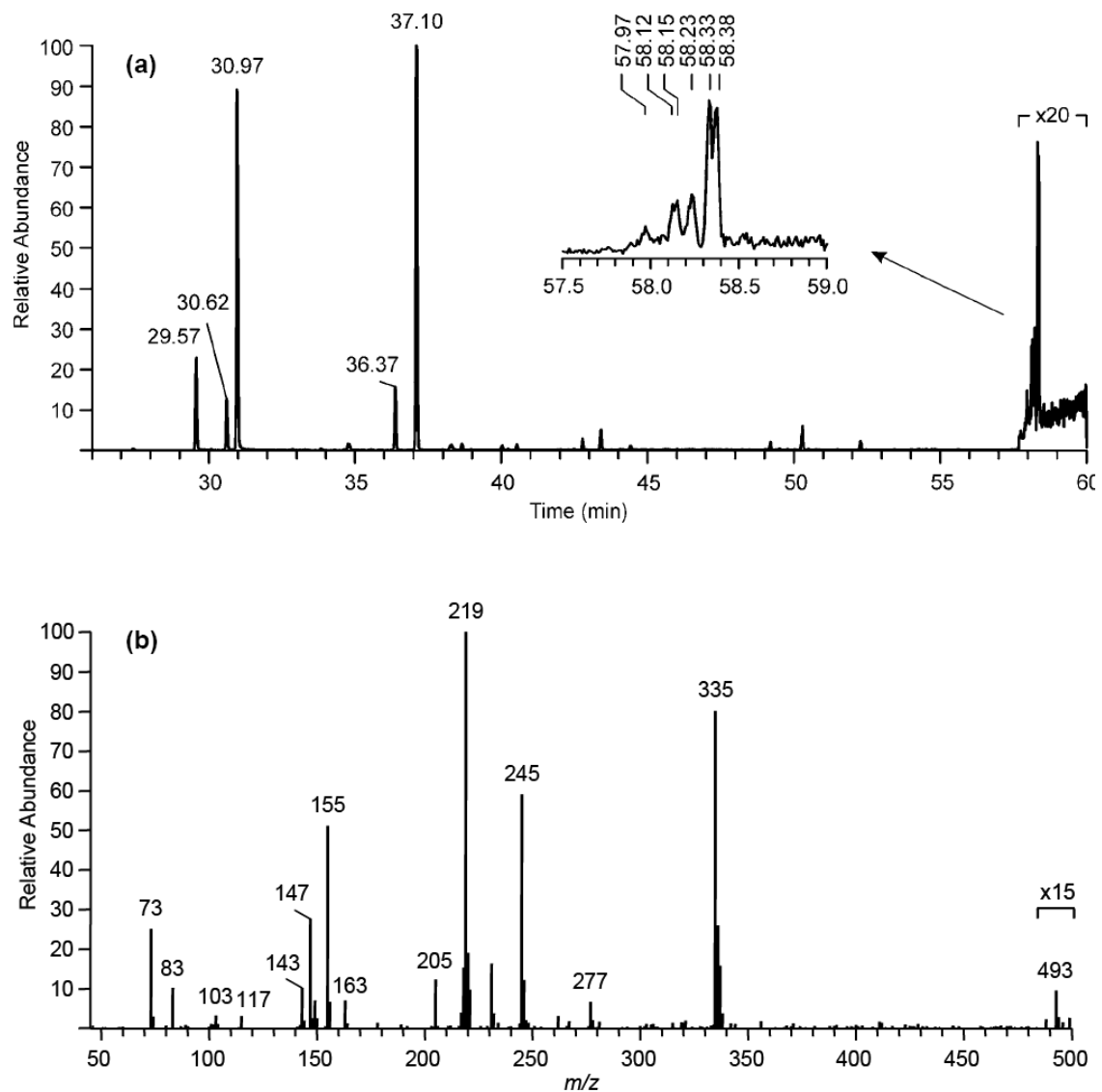
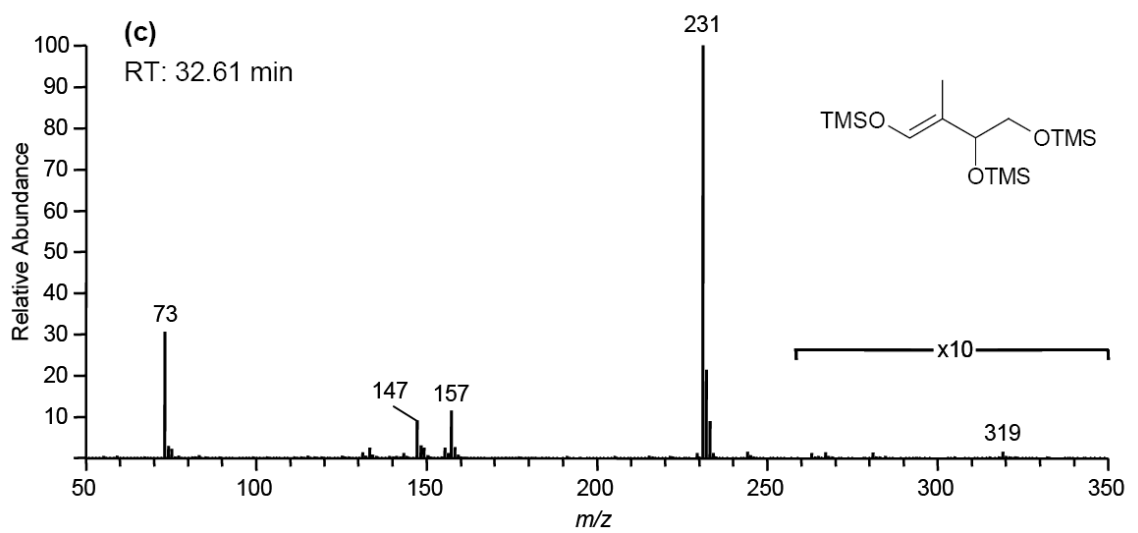
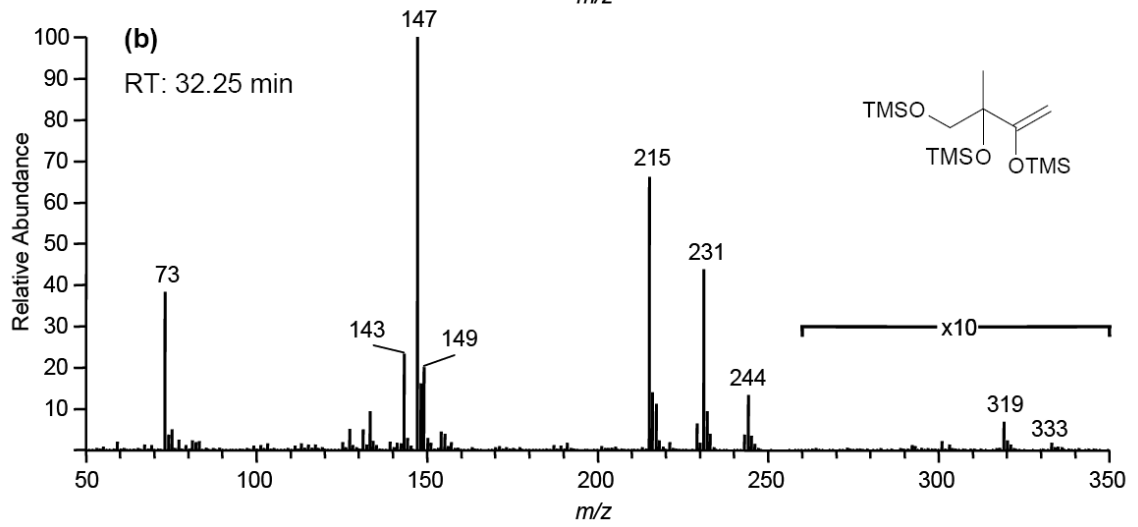
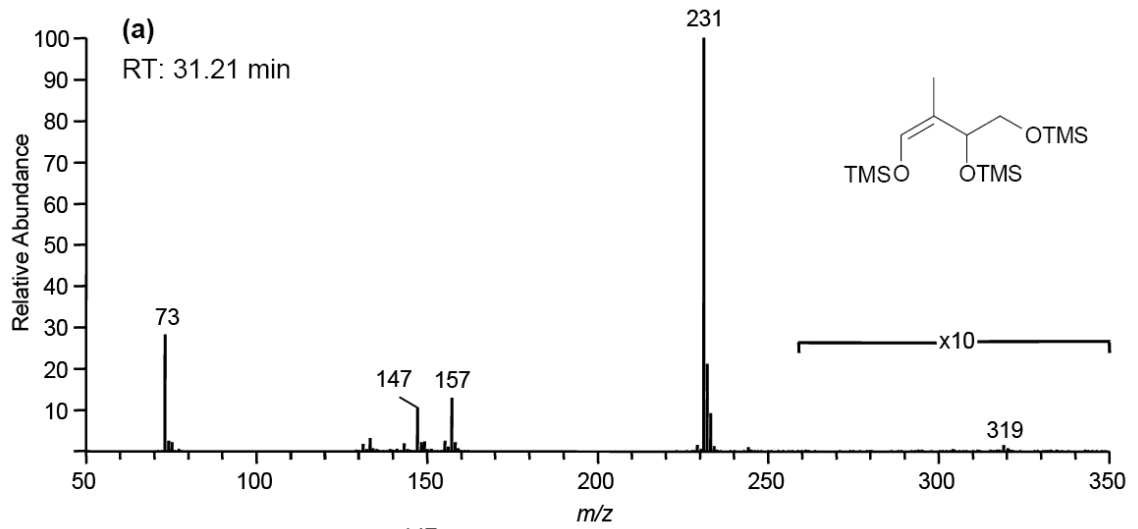
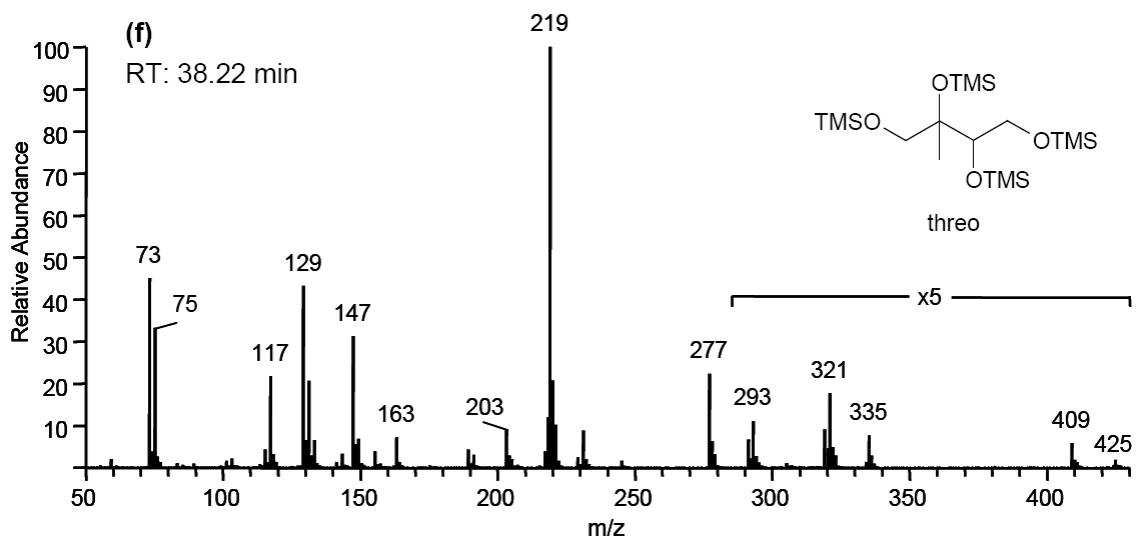
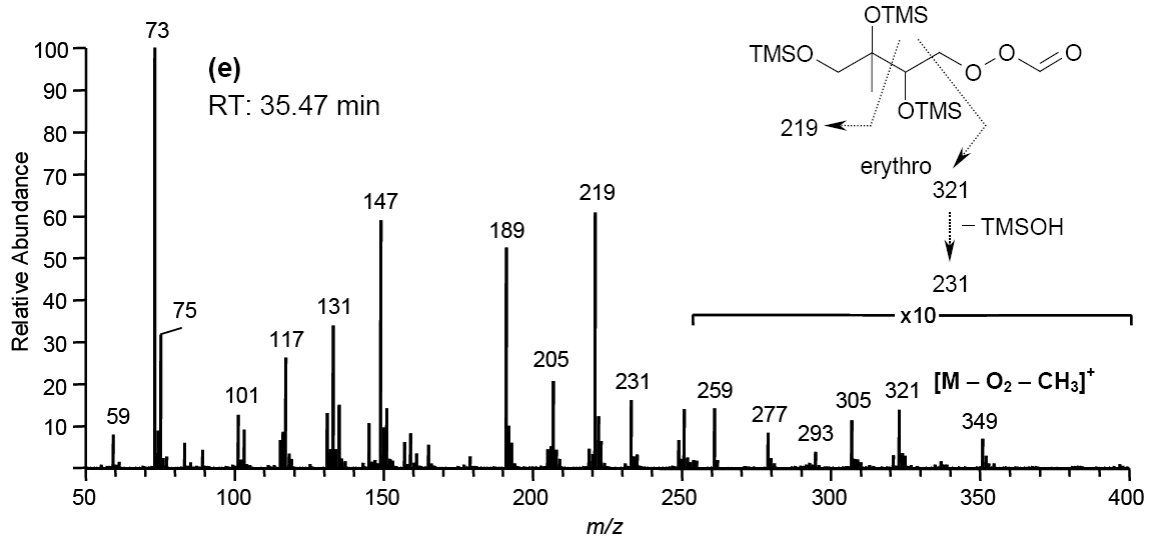
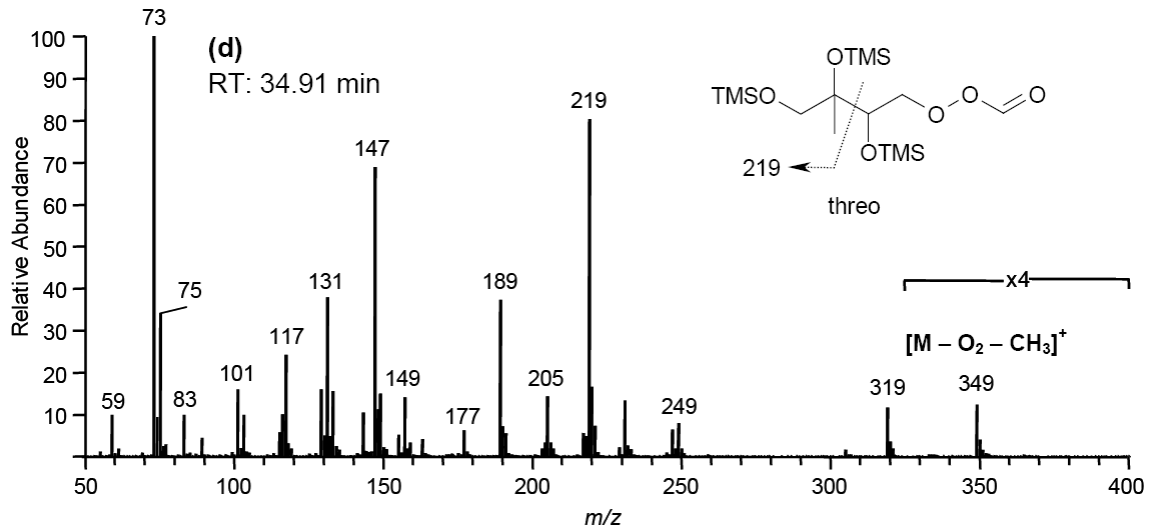


Figure 2.19. (a) GC/MS EIC using specific ions for the TMS derivatives of 2-methyltetrols (m/z 219), C_5 alkene triols (m/z 231), and hemiacetal dimers (m/z 219 and 335) for a $PM_{2.5}$ aerosol sample collected in Rondônia, Brazil, during the onset of the wet season from 10-12 November 2002 (39 h collection time). The insert shows a detail of the isomeric hemiacetal dimers, formed between 2-methyltetrols and C_5 dihydroxycarbonyls, which elute between 57 and 59 min; (b) averaged EI mass spectrum (only limited mass range m/z 50 – 500 available) for the TMS derivatives of the isomeric hemiacetal dimers.





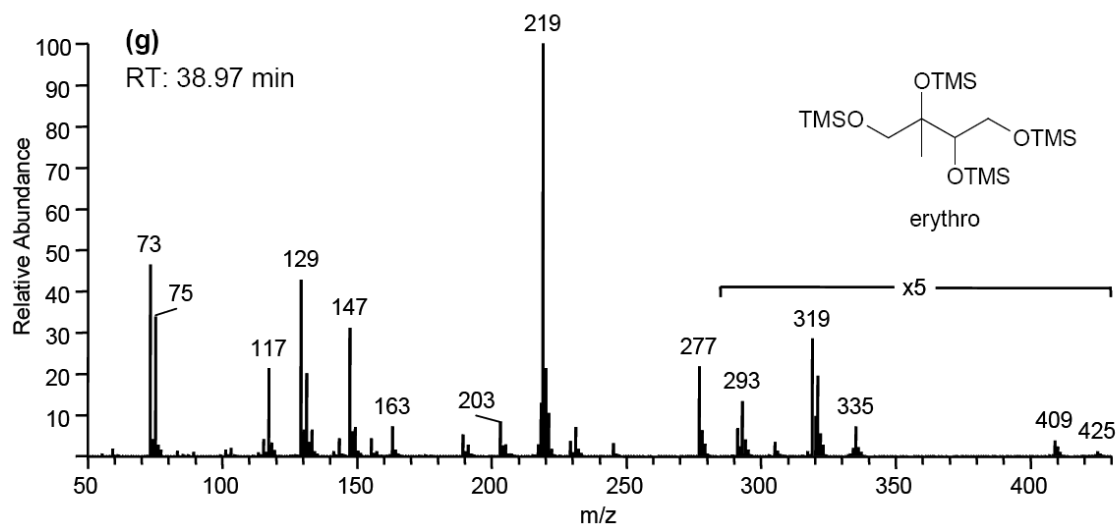


Figure 2.20. EI mass spectra for low-NO_x SOA products detected in the GC/MS TIC of Figure 2.10a. (a), (b), and (c) correspond to mass spectra of isomeric C₅ alkene triols. (d) and (e) correspond to mass spectra of diastereoisomeric 2-methyltetrol performate derivatives. (f) and (g) correspond to mass spectra of diastereoisomeric 2-methyltetrols.

Chapter 3

Secondary Aerosol Formation from Atmospheric Reactions of Aliphatic Amines*

*This chapter is reproduced by permission from “Secondary aerosol formation from atmospheric reactions of aliphatic amines.” by S.M. Murphy, A. Sorooshian, J. H. Kroll, N. L. Ng, P. Chhabra, C. Tong, J.D. Surratt, E. Knipping, R. C. Flagan, and J. H. Seinfeld, *Atmospheric Chemistry and Physics*, 7(9), 2313-2337, 2007. Copyright 2007 Authors. This work is licensed under a Creative Commons License.

3.1 Abstract

Although aliphatic amines have been detected in both urban and rural atmospheric aerosols, little is known about the chemistry leading to particle formation or the potential aerosol yields from reactions of gas-phase amines. We present here the first systematic study of aerosol formation from the atmospheric reactions of amines. Based on laboratory chamber experiments and theoretical calculations, we evaluate aerosol formation from reaction of OH, ozone, and nitric acid with trimethylamine, methylamine, triethylamine, diethylamine, ethylamine, and ethanolamine. Entropies of formation for alkylammonium nitrate salts are estimated by molecular dynamics calculations enabling us to estimate equilibrium constants for the reactions of amines with nitric acid. Though subject to significant uncertainty, the calculated dissociation equilibrium constant for diethylammonium nitrate is found to be sufficiently small to allow for its atmospheric formation, even in the presence of ammonia which competes for available nitric acid. Experimental chamber studies indicate that the dissociation equilibrium constant for triethylammonium nitrate is of the same order of magnitude as that for ammonium nitrate. All amines studied form aerosol when photooxidized in the presence of NO_x with the majority of the aerosol mass present at the peak of aerosol growth consisting of aminium (R_3NH^+) nitrate salts, which re-partition back to the gas phase as the parent amine is consumed. Only the two tertiary amines studied, trimethylamine and triethylamine, are found to form significant non-salt organic aerosol when oxidized by OH or ozone; calculated organic mass yields for the experiments conducted are similar for ozonolysis (15% and 5% respectively) and photooxidation (23% and 8% respectively). The non-salt organic aerosol formed appears to be more stable than the

nitrate salts and does not quickly repartition back to the gas phase.

3.2 Introduction

Amines are emitted into the atmosphere from a variety of sources including meat cooking, biomass burning, motor vehicle exhaust, industrial processes, and marine organisms. The dominant anthropogenic source is emissions from animal husbandry operations (Table 3.1). While amine emissions from animal husbandry are typically reported to be two to three orders of magnitude less than those of ammonia (Ngwabie and Hintz, 2005; Schade and Crutzen, 1995), at least one study has reported gas-phase concentrations of amines in the hundreds of ppb in areas of intense animal husbandry (Rabaud et al., 2003). Though emission estimates vary widely, amines have been detected in marine, rural, and urban atmospheres in the gas phase, particle phase, and within aqueous fog and rain drops (Zhang and Anastasio, 2003). Mass spectrometric studies by both Murphy (1997) and Angelino (2001) have shown that molecular ions typically associated with amines are present in ambient particles, especially in air masses from agricultural regions. Tan et al. (2002) identified particle phase amines during multiple smog events in Toronto's winter atmosphere. Recent field studies suggest that organic nitrogen species could be an appreciable fraction of organic aerosol mass (Beddows et al., 2004; Mace et al., 2003; Makela et al., 2001; McGregor and Anastasio, 2001; Neff et al., 2002; Simoneit et al., 2003; Tan et al., 2002), although the relative importance of amines as a source of particulate organic nitrogen remains unclear.

During the 1970's, interest in the gas-phase atmospheric chemistry of amines focused on carcinogenic nitrosamines formed when amines are photooxidized (Pitts et al., 1978). It was subsequently determined that gas-phase nitrosamines photolyze rapidly in

the troposphere and are believed to pose a minimal threat to human health. More recently, toxicology studies have demonstrated that particulate organic nitrogen species are associated with adverse health effects (Hamoir et al., 2003). Nemmar (2002) found that particles coated with amines produced a significant increase in the rate of blood clots (by nearly 4 times) when installed in the trachea of hamsters; in contrast, the effects of particles coated with carboxylic acids and unmodified polystyrene particles were not statistically significant when compared to the control group of hamsters.

Amines are oxidized in the atmosphere by the hydroxyl radical (OH), ozone (O₃), and possibly by the nitrate radical (NO₃), with measured rate constants suggesting that the reaction rates of ozone and OH with amines are competitive during the day if ozone levels are in the tens to hundreds of ppb (Tuazon et al., 1994). The nitrate radical may play a significant role in amine oxidation at night, though very little is known about this pathway. While many of the gas-phase oxidation pathways involving OH and ozone have been elucidated, secondary aerosol formation resulting from the photooxidation of amines has received limited attention. Also, because amines are basic compounds, they can form particulate salts through reactions with gas-phase acids present in the atmosphere (HNO₃, H₂SO₄),



Reactions (R1) and (R2) are analogous to those of ammonia to form ammonium sulfate and ammonium nitrate. While the equilibria between gas-phase ammonia and nitric or sulfuric acid to form particle-phase salts have been thoroughly investigated and the thermodynamic parameters governing these reactions are well known (Mozurkewich,

1993; Stelson and Seinfeld, 1982), similar thermodynamic parameters for amine systems were not available prior to this study.

There have been a limited number of laboratory chamber experiments in which aerosol resulting from amine photooxidation was observed (Angelino et al., 2001; Pitts et al., 1978). Aerosol yields, the relative importance of acid-base chemistry, and the oxidative pathways leading to particle formation remain poorly understood. The goal of the present work is to use controlled laboratory chamber studies to evaluate the aerosol forming potential, by acid-base reactions, photooxidation and ozonolysis, of aliphatic amines known to be present in the atmosphere. The amines studied (with abbreviation used) are: trimethylamine (TMA), methylamine (MA), triethylamine (TEA), diethylamine (DEA), ethylamine (EA), and monoethanolamine (MEA), which will be referred to as ethanolamine in this paper.

3.3 Experimental

All experiments (Table 3.2) were carried out in the Caltech dual 28 m³ FEP Teflon chambers (Cocker et al., 2001; Keywood et al., 2004). The chambers are surrounded by banks of black lights (276GE350BL) which output ultraviolet light predominantly between 300 and 400 nm, with a maximum at 354 nm. Ports allow for the introduction of clean, dry (< 10% RH) air, gas-phase reagents, inorganic seed aerosol, and for measurement of NO, NO_x, O₃, RH, temperature, and particulate mass, size, number concentration, and chemistry. Temperature is held at 20°C, increasing to 25°C during photooxidation experiments using the black lights. Commercial monitors (Horiba) are used to measure O₃ (by UV absorption) and NO/NO_x (NO_x conversion to NO by

activated carbon, followed by NO + O₃ chemiluminescence). Both amines and nitric acid (when added) were injected into the chamber by passing a stream of dry, clean air over a known volume of high purity liquid phase compound. The purity and source of the amines used in this study are: trimethylamine (45% solution in H₂O, Fluka), methylamine (40 wt.% solution in H₂O, Sigma-Aldrich), triethylamine (>99.5% purity, Sigma Aldrich), diethylamine (> 99.5% purity, Sigma Aldrich), ethylamine (70 wt.% solution in H₂O, Aldrich), ethanolamine, (≥ 99% purity, Sigma Aldrich). Gas-phase concentrations of amines and nitric acid were not directly measured and were instead estimated based on the volume of liquid phase amine injected; these concentrations represent the maximum possible within the chamber in the absence of wall loss.

“Seed” aerosol was generated by atomizing a solution of 0.015 M ammonium sulfate or 0.75 M ammonium nitrate. Particle-phase measurements were made by an Aerodyne Time of Flight Aerosol Mass Spectrometer (cToF-AMS), a Particle-Into-Liquid Sampler coupled to Ion Chromatography (PILS-IC), and a differential mobility analyzer (DMA, TSI 3760). During experiment number 20 (Table 3.2), chamber particles were collected onto a Teflon (PALL Life Sciences, 47-mm diameter, 1.0-μm pore size) filter for analysis by mass spectrometry using both Matrix Assisted Laser Desorption Ionization (MALDI) and electrospray ionization (ESI) to determine how spectra from these ionization techniques compared to the electron impact ionization spectra of the cToF-AMS. Details of the extraction and analysis methodology used for the Teflon filter are given in Surratt et al. (2006).

3.3.1 PILS-IC

The particle-into-liquid sampler coupled with ion chromatography is a quantitative technique for measuring water-soluble ions, including inorganic, organic acid, and amine ions in aerosol particles. The PILS-IC used in this study (Sorooshian et al., 2006) is based on the prototype design (Weber et al., 2001) with key modifications, including integration of a liquid sample fraction collector and real-time control of the steam injection tip temperature. Chamber air is sampled through a 1 μm cut-size impactor and a set of three denuders (URG and Sunset Laboratories) to remove inorganic (basic and acidic) and organic gases that would otherwise bias aerosol measurements. Sample air mixes with steam in a condensation chamber where rapid adiabatic mixing produces a high water supersaturation. Droplets grow sufficiently large to be collected by inertial impaction before being delivered to vials held on a rotating carousel. The contents of the vials are subsequently analyzed off-line using a dual IC system (ICS-2000 with 25 μL sample loop, Dionex, Inc.) for simultaneous anion and cation analysis.

Data for the following ions are reported: acetate, formate, nitrate, sulfate ammonium, methylammonium, dimethylammonium, trimethylammonium, ethylammonium, diethylammonium, and triethylammonium. The PILS-IC technique cannot be used to speciate many of the organic compounds that make up the total aerosol mass since these are not sufficiently ionic in water to have affinity for the IC columns used (anion: Dionex AS-11 column 2 \times 250 mm, ASRS Ultra II 2-mm suppressor, potassium hydroxide eluent; cation: CS12A column 2 \times 250 mm, CSRS Ultra II 2-mm suppressor, methanesulfonic acid eluent); nevertheless, all of the amine salts formed in the experiments reported here were successfully speciated. It should be noted that ammonium, methylammonium, and ethylammonium co-elute; additional co-eluting pairs

are diethylammonium:trimethylammonium and potassium:dimethylammonium. While potassium was never expected to be present and ammonium formation was not anticipated for many of the experiments, background levels of these species in the IC baseline noise did interfere with quantification of co-eluting species. The limit of detection (LOD) for each ion (NH_4^+ , NO_3^- , acetate, formate, and the six aforementioned amine species) is defined in this study as the air-equivalent concentration of the lowest concentration standard that is distinct from baseline noise in the IC plus three times the standard deviation ($n=3$) of this measurement. The LOD's for the ions measured using the PILS-IC technique for this study are all below $0.1 \mu\text{g m}^{-3}$, with the exceptions of trimethylamine and triethylamine, which have LOD's of 0.60 and $0.89 \mu\text{g m}^{-3}$, respectively. In all experiments, chamber air containing gas-phase amine and nitric acid (when added) was run through a particle filter and sampled by the PILS-IC; none of the amines was ever detected in these filtered vials, confirming that the carbon denuder was able to completely remove gas-phase species and that the PILS-IC signal is entirely a result of aerosol-phase compounds.

3.3.2 Aerodyne cToF-AMS

The design parameters and capabilities of the cToF-AMS instrument are described in detail elsewhere (Drewnick et al., 2004a, b). Briefly, chamber air enters the instrument through a $100 \mu\text{m}$ critical orifice at a flowrate of $1.4 \text{ cm}^3 \text{ s}^{-1}$. Particles with a vacuum aerodynamic diameter between roughly 50 and 800 nm are efficiently focused by an aerodynamic lens, passed through a 1% chopper, and then impacted onto a tungsten vaporizer. The chopper can be operated in three modes: (1) completely blocking the beam

to gather background mass spectra; (2) out of the beam's path to collect ensemble average mass spectra over all particles sizes; (3) chopping the beam to create size-resolved mass spectra. The vaporizer is set at ~ 550 °C to ensure complete volatilization of the aerosol. Once vaporized, molecules undergo electron impact ionization at 70 eV and are orthogonally pulsed every 19 μs into the time of flight mass analyzer. The resolution of the mass analyzer is ~ 800 ($M/\Delta M$). For all mass spectra shown in this work the ion signal is represented as sticks, the height of which represent the raw ion signal integrated over 1 amu bins. These stick mass spectra are divided into different chemical species based on the methodology of Allan et al. (2003), with exceptions noted in the text. The limits of detection, calculated as three times the standard deviation of the noise for particle filtered air are $< 0.05 \mu\text{g m}^{-3}$ for all species measured.

3.3.3 Effective density

Calculating the density of aerosol particles is important for two reasons. First, multiplying the aerosol volume measured by the DMA by the material density allows one to calculate aerosol mass yields. (The cToF-AMS cannot be used to directly quantify aerosol mass because the fraction of particles that bounce off of the vaporizer is unknown and the PILS-IC does not measure the mass of non-ionic species) Second, changes in the density give an indication of alterations in particle morphology during secondary aerosol formation.

The effective density (ρ_{eff}) is a function of the vacuum aerodynamic diameter (d_{va}) measured by the cToF-AMS and the mobility diameter (d_m) measured by the DMA (DeCarlo et al., 2004), where ρ_o is unit density (1 g cm^{-3}), ρ_m is the material density, C_c is

the slip correction factor, d_{ve} is the volume equivalent diameter, δ is a measure of the internal void space defined by $\delta=(\rho_m/\rho_p)^{1/3}$

$$\rho_{eff} = \frac{d_{va}}{d_m} \rho_o = \rho_m \frac{C_c(d_{ve})}{\delta^3 \chi_t \chi_v C_c(d_m)} \quad (1)$$

where ρ_p is the particle density, χ_t is the dynamic shape factor in the transition regime, and χ_v is the dynamic shape factor in the free molecular regime.

As described in Bahreini et al. (2005) and Decarlo et al. (2004), the effective density is equivalent to the material density if the shape factor and slip correction factor are unity and the internal void fraction is zero. These assumptions are probably slightly incorrect for amine salts and amine oxidation products, given that ammonium nitrate particles have an effective density 20 percent less than the material density of ammonium nitrate when ρ_{eff} is calculated using simultaneous cToF-AMS and DMA measurements (Jayne et al., 2000). Indeed the effective densities calculated in this way for the ammonium nitrates are less than the literature values. While there is no need to use effective densities to calculate the mass of pure salts (the PILS-IC is able quantitatively measure these), it is necessary to use effective densities (as an approximation of the material density) to calculate the mass of aerosol formed during photooxidation and ozonolysis because non-ionic species are present.

To calculate the effective density, one represents the DMA volume distribution, normally expressed as $dV/d\log(d_m)$, as $dV/d\log(\rho_{eff}d_m)$ and adjusts ρ_{eff} until this distribution (with peak height normalized to 1) aligns in diameter space with the mass distribution from the cToF-AMS, $dM/d\log(d_{va})$ (peak height also normalized to 1). The two distributions align when the correct effective density is used because $\rho_{eff}d_m = d_{va}\rho_o$ (if unity shape and slip correction factors and zero internal void fraction are assumed).

Figure 3.1a shows the calculated effective density of triethylammonium nitrate (TEAN) is $1.0 \pm 0.1 \text{ g cm}^{-3}$ while the effective density of the aerosol formed from photolysis of TEA (mixed TEAN and products from TEA oxidation) has a slightly increased effective density of $1.1 \pm 0.1 \text{ g cm}^{-3}$.

3.3.4 Oxidation experiments

Three types of amine oxidation experiments were conducted in this study: (1) Photooxidation in the absence of NO_x , (2) Photooxidation in the presence of NO_x , and (3) dark ozonolysis. Hydrogen peroxide (H_2O_2) was used as the OH radical precursor for all of the NO_x -free photooxidation experiments and many of the high NO_x experiments (see Table 3.2 for details). H_2O_2 is introduced by bubbling 5 L min^{-1} of humidified room-temperature air for 2.5 h through a 50% H_2O_2 solution (Aldrich), through a particle filter to avoid the introduction of droplets, and finally into the chamber. The mixing ratio of H_2O_2 achieved using this method has been previously estimated to be between 3 and 5 ppm (Kroll et al., 2006). To minimize potential uptake of H_2O_2 by the aerosol, all experiments were carried out under dry ($\text{RH} < 10\%$) conditions. To determine if the presence of hydrogen peroxide significantly affected the particle-phase chemistry, numerous high NO_x photooxidation experiments were conducted in the absence of H_2O_2 , some with the gas-phase amine and NO_x alone, and others where propene was added to generate higher levels of OH in the chamber and increase the rate of oxidation (see Table 3.2 for details). For all photooxidation studies, H_2O_2 , NO_x , propene, or a combination of these was injected first. For many experiments using NO_x , this step was followed by the injection of nitric acid or, occasionally, ammonium sulfate (see Table 3.2 for details).

After the HNO_3 or ammonium sulfate had mixed throughout the chamber, the amine was added. When nitric acid is present, formation of aminium nitrate salt occurs once the amine is injected. By using a similar concentration of HNO_3 in all experiments, we were able to roughly control the size distribution of the aerosol. Nucleating the aminium nitrate before the start of oxidation also allowed us to measure the chemistry of pure salt particles in situ with the cToF-AMS and PILS-IC. Photooxidation reactions were initiated by irradiation from the black lights surrounding the chamber. Ozonolysis experiments were conducted in the dark in the absence of an OH scavenger. The order of reactant introduction for ozonolysis experiments was: nitric acid, amine, and finally ozone. Between experiments, the chamber was continuously flushed with clean air and irradiated with UV light. Contamination from previous experiments was occasionally observed and has been accounted for in the analyses.

3.4 Atmospheric reaction pathways of amines

At the outset, it is useful to frame the results of this study by outlining a hypothesis for the atmospheric reaction pathways of amines. Direct or indirect evidence of most of these pathways has been observed during the chamber experiments in this study.

Because amines are one of relatively few basic atmospheric compounds, they have the potential to undergo rapid acid-base reactions to form salt particles in the presence of nitric or sulfuric acid. Formation of salt particles depends on temperature, the identity of the amine, and the concentrations and identities of acidic species present. Formation of aminium salts also depends indirectly on the concentration of ammonia,

which will compete with amines for acidic molecules. Once aminium-salt particles are formed, they can revolatilize, undergo particle-phase reactions (including oxidation), or serve as a site for condensation of other organic species. Condensation of organics onto the salts particles may form a barrier that prevents the salts from remaining at equilibrium with the gas phase.

Gas-phase amines can be oxidized by OH, O₃ and possibly NO₃ (OH and O₃ are known to be competitive oxidation agents of amines at atmospherically relevant concentrations while the rate of NO₃ oxidation remains unexplored). Specifics of the known oxidation pathways will be discussed thoroughly in Sect. 3.6. Briefly, the products formed depend on the oxidizing species and the NO_x level. Many of the oxidation products of amines are themselves basic and can undergo reactions with atmospheric acids to form additional salts. Other oxidation products are sufficiently non-volatile to condense directly onto particles without forming salts. Finally, it is possible that certain amines, or their oxidation products, that are too volatile to condense onto dry particles will condense into, and ionize within, aqueous aerosols. Once condensed, amines and their oxidation products may undergo particle-phase reactions to form high molecular weight compounds, or they may be further oxidized into volatile species.

The remainder of the paper is divided into two main sections. In the first section, we investigate salt aerosol formation from acid-base reactions of amines through both laboratory chamber experiments and theoretical estimates. In the second section, aerosol formation resulting from photooxidation and ozonolysis of amines under varying NO_x conditions is addressed.

3.5 Salt aerosol formation from acid-base reactions of amines

3.5.1 Detection of aminium nitrate salts

As described in the Experimental section, nitrate salts were formed by adding the amine of interest to a chamber containing gaseous nitric acid (HNO_3). In all cases, particle nucleation occurred within a few minutes of amine injection. All of the aminium nitrate salts investigated were detected by the cToF-AMS, PILS-IC, and DMA instruments. The mass spectra for the nitrate salts of the amines studied are shown in Fig. 3.2. The spectra are similar to reference electron impact spectra in the NIST database for the gas-phase amines except for additional intensity at m/z 30 and m/z 46 caused by NO^+ and NO_2^+ ion fragments from nitrate (Stein, 2005). The only previous chamber study to focus on aerosol-phase amines was conducted by Angelino et al. (2001) using a laser desorption aerosol time of flight mass spectrometer (ATOFMS). In their study, the spectra of dialkyl ammonium salts exhibited prominent peaks $(M+13)^+$, attributed to ion-molecule reactions within the ionization region of the instrument. We do not observe peaks larger than the molecular ion for any of the salts, indicating that ion-molecule reactions do not occur in the ionization region of the Aerodyne cToF-AMS; this absence of ion-molecule reactions dramatically simplifies mass spectral interpretation.

Though we did not observe ion-molecule reactions, it is important to note that we did observe a dramatic increase in the number of ions detected by the cToF-AMS when the voltages that extract ions from the electron impact region into the flight chamber of the mass spectrometer were altered by a few percent. When the voltages were in this altered state, we observed a further increase in both molecular and fragment amine ions with increasing vaporizer temperature above 550°C . No such correlation between

increased vaporizer temperature and ion signal is observed when the extraction voltages are not in the altered state. Because altering the extraction voltages allows ions formed on the vaporizer surface to enter the mass spectrometer and because amines have low ionization potentials, we believe that the additional ions are formed on the high temperature tungsten surface of the vaporizer. The artificial signal enhancement (increased ion rate) caused by this proposed surface ionization indicates that there is a potential for overestimates of amine concentrations measured by the Aerodyne cToF-AMS if the instrument is not carefully calibrated and tuned. Similar effects caused by the unusually low ionization energy of amines may also occur in other aerosol mass spectrometry instruments. We observed enhancement of up to an order of magnitude by changing the voltages in the instrument a few percent. The m/z with the most prominent increase in ion rate was that corresponding to the molecular ion of the amine being studied. The fact that the molecular ion showed the most dramatic increase further supports the hypothesis that a non-electron impact surface ionization is occurring; 70 eV electron impact ionization typically induces alpha cleavage of amines and little, non-fragmented, molecular ion signal is observed. It should be noted that we have not observed an increase in detected ions when the extraction voltages are shifted when studying aerosol that does not contain amines. Though not investigated further, these observations raise the possibility that this type of tuning might be intentionally used to detect the presence of molecular amine ions.

3.5.2 Atmospheric formation of aminium nitrate salts: theory

Having confirmed that aminium nitrate salts can be generated and detected, we wish to estimate the potential atmospheric importance of aminium nitrate salts relative to ammonium nitrate (typically assumed to be the dominant atmospheric nitrate salt in the fine mode). Based on theory, we estimate the dissociation constants ($K_p = p_{HNO_3} / p_{amine}$) for the gas-particle equilibrium of all amines studied except for ethanolamine, while noting that the estimates have large uncertainties resulting from discrepancies in the literature values for the heats of formation of the aminium nitrate salts. If the required thermodynamic parameters are known, the dissociation constant for a given amine-nitric acid system can be obtained using the integrated form of the Van't Hoff equation,

$$\ln K_p = \frac{\Delta S_{diss}^\circ - \Delta C_{P,diss}}{R} - \frac{\Delta H_{diss}^\circ - T_0 \Delta C_{P,diss}}{RT} + \frac{\Delta C_{P,diss}}{R} \ln \left(\frac{T}{T_0} \right) \quad (2)$$

Entropies of formation for aminium nitrate salts have apparently not been reported in the literature; we estimate them using a molecular dynamics approach described in Section 3.8. Also given in Section 3.8 are literature sources and values for the other thermodynamic parameters in Eq. (2). The calculated dissociation constants for all of the amines studied (except ethanolamine, for which the entropy was not estimated) are given in Table 3.3. Even if we assume that the estimated entropies are accurate, the results in Table 3.3 show that discrepancies in the literature values for the heats of formation lead to significant uncertainty in the calculated dissociation constants. While this uncertainty precludes us from gaining meaningful insight into how MA, DMA, or TEA might compete with ammonia for HNO_3 in the atmosphere, we are able to draw conclusions about the other salts. As mentioned earlier, most studies show that ambient ammonia concentrations tend to be an order of magnitude greater than amine concentrations,

except perhaps in the immediate vicinity of an amine emissions source. Given this, and assuming that the calculated entropies are reasonable, it is improbable that nitrate salts of TMA or EA would form in the presence of typical ambient ammonia levels, because the K_p values for these two systems are greater than or equal to that of ammonium nitrate, independent of the precise value of the heat of formation. By contrast, the value of the dissociation constant for DEA is 2 to 3 orders of magnitude smaller than that of ammonium nitrate (independent of the uncertainty in the heat of formation), indicating that formation of DEAN particles under typical atmospheric mixing ratios is possible.

3.5.3 Atmospheric formation of aminium nitrate salts; experimental

We conducted chamber experiments to evaluate and constrain the theoretical estimate for the dissociation constant of triethylammonium nitrate (TEAN), the highest molecular weight aminium nitrate studied.

The first experiment was carried out to study TEAN formation at atmospherically relevant ratios of ammonia:TEA (Fig. 3.3). Initially, 100 ppb of gas-phase ammonia was mixed in a chamber containing ~ 5 ppb of nitric acid, leading to nucleation of ammonium nitrate particles. Once the ammonium nitrate particle concentration and mass had stabilized, aliquots of TEA were injected into the chamber. As can be seen in Fig. 3.3, the concentration of TEAN salt, indicated by simultaneous shifts in the nitrate and organic signals, increased dramatically when TEA was added because the injection plume provided a high concentration region for particle formation. As the amine mixed throughout the chamber and became more dilute, the equilibrium shifted back to the gas phase, the salt returned to pure ammonium nitrate, and the organic signal = 0. This

sequence of events occurred after each injection, including a second addition of 5 ppb of nitric acid to the chamber.

After concluding that TEA would be unable to form nitrate salts at ratios of TEA:NH₃ typically found in the atmosphere (except possibly near emissions sources), we developed an experimental technique to estimate the gas-particle equilibrium constant for TEAN. The procedure consists of adding an equimolar mixture of amine and ammonia to a chamber containing nitric acid (it is necessary to inject both ammonia and amine because we are unable to accurately measure gas-phase amine or nitric acid concentrations). Once ammonia, TEA, and nitric acid are injected, the following equilibria are established:

$$K_{P1} = p_{HNO_3} p_{NH_3} \quad (3)$$

$$K_{P2} = p_{HNO_3} p_{TEA} \quad (4)$$

where p_{HNO_3} , p_{NH_3} , and p_{TEA} are the partial pressures of nitric acid, ammonia, and triethylamine, and K_{P1} and K_{P2} are the dissociation constants for ammonium nitrate and triethylammonium nitrate, respectively. Using the values in Table 3.5 in Eq. (2), K_{P1} for the ammonium nitrate system is calculated to be $1.916E-7 \text{ Pa}^2$ at 293 K. The partial pressures of NH₃ and TEA can be determined by subtracting the measured mass of each species in the aerosol phase from that which was injected, assuming negligible wall loss. Thus K_{P2} and p_{HNO_3} are the two unknown quantities to be determined. Although the PILS-IC can measure the amount of nitrate in the aerosol phase, this measurement was not used to calculate p_{HNO_3} , as nitric acid is subject to significant wall losses.

We report here an experiment in which 50 ppb of TEA and 50 ppb of ammonia were added simultaneously to a chamber containing 8 ppb of nitric acid. Upon injection

of the amine/ammonia mixture, a rapid particle nucleation event was detected by the cToF-AMS (similar to those shown in Fig. 3.3). As the plume of ammonia and TEA mixed through the chamber, the mass loading of particles detected by the cToF-AMS decreased, and the other particle instruments (PILS-IC and DMA, which are not aligned with the injection port) began to detect particle loadings consistent with those of the cToF-AMS. After all of the instruments gave consistent readings and the particle concentration was stable (other than a slow decrease from wall loss), the triethylammonium and ammonium contents of the aerosol-phase were measured by the PILS-IC, which unambiguously and quantitatively detects these two species. The dissociation constant of triethylammonium nitrate determined from this experiment, using Eq. (4), is $1.85\text{E-}7 \text{ Pa}^2$. Although wall losses and slight contamination from other amine compounds from previous experiments influenced this result, the likely effect of these influences is judged to be too small to affect the conclusion that the dissociation constant for TEAN is close to that of ammonium nitrate. This conclusion is consistent with the previous experiment and the estimated dissociation constant falls within the large range of values predicted theoretically.

The two chamber experiments described above confirm that TEA does not form nitrate salts unless the ammonia concentration is roughly equivalent to that of TEA or there is a large excess of nitric acid. Experimental testing of all of the amines was beyond the scope of this study and further studies of this type are warranted, but these initial results indicate that the calculated dissociation constants, although subject to considerable uncertainty, are reasonable.

3.5.4 Aminium sulfate salts

Amines have the potential to form sulfate salts analogous to ammonium sulfate. Although nitrate salts are probably more relevant in agricultural settings, aminium sulfate salts may form in the presence of high sulfate concentrations. Figure 3.4 shows results from the addition of 100 ppb methylamine (MA) to pure ammonium sulfate seed in a dry (less than 10% RH) chamber (the chamber also contained ozone because the experiment was designed for MA ozonolysis). The DMA data show a $3 \mu\text{m cm}^{-3}$ increase in particle volume and new particle formation when methylamine is injected. The new particles are formed from the reaction of methylamine with residual nitric acid in the chamber.

Intriguingly, the mass of methylammonium (labeled “organic” in Fig. 3.4) detected by the cToF-AMS is roughly 8 times the mass needed to neutralize the nitrate. Additionally, the time series from the cToF-AMS also shows a sharp decrease in the ammonium signal as the methylamine signal increases. The effective density of the particles decreases slightly ($\sim 0.1 \pm 0.1 \text{ g cm}^{-3}$) as the organic signal increases. All of these trends indicate that the methylamine is displacing ammonia and forming methylammonium sulfate. One oddity is the apparent increase in sulfate observed by the cToF-AMS. The sulfate time series from the PILS-IC shows that there is no increase in sulfate loading after methylamine is injected (the growth of methylammonium cannot be followed by the PILS-IC because the IC column used is unable to distinguish between ammonium and methylammonium cations). The increase in sulfate signal from the cToF-AMS can most easily be explained as an artifact, often seen in chamber studies, resulting from an increase in collection efficiency as the physical properties of the aerosol change (Bahreini et al., 2005; Huffman et al., 2005). We hypothesize that replacement of the

ammonium cation by methylammonium alters the physical characteristics of the particle which, in turn, causes fewer particles to bounce from the vaporizer surface, increasing collection efficiency. All of the signals from the cToF-AMS (sulfate, organic, nitrate and ammonium) have been scaled by a factor that causes the cToF-AMS sulfate mass to match the PILS-IC sulfate mass after the increase in collection efficiency. Accordingly, the masses shown for the cToF-AMS before the collection efficiency increase are low.

Though the gas-phase concentration of methylamine in this experiment is relatively large, a nearly complete conversion from ammonium sulfate to methylammonium sulfate was observed. The extent of this type of displacement at lower gas-phase amine concentrations, for other amines, and as a function of RH all warrant further study.

3.6 Aerosol formation from photooxidation and ozonolysis of amines

We begin this section by describing common trends observed during the oxidation experiments of all amines. The following subsections give the data and details for the oxidation of individual amines.

During all of the photooxidation experiments with NO_x , we observed aerosol growth resulting from a combination of ammonium nitrate salt formation and condensation of nonvolatile oxidized compounds (growth from the dissolution of water soluble amines was limited by the low, $<10\%$, RH of the chamber). For all of the amines studied, some of the ammonium nitrate salt that was initially formed during photooxidation partitioned back into the gas-phase as more of the parent amine was reacted away. The particle-phase salt repartitions back to the gas phase because the continued oxidation of the parent

amine depletes its concentration in the gas phase and drives the equilibrium back towards gas-phase amine and nitric acid. For methylamine, ethylamine, ethanolamine, and diethylamine nearly 100 percent of the nitrate salt revolatilized while for trimethylamine and triethylamine the nitrate salts appeared to be more stable and did not return completely to the gas phase. All experiments were carried out until the mass of aerosol was stable, no further growth or decay other than a slow decay caused by particle loss to the walls. Based on estimates of the OH concentration in our chamber (Kroll et al., 2006) and measured ozone concentrations, the cessation of aerosol growth is not caused by a depletion of oxidant. Typically, one defines a mass yield of secondary organic aerosol (ratio of organic aerosol mass to the mass of hydrocarbon reacted), but for the amines the mass yield of aerosol depends on the concentration of nitric acid in the system. If ample nitric acid is formed during photooxidation, nearly all of the amine will form aminium nitrate salts, while in the absence of nitric acid, nitrate salts are not formed and the yield reflects the formation of nonvolatile compounds from reaction of OH and O₃ with the amine. Additional complexity arises because many of the oxidation products of amines are themselves basic and can form salts with nitric acid (e.g. amides and imines can all form salts with HNO₃). These factors create a situation in which the yield of aerosol is related in a complex manner to the rate of formation of nitric acid in the system.

If all of the nitrate salts return to the gas phase as the parent amine is reacted away, the final aerosol mass yield would be relatively independent of the nitric acid concentration. Intriguingly, this is not the case for experiments involving TMA or TEA, as the PILS-IC detects significant loadings of salt at the end of these experiments. As described in detail later in this section, TMA and TEA are the only two amines that

formed significant non-salt organic aerosol during oxidation. One explanation for the persistence of the aminium nitrate salts in these two systems is that the salt has been “trapped” inside an external layer of oxidized aerosol and is no longer in equilibrium with the gas phase. However, the timescale for diffusion through the organic layers formed in these experiments, which are less than 200 nm thick, is small and, unless the gas phase amine was completely insoluble in the organic layer, it is improbable that this layer could “trap” the salt for any significant amount of time. It is possible that mixing of organic material with the salt in the particle phase somehow lowers the volatility of the salt. Another possibility is that gas-phase concentrations of nitric acid are sufficiently high to force the equilibrium towards the particle phase even when the concentration of the parent amine is very low. Finally, given the large uncertainties in the calculated gas-particle equilibrium constants for the amines, it is possible that certain amines favor the particle phase even at very low gas-phase concentrations.

Regardless of the mechanism by which the salts persist, the formation of nitrate salts biases the calculated mass yields of the photooxidation experiments to be higher than they would be as a result of oxidation alone. In an attempt to estimate the purely oxidative yield in the absence of salt formation we conducted ozonolysis experiments and photooxidation experiments in the absence of NO_x . The aerosol mass yields for the different amines during photooxidation (with and without NO_x) and ozonolysis are given in Table 3.4. It is important to note that these yields are derived from experiments run under a single set of conditions and are given to show relative differences in the behavior of the different amines; they are not quantitative yield estimates for the individual amines. Indeed, runs conducted with higher initial concentrations of amine give higher

yields because of the increased particle-phase organic mass into which organics can condense (Seinfeld and Pankow, 2003). It is even possible that the mass of salt formed can affect the yield if the condensable organics formed are soluble in the nitrate salts. Because of the exploratory nature of this study and because of the complex behavior of amines forming aerosol both through salt formation and oxidation, we do not attempt to derive yield curves from these data.

The non-salt photooxidation yields given in Table 3.4 were obtained using the following method: first, the aerosol volume measured by the DMA was multiplied by the effective density; second, the salt fraction of the aerosol mass was determined as (PILS-IC mass)/(DMA volume \times effective density). Finally, the wall-loss corrected DMA volume was multiplied by the effective density and then by the fraction of non-salt aerosol mass to give the mass of non-salt secondary organic aerosol (SOA). The yields were calculated using data from the period after aerosol growth and decay appeared to have ceased other than from loss to the chamber walls. These yield results will be discussed in detail later, although it is immediately evident that while all of the amines can generate aerosol mass by forming nitrate salts, several do not form aerosol mass through oxidation.

Before discussing results from individual photooxidation and ozonolysis experiments, it is useful to consider the general mechanisms by which OH and ozone oxidize aliphatic amines. The gas-phase chemistry of amine oxidation by OH (in the presence of NO_x) and by ozone (without NO_x) have been studied (Schade and Crutzen, 1995; Tuazon et al., 1994), and the major products formed by these reactions have been identified. For many of the oxidation pathways, the products of OH and ozone oxidation

are similar, if not identical. The gas-phase products formed from oxidation of aliphatic amines by OH in low NO_x environments are unknown.

Figure 3.5a shows the most common oxidation pathways for OH attack of an aliphatic amine in the presence of NO_x (Angelino et al., 2001; Schade and Crutzen, 1995). Abstraction of hydrogen from the secondary carbon is believed to be the dominant pathway (Finlayson-Pitts and Pitts, 1986). Abstraction of a hydrogen atom bound directly to the nitrogen in a primary or secondary amine is also possible but is believed to play a less significant role (Schade and Crutzen, 1995). The gas-phase oxidation products formed are amides, nitramines, and imines. All of the products shown have the potential to partition to the aerosol phase, although amides are particularly water soluble and have the lowest vapor pressures. An unexpected product, alkylamine-N-oxide, was first detected by Angelino et al. (2001) in the aerosol phase and was again detected in the particle phase during the current study.

Figure 3.5b shows the pathways for ozone reaction with an aliphatic amine. While the loss of an alkyl group from the high energy amine oxide generates products distinct from those generated by reaction with OH, rearrangement of the amine oxide and subsequent loss of OH leads to alkoxy radicals similar to those generated from hydrogen abstraction by OH followed by loss of an oxygen atom to NO. Following this branch of the reaction diagram leads to similar, and in many cases identical, products as those formed by reaction with OH.

Figure 3.5c shows the beginning of the reaction pathways for amine oxidation by OH in the absence of NO_x. Presumably, a number of the condensable species in this

system consist of hydroperoxides and alkyl peroxides. Many of the same products formed in the high NO_x and ozone systems are formed if, rather than forming peroxides, RO₂ + RO₂ and RO₂ + HO₂ reactions form alkoxy radicals.

Many of the photooxidation experiments reported here employed hydrogen peroxide (H₂O₂) as an OH source. As detailed in the Experimental section, a relatively large amount (3–5 ppm) of hydrogen peroxide must be introduced into the chamber to achieve sufficient levels of OH for rapid reaction. Because the reaction between OH and H₂O₂ forms HO₂ and because hydrogen peroxide itself may affect the chemistry of the aerosol formed, we conducted additional photooxidation experiments using mixtures of propene and NO_x as well as NO_x alone. We found no major differences in chemistry between the systems with and without H₂O₂, although the reactions occurred much faster in the presence of hydrogen peroxide, as expected. All of the ozonolysis reactions were carried out in the absence of NO_x.

3.6.1 Experimental protocol

The same procedure was used for all photooxidation and ozonolysis experiments. For photooxidation experiments, the first step is the injection of either: H₂O₂, a H₂O₂ and NO_x mixture, a NO_x and propene mixture, or NO_x alone. Table 3.2 gives the oxidant used and NO_x mixing ratio for each photooxidation experiment. For all types of experiments, except NO_x-free photooxidations, the next step was to add a small amount (~10 ppb) of HNO₃. Once the HNO₃ had mixed, the amine was injected at a much higher concentration than the nitric acid (typically ~ 100 ppb) causing nucleation of aminium nitrate salt while the vast majority of the amine remained in the gas phase. The

concentration of nucleated salt particles was always observed to peak soon after the injection of the amine, followed by a sharp decrease in mass as mixing occurred and gas-particle equilibrium was established.

After the concentration of the nucleated particles became steady and sufficient time had elapsed to collect composition data with the cToF-AMS and the PILS-IC, oxidation was initiated. For photooxidation experiments, oxidation was initiated by turning on the black lights surrounding the chamber, while for ozonolysis ozone was injected into the chamber. All experiments were continued until there were no further changes in particle mass or volume, except for slow decay in mass and volume caused by particle loss to the chamber walls.

3.6.2 Trimethylamine (TMA) photooxidation

Trimethylamine (TMA) is one of the more abundant ambient alkyl amines near animal husbandry operations (Rabaud et al., 2003; Schade and Crutzen, 1995). Figure 3.6 shows the time profiles for NO_x , O_3 , particle volume (DMA), ionic particle mass (PILS-IC), and particle mass (cToF-AMS) during the photooxidation of TMA. For this experiment (number 3, Table 3.2), 300 ppb of NO_2 , 10 ppb of HNO_3 and 100 ppb of TMA were used. As expected, trimethylammonium nitrate (TMAN) salt began to nucleate soon after the injection of TMA. Approximately 30 min after the TMA injection the aerosol mass stabilized as the system reached gas-particle equilibrium. The composition of the TMAN particles was measured for an additional 30 min with the cToF-AMS and the PILS-IC before the black lights surrounding the chamber were turned on, initiating photooxidation.

When photooxidation begins, because of the large excess of TMA injected relative to HNO_3 , much of the nitric acid has been converted into particle-phase nitrate. Assuming negligible wall loss, ~ 90 ppb of TEA remains in the gas phase at the time the lights are turned on. Upon irradiation, there is a brief spike in NO from the photolysis of NO_2 ; as the TMA is oxidized by OH, RO_2 radicals are formed that convert the NO back to NO_2 , and ozone formation begins. NO_x gradually decreases throughout the course of the experiment as NO_2 is converted to HNO_3 by reaction with OH. Particle formation begins within ~ 10 min of the start of irradiation.

Figure 3.6c-e shows the particle composition as measured by the cToF-AMS and the PILS-IC instruments. The PILS-IC data show that at the peak of particle growth, $62 \mu\text{gm}^{-3}$ of the particle mass consists of TMAN salt. The volume measured by the DMA is $78 \mu\text{mcm}^{-3}$ at the peak of particle growth. Based on a calculated effective density of (1.3 ± 0.2) , nearly 80% of the particle mass is composed of the nitrate salt at the peak of particle growth. In addition to the salt present at the start of irradiation, additional salt is formed as TMA reacts with nitric acid formed as OH reacts with NO_2 . After the peak of particle growth, both the mass and volume of aerosol drop dramatically. The drop in particle mass can be accounted for almost entirely by the volatilization of TMAN, and after 4.4 h of reaction TMAN salt accounts for less than 35% of the particle mass. Volatilization of TMAN is a direct consequence of the gas-particle equilibrium of the nitrate salt; as oxidation proceeds and gas-phase TMA is reacted away (and as nitric acid is lost to the walls of the chamber), the equilibrium for the salt shifts back towards the gas phase. Figure 3.6d-e shows time traces of signals from the cToF-AMS associated with trimethylammonium (m/z 58 $(\text{CH}_3)_2\text{NCH}_2^+$), methylammonium (m/z 31 CH_3NH_2^+),

nitrate (m/z 30 NO^+ , m/z 46 NO_2^+) and oxidized fragments (m/z 44 CO_2^+ , m/z 29 CHO^+). The signals associated with trimethylammonium and nitrate all decrease quickly after the peak of particle growth while those associated with oxidized fragments and methylamine are relatively flat (some show slight decreases associated with the slow loss of particles to the chamber walls). The time trends of these fragments lend support to the hypothesis that TMAN salt is repartitioning to the gas phase while compounds formed from TMA oxidation are condensing.

Over the course of the reaction, both the cToF-AMS and the PILS-IC detected signals consistent with the presence of particle-phase methylammonium. Based on the PILS-IC data, nearly 10% of the particle mass at the peak of aerosol growth is methylammonium. The most plausible explanation for the detection of this species is that imines formed in the gas phase (see Fig. 3.5a) partition to the particle phase through either nitrate salt formation or direct condensation. Imines exposed to liquid water readily decompose into an amine and an aldehyde (Fig. 3.5a). It is possible that this reaction occurs in the particle phase, though it is unclear if sufficient particle-phase water existed to drive this reaction. The experiments are carried out at low RH (<10%) but both the TEA and nitric acid were bubbled into the chamber from aqueous solutions and the efflorescence behavior of ammonium nitrate particles is unknown (although if their behavior is similar to that of ammonium nitrate, the particles may retain water at low RH). Independent of the amount of particle water, because the PILS-IC dissolves collected aerosol particles into water droplets, the imines would almost certainly react with water inside of the instrument if this reaction had not already occurred in the chamber. The fact that more methylammonium nitrate is detected by the PILS-IC than

dimethylammonium nitrate further supports the imine reaction pathway because this pathway does not lead to dimethylammonium nitrate. The PILS-IC data also show an increase in the abundance of formate, which is a byproduct of hydrolysis of imines. While the cToF-AMS peak at m/z 31 could be a fragment from oxidized forms of TMA and not from methylammonium, it is improbable that this peak is a fragment from TMAN itself because it does not follow the same time profiles as m/z 58 (the dominant peak for TMAN). The small amounts of dimethylammonium nitrate detected by the PILS-IC could be formed through hydrolysis of amides in the particle phase as shown in Fig. 3.5a.

Figure 3.7 shows the spectra from the cToF-AMS during different stages of the same photooxidation experiment discussed above (experiment 3, Table 3.2). As in Fig. 3.6, the growing importance of oxidized fragments relative to trimethylammonium nitrate fragments is evident. Of note is the relative prominence of m/z 88, which is the expected dominant peak (resulting from alpha-cleavage) of the carboxylic acid of TMA (shown in the bottom of Fig. 3.5a). Also of note is the increase in abundance of higher molecular weight species which could be the result of particle-phase reactions or multiple oxidations in the gas phase. The gas-phase route seems somewhat implausible for molecular weights above 150 ($RO_2 + RO_2 = 148$ amu for TMA) because formation of these high molecular weight compounds would require multiple RO_2+RO_2 or RO_2+HO_2 reactions.

3.6.3 Trimethylamine (TMA) ozonolysis

During the photooxidation of trimethylamine a large amount of ozone is formed, and, based on reported rate constants (Atkinson et al., 1978; Tuazon et al., 1994), ozone and

OH reactions with TMA are competitive under these conditions. To determine if the products of the ozone reaction form aerosol, we conducted a TMA ozonolysis experiment. Figure 3.8 shows the time series of the DMA, cToF-AMS, and PILS-IC for this experiment. At time = 0, 100 ppb of TMA was added to 16 ppb of HNO₃ already in the chamber, forming trimethylammonium nitrate (TMAN). The TMAN salt remained in the chamber for ~3 h during which time nearly all of it deposited on the chamber walls or volatilized. Oxidation was initiated by adding 200 ppb of ozone to the remaining gas-phase TMA in the system (~ 85 ppb assuming negligible wall loss of gas phase TMA and assuming all of the particulate TMAN was lost to the walls). During the ozonolysis, the vast majority (> 90%) of the aerosol formed was nonionic and accordingly was not detected by the PILS-IC. After 3 h of ozonolysis, aerosol growth had reached a peak. At this point, nitric acid was added (not shown in Fig. 3.8) to induce nitrate salt formation of gas-phase products too volatile to condense. The addition of nitric acid led to 9 μm³ cm⁻³ of aerosol growth, which was predominantly TMAN with a small contribution from methylammonium nitrate.

Though a large excess of ozone remained after the peak of aerosol growth, the aerosol formed appeared to be stable towards further oxidation and did not rapidly revolatilize. The mass yield of non-salt aerosol (before additional nitric acid was injected) was ~ 15% (assuming 85 ppb as the starting concentration of amine). Interestingly, the yield from the ozonolysis is similar to the 23% yield of oxidized (non-salt) SOA formed during photooxidation with NO_x.

The bottom panel of Fig. 3.7 shows a spectrum from the cToF-AMS after three hours of ozone oxidation. The similarity between this spectrum and that in the middle

panel of the figure (after photooxidation) is striking, with the one obvious difference being that the nitrate fragments (m/z 30 and 46) are less prominent because nitrate salts represent a smaller fraction of the particulate mass in the ozonolysis experiment. The similarity of the spectra indicates that ozonolysis generates similar condensable compounds to those from photooxidation. It should be noted that OH can be created during ozonolysis (see Fig. 3.5) and some of the compounds formed in ozonolysis could potentially be formed from amine reaction with OH.

3.6.4 Methylamine (MA) photooxidation

In addition to being formed through oxidation and hydrolysis of TMA, methylamine (MA) is itself a major emission from animal husbandry operations. In the study of Schade and Crutzen (1995) methylamine and trimethylamine were the only two aliphatic amines detected near animal husbandry operations. Figure 3.9 shows the time series for the photooxidation of methylamine (experiment 6, Table 3.2) using H_2O_2 as the OH precursor. Nitric acid, in the amount of 10 ppb, was added before methylamine was injected, and NO_x was added as 100 ppb of NO, instead of as NO_2 . Injection of the methylamine caused the nucleation of methylammonium nitrate, which was allowed to equilibrate and mix for approximately two hours before the black lights were turned on 2.5 h after injection of the amine. When irradiation began, NO was quickly converted to NO_2 through reactions with RO_2 and HO_2 . As NO was removed, ozone formation began, NO_2 started to convert to HNO_3 , and aerosol formation began. The aerosol volume shows the same behavior as that during the TMA photooxidation, growing to a peak as methylammonium nitrate is formed then rapidly decaying as gas-phase methylamine is

oxidized. Subtracting the mass of all the ionic species detected by the PILS-IC from the aerosol mass calculated by multiplying the DMA volume by the effective density of 1.1 ± 0.2 , one finds that nearly 100% of the aerosol formed at the peak of aerosol growth is methylammonium nitrate. There is a small signal in the PILS-IC from contaminant TMA which decreases as the experiment progresses. In contrast to the TMA photooxidation, there is little aerosol remaining after the rapid decay of the salt; $< 1 \mu\text{g m}^{-3}$ of non-salt organic aerosol is present in the system after 4 h of photooxidation relative to more than $20 \mu\text{g m}^{-3}$ remaining for the TMA with similar starting concentrations of amine. Though the mass of non-salt aerosol formed from the photooxidation was small, Panel (D) of Fig. 3.9 shows that the relative importance of non-salt organic aerosol increases throughout the experiment. Methanimine, one of the most abundant gas-phase products from methylamine photooxidation is known to polymerize on surfaces and may be a source of the nonionic aerosol detected (Schade and Crutzen, 1995).

3.6.5 Methylamine (MA) ozonolysis

Because the vast majority of the aerosol formed during the photooxidation of methylamine is methylammonium nitrate, we performed an ozonolysis experiment to confirm that methylamine is unable to generate significant aerosol mass through oxidative routes. Time series from the ozonolysis have already been shown, though in the context of sulfate salt formation, in Fig. 3.4. Ammonium sulfate seed was added to the methylamine-ozonolysis system to provide a surface for condensation if the system did not generate enough condensable products to induce nucleation. Ozone, in the amount of

200 ppb, was added to the chamber along with ~ 100 ppb of methylamine. As discussed previously, the methylamine replaced the ammonium from the ammonium sulfate seed, but after this initial phase of growth by displacement, negligible further growth was observed, confirming the result of negligible non-salt organic mass yield observed during the photooxidation.

3.6.6 Triethylamine (TEA) photooxidation

Results from the photooxidation of 500 ppb of triethylamine with NO_x using hydrogen peroxide as an OH precursor are shown in Fig. 3.10. For all TEA photooxidations, independent of OH source or starting concentration, rapid decay of aerosol mass after the peak growth was not observed. The reason for the observed stability of the salt formed is unclear. It probably indicates that TEAN has a smaller dissociation constant than the other amines studied. It could also indicate that there is interaction between the organic material and the salt lowering the volatility of the TEAN. Finally, it could be the result of salt formation by products of TEA oxidation. During all TEA photooxidations, diethylammonium and ethylammonium were detected by the PILS-IC with diethylammonium being formed at higher concentrations in the particle phase than ethylammonium. Based on our knowledge of the gas-phase oxidation reactions, it seems most plausible that the diethylammonium is formed by the particle-phase hydrolysis of N,N diethylacetamide (the amide shown in Fig. 3.5a if all R groups are ethyl groups. As mentioned earlier, it is possible that hydrolysis of the amide occurs in the PILS-IC instrument itself rather than in the chamber.) The detection of acetate by the PILS-IC during the experiment is consistent with the proposed mechanism of diethylammonium

formation from hydrolysis of N,N diethylacetamide . The ethylammonium detected by the PILS-IC could be formed in two ways. First, it could result from aqueous reaction of the imine as shown in Fig. 3.5a (if all R groups being ethyl). Second, it could be the result of two successive amide hydrolysis reactions. The detection of higher levels of diethylammonium than ethylammonium contrasts with the results from the oxidation of trimethylamine for which higher levels of methylamine were detected than for dimethylamine. This difference suggests that more aerosol is formed through the imine route for trimethylamine whereas more aerosol is formed through the amide route for triethylamine.

During one photooxidation of TEA (experiment 20), a filter of the aerosol was collected and analyzed by LC/MS with electrospray ionization. All of the mass spectral peaks observed using LC/MS were consistent with the nitrate salt and oxidation products already discussed, except for a peak at m/z 118 detected in the positive mode. Peaks detected in the positive mode from electrospray ionization are typically $[M+H]^+$ ions, making the molecular weight of the species detected 117 amu. This molecular weight is consistent with triethylamine-N-oxide (shown in Figs. 3.5a and b with R=ethyl group), a species that was previously detected by Angelino et al. (2001). There is not a significant peak in the spectrum from the cToF-AMS at m/z 117 (or m/z 116 which would be the expected largest fragment ion peak resulting from the alpha cleavage of a hydrogen from triethylamine-N-oxide); this is not particularly surprising because a high energy oxide of this type would be expected to fragment under electron impact ionization if it had not already thermally fragmented on the vaporizer. The extracted ion chromatogram (EIC) of m/z 118 from the LC/MS system gives three distinct peaks with retention times of 1.38,

2.00, and 2.30 min, indicating the presence of three distinct isomers of this species. The structures of these isomers remain unknown.

3.6.7 Triethylamine (TEA) ozonolysis

Ozonolysis of TEA was conducted using the same procedure as for the ozonolysis of TMA and MA. First, nucleation of triethylammonium nitrate (TEAN) was initiated by adding 100 ppb of TEA to a chamber containing 8 ppb of nitric acid. After allowing the TEAN to equilibrate for 2 h, 350 ppb of ozone was slowly added to the chamber causing further aerosol growth that peaked, after ~ 3 h of ozone exposure, at a maximum of $15 \mu\text{m}^3 \text{cm}^{-3}$, or $\sim 18 \mu\text{g m}^{-3}$ (effective density = 1.2 ± 0.2) of additional growth. The mass yield from ozonolysis is 5%.

During ozonolysis, diethylammonium and ethylammonium were formed as they were during photooxidation, but there was no corresponding growth in the nitrate signal (either on the cToF-AMS or the PILS-IC) indicating that these compounds condensed in the particle phase in a form other than nitrate salts. At the peak of aerosol growth (3 h of oxidation), diethylammonium constituted 23% of the aerosol mass formed after ozone injection and ethylammonium accounted for 3% of the mass from ozonolysis. After the aerosol growth had peaked, an additional 8 ppb of nitric acid was added causing a further $30 \mu\text{g m}^{-3}$ of aerosol growth. The aerosol generated by this second addition of nitric acid was a mix of diethylammonium ($8.7 \mu\text{g m}^{-3}$), ethylammonium ($4.5 \mu\text{g m}^{-3}$), triethylammonium ($0.5 \mu\text{g m}^{-3}$), and nitrate ($14.5 \mu\text{g m}^{-3}$). The near perfect ion balance between the positive amine ions and the negative nitrate ions (3% negative charge imbalance) substantiates that all of the additional growth was in the form of nitrate salts.

The negligible increase in triethylammonium mass during the second addition of nitric acid indicates that nearly all of the starting TEA had been oxidized. The final aerosol, composed of nitrate salts and oxidized SOA, did not rapidly decay. The PILS-IC data showed that nitrate decayed 7 percent faster than ethylammonium and 14 percent faster than diethylammonium further supporting the idea that these species are not entirely nitrate salts and that nitrate salts decay more rapidly than SOA formed through oxidation.

3.6.8 Diethylamine (DEA) photooxidation

Figure 3.12 shows the photooxidation of 100 ppb of diethylamine, conducted in the same manner as the previously discussed photooxidations using hydrogen peroxide as an OH precursor. Diethylammonium nitrate nucleates upon injection of DEA followed by a burst of aerosol mass when the lights are turned on that quickly decays away. The rapid decay is similar to the behavior of TMA and MA during photooxidation, with DEA being more similar to MA in that nearly all of the aerosol formed is nitrate salt. Experiments using different OH sources also yielded negligible non-salt aerosol. This is an intriguing result, because by molecular weight alone, DEA would be predicted to form more secondary organic aerosol when oxidized than TMA. Clearly, in this case, the chemical nature of the compound is more important than molecular weight alone. Though the specific reactions that lead to the difference in yield between TEA and DEA remain unclear, Fig. 3.5 shows that there are several compounds that can be formed by tertiary amines through the loss of one of the alkyl groups, a reaction pathway that is not available for secondary or primary amines. Though believed to be a minor channel, OH can also extract a hydrogen atom directly from the nitrogen of primary and secondary

amines; it is possible that this reaction pathway leads to more volatile compounds.

Because photooxidation yielded no non-salt organic aerosol, an ozonolysis experiment was not conducted for DEA.

3.6.9 Ethylamine (EA) photooxidation

One photooxidation of ethylamine was conducted and yielded negligible non-salt aerosol mass. Though there was contamination from a previous DEA experiment, it is doubtful that this affected the amount of organic aerosol formed. Ethylamine ozonolysis was not pursued because of the negligible non-salt yield during photooxidation.

3.6.10 Ethanolamine (MEA) photooxidation and ozonolysis

Figure 3.13 shows the photooxidation of ethanolamine. Aerosol growth follows the same pattern as for the other amines with the majority of the initial growth being composed of nitrate salts that repartition back to the gas phase as the amine reacts away. Non-salt organic aerosol forms (~ 2% mass yield), but the yield is small as it is for the other non-tertiary amines studied. The cToF-AMS data show that oxidized fragments (m/z 44, CO_2^+) grow in more gradually and decay less than fragments associated with ethanolammonium nitrate (m/z 46 NO_2^+ and m/z 30 NO^+ and the major ion fragment from ethanolammonium itself). The PILS-IC shows growth of diethylammonium though this is probably a result of contamination because it is unclear how ethanolamine could react to form diethylammonium. The yield from ozonolysis of ethanolamine was small (~ 3%), as expected from the small yield observed during photooxidation.

3.6.11 Photooxidation in the absence of NO_x

NO_x-free photooxidation experiments were conducted for both TEA and DEA. In both cases, negligible mass from nitrate salts was detected by the PILS-IC. Following the trends of the high NO_x photooxidation and ozonolysis results, 500 ppb of TEA formed 260 μg m⁻³ of aerosol (mass yield of ~ 12%) while 500 ppb DEA formed less than 2 μg m⁻³ (mass yield of ~ 0.1%). The cToF-AMS mass spectrum from the NO_x-free photooxidation of TEA is shown in Fig. 3.14. No dramatic changes in the mass spectrum occur during the course of the experiment.

3.6.12 Effect of oxidation conditions on particle chemistry

Figure 3.14 shows cToF-AMS spectra from particles formed by oxidation of TEA using four different systems: (1) photooxidation with NO_x alone, (2) photooxidation with NO_x using H₂O₂ as an OH precursor, (3) ozonolysis in the absence of NO_x, and (4) photooxidation in the absence of NO_x using H₂O₂ as an OH precursor. Because the cToF-AMS uses electron impact ionization, differences in the peak height ratios can be used to assess chemical similarity between the systems even though the spectra are highly fragmented. Aerosol formed in the two different photooxidation systems containing NO_x have similar spectra with large peaks corresponding to fragments from the nitrate salt mixed with oxidized fragments (m/z 29 HCO⁺, m/z 44 COO⁺, m/z 43 C₂H₃O⁺, etc.). The spectrum of aerosol generated by photooxidation (using hydrogen peroxide as an OH precursor) in the absence of NO_x is the most distinct from all other spectra, with dramatically different peak height ratios (m/z 43 is the most intense signal) and more high molecular weight fragments than the other systems. The ozone spectrum shows

characteristics of both the high and low NO_x spectra including a relatively large, yet not dominant, m/z 43 peak.

The spectra from different oxidation systems show that in addition to affecting how much nitrate salt is formed, oxidant (OH, O₃) and NO_x levels also affect the chemical composition of the oxidized aerosol. At the same time, the similarities between the spectra from high NO_x photooxidation systems with and without H₂O₂ indicate that similar species condense independent of the OH source. All of the amines studied formed aerosol with similar spectra during photooxidation whether or not hydrogen peroxide was used as an OH precursor.

3.6.13 Effective density shifts

During the photooxidations of TEA and TMA the effective density of the aerosol continually increased as non-salt organic mass condensed. Figure 3.1 shows the increase observed during the photooxidation of TEA. The effective density of the aerosol formed during ozonolysis was higher than that of the salt for both TEA and TMA. Additionally, TEA formed aerosol with a higher effective density than TEAN when photooxidized in the absence of NO_x. The increases in effective densities observed in particles with a higher fraction of non-salt mass indicates that either: (1) the non-salt aerosol is more dense; or (2) the salt aerosol is either non-spherical or has void volumes, and the condensation of organic aerosol onto the salt alters these physical characteristics. In either case, it is evident that the physical morphology of the particles depends on the ratio of non-salt to salt mass.

3.7 Implications

Amines can undergo similar acid-base reactions as ammonia to form atmospheric nitrate and sulfate salts when in the presence of HNO_3 or H_2SO_4 . Whether amines, in fact, will form such aminium salts depends not only on the concentration of the amine and the acid, but also on the concentration of ammonia which competes for acidic molecules. Thermodynamic calculations using entropies estimated from quantum mechanics and molecular dynamics indicate that diethylammonium nitrate will be able to form when ammonia mixing ratios are greater than those of diethylamine. Triethylamine was shown experimentally to have a dissociation equilibrium constant similar to that of ammonia. Ethylammonium nitrate and trimethylammonium nitrate are predicted to be unable to form unless their mixing ratios are near to or greater than that of ammonia. We note that thermodynamic parameters for the aminium salts have large uncertainties that preclude us from making conclusions regarding the formation, in the presence of ammonia, of the other aminium salts studied.

Gas-phase amines are subject to atmospheric oxidation by the OH radical and ozone, leading to secondary organic aerosol formation. If nitric or sulfuric acid is present during the oxidation, aminium salts of the parent amine can form simultaneously with the SOA resulting from oxidation. The products of amine oxidation can also be basic and form additional aminium salts. Aminium salts will most often form in source-rich areas. As the parent amine is reacted away or as the air mass undergoes dilution, aminium salts can be expected to repartition back to the gas phase. SOA resulting from amine oxidation appears to be more stable in the particle phase than the aminium salts.

Table 3.4 gives the non-salt organic aerosol yields for all of the amines studied under a number of different oxidative conditions. While the yields shown are only

applicable to the amine:oxidant and oxidant:NO_x ratios of the particular experiments, we can draw the general conclusion that the tertiary amines (TMA and TEA) are able to form significant yields of non-salt SOA while the primary and secondary amines studied are not. Ethanolamine showed a small growth during ozonolysis which may be an indication that adding functional groups to the amines increases their organic (non-salt) aerosol yield.

3.8 Thermodynamic data for amine systems

Table 3.5 lists available thermodynamic data for common amine systems. Multiple heats of formation values of alkylammonium nitrates are listed to highlight their uncertainty. Data on entropy and heat capacities for alkylammonium nitrates, with the exception of ammonium nitrate, do not appear to be available.

One approach is to extract the entropy information from atomistic classical and quantum simulation. Lin et al. (2003) developed a 2-phase thermodynamic approach for calculating the thermodynamic properties of complex systems from single molecular dynamics simulation trajectories. In general the Fourier transform of the velocity autocorrelation function, obtained from a molecular dynamics trajectory is used to obtain the vibrational density of states, which is then used to calculate the thermodynamic properties by applying quantum statistics assuming each vibrational mode is a harmonic oscillator. This approach is quite accurate for solids, but leads to significant errors for liquids. Lin et al. (2003) extend this approach to fluids by applying the 2-phase model in which the density of states of the fluid systems are partitioned into gas and solid like

components. However, for aminium nitrates that are solids in ambient conditions, the harmonic approximation is sufficiently accurate for entropy estimation.

Of the alkylammonium nitrates, crystal structures were only found for ammonium nitrate (Herrmann et al., 1994) and methylammonium nitrate (Mylrajan et al., 1985). For the compounds with experimental crystal structures, the periodic quantum mechanical (QM) Mulliken charge distributions were determined by the SeqQuest program (Feibelman, 1987; Verdozzi et al., 2002). For the compounds lacking experimental crystal structure, the solid structures were estimated by modifying the methylammonium nitrate crystal. For instance, methyl groups were replaced by ethyl groups in order to create the ethylammonium nitrate crystal structure. The QM charges were obtained using Density Functional Theory (DFT), B3LYP (Becke, 1993) functions as implemented in the Jaguar program (Jaguar, 2005) using basis sets aug-cc-pvtz (Kendall et al., 1992). Solid structures were built using this method for di and trimethylammonium nitrate, mono, di and triethylammonium nitrate in CERIOUS2 (Cerius2, 1999). Molecular dynamic (MD) simulation at constant pressure, temperature and number of particles (NPT) were performed to equilibrate these solid structures. NVT simulations were then carried out for these experimental crystals or equilibrated solids for a total of 50 ps. Long-range interactions are included using the Ewald sum method and the Nose-Hoover thermostat. Using the MD trajectories, the density of states can be obtained, and the entropies can then be determined from quantum statistics (Lin et al., 2003).

The QM entropy is expected to be quite accurate for crystalline systems. Indeed, the QM entropy agrees rather well with the experimental values for ammonium nitrate

(141.56 J/molK vs. 146.44 J/molK). Unfortunately, experimental entropy is available only for ammonium nitrate so further comparison cannot be done. Since crystal structure was also available for methylammonium nitrate, we expect its QM entropy to be reasonably accurate. For other aminium nitrates, the accuracy of the calculated entropies remains undetermined although we observed a sensible correlation between the “flexibility” of the alkyl groups and the entropies.

3.9 Acknowledgements

This work was supported by the Electric Power Research Institute.

3.10 References

- Allan, J. D., Jimenez, J. L., Williams, P. I., Alfarra, M. R., Bower, K. N., Jayne, J. T., Coe, H., and Worsnop, D. R.: Quantitative sampling using an Aerodyne aerosol mass spectrometer: 1. Techniques of data interpretation and error analysis, *J. Geophys. Res.*, 108(D3), doi:10.1029/2002JD002358, 2003.
- Allen, M., Evans, D. F., and Lumry, R.: Thermodynamic properties of the ethylammonium nitrate + water-system - partial molar volumes, heat-capacities, and expansivities, *Journal of Solution Chemistry*, 14(8), 549-560, 1985.
- Angelino, S., Suess, D. T., and Prather, K. A.: Formation of aerosol particles from reactions of secondary and tertiary alkylamines: Characterization by aerosol time-of-flight mass spectrometry, *Environ. Sci. Technol.*, 35(15), 3130-3138, 2001.

- Atkinson, R., Perry, R. A., and Pitts, J. N.: Rate constants for reactions of OH radical with $(\text{CH}_3)_2\text{NH}$, $(\text{CH}_3)_3\text{N}$, and $\text{C}_2\text{H}_5\text{NH}_2$ over temperature range 298-426 degrees K, *J. Chem. Phys.*, 68(4), 1850-1853, 1978.
- Bahreini, R., Keywood, M. D., Ng, N. L., Varutbangkul, V., Gao, S., Flagan, R. C., Seinfeld, J. H., Worsnop, D. R., and Jimenez, J. L.: Measurements of secondary organic aerosol from oxidation of cycloalkenes, terpenes, and m-xylene using an Aerodyne aerosol mass spectrometer, *Environ. Sci. Technol.*, 39(15), 5674-5688, 2005.
- Becke, A. D.: Density-functional thermochemistry III. The role of exact exchange, *Journal of Chemical Physics*, 98(7), 5648-5652, 1993.
- Beddows, D. C. S., Donovan, R. J., Harrison, R. M., Heal, M. R., Kinnersley, R. P., King, M. D., Nicholson, D. H., and Thompson, K. C.: Correlations in the chemical composition of rural background atmospheric aerosol in the UK determined in real time using time-of-flight mass spectrometry, *J. Environ. Monit.*, 6(2), 124-133, 2004.
- Cerius2, v. 4.0, Accelrys, San Diego, CA, 1999
- Chase, M. W.: NIST-JANAF thermochemical tables, fourth edition, *J. Phys. Chem. Ref. Data*, Monograph9, 1343-1290, 1951, 1998.
- Cocker, D. R., Flagan, R. C., and Seinfeld, J. H.: State-of-the-art chamber facility for studying atmospheric aerosol chemistry, *Environ. Sci. Technol.*, 35(12), 2594-2601, 2001.

- Cottrell, T. L., and Gill, J. E.: The preparation and heats of combustion of some amine nitrates, *Journal of the Chemical Society*, (Jul), 1798-1800, 1951.
- Cox, J. D., Harrop, D., and Head, A. J.: Standard enthalpy of formation of ammonium-nitrate and of the nitrate ion, *Journal of Chemical Thermodynamics*, 11(8), 811-814, 1979.
- DeCarlo, P. F., Slowik, J. G., Worsnop, D. R., Davidovits, P., and Jimenez, J. L.: Particle morphology and density characterization by combined mobility and aerodynamic diameter measurements. Part 1: Theory, *Aerosol Sci. Technol.*, 38(12), 1185-1205, 2004.
- Drewnick, F., Jayne, J. T., Canagaratna, M., Worsnop, D. R., and Demerjian, K. L.: Measurement of ambient aerosol composition during the PMTACS-NY 2001 using an aerosol mass spectrometer. Part II: Chemically speciated mass distributions, *Aerosol Sci. Technol.*, 38, 104-117, 2004a.
- Drewnick, F., Schwab, J. J., Jayne, J. T., Canagaratna, M., Worsnop, D. R., and Demerjian, K. L.: Measurement of ambient aerosol composition during the PMTACS-NY 2001 using an aerosol mass spectrometer. Part I: Mass concentrations, *Aerosol Sci. Technol.*, 38, 92-103, 2004b.
- Eichenau, W., and Liebsche, D.: Die molwärme des ammoniumnitrats zwischen 11 und 280 degrees K, *Zeitschrift Fur Naturforschung Part a-Astrophysik Physik Und Physikalische Chemie*, A 20(1), 160, 1965.
- Feibelman, P. J.: Force and total-energy calculations for a spatially compact adsorbate on an extended, metallic crystal surface, *Physical Review B*, 35(6), 2626-2646, 1987.

- Finlayson-Pitts, B. J., and Pitts, J. N. J.: Atmospheric chemistry : Fundamentals and experimental techniques, Wiley, New York, 1986.
- Haar, L.: Thermodynamic properties of ammonia as an ideal gas, Journal of Research of the National Bureau of Standards Section a-Physics and Chemistry, A 72(2), 207, 1968.
- Hamoir, J., Nemmar, A., Halloy, D., Wirth, D., Vincke, G., Vanderplasschen, A., Nemery, B., and Gustin, P.: Effect of polystyrene particles on lung microvascular permeability in isolated perfused rabbit lungs: Role of size and surface properties, Toxicology and Applied Pharmacology, 190(3), 278-285, 2003.
- Herrmann, M., Engel, W., Schneider, J., and Goebel, H.: Rietveld refinement of the phase of NH₄NO₃ measured in-situ under different diffraction geometries, Materials Science Forum, 166, 489-494, 1994.
- Huffman, J. A., Jayne, J. T., Drewnick, F., Aiken, A. C., Onasch, T., Worsnop, D. R., and Jimenez, J. L.: Design, modeling, optimization, and experimental tests of a particle beam width probe for the aerodyne aerosol mass spectrometer, Aerosol Sci. Technol., 39(12), 1143-1163, 2005.
- Jaguar, v. 6.5, Schrodinger, LLC, New York, NY, 2005
- Jayne, J. T., Leard, D. C., Zhang, X. F., Davidovits, P., Smith, K. A., Kolb, C. E., and Worsnop, D. R.: Development of an aerosol mass spectrometer for size and composition analysis of submicron particles, Aerosol Sci. Technol., 33(1-2), 49-70, 2000.

- Kendall, R. A., Dunning Jr., T. H., and Harrison, R. J.: Electron affinities of the first-row atom revisited. Systematic basis sets and wave functions, *Journal of Chemical Physics*, 96(9), 6796-6806, 1992.
- Keywood, M. D., Varutbangkul, V., Bahreini, R., Flagan, R. C., and Seinfeld, J. H.: Secondary organic aerosol formation from the ozonolysis of cycloalkenes and related compounds, *Environ. Sci. Technol.*, 38(15), 4157-4164, 2004.
- Kroll, J. H., Ng, N. L., Murphy, S. M., Flagan, R. C., and Seinfeld, J. H.: Secondary organic aerosol formation from isoprene photooxidation, *Environ. Sci. Technol.*, 40(6), 1869-1877, 2006.
- Lin, S.-T., Blanco, M., and Goddard III, W. A.: The two-phase model for calculating thermodynamic properties of liquids from molecular dynamics: Validation for the phase diagram of lennard-jones fluids, *Journal of Chemical Physics*, 119(22), 11792-11805, 2003.
- Mace, K. A., Artaxo, P., and Duce, R. A.: Water-soluble organic nitrogen in amazon basin aerosols during the dry (biomass burning) and wet seasons, *J. Geophys. Res.*, 108(D16), doi:10.1029/2003JD003557, 2003.
- Makela, J. M., Yli-Koivisto, S., Hiltunen, V., Seidl, W., Swietlicki, E., Teinila, K., Sillanpaa, M., Koponen, I. K., Paatero, J., Rosman, K., and Hameri, K.: Chemical composition of aerosol during particle formation events in boreal forest, *Tellus Series B-Chemical and Physical Meteorology*, 53(4), 380-393, 2001.
- McGregor, K. G., and Anastasio, C.: Chemistry of fog waters in california's central valley: 2. Photochemical transformations of amino acids and alkyl amines, *Atmos. Environ.*, 35(6), 1091-1104, 2001.

- Mozurkewich, M.: The dissociation-constant of ammonium-nitrate and its dependence on temperature, relative-humidity and particle-size, *Atmospheric Environment Part a-General Topics*, 27(2), 261-270, 1993.
- Murphy, D. M., and Thomson, D. S.: Chemical composition of single aerosol particles at Idaho hill: Positive ion measurements, *J. Geophys. Res.*, 102(D5), 6341-6352, 1997.
- Mylrajan, M., Srinivasan, T. K. K., and Sreenivasamurthy, G.: Crystal structure of monomethylammonium nitrate, *Journal of Crystallographic and Spectroscopic Research*, 15(5), 493-500, 1985.
- Neff, J. C., Holland, E. A., Dentener, F. J., McDowell, W. H., and Russell, K. M.: The origin, composition and rates of organic nitrogen deposition: A missing piece of the nitrogen cycle?, *Biogeochemistry*, 57(1), 99-136, 2002.
- Nemmar, A., Hoylaerts, M. F., Hoet, P. H. M., Dinsdale, D., Smith, T., Xu, H. Y., Vermynen, J., Nemery, B., and Nemery, B.: Ultrafine particles affect experimental thrombosis in an in vivo hamster model, *American Journal of Respiratory and Critical Care Medicine*, 166(7), 998-1004, 2002.
- Ngwabie, N. M., and Hintz, T.: Mixing ratio measurements and flux estimates of volatile organic compounds (voc) from a cowshed with conventional manure treatment indicate significant emissions to the atmosphere, *Geographical Research Abstracts*, 7(01175), 2005.
- Perry, R. H., Green, D. W., and Maloney, J. O.: *Perry's chemical engineers' handbook*, McGraw-Hill, New York, 1997.

- Pitts, J. N., Grosjean, D., Vancauwenberghe, K., Schmid, J. P., and Fitz, D. R.: Photo-oxidation of aliphatic-amines under simulated atmospheric conditions - formation of nitrosamines, nitramines, amides, and photo-chemical oxidant, *Environ. Sci. Technol.*, 12(8), 946-953, 1978.
- Rabaud, N. E., Ebeler, S. E., Ashbaugh, L. L., and Flocchini, R. G.: Characterization and quantification of odorous and non-odorous volatile organic compounds near a commercial dairy in California, *Atmos. Environ.*, 37(7), 933-940, 2003.
- Schade, G. W., and Crutzen, P. J.: Emission of aliphatic-amines from animal husbandry and their reactions - potential source of N₂O and HCN, *J. Atmos. Chem.*, 22(3), 319-346, 1995.
- Schmitz, L. R., Chen, K. H., Labanowski, J., and Allinger, N. L.: Heats of formation of organic molecules calculated by density functional theory. III - amines, *Journal of Physical Organic Chemistry*, 14(2), 90-96, 2001.
- Seinfeld, J. H., and Pankow, J. F.: Organic atmospheric particulate material, *Annu. Rev. Phys. Chem.*, 54, 121-140, 2003.
- Simoneit, B. R. T., Rushdi, A. I., Bin Abas, M. R., and Didyk, B. M.: Alkyl amides and nitriles as novel tracers for biomass burning, *Environ. Sci. Technol.*, 37(1), 16-21, 2003.
- Sorooshian, A., Brechtel, F. J., Ma, Y. L., Weber, R. J., Corless, A., Flagan, R. C., and Seinfeld, J. H.: Modeling and characterization of a particle-into-liquid sampler (pils), *Aerosol Sci. Technol.*, 40(6), 396-409, 2006.
- Stein, S. E.: Mass spectra by NIST mass spec data center, NIST chemistry webbook, NIST standard reference database number 69, Eds. Linstrom PJ, Mallard WG,

- National Institute of Standards and Technology, Gaithersburg MD, 2005.
(<http://webbook.nist.gov>).
- Stelson, A. W., and Seinfeld, J. H.: Relative-humidity and temperature-dependence of the ammonium-nitrate dissociation-constant, *Atmos. Environ.*, 16(5), 983-992, 1982.
- Surratt, J. D., Murphy, S. M., Kroll, J. H., Ng, N. L., Hildebrandt, L., Sorooshian, A., Szmigielski, R., Vermeulen, R., Maenhaut, W., Claeys, M., Flagan, R. C., and Seinfeld, J. H.: Chemical composition of secondary organic aerosol formed from the photooxidation of isoprene, *J. Phys. Chem. A*, 110(31), 9665-9690, 2006.
- Tan, P. V., Evans, G. J., Tsai, J., Owega, S., Fila, M. S., and Malpica, O.: On-line analysis of urban particulate matter focusing on elevated wintertime aerosol concentrations, *Environ. Sci. Technol.*, 36(16), 3512-3518, 2002.
- Tuazon, E. C., Atkinson, R., Aschmann, S. M., and Arey, J.: Kinetics and products of the gas-phase reactions of O₃ with amines and related-compounds, *Res. Chem. Intermed.*, 20(3-5), 303-320, 1994.
- Verdozzi, C., Schultz, P. A., Wu, R., Edwards, A. H., and Kioussis, N.: Layer intermixing during metal/metal oxide adsorption: Ti/sapphire(0001), *Physical Review B*, 66, 125408, 2002.
- Wagman, D. D., Evans, W. H., Parker, V. B., Halow, I., Bailey, S. M., and Schumm, R. H.: Selected values of chemical thermodynamic properties; tables for the first thirty-four elements in the standard order of arrangement, NBS Technical Note, 270(3), 1968.
- Wagman, D. D., Evans, W. H., Parker, V. B., Schumm, R. H., Halow, I., Bailey, S. M., Churney, K. L., and Nuttall, R. L.: The nbs tables of chemical thermodynamic

properties - selected values for inorganic and C-1 and C-2 organic-substances in si units, *Journal of Physical and Chemical Reference Data*, 11, 1-&, 1982.

Weber, R. J., Orsini, D., Daun, Y., Lee, Y. N., Klotz, P. J., and Brechtel, F.: A particle-into-liquid collector for rapid measurement of aerosol bulk chemical composition, *Aerosol Sci. Technol.*, 35(3), 718-727, 2001.

Yaws, C. L.: *Yaws' handbook of thermodynamic and physical properties of chemical compounds*, Knovel. 2003.

Zhang, Q., and Anastasio, C.: Free and combined amino compounds in atmospheric fine particles (pm2.5) and fog waters from northern California, *Atmos. Environ.*, 37(16), 2247-2258, 2003.

Table 3.1: Summary of structures of amines studied and estimated global emissions from animal husbandry.

Amine (abbrev)	Formula	Estimated Global Emissions, Gg N y⁻¹ (Schade and Crutzen, 1995)
Ammonia	NH ₃	23,300
Methylamine (MA)	CH ₃ NH ₂	24 ± 15
Trimethylamine (TMA)	(CH ₃) ₃ N	108 ± 30
Diethylamine (DEA)	(CH ₃ CH ₂) ₂ NH	-
Triethylamine (TEA)	(CH ₃ CH ₂) ₃ N	-
Ethanolamine (MEA)	(CH ₂ OH)CH ₂ NH ₂	-

Table 3.2 Initial conditions of all experiments conducted.

<i>Exp.</i>	<i>Amine</i>	<i>Estimated Initial Mixing Ratios (ppb)</i>	<i>Oxidant</i>	<i>Initial NO_x Mixing Ratios (ppb)</i>	<i>HNO₃ Injected (ppb)</i>	<i>Atomized Seed Aerosol</i>
1	TMA	100	NO _x , Propene	100 (NO ₂)	NA	-
2	TMA	100	NO _x , Propene	100 (NO ₂)	10	-
3	TMA	100	H ₂ O ₂	100 (NO ₂)	10	-
4	TMA	100	Ozone	-	18	-
5	MA	100	NO _x	100 (NO ₂)	10	-
6	MA	100	H ₂ O ₂	100 (NO)	10	-
7	MA	100	Ozone	-	-	(NH ₄) ₂ SO ₄
8	TEA	500	H ₂ O ₂	No NO _x	-	-
9	TEA	500	H ₂ O ₂	400 (NO)	-	-
10	TEA	100	NO _x	100 (NO)	-	-
					-	-
11	TEA	100	NO _x	100 (NO) 100 (NO ₂)	-	-
12	TEA	100	NO _x	140 (NO ₂)	-	-
13	TEA	100	NO _x	100 (NO ₂)	-	-
14	TEA	100	NO _x	100 (NO ₂)	10	-
15	TEA	50	NO _x , Propene	100 (NO ₂)	100	-
16	TEA	100	O ₃	-	8	-
17	TEA	100	HNO ₃	-	100	-
18	TEA	20 ppb TEA aliquots	-	-	-	NH ₄ NO ₃
19	TEA	100 ppb NH ₃ inject TEA in aliquots	-	-	5 (twice)	-
20	TEA	50 ppb TEA 50 ppb NH ₃	-	-	8	-
21	DEA	100	H ₂ O ₂	No NO _x	-	-
22	DEA	100	H ₂ O ₂	80 (NO)	-	-
23	DEA	100	NO _x , Propene	100 (NO)	-	-
24	DEA	100	NO _x	100 (NO)	-	-
25	DEA	100	NO _x	100 (NO ₂)	-	(NH ₄) ₂ SO ₄
26	DEA	100	NO _x	100 (NO ₂)	10	-
27	ethylamine	100	NO _x	100 (NO ₂)	10	-
28	MEA	100	NO _x , Propene	NO/NO ₂	-	-
29	MEA	100	NO _x , Propene	NO ₂	-	-
30	MEA	300	NO _x , Propene	100 (NO ₂)	-	-
31	MEA	100	-	-	-	(NH ₄) ₂ SO ₄ mixed with H ₂ SO ₄ (aq)
32	MEA	100	H ₂ O ₂	100	100	-
33	MEA	100	O ₃	-	-	-
34	NH ₃	100	NO _x , Propene	100 (NO ₂)	10	-

Table 3.3: Theoretically calculated dissociation constants for different nitrate systems.
 $K_{P,298}$ for ammonium nitrate = $7.14\text{E-}7 \text{ Pa}^2$

Species	$K_{P,298} (\text{Pa}^2)$	
	$\Delta H^\circ\text{f}$ from Cottrell and Gill (1951)	$\Delta H^\circ\text{f}$ from NBS (1982)
Methylammonium nitrate	7.90E-06	8.56E-09
Dimethylammonium nitrate	1.01E-05	3.95E-09
Trimethylammonium nitrate	2.27E+00	5.29E-07
Ethylammonium nitrate	3.29E-06	9.56E-07
Diethylammonium nitrate	3.11E-10	3.30E-11
Triethylammonium nitrate	1.37E-05	1.18E-12

Table 3.4: Estimated percent mass yields^a of non-salt aerosol during ozonolysis and photooxidation. All yields have an uncertainty of ~ 25% of their magnitude.

Amine	Ozonolysis Yield	High NO _x Photooxidation Yield	Zero NO _x Photooxidation Yield
Trimethylamine	15	23 ^b	-
Methylamine	<1	<1 ^b	-
Triethylamine	5	8 ^c	12 ^b
Diethylamine	<1	<1 ^b	<1 ^b
Ethylamine	-	<1 ^c	-
Ethanolamine	3	2 ^c	-

^aAll yields for high NO_x and ozonolysis are derived from experiments using 100 ppb initial concentrations of amine (high NO_x photooxidations were run with 100 ppb of NO_x). The zero NO_x yields are from experiments using 500 ppb initial amine concentrations. These yields are given to demonstrate trends in the aerosol forming potential of the different amines and are not meant to represent definitive yields for the systems shown.

^bH₂O₂ as OH precursor

^c Photooxidation without H₂O₂. Photooxidation of 500 ppb TEA using H₂O₂ gave a mass yield of non-salt SOA of > 20%

Table 3.5: Thermodynamic data for various amine nitrate systems. Amines and nitric acid are in the gas phase and nitrates are solid.

Substance	ΔH_f° (kJ/mol)	S° (J/mol K)	C_P (J/mol K)
ammonia	-45.90 ^d	192.77 ^e	35.65 ^d
methylamine	-23.0 ^f	243 ^g	53 ^g
dimethylamine	-18.5 ^f	273 ^g	70.8 ^g
trimethylamine	-23.7 ^f	287 ^g	91.8 ^g
ethylamine	-47.5 ^f	285 ^g	72.7 ^g
diethylamine	-72.6 ^f	352 ^g	115.7 ^g
triethylamine	-92.4 ^f	405 ^g	160.9 ^g
ethanolamine	-210.2 ^j	321 ^j	85.3 ^j
ammonium nitrate	-365.61 ^a	146.44 ^b 141.56*	140 ^c
methylammonium nitrate	-337 ^h -354.4 ^k	194.7*	
dimethylammonium nitrate	-331 ^h -350.2 ^k	229.9*	
trimethylammonium nitrate	-407 ^h -343.9 ^k	243.5*	
ethylammonium nitrate	-364 ^h -366.9 ^k	237.2*	206 ⁱ
diethylammonium nitrate	-413 ^h -418.8 ^k	299.9*	
triethylammonium nitrate	-407 ^h -447.7 ^k	350.3*	
ethanolammonium nitrate	-576 ^h -577 ^k		
nitric acid	-134.31 ^d	266.39 ^d	53.31 ^d

*values estimated from quantum mechanics/molecular dynamics

^aCox et al.(1979)

^bEichenauer and Liebscher(1965)

^cWagman et al.(1968)

^dChase et al.(1998)

^eHaar(1968)

^fSchmitz et al.(2001)

^gPerry et al.(1997)

^hCottrell and Gill(1951)

ⁱAllen et al.(1985)

^jYaws(2003)

^kWagman et al.(1982)

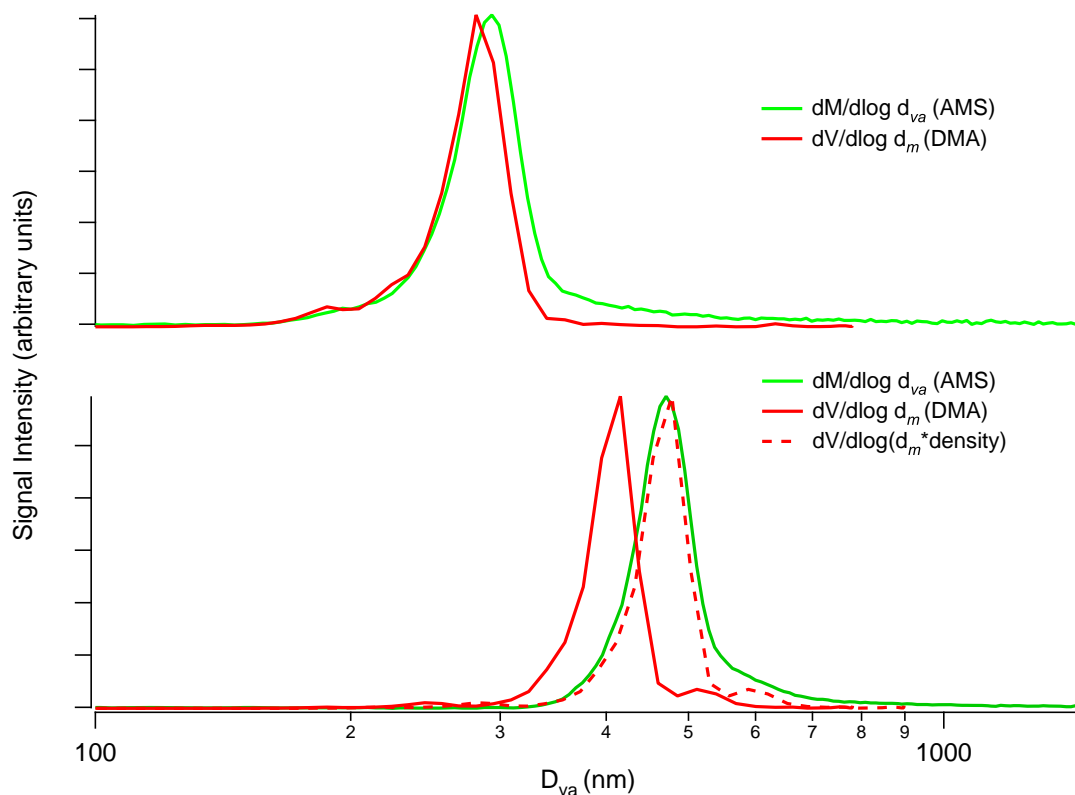


Figure 3.1: Calculation of the effective density (data from exp. 14, Table 3.2). **Panel (A)** Volume distribution from the DMA ($dV/d\log dm$, solid red line) and mass distribution from the cToF-AMS ($dM/d\log(dva)$, solid green line) of triethylammonium nitrate (TEAN). The fact that the two distributions are aligned indicates the effective density of TEAN is ~ 1 . The slight tailing of the cToF-AMS signal could be caused by slow vaporization or higher uncertainty in the size calibration for larger particles. **Panel (B)** The same distributions shown in (A) after products from TEA photooxidation have condensed onto the nitrate salt shown in (A) for 7 h. The particles have grown larger from the condensation process. The dashed red line ($dV/d\log(\rho_{eff} dm)$) is created by adjusting the effective density (ρ_{eff}) until the dotted red line aligns with the solid green line ($\rho_{eff} = 1.1 \text{ g cm}^{-3}$).

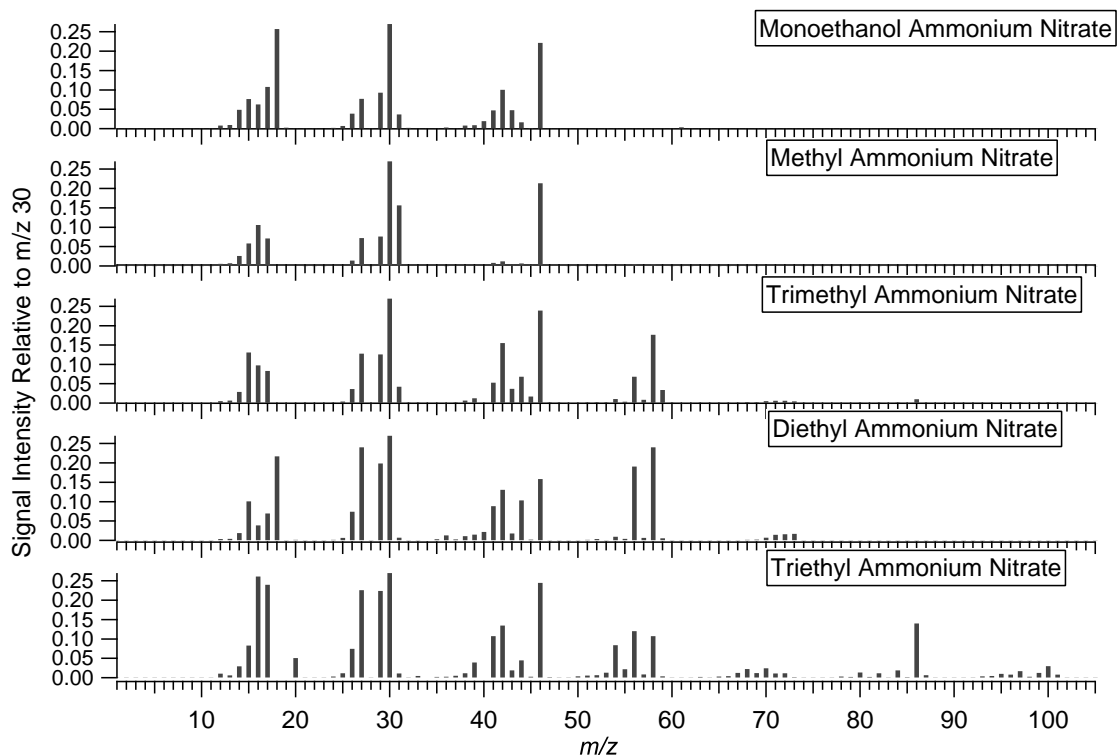


Figure 3.2: Mass spectra for the nitrate salts of the amines studied. On the ~ 550 °C surface of the vaporizer, all nitrate salts decompose into nitric acid and the parent amine. Signals at m/z 30 and 46 are generated from the nitrate fragments NO^+ and NO_2^+ and are common to all spectra. Signal at m/z 30 is a combination of signal from NO^+ and from amine fragments resulting from rearrangements after electron impact ionization. For all spectra, molecular ions have significantly less signal intensity than the fragments resulting from the cleavage of the chemical group alpha to the nitrogen (alpha cleavage). For the ethyl amines, loss of methyl groups alpha to the nitrogen give fragments at $[\text{M}-15]^+$ while for the methyl amines, loss of hydrogen atoms alpha to the nitrogen give fragments at $[\text{M}-1]^+$.

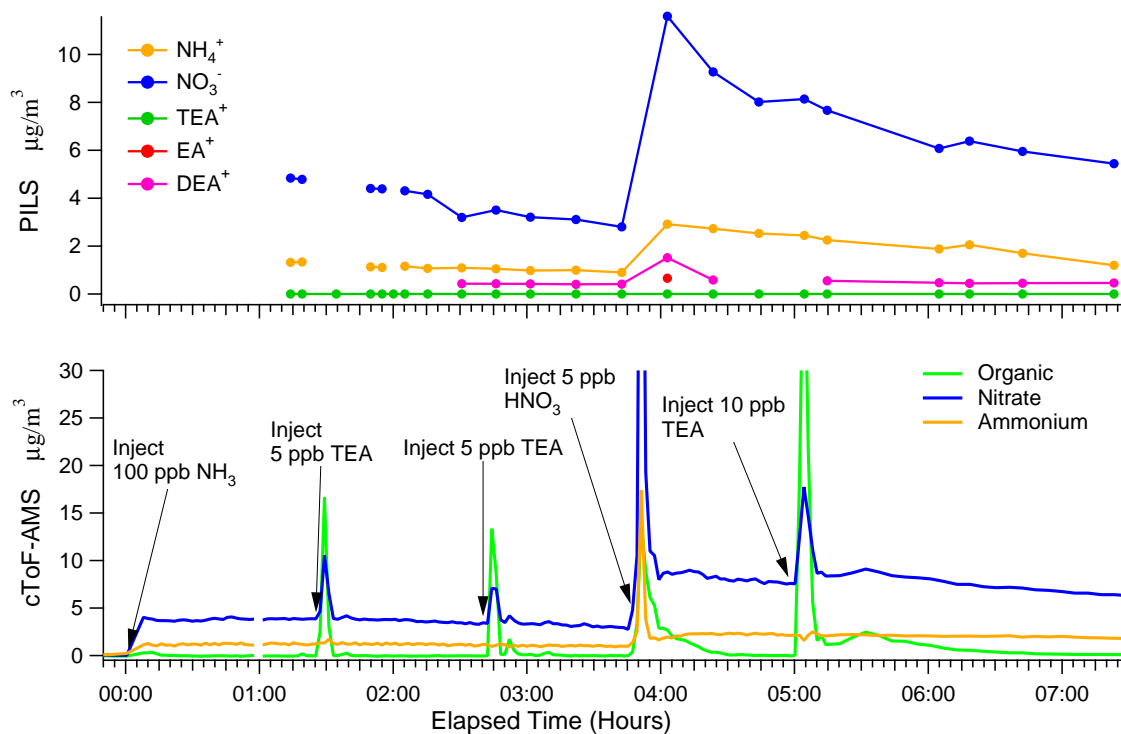


Figure 3.3: Time series from exp. 19 in Table 3.2 of the cToF-AMS (bottom) and the PILS-IC (top) showing rapid particle growth and evaporation after TEA and nitric acid were added in small aliquots to a chamber containing equilibrated ammonium nitrate particles. The transient spikes in particle loading do not appear in the PILS-IC data because of the relatively long averaging time (5 min) of measurements and because the PILS-IC inlet is not in the path of the highly concentrated injection plume.

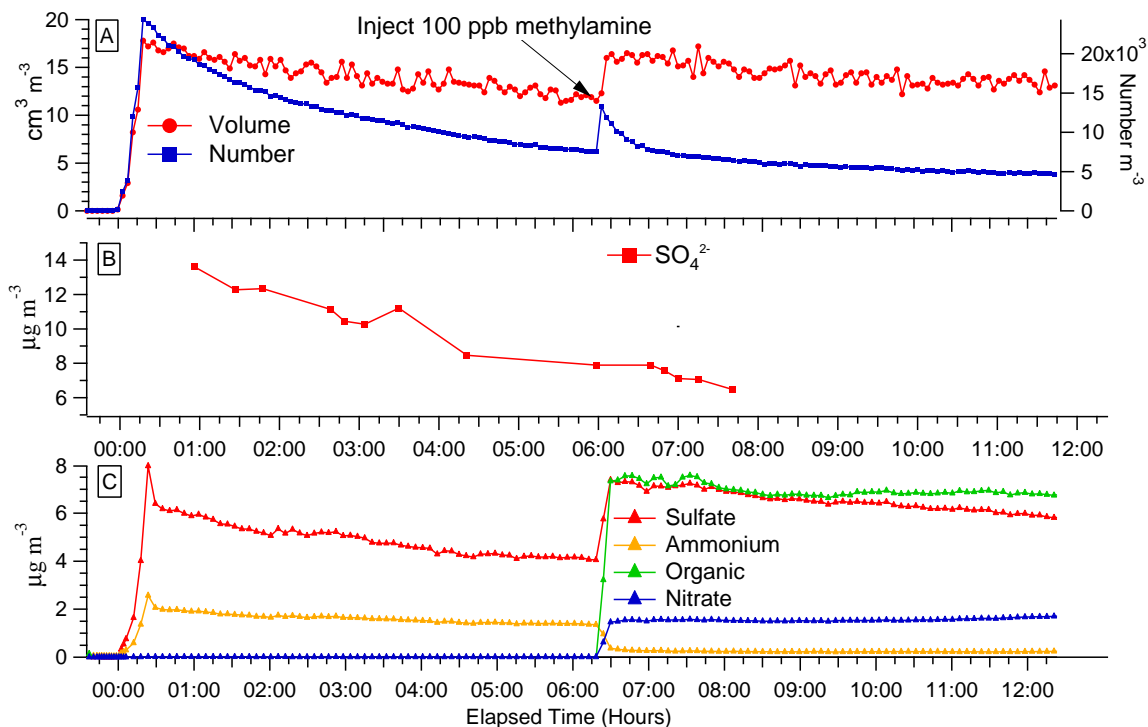
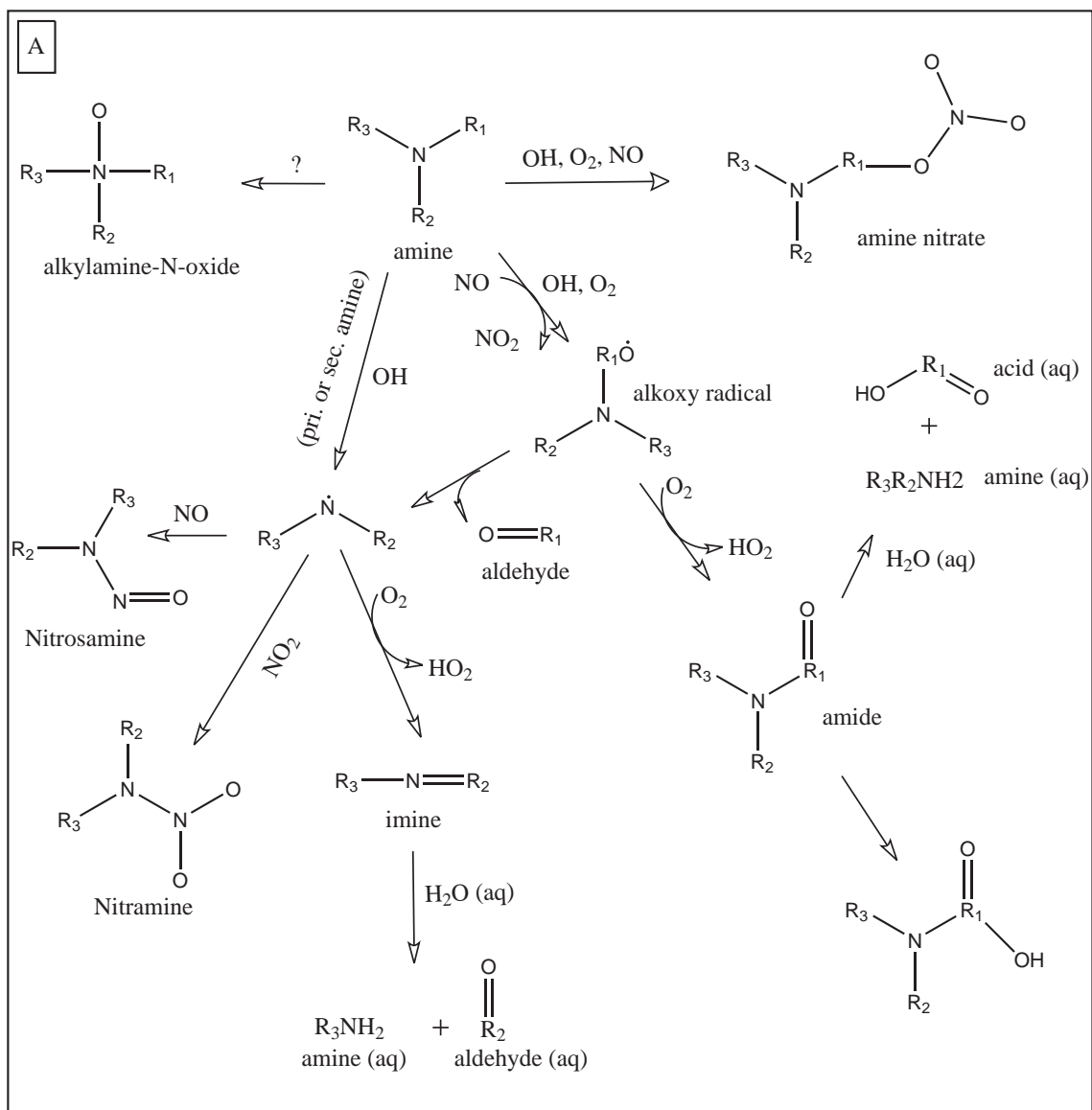


Figure 3.4: Time Series of data from the DMA (**Panel A**), PILS-IC (**Panel B**), and cToF-AMS (**Panel C**) showing rapid replacement of ammonium sulfate by methylammonium sulfate during the injection of 100 ppb of methylamine into a chamber containing ammonium sulfate seed and ozone. The increase in the ratio of organic signal to sulfate signal near the end of the experiment results from the slow reaction of methylamine with ozone forming a small mass of organic aerosol.



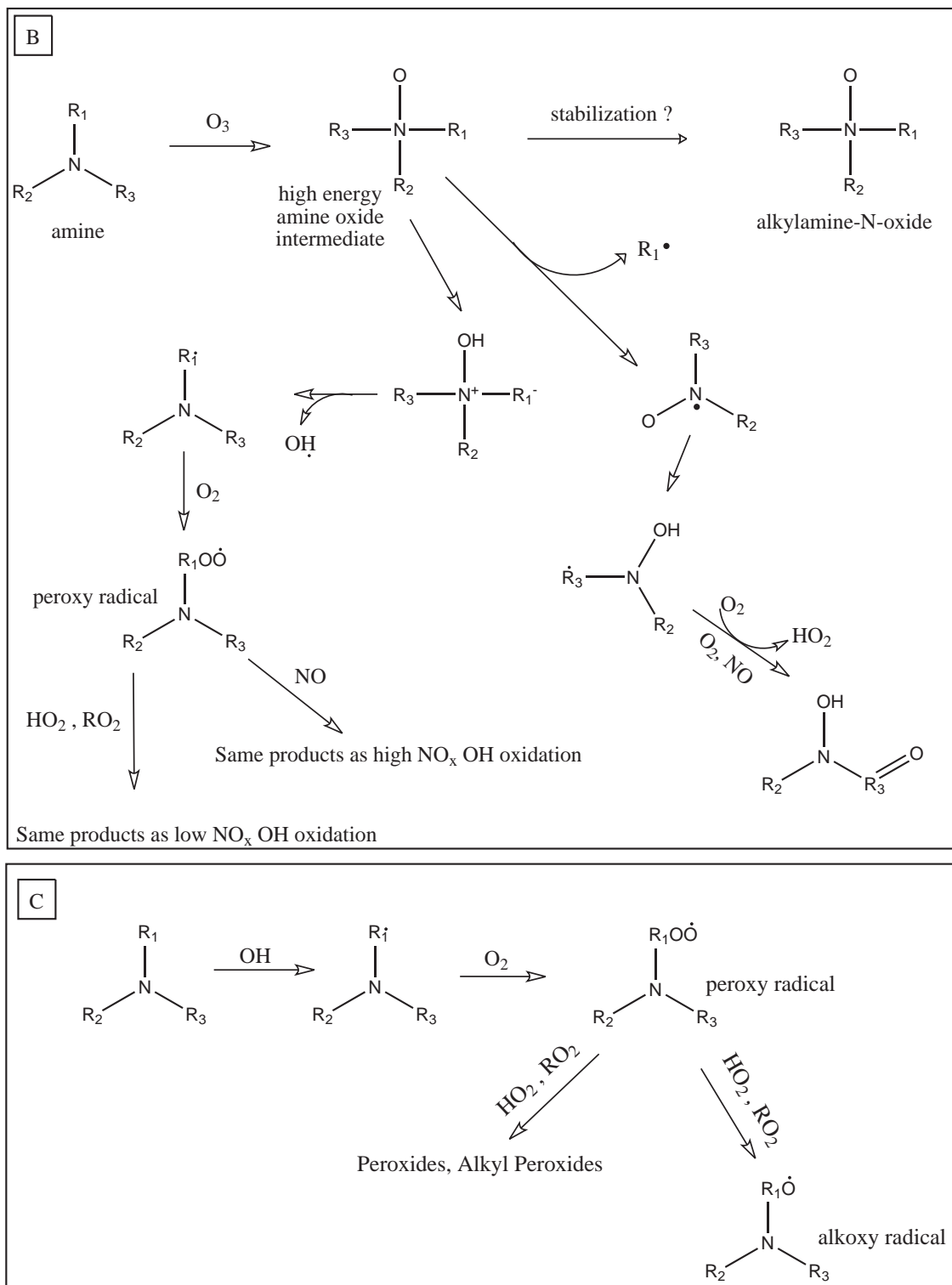


Figure 3.5: Mechanisms of amine oxidation by: (A) OH in the presence of NO_x (Schade and Crutzen, 1995), (B) Ozone, in the absence of NO_x (Tuazon et al., 1994), (C) OH in the absence of NO_x . A ? indicates an unknown oxidation mechanism to form the product shown.

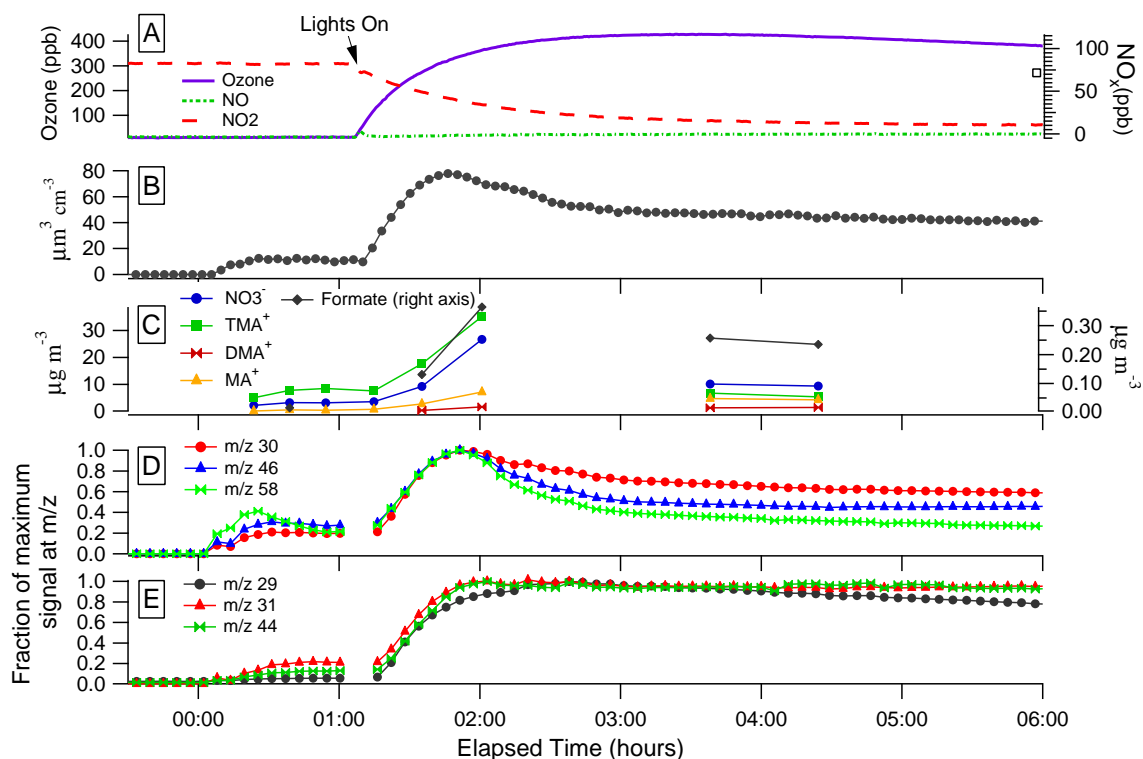


Figure 3.6: Photooxidation of trimethylamine (experiment 3 from Table 3.2). **Panel (A)** NO_x and ozone concentrations. **Panel (B)** Particle volume measured by the DMA. **Panel (C)** Growth of ionic species measured by the PILS-IC. **Panels (D) and (E)** Fragment ions from the cToF-AMS. When injected, the TMA reacts with nitric acid in the chamber to form trimethylammonium nitrate. Upon activation of the black lights, there is an initial burst of particle growth followed by a rapid decay in particle mass and volume. The PILS-IC data show that much of the decay is a result of volatilization of the methylammonium nitrate salt. The cToF-AMS traces show that while m/z 's corresponding to trimethylammonium nitrate salt fragments (30 NO⁺, 46 NO₂⁺, 58 ((CH₃)₂NCH₂)⁺) rapidly decrease after the peak in growth, m/z 's corresponding to methylammonium nitrate (31 CH₃NH₂⁺) and oxidized fragments (29 HCO⁺, 44 CO₂⁺) are level or decrease much more gradually.

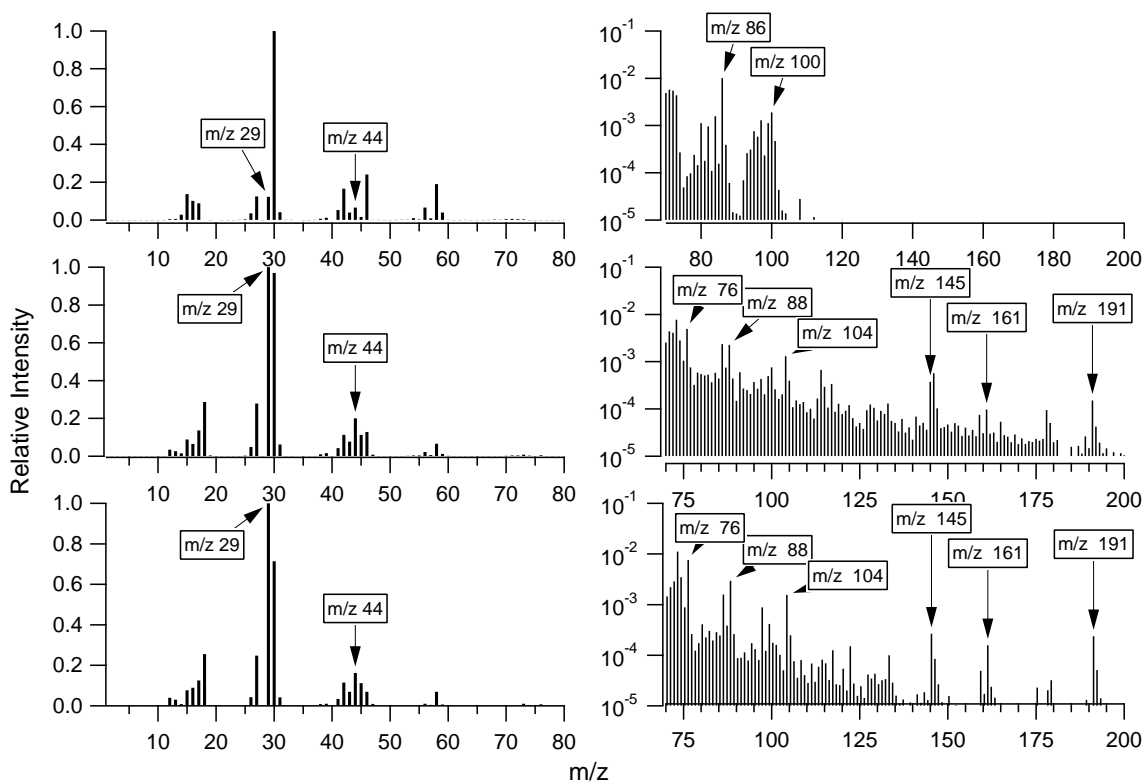


Figure 3.7: Aerosol mass spectra from the cToF-AMS during different stages of trimethylamine photooxidation (Figure 3.6) and ozonolysis (Figure 3.8). The top panel shows trimethylammonium nitrate before oxidation while the middle panel is from the end of the photooxidation experiment (8 h elapsed time). The bottom panel shows the spectra from aerosol formed from TMA after ~ 3 h of ozone exposure. The right and left panels show different m/z ranges of the same spectra. The major peaks shift during the photooxidation from peaks corresponding to the trimethylammonium nitrate salt to more oxidized peaks (29 HCO^+ , 44 CO_2^+). There is also a significant increase in the fraction of higher molecular weight species.

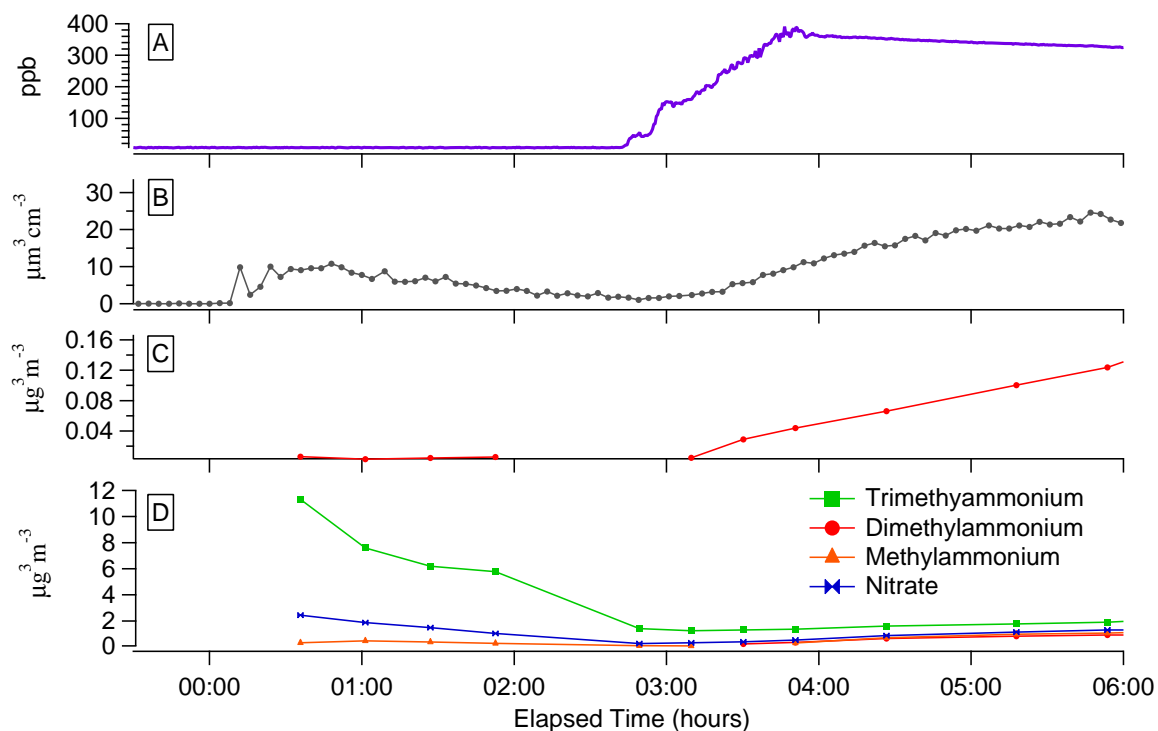


Figure 3.8: Ozonolysis of trimethylamine (exp. 4, Table 3.2). Trimethylamine is injected into a chamber containing 18 ppb of nitric acid at time = 0. The salt is allowed to decay away before 400 ppb of ozone is injected over ~1 h. **Panel (A)** Ozone concentration. **Panel (B)** DMA volume showing significant aerosol growth as the TMA is oxidized. **Panel (C)** Formate concentration measured by the PILS-IC. **Panel (D)** Ions measured by the PILS-IC, showing that there is little increase in salt concentrations during the ozonolysis.

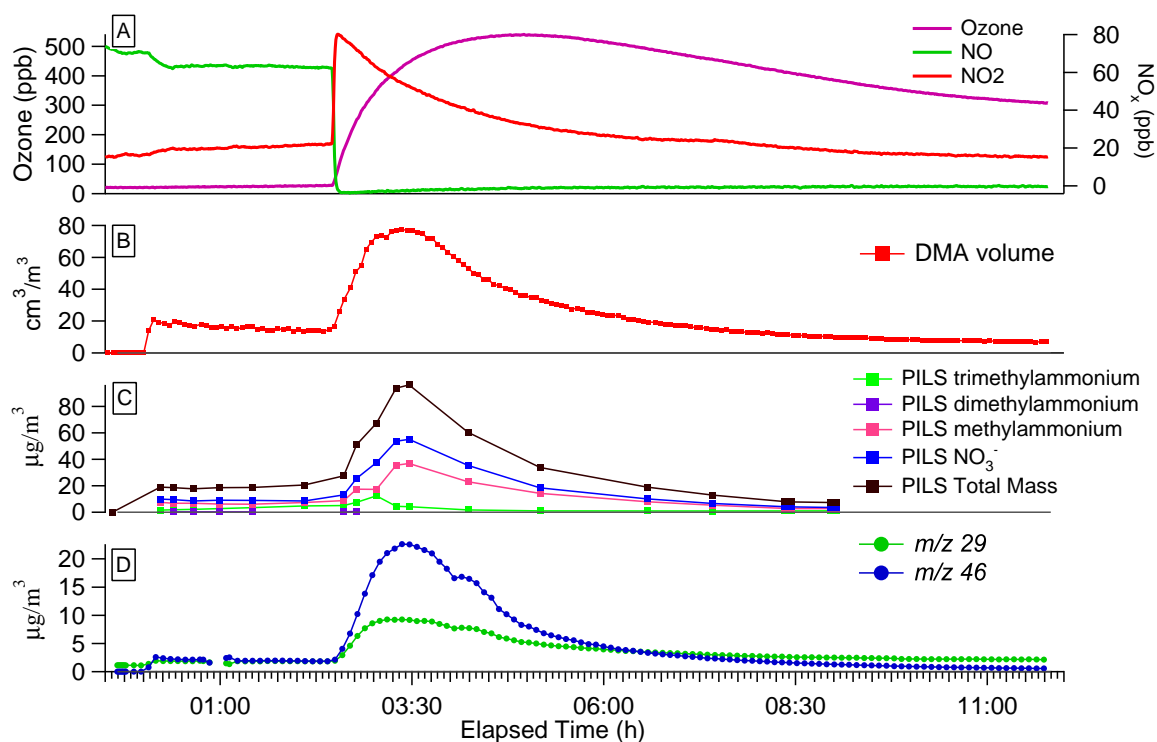


Figure 3.9: Methylamine photooxidation (exp. 6, Table 3.2). **Panel (A)** Ozone and NO_x concentrations. **Panel (B)** Time series for the DMA volume showing rapid decay after the peak of aerosol growth. **Panel (C)** Time series for the PILS-IC showing that most of the rapid mass decay is due to vaporization of the methylammonium nitrate salt. **Panel (D)** Fragment ions from the cToF-AMS. Signal from *m/z* 29, which is a mix of oxidized organic fragments (CHO⁺) and salt fragments gradually grows more important than signal from from salt alone (*m/z* 46 NO₂⁺).

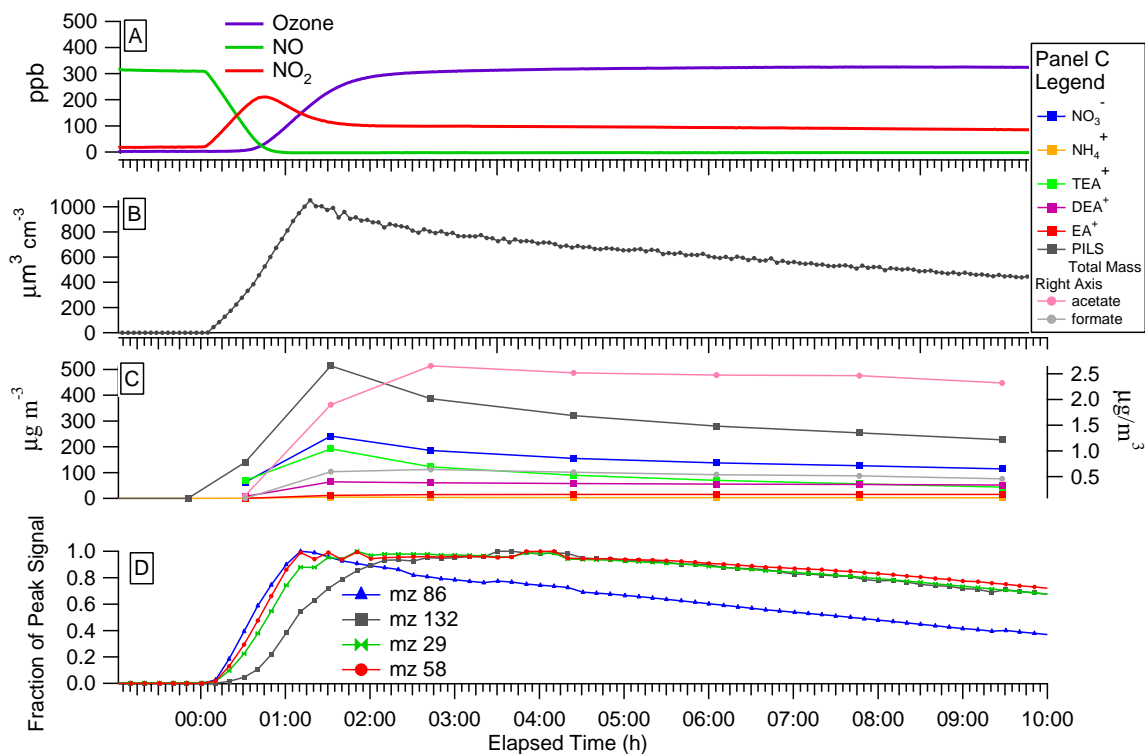


Figure 3.10: Photooxidation of 500 ppb triethylamine (TEA) (exp. 9, Table 3.2). Irradiation is initiated at $t=0$. **Panel (A)** Evolution of ozone and NO_x. **Panel (B)** DMA volume. **Panel (C)** Time profile of species detected by the PILS-IC showing that diethylammonium and ethylammonium are formed during the photooxidation, with significantly more diethylammonium being formed. **Panel (D)** Fragments from the cToF-AMS. The most intense fragment of TEA (m/z 86 $\text{N}(\text{CH}_2\text{CH}_3)_2\text{CH}_2^+$) grows in first followed by the major peak for DEA (m/z 58 $\text{NH}(\text{CH}_2\text{CH}_3)\text{CH}_2^+$) and oxidized fragments (m/z 29 CHO^+). Higher molecular weight fragments (m/z 132) grow in more slowly.

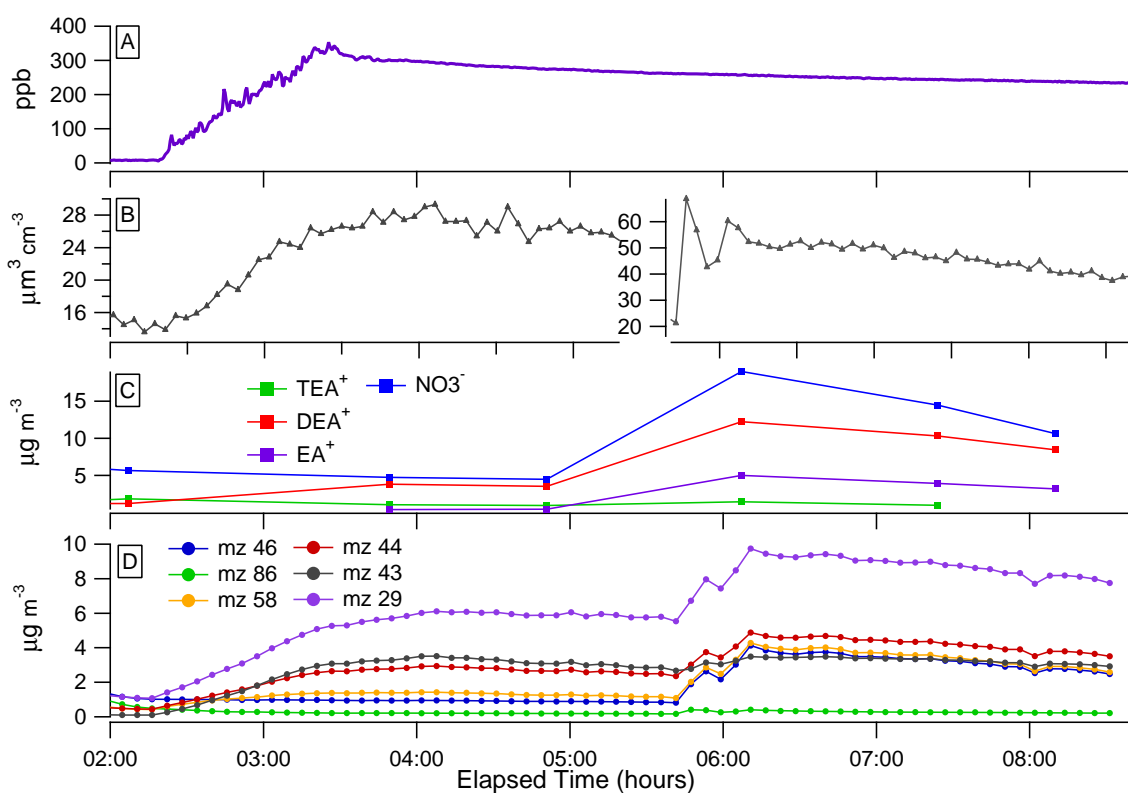


Figure 3.11: Ozonolysis of triethylamine (TEA) (exp. 16, Table 3.2). At $t=0$ (not shown) 100 ppb of TEA is injected into a chamber containing 8 ppb of nitric acid, nucleating triethylammonium nitrate (TEAN) particles, which are still present when ozone is injected at $t=2\text{h } 12\text{min}$. After growth of secondary aerosol formed through ozonolysis had ceased, an additional 8 ppb of nitric acid was injected at $5\text{h } 31\text{min}$. **Panel (A)** Time series of ozone mixing ratio **Panel (B)** Aerosol volume as measured by the DMA (the time axis is coincident with all of the other panels, two y-axes have been used to show more precisely the growth resulting from ozonolysis). **Panel (C)** Ionic species measured by the PILS-IC showing an increase in DEA throughout the reaction and condensation of EA when additional HNO_3 is added **Panel (D)** Ion fragments detected by the cToF-AMS: m/z 46 NO_2^+ , m/z 86 $\text{N}(\text{CH}_2\text{CH}_3)_2\text{CH}_2^+$ (largest peak from triethylammonium), m/z 58 $\text{NH}(\text{CH}_2\text{CH}_3)\text{CH}_2^+$ (largest peak from Diethylammonium), m/z 44 CO_2^+ , m/z 43 $\text{C}_2\text{H}_3\text{O}^+$, m/z 29 CHO^+ .

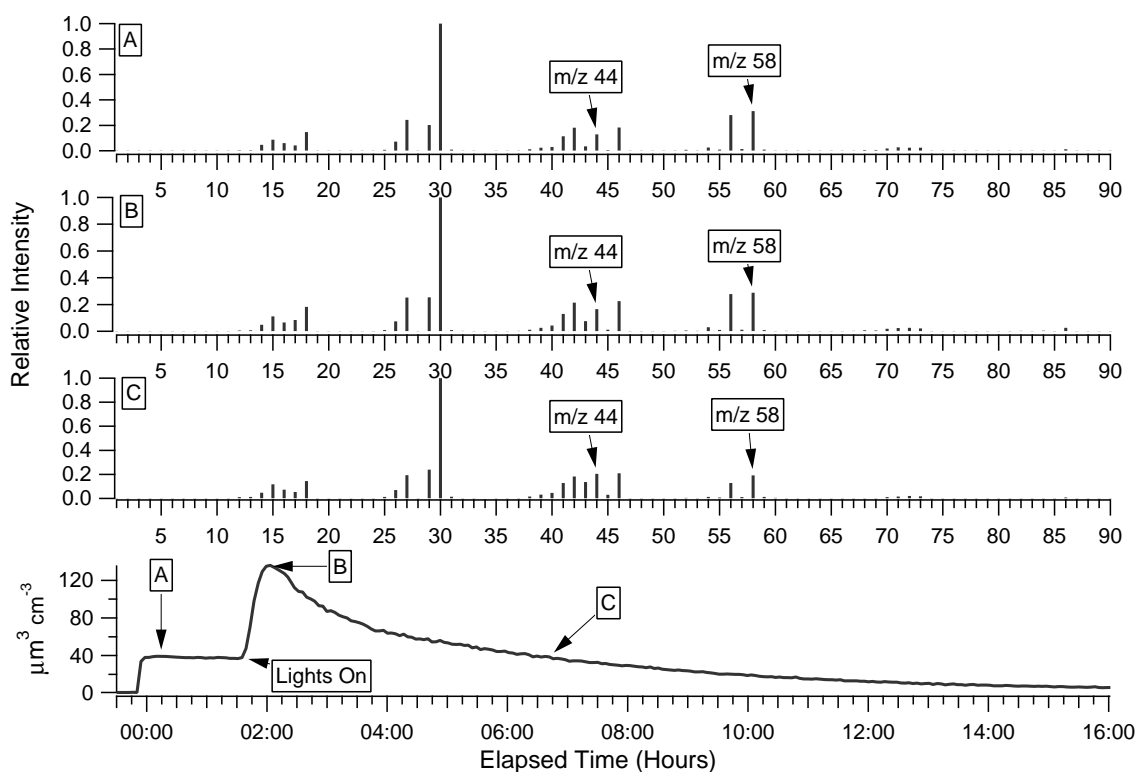


Figure 3.12: Photooxidation of diethylamine (exp. 22, Table 3.2). The volume trace from the DMA (bottom panel) shows that the aerosol formed decays quickly back to the volume present before the irradiation. The prominent peaks in the cToF-AMS spectra (Panels A-C) show little change throughout the course of the experiment, except for a slight increase in the relative intensity of oxidized peaks at m/z 44 (CO_2^+) and m/z 43 ($\text{C}_2\text{H}_3\text{O}^+$). There was also little change in the high m/z spectra indicating negligible growth of high molecular weight species.

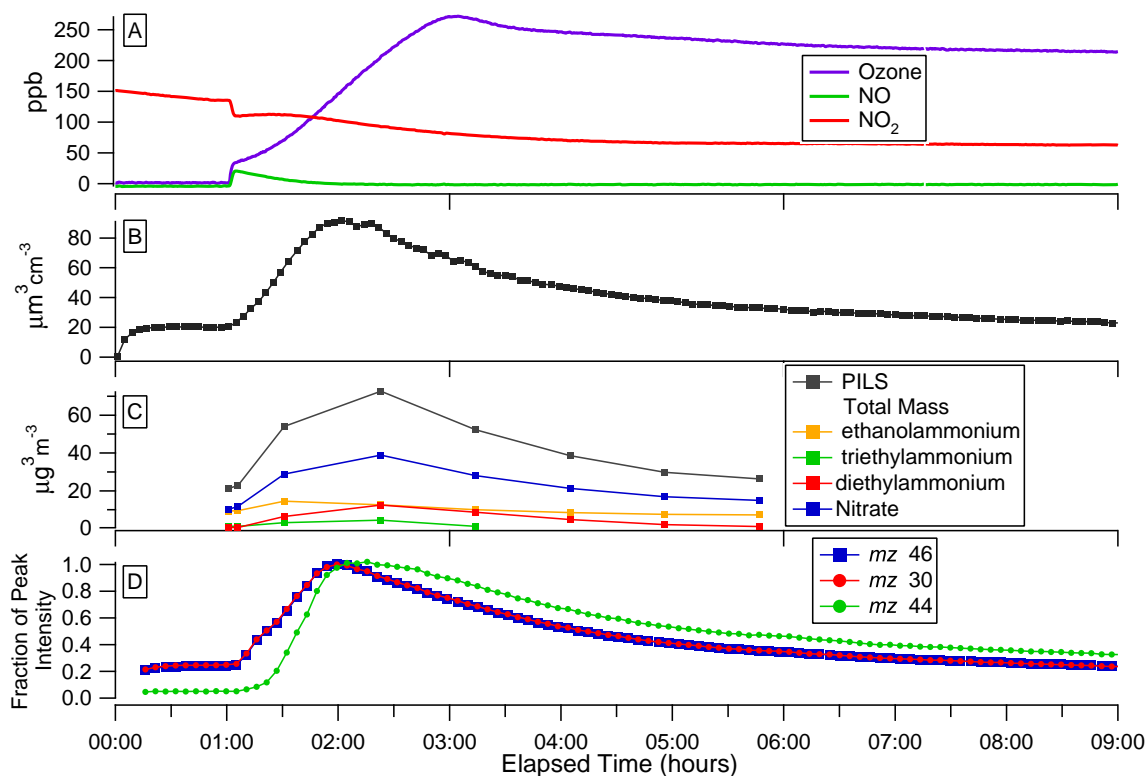


Figure 3.13: Photooxidation of 100 ppb of ethanolamine (EtOHA) (exp. 29, Table 3.2). Ethanolamine is injected at $t=0$ forming ethanolammonium nitrate. **Panel (A)** Evolution of ozone and NO_x mixing ratios. **Panel (B)** DMA volume. **Panel (C)** PILS-IC data. **Panel (D)** Fragments from the cToF-AMS. Oxidized fragment ions (m/z 44 CO_2^+) grow in slowly and decay less quickly than nitrate fragment ions (m/z 46 NO_2^+ and m/z 30 NO^+) or ethanolammonium fragment ions (m/z 30 is the base peak for ethanolammonium in the cToF-AMS).

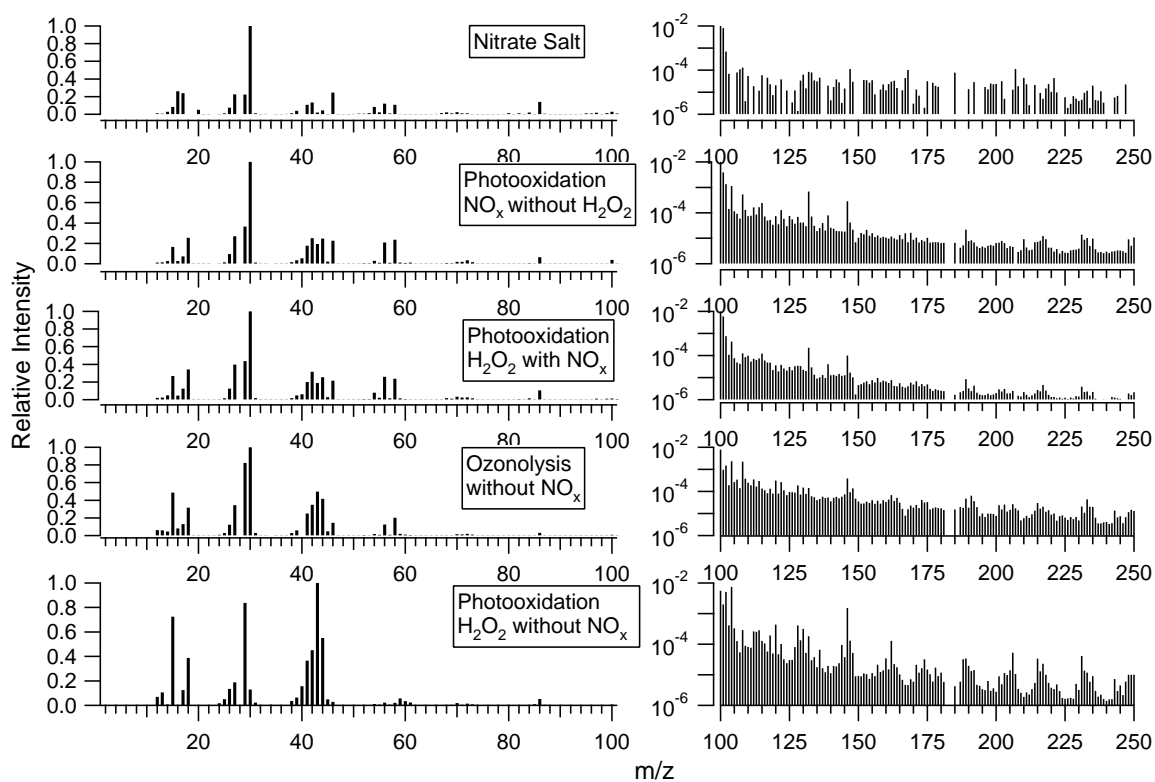


Figure 3.14: cToF-AMS spectra (normalized to the largest peak) of aerosol generated from TEA oxidation under various conditions. In all cases, except for hydrogen peroxide without NO_x , the nitrate salt was intentionally formed by mixing TEA with nitric acid in the chamber before the start of oxidation. All spectra were collected after the peak of aerosol growth had been reached.

Chapter 4

Comprehensive Airborne Characterization of Aerosol from a Major Bovine Source

*This chapter is reproduced by permission from “Comprehensive Airborne Characterization of Aerosol From a Major Bovine Source” by A. Sorooshian, S. M. Murphy, S. Hersey, H. Gates, L. T. Padró, A. Nenes, F. J. Brechtel, H. Jonsson, R. C. Flagan, and J. H. Seinfeld¹, *Atmospheric Chemistry and Physics*, 8, 5489, 2008. Copyright 2008 Authors. This work is licensed under a Creative Commons License.

4.1 Abstract

We report an extensive airborne characterization of aerosol downwind of a massive bovine source in the San Joaquin Valley (California) on two flights during July 2007. The Center for Interdisciplinary Remotely-Piloted Aircraft Studies (CIRPAS) Twin Otter probed chemical composition, particle size distribution, mixing state, sub- and supersaturated water uptake behavior, light scattering properties, and the interrelationship between these parameters and meteorology. Total $PM_{1.0}$ levels and concentrations of organics, nitrate, and ammonium were enhanced in the plume from the source as compared to the background aerosol. Organics dominated the plume aerosol mass (~ 56 - 64%), followed either by sulfate or nitrate, and then ammonium. Particulate amines were detected in the plume aerosol by a particle-into-liquid sampler (PILS) and via mass spectral markers in the Aerodyne C-ToF-AMS. Amines were found to be a significant atmospheric base even in the presence of ammonia; particulate amine concentrations are estimated as at least 14 – 23% of that of ammonium in the plume. Enhanced sub- and supersaturated water uptake and reduced refractive indices were coincident with lower organic mass fractions, higher nitrate mass fractions, and the detection of amines. The likelihood of suppressed droplet growth owing to kinetic limitations from hydrophobic organic material is explored. After removing effects associated with size distribution and mixing state, the normalized activated fraction of cloud condensation nuclei (CCN) increased as a function of the subsaturated hygroscopic growth factor, with the highest activated fractions being consistent with relatively lower organic mass fractions and higher nitrate mass fractions. Subsaturated hygroscopic growth factors for the organic fraction of the aerosol are estimated based on employing the Zdanovskii-Stokes Robinson

(ZSR) mixing rule. Representative values for a parameterization treating particle water uptake in both the sub- and supersaturated regimes are reported for incorporation into atmospheric models.

4.2 Introduction

Bovine emissions are major sources of methane (CH_4), nitrous oxide (N_2O), and ammonia (NH_3); they are also the dominant anthropogenic source for amines (Schade and Crutzen, 1995). Ammonia is the dominant base in the atmosphere, efficiently neutralizing acidic substances. The main global sources of ammonia are from livestock waste, fertilizer applications, biomass burning, motor vehicle emissions, and coal combustion (Apsimon et al., 1987; Asman and Janssen, 1987; Kleeman et al., 1999; Anderson et al., 2003; Battye et al., 2003). Typical ammonia mixing ratios over continents range between 0.1 and 10 ppb (Edgerton et al., 2007, and references therein), while levels as high as a few ppm have been reported near areas of extensive livestock operations (Rumburg et al., 2006).

The principal inorganic aerosol components involving ammonia are ammonium nitrate and ammonium sulfate. The formation of these inorganic salts depends on temperature, relative humidity (RH), and concentrations of NH_3 , nitric acid (HNO_3) and sulfur dioxide (SO_2). Ammonium nitrate tends to form after sulfuric acid is completely neutralized. Atmospheric ammonium nitrate generally obeys thermodynamic equilibrium with gaseous nitric acid and ammonia (Stelson et al., 1979; Doyle et al., 1979; Stelson and Seinfeld, 1982a, 1982b; Russell et al., 1983; Hildemann et al., 1984; Zhang et al., 2002; Takahama et al., 2004; Yu et al., 2005), although some studies have pointed out

that factors such as mass transport limitations can, at times, result in departures from equilibrium (Wexler and Seinfeld, 1992; Meng and Seinfeld, 1996; Fridlind and Jacobson, 2000; Fridlind et al., 2000). The equilibrium between particulate ammonium nitrate and gaseous nitric acid and ammonia shifts to the gas phase as ambient temperature increases, and RH decreases. Similar to ammonia, amines undergo neutralization reactions with nitric and sulfuric acids to form amine salts (Mozurkewich, 1993; Stelson and Seinfeld, 1982a; Angelino et al., 2001; Murphy et al., 2007). The photooxidation of gas-phase amines has been shown to form aerosol based on recent laboratory experiments (Angelino et al., 2001; Murphy et al., 2007).

Gaseous amines, including methylamine, dimethylamine, trimethylamine, ethylamine, diethylamine, triethylamine, ethanoloamine, *n*-butylamine, amylamine, 1,4-butanediamine, isobutylamine, and isopropylamine, have been identified in emissions from bovine sources (Mosier et al., 1973; Hutchinson et al., 1982; Schade and Crutzen, 1995; Rabaud et al., 2003; Ngwabie et al., 2005). Amine emission rates from animal husbandry sources are typically two to three orders of magnitude lower than those of ammonia (Schade and Crutzen, 1995; Ngwabie et al., 2005). Gaseous amines are also present in vehicular exhaust (Cadle and Mulawa, 1980; Westerholm et al., 1993), the marine atmosphere (Vanneste et al., 1987), biomass burning plumes (Lobert et al., 1991), as well as emissions from decaying organic matter, waste incineration, and sewage treatment plants (Manahan, 2005). Amine salts have sufficiently low vapor pressures to partition to the aerosol phase; moreover, they exhibit greater water-solubility as compared to other particulate organic nitrogen species (Milne and Zika, 1993; Gorzelska et al., 1994; Murphy and Thomson, 1997; Glagolenko and Phares, 1994; Abalos et al.,

1999; Angelino et al., 2001; Makela et al., 2001; Tan et al., 2002; Zhang et al., 2002; Zhang and Anastasio, 2003; Maria et al., 2003; Beddows et al., 2004; Denkenberger et al., 2007; Murphy et al., 2007; Sorooshian et al., 2007a).

The availability of a massive, concentrated source of ammonia and amines offers a unique opportunity to probe the response of the resulting aerosol. During July 2007, the Center for Interdisciplinary Remotely Piloted Aircraft Studies (CIRPAS) Twin Otter probed the aerosol downwind of a major cattle feedlot in the San Joaquin Valley in California. The San Joaquin Valley, the major geographical feature in central California, is bordered on its west and east sides by mountain ranges and is characterized by relatively stagnant air circulation (Fig. 4.1A). Consequently, this region is one of the largest nonattainment areas for ozone and particulate matter in the United States (Chow et al., 2006). The San Joaquin Valley contains numerous animal husbandry operations, the largest of which is the focus of this study. This feedlot operation covers several hundred acres and contains up to 100,000 head of cattle at any one time. Although gas-phase measurements were not carried out, the presence of ammonia and amines is inferred from established emissions inventories from animal husbandry sources and from measurements of the ammonium and amine content of the aerosol downwind of the plume source.

The goal of the present study is to provide a comprehensive airborne characterization of the aerosol downwind of a major bovine source. First, the aircraft instrument payload and flight path strategy are presented. Detailed measurements were obtained for: meteorology, aerosol size distributions and number concentrations, aerosol composition, mixing state, refractive index, hygroscopic growth factors at three different

relative humidities, and cloud condensation nucleus (CCN) behavior. Special attention is given to the sub- and supersaturated water uptake properties of the aerosol, and how these relate to chemical composition. Subsaturated hygroscopic growth factors for the organic fraction of the aerosol are reported based on a closure analysis employing the Zdanovskii-Stokes Robinson mixing rule. Subsaturated hygroscopic growth data are then compared to measured supersaturated CCN activity to evaluate the level of consistency between observed water uptake in the two regimes.

4.3 Experimental Methods

The data on which the present study is based were acquired during two clear air flights in the San Joaquin Valley on 12 July 2007 and 30 July 2007. Henceforth, these two flights will be termed flight A (12 July 2007) and flight B (30 July 2007). The aircraft total aerosol inlet, characterized by Hegg et al. (2005), provided sample air to instruments on the aircraft. The instrument payload on the Twin Otter aircraft is described elsewhere (<http://www.cirpas.org>), however, attention is given below to those instruments the data from which will be discussed in detail.

4.3.1 Aerosol Chemical Composition (Aerodyne C-ToF-AMS)

Chemical composition measurements for non-refractory aerosol species (sulfate, nitrate, ammonium, and organics) were performed using an Aerodyne compact Time of Flight Aerosol Mass Spectrometer (C-ToF-AMS; Drewnick et al., 2005). At the entrance to the instrument, an aerodynamic lens focuses particles with vacuum aerodynamic diameters between approximately 50 nm and 800 nm through a 3.5% chopper and onto a

tungsten vaporizer ($\sim 550^\circ \text{C}$) (Murphy et al., 2007). The chopper can be operated in three modes to gather either background mass spectra, ensemble average mass spectra over all particle sizes, or size-resolved mass spectra. Once vaporized, molecules undergo electron impact ionization and travel through a time of flight mass analyzer. The C-ToF-AMS detects the presence of amines in the form of characteristic amine peaks at m/z 30, 56, and 86 (McLafferty and Turecek, 1993; Angelino et al., 2001; Murphy et al., 2007). The detection limit, calculated as three times the standard deviation of the noise for filtered air, is $< 0.05 \mu\text{g}/\text{m}^3$ for all species measured.

The C-ToF-AMS can be used to calculate a quantity that will be referred to subsequently as *excess nitrate*. *Excess nitrate* is defined as the nitrate mass, derived from C-ToF-AMS spectra, remaining after both sulfate and nitrate have been fully neutralized by ammonium. A zero or slightly negative value indicates that sufficient ammonia exists to neutralize both sulfate and nitrate, while a positive value indicates that some nitrate is associated with other cations besides ammonium. C-ToF-AMS calibrations allow an assessment of the error associated with the *excess nitrate* calculation; introducing pure ammonium nitrate into the instrument should result in an *excess nitrate* value of zero. After flight A, calibrations were conducted with monodisperse ammonium nitrate particles ranging from 50 nm to 400 nm and mass concentrations ranging from $1.5 \mu\text{g}/\text{m}^3$ to $7.0 \mu\text{g}/\text{m}^3$, similar to concentrations in flight. Thirty-three calibration points were collected that exhibited an average *excess nitrate* of $0.08 \pm 0.31 \mu\text{g}/\text{m}^3$. Similarly during a calibration on the day of flight B, 350 and 400 nm ammonium nitrate particles were introduced into the instrument at levels near $\sim 3 \mu\text{g}/\text{m}^3$, which exceeds the peak nitrate concentration observed during the flight. The average *excess nitrate* was -0.014 ± 0.095

$\mu\text{g}/\text{m}^3$ ($n = 17$). As will be shown, ambient *excess nitrate* concentrations in the plume aerosol significantly exceeded the background values for pure ammonium nitrate.

Nitrate species can be detected by peaks at m/z 30 and 46. A problem innate to C-ToF-AMS unit mass-resolution spectra is differentiating between NO^+ , CH_2O^+ , and C_2H_6^+ , all of which give peaks at m/z 30. If the contribution of organic fragments to the signal at m/z 30 is not correctly accounted for, the mass of nitrate, as inferred from NO^+ , can be overestimated. A relatively conservative approach is to calculate nitrate mass using the peak intensity at m/z 46 (NO_2^+), which rarely corresponds to an organic fragment (McLafferty and Turecek, 1993). Calibration of the instrument with pure ammonium nitrate allows observation of the ratio of the peak intensities at m/z 30 and 46 when NO^+ and NO_2^+ are present without organic interference. During such a calibration conducted after flight A, the peak at m/z 30 was observed to be 2.2 times that at m/z 46. Thus, for this flight, nitrate mass at m/z 30 was calculated to be 2.2 times the mass at m/z 46. Based on calibrations on the day of flight B, the peak at m/z 30 was observed to be 2.8 times that at m/z 46. The two calibrations were seventeen days apart, and instrumental drift is responsible for the difference in the m/z 30:46 ratio between the two days; typical values observed with this instrument range between two and three. The mass remaining at m/z 30 after the nitrate contribution is subtracted is assumed to be organic, including amine species, which often exhibit a major peak here.

4.3.2 Aerosol Chemical Composition (PILS)

Water-soluble aerosol chemical composition was measured by a particle-into-liquid sampler (PILS, Brechtel Mfg Inc.; Sorooshian et al., 2006a). In the PILS,

submicrometer ambient particles are grown into droplets sufficiently large to be collected by inertial impaction for subsequent chemical analysis. At the entrance to the instrument a series of three denuders (URG and Sunset Laboratories) remove inorganic (basic and acidic) and organic gases that would otherwise bias aerosol measurements. The impacted droplets are delivered to a rotating carousel containing 72 vials, with each vial containing material representing a period of ~ 5 min of flight, or alternatively, a distance of 15 km in flight (aircraft speed ~ 50 m/s). The contents of the vials are subsequently analyzed off-line using a dual ion chromatography (IC) system (ICS-2000, Dionex, Inc.) for simultaneous anion and cation analysis.

The PILS-IC instrument uncertainty has been established as $\pm 7\%$, and the detection limit (calculated as air-equivalent concentration of the lowest concentration standard that is distinct from baseline noise in the IC plus three times the standard deviation of this measurement) is $< 0.1 \mu\text{g}/\text{m}^3$ for the inorganic ions (Na^+ , NH_4^+ , K^+ , Mg^{2+} , Ca^{2+} , Cl^- , NO_2^- , NO_3^- , and SO_4^{2-}) and $< 0.01 \mu\text{g}/\text{m}^3$ for the organic acid ions (carboxylic acids with one to nine carbon atoms) (Sorooshian et al., 2007b). The PILS-IC technique has been demonstrated to speciate amines, including ethylamine, diethylamine, triethylamine, methylamine, dimethylamine, and trimethylamine (Sorooshian et al., 2007a); however, only ethylamine and diethylamine were measured above detection limits ($0.01 \mu\text{g}/\text{m}^3$) in the present study. It should be noted that ammonium and ethylamine co-elute in the IC cation column; however, ethylamine was detected at sufficiently high concentrations for its peak to be distinguishable from that of ammonium. The reported concentrations of ethylamine represent a lower limit due to this co-elution effect. Since acetate, lactate, and glycolate also co-elute, these three species

are reported as a collective mass using the calibration equation of acetate; therefore, the contribution of acetate reported is likely an overestimate. As compared to acetate, using the calibration equation of glycolate would reduce the estimates by < 10%.

An important issue during this study was the potential for denuder breakthrough in the PILS because the sampling site represents the most concentrated ambient source of ammonia and amines encountered by this PILS. The denuders have been shown to successfully remove gaseous amine species in laboratory chamber experiments (Murphy et al., 2007); estimated initial mixing ratios for gaseous amines in those experiments ranged between 50 – 500 ppb, which is expected to represent levels expected in areas of intense animal husbandry. To check for evidence of ammonia breakthrough, the ammonium levels measured by the PILS and C-ToF-AMS, which is not prone to gaseous artifacts, are compared. For the following calculations it is assumed that the C-ToF-AMS collection efficiency for ammonium was constant throughout the flights and was identical to that of sulfate, even though external mixing was evident. The average of the ammonium ratio (PILS:C-ToF-AMS) was 0.90 ± 0.11 during flight A and 0.87 ± 0.21 during flight B. There was no clear enhancement in the ratio of PILS:C-ToF-AMS ammonium levels within the plume either flight. These data suggest that ammonia breakthrough did not lead to a positive artifact in the PILS, and even if so, it was masked by some other effect such as volatilization of ammonium in the PILS or an inaccurate collection efficiency applied to C-ToF-AMS ammonium data. Sorooshian et al. (2006a) showed that approximately 12% of ammonium in laboratory-generated ammonium sulfate particles is lost by volatilization at similar PILS operating conditions as implemented during this study, and the PILS data here are corrected for this 12%.

Therefore, it is uncertain as to why the PILS ammonium levels were on average less than those of the C-ToF-AMS.

4.3.3 Aerosol Hygroscopicity and Refractive Index (DASH-SP)

A differential aerosol sizing and hygroscopicity spectrometer probe (DASH-SP; Brechtel Mfg Inc.; Sorooshian et al., 2008) was included in the instrument payload on the aircraft. The DASH-SP consists of a single classification differential mobility analyzer (DMA) followed by a set of parallel hygroscopic growth chambers operated at different relative humidities. A ~ 0.5 LPM aerosol sample flow passes first through a Nafion drier, and then through a ^{210}Po neutralizer that brings the dried particles to a stable, steady-state charge distribution. A cylindrical DMA selects particles in a narrow interval of mobility-equivalent diameters in the 0.1 to 1.0 μm range. The classified aerosol leaving the DMA is split into five separate flows. In one of the five streams, the total concentration of classified particles is determined using an integral TSI Model 3831 water-based condensation particle counter (CPC). The remaining four classified aerosol flows pass through a Nafion humidifier (Perma Pure, LLP, Model MD-070-24FS-4) to achieve thermodynamic equilibrium with water vapor at a constant, predetermined RH. The four conditioned aerosol flows pass directly to dedicated, custom-built OPCs ($\lambda = 532$ nm, World Star Technologies, Model TECGL-30) designed to size particles in the 100 nm to 3 μm diameter size range. An iterative data processing algorithm quantifies an ‘effective’ aerosol refractive index that is used to calculate hygroscopic growth factors ($GF = D_{p,wet}/D_{p,dry}$) corrected for the refractive-index dependence of the OPC response (Sorooshian et al., 2008). During this study, the DASH-SP provided simultaneous

measurements of GFs at different RHs for dry DMA-selected particle diameters between $D_p = 150 - 200$ nm. One humidifier was operated dry (RH < 8%), and the other three were at RHs of 74%, 85%, and 92%. (No data from the RH = 85% channel were available during flight A.) The uncertainty associated with growth factor measurements is $\sim \pm 4.5\%$, and the uncertainty in the RH is $\pm 1.5\%$.

4.3.4 Cloud Condensation Nuclei Counter (CCNc)

A continuous flow thermal gradient cloud condensation nuclei counter (CCNc, Droplet Measurement Technologies Inc.; Roberts and Nenes, 2005; Lance et al., 2006) was used to quantify the number of particles that activate at supersaturations ranging from 0.1% to 0.6%. In the instrument a supersaturation is generated in an axisymmetric flow by applying a constant streamwise temperature gradient, using three sets of thermal electric coolers across a wetted column. At the exit of the CCNc column, those particles that activate and grow sufficiently large ($D_p > 0.75 \mu\text{m}$) for detection by an OPC were quantified. The activated fraction is determined as the ratio of the CCN number concentration to the total particle (CN) number concentration.

The CCNc was calibrated numerous times throughout this study and a brief description of the procedure now follows; we refer the reader to Appendix A for a more detailed explanation. Dried ammonium sulfate particles are sent to a DMA (Model 3081L, TSI, Inc.) for size selection. The resulting monodisperse aerosol stream is split and sent to both a condensation particle counter (Model 3010, TSI, Inc.) and a continuous-flow streamwise thermal gradient chamber (operated at constant flow rate, temperature gradient, and pressure) to measure CN and CCN, respectively. The level of

supersaturation in the instrument is determined from the minimum dry particle diameter, D_{p50} (dry diameter for which the $CCN/CN = 0.50$), that activates in the instrument. The instrument supersaturation is related to D_{p50} by applying Köhler theory assuming ammonium sulfate has a density of 1760 kg/m^3 , surface tension of water, molar mass of 0.132 kg/mol , and an effective van't Hoff factor of 2.5; studies have found the latter value to lie between 2 and 2.5 (Gerber et al., 1977; Brechtel and Kreidenweis, 2000; Kumar et al., 2003; Rose et al., 2008).

4.3.5 Size Distributions and Particle Number Concentration

Aerosol size distribution data were obtained by a DMA ($D_p = 10 - 800 \text{ nm}$) and an external passive cavity aerosol spectrometer probe ($0.1 - 3 \text{ }\mu\text{m}$) (PCASP, PMS Inc., modified by DMT Inc.). Particle number concentrations were quantified with two condensation particle counters (CPC Model 3010, TSI Inc., $D_p > 10 \text{ nm}$; UFCPC Model 3025, TSI Inc., $D_p > 3 \text{ nm}$). When the two CPCs experienced electrical saturation, particle number concentrations from the DMA are reported. The DMA time resolution is 74 s as opposed to 1 s for the CPCs.

4.3.6 Flight Strategy

Complete flight tracks from flights A and B are shown in Fig. 4.1A. Both flights were intended to resemble each other in the time of the day and flight path. Starting from the Marina, CA airport, the aircraft transited east before descending to 50 m above the surface of the San Joaquin Valley. Then the aircraft flew southeast directly towards the feedlot, approaching to within one kilometer of the feedlot. A close-up of the flight

tracks near the plume source with step-by-step details of the flight strategy is shown in Fig. 4.1B/C. In each flight, the Twin Otter circled above the perimeter of the source several times, performed a spiral ascent to characterize the meteorological profile, performed several downwind transects of the plume at various altitudes below the boundary layer top, flew directly in the plume for several legs (only flight B), and transited northwest back up the valley. Sampling lasted for more than three hours starting just before noon during both flights. The feedlot operation is slightly larger than 3 km² in area (~ 800 acres). The feedlot is bordered on the west side by the Interstate 5 roadway, which is a major transportation route and source of vehicular emissions, connecting northern and southern California.

4.4 Results

4.4.1 Meteorology

Figures 4.2 (flight A) and 4.3 (flight B) display the time evolution of meteorological and particle number concentration data, while Fig. 4.4 presents vertical profiles. During flight B, ambient temperatures ($27.5 \pm 2.4^\circ \text{C}$) were higher and RHs ($25.8 \pm 5.9\%$) were lower than observed in flight A ($21.8 \pm 2.3^\circ \text{C}$; $49.0 \pm 7.8\%$). During both flights, the aircraft performed three vertical profiles of the boundary layer. The temperature inversions were weak ($< 1^\circ \text{C}$), so decreases in RH and particle number concentrations, as quantified by the DMA and PCASP, are used as indicators for inversion layers. The boundary layer exhibited multiple inversions, the highest of which was observed at the end of the flights (~ 3 PM local time) at ~ 630 m. The depth of the inversion layers increased with time as the surface warmed. The vertical temperature and

RH profiles, and the relatively uniform particle concentrations with altitude (Fig. 4.4) provide evidence for a vigorously-mixed boundary layer, as was previously observed by Neuman et al. (2003) in the San Joaquin Valley in May 2002.

Five-day back-trajectories, computed using the NOAA HYSPLIT model (Draxler and Rolph, 2003), show that the background air during flight A originated over the Pacific Ocean, whereas the background air during flight B was transported over land from the north (Fig. 4.5). This suggests that the background aerosol in flight A may have carried the signature of cleaner marine air, while that measured during flight B was more exposed to urban and agricultural emissions.

4.4.2 Particle Number Concentrations and Size Distributions

Average submicrometer particle number concentrations in the plume were $30,528 \pm 8,987 \text{ cm}^{-3}$ (flight A) and $16,606 \pm 4,286 \text{ cm}^{-3}$ (flight B) (Table 4.1). Particle number concentrations in and out of the plume were similar, indicating the absence of significant emissions of particles from the source. (As noted in Sect. 4.4.3, nitrate enhancement is used to identify the location of the plume.) During the downwind plume transects, number concentrations decreased slightly with increasing altitude until a sharp decrease near the top of the boundary layer to below 300 cm^{-3} (flight A) and 800 cm^{-3} (flight B) at altitudes of 550 m and 400 m, respectively. The ratio of the number concentration of particles with $D_p > 3 \text{ nm}$ to the number concentration of particles with $D_p > 10 \text{ nm}$ was 1.1 ± 0.1 and 1.2 ± 0.1 for flights A and B, respectively. This ratio showed no difference in and out of the plume and decreased with altitude.

The vertical structure of the PCASP ($D_p = 0.1 - 3 \mu\text{m}$) and CPC number concentrations were similar. Average PCASP concentrations in the plume for flights A and B were $1,065 \pm 330$ and $675 \pm 220 \text{ cm}^{-3}$, respectively, indicating that most of the particles were smaller than 100 nm in diameter. The number of 0.1 to 3 μm diameter particles in the plume was enhanced by a factor of 2.5 - 3 times as much over that in the background aerosol. This is especially evident by the increase in number concentration ($D_p > 100 \text{ nm}$) observed when passing through the beginning of the plume over the perimeter of the source (upper panels of Fig. 4.2/4.3; see the flight segments labeled “2” when the aircraft was circling the perimeter of the plume source); this likely is a result of smaller particles growing into this size range. However, the increase in number concentration for particles with $D_p = 0.1 - 3 \mu\text{m}$ was not sufficiently large to result in a significant difference in the submicrometer number concentration ($D_p = 0.01 - 1 \mu\text{m}$) in and out of the plume.

Aerosol number and volume distributions were similar both between the two flights, and in and out of the plume. Multiple modes normally existed in the number and volume distributions. A number concentration mode was generally present between $D_p = 20 - 60 \text{ nm}$, with a weaker mode between $D_p = 60 - 100 \text{ nm}$ (lower panels of Fig. 4.2/4.3). There was also a dominant number concentration mode, which will be referred to as the nucleation mode, at sizes smaller than the detection limit of the DMA (10 nm); this mode is evident from the difference in number concentration measured by the DMA and the UFCPC 3025. Volume concentration modes existed at $D_p = 30 - 60 \text{ nm}$, $D_p \sim 100 \text{ nm}$, and frequently at $D_p > 100 \text{ nm}$. The number and volume distributions in the plume shifted slightly to larger sizes with downwind distance from the plume source.

4.4.3 Submicrometer Aerosol Chemical Composition

Figures 4.6 (time series), 4.7/4.8 (spatial distribution), and 4.9 (vertical distribution) summarize the submicrometer aerosol composition data, in addition to Table 4.1, which reports the background and in-plume composition for both flights. The reported total organic mass is non-refractory organic mass that was measured by the C-ToF-AMS. The total aerosol mass is determined as the sum of inorganic mass, as determined by the PILS and C-ToF-AMS, and non-refractory organic mass from the C-ToF-AMS. Nitrate enhancement is used to define the location of the plume. Then, knowing where the plume is, local enhancements in other species concentrations and aerosol properties can be determined. Plume ages are noted on the spatial plots in Fig. 4.1B/C and were calculated using downwind distance and average wind speed in the vicinity of the source. The highest plume age encountered in flights A and B was 0.9 h and 1.2 h, respectively.

4.4.3.1 Total Aerosol Mass and Major Components

The average total aerosol mass in the boundary layer was $8.85 \pm 1.79 \mu\text{g}/\text{m}^3$ and $3.40 \pm 0.98 \mu\text{g}/\text{m}^3$ during flights A and B, respectively, with significant enhancements in the plume (Table 4.1). The highest concentrations, $17.07 \mu\text{g}/\text{m}^3$ (flight A) and $6.27 \mu\text{g}/\text{m}^3$ (flight B), occurred in the plume while the lowest concentrations were observed at the highest altitudes when the aircraft performed spiral ascents (flight A = $1.40 \mu\text{g}/\text{m}^3$; flight B = $0.24 \mu\text{g}/\text{m}^3$).

Overall, organic species dominated the total mass. Organics accounted for $61.9\% \pm 2.6\%$ (flight A) and $55.5\% \pm 6.4\%$ (flight B) of the plume aerosol mass, and $63.5\% \pm 3.3\%$ (flight A) and $63.1\% \pm 11.9\%$ (flight B) of the background aerosol mass. The organic mass concentration in the plume was $6.48 \pm 0.98 \mu\text{g}/\text{m}^3$ (flight A) and $2.46 \pm 0.29 \mu\text{g}/\text{m}^3$ (flight B), and in the background aerosol was $5.10 \pm 1.07 \mu\text{g}/\text{m}^3$ (flight A) and $1.73 \pm 0.70 \mu\text{g}/\text{m}^3$ (flight B). The next largest contributor to the particulate mass was either sulfate or nitrate, depending on the day and aerosol type, followed by either ammonium or nitrate (see Table 4.1). The ratio of organic mass to inorganic mass in the plume was 1.64 ± 0.19 (flight A) and 1.30 ± 0.39 (flight B), while the ratio in the background aerosol was 1.77 ± 0.29 (flight A) and 1.92 ± 0.68 (flight B). Previous measurements in the San Joaquin Valley have also shown that organic aerosol contributes significantly to the fine particle mass (Chow et al., 1996; Neuman et al., 2003).

4.4.3.2 Inorganic Aerosol

Within the source plume, the levels of nitrate and ammonium increased significantly above their respective values in the background valley aerosol (Fig. 4.6 – 4.8). The ammonium-to-sulfate molar ratio is an important indicator of the level of partitioning of ammonium nitrate between the gas and aerosol phases. Since this ratio usually exceeded two, ammonia was available to foster partitioning of nitrate to the aerosol phase in the plume. The vertical distribution of nitrate and ammonium exhibited similar trends in each flight, unlike sulfate, which did not increase in concentration at plume altitudes ($\sim 100 - 300$ m) (Fig. 4.9).

Generally, other inorganic species, including chloride, sodium, potassium, calcium, magnesium, and nitrite, did not contribute significantly ($> 0.1 \mu\text{g}/\text{m}^3$) to the aerosol mass. Many of these species are expected to be found primarily in the coarse particle fraction ($D_p > 1 \mu\text{m}$), owing to their origins in sea salt (Na^+ , Cl^-) and dust and soil (Ca^{2+} , Mg^{2+} , Na^+ , K^+). Magnesium, calcium, and potassium concentrations were all below detection limits ($< 0.05 \mu\text{g}/\text{m}^3$). Sodium and chloride were sparsely detected in both flights, usually in the background aerosol during the transits, with concentrations near $\sim 0.1 \mu\text{g}/\text{m}^3$. Nitrite above detection limits was found in only one PILS sample ($0.10 \mu\text{g}/\text{m}^3$) during flight A while circling the feedlot near the beginning of the flight (UT $\sim 19:00$).

4.4.3.3 Organic Aerosol

The concentration of total organics, as determined by the C-ToF-AMS, in the plume aerosol significantly exceeded those in the background valley aerosol (Fig. 4.6 - 4.8). The vertical distribution of total organic concentrations was somewhat similar to those of nitrate and ammonium, with the exception that there was not as sharp an enhancement in concentration at plume altitudes, as was especially evident in flight B (Fig. 4.9).

Figure 4.10 shows the representative mass spectra of the organic fragments detected by the C-ToF-AMS in the background valley aerosol, the plume aerosol close to the source, and farther downwind. All non-organic contributions to the mass spectra have been removed using the methodology described in Allan et al. (2004); fragmentation at m/z 30 was further modified as described in Sect. 4.3.1. Figure 4.11

indicates that the signal at m/z 30 represents a large fragment for organics, including amines. The chemical signatures of the organic aerosol in the three categories appear to be quite similar. One difference, which is highlighted also in Fig. 4.10, is that the m/z 30 (common amine marker) peak intensity is enhanced by $\sim 150\%$ at the closest point to the plume source as compared to background aerosol, and decreases by $\sim 25\%$ at the farthest downwind distance. Figure 4.11 shows comparisons of the plume aerosol organic mass spectra to the background spectra for both flights. The overall organic aerosol appears to be similar in and out of the plume; however, peak intensities at m/z 30, 56, and 86 are enhanced in plume. These are all peaks in the electron impact mass spectrum of amines, including diethylamine and triethylamine (McLafferty and Turecek, 1993; Angelino et al., 2001; Murphy et al., 2007). A similar analysis for plume organics close to the feedlot and farther downwind reveals no significant difference in most peaks, although the intensity of the m/z 30 peak decreases with increasing plume age; as will be discussed subsequently, this is likely attributed to increased partitioning of particulate amines to the gas phase to maintain thermodynamic equilibrium as the plume dilutes with background air. An analysis of the background valley aerosol spectra during the transit portions of the flights indicates that the organic aerosol composition was similar throughout the valley.

Two amines were detected by the PILS, diethylamine and ethylamine; these were found only in the plume (Fig. 4.6 - 4.8). Diethylamine reached higher concentrations (up to $0.18 \mu\text{g}/\text{m}^3$ and 6.0% of the organic mass) and was more abundant farther downwind of the feedlot as compared to ethylamine; diethylamine was observed at plume ages up to 0.9 h (flight A) and 0.7 h (flight B). Ethylamine was detected by the PILS only in three samples collected during the two flights. It was found immediately downwind of the

feedlot up to plume ages of 0.7 h (flight A) and 0.3 h (flight B) at concentrations near $0.02 \mu\text{g}/\text{m}^3$, which corresponds to 0.8% of the total organic mass, as inferred from the C-ToF-AMS data.

The collective organic acid concentration, as determined by the PILS, reached levels of up to $0.23 \mu\text{g}/\text{m}^3$ (flight A) and $0.41 \mu\text{g}/\text{m}^3$ (flight B), accounting for 0.4% ($\pm 0.8\%$) and 0.4% ($\pm 0.6\%$) of the C-ToF-AMS total organic mass during flights A and B, respectively. Oxalate was the most abundant organic acid, followed by succinate, formate, and acetate. The concentration of the organic acids ($\text{C}_1 - \text{C}_9$) were not found to be correlated with those of total organics, amines, or any inorganic species.

4.4.4 Aerosol Mixing State

Figure 4.12 shows speciated size distributions for the background and in-plume aerosol at various downwind distances for both flights. Organics, nitrate, and sulfate all appear to be externally mixed to some extent. This is especially clear when examining the plume aerosol at various downwind distances in flight B; the distribution of nitrate aerosol grows in diameter, while the organic distribution shows relatively less growth and the sulfate distribution does not exhibit any corresponding shift in size. Speciated size distributions for the valley aerosol during transit are similar to the background aerosol in the vicinity of the feedlot, indicating chemically similar particles.

4.4.5 Refractive Index

The background aerosol exhibited a consistent average dry-particle refractive index of 1.54 ± 0.07 and 1.54 ± 0.04 for flights A and B, respectively (Table 4.2). Since

these values are close to those of ammonium nitrate (1.55) and ammonium sulfate (1.52 – 1.53) (Weast, 1987; Tang, 1996), which are the dominant inorganic components of the aerosol, assuming a volume-weighted overall refractive index, the organic component refractive index is calculated also to be 1.54. Notably, Zhang et al. (1994) reported a similar refractive index of 1.55 for particulate organic compounds in Grand Canyon aerosol. The overall aerosol refractive indices were slightly lower in the plume, with the lowest values observed closest to the feedlot during the aircraft circling maneuvers (1.48 ± 0.09 and 1.51 ± 0.01 for flights A and B, respectively). Organic species, such as amines, may be responsible for this decrease as the organic mass fraction dominated the total mass; ethylamine and diethylamine have refractive indices of 1.37 and 1.39, respectively (Dean, 1999). Although only two particulate amines were speciated at low concentrations (< 4% of total mass), other amine compounds may well have existed in the total organic mass with comparable refractive indices.

4.4.6 Hygroscopic Properties of the Aerosol

4.4.6.1 Subsaturated Water Uptake

Figures 4.13 and 4.14 present the spatial distribution of hygroscopic growth factors at the RHs studied for flights A and B, respectively. Aerosol growth factors ranged from 1.00 to 1.27 at 74% RH, 1.21 to 1.62 at 85% RH, and 1.30 to 2.04 at 92% RH (Table 4.2), depending on location, altitude, and proximity to the plume source. For reference, growth factors for pure ammonium nitrate ($D_{p,dry} = 150$ nm) at RHs of 74%, 85%, and 92% are 1.37, 1.60, and 1.94, respectively (deliquescence RH = 61.8%; Brechtel and Kreidenweis, 2000). Growth factors for pure ammonium sulfate ($D_{p,dry} =$

150 nm) at RHs of 85% and 92% are 1.56 and 1.80, respectively (deliquescence RH = 79.9%; Brechtel and Kreidenweis, 2000). Overall, the plume aerosol exhibited higher hygroscopic growth factors as compared to the background aerosol. Hygroscopic growth factors in the immediate vicinity of the source were usually between 1.75 – 1.90 at RH = 92%.

Hygroscopic growth factors are now related to the mass fractions of the aerosol components. Figure 4.15 shows the dependence of growth factors at an RH of 92% on mass fractions of nitrate and organics measured for flight B. (Similar effects occur at the other RHs.) Increasing growth factors coincide with higher nitrate mass fractions. This effect is most evident during flight B, in terms of slope (0.31) and correlation ($r^2 = 0.43$), partly because of the larger range of nitrate mass fractions observed. In addition, growth factors exhibited a negative correlation ($r^2 = 0.46$, slope = -0.28) with organic mass fractions. Less correlation exists between observed growth factors and mass fractions of ammonium and sulfate ($r^2 < 0.21$). The data show that subsaturated hygroscopicity increases as a function of increasing fraction of ammonium nitrate, a highly hygroscopic salt, and decreasing fraction of organics, the growth factor of which will be explored subsequently.

4.4.6.2 CCN

The CCN data acquired are summarized in Table 4.3 and Fig. 4.16. Owing to the large number of particles with diameters below about 60 nm, in the background atmosphere as well as in the plume, the activated fractions were quite small. An

enhancement in activated fraction was observed in the plume, which is consistent with the observed behavior of subsaturated hygroscopic growth factors.

An important issue is the extent to which aerosol composition influences CCN behavior. This can be manifested in two ways: (1) by affecting the critical supersaturation of the particles; and (2) by influencing the growth rate once the particle activates. Figure 4.17 shows the normalized activation fraction as a function of hygroscopic growth factor for flight B. The normalization is done by computing the activation fraction assuming the CCN are composed of pure ammonium sulfate. The normalization removes any variations due to shifts in the shape of the size distribution. It is noted that, in general, higher supersaturations are required to activate particles composed of less hygroscopic material.

Regarding the effect of particle composition on growth rate, consider two particles each having the same critical supersaturation. If the ambient supersaturation exceeds the critical supersaturation, then each particle will activate. The subsequent rate of growth by water condensation depends on the uptake of water molecules. If the two particles have different composition, then the uptake coefficients for water vapor can be different; the particle with the smaller water uptake coefficient will exhibit a slower rate of growth after activation. In a CCN instrument, like the CCNc employed here, the more slowly growing particle may not reach its ultimate size before it exits the growth chamber of the instrument and is detected by the OPC. The growth rate of pure ammonium sulfate particles of the same critical supersaturation as that of the particle in question can be taken as the standard against which particle growth rates can be compared. Since an entire distribution of particles enter the CCNc, with different critical supersaturations (as

a result of size and composition), the standard used is ammonium sulfate with a critical supersaturation equal to the supersaturation of the instrument. Based on this standard, if all particles grow as quickly as those composed entirely of ammonium sulfate, all particles will have droplet sizes equal to or larger than the standard. Hence, at a given supersaturation, the presence of droplets with a size less than that of the standard indicates retarded growth. We express this effect in terms of the fraction of droplets less than the standard at the supersaturation of the instrument.

Figure 4.18 shows the C-ToF-AMS – derived ratio of m/z 57:44 as a function of organic mass fraction. (A larger m/z 57:44 ratio is correlated with the organic material being less oxidized, and hence more hydrophobic.) The color coding of the data points corresponds to the fraction of droplets that have a size (D_i) less than the ammonium sulfate standard (D_{AS}), as described above. The size of the symbols reflects the hygroscopic growth factor at 92% RH. The data indicate that at high organic mass fractions when the particles are composed of less oxidized material, there is a tendency, although weak, towards retardation of growth. The degree of correlation (r^2) between the fraction of droplets with $D_i < D_{AS}$ and various measurements of the organic material are as follows: m/z 57:44 (0.11), organic mass fraction (0.03), product of m/z 57:44 and organic mass fraction (0.01). The growth factor exhibits a clear anti-correlation with organic mass fraction.

4.5 Discussion

In this section we explore key findings in this study. The observations reveal significant differences in aerosol properties in and out of the plume, and as a function of

plume age. Significant enhancements in nitrate, ammonium, and organic levels in the plume were observed; this coincided with an increased potential for water uptake in both the sub- and supersaturated regimes. While trends in the data from the two flights were similar, particle number and mass concentrations were larger in flight A. Explanations for this discrepancy will be pursued.

Owing to the range of organic fractions observed, the present study provides an opportunity to evaluate the sensitivity of mixed inorganic/organic particle hygroscopicity to the organic fraction. Subsaturated hygroscopic growth factors are calculated for the organic fraction based on a closure analysis using the Zdanovskii-Stokes Robinson (ZSR) mixing rule. Measurement of CCN activity in this study also presents an opportunity to assess the consistency of observed supersaturated water uptake with the subsaturated water uptake measurements.

4.5.1 Enhancements in Mass Production and Water Uptake in the Plume Aerosol

Significant production of ammonium nitrate and organic mass in the plume occurred during both flights. Ammonium nitrate production is expected due to the high ammonia levels and the presumed abundance of nitric acid from the daytime photochemistry. Organic aerosol mass production results from both condensation of semi-volatile organic species and acid – base chemistry of amines, followed by condensation of low-volatility products onto pre-existing aerosols.

Enhanced sub- and supersaturated water uptake coincides with greater fractions of ammonium, nitrate, and amines. Dinar et al. (2008) have shown, for example, that the reactive uptake of ammonia by aerosols containing slightly soluble organics leads to

substantial increases in hygroscopic growth and CCN activity. This observation appears to be consistent with the present measurements. Speciated size distributions show that the aerosol is, in part, externally mixed, with different species growing independently during plume aging (Fig. 4.12). The high organic fractions, particularly during flight A, may have masked the expected and significant growth exhibited by pure ammonium nitrate and ammonium sulfate salts; however, amines, which represent one class of organic species in the plume, are thought to be highly hygroscopic. Aklilu et al. (2006) also suggested that the organic fraction of the aerosol can suppress the growth normally associated with nitrate based on ambient measurements at two rural, urban-influenced sites.

4.5.2 Amines as an Atmospheric Base

4.5.2.1 Is Nitric Acid or Ammonia the Limiting Reactant?

Previous studies of particulate ammonium nitrate formation in the San Joaquin Valley suggest that the limiting reactant is nitric acid because of abundant ammonia emissions (Blanchard et al., 2000; Pun and Seigneur, 1999). During an aircraft study in the San Joaquin Valley in May 2002, Neuman et al. (2003) reported simultaneous nitric acid depletion and aerosol mass enhancements when the aircraft either encountered large ammonia sources or reached lower temperatures at higher altitudes in the boundary layer. Ammonia is emitted from the ground, whereas nitric acid is efficiently produced photochemically throughout the entire boundary layer, especially during the summer in the daytime San Joaquin Valley atmosphere.

Since gas-phase ammonia and nitric acid were not measured in the present study, observed particulate levels of ammonium, nitrate, sulfate, and amines can help determine the limiting reactant in chemical processing inside the plume. *Excess nitrate* is most abundant within the plume, reaching levels as high as $1.72 \mu\text{g}/\text{m}^3$ (flight A) and $0.89 \mu\text{g}/\text{m}^3$ (flight B). (As defined in Sect. 4.3.1, *excess nitrate* is the amount of nitrate remaining after both sulfate and nitrate have been fully neutralized by ammonium.) The greatest *excess nitrate* values coincide with relatively lower ambient temperatures, higher altitudes, the presence of diethylamine and ethylamine, and are correlated with amine markers in the C-ToF-AMS spectra (m/z 56 and 86) (Fig. 4.7B/4.8B/4.9). The background aerosol tends to exhibit *excess nitrate* values close to zero, indicating that just enough ammonia was present, on average, to neutralize both sulfate and nitrate. The data suggest either of two conclusions: (1) insufficient ammonia was present to neutralize both sulfate and nitrate within the plume, thereby distinguishing ammonia as the limiting reactant; or (2) sufficient ammonia was present, but a significant amount of nitric acid formed salts preferentially with amines rather than ammonia. The detection of amines by the PILS and the large amount of organic mass, with representative amine markers detected by the C-ToF-AMS, suggests that the second explanation may be more plausible. This is a significant finding in the atmosphere that is consistent with laboratory observations made in photooxidation experiments of aliphatic amines (Angelino et al., 2001; Murphy et al., 2007). The affinity of inorganic acids for amines in the presence of ammonia could possibly have greater implications under conditions of lower temperatures and higher RHs due to increased partitioning of both ammonium nitrate and amine salts into the aerosol phase. However, caution must be taken to extrapolate the

current results to other atmospheric conditions such as stronger pollution events, especially during winter stagnation events in the San Joaquin Valley, where a great excess of ammonia can exist over nitric acid.

4.5.2.2 Sources and Character of Amines

The formation of particulate amine salts depends on temperature, the identity and concentrations of the amine and acidic species present, and the concentration of ammonia that competes with amines for the acidic species. Once the particulate amine salts are formed, they may revolatilize, undergo subsequent particle-phase reactions including oxidation, or serve as a site for the condensation of other organic compounds. Chamber experiments performed by Murphy et al. (2007) showed that the dominant formation mechanism for amines is that of acid-base reactions (amine + nitric acid) rather than from photooxidation to form non-salt condensable organics. These experiments showed that nitric acid preferentially reacts with amines, depending on the species, rather than ammonia. It is expected that particulate amines should be prevalent close to the source of amine emissions where gaseous amine concentrations are highest. If the temperature dependence of amine salt equilibria resembles that of ammonium nitrate, then amines should partition more favorably to the aerosol phase at lower temperature (higher altitudes) within the plume. Of the six amines studied by Murphy et al. (2007), diethylamine was shown to have the most favorable equilibrium constant for salt formation in the presence of ammonia, an observation that is consistent with the present field measurements since diethylamine was the most abundant amine detected in the aerosol. The amine salts produced in the laboratory chamber experiments eventually

repartitioned back to the gas phase. In the present study, amine concentrations decreased as a function of plume age, as evident in the m/z 30 peak intensity data from the C-ToF-AMS (Fig. 4.10). The decreasing amine levels in the aerosol phase presumably occur because of two reasons: (1) amine concentrations, like those of ammonium and nitrate, decrease due to dilution as a function of plume age; and (2) amines partition back to the gas phase to maintain thermodynamic equilibrium due to the decreasing gas-phase concentrations owing to dilution.

Diethylamine, measured exclusively in the plume, exhibited a strong and positive correlation with nitrate, ammonium, sulfate, and total organics during flight A ($n = 8$, r^2 : nitrate = 0.65, ammonium = 0.73, sulfate = 0.72, organics = 0.68), but showed a weaker correlation with the same species during flight B ($n = 7$, r^2 : nitrate = 0.35, ammonium = 0.04, sulfate = 0.13, total organics = 0.40). The positive correlation between diethylamine and nitrate suggests that nitric acid exhibits an affinity for amines as an atmospheric base, even in the presence of ammonia. Diethylamine concentrations correlated more weakly with sulfate than to nitrate during flight B, possibly because nitric acid levels were higher than those of sulfuric acid causing the formation of particulate amines to proceed only through the amine + HNO_3 acid-base reaction. When diethylamine was detected, its average mass ratio relative to nitrate was 0.31 (flight A) and 0.36 (flight B); relative to sulfate it was 0.16 (flight A) and 0.36 (flight B), and relative to ammonium it was 0.31 (flight A) and 0.17 (flight B).

4.5.2.3 Total Amine Mass Calculations

One can estimate the total mass of amines present in the plume. This calculation assumes that *excess nitrate* is in a 1:1 molar ratio with amines. Amine mass is then determined by assuming a representative molecular weight for the amine population. We choose to use methylamine and triethylamine as lower and upper limits, respectively, since these species represent the smallest and largest amines that can be speciated using the PILS-IC technique (Murphy et al., 2007); the molecular weight of the two amines detected in this study, ethylamine and diethylamine, fall within the range of those of methylamine and triethylamine.

On the basis of the molecular weight of methylamine (31.1 g/mol), average amine concentrations in the plume are calculated to have been $0.23 \pm 0.13 \mu\text{g}/\text{m}^3$ (4% of total organic mass) (flight A) and $0.06 \pm 0.10 \mu\text{g}/\text{m}^3$ (2% of total organic mass) (flight B), while maximum plume concentrations were $0.86 \mu\text{g}/\text{m}^3$ (13% of total organic mass) (flight A) and $0.44 \mu\text{g}/\text{m}^3$ (19% of total organic mass) (flight B). On the basis of the molecular weight of triethylamine (101.1 g/mol), average amine concentrations are calculated to have been $0.76 \pm 0.43 \mu\text{g}/\text{m}^3$ (12% of total organic mass) (flight A) and $0.20 \pm 0.32 \mu\text{g}/\text{m}^3$ (8% of total organic mass) (flight B), while maximum levels were $2.81 \mu\text{g}/\text{m}^3$ (43% of total organic mass) (flight A) and $1.45 \mu\text{g}/\text{m}^3$ (63% of total organic mass) (flight B). Using the conservative molecular weight of methylamine, amine mass was at least 23% (flight A) and 14% (flight B) of ammonium mass in this plume. In addition, speciated amines (ethylamine and diethylamine via the PILS) accounted for at least 25% (flight A) and 45% (flight B) of the estimated total amine mass (via the *excess nitrate* calculation from the C-ToF-AMS).

4.5.3 Degree of Oxidation and Volatility in the Aerosol

In the absence of strong signals in the data representing primary particulate emission sources, the submicrometer aerosol in the sampling region is presumed to originate mainly from secondary production. No obvious signs of primary aerosol vehicular emissions existed based on organic markers in the C-ToF-AMS spectra. The ratio of m/z 57:44 peak intensities from the C-ToF-AMS can provide some insight into the relative ratio of hydrocarbon-like (HOA) and oxygenated organic (OOA) aerosols (Zhang et al., 2005); m/z 57 is representative of hydrocarbon-like structures (typically $C_4H_9^+$), while m/z 44 (typically CO_2^+ ion) arises only from oxygenated compounds (Alfarra et al., 2004; Cubison et al., 2006). To provide a framework, values of the m/z 57:44 ratio have been observed to range between 1 – 2 at urban sites in Canada and the UK, less than 0.10 at a rural site in Canada, less than 0.10 above the Eastern Pacific Ocean, and between 0.5 – 2.0 in the exhaust plume of a container ship (<http://cires.colorado.edu/jimenez-group/AMSSd/>; Alfarra et al., 2004; Ulbrich et al., 2008; Murphy et al., submitted). This ratio was $\sim 0.07 \pm 0.01$ during both flights, with no major changes during the flights, nor between plume and background aerosol (Table 4.1). Based on this ratio, it appears that the aerosol was highly oxygenated with relatively little hydrocarbon-like organic aerosol (HOA). The ratio of the peak intensity between m/z 44 and total organics was, on average, 0.10 ± 0.01 in the plume aerosol and 0.11 ± 0.02 in the background aerosol (Table 4.1). Peak intensities at m/z 44 (and 29 for flight A) are slightly greater in the background aerosol relative to plume aerosol, indicating a greater degree of oxidation out of the plume than within it (Fig. 4.11). This is presumably because the background aerosol had aged longer than the fresh emissions in the plume.

The atomic ratio O:C, which is indicative of the oxidation state of the organic aerosol (OA), can be derived from the ratio of m/z 44:OA using the data inventory and methodology presented by Aiken et al. (2008). They determined that O:C values range between 0.2 and 0.8 for ambient urban OA, with a diurnal cycle marked by decreases with primary emissions and increases due to photochemical processing and secondary organic aerosol (SOA) production. In the present study, the O:C ratio is typically between 0.45 and 0.50 both in and out of the plume (Table 4.1); these values are consistent with what would be expected from fresh SOA.

Organic acids represent a pool of organic species that are water-soluble and highly oxidized. In previous aircraft measurements, organic acids ($C_1 - C_9$) contributed $3.4 \pm 3.7\%$ to the total PILS mass in an urban atmosphere (Houston, Texas; Sorooshian et al., 2007a) and $3.5 \pm 3.1\%$ in a marine atmosphere (Eastern Pacific Ocean; Sorooshian et al., 2007b). In the present study, organic acids contributed $2.4 \pm 5.5\%$ to the total PILS mass, indicating greater variability and a lower average mass fraction of organic acids than seen in the other field data. Gas-particle partitioning of these water-soluble organic species may have been affected by the high ambient temperatures in the present flights. In addition, the relatively low humidities and lack of clouds prevented organic acid production via aqueous-phase processing during the measurement period (Sorooshian et al., 2006b). Assuming that photochemical reactions efficiently take place in the aqueous phase, the possibility also exists that photochemical processing is less effective in the absence of an aqueous medium. Organic acid concentrations were not correlated with ammonium or nitrate, which represent semi-volatile species, during the present flights. The ammonium nitrate levels varied significantly in the plume, but concentrations of the

organic acids were relatively stable. Thus, the data do not allow one to conclude whether volatility or RH was the dominant factor controlling organic acid levels.

4.5.4 Factors Influencing Aerosol Number/Mass Concentrations

Particle number and mass concentrations were significantly higher during flight A than in flight B. The presence of nucleation cannot explain this discrepancy, especially in terms of mass concentration (Table 4.1). The background aerosol concentration in the valley was also higher during flight A than in flight B. Since there are no significant sources of SO₂ in the sampling region, sulfate can be employed as a tracer for accumulated aerosol originating from long-range transport. It should be noted that comparable levels of vehicular emissions could be expected both days as both flights occurred on weekdays. Sulfate concentrations were significantly higher during flight A. The lower temperatures and higher RH during flight A favored partitioning of semi-volatile species, such as ammonium nitrate and organics, to the aerosol phase. The back-trajectory analysis indicates that the sampled air mass during flight A originated three days previously over the Pacific Ocean, while the air sampled in flight B originated in a more polluted inland area (Fig. 4.5). We conclude that ventilation of the valley during flight B was more effective than in flight A, reducing aerosol number and mass concentrations.

Over the flight durations, aerosol concentrations were influenced by competition between a growing boundary layer, decreasing RH, and increasing temperatures. Although the aerosol was well-mixed locally in the valley, the timescale for equilibration between the gas and particle phases is shorter than the boundary layer mixing time

(Neuman et al., 2003); this may explain fluctuations in the concentrations of aerosol species at various altitudes and distances downwind of the plume source. The topography of the sampling region downwind of the source and general buoyancy in the boundary layer facilitated vertical transport of emissions to lower temperature regions, reducing the dissociation constant of ammonium nitrate aerosol and, presumably, semi-volatile organics (Fig. 4.7–4.9). This might explain why the concentrations of organics (diethylamine in particular), nitrate, and ammonium peaked at the highest altitude and farthest downwind distance from the plume source in flight A (Fig. 4.7 and 4.9).

4.5.5 Estimated Subsaturated Hygroscopic Growth Factors for the Organic Fraction

Calculations were carried out to determine the effective growth factor for the organic fraction needed to achieve composition – hygroscopicity closure. Due to its simplicity and frequent application (Cruz and Pandis, 2000; Dick et al., 2000; Choi and Chan, 2002a, 2002b; Prenni et al., 2003; Wise et al., 2003; Clegg et al., 2003; Clegg and Seinfeld, 2004, 2006a, 2006b; Khlystov et al., 2005; Rissler et al., 2005; Aklilu et al., 2006; Svenningsson et al., 2006; Varutbangkul et al., 2006; Gysel et al., 2007; Sjogren et al., 2007; Dinar et al., 2008), the Zdanovskii-Stokes Robinson (ZSR) (Zdanovskii, 1948; Stokes and Robinson, 1966) mixing rule is employed to predict hygroscopic growth factors. This procedure of estimating hygroscopic growth based on specified composition is based on the assumption that water uptake by each individual component of a particle is independent and additive. We use the following form of the ZSR mixing rule (Aklilu et al., 2006; Gysel et al., 2007):

$$GF_{mixed}(a_w) \approx \left(\sum_i \varepsilon_i GF_i(a_w)^3 \right)^{\frac{1}{3}} \quad (1)$$

where GF_{mixed} is the hygroscopic growth factor of the mixed particle, GF_i is the hygroscopic growth factor of pure compound i , a_w is the activity coefficient of water, and ε_i is the volume fraction of pure compound i in the dry particle. $a_w = RH$ in Eq. (1) (Seinfeld and Pandis, 2006). Growth factors for the pure inorganic components were obtained from the Aerosol Inorganics Model (AIM; <http://mae.ucdavis.edu/~sclegg/aim.html>; Clegg et al., 1998). At an RH of 74%, a growth factor of unity is employed for ammonium sulfate rather than the predicted value of 1.40 on its metastable branch of the hygroscopic hysteresis. It is reasonable to assume that the sampled aerosol did not have sufficient time to be processed in the atmosphere at high RHs. A growth factor of unity is also assumed for EC, as suggested by Aklilu et al. (2006). Bulk composition data is used to calculate volume fractions in Eq. (1). Although there is evidence for externally-mixed particles in the plume (Fig. 4.12), assuming an internal mixture for the purposes of calculating volume fractions eliminates uncertainties associated with converting vacuum aerodynamic diameters from the C-ToF-AMS to mobility-equivalent diameters between 150 – 200 nm for particles of different densities (the measured growth factors are for dry particle mobility-equivalent diameters between 150 – 200 nm). Therefore, the assumption of an internal mixture is not entirely correct but it will provide for a fairly accurate representation of the composition for the majority of the size distribution.

Assuming an internal mixture, calculating the individual volume fractions requires an estimate of the organic density. If it is assumed that the aerosol is composed

of ammonium sulfate (AS), ammonium nitrate (AN), organic carbon (OC), and elemental carbon (EC), then total aerosol density can be expressed as:

$$\rho = x_{OC}\rho_{OC} + x_{AS}\rho_{AS} + x_{AN}\rho_{AN} + x_{EC}\rho_{EC} \quad (2)$$

where x_i are mass fractions and ρ is density of the multicomponent particle, as determined by the ratio of aerosol volume (via the DMA) to the aerosol mass (via the PILS and C-ToF-AMS); in Eq. (2), ρ_{OC} is the unknown quantity that we desire to determine. Elemental carbon was not quantified in the present study; however, based on extensive chemical characterization of San Joaquin Valley PM_{2.5} by Chow et al. (2006), the mass fraction of EC tends to be ~ 5 – 10% near the present sampling site. In the absence of a quantitative measure of EC, it is assumed that 5% of the total submicrometer mass is composed of EC. It is assumed for the purpose of this calculation that all of the sulfate is neutralized by ammonium, and the remaining ammonium occurs as ammonium nitrate. Densities of 1.725, 1.769, and 1.9 g/cm³ are used for AN, AS, and EC respectively. A wide range of densities are reported for EC (0.625 – 2.25 g/cm³) (Fuller et al., 1999); here we assume a value of 1.9 g/cm³, similar to that employed by Dillner et al. (2001). From the mass concentrations and respective densities of AN, AS, OC, and EC, the volume fraction of each component can be calculated.

On average, the in-plume organic growth factors needed to match the data (flight A/B) are 1.07/1.02 (74% RH), NA/1.28 (85% RH), and 1.49/1.53 (92% RH) (Fig. 4.19). The background aerosol organic growth factors (flight A/B) are 1.08/1.03 (74% RH), NA/1.21 (85% RH), and 1.29/1.24 (92% RH). Flight B is characterized by a wider range in the mass fractions of organics, thus this flight presents a better indication of trends in organic growth factor with changing mass fractions. During this flight, inferred organic

growth factors increase in the plume as a function of decreasing organic fraction. The lowest organic fractions in flight B coincide with the detection of amines, which likely enhance the hygroscopicity of the organic fraction. There is a significant amount of variation in predicted growth factors at constant organic mass fractions and the absolute values of some of the predicted organic growth factors (< 1 and > 2) are unrealistic. Possible explanations for the unrealistic organic hygroscopic growth factors include: (1) complex particle morphology; (2) complex interactions between the components in the particles leading to non-additive water uptake among the individual components; and (3) errors associated with the calculation of the volume fractions and uncertainties in the measurements.

4.5.6 Relationship Between Sub- and Supersaturated Water Uptake

One anticipates a direct correspondence between subsaturated hygroscopic behavior and supersaturated CCN activity. For example, Mochida et al. (2006) explored the relationship between hygroscopicity and CCN activity for urban aerosols using a hygroscopic tandem DMA (HTDMA) coupled in series to a CCNc; enhanced CCN activity coincided with higher subsaturated growth factors. A similar analysis for the present data (Fig. 4.17) shows that the normalized CCN activation ratio is generally consistent with water uptake in the subsaturated regime. One interesting feature is the tendency towards relatively higher normalized activation ratios at a supersaturation of 0.25%; we do not have a clear explanation for this other than to point out that more data points were available at this supersaturation, and that temporal and spatial factors during these specific measurements may have played a role. Also, higher activated fractions are

consistent with smaller markers, which represent lower organic mass fractions and higher nitrate mass fractions. Enhancements in water uptake for aerosols with lower organic content are likely due to increasing dissolution of water-soluble species, including ammonium nitrate and amine salts, and the possible reduction in surface tension by surface-active species. Organics have previously been shown to influence CCN activity by adding solute and suppressing surface tension (Shulman et al., 1996; Facchini et al., 1999; Feingold and Chuang, 2002; Nenes et al., 2002).

Recent work has shown that kinetic limitations, including surface films and slow dissolution of particulate substances, can suppress droplet growth (Asa-Awuku and Nenes, 2007; Ruehl et al., 2008). With few exceptions including solute being physically “trapped” within some type of waxy material, dissolution kinetics is governed by diffusion of solute from the solid “core” at the center of a droplet to the growing droplet. It has been argued that the latter process is slow enough for compounds with high molecular weights to influence droplet growth kinetics and the Köhler curve (Asa-Awuku and Nenes, 2007; Taraniuk et al., 2007; Moore et al., 2008). According to Fig. 4.18, droplet growth was at times less than that expected for pure ammonium sulfate. In addition, it is shown to some extent that the droplet growth was suppressed for CCN with relatively greater amounts of hydrophobic organic material. This suggests kinetic limitations may have played a role in suppressing water uptake. This issue will be revisited in subsequent work that will address size-resolved CCN data from this experiment.

4.5.7 Parameterization for Sub- and Supersaturated Water Uptake

To effectively represent the process of water uptake by multicomponent particles in atmospheric models, parameterizations are used. A number of investigators have attempted to introduce parameters to describe water uptake in both the sub- and supersaturated regimes. Expanding upon the earlier work of Fitzgerald et al. (1982), Svenningsson et al. (1992) used a parameter termed ε to link subsaturated water uptake to cloud and fog activation. Subsequent work introduced closely related parameters for sub- and supersaturated regimes (Kreidenweis et al., 2005; Rissler et al., 2006; Petters and Kreidenweis, 2007). A recently introduced parameter, κ (Petters and Kreidenweis, 2007), can be calculated without knowledge of the particle properties such as density, molecular weight, and surface tension.

Kappa can be determined from either CCN activity data or subsaturated hygroscopic growth data. Since the subsaturated DASH-SP growth factors are measured for size-resolved particles, we use the subsaturated hygroscopicity data to predict the value of κ with the following equation (Petters and Kreidenweis, 2007):

$$\frac{RH}{\exp\left(\frac{A}{D_d GF}\right)} = \frac{GF^3 - 1}{GF^3 - (1 - \kappa)} \quad (3)$$

where $A = \frac{4\sigma_{s/a}M_w}{RT\rho_w}$, D_d is the dry particle diameter, GF is the growth factor at the corresponding RH, M_w is the molecular weight of water, ρ_w is the density of water, R is the universal gas constant, T is temperature, and $\sigma_{s/a}$ is the surface tension at the air/water interface. The water surface tension of 0.072 J/m² is assumed, as in the analysis of

Petters and Kreidenweis (2007). Briefly, κ values of 0.5 to 1.4 represent highly hygroscopic salts such as sodium chloride, values of 0.01 to 0.5 represent slightly to very hygroscopic organics, and a value of 0 represents a non-hygroscopic component (Petters and Kreidenweis, 2007; see Table 4.1). κ values representative of urban, maritime, continental, and remote areas, as derived by Petters and Kreidenweis (2007) using data from previous ambient studies (Fitzgerald and Hoppel, 1982; Hudson and Da, 1996; Dusek et al., 2006), have been reported to range from 0.1 to 0.94.

Table 4.4 summarizes the values of κ derived in the present study for both the total aerosol and the organic component of the aerosol. A noticeable enhancement in κ occurs within the plume as compared to the background aerosol, which is consistent with the enhancement in subsaturated growth factors. κ for the total aerosol is enhanced by between 21% and 67% in the plume, with typical values being between 0.36 – 0.44. The range of κ values, based on DASH-SP data at RHs of 85% and 92%, is 0.11 – 0.87. The correlation between κ values and the mass fraction of organics is more pronounced for flight B; κ increases as the mass fraction of organics decreases and that of nitrate increases. A clear enhancement in the κ values for the organic fraction of the aerosol is observed in the plume; typical values are between 0.10 and 0.15 inside the plume and near zero for the background aerosol. Representative κ values are assigned to two categories: aerosol from the strong bovine source ($\kappa = 0.40$) and aerosol in an agricultural area ($\kappa = 0.30$). Values of κ determined here fall within the range of those derived from previous ambient studies.

4.6 Conclusions

An extensive set of airborne aerosol and meteorological measurements were performed downwind of a massive bovine source in the San Joaquin Valley of California during two flights in July 2007; these include meteorology, particle size distributions, aerosol composition and mixing state, sub- and supersaturated water uptake behavior, aerosol refractive index, and interrelationships between these properties.

Concentrations of total mass, organics, nitrate, and ammonium were elevated within the plume as compared to the background aerosol during both flights. Evidence exists of some degree of external mixing of particles in the plume. Organics constituted the dominant fraction of the total mass in the plume and background aerosol (~ 56 – 64%), followed either by sulfate or nitrate, and then ammonium. The O:C atomic ratio of the organic fraction is estimated to have been typically between 0.45 and 0.50 both in and out of the plume. Particulate amines were detected in the plume and are shown to be a significant atmospheric base even in the presence of ammonia; the total amine concentration accounted for at least 23% (flight A) and 14% (flight B) of that of ammonium.

The refractive index of the background aerosol in the valley was on average 1.54, but reductions were observed in the plume, especially in the immediate vicinity of the plume source (flight A ~ 1.48; flight B ~ 1.51). Measurements indicate that increasing uptake of ammonia by aerosols, in the form of ammonium nitrate and ammonium sulfate, relative to the organic fraction, results in an enhancement in particle water uptake and a reduction in refractive index. Amine salts are also hypothesized to have contributed to significant hygroscopic growth in the plume. Hygroscopic growth factors in the immediate vicinity of the source were generally between 1.75 – 1.90 at RH = 92%.

Estimated hygroscopic growth factors ($RH = 92\%$) for the organic fraction on average were 1.49 – 1.53 in the plume and 1.24 – 1.29 in the background aerosol. Kinetic limitations associated with hydrophobic organic species may have possibly suppressed droplet growth, but the tendency is shown to be weak in this study. After removing effects associated with size distribution and mixing state, enhanced CCN activated fractions were generally observed as a function of increasing subsaturated growth factors, with the highest activated fractions being consistent with the lowest organic mass fractions. Representative κ values (Petters and Kreidenweis, 2007) are assigned to two categories: aerosol from the bovine source ($\kappa = 0.40$) and aerosol in an agricultural area ($\kappa = 0.30$). There was a clear enhancement in the values of κ representing the organic fraction of the aerosol within the plume, with average values of 0.13 and 0.14 for the two flights.

4.7 Appendix

This appendix details the calibration procedure for the CCNc. The instrument used in this study was calibrated using ammonium sulfate particles classified with a DMA as follows. An aqueous solution of ammonium sulfate was atomized via a collision-type atomizer operated at 4 psig. The droplet stream was passed through multiple diffusional driers (operating at 5-10% RH), resulting in a polydisperse dry aerosol (with modal diameter ~ 50 nm), which was sent through a DMA (Model 3081L, TSI Inc.) operated with a sheath-to-aerosol flow ratio of 10:1. The classified aerosol stream was then sent to a CPC (Model 3010, TSI Inc.) and the Continuous-flow Streamwise Thermal Gradient Chamber (CFSTGC) (operated at constant flow rate,

temperature gradient, and pressure) to measure the total aerosol concentration and the total activated particles, respectively. The level of supersaturation in the instrument is determined from the minimum dry particle diameter, D_{p50} , that activates in the instrument, found by plotting the ratio of CCN to CN concentration as a function of mobility particle diameter. A sigmoidal fit to the data (neglecting the effects of multiple particle charging, which is minor for the aerosol used) then determines D_{p50} as the dry diameter for which $CCN/CN = 0.50$. The instrument supersaturation is related to D_{p50} by applying Köhler theory assuming that ammonium sulfate has a density of 1760 kg m^{-3} , surface tension of water, molar mass of $0.132 \text{ kg mol}^{-1}$ and an effective van't Hoff factor of 2.5. The standard deviation in the supersaturation was determined from the standard deviation observed in the D_{p50} . The error bars in the temperature difference are 1σ of the observed variation during the calibrations. Droplet diameter of activated CCN at the exit of the growth column is also measured; in this study, the growth rate of ammonium sulfate particles is characterized by the average size of droplets formed from particles with dry diameter equal to D_{p50} .

The instrument was calibrated numerous times throughout the study for supersaturations ranging from 0.1 to 1.4% SS, for pressures between 700 and 1000 mb, and for flow rates ranging between 500 and 1000 cm^3/min . The resulting calibration curves are presented in Fig. 4.20 and 4.21. The average size of activated droplets, together with 1σ error bars, are shown in Fig. 4.22 and 4.23.

The instrument was not operated at constant pressure during flights; instead, the pressure was allowed to vary with altitude. As a result, some transition time is required for the instrument supersaturation to adjust every time altitude changes; the data used in

the closure study was filtered for transients resulting from changes in instrument pressure and temperature gradient. The calibration curves are then interpolated with respect to temperature gradient and pressure to determine the in-flight supersaturation.

4.8 Acknowledgements.

This work was supported, in part, by NOAA grant NA06OAR4310082. A. N. acknowledges support from an NSF CAREER award, NOAA, and NASA. L. T. P. acknowledges support from a NASA Earth System Science Fellowship. The authors gratefully acknowledge the NOAA Air Resources Laboratory (ARL) for provision of the HYSPLIT transport and dispersion model.

4.9 References

Abalos, M., Bayona, J. M., and Ventura, F.: Development of a solid-phase microextraction GC-NPD procedure for the determination of free volatile amines in wastewater and sewage-polluted waters, *Anal. Chem.*, 71, 3531-3537, 1999.

Aiken, A. C., Decarlo, P. F., Kroll, J. H., Worsnop, D. R., Huffman, J. A., Docherty, K. S., Ulbrich, I. M., Mohr, C., Kimmel, J. R., Sueper, D., Sun, Y., Zhang, Q., Trimborn, A., Northway, M., Ziemann, P. J., Canagaratna, M. R., Onasch, T. B., Alfarra, M. R., Prevot, A. S. H., Dommen, J., Duplissy, J., Metzger, A., Baltensperger, U., and Jimenez, J. L.: O/C and OM/OC ratios of primary, secondary, and ambient organic aerosols with high-resolution time-of-flight aerosol mass spectrometry, *Environ. Sci. Technol.*, 42, 4478-4485, 2008.

Aklilu, Y., Mozurkewich, M., Prenni, A. J., Kreidenweis, S. M., Alfarra, M. R., Allan, J. D., Anlauf, K., Brook, J., Leaitch, W. R., Sharma, S., Boudries, H., and Worsnop, D. R.: Hygroscopicity of particles at two rural, urban influenced sites during Pacific 2001: Comparison with estimates of water uptake from particle composition, *Atmos. Environ.*, 40, 2650-2661, 2006.

Alfarra, M. R., Coe, H., Allan, J. D., Bower, K. N., Boudries, H., Canagaratna, M. R., Jimenez, J. L., Jayne, J. T., Garforth, A. A., Li, S. M., and Worsnop, D. R.: Characterization of urban and rural organic particulate in the lower Fraser valley using two aerodyne aerosol mass spectrometers, *Atmos. Environ.*, 38, 5745-5758, 2004.

Allan, J. D., Delia, A. E., Coe, H., Bower, K. N., Alfarra, M. R., Jimenez, J. L., Middlebrook, A. M., Drewnick, F., Onasch, T. B., Canagaratna, M. R., Jayne, J. T., and Worsnop, D. R.: A generalised method for the extraction of chemically resolved mass spectra from aerodyne aerosol mass spectrometer data, *J. Aerosol Sci.*, 35, 909-922, 2004.

Anderson, N., Strader, R., and Davidson, C.: Airborne reduced nitrogen: ammonia emissions from agriculture and other sources, *Environ. Int.*, 29, 277-286, 2003.

Angelino, S., Suess, D. T., and Prather, K. A.: Formation of aerosol particles from reactions of secondary and tertiary alkylamines: Characterization by aerosol time-of-flight mass spectrometry, *Environ. Sci. Technol.*, 35, 3130-3138, 2001.

Apsimon, H. M., Kruse, M., and Bell, J. N. B.: Ammonia emissions and their role in acid deposition, *Atmos. Environ.*, 21, 1939-1946, 1987.

Asa-Awuku, A. and Nenes, A.: Effect of solute dissolution kinetics on cloud droplet formation: Extended Kohler theory, *J. Geophys. Res.*, 112, D22201, doi:10.1029/2005JD006934, 2007.

Asman, W. A. H. and Janssen, A. J.: A long-range transport model for ammonia and ammonium for Europe, *Atmos. Environ.*, 21, 2099-2119, 1987.

Battye, W., Aneja, V. P., and Roelle, P. A.: Evaluation and improvement of ammonia emissions inventories, *Atmos. Environ.*, 37, 3873-3883, 2003.

Beddows, D. C. S., Donovan, R. J., Harrison, R. M., Heal, M. R., Kinnersley, R. P., King, M. D., Nicholson, D. H., and Thompson, K. C.: Correlations in the chemical composition of rural background atmospheric aerosol in the UK determined in real time using time-of-flight mass spectrometry, *J. Environ. Monitor.*, 6, 124-133, 2004.

Blanchard, C. L., Roth, P. M., Tanenbaum, S. J., Ziman, S. D., and Seinfeld, J. H.: The use of ambient measurements to identify which precursor species limit aerosol nitrate formation, *J. Air Waste Manage.*, 50, 2073-2084, 2000.

Brechtel, F. J. and Kreidenweis, S. M.: Predicting particle critical supersaturation from hygroscopic growth measurements in the humidified TDMA. part I: Theory and sensitivity studies, *J. Atmos. Sci.*, 57, 1854-1871, 2000.

Cadle, S. H. and Mulawa, P. A.: Low-molecular weight aliphatic-amines in exhaust from catalyzed-equipped cars, *Environ. Sci. Technol.*, 14, 718-723, 1980.

Choi, M. Y. and Chan, C. K.: The effects of organic species on the hygroscopic behaviors of inorganic aerosols, *Environ. Sci. Technol.*, 36, 2422-2428, 2002a.

Choi, M. Y. and Chan, C. K.: Continuous measurements of the water activities of aqueous droplets of water-soluble organic compounds, *J. Phys. Chem. A*, 106, 4566-4572, 2002b.

Chow, J. C., Watson, J. G., Lu, Z. Q., Lowenthal, D. H., Frazier, C. A., Solomon, P. A., Thuillier, R. H., and Magliano, K.: Descriptive analysis of PM(2.5) and PM(10) at regionally representative locations during SJVAQS/AUSPEX, *Atmos. Environ.*, 30, 2079-2112, 1996.

Chow, J. C., Chen, L. W. A., Watson, J. G., Lowenthal, D. H., Magliano, K. A., Turkiewicz, K., and Lehrman, D. E.: PM_{2.5} chemical composition and spatiotemporal variability during the California Regional PM₁₀/PM_{2.5} Air Quality Study (CRPAQS), *J. Geophys. Res.*, 111, D10S04, doi:10.1029/2005JD006457, 2006.

Chuang, P. Y.: Measurement of the timescale of hygroscopic growth for atmospheric aerosols, *J. Geophys. Res.*, 108, 4282, doi:10.1029/2002JD002757, 2003.

Clegg, S. L., Brimblecombe, P., and Wexler, A. S.: Thermodynamic model of the system H⁺-NH₄⁺-Na⁺-SO₄²⁻-NO₃⁻-Cl⁻-H₂O at 298.15 K, *J. Phys. Chem. A*, 102, 2155-2171, 1998.

Clegg, S. L., Seinfeld, J. H., and Edney, E. O.: Thermodynamic modelling of aqueous aerosols containing electrolytes and dissolved organic compounds. II. An extended Zdanovskii-Stokes-Robinson approach, *J. Aerosol Sci.*, 34, 667-690, 2003.

Clegg, S. L. and Seinfeld, J. H.: Improvement of the Zdanovskii-Stokes-Robinson model for mixtures containing solutes of different charge types, *J. Phys. Chem. A*, 108, 1008-1017, 2004.

Clegg, S. L. and Seinfeld, J. H.: Thermodynamic models of aqueous solutions containing inorganic electrolytes and dicarboxylic acids at 298.15 K. 1. The acids as nondissociating components, *J. Phys. Chem. A*, 110, 5692-5717, 2006a.

Clegg, S. L. and Seinfeld, J. H.: Thermodynamic models of aqueous solutions containing inorganic electrolytes and dicarboxylic acids at 298.15 K. 2. Systems including dissociation equilibria, *J. Phys. Chem. A*, 110, 5718-5734, 2006b.

Cruz, C. N. and Pandis, S. N.: Deliquescence and hygroscopic growth of mixed inorganic-organic atmospheric aerosol, *Environ. Sci. Technol.*, 34, 4313-4319, 2000.

Cubison, M. J., Alfarra, M. R., Allan, J., Bower, K. N., Coe, H., McFiggans, G. B., Whitehead, J. D., Williams, P. I., Zhang, Q., Jimenez, J. L., Hopkins, J., and Lee, J.: The characterisation of pollution aerosol in a changing photochemical environment, *Atmos. Chem. Phys.*, 6, 5573-5588, 2006

Dean, J. A.: *Lange's Handbook of Chemistry*, Fifteenth Edition, McGraw-Hill, 1999.

Denkenberger, K. A., Moffet, R. C., Holecek, J. C., Rebotier, T. P., and Prather, K. A.: Real-time, single-particle measurements of oligomers in aged ambient aerosol particles, *Environ. Sci. Technol.*, 41, 5439-5446, 2007.

Dick, W. D., Saxena, P., and McMurry, P. H.: Estimation of water uptake by organic compounds in submicron aerosols measured during the Southeastern Aerosol and Visibility Study, *J. Geophys. Res.*, 105, 1471-1479, 2000.

Dillner, A. M., Stein, C., Larson, S. M., and Hitzenberger, R.: Measuring the mass extinction efficiency of elemental carbon in rural aerosol, *Aerosol Sci. Tech.*, 35, 1009-1021, 2001.

Dinar, E., Anttila, T., and Rudich, Y.: CCN activity and hygroscopic growth of organic aerosols following reactive uptake of ammonia, *Environ. Sci. Technol.*, 42, 793-799, 2008.

Doyle, G. J., Tuazon, E. C., Graham, R. A., Mischke, T. M., Winer, A. M., and Pitts, J. N.: Simultaneous concentrations of ammonia and nitric-acid in a polluted atmosphere and their equilibrium relationship to particulate ammonium-nitrate, *Environ. Sci. Technol.*, 13, 1416-1419, 1979.

Draxler, R. R. and Rolph, G. D.: HYSPLIT (HYbrid Single-Particle Lagrangian Integrated Trajectory) Model access via NOAA ARL READY Website (<http://www.arl.noaa.gov/ready/hysplit4.html>), NOAA Air Resources Laboratory, Silver Spring, MD, 2003.

Drewnick, F., Hings, S. S., DeCarlo, P., Jayne, J. T., Gonin, M., Fuhrer, K., Weimer, S., Jimenez, J. L., Demerjian, K. L., Borrmann, S., and Worsnop, D. R.: A new time-of-flight aerosol mass spectrometer (tof-ams) - instrument description and first field deployment, *Aerosol Sci. Tech.*, 39, 637-658, 2005.

Dusek, U., Frank, G. P., Hildebrandt, L., Curtius, J., Schneider, J., Walter, S., Chand, D., Drewnick, F., Hings, S., Jung, D., Borrmann, S., and Andreae, M. O.: Size matters more than chemistry for cloud-nucleating ability of aerosol particles, *Science*, 312, 1375-1378, 2006.

Edgerton, E. S., Saylor, R. D., Hartsell, B. E., Jansen, J. J., and Hansen, D. A.: Ammonia and ammonium measurements from the southeastern United States, *Atmos. Environ.*, 41, 3339-3351, 2007.

Facchini, M. C., Mircea, M., Fuzzi, S., and Charlson, R. J.: Cloud albedo enhancement by surface-active organic solutes in growing droplets, *Nature*, 401, 257-259, 1999.

Feingold, G. and Chuang, P. Y.: Analysis of the influence of film-forming compounds on droplet growth: Implications for cloud microphysical processes and climate, *J. Atmos. Sci.*, 59, 2006-2018, 2002.

Fitzgerald, J. W., Hoppel, W. A., and Vietti, M. A.: The size and scattering coefficient of urban aerosol-particles at Washington, DC as a function of relative-humidity, *J. Atmos. Sci.*, 39, 1838-1852, 1982.

Fitzgerald, J. W. and Hoppel, W. A.: Measurement of the relationship between the dry size and critical supersaturation of natural aerosol particles, *J. Hung. Meteorol. Serv.*, 86, 242-248, 1982.

Fridlind, A. M. and Jacobson, M. Z.: A study of gas-aerosol equilibrium and aerosol pH in the remote marine boundary layer during the First Aerosol Characterization Experiment (ACE 1), *J. Geophys. Res.*, 105, 17325-17340, 2000.

Fridlind, A. M., Jacobson, M. Z., Kerminen, V. M., Hillamo, R. E., Ricard, V., and Jaffrezo, J. L.: Analysis of gas-aerosol partitioning in the Arctic: Comparison of size-resolved equilibrium model results with field data, *J. Geophys. Res.*, 105, 19891-19903, 2000.

Fuller, K. A., Malm, W. C., and Kreidenweis, S. M.: Effects of mixing on extinction by carbonaceous particles, *J. Geophys. Res.*, 104, 15941-15954, 1999.

Gerber, H. E., Hoppel, W. A., and Wojciechowski, T. A.: Experimental verification of the theoretical relationship between size and critical supersaturation of salt nuclei, *J. Atmos. Sci.*, 34, 1836 - 1841, 1977.

Glagolenko, S. and Phares, D. J.: Single-particle analysis of ultrafine aerosol in College Station, Texas. *J. Geophys. Res.*, 109, D18205, doi:10.1029/2004JD004621, 2004.

Gorzelska, K., Talbot, R. W., Klemm, K., Lefer, B., Klemm, O., Gregory, G. L., Anderson, B., and Barrie, L. A.: Chemical-composition of the atmospheric aerosol in the troposphere over the Hudson-Bay Lowlands and Quebec-Labrador Regions of Canada. *J. Geophys. Res.*, 99, 1763-1779, 1994.

Gysel, M., Crosier, J., Topping, D. O., Whitehead, J. D., Bower, K. N., Cubison, M. J., Williams, P. I., Flynn, M. J., McFiggans, G. B., and Coe, H.: Closure study between chemical composition and hygroscopic growth of aerosol particles during TORCH2, *Atmos. Chem. Phys.*, 7, 6131-6144, 2007.

Hegg, D. A., Covert, D. S., Jonsson, H., and Covert, P. A.: Determination of the transmission efficiency of an aircraft aerosol inlet, *Aerosol Sci. Tech.*, 39, 966-971, 2005.

Hildemann, L. M., Russell, A. G., and Cass, G. R.: Ammonia and nitric-acid concentrations in equilibrium with atmospheric aerosols - experiment vs theory, *Atmos. Environ.*, 18, 1737-1750, 1984.

Hudson, J. G. and Da, X. Y.: Volatility and size of cloud condensation nuclei, *J. Geophys. Res.*, 101, 4435-4442, 1996.

Hutchinson, G. L., Mosier, A. R., and Andre, C. E.: Ammonia and amine emissions from a large cattle feedlot, *J. Environ. Qual.*, 11, 288-293, 1982.

Khlystov, A., Stanier, C. O., Takahama, S., and Pandis, S. N.: Water content of ambient aerosol during the Pittsburgh air quality study, *J. Geophys. Res.*, 110, D07S10, doi:10.1029/2004JD004651, 2005.

Kleeman, M. J., Hughes, L. S., Allen, J. O., and Cass, G. R.: Source contributions to the size and composition distribution of atmospheric particles: Southern California in September 1996, *Environ. Sci. Technol.*, 33, 4331-4341, 1999.

Kreidenweis, S. M., Koehler, K., DeMott, P. J., Prenni, A. J., Carrico, C., and Ervens, B.: Water activity and activation diameters from hygroscopicity data - Part I: Theory and application to inorganic salts, *Atmos. Chem. Phys.*, 5, 1357-1370, 2005.

Kumar, P. P., Broekhuizen, K., and Abbatt, J. P. D.: Organic acids as cloud condensation nuclei: Laboratory studies of highly soluble and insoluble species, *Atmos. Chem. Phys.*, 3, 509-520, 2003.

Lance, S., Medina, J., Smith, J. N., and Nenes, A.: Mapping the operation of the DMT Continuous Flow CCN counter, *Aerosol Sci. Tech.*, 40, 242-254, 2006.

Lobert, J. M., Scharffe, D. H., Hao, W. M., Kuhlbusch, T. A., Warneck, P., and Crutzen, P. J.: Experimental evaluation of biomass burning emissions: Nitrogen and carbon containing compounds, in J. S. Levine (ed.), *Global Biomass Burning: Atmospheric, Climate and Biospheric Implications*, MIT Press, Cambridge, MA, 1991.

Makela, J. M., Yli-Koivisto, S., Hiltunen, V., Seidl, W., Swietlicki, E., Teinila, K., Sillanpaa, M., Koponen, I. K., Paatero, J., Rosman, K., and Hameri, K.: Chemical composition of aerosol during particle formation events in boreal forest, *Tellus B*, 53, 380-393, 2001.

Manahan, S. E.: *Environmental Chemistry*, Eighth Edition, CRC Press, Boca Raton, Florida, 2005.

Maria, S. F., Russell, L. M., Turpin, B. J., Porcja, R. J., Campos, T. L., Weber, R. J., and Huebert, B. J.: Source signatures of carbon monoxide and organic functional groups in Asian Pacific Regional Aerosol Characterization Experiment (ACE-Asia) submicron aerosol types, *J. Geophys. Res.*, 108, 8637, doi:10.1029/2003JD003703, 2003.

McLafferty, F. W. and Turecek, F.: *Interpretation of Mass Spectra*, Fourth Edition, University Science Books, Mill Valley, California, 1993.

Meng, Z. Y. and Seinfeld, J. H.: Time scales to achieve atmospheric gas-aerosol equilibrium for volatile species, *Atmos Environ.*, 30, 2889-2900, 1996.

Milne, P. J. and Zika, R. G.: Amino-acid nitrogen in atmospheric aerosols - occurrence, sources and photochemical modification, *J. Atmos. Chem.*, 16, 361-398, 1993.

Mochida, M., Kuwata, M., Miyakawa, T., Takegawa, N., Kawamura, K., and Kondo, Y.: Relationship between hygroscopicity and cloud condensation nuclei activity for urban aerosols in Tokyo, *J. Geophys. Res.*, 111, D23204, doi:10.1029/2005JD006980, 2006.

Moore, R. H., Ingall, E. D., Sorooshian, A., and Nenes, A.: Molar mass, surface tension, and droplet growth kinetics of marine organics from measurements of CCN activity, *Geophys. Res. Lett.*, 35, L07801, doi:10.1029/2008GL033350, 2008.

Mosier, A. R., Andre, C. E., and Viets, F. G.: Identification of Aliphatic-Amines Volatilized from Cattle Feedyard, *Environ. Sci. Technol.*, 7, 642-644, 1973.

Mozurkewich, M.: The dissociation-constant of ammonium-nitrate and Its dependence on temperature, relative-humidity and particle-size, *Atmos Environ.*, 27, 261-270, 1993.

Murphy, D. M. and Thomson, D. S.: Chemical composition of single aerosol particles at Idaho Hill: Positive ion measurements, *J. Geophys. Res.*, 102, 6341-6352, 1997.

Murphy, S. M., Sorooshian, A., Kroll, J. H., Ng, N. L., Chhabra, P., Tong, C., Surratt, J. D., Knipping, E., Flagan, R. C., and Seinfeld, J. H.: Secondary aerosol formation from atmospheric reactions of aliphatic amines, *Atmos. Chem. Phys.*, 7, 2313-2337, 2007.

Murphy, S. M., Agrawal, H., Sorooshian, A., Padró, L. T., Gates, H., Hersey, S., Miller, J. W., Cocker III, D. R., Nenes, A., Jonsson, H., Flagan, R. C., and Seinfeld, J. H.: Comprehensive simultaneous on-board and airborne characterization of exhaust from a Panamax-size cargo ship at sea, *Environ. Sci. Technol.*, submitted.

Nenes, A., Charlson, R. J., Facchini, M. C., Kulmala, M., Laaksonen, A., and Seinfeld, J. H.: Can chemical effects on cloud droplet number rival the first indirect effect?, *Geophys. Res. Lett.*, 29, 1848, doi:10.1029/2002GL015295, 2002.

Neuman, J. A., Nowak, J. B., Brock, C. A., Trainer, M., Fehsenfeld, F. C., Holloway, J. S., Hubler, G., Hudson, P. K., Murphy, D. M., Nicks, D. K., Orsini, D., Parrish, D. D., Ryerson, T. B., Sueper, D. T., Sullivan, A., and Weber, R.: Variability in ammonium nitrate formation and nitric acid depletion with altitude and location over California, *J. Geophys. Res.*, 108, 4557, doi:10.1029/2003JD003616, 2003.

Ngwabie, N. M., Custer, T. G., Schade, G. W., Linke, S., and Hinz, T.: Mixing ratio measurements and flux estimates of volatile organic compounds (VOC) from a cowshed with conventional manure treatment indicate significant emissions to the atmosphere, *Geophys. Res. Abstr.*, 7(01175), 2005.

Petters, M. D. and Kreidenweis, S. M.: A single parameter representation of hygroscopic growth and cloud condensation nucleus activity." *Atmos. Chem. Phys.*, 7, 1961-1971, 2007.

Prenni, A. J., De Mott, P. J., and Kreidenweis, S. M.: Water uptake of internally mixed particles containing ammonium sulfate and dicarboxylic acids, *Atmos Environ.*, 37, 4243-4251, 2003.

Pun, B. K. and Seigneur, C.: Understanding particulate matter formation in the California San Joaquin Valley: conceptual model and data needs, *Atmos. Environ.*, 33, 4865-4875, 1999.

Rabaud, N. E., Ebeler, S. E., Ashbaugh, L. L., and Flocchini, R. G.: Characterization and quantification of odorous and non-odorous volatile organic compounds near a commercial dairy in California, *Atmos. Environ.*, 37, 933-940, 2003.

Rissler, J., Pagels, J., Swietlicki, E., Wierzbicka, A., Strand, M., Lillieblad, L., Sanati, M., and Bohgard, M.: Hygroscopic behavior of aerosol particles emitted from biomass fired grate boilers, *Aerosol Sci. Tech.*, 39, 919-930, 2005.

Rissler, J., Vestin, A., Swietlicki, E., Fisch, G., Zhou, J., Artaxo, P., and Andreae, M. O.: Size distribution and hygroscopic properties of aerosol particles from dry-season biomass burning in Amazonia, *Atmos. Chem. Phys.*, 6, 471-491, 2006.

Roberts, G. C. and Nenes, A.: A continuous-flow streamwise thermal-gradient CCN chamber for atmospheric measurements, *Aerosol Sci. Tech.*, 39, 206-221, 2005.

Rose, D., Gunthe, S. S., Mikhailov, E., Frank, G. P., Dusek, U., Andreae, M. O., and Poschl, U.: Calibration and measurement uncertainties of a continuous-flow cloud condensation nuclei counter (DMT-CCNC): CCN activation of ammonium sulfate and sodium chloride aerosol particles in theory and experiment, *Atmos. Chem. Phys.*, 8, 1153-1179, 2008.

Ruehl, C. R., Chuang, P. Y., and Nenes, A.: How quickly do cloud droplets form on atmospheric particles?, *Atmos. Chem. Phys.*, 8, 1043-1055, 2008.

Rumburg, B., Mount, G. H., Yonge, D., Lamb, B., Westberg, H., Filipy, J., Bays, J., Kincaid, R., and Johnson, K.: Atmospheric flux of ammonia from sprinkler application of dairy waste, *Atmos Environ.*, 40, 7246-7258, 2006.

Russell, A. G., Mcrae, G. J., and Cass, G. R.: Mathematical-modeling of the formation and transport of ammonium-nitrate aerosol, *Atmos. Environ.*, 17, 949-964, 1983.

Schade, G. W. and Crutzen, P. J.: Emission of aliphatic-amines from animal husbandry and their reactions - potential source of N₂O and HCN, *J. Atmos. Chem.*, 22, 319-346, 1995.

Seinfeld, J. H. and Pandis, S. N.: Atmospheric Chemistry and Physics, Second Edition, Wiley-Interscience, New York, 2006.

Shulman, M. L., Jacobson, M. C., Carlson, R. J., Synovec, R. E., and Young, T. E.: Dissolution behavior and surface tension effects of organic compounds in nucleating cloud droplets, *Geophys. Res. Lett.*, 23, 277-280, 1996.

Sjogren, S., Gysel, M., Weingartner, E., Baltensperger, U., Cubison, M. J., Coe, H., Zardini, A. A., Marcolli, C., Krieger, U. K., and Peter, T.: Hygroscopic growth and water uptake kinetics of two-phase aerosol particles consisting of ammonium sulfate, adipic and humic acid mixtures, *J. Aerosol Sci.*, 38, 157-171, 2007.

Sorooshian, A., Brechtel, F. J., Ma, Y. L., Weber, R. J., Corless, A., Flagan, R. C., and Seinfeld, J. H.: Modeling and characterization of a particle-into-liquid sampler (PILS), *Aerosol Sci. Tech.*, 40, 396-409, 2006a.

Sorooshian, A., Varutbangkul, V., Brechtel, F. J., Ervens, B., Feingold, G., Bahreini, R., Murphy, S. M., Holloway, J. S., Atlas, E. L., Buzorius, G., Jonsson, H., Flagan, R. C., and Seinfeld, J. H.: Oxalic acid in clear and cloudy atmospheres: Analysis of data from International Consortium for Atmospheric Research on Transport and Transformation 2004, *J. Geophys. Res.*, 111, D23S45, doi:10.1029/2005JD006880, 2006b.

Sorooshian, A., Ng, N. L., Chan, A. W. H., Feingold, G., Flagan, R. C., and Seinfeld, J. H.: Particulate organic acids and overall water-soluble aerosol composition measurements from the 2006 Gulf of Mexico Atmospheric Composition and Climate Study (GoMACCS), *J. Geophys. Res.*, 112, D13201, doi:10.1029/2007JD008537, 2007a.

Sorooshian, A., Lu, M. L., Brechtel, F. J., Jonsson, H., Feingold, G., Flagan, R. C., and Seinfeld, J. H.: On the source of organic acid aerosol layers above clouds, *Environ. Sci. Technol.*, 41, 4647-4654, 2007b.

Sorooshian, A., S. Hersey, F. J. Brechtel, A. Corless, R. C. Flagan, and Seinfeld, J. H.: Rapid, size-resolved aerosol hygroscopic growth measurements: differential aerosol sizing and hygroscopicity spectrometer probe (DASH-SP), *Aerosol Sci. Tech.*, 42, 445-464, 2008.

Stelson, A. W., Friedlander, S. K., and Seinfeld, J. H.: Note on the equilibrium relationship between ammonia and nitric-acid and particulate ammonium-nitrate, *Atmos. Environ.*, 13, 369-371, 1979.

Stelson, A. W. and Seinfeld, J. H.: Relative-humidity and temperature-dependence of the ammonium-nitrate dissociation-constant, *Atmos. Environ.*, 16, 983-992, 1982a.

Stelson, A. W. and Seinfeld, J. H.: Relative-humidity and Ph-dependence of the vapor-pressure of ammonium-nitrate nitric acid-solutions at 25 degrees C, *Atmos. Environ.*, 16, 993-1000, 1982b.

Stokes, R. H. and Robinson, R. A.: Interactions in aqueous nonelectrolyte solutions .I. Solute-solvent equilibria, *J. Phys. Chem.*, 70, 2126-2130, 1966.

Svenningsson, I. B., Hansson, H. C., Wiedensohler, A., Ogren, J. A., Noone, K. J., and Hallberg, A.: Hygroscopic growth of aerosol-particles in the Po Valley, *Tellus B*, 44, 556-569, 1992.

Svenningsson, B., Rissler, J., Swietlicki, E., Mircea, M., Bilde, M., Facchini, M. C., Decesari, S., Fuzzi, S., Zhou, J., Monster, J., and Rosenorn, T.: Hygroscopic growth and critical supersaturations for mixed aerosol particles of inorganic and organic compounds of atmospheric relevance, *Atmos. Chem. Phys.*, 6, 1937-1952, 2006.

Takahama, S., Wittig, A. E., Vayenas, D. V., Davidson, C. I., and Pandis, S. N.: Modeling the diurnal variation of nitrate during the Pittsburgh Air Quality Study, *J. Geophys. Res.*, 109, D16S06, doi:10.1029/2003JD004149, 2004.

Tan, P. V., Evans, G. J., Tsai, J., Owega, S., Fila, M. S., and Malpica, O.: On-line analysis of urban particulate matter focusing on elevated wintertime aerosol concentrations, *Environ. Sci. Technol.*, 36, 3512-3518, 2002.

Tang, I. N.: Chemical and size effects of hygroscopic aerosols on light scattering coefficients, *J. Geophys. Res.*, 101, 19245-19250, 1996.

Taraniuk, I., Graber, E. R., Kostinski, A., and Rudich, Y.: Surfactant properties of atmospheric and model humic-like substances (HULIS), *Geophys. Res. Lett.*, 34, L16807, doi:10.1029/2007GL029576, 2007.

Ulbrich, I. M., Lechner, M., and Jimenez, J. L.: AMS Spectral Database. URL: <http://cires.colorado.edu/jimenez-group/AMSSd/>, 2008.

Ulbrich, I. M., Canagaratna, M. R., Zhang, Q., Worsnop, D. R., and Jimenez, J. L.: Interpretation of organic components from positive matrix factorization of aerosol mass spectrometric data, *Atmos. Chem. Phys. Disc.*, 8, 6729-6791, 2008.

Vanneste, A., Duce, R. A., and Lee, C.: Methylamines in the marine atmosphere, *Geophys. Res. Lett.*, 14, 711-714, 1987.

Varutbangkul, V., Brechtel, F. J., Bahreini, R., Ng, N. L., Keywood, M. D., Kroll, J. H., Flagan, R. C., Seinfeld, J. H., Lee, A., and Goldstein, A. H.: Hygroscopicity of secondary organic aerosols formed by oxidation of cycloalkenes, monoterpenes, sesquiterpenes, and related compounds, *Atmos. Chem. Phys.*, 6, 2367-2388, 2006.

Weast, R. C.: CRC Handbook of Chemistry and Physics, Sixty Eighth Edition, CRC Press, Florida, 1987.

Westerholm, R., Li, H., and Almen, J.: Estimation of aliphatic amine emissions in automobile exhausts, *Chemosphere*, 27, 1381-1384, 1993.

Wexler, A. S. and Seinfeld, J. H.: Analysis of aerosol ammonium-nitrate - departures from equilibrium during Scaqs, *Atmos. Environ.*, 26, 579-591, 1992.

Wise, M. E., Surratt, J. D., Curtis, D. B., Shilling, J. E., and Tolbert, M. A.: Hygroscopic growth of ammonium sulfate/dicarboxylic acids, *J. Geophys. Res.*, 108, 4638, doi:10.1029/2003JD003775, 2003.

Xiong, J. Q., Zhong, M. H., Fang, C. P., Chen, L. C., and Lippmann, M.: Influence of organic films on the hygroscopicity of ultrafine sulfuric acid aerosol, *Environ. Sci. Technol.*, 32, 3536-3541, 1998.

Yu, S. C., Dennis, R., Roselle, S., Nenes, A., Walker, J., Eder, B., Schere, K., Swall, J., and Robarge, W.: An assessment of the ability of three-dimensional air quality models with current thermodynamic equilibrium models to predict aerosol NO_3^- , *J. Geophys. Res.*, 110, D07S13, doi:10.1029/2004JD004718, 2005.

Zdanovskii, A.: New methods for calculating solubilities of electrolytes in multicomponent systems, *Zhur. Fiz. Khim.*, 22, 1475-1485, 1948.

Zhang, J., Chameides, W. L., Weber, R., Cass, G., Orsini, D., Edgerton, E., Jongejan, P., and Slanina, J.: An evaluation of the thermodynamic equilibrium assumption for fine particulate composition: Nitrate and ammonium during the 1999 Atlanta Supersite Experiment, *J. Geophys. Res.*, 108, 8414, doi:10.1029/2001JD001592, 2002.

Zhang, X. Q., Turpin, B. J., McMurry, P. H., Hering, S. V., and Stolzenburg, M. R.: Mie theory evaluation of species contributions to 1990 wintertime visibility reduction in the Grand-Canyon, *J. Air Waste Manage.*, 44, 153-162, 1994.

Zhang, Q., Anastasio, C., and Jimenez-Cruz, M.: Water-soluble organic nitrogen in atmospheric fine particles ($\text{PM}_{2.5}$) from northern California, *J. Geophys. Res.*, 107, 4112, doi:10.1029/2001JD000870, 2002.

Zhang, Q. and Anastasio, C.: Free and combined amino compounds in atmospheric fine particles ($\text{PM}_{2.5}$) and fog waters from Northern California, *Atmos. Environ.*, 37, 2247-2258, 2003.

Zhang, Q., Alfarra, M. R., Worsnop, D. R., Allan, J. D., Coe, H., Canagaratna, M. R., and Jimenez, J. L.: Deconvolution and quantification of hydrocarbon-like and oxygenated organic aerosols based on aerosol mass spectrometry, *Environ. Sci. Technol.*, 39, 4938-4952, 2005.

Table 4.1 Summary of in-plume and out-of-plume measurements of composition and particle number and mass concentration.

	Flight A In Plume		Flight A Out of Plume		Flight B In Plume		Flight B Out of Plume	
	AVE	ST DEV	AVE	ST DEV	AVE	ST DEV	AVE	ST DEV
Total Mass ($\mu\text{g m}^{-3}$)	10.48	1.64	8.01	1.48	4.53	0.87	2.65	0.95
Organic ($\mu\text{g m}^{-3}$)	6.48	0.98	5.10	1.07	2.46	0.29	1.73	0.70
NO_3^- ($\mu\text{g m}^{-3}$)	0.93	0.40	0.30	0.11	1.08	0.50	0.19	0.12
SO_4^{2-} ($\mu\text{g m}^{-3}$)	2.06	0.24	1.81	0.31	0.54	0.10	0.56	0.26
NH_4^+ ($\mu\text{g m}^{-3}$)	1.02	0.23	0.80	0.17	0.44	0.14	0.19	0.10
Excess NO_3^- ($\mu\text{g m}^{-3}$)	0.04	0.50	-0.16	0.41	0.02	0.34	0.00	0.21
$[\text{NH}_4^+ : \text{SO}_4^{2-}]$ molar ratio	2.64	0.51	2.38	0.47	4.61	2.25	1.94	1.42
% Organic	61.9	2.6	63.5	3.3	55.5	6.4	63.1	11.9
% NO_3^-	8.6	2.4	3.7	1.1	22.7	7.3	7.2	2.4
% SO_4^{2-}	19.8	1.7	22.8	2.6	12.3	3.0	23.1	11.0
% NH_4^+	9.7	1.7	10.1	1.8	9.6	2.1	7.0	3.8
DMA particle concentration ($\# \text{cm}^{-3}$)	30528	8987	30778	11026	16606	4286	18139	8910
(UFPCPC 3025/ CPC 3010) ^a	1.1	0.0	1.1	0.0	1.2	0.1	1.2	0.1
cToF-AMS m/z 57:44	0.07	0.01	0.07	0.02	0.07	0.02	0.09	0.08
cToF-AMS m/z 44: Total Organic	0.10	0.01	0.10	0.01	0.11	0.01	0.12	0.02
O:C atomic ratio ^b	0.45	0.02	0.45	0.02	0.48	0.04	0.53	0.09

^aThe ratio of the particle number concentration for $D_p > 3$ nm (UFPCPC 3025) to that for $D_p > 10$ nm (CPC 3010).

^bThe O:C atomic ratio was calculated using the data inventory and slope equation presented by Aiken et al. (2008; Fig. 4.4b).

Table 4.2 DASH-SP hygroscopicity and dry particle refractive index data categorized by the time of flight as shown in Fig. 4.1. Data at RH = 85% are not available for flight A.

		<i>GF</i> (74%)	<i>GF</i> (85%)	<i>GF</i> (92%)	Dry Refractive Index
Flight A	Valley transit	1.10 ± 0.05		1.64 ± 0.17	1.52 ± 0.08
	Circle above plume source	1.16 ± 0.12		1.79 ± 0.22	1.48 ± 0.08
	First set of transects (1 - 4)	1.07 ± 0.03		1.55 ± 0.19	1.52 ± 0.06
	Transect 1 (plume age = 0.3 h)	1.04 ± 0.03		1.59 ± 0.17	1.54 ± 0.04
	Transect 2 (plume age = 0.5 h)	1.05 ± 0.03		1.51 ± 0.22	1.56 ± 0.05
	Transect 3 (plume age = 1.1 h)	1.08 ± 0.03		1.70 ± 0.18	1.48 ± 0.05
	Transect 4 (plume age = 1.5 h)	1.06 ± 0.01		1.74 ± 0.08	1.51 ± 0.01
	Spiral up to 600 m	1.07 ± 0.05		1.47 ± 0.15	1.53 ± 0.10
	Second set of transects (5 - 7)	1.09 ± 0.04		1.61 ± 0.13	1.54 ± 0.05
	Transect 5 (plume age = 1.2 h)	1.06 ± 0.01		1.68 ± 0.06	1.54 ± 0.05
	Transect 6 (plume age = 1.3 h)	1.12 ± 0.05		1.60 ± 0.08	1.54 ± 0.05
	Transect 7 (plume age = 0.8 h)	1.12 ± 0.01		1.69 ± 0.16	1.54 ± 0.09
	Spiral down above plume source	1.33 ± 0.30		1.80 ± 0.19	1.40 ± 0.10
	Valley transit	1.06 ± 0.02		1.53 ± 0.15	1.56 ± 0.05
Flight B	Valley transit	1.03 ± 0.04	1.35 ± 0.06	1.49 ± 0.07	1.55 ± 0.04
	Circle above plume source	1.10 ± 0.07	1.50 ± 0.10	1.88 ± 0.22	1.51 ± 0.01
	First set of transects (plume age < 0.9 h)	1.12 ± 0.05	1.39 ± 0.08	1.65 ± 0.20	1.52 ± 0.01
	Directly in plume (plume age < 0.9 h)	1.15 ± 0.06	1.44 ± 0.06	1.86 ± 0.14	1.52 ± 0.01
	Spiral up to 400 m	1.07 ± 0.04	1.37 ± 0.06	1.57 ± 0.07	1.52 ± 0.01
	Second set of transects (plume age < 0.9 h)	1.08 ± 0.04	1.39 ± 0.06	1.65 ± 0.17	1.53 ± 0.03
	Directly in plume (plume age < 0.9 h)	1.09 ± 0.05	1.40 ± 0.09	1.65 ± 0.16	1.51 ± 0.02
	Valley transit	1.11 ± 0.04	1.39 ± 0.08	1.55 ± 0.11	1.53 ± 0.05

Table 4.3 Summary of CCN data for flights A and B.

			CCN (#/ cm^3)	Activated fraction								
			SS ~ 0.1%		SS ~ 0.2%		SS ~ 0.3%		SS ~ 0.4 - 0.45%		SS ~ 0.5%	
Flight A	In plume	AVE	92	0.01	329	0.02	1114	0.06	1882	0.08	2265	0.08
		ST DEV	123	0.01	354	0.02	628	0.05	526	0.04	478	0.02
	Out of plume	AVE	141	0.01	252	0.01	1124	0.05	1641	0.06	1966	0.08
		ST DEV	218	0.01	295	0.01	561	0.03	484	0.02	478	0.02
			SS ~ 0.2%		SS ~ 0.25 - 0.35%		SS ~ 0.4 - 0.45%		SS ~ 0.6%			
Flight B	In plume	AVE	855	0.05	1246	0.07	2027	0.11	2436	0.15		
		ST DEV	584	0.03	713	0.04	523	0.03	834	0.05		
	Out of plume	AVE	707	0.04	1073	0.06	1796	0.08	4168	0.14		
		ST DEV	596	0.03	770	0.05	768	0.03	2052	0.04		

Table 4.4 Summary of κ values (Petters and Kreidenweis, 2007) for the total aerosol and the organic component of the aerosol, as derived from subsaturated hygroscopic growth factor data at the respective RHs shown. Data at RH = 85% are not available for flight A. The organic κ values were calculated using equation 7 from Petters and Kreidenweis (2007), CCN-derived values of κ for ammonium sulfate and ammonium nitrate from their Table 4.1, the total κ value calculated at RH = 92%, and measured volume fractions of ammonium nitrate, ammonium sulfate, and organics.

	In plume		Out of plume	
	Flight A	Flight B	Flight A	Flight B
κ_{total} (85%)	NA	0.40 ± 0.12	NA	0.33 ± 0.09
κ_{total} (92%)	0.36 ± 0.12	0.44 ± 0.19	0.29 ± 0.12	0.28 ± 0.10
κ_{organic} (92%)	0.13 ± 0.08	0.14 ± 0.15	0.06 ± 0.07	-0.06 ± 0.23

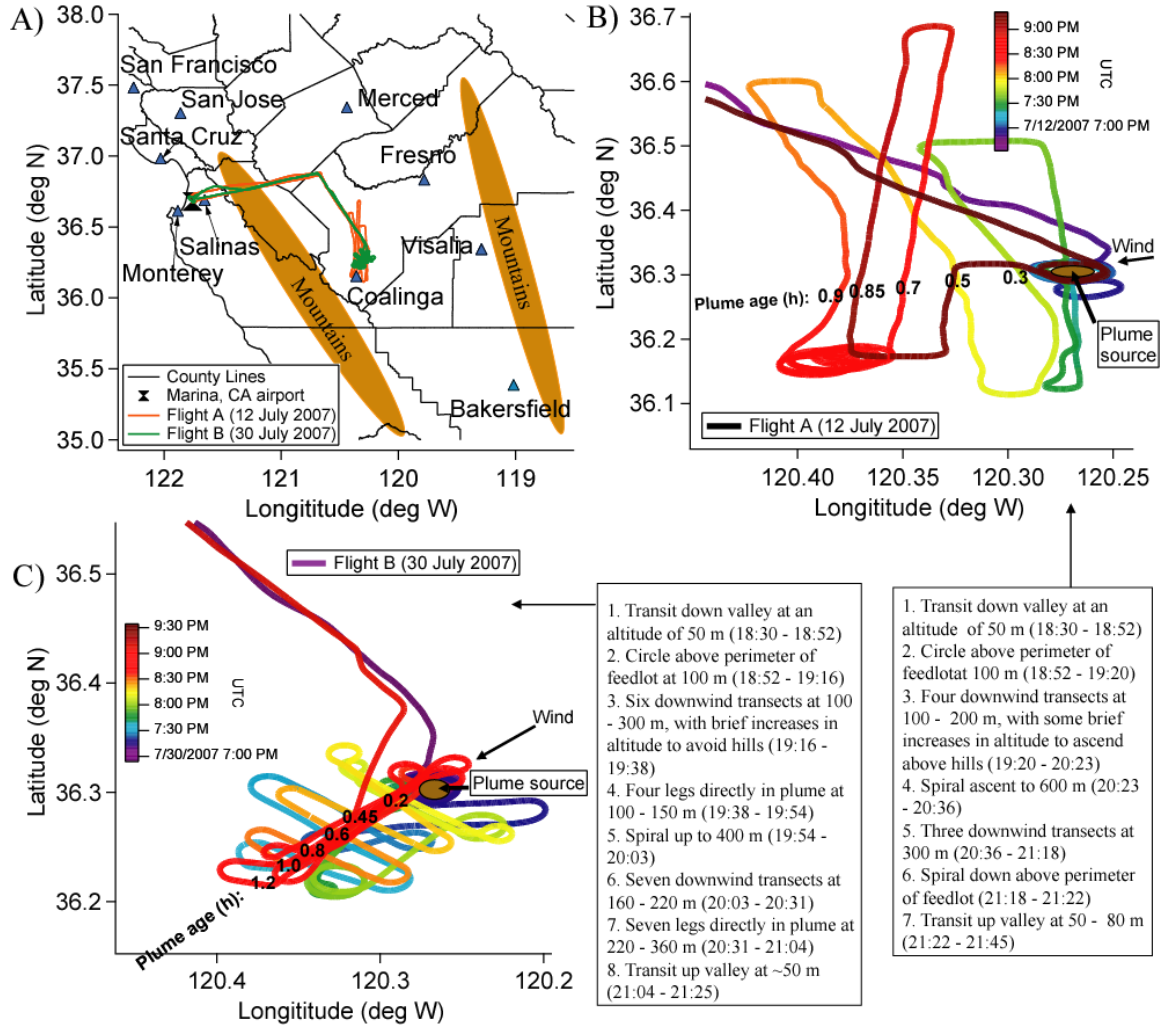


Fig. 4.1 A) Complete flight tracks for the two flights in the San Joaquin Valley of California. The shaded mountain areas are meant to provide a relative view of how the San Joaquin Valley is bordered by major topographical features. B/C) Detailed tracks for flights A (12 July 2007) and B (30 July 2007) with a step-by-step description of the aircraft maneuvers. Plume ages were calculated using downwind distance and average wind speed in the vicinity of the feedlot.

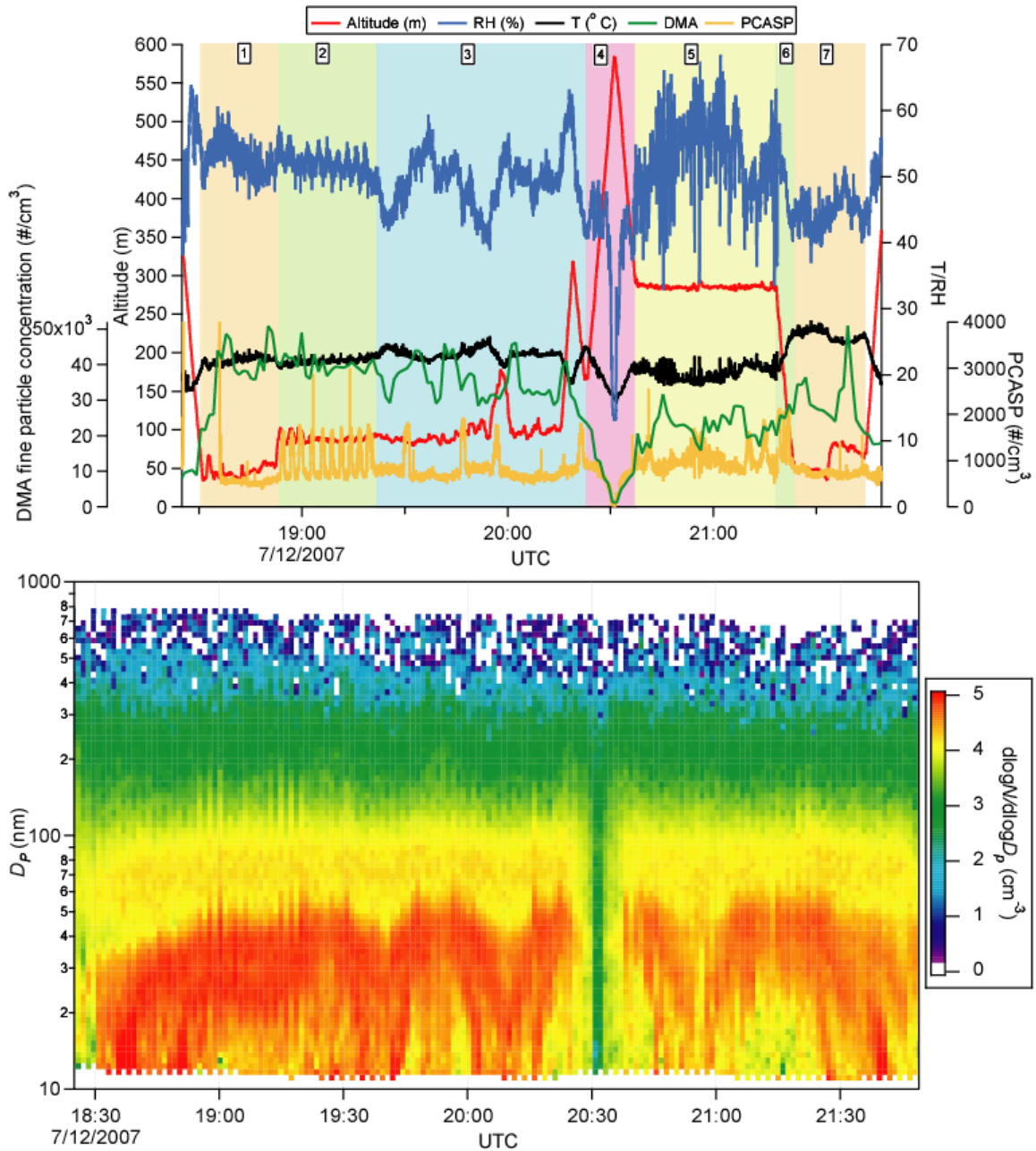


Fig. 4.2 Upper panel) Time series of particle number concentration and meteorological data for flight A. Lower panel) Time series of aerosol size distribution. The number labels at the top of each shaded block correspond to the respective flight segment listed in Fig. 4.1.

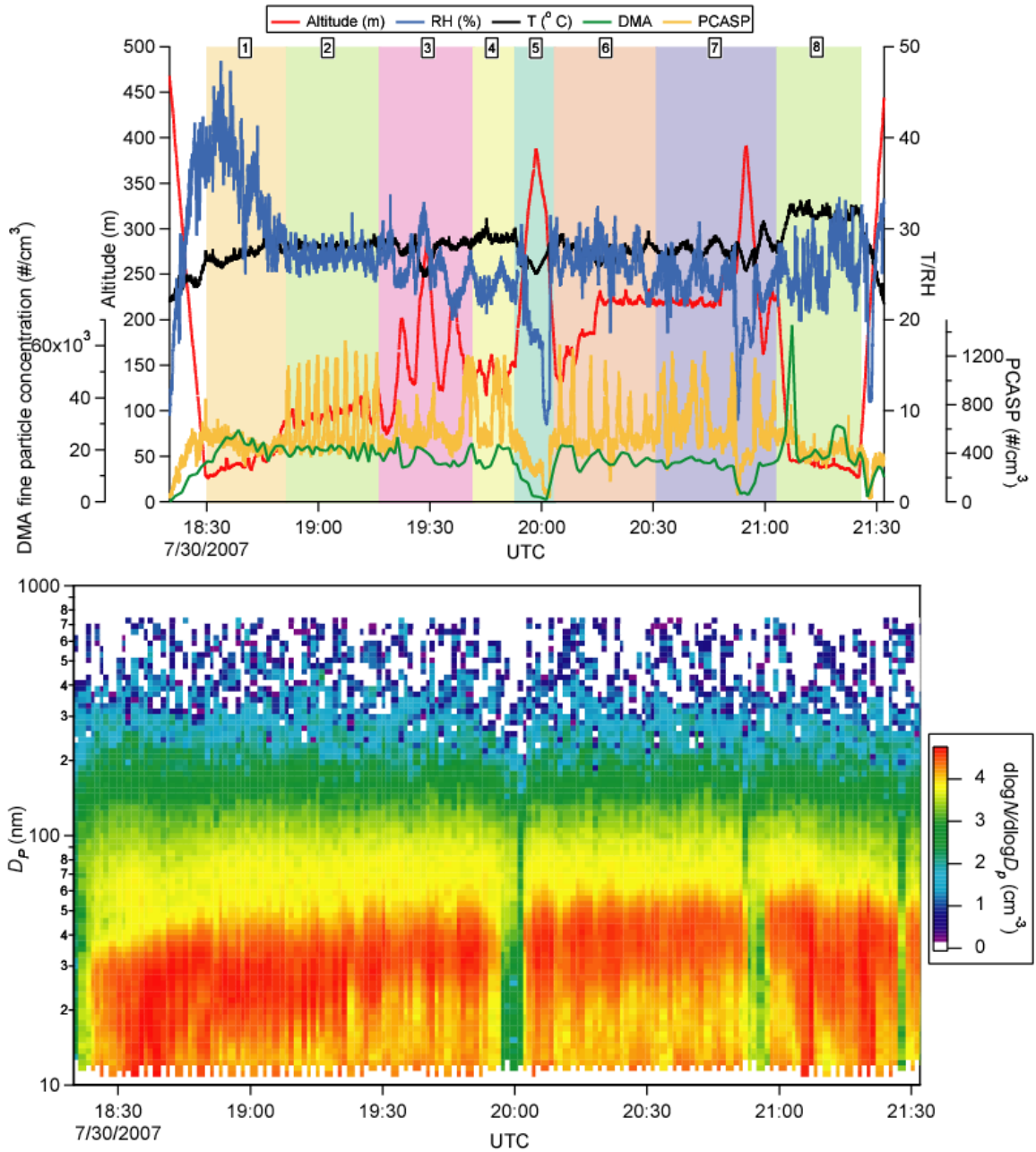


Fig. 4.3 Upper panel) Time series of particle number concentration and meteorological data for flight B. Lower panel) Time series of aerosol size distribution. The number labels at the top of each shaded block correspond to the respective flight segment listed in Fig. 4.1.

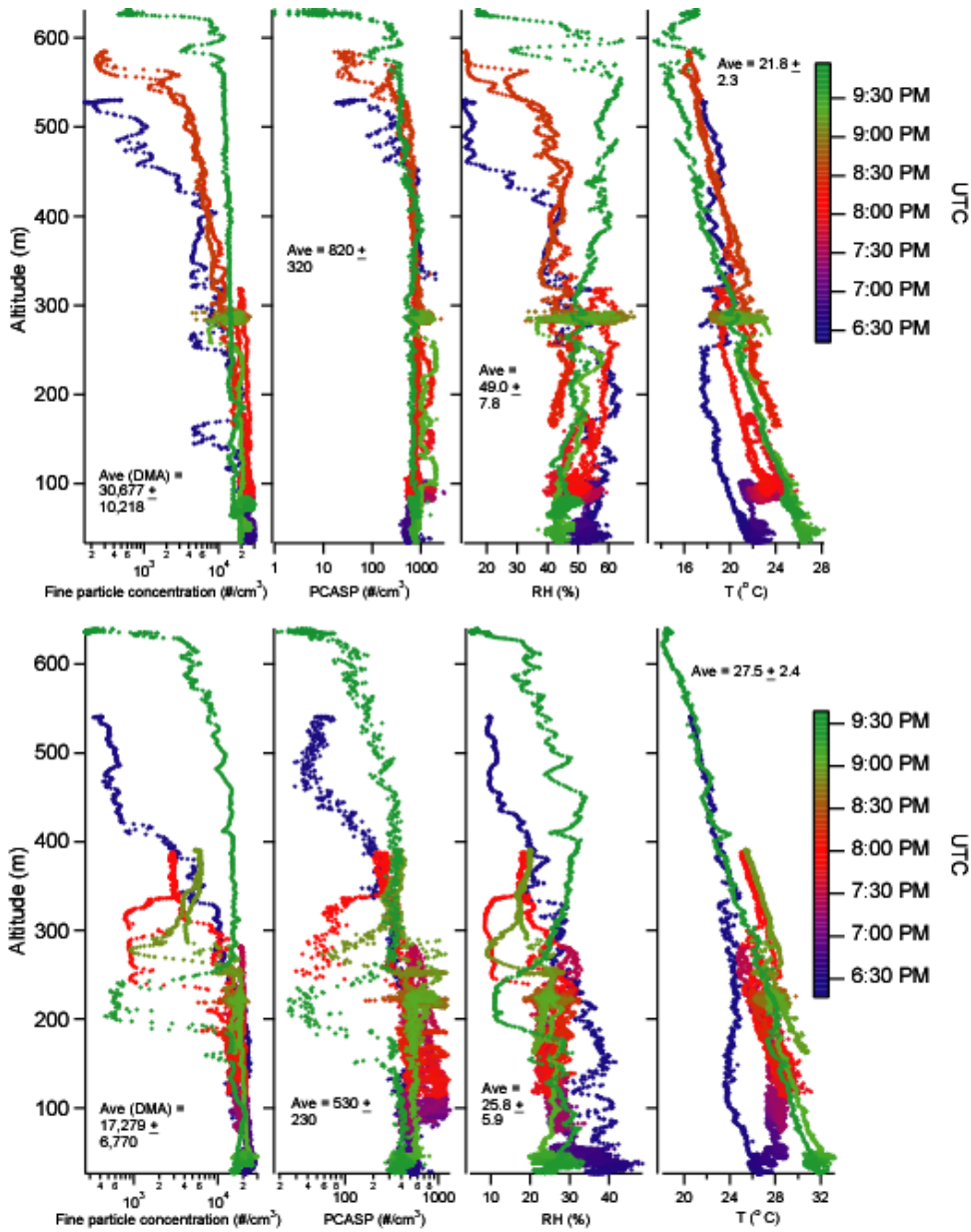


Fig. 4.4 Vertical profiles of particle number concentration and meteorological data for flights A (upper panel) and B (lower panel). For the submicrometer particle concentration data (CPC 3010), it should be noted that the absolute concentrations are not accurate due to electrical saturation of the instrument; these data are plotted because of the 1 s time resolution of the data. The DMA and CPC 3010 number concentrations were proportional throughout both flights, therefore, the CPC 3010 values are useful for qualitative purposes to identify the mixing layer height. DMA number concentrations indicated are accurate.

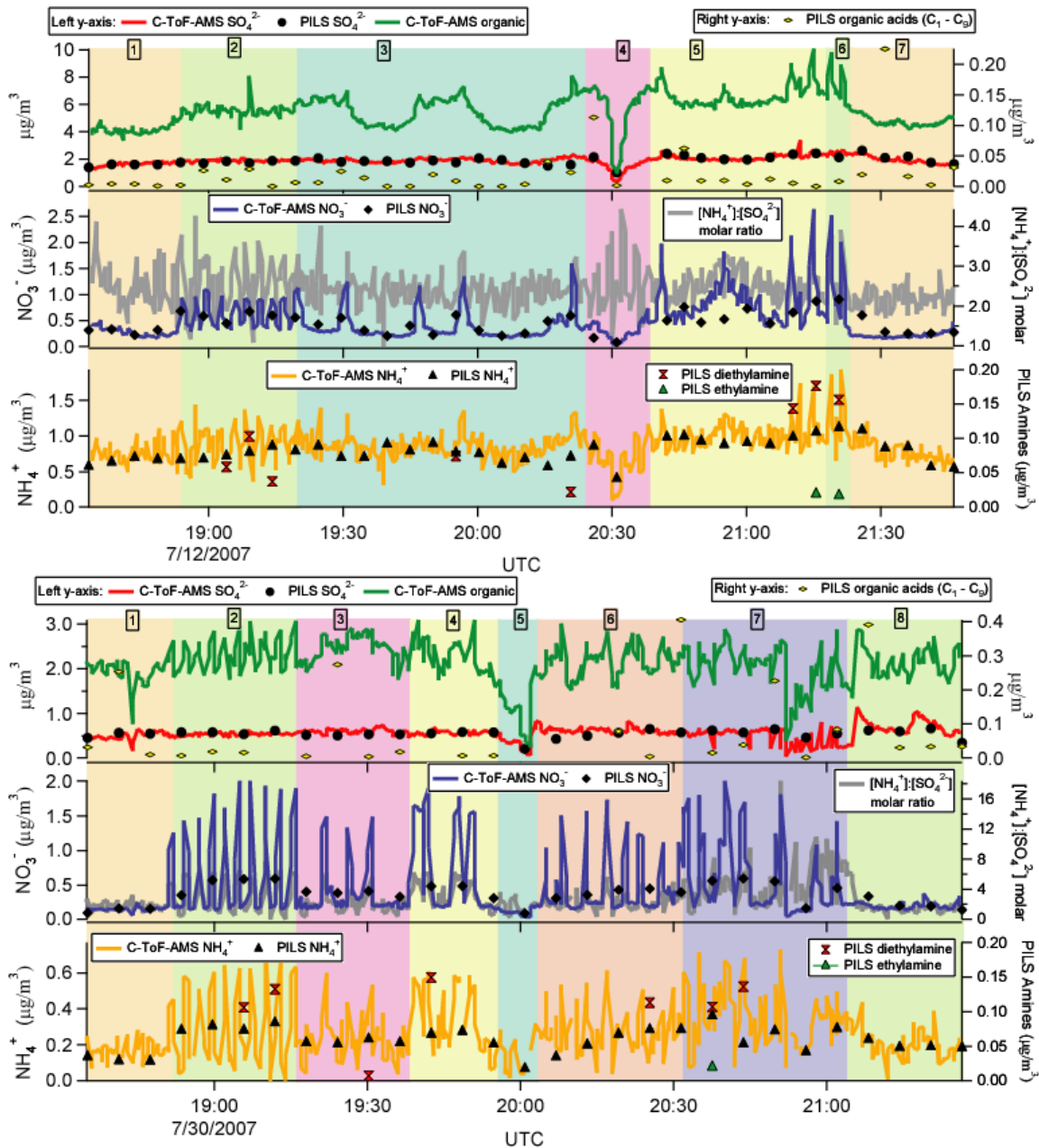


Fig. 4.6 Time series of Pils water-soluble aerosol composition and C-ToF-AMS composition for flights A (upper panel) and B (lower panel). The number labels for each shaded box correspond to the portion of each flight represented in Fig. 4.1. The shaded areas representing the plume are characterized by significant increases in organics, ammonium, nitrate, and amines. The ammonium-to-sulfate molar ratio exceeds 2.0 in the plume, allowing nitrate to partition into the aerosol phase. The multiple C-ToF-AMS spikes in the species concentrations cannot be resolved by the Pils since the 5-min time intervals for sample collection average out the quick plume passes with the longer legs outside of the plume. Agreement between the Pils and C-ToF-AMS is most evident for sulfate, since this species was relatively level in concentration during the flights.

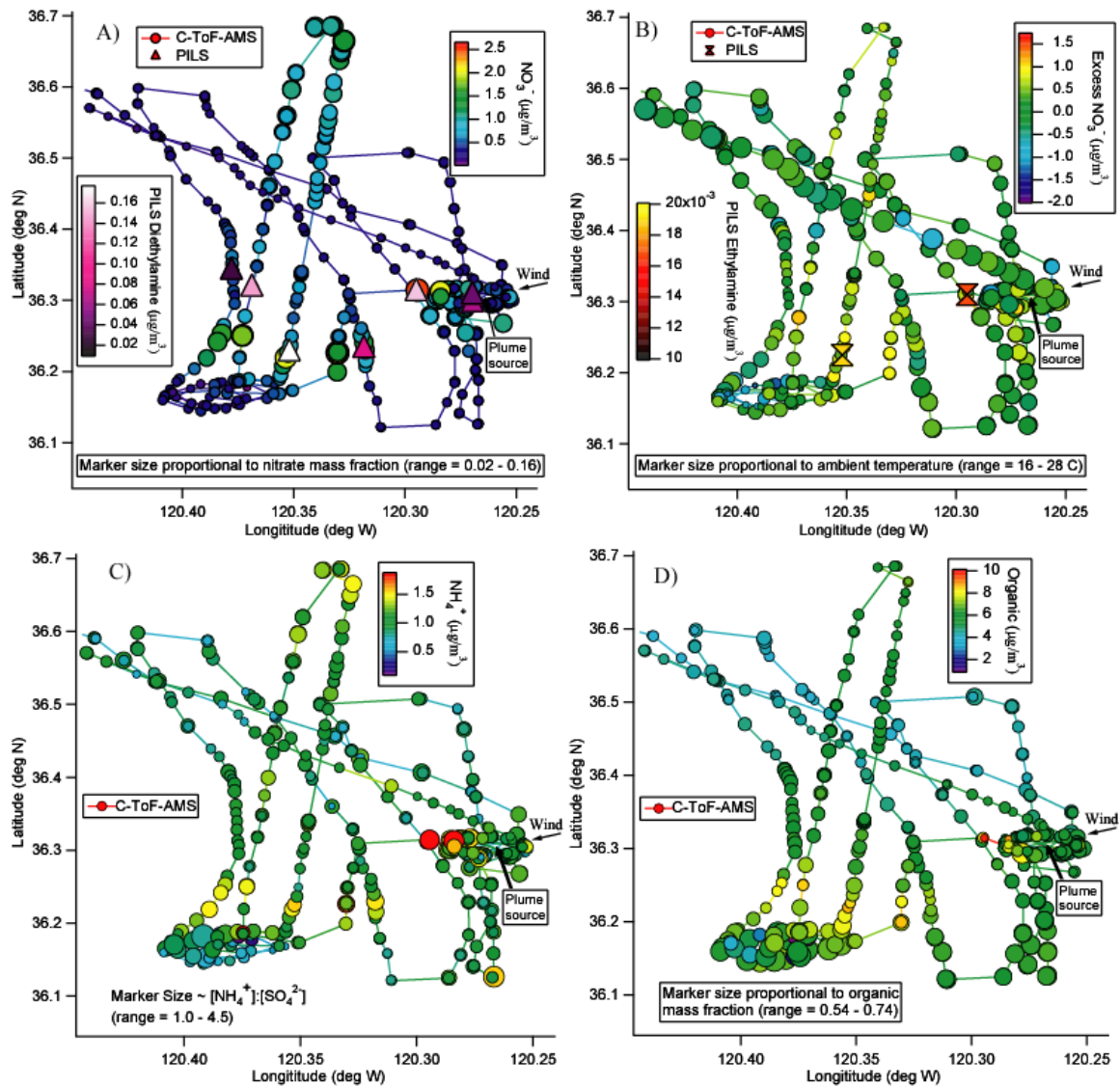


Fig. 4.7 Spatial distribution of various aerosol species during flight A. A) C-ToF-AMS nitrate and PILS diethylamine, with marker size proportional to nitrate mass fraction; B) PILS ethylamine and *excess nitrate* remaining after both sulfate and nitrate have been neutralized by ammonium (see Sect. 4.3.1 for further explanation), with marker size proportional to ambient temperature; C) C-ToF-AMS ammonium, with marker size proportional to the ammonium-to-sulfate molar ratio; D) C-ToF-AMS organic, with marker size proportional to organic mass fraction. The PILS markers are spatially placed wherever the aircraft was at the midpoint of the time when a particular sample was collected (after being corrected for liquid residence time in the instrument); therefore the amine markers are spatially distinct from the core of the plume (especially the two markers representing the highest plume ages).

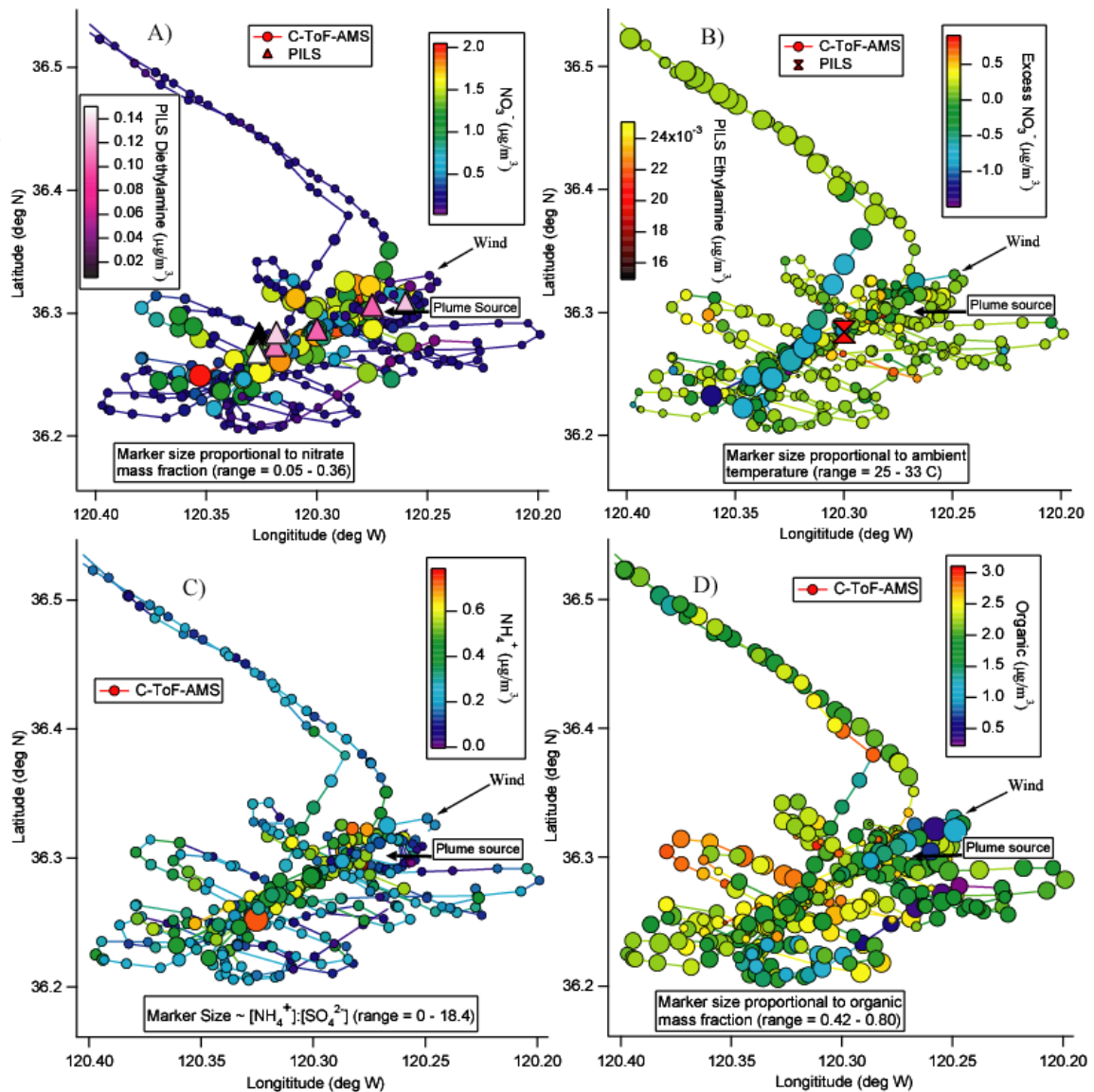


Fig. 4.8 Spatial distribution of various aerosol species during flight B. A) C-ToF-AMS nitrate and PILS diethylamine, with marker size proportional to nitrate mass fraction; B) PILS ethylamine and *excess nitrate* remaining after both sulfate and nitrate have been neutralized by ammonium (see Sect. 4.3.1 for further explanation), with marker size proportional to ambient temperature; C) C-ToF-AMS ammonium, with marker size proportional to the ammonium-to-sulfate molar ratio; D) C-ToF-AMS organic, with marker size proportional to organic mass fraction. The PILS markers are spatially placed wherever the aircraft was at the midpoint of the time when a particular sample was collected (after being corrected for liquid residence time in the instrument).

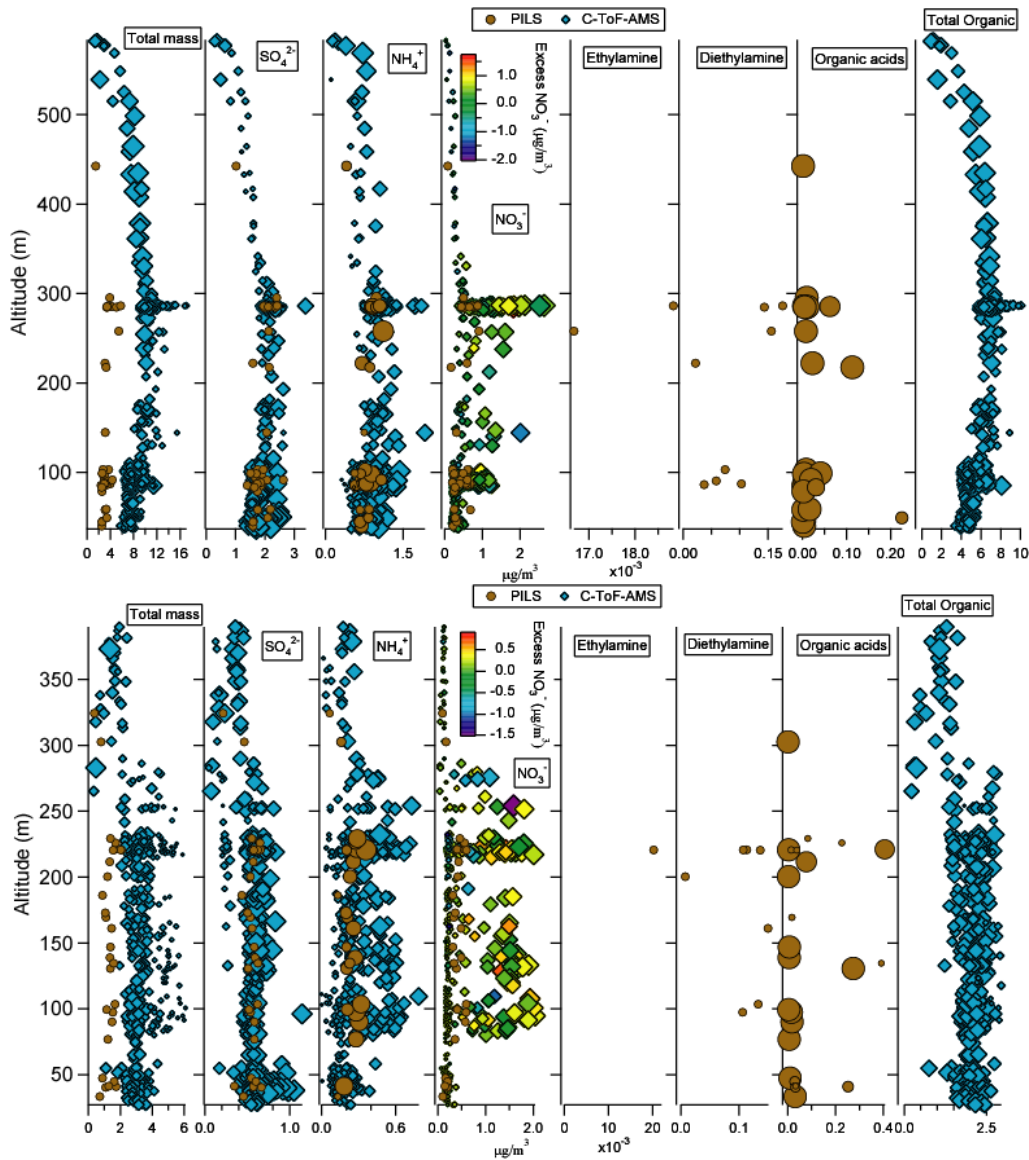


Fig. 4.9 Vertical distribution of total submicrometer particulate mass and species concentrations from both the PILS and C-ToF-AMS, for flights A (upper panel) and B (lower panel). The C-ToF-AMS marker sizes for ‘Total mass’ are proportional to the organic:inorganic ratio. Marker sizes for the individual C-ToF-AMS species are proportional to the respective mass fraction of that species. Marker sizes for PILS ‘Organic acids’ are proportional to the relative contribution by oxalate. Marker sizes for PILS ammonium are proportional to the ammonium-to-sulfate molar ratio. Total mass, nitrate, ammonium, and organics increase in concentration with increasing altitude up to $\sim 250 - 300$ m, before decreasing in both flights. C-ToF-AMS concentrations exceed those of the PILS for commonly detected species in the plume, especially nitrate and ammonium, since the PILS averages 5-min worth of aerosol composition whereas the C-ToF-AMS has a time resolution of $\sim 20 - 30$ s. Total PILS mass includes inorganics and organic acids, whereas total C-ToF-AMS mass includes inorganics and nonrefractory organic mass.

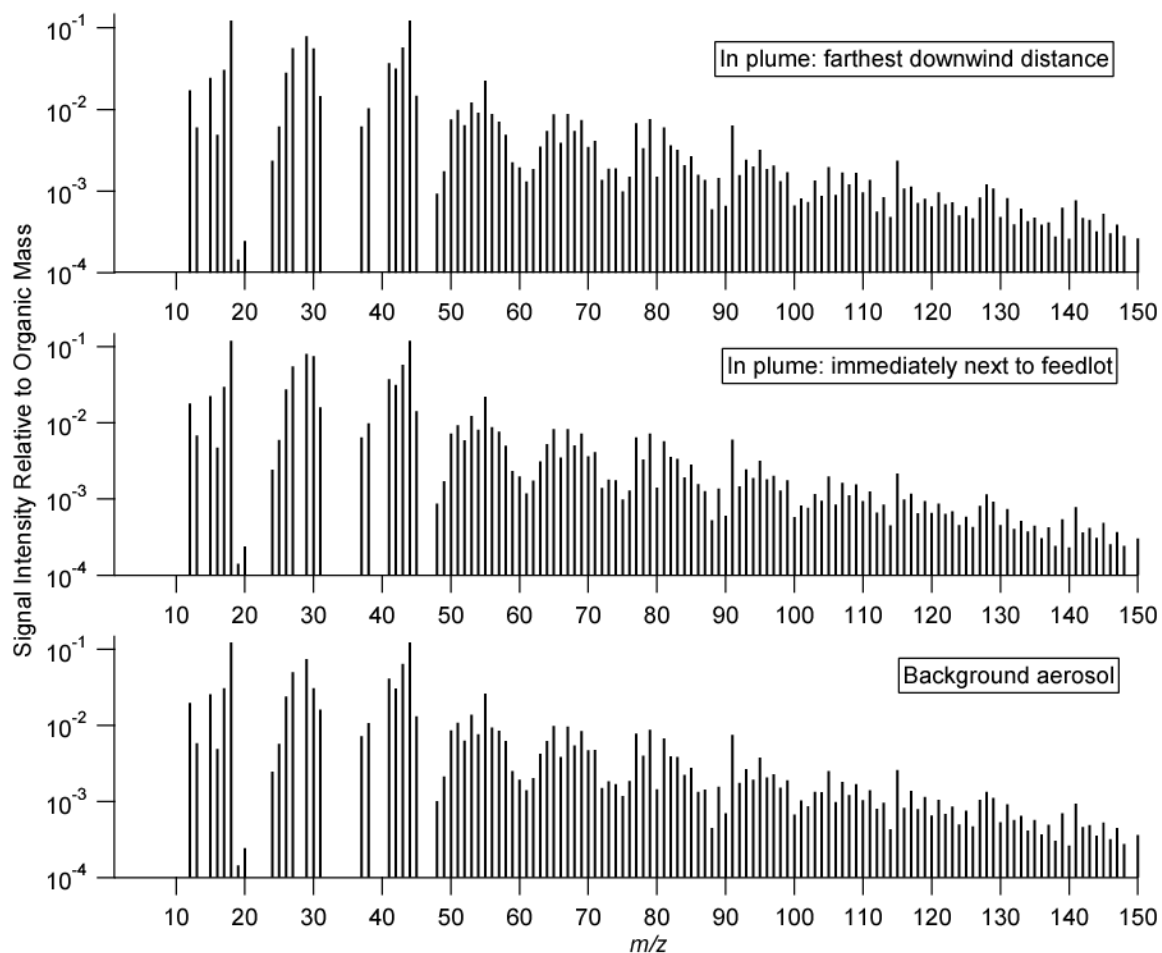


Fig. 4.10 Aerosol mass spectra from the C-ToF-AMS in the background aerosol and in the plume at various downwind distances from the feedlot for flight B. There is no significant difference in the chemical signature of the aerosol in the three categories shown, with the notable exception of an enhancement in the m/z 30 peak, a common amine marker, at the closest point to the source. The flight A spectra are similar to those presented here.

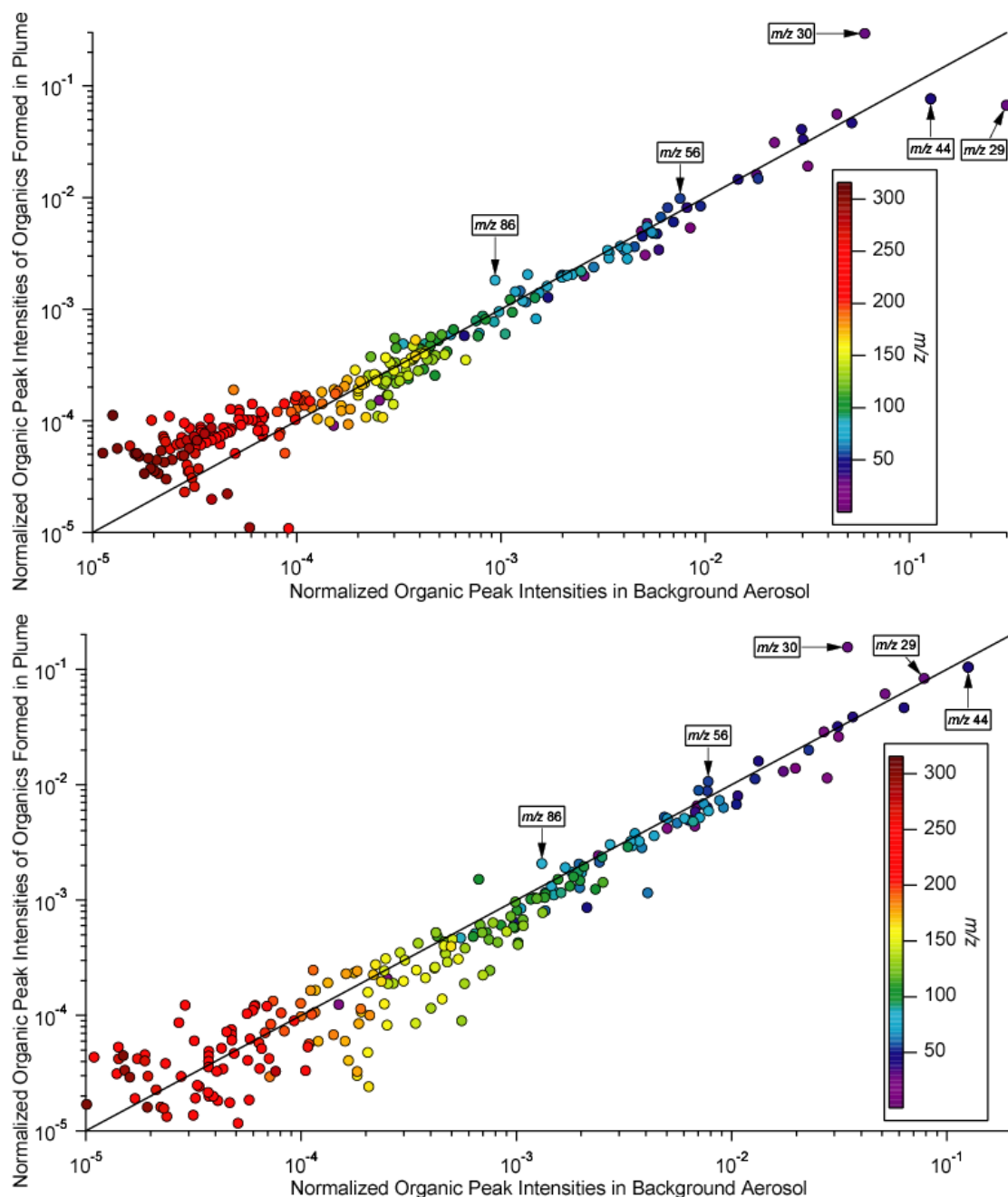


Fig. 4.11 A comparison of the plume organic mass spectra versus the background aerosol organic mass spectra for flights A (upper panel) and B (lower panel). All non-organic contributions to the mass spectra have been removed by fragmentation calculations described in Sect. 4.4.3.3. This means that the signal at m/z 30 represents a fragment of organics, including amines. The data on the y-axis were generated by taking the difference in the organic spectra in the plume and out of the plume. The organic aerosol appears to be very similar except this plot shows that there is an increase in peak intensities at m/z 30, 56, and 86, common amine peaks, in the plume. The peak intensity at m/z 44 (and 29 in flight A) are greater in the background aerosol spectra indicating increased oxidation out of the plume as compared to inside the plume.

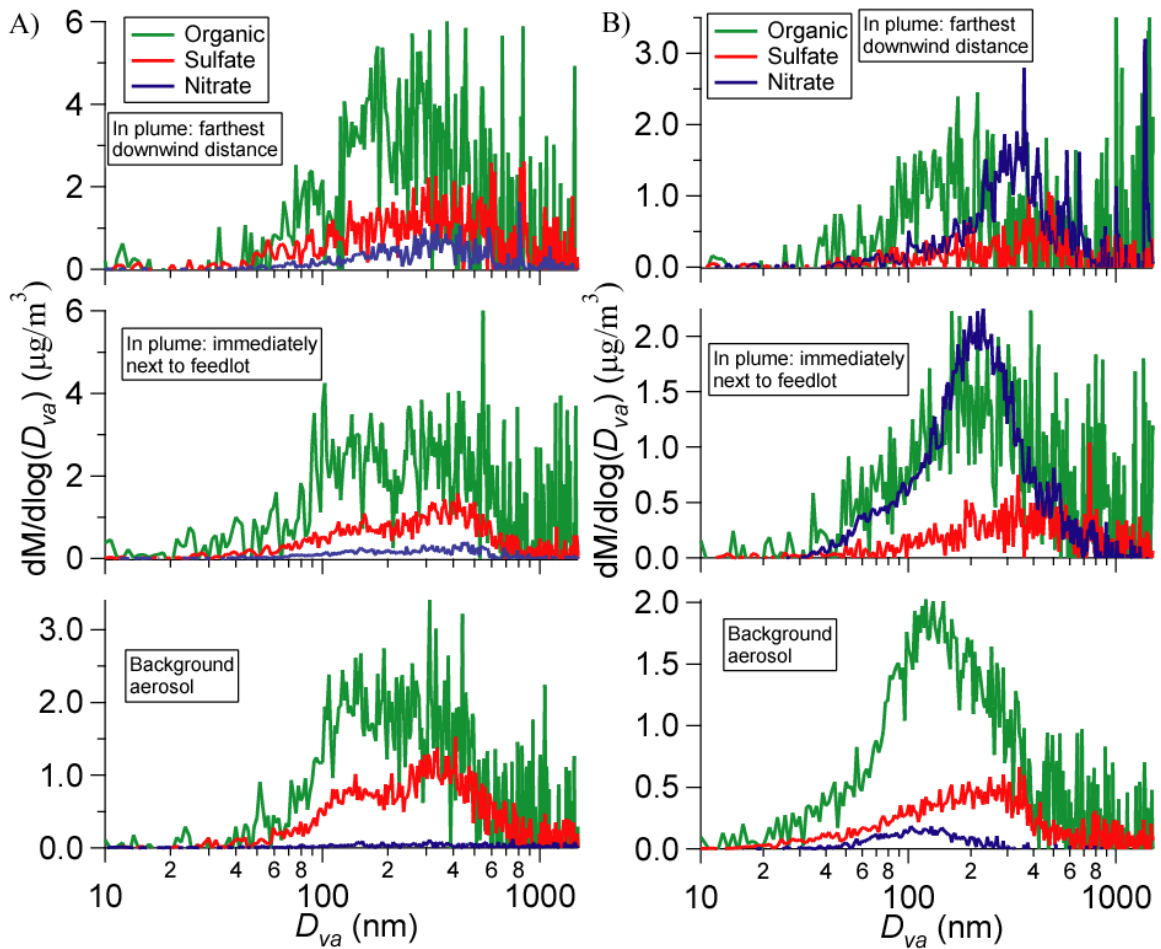


Fig. 4.12 Speciated size distributions as determined by the C-ToF-AMS for flights A (panel A) and B (panel B). The x-axis is the vacuum aerodynamic diameter. There is evidence of externally mixed aerosols, evident by the independent shifts of various species as a function of increasing plume age. This is clearest in flight B where nitrate is shown to grow in size with plume age with less growth for organics and no growth for sulfate.

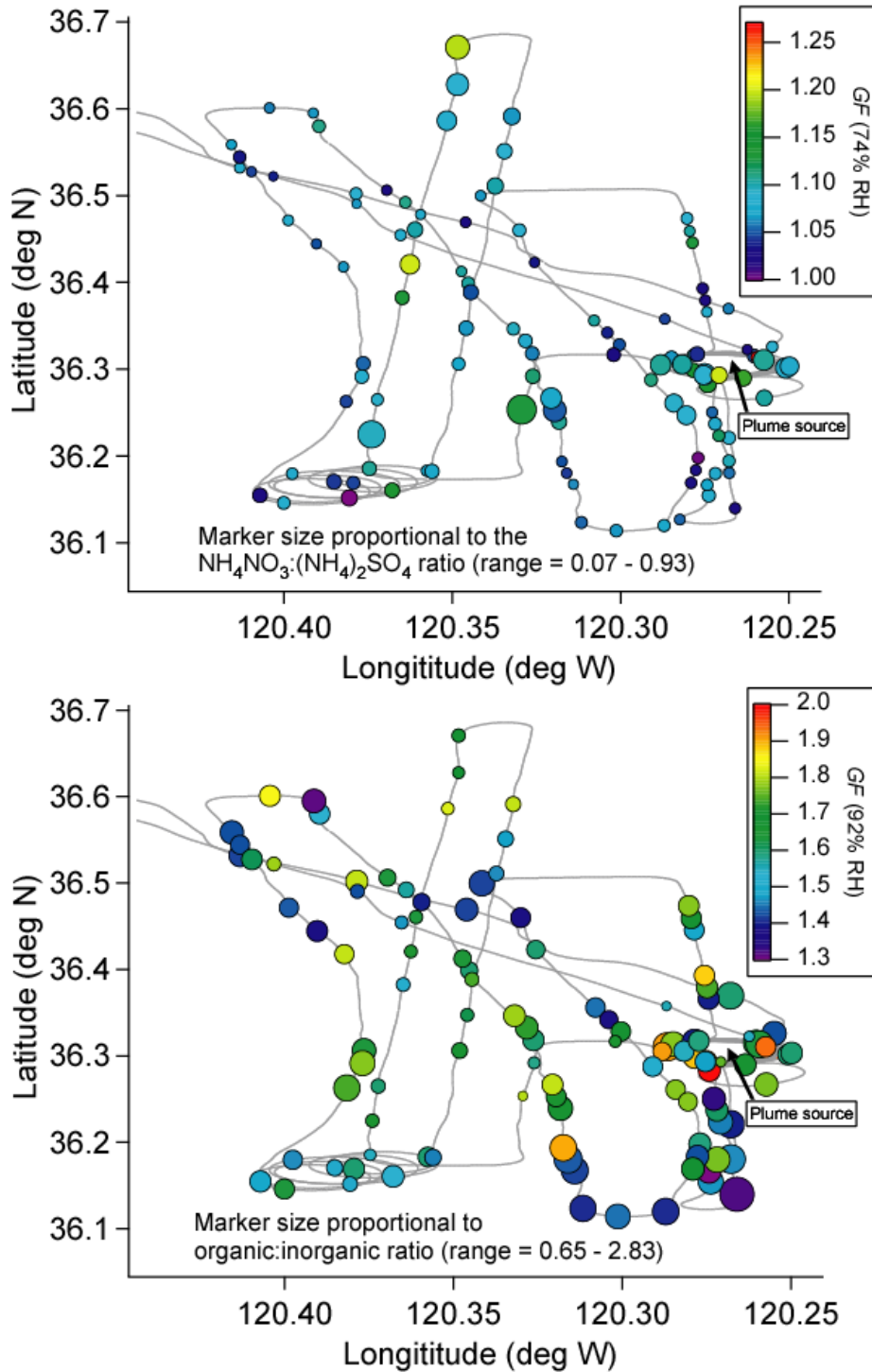


Fig. 4.13 Growth factor data from flight A at RHs of 74% (upper panel) and 92% (lower panel). The markers represent individual DASH-SP scans at dry diameters between 150 and 200 nm. Marker sizes in upper panel are proportional to the ammonium nitrate:ammonium sulfate ratio, while marker sizes in the lower panel are proportional to the organic:inorganic ratio (inorganic = ammonium sulfate + ammonium nitrate).

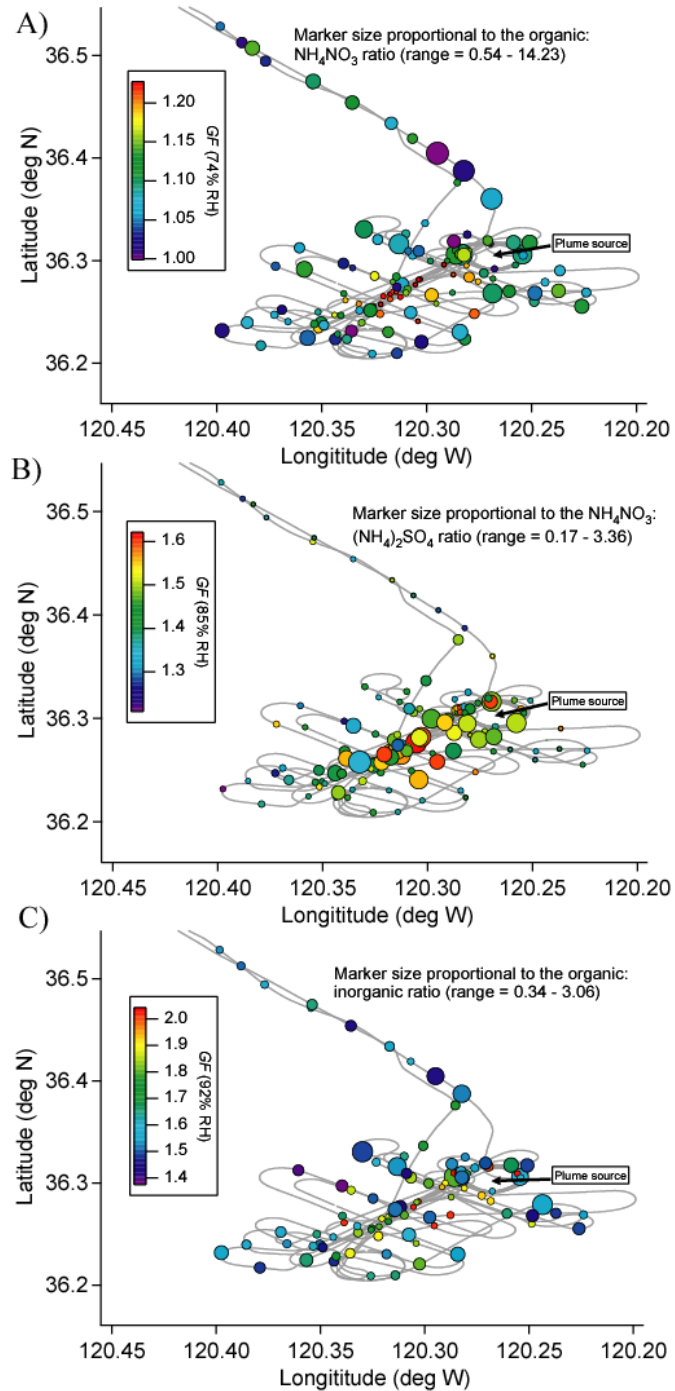


Fig. 4.14 Growth factor data from flight B at RHs of 74% (A), 85% (B) and 92% (C). The markers represent individual DASH-SP scans at dry diameters between 150 and 200 nm. A) marker sizes are proportional to the organic:ammonium nitrate ratio; B) marker sizes are proportional to the ammonium nitrate:ammonium sulfate ratio; C) marker sizes are proportional to the organic:inorganic ratio (inorganic = ammonium sulfate + ammonium nitrate).

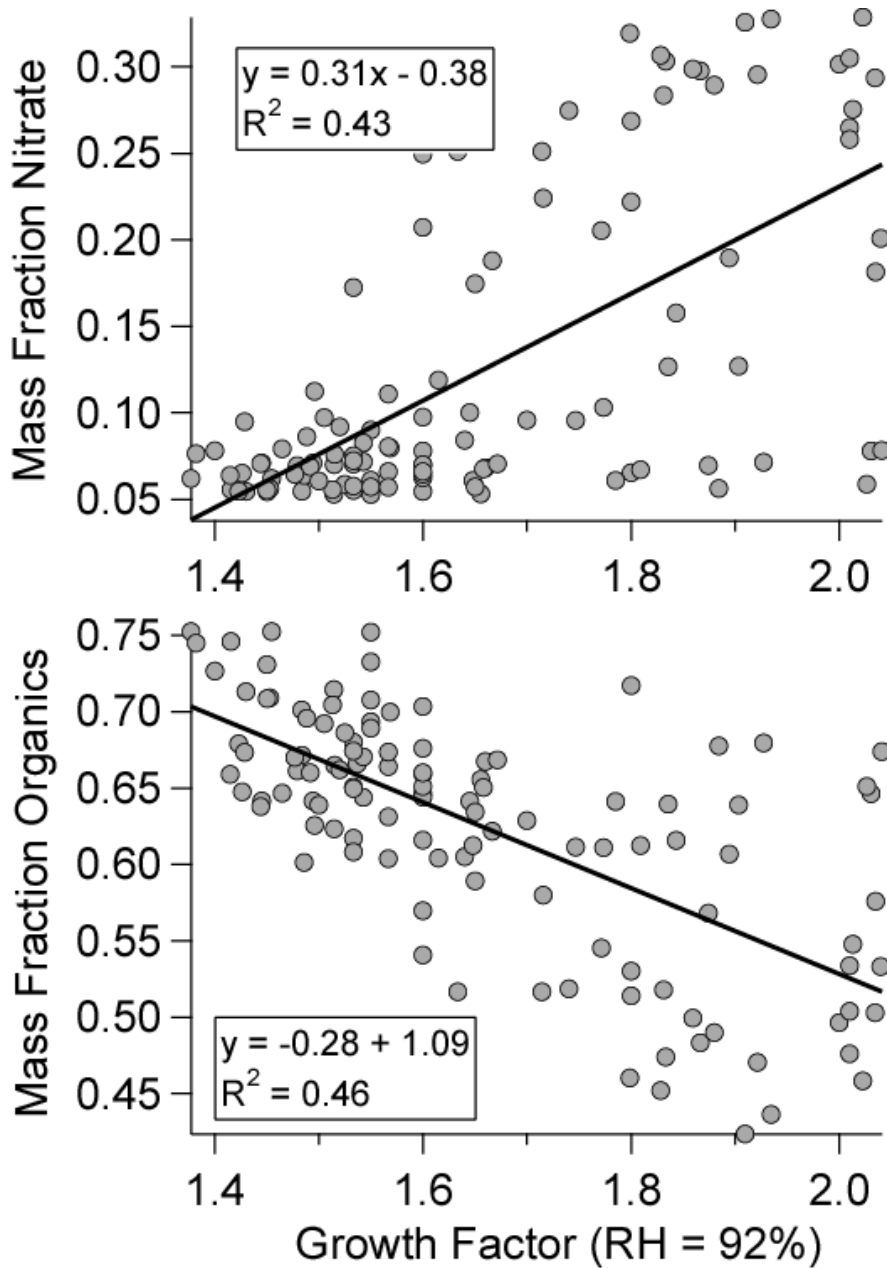


Fig. 4.15 Relationship between the hygroscopic growth factor at 92% RH and mass fractions of nitrate and organics during flight B. Less correlation exists between the subsaturated hygroscopic growth factors and the mass fractions of ammonium ($r^2 = 0.19$, slope = 0.07) and sulfate ($r^2 = 0.21$, slope = -0.10).

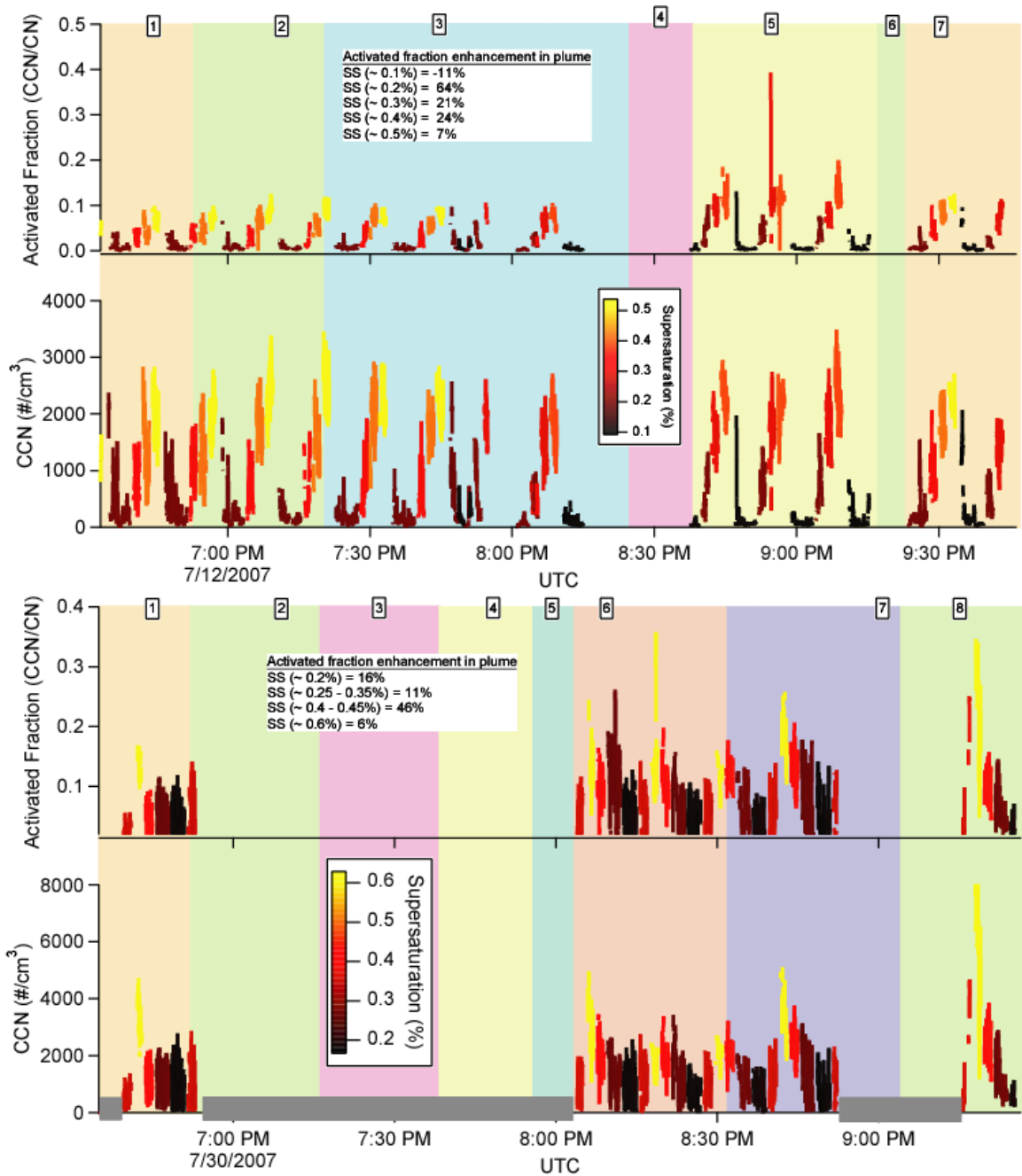


Fig. 4.16 Time series of activated fraction of aerosol (CCN/CN), and total CCN concentration during flights A (upper panel) and B (lower panel). Data points are color-coded with instrument supersaturation. The shaded gray boxes in the lower panel indicate portions of flight B when the CCNc was operating in an alternative mode and those data are not presented here.

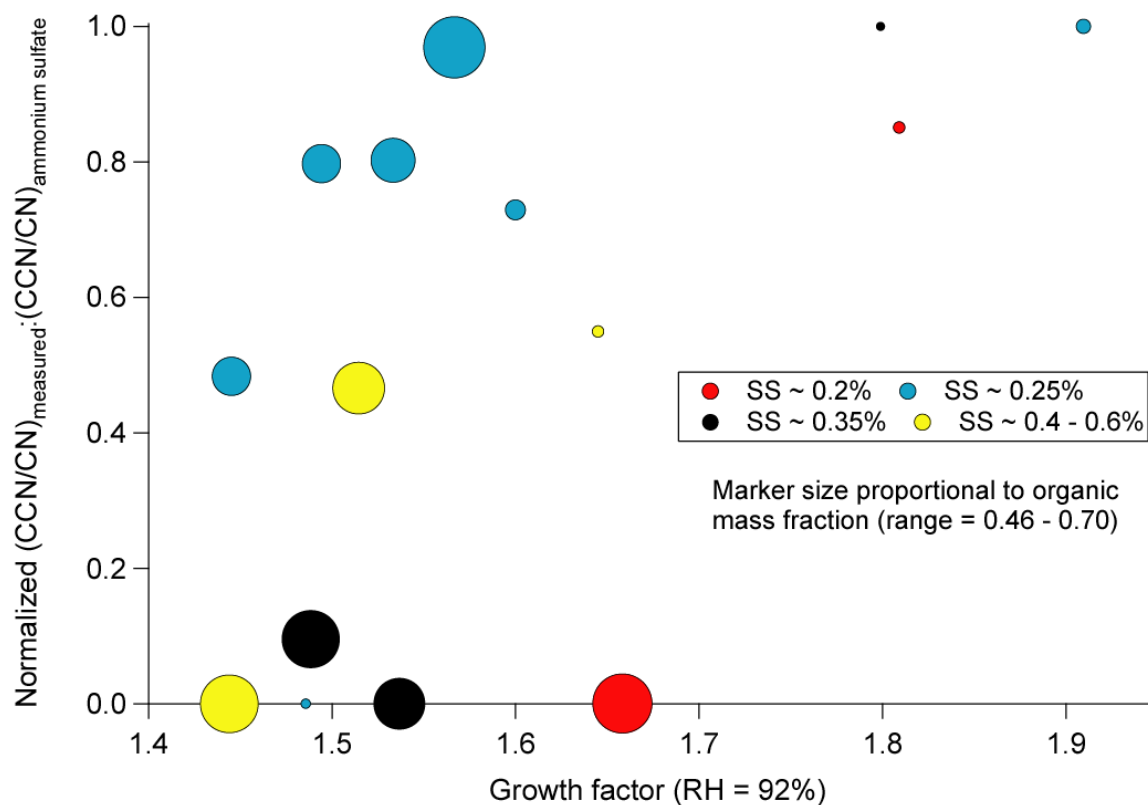


Fig. 4.17 Normalized CCN activation ratio, $(\text{CCN}/\text{CN})_{\text{measured}}:(\text{CCN}/\text{CN})_{\text{ammonium sulfate}}$, as a function of hygroscopic growth factors for flight B. The effects of size distribution and mixing state have been removed from the data and the calculated activation ratio to isolate the impact of composition on the relationship between water uptake in the sub- and supersaturated regimes (see Sect. 4.4.6.2).

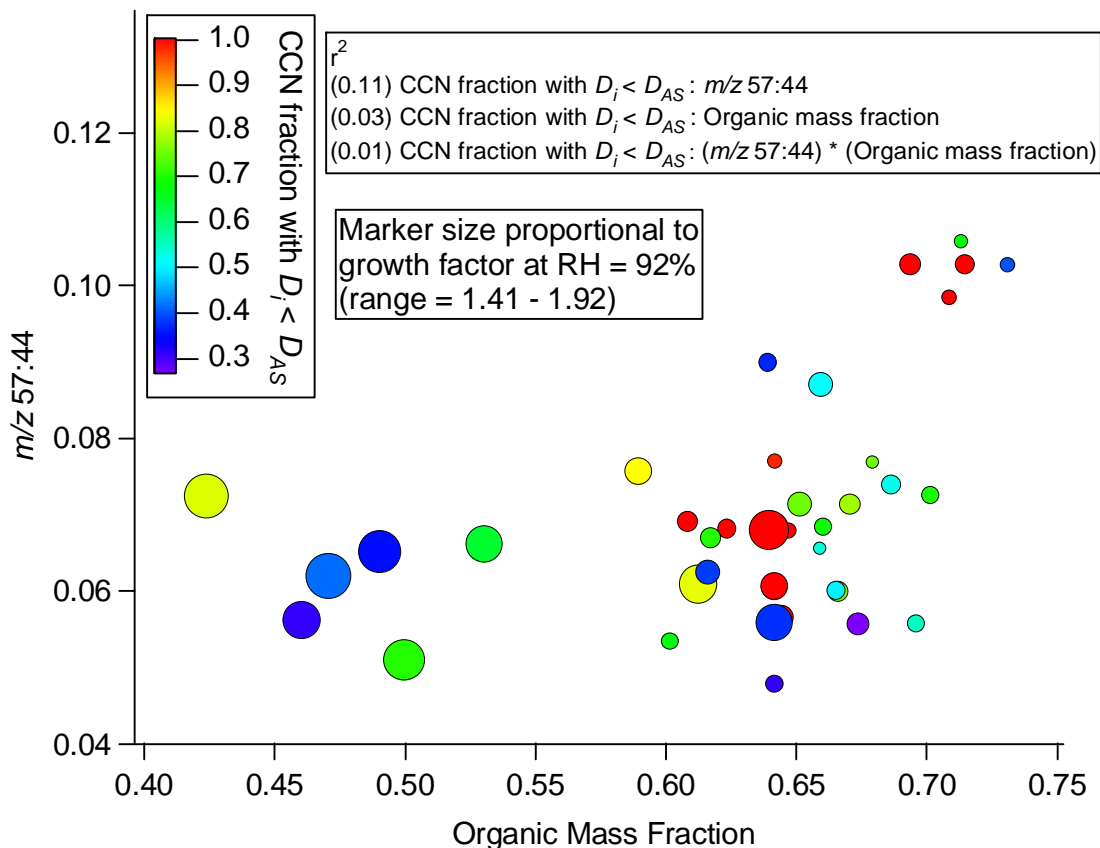


Fig. 4.18 The relationship between the m/z 57:44 ratio, the organic mass fraction, the CCN fraction with less droplet growth than ammonium sulfate ($D_i < D_{AS}$), and the hygroscopic growth factor at $RH = 92\%$. The CCN fraction with $D_i < D_{AS}$ is a qualitative measure of kinetic limitations to droplet growth. The majority of the markers representing the lowest values of $D_i < D_{AS}$ occur at m/z 57:44 < 0.07 , while most of the higher values of $D_i < D_{AS}$ coincide with the highest organic mass fractions (> 0.6). The highest growth factors at $RH = 92\%$ occur at the lowest organic mass fractions and m/z 57/44 ratios.

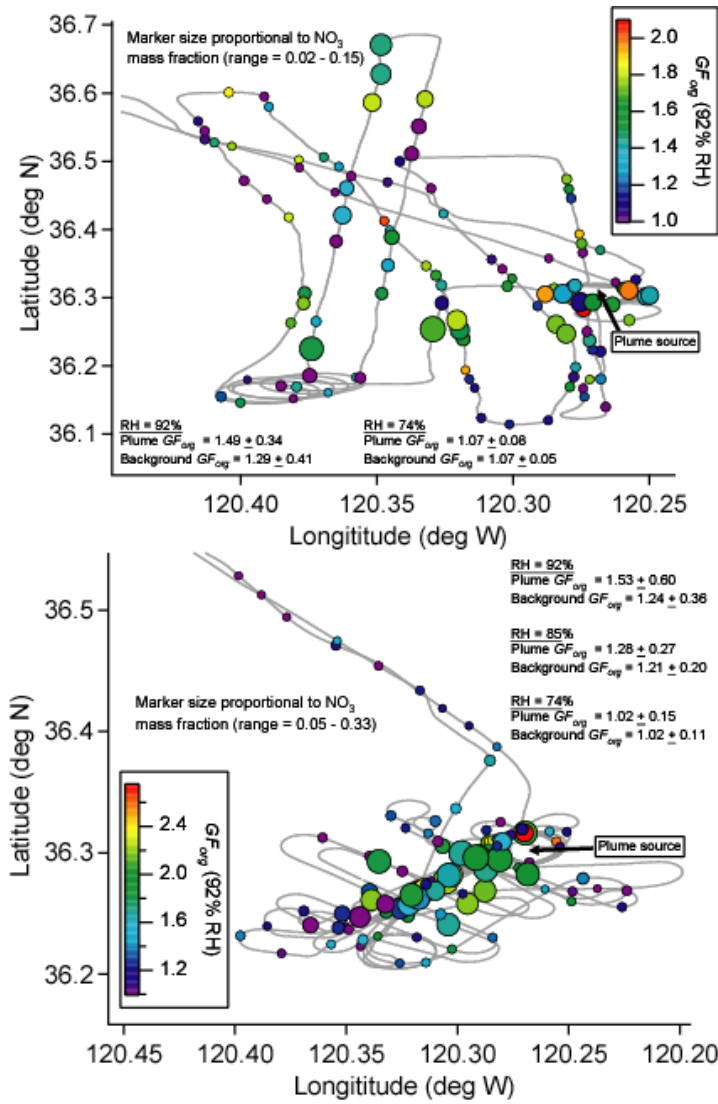


Fig. 4.19 Spatial distribution of the calculated organic growth factors, using the ZSR mixing rule, for flights A (upper panel) and B (lower panel). Marker sizes are proportional to the mass fraction of nitrate.

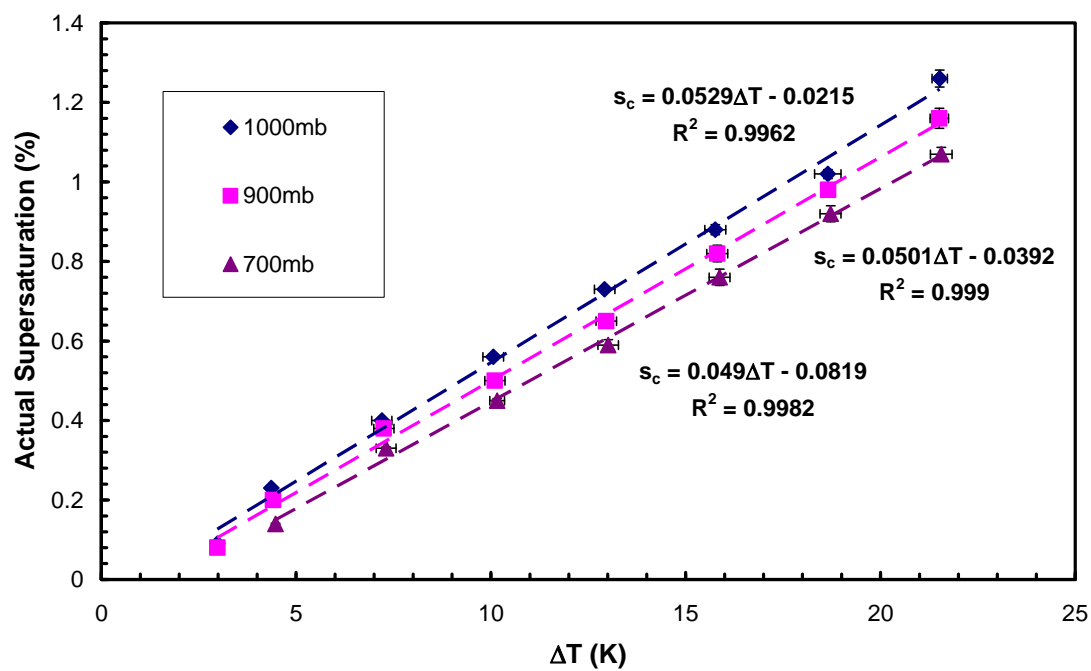


Fig. 4.20 Critical supersaturation versus delta T calibration for ammonium sulfate aerosol. Calibration was performed at 500 cm³/min at 700, 900, and 1000 mb.

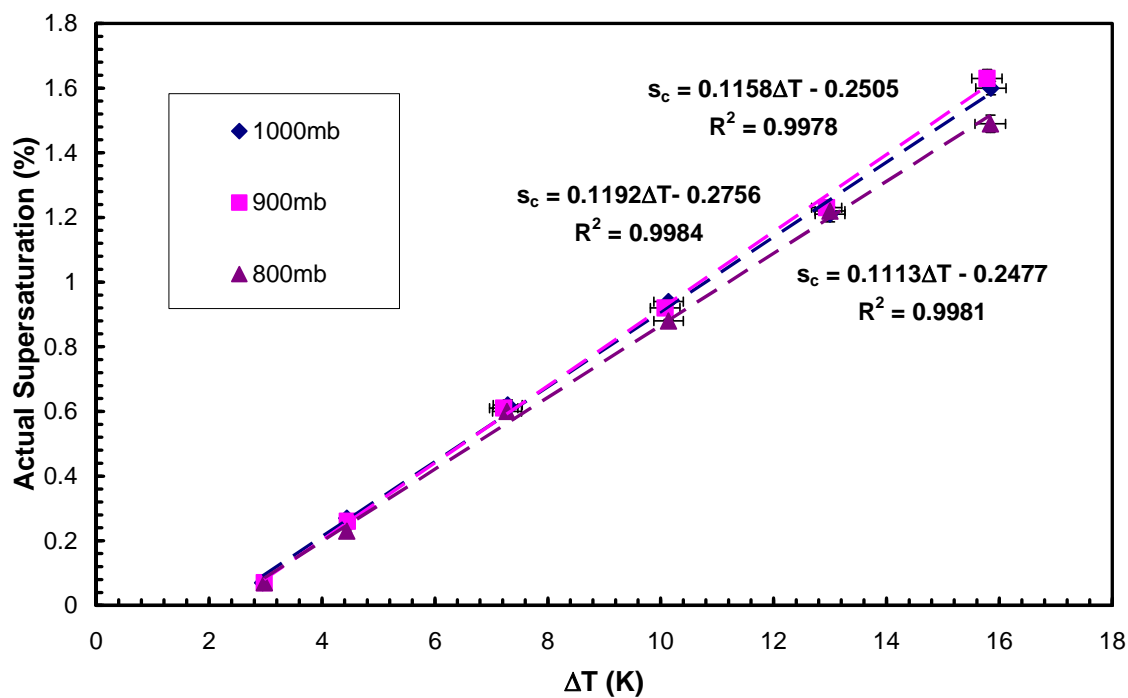


Fig. 4.21 Critical supersaturation versus delta T calibration for ammonium sulfate aerosol. Calibration was performed at 1000 cm³/min at 800, 900, and 1000 mb.

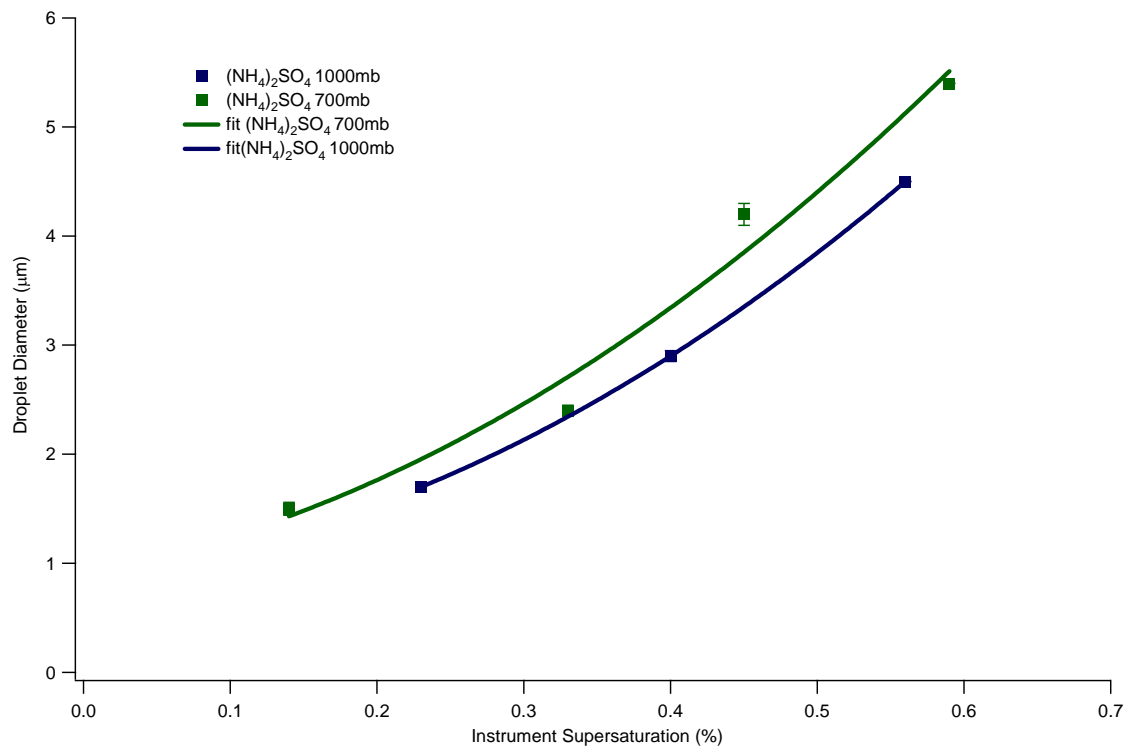


Fig. 4.22 Growth kinetics plots for ammonium sulfate aerosol. Calibration was performed at $500 \text{ cm}^3/\text{min}$ at 700 and 1000 mb.

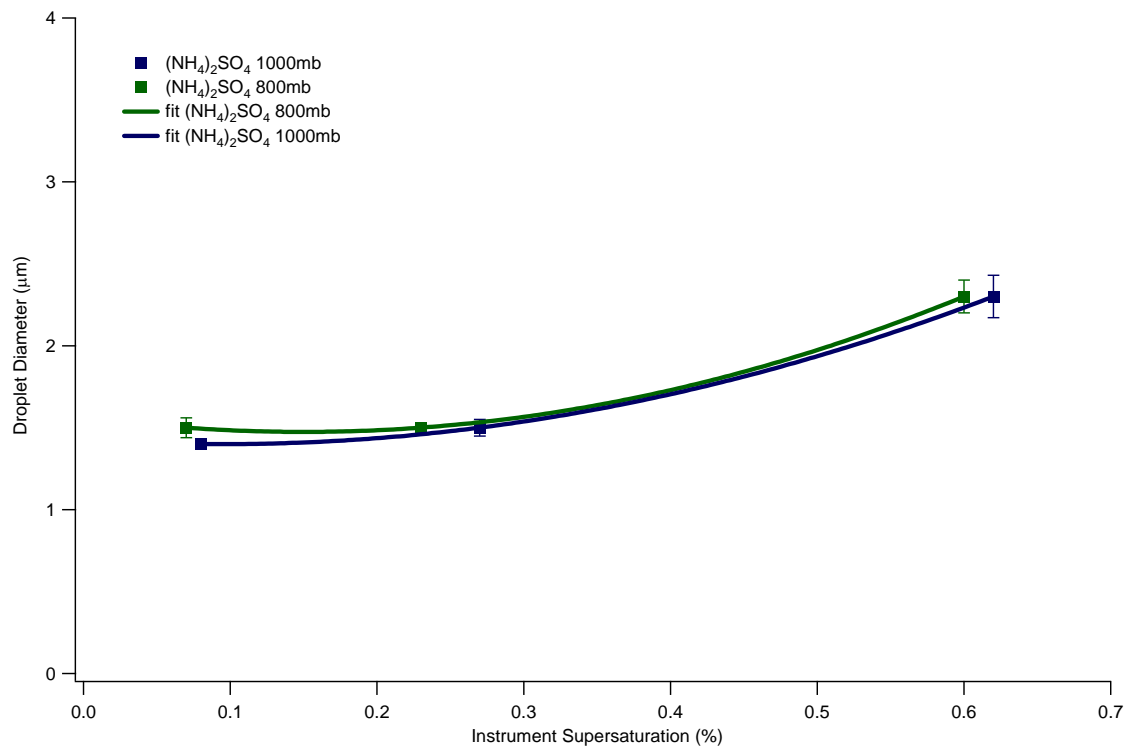


Fig. 4.23 Growth kinetics plots for ammonium sulfate aerosol. Calibration was performed at 1000 cm³/min at 800 and 1000 mb.

Chapter 5

Comprehensive Simultaneous Shipboard and Airborne Characterization of Exhaust from a Modern Container Ship at Sea

*This chapter is reproduced by permission from “Comprehensive simultaneous shipboard and airborne characterization of exhaust from a modern container ship at sea.” Shane M. Murphy, H. Agrawal, A. Sorooshian, L. T. Padró, H. Gates, S. Hersey, W.A. Welch, H. Jung, J. W. Miller, D.R. Cocker, A. Nenes, H. Jonsson, R.C. Flagan, J.H. Seinfeld, *Environmental Science and Technology*, Article ASAP, 2009. Copyright 2009 American Chemical Society

5.1 Abstract

We report the first joint shipboard and airborne study focused on the chemical composition and water-uptake behavior of particulate ship emissions. The study focuses on emissions from the main propulsion engine of a Post-Panamax class container ship cruising off the Central Coast of California and burning heavy fuel oil. Shipboard sampling included Micro-Orifice Uniform Deposit Impactors (MOUDI) with subsequent off-line analysis, whereas airborne measurements involved a number of real-time analyzers to characterize the plume aerosol, aged from a few seconds to over an hour. The mass ratio of particulate organic carbon to sulfate at the base of the ship stack was 0.23 ± 0.03 , and increased to 0.30 ± 0.01 in the airborne exhaust plume, with the additional organic mass in the airborne plume being concentrated largely in particles below 100 nm in diameter. The organic to sulfate mass ratio in the exhaust aerosol remained constant during the first hour of plume dilution into the marine boundary layer. The mass spectrum of the organic fraction of the exhaust aerosol strongly resembles that of emissions from other diesel sources and appears to be predominantly hydrocarbon-like organic (HOA) material. Background aerosol which, based on air mass back trajectories, probably consisted of aged ship emissions and marine aerosol, contained a lower organic mass fraction than the fresh plume and had a much more oxidized organic component. A volume-weighted mixing rule is able to accurately predict hygroscopic growth factors in the background aerosol but measured and calculated growth factors do not agree for aerosols in the ship exhaust plume. Calculated CCN concentrations, at supersaturations ranging from 0.1% to 0.33%, agree well with measurements in the ship-exhaust plume. Using size-resolved chemical composition instead of bulk sub-micron composition has

little effect on the predicted CCN concentrations because the cutoff diameter for CCN activation is larger than the diameter where the mass fraction of organic aerosol begins to increase significantly. The particle number emission factor estimated from this study is $1.3 \times 10^{16} \text{ (kg fuel)}^{-1}$, with less than one-tenth of the particles having diameters above 100 nm; 24% of particles (> 10 nm in diameter) activate into cloud droplets at 0.3% supersaturation.

5.2 Introduction

Ship exhaust is estimated to represent an appreciable fraction of global NO_x (21 Tg y^{-1}), SO_x (12 Tg y^{-1}), and hydrocarbon emissions (1.96 Tg y^{-1}) (1). Ship emissions are also thought to be a significant contributor to global particulate mass (PM, 1.67 Tg y^{-1}), though emission factors for PM remain highly uncertain (1-3). Particles emitted from ships impact climate through both direct and indirect effects and are often emitted close to populated coastlines where they impact air quality (2, 4, 5). In their 2003 study on the global impact of ship emissions, Corbett and Koehler (6) state that error in the estimated fuel consumption of the world fleet (based on estimates of the number, type, and activity level of vessels in different regions of the world) is the most important uncertainty for every type of ship emission except PM, for which the emission factor itself remains the dominant uncertainty. Relatively little data exist concerning the composition of particles emitted from ships and the ability of those particles to grow by hygroscopic water uptake and act as cloud condensation nuclei (1, 3, 7). While it has been established that fresh particulate emissions from ships consist of sulfuric acid, organics, and soot, estimates of the organic mass fraction vary widely (8-10). Undoubtedly, much of the variation in the particulate composition stems from the type of fuel used, but because heavy fuel oil

(HFO) represents over 80% of the fuel consumed by the world fleet, emissions from HFO clearly need to be characterized. Another source of variation in particulate emissions is ship type, though the majority of worldwide emissions are from large cargo or container vessels (6). Finally, engine type and load can significantly influence both particle number and composition, though the amount of time ships spend entering and exiting port with highly varying engine loads is a relatively small fraction of overall operating time.

Emission studies conducted on engine test beds offer obvious advantages in that engine load can be controlled, fuel characteristics are precisely known, and testing can be conducted in a stationary, stable environment (8, 11). While these test-bed studies provide important insight into the emission characteristics of different engines at various loads, they need to be evaluated against measured emissions from engines in actual usage at sea. To determine the relationship between test-bed results and in-situ emissions, groups have begun to measure emissions inside the stacks of vessels under sail (12, 13). Other groups have used airborne platforms to characterize particulate ship emissions in the marine atmosphere (3, 7, 11). However, when there is limited knowledge of the fuel being used or the operating conditions of the vessel, it is difficult to relate airborne emissions measurements to fuel consumption inventories. Corbett (14) summarized the gap in the current literature as follows, “By directly measuring what the engine emits at the stack with pollution chemistry ‘seen by the environment’ in the aging plume, we may improve large-scale inventories used in chemical transport models.”

We report here the first study with simultaneous in-stack and airborne measurements of emissions from a container ship. Shipboard measurements give detailed

gas and particle-phase emissions for a wide range of chemical species, while airborne measurements are focused on particulate number, mass, composition, hygroscopic growth, and CCN activity. We evaluate the relationship between shipboard and airborne measurements and explore how these findings impact the characterization of emissions from this important class of ships.

5.3 Methods

5.3.1 Container Ship

The ship, representative of a modern Post-Panamax class container ship (Panamax = maximum size allowed through the Panama Canal), was 347 m long, with a gross tonnage (GT) of 91,690 and a capacity of 8680 TEUs (Twenty-foot Equivalent Unit). The main propulsion engine (ME) of the vessel was a 2-stroke, slow-speed diesel engine (12k90MC, Build: Hitachi MAN B&W 12K90Mk mk 6 (1998)). The engine's rated power and speed are 54840 kW and 94 r/min with a maximum pressure at maximum continuous rating (MCR) of 141 bar. During the study, load was stable with ME running at 57% of maximum power, approximately 31.2 MW, and 81 revolutions per minute. The ME operated on heavy fuel oil (HFO); selected properties are in Table 5.1, and the ME exhaust included a heat recovery section after the on-board sampling section.

5.3.2 Shipboard Platform Measurements

A detailed description of the shipboard methods for sampling and analysis of gases and particulate matter (PM) is given in Section 5.8.1 of the Supporting Information and briefly described here. In-stack measurements conformed to the requirements of ISO 8178-1 (15). The sampling approach for PM and speciated hydrocarbons involved the

use of a partial flow dilution system with single venturi and is shown in Figure 5.12 and described in Agrawal et al. (13). While ISO 8178-1 allows a transfer line of 5 m, no transfer line was used in this study based on previous experience showing significant loss of particulate mass in the transfer line. Concentrations of CO₂ and NO_x were measured in both the raw exhaust gas and dilution tunnel using the exhaust gas analyzer (EGA). The dilution ratio in the dilution tunnel, determined from either CO₂ or NO_x concentrations, agreed within 5%, as specified in the reference method (15).

Emission measurement of different gases, PM_{2.5} (particulate matter of diameter < 2.5 μm) mass, size resolved PM composition, metals, ions, elemental and organic carbon, selected hydrocarbon species, including polycyclic aromatic hydrocarbons (PAHs), carbonyls, and n-alkanes, were performed off-line following standard methods (15-19). The SO₂ data are calculated from the sulfur level in the fuel as per ISO 8178-1 (15). Other PM measurements were made with: a MOUDI, a thermophoretic sampler with Transmission Electron Microscopy (TEM) grids (model 3320C-CF, SPI Inc.), and Dekati Mass Monitor (20). TEM grids were analyzed for non-organic elemental composition using EDS (Energy Dispersive X-Ray Spectroscopy).

5.3.3 Aircraft-Based Measurements

The Center for Interdisciplinary Remotely Piloted Aircraft Studies (CIRPAS) Twin Otter aircraft performed a series of passes through the exhaust plume of the container ship on July 16, 2007. The ship-plane rendezvous occurred in the Pacific Ocean 65 km west of the Central California Coast at 122° west longitude and 35° north latitude. The Twin Otter remained in the vicinity of the ship for roughly 2.5 h,

characterizing the aerosol properties within the plume and background air. Plume aerosol was measured at ages ranging from a few seconds to over an hour.

5.3.3.1 Aerosol Number and Volume

Aerosol number concentrations were measured by three independent condensation particle counters (CPC's), two TSI Model 3010 counters with a minimum detection diameter of 10 nm, a saturation threshold of 10^4 particles cm^{-3} , and one ultrafine condensation particle counter (TSI Model 3025) with a minimum detection diameter of 3 nm and a saturation threshold of 10^6 particles cm^{-3} . In the concentrated exhaust plume just behind the ship, all three CPC's were saturated; when this occurred, number concentration data were obtained from the differential mobility analyzer (DMA) ($D_p = 10 - 800$ nm) which is not subject to saturation until much higher concentrations because it classifies the aerosol before optical counting. However, the time resolution of the DMA is much slower (74 s) than the CPC's (1 s).

Aerosol volume was determined by the DMA and an external passive cavity aerosol spectrometer probe (0.1 – 3 μm) (PCASP, PMS Inc., modified by DMT Inc.). The response of the PCASP probe to different diameter particles was calibrated using polystyrene latex spheres (refractive index = 1.58) and this calibration was used for all data analysis. While the PCASP cannot measure particles below 100 nm, it offers the advantage of 1 s time resolution. The PCASP nominally operates at ambient relative humidity while during this flight, because of problems with the Nafion drier, the DMA was operated at relative humidities between 40% and 50%

5.3.3.2 Aerosol Mass, Chemistry, and Absorption

Sub-micron aerosol mass and size-resolved chemical composition were measured by an Aerodyne compact Time of Flight Aerosol Mass Spectrometer (C-ToF-AMS). Sub-micron water-soluble ions were measured by a Particle Into Liquid Sampler – Ion Chromatograph (PILS-IC, Brechtel Mfg. Inc.). Aerosol optical absorption was measured by a three-wavelength Particle Soot Absorption Photometer (PSAP, Radiance Research).

Details concerning the C-ToF-AMS can be found in Drewnick et al. (21). For this airborne deployment the C-ToF-AMS was fitted with a pressure-controlled inlet (22), a 3.5 % chopper, the vaporizer was operated at 550 °C, and ion extraction occurred at a rate of ~ 60 kHz. Detection limits for the instrument, calculated as three times the standard deviation of the noise for filtered air, are $< 0.05 \mu\text{g m}^{-3}$ for all species measured, though, in practice, detection is limited by counting statistics at low aerosol loadings. One important issue concerning C-ToF-AMS data is the collection efficiency of particles within the instrument (23). In this study, all C-ToF-AMS mass loadings were multiplied by a factor of 2 (collection efficiency = 0.5) to attain agreement between the sulfate measurements of the C-ToF-AMS and the PILS-IC during periods where there were no rapid fluctuations in particulate mass loading. A collection efficiency of 0.5 has been observed in numerous other field studies with the AMS (24) and in this study it gives excellent agreement with both the PILS sulfate measurement and DMA derived mass loadings, as described in Section 3.3.

The PILS-IC is described in Sorooshian et al. (25) with specifics related to airborne operation given in Sorooshian et al. (26). For this study, instrument uncertainty was established as $\pm 7\%$. Collected aerosol in solution was delivered to a rotating

carousel containing 72 vials, each of which contains material representing a period of ~ 5 min of flight, or alternatively, a distance of 15 km in flight (aircraft speed ~ 50 m/s).

The design of the three wavelength PSAP used in this study is described in Virkkula et al. (27). The PSAP measures cumulative light absorption at 467, 530 and 660 nm as particles are collected onto a filter. All absorption measurements presented in this paper have been corrected for scatter using the methods described in Virkkula et al. (27).

5.3.3.3 Aerosol Hygroscopic Growth and Cloud Condensation Nuclei Activity

Subsaturated aerosol water uptake was measured by a recently developed instrument, the Differential Aerosol Sizing and Hygroscopicity Spectrometer Probe (DASH-SP; Brechtel Mfg Inc.) while activation of cloud condensation nuclei (CCN) was measured by a flow thermal gradient cloud condensation nuclei counter (CCNc, Droplet Measurement Technologies Inc.) The DASH-SP is described in detail in Sorooshian et al. (28). During this study, the DASH-SP provided simultaneous measurements of growth factor at different relative humidities (RH) for dry DMA-selected particle diameters between $D_p = 150 - 200$ nm; the time resolution for this size range inside and outside of the plume was 1 - 10 s and 10 - 30 s, respectively. One humidifier was operated dry (RH < 8%), and the other three were at RH settings of 74%, 85%, and 92%. The uncertainty associated with growth factor measurements is $\pm 4.5\%$, and the uncertainty in the RH measurement is $\pm 1.5\%$. The CCNc is described in detail in Roberts and Nenes (29) and Lance et al. (30). For this study, the instrument was operated at supersaturations between 0.1% and 0.4%.

5.3.4 Theory for Predicting Subsaturated Hygroscopic Growth

Owing to its simplicity and frequent application, an assumption of independent and additive water uptake by each individual chemical component of a particle was used to predict hygroscopic growth in this study with composition measurements obtained from the C-ToF-AMS (31, 32):

$$GF_{mixed}(a_w) = \left(\sum_i \varepsilon_i GF_i(a_w)^3 \right)^{\frac{1}{3}} \quad (1)$$

where GF_{mixed} is the hygroscopic growth factor of the mixed particle, GF_i is the hygroscopic growth factor of pure compound i , a_w is the activity coefficient of water, and ε_i is the volume fraction of pure compound i in the dry particle. In applying eq 1 we set $a_w = RH$ (33). Growth factors for the pure inorganic components were obtained from the Aerosol Inorganics Model (34, 35). In the DASH-SP, particles are processed at an RH very near zero before being re-humidified. Since ammonium sulfate does not deliquesce until 79% (33), it is assigned a growth factor of unity at 74% RH. Because C-ToF-AMS results indicate a hydrocarbon-like and presumably hydrophobic organic aerosol component in the ship-exhaust plume, the growth factor for organic material is assumed to be unity at all RH settings.

5.3.5 Theory for Cloud Condensation Nuclei (CCN) Closure

“CCN closure,” that is, comparison of CCN predictions based on knowledge of particle size and composition with direct measurements of CCN concentrations, is an evaluation of the extent to which CCN behavior can be predicted theoretically using Köhler theory (36). CCN closure calculations within the exhaust plume of the ship were

performed at supersaturations ranging from 0.1% to 0.33%. Because the DMA was operated at relative humidities ranging from 40%-50% during the study, measured aerosol particles contained significant amounts of water, especially in the ship plume where sulfuric acid was the most abundant species. Because prediction of CCN concentrations requires knowledge of the dry size and composition of particles, an algorithm was developed to calculate dry size distributions from the measured humid distributions. First, size-resolved C-ToF-AMS data (averaged over the 74 s scan time of the DMA) were shifted in diameter space until they aligned with the volume distribution from the DMA. Once the mass and volume distributions were aligned, the non-refractory particle composition of each DMA diameter bin was determined from the C-ToF-AMS data (see Section 3.3 for a discussion of why the dry composition from the C-ToF-AMS, measured versus vacuum aerodynamic diameter, can be aligned with the humid volume distribution from the DMA, measured versus electrical mobility diameter). Next, with knowledge of the composition of each DMA diameter bin, the ISORROPIA program (37) was used to determine the amount of water that the particles in each diameter bin contain at thermodynamic equilibrium at the operating relative humidity of the DMA. Finally the particle volume without water was calculated (assuming volume additivity), particles were rebinned into new smaller size bins, and the average composition of the new diameter bins was calculated. Following this procedure, particle diameters within the ship exhaust plume were found to be between 15 to 28% smaller when dry than when measured by the DMA at $\sim 45\%$ RH. The percentage decrease in diameter was almost exclusively determined by the mass fraction of organic (assumed insoluble) present in a given DMA diameter bin. Data from the CCNc were also averaged to match the time

resolution of the scanning DMA meaning one closure calculation can be performed every 74 s except when the CCNc instrument is switching between supersaturations.

Based on C-ToF-AMS and DASH-SP results to be discussed, the aerosol was treated as an internal mixture when predicting CCN concentrations. Because the C-ToF-AMS cannot measure refractory material, black carbon and ash are assumed to be negligible in this closure study (impacts of this assumption are discussed in Section 4.4). Two chemical composition scenarios were considered in the closure: a) bulk composition, which assumes all particles have the same composition, and, b) size-resolved composition, which assigns a specific composition to each particle size. In each of these compositional scenarios, the measured sulfate molar ratio, $SR = [\text{NH}_4^+]/[\text{SO}_4^{2-}]$, was used to estimate the composition of the inorganic fraction. When $SR \leq 1$, the sulfate is assumed to be a mixture of NH_4HSO_4 and H_2SO_4 , when $1 < SR < 2$, the sulfate is assumed to be a mixture of NH_4HSO_4 and $(\text{NH}_4)_2\text{SO}_4$, and when $SR \geq 2$, the sulfate is considered to be solely $(\text{NH}_4)_2\text{SO}_4$. In the exhaust plume, the sulfate fraction consisted mainly of H_2SO_4 . Because ammonium levels were very low in the ship-exhaust plume ($SR \sim 0.1$) the size-resolved ammonium measurements from the C-ToF-AMS were too noisy to be used in CCN closure calculations. Instead, the mass ratio of ammonium to sulfate from the bulk composition was assumed at all sizes. Particles were assumed to have the surface tension of water and organics were treated as insoluble.

The effective van't Hoff factor, v_s (which includes an estimate of the osmotic coefficient), is assumed to be 2.5 for ammonium sulfate, obtained from Pitzer activity coefficients (38, 39) for ammonium sulfate CCN with critical supersaturation between 0.2 and 0.6%. Effective van't Hoff factors for sulfuric acid and ammonium bisulfate are

assumed to be 2 and 2.5 respectively (38-40). The critical supersaturation, s_c , for each particle with dry diameter d , is calculated from Köhler theory (33),

$$s_c = \left[\frac{256}{27} \left(\frac{M_w \sigma}{RT \rho_w} \right)^3 \left(\frac{M_s}{\rho_s} \right) \left(\frac{\rho_w}{M_w} \right) \frac{d^3}{\varepsilon_s \nu_s} \right]^{1/2} \quad (2)$$

where R is the universal gas constant, T is the ambient temperature, σ is the surface tension of the CCN at the point of activation, M_s is the molar mass of the solute, and M_w and ρ_w are the molar mass and density of water, respectively. The volume fraction of solute, ε_s , can be calculated as a function of the mass fraction of solute, m_s , and its density, ρ_s ,

$$\varepsilon_s = \frac{\frac{m_s}{\rho_s}}{\frac{m_s}{\rho_s} + \frac{1 - m_s}{\rho_i}} \quad (3)$$

where ρ_i is the density of the organic (assumed to be 1.6 g cm^{-3} , as discussed subsequently). A particle is counted as a CCN when its calculated s_c is less than or equal to the supersaturation of the CCNc. Predicted and measured CCN are then compared to assess closure.

5.4 Results

5.4.1 Flight Tracks and Meteorology

Figure 5.1 is a photo taken from the Twin Otter aircraft during the study; the plume was visible to the naked eye for a considerable distance downwind of the ship. There was a steady $10 - 15 \text{ m s}^{-1}$ wind from 311° NW which was blowing at a 10° angle

to the ship's path, as can be seen by the different paths of the exhaust plume and ship wake in Figure 5.1. The flight track for the CIRPAS Twin Otter is shown in Figure 5.2. Marker size is proportional to sulfate concentration and indicates the relative dilution of the exhaust plume being emitted from the ship. Plume age was estimated from a simple calculation based on the distance between the ship and the aircraft at the time of measurement, knowledge of the ship's velocity (11.3 m s^{-1}) and heading (322° NW), and the average wind speed (11.4 m s^{-1}) and direction (311° NW) during the period between when the exhaust was emitted from the ship and measurement by the aircraft.

The marine boundary layer was well mixed during the 2.5 h period that the Twin Otter probed the ship plume with a temperature of $14.3 \pm 0.4 \text{ }^\circ\text{C}$ ($\theta = 287.9 \pm 0.1$) and a relative humidity of 90-98%. Vertical profiles (Figure 5.13) show an abrupt increase in potential temperature and decrease in relative humidity at approximately 200 m, which is assumed to be the top of the marine boundary layer. Three-day Hysplit back trajectories (Figure 5.14) indicate that the air mass present during the study originated in the Pacific Ocean and that there was no direct continental or urban influence on it during the previous 3 days. There is little variation in the back trajectories with altitude, giving further confidence that the measured air was not contaminated by continental outflow (41).

Two different flight strategies were used. In the first half of the flight, four direct approaches were made toward the ship, flying in what was estimated to be the center of the plume. Each approach was initiated at a point that was as far from the ship as possible but where the plume was still clearly distinguishable from background aerosol. In these approaches down the ship plume, it was possible to obtain number, volume, and

mass distributions and, importantly, to accurately measure the chemical composition of the ship-exhaust aerosol in a region with very high signal to noise. Because negligible differences were observed in any of the measured variables between the four direct approaches in the plume, generally we present data only from the first approach, in which the plume was detected at the farthest distance from the ship. The second half of the flight consisted of a number of plume transects made at progressively farther distances from the ship and at altitudes between 30 and 200 m. In this part of the flight the crosswind and vertical structure of the plume and particle aging at longer time scales were examined.

5.4.2 In-Stack Composition

Table 5.2 gives emission factors for all of the gas-phase and mixed (gas and particle) phase species measured from the ship's stack. The data represent the average of triplicate measurements made during the period when the aircraft was probing the exhaust plume; the values are similar to those reported by the engine manufacturer on this vessel. In addition to CO₂, NO_x, and SO₂, a wide array of volatile organic compounds were measured, with naphthalene, formaldehyde, acetaldehyde, and acetone being the most abundant.

Table 5.3 gives the average in-stack emission factors for particulate-phase species. While sulfate is the dominant emission by mass, there is a significant fraction of organic carbon. The cumulative masses of hydrated sulfate, organic carbon, elemental carbon, and estimated ash is about 20% less than the measured particulate mass. The lack of mass closure is most likely the result of uncertainty in the number of water

molecules associated with each sulfate molecule. A ratio of 6.5 H₂O molecules to a H₂SO₄ molecule was used because it represents the lowest energy state for a sulfate-water complex (12, 13). Another reason for poor mass closure is that the organic carbon (OC) has not been converted to organic mass (OM). While this would improve closure, it may not be justified given that previous filter-based measurements of diesel exhaust, where denuders were used to remove gas-phase organics, have shown an overestimation of OC mass of approximately 30% caused by adsorption of gas-phase organics onto the filter (42). Figure 5.3 shows size-resolved chemical composition measurements of particulate matter within the ship's stack obtained using a Micro-Orifice Uniform Deposit Impactor (MOUDI, described in Section 5.8.1.4 in the Supporting Information). The mass ratio of total carbon to hydrated sulfate (H₂SO₄ + 6.5 H₂O) remains relatively constant with size at 0.12 ± 0.02 , but the fraction of unknown mass is much higher at small particle sizes (note that there was too little PM present in size bins above 0.32 microns to exceed the detection limit for sulfate measurement and total PM cannot be measured for the smallest size bin as described in Section 5.8.1.4 of the Supporting Information).

Figure 5.4 shows a TEM image from the in-stack thermophoretic sampler. Two populations of nanoparticles are observed; one population ranging from 5 to 8 nm and the other ranging from 30 to 100 nm. The 5 to 8 nm nanoparticles outnumber the larger nanoparticles, a finding that is consistent with airborne measurements with an ultrafine CPC, discussed subsequently, that show significant number of particles between 3 and 10 nm. EDS analysis shows distinctive peaks of sulfur and vanadium from both populations of particles.

5.4.3 Particle Number, Volume, and Mass in the Airborne Exhaust Plume

Figure 5.5 shows particle number concentrations during a series of airborne transects made at progressively farther distances from the ship. Data from the three different CPCs and the PCASP are shown. During the first two transects all three CPCs were saturated, consistent with a DMA-measured concentration of 7.8×10^5 particles cm^{-3} near the ship. The relatively low particle number concentrations reported by the PCASP indicate that the vast majority of particles were less than 100 nm in size. On the third transect, the number concentrations recorded by the ultrafine TSI 3025 CPC dropped below the instrument saturation level of 10^5 particles cm^{-3} . The particle number concentration in the center of the plume during all of the transects exceeded 10^4 cm^{-3} , a level at which the TSI 3010 data are unreliable (7.4 % coincidence at 10^4 particles cm^{-3}). On the edges of the plume transects, the ultrafine TSI 3025 detected much higher loadings of particles than either TSI 3010, indicating the presence of significant numbers of particles between 3 nm and 10 nm (the cutoff points for the TSI 3025 and 3010 CPCs respectively). The ultrafine particles persist even at the longest plume age observed of 62 min.

Figure 5.6 shows time series from the C-ToF-AMS, PILS, PCASP and DMA during the first in-plume approach to the ship. Background aerosol, at loadings typical for marine air in this region, is observed until the plume is first encountered at 21:32 UTC. Following plume identification, the aircraft flew in the plume towards the ship until reaching it at 21:49. The particle volumes measured by the PCASP were much lower than those of the other instruments, indicating that not only the majority of the

particle number distribution, but also the majority of the particulate volume and mass distributions were below a diameter of 100 nm.

In Figure 5.6 and all subsequent figures, the mass loadings shown for the C-ToF-AMS have been multiplied by a factor of 2 to correct for particle bounce off the instrument's vaporizer (see Section 2.3.2). The maximum sulfate loadings determined by the C-ToF-AMS inside the exhaust plume are significantly higher than those determined by the PILS, presumably the result of the longer, 5 min, averaging time for a PILS measurement. To confirm that the higher loadings observed in the C-ToF-AMS were not caused by an increase in collection efficiency related to the high concentrations of sulfuric acid in the exhaust plume (24), C-ToF-AMS results are compared with measurements from the DMA, which has enhanced time resolution (74 s scans) relative to the PILS. Comparing the volume measured by the DMA to the C-ToF-AMS mass measurement requires an estimate of the aerosol density. The C-ToF-AMS measures particle vacuum aerodynamic diameter (D_{va}) while the DMA measures electrical mobility diameter (D_m) allowing determination of particle density (ρ_p) (43). If one assumes that the aerosol consists of an internal mixture of spherical particles, the relationship between the two diameters is $\rho_p = (D_{va} / D_m) \rho_o$, where ρ_o is unit density (1 g cm^{-3}).

Figure 5.7 shows the chemically-resolved mass distribution of the in-plume aerosol measured by the C-ToF-AMS along with the number and volume distributions from the DMA. While there is a higher fraction of organic matter in the smaller particles, an assumption of internal mixing appears reasonable in determining an average particle density. Based on the diameter offset between the mass distribution (plotted vs. D_{va}) and

the volume distribution (plotted vs. D_p), the average in-plume particle density is calculated to be 1.4 g cm^{-3} .

Because the DMA was run at relative humidities between 40% and 50%, this represents a wet particle density. It may seem inconsistent to use C-ToF-AMS data where particles are essentially dry (a small amount of water is retained by sulfuric acid in the C-ToF-AMS) and DMA data where they are wet. However, this is reasonable because of the fortuitous fact that the vacuum aerodynamic diameter of particles composed of sulfuric acid and hydrophobic organic remains virtually unchanged as the particle is dried from 50% to 0% RH. This is because the reduction in size caused by the loss of water is almost exactly compensated for by the increase in density. Using the wet particle density of 1.4 g cm^{-3} , mass loadings can be derived from the DMA volume data.

When total particulate mass measured by the C-ToF-AMS is plotted versus the DMA volume multiplied by a wet density of 1.4 g cm^{-3} , the resulting loadings agree within $\pm 10\%$ throughout the plume, except for the point nearest the ship where sufficient time did not exist to complete a full DMA scan. Even at this last point where the highest loading was observed, the two instruments agree to within 20%, with the C-ToF-AMS measuring $470 \text{ } \mu\text{g m}^{-3}$ and the DMA, $380 \text{ } \mu\text{g m}^{-3}$. The extent of agreement between the mass measured by the PILS, the C-ToF-AMS, and the DMA-derived mass gives confidence that none of these instruments was subject to obvious saturation issues and that the collection efficiency of the AMS remained constant throughout the flight.

5.4.4 Airborne Particulate Composition

Table 5.4 gives the mass fractions of organic, ammonium, sulfate, and nitrate in the particles directly behind the ship and during successive downwind transects of the exhaust plume. Also given are the contributions of m/z 44 (CO_2^+ , higher fractions indicate more oxidation) and 57 (C_4H_9^+ , higher fraction indicate less oxidation) (44) to the organic mass, the ammonium-to-sulfate molar ratio, and the fraction of the organic mass (measured by the C-ToF-AMS) accounted for by oxalate and other organic acids (measured by the PILS). Organic acid concentrations in the final transect represent primarily background aerosol because the plume transect itself lasted for a few seconds while a PILS vial represents average particle concentrations for a five-minute period. Measurements from the PSAP instrument of aerosol light absorption are an indirect measure of particulate black carbon concentration.

Organics comprise 31% of the aerosol mass immediately aft of the ship. This fraction does not change significantly with age, remaining at 28% after the plume has aged for over an hour. The non-organic aerosol mass appears to be almost entirely sulfuric acid, given the very low mass fractions of either ammonium or nitrate within the plume. The low mass fraction of organic acids in the plume and the large contribution of m/z 57 relative to m/z 44 indicate that the organic is not well oxidized or readily water soluble (45, 46). The estimated O:C atomic ratio for the plume organic aerosol is 0.20 versus 0.74 for the background aerosol (O:C estimates based on eq 4 and discussed in Section 4.1) (47). Figure 5.8 shows aerosol mass spectra taken in the fresh ship exhaust, in the exhaust plume after it had aged for 62 min, and in the background marine boundary layer. Also shown in Figure 5.8 is a reference Aerodyne AMS mass spectrum from the exhaust of a diesel bus (48). While the relative magnitude of the major peaks is slightly

different in the diesel bus and ship exhaust particulate mass spectra, the major peaks themselves are the same. These are the same major peaks observed by Phinney et al. (49) during previous observations of particulate ship exhaust with an Aerodyne AMS and they indicate particles composed of saturated and unsaturated hydrocarbons (alkanes, m/z 29, 43, 57, 71, 85, ...; alkenes and cycloalkanes, m/z 27, 41, 55, 69, 83, ...; dienes, alkynes, and cycloalkenes, m/z 67, 81, 95, ...; phenylalkanes, m/z 77, 91, 105, 119, ...) (50). Peaks known to be associated with PAHs were also observed in the C-ToF-AMS mass spectrum at m/z values above 200. Also evident in Figure 5.8 is an increase in the mass fraction of m/z 44 and a decrease in the mass fraction m/z 57 in the more aged spectra, though this is thought to be primarily caused by the influence of the more highly oxidized background aerosol mixing in when the plume dilutes, as will be discussed subsequently.

5.4.5 Aerosol Hygroscopicity

Figure 5.9 shows the particle hygroscopic growth factors measured by the DASH-SP and predicted by eq 1 with compositional inputs obtained from the C-ToF-AMS. Average growth factors are given for “in plume”, defined as regions where particulate sulfate mass and CN number were more than double those of the background aerosol, and “out of plume,” classified as all non-plume measurements made at similar altitudes to the in-plume measurements. The sulfate molar ratio, $SR = [NH_4^+]/[SO_4^{2-}]$, was used to determine the composition of the inorganic fraction. The same scheme (described in Section 2.4.2) was used to define the relative amounts of sulfuric acid, ammonium bisulfate and ammonium sulfate in both sub-saturated hygroscopic growth and CCN calculations. Predicted particle growth factors were calculated using bulk composition

(the average composition of all sub-micron particles). While the DASH-SP measures particles with mobility diameters between 150 and 200 nm, bulk composition was used because the improvement in signal to noise was judged to be more important than the rather negligible difference (typically < 5 percent) between bulk composition and the composition of particles in this size range. Organics were assumed to be hydrophobic and assigned a growth factor of unity when calculating hygroscopic growth factors, both in the ship exhaust plume and in the background air.

Because eq 1 requires volume fractions of individual chemical species in the aerosol and the C-ToF-AMS measures mass fractions, it is necessary to estimate the density of each individual chemical component within the particle. Using the techniques described in Section 3.3, the average particle density (at ~ 45% RH) was determined to be 1.4 g cm^{-3} in the ship-exhaust plume and 1.55 g cm^{-3} outside of the plume. Given the average particle density, the density of the organic fraction can be estimated using the mass fraction of organic and inorganic species from the C-ToF-AMS, the mass fraction of water from ISORROPIA, assuming volume additivity, and assuming dry densities of 1.83 g cm^{-3} for sulfuric acid, 1.79 g cm^{-3} for ammonium bisulfate, and 1.77 g cm^{-3} for ammonium sulfate. For the purpose of calculating the organic density, all in-plume sulfate was assumed to be sulfuric acid and all out-of-plume sulfate was assumed to be in the form of ammonium sulfate. Organics were found to have a density of $\sim 1.6 \text{ g cm}^{-3}$ in the exhaust plume while outside of the exhaust plume there was high variability in the calculated organic density and a typical organic density of 1.4 g cm^{-3} was assumed. It is important to note that changing the organic density from 1.4 to 1.6 g cm^{-3} results in an $\sim 1\%$ change in predicted growth factor.

Hygroscopic growth factors of in-plume aerosol are suppressed relative to those measured in the background aerosol. In-plume aerosol has a higher fraction of organic mass (0.28 ± 0.02 vs. 0.20 ± 0.15 out of plume), but also has more acidic sulfate (see Table 5.4). Based on measured composition and the assumptions noted above, both in- and out-of-plume hygroscopic growth factors are overpredicted by eq 1, and the overprediction within the plume is more substantial. The color bar in Figure 5.9 shows the hygroscopic growth factor of the organic fraction that would need to be assumed to achieve closure between the predicted and measured growth factors. While physically unrealistic, organic growth factors less than 1 indicate that observed growth factors are less than those predicted based on water uptake by the inorganic fraction alone. The presence of negative organic growth factors indicates that the measured growth factors are substantially less than predicted. Using size-resolved chemistry from the C-ToF-AMS in eq 1 would result in a slightly lower mass fraction of organics, eliminating the possibility that a high organic mass fraction was masked by averaging across particle sizes. None of the wet number distributions from the DASH-SP (74%, 85%, and 92% RH) shows signs of a bimodal distribution, making it improbable that an externally mixed, hydrophobic mode existed to explain the overpredicted particle hygroscopic growth factors. Potential explanations for the suppressed growth factors observed will be discussed subsequently.

5.4.6 CCN Activity

Figure 5.10 shows predicted and measured CCN concentrations for a number of points within the ship exhaust plume. These particular in-plume points were chosen

because the particle concentrations were relatively stable during an entire scan of the DMA. Again, the sulfate molar ratio, $SR = [NH_4^+]/[SO_4^{2-}]$, was used to determine the composition of the inorganic fraction (see Section 2.5). As noted earlier, the low SR suggests that the aerosol sulfate was present mostly as H_2SO_4 in the exhaust plume, while out of plume the particulate sulfate was partially neutralized. All predictions shown are based on eqs 2 and 3, but with different inputs for particulate chemical composition. Before CCN prediction calculations were performed, the dry particle size distribution was estimated based on the measured humid DMA size distribution and C-ToF-AMS measured composition as described in Section 2.5. Because the particulate composition in the ship exhaust plume did not change significantly with distance from the ship, the dry size distribution was consistently between 15 and 28% smaller than the humid distributions shown in Figure 5.7. Organics were treated as hydrophobic (based on AMS spectra and DASH-SP results) with a density of 1.6 g cm^{-3} and were assumed to have no effect on surface tension. Assuming an internal mixture and using bulk composition results in an overprediction of CCN number by an average of $23 \pm 6\%$ (Figure 5.10, top). Using size-resolved composition improves the closure slightly, resulting in an average overprediction of $16 \pm 6\%$ (Figure 5.10, bottom). The slight improvement in closure using size resolved chemistry occurs because at the higher supersaturations (above $\sim 0.25\%$) the CCN activation diameter moves towards smaller particles, which have a higher mass fraction of hydrophobic organics and are less CCN active.

Figure 5.11, which will be referred to as a growth kinetics plot, shows the average diameter achieved by activated particles when exiting the CCNc growth chamber as a function of the instrument supersaturation. Because the aerosol introduced into the

CCNc is polydisperse, the particles leaving the activation columns will always exhibit a range of final sizes (this occurs even if the particles are pure ammonium sulfate, because initially larger particles will grow to correspondingly larger sizes). The smallest size that an ammonium sulfate particle can reach is that attained by a particle of the minimum diameter required for activation at the operating supersaturation of the instrument; the lines shown in the figure represent this minimum size for ammonium sulfate particles. Any particles attaining a final size smaller than this minimum are likely to be subject to mass transfer limitations; that is, water is taken up more slowly such that the particles activate at a later time within the CCNc growth chamber than ammonium sulfate. It is clear that in-plume particles tend to achieve a smaller size within the CCNc growth chamber than the reference ammonium sulfate particles. The effect is not thought to be the result of depleted supersaturation in the column which has been shown not to occur for CCN concentrations $<10^4 \text{ cm}^{-3}$. This suggests that particles with critical supersaturation between 0.1 and 0.35% may have slower water uptake kinetics than ammonium sulfate. On the contrary, the vast majority of particles outside the ship plume do not exhibit slower water vapor uptake kinetics relative to $(\text{NH}_4)_2\text{SO}_4$.

5.5 Discussion

5.5.1 Comparison of Ship and Airborne Data

One goal of the present study is to determine the extent to which in-stack measurements of particulate ship emissions reflect particle properties in the airborne exhaust plume. Owing to a lack of measurements of gas-phase tracers of dispersion (e.g.

CO₂ or CO), it is not possible to relate the absolute particulate mass measured in the stack to that in the air, but it is possible to assess agreement between composition measurements. In-stack particulate composition data are summarized in Table 5.3, while the airborne measurements are given in Table 5.4. The airborne measurements for sulfate are reported without associated water. Accordingly, the 6.5 H₂O molecules assumed to be associated with a sulfate molecule in the stack can be removed to give a dry sulfate emission factor of 0.84 g kWh⁻¹. To relate the shipboard and airborne organic measurements, it is necessary to estimate a conversion from organic carbon (OC), measured in the stack, to organic mass (OM) measured by the airborne C-ToF-AMS.

Aiken et al. (47) used a high resolution Aerodyne aerosol mass spectrometer, capable of unambiguously measuring the oxygen and carbon content of an aerosol, to relate the O:C atomic ratio to the fraction of signal intensity observed at m/z 44 on unit mass resolution AMS instruments. The relationship, derived from several ground-based and airborne studies, between the fraction of the organic aerosol signal (OA) present at m/z 44 and the atomic ratio of oxygen to carbon (O:C), given with 95% confidence intervals, is ($R^2 = 0.84$):

$$\text{O:C} = (0.0382 \pm 0.0005)(\% \text{ of OA from } m/z \text{ 44}) + (0.0794 \pm 0.0070) \quad (4)$$

Aiken et al. (47) used an even broader data set, including several chamber studies in addition to the previously mentioned field studies, to derive a relationship between organic mass (OM) and the O:C atomic ratio ($R^2 = 0.997$):

$$\text{OM/OC} = (1.260 \pm 0.002)(\text{O:C}) + (1.180 \pm 0.001) \quad (5)$$

In Table 5.4, the percentage of the organic mass spectrum represented by signal at m/z 44 for particles within the exhaust plume is 3.5%, which, using eqs 4 and 5, leads to an OM:OC ratio of 1.45. The in-plume percentage of non-refractory organic mass was measured to be 31% by the C-ToF-AMS which converts to 21% organic carbon using this estimated OM:OC ratio. Based on the arguments above, the estimated ratio of organic carbon to dry sulfate mass (OC:SO_{4dry}) measured in the ship's stack is 0.23 ± 0.03 . The estimated airborne measurement of OM:SO_{4dry} = 0.43 ± 0.01 , which converts (again assuming an OM:OC ratio of 1.45) to OC: SO_{4dry} = 0.30 ± 0.01 . However, this relatively good agreement between airborne and shipboard measurements is a best case scenario given the previously mentioned overestimation of organic carbon mass in the shipboard measurement caused by adsorption of gas-phase organics onto the filter (estimated to be ~ 30% based on Shah et al. (42)). Because there was no correction for absorption of gas-phase organics in this study, 0.23 represents an upper limit of the organic carbon to dry sulfate mass ratio measured within the ship's stack.

There are several possible explanations for the higher fraction of organic mass measured in the airborne plume. The in-stack measurements were made at a dilution ratio of about 5:1 which is less dilute than the airborne measurements, even close to the stack. However, additional dilution should cause semivolatile organics to revolatilize and cause less organic mass to be present in the airborne plume. Loss of particulate or semivolatile gaseous organics during the transition from the stack to the filter is likely to be a negligible effect because a transfer line was not used in this study. The slightly

higher temperature of the collection point for the filters (~ 25 °C) versus the ambient temperature of the marine boundary layer (14.3 ± 0.4 °C) is also judged to be relatively unimportant based on previous studies in which diesel exhaust filters were collected at different temperatures (51). However, it should be noted that the volatilities of the organics in the Heavy Fuel Oil may have quite different temperature dependencies than those of organics in diesel fuels previously tested.

Given that the higher fraction of particulate organic mass observed in the airborne measurements does not appear to be an artifact of the shipboard measurement methods, the organic material must condense from the gas phase into the particle phase between the point where the stack measurements are made (at the bottom of the stack) and the point at which airborne measurements are first made (~ 100 m behind the ship). Between the two measurement points, the exhaust gas from the stack passes through a heat exchanger designed to use the otherwise waste heat of exhaust (also called a waste heat boiler). The heat exchanger can lower the temperature of exhaust to ~ 75 -100 °C. This temperature decrease occurs without dilution of the exhaust as opposed to the dilution tunnel system used for in-stack measurements where the exhaust was cooled and diluted simultaneously. The hypothesis that organics condense in the upper regions of the stack and in the waste heat boiler is supported by Figures 5.3 and 5.7, which show that the fraction of organic mass is constant with particle size in the stack measurements but that organic mass is enriched on smaller airborne particles. This pattern of larger mass fraction on smaller particles, which have more surface area, is consistent with a gas-to-particle condensational process (assuming the condensing organic is non-volatile

enough not to be affected by the higher vapor pressure caused by the increased curvature of the smaller particles).

5.5.2 Plume Dilution and Aging

Because of the favorable wind and cloudless conditions during the study, it was possible to fly directly in the exhaust plume until it had reached an estimated age of 24 min and to detect the plume in transects up to an estimated age of 62 min. Measurements of plume composition at different ages are given in Table 5.4. Of significance is the fact that there is essentially no change in the organic:sulfate mass ratio with time. This constant ratio indicates that condensed organics in the particulate phase were not volatile enough to repartition back to the gas phase as the plume diluted and gas-phase organic concentrations decreased. Additionally, while organic matter does appear to condense into the particle phase between the lower stack (where in-stack measurements were made) and the point where airborne measurements were first made (a few hundred meters behind the ship), no further organic matter condenses into the particle phase as the plume ages after the point of the first airborne measurements.

While the ratio of organic:sulfate mass remains essentially constant, the fraction of the mass spectrum represented by the peak at m/z 44 does increase significantly with increasing plume age, indicating an increasingly oxidized aerosol. This appears to be the result of the mixing of plume and background aerosol. As shown in Figure 5.8 and tabulated in Table 5.4, the fraction of the organic signal at m/z 44 is significantly higher (17%) in the background marine aerosol than it is in the freshly emitted plume (3%). The average mass loading of organic aerosol in the background air is $0.48 \mu\text{g m}^{-3}$, while

closest to the ship it is $148 \mu\text{g m}^{-3}$. During the transect at a plume age of 62 min, the peak organic mass loading observed was $2.0 \mu\text{g m}^{-3}$. Accordingly, one can approximate the organic mass spectrum during this transect as a linear combination of $0.48 \mu\text{g m}^{-3}$ (24%) background aerosol and $1.52 \mu\text{g m}^{-3}$ (76%) plume aerosol. Assuming the mass spectrum of the plume aerosol remains unchanged after 62 min of aging, this simple linear combination of plume and background aerosol predicts that 6.4% of the organic signal will be present in the peak at m/z 44, which is close to the 8% that is observed. From this analysis, it appears that there is little change in the mass spectrum of the particulate organic during the first hour after emission. The conclusion that the increase in signal at m/z 44 with plume age is a result primarily of dilution lends further confidence to the hypothesis that the mass fraction and composition of particulate organics are determined soon after the exhaust is emitted from the ship.

5.5.3 Hygroscopic Growth

Particulate hygroscopic growth is suppressed in the ship exhaust plume relative to the background aerosol. While there is a higher fraction of organic mass inside the plume (31%) relative to the background aerosol (18%), the closure study using the volume-weighted mixing rule shows that when this organic mass is accounted for there is relatively good closure between predicted and measured growth factors outside of the exhaust plume but very poor closure within it. It is worth noting that while the closure outside the exhaust plume is reasonable, it was obtained by assuming that organics have the lowest physically realistic growth factor of unity. It is somewhat surprising that a growth factor of unity would be appropriate for the highly oxidized organics found

outside of the exhaust plume, though significant mass fractions of insoluble organics and lower than predicted growth factors have been previously observed in marine aerosols in this region (52).

The fact that the simple volume-weighted mixing rule with compositional inputs from C-ToF-AMS measurements is unable to realistically represent the hygroscopic behavior of the mixture of fresh, hydrocarbon-like organic and sulfuric acid found within the plume could be explained in several ways. First and most probable, the DASH-SP may not be able to fully dry the exhaust-plume particles which contain large amounts of sulfuric acid. If the particles are not fully dried before they are humidified, then the measured growth factor will be underestimated because the particle's dry size is overestimated. A second possibility is that the organic material in the exhaust plume may be slowing uptake of water onto the particles. A simple model of the DASH-SP growth chamber, which has a particle residence time of ~ 4 s, indicates that an accommodation coefficient (α) of $\sim 10^{-4}$ (or equivalently slow mass transfer through the organic layer) is required to simulate the measured growth factors at 85 and 92% RH (an even smaller α ($\sim 10^{-5}$) is required to simulate the measured growth factor at 74% RH, but the sizing of OPC in the DASH-SP is questionable at this lower RH because of uncertainties in the refractive index).

The final possibility is that the volume fraction of organics has been incorrectly estimated. This is possible because the particles that the DASH-SP measures (150-200 nm) are at the edge of the volume/mass distribution where there is relatively poor signal to noise. Figure 5.7 clearly shows that a 200 nm mobility diameter particle is at the tail end of the volume distribution and that the corresponding C-ToF-AMS composition

measurements in this region of the mass distribution are rather uncertain. It is also important to remember that the volume distribution given in Figure 5.7 is given at $\sim 45\%$ RH and would be shifted to smaller sizes (by $\sim 20\%$, see section 2.5) if it were dry. However, there is no obvious indication that the fraction of organics would dramatically increase at larger particle sizes and a brief sensitivity study showed that a 60% reduction in sulfate volume fraction is needed to predict the growth factors measured in the exhaust plume at 85% and 92% RH (an even further reduction of sulfate volume fraction would be needed to simulate the measurements at 74% RH). This type of reduction in sulfate seems improbable.

For completeness, it is important to note that black carbon is not detected by the C-ToF-AMS, though it is clearly present in the exhaust plume as shown by the PSAP measurements. Particles containing significant fractions of black carbon will be assigned erroneously high volume fractions of water-soluble inorganics based on C-ToF-AMS composition measurements. Despite this, the effect of black carbon is estimated to be relatively minor overall given the good agreement between C-ToF-AMS measured particle mass and DMA measured particle volume and given the low ash content in the fuel.

5.5.4 CCN Closure

Ship emissions are clearly a source of particles in the marine boundary layer, but because these particles typically have a smaller mean diameter and contain more organic than background marine particles, it is uncertain what fraction act as CCN under the relatively low supersaturations of marine stratocumulus clouds. The results of this study

imply that, for the size distribution of particles emitted from this ship, knowledge of the size-resolved chemical composition is relatively unimportant for supersaturations below 0.3%. However, if the supersaturation is above 0.3% or if the emitted particles are slightly larger, knowledge of the size-resolved composition becomes critical for accurately predicting CCN because of the high mass fractions of hydrophobic organics, which inhibit CCN formation, observed at smaller particle sizes.

The impact of soot (black carbon) and ash particles on CCN closure was also considered. Because the C-ToF-AMS cannot detect refractory material, the presence of soot or ash will lead to overprediction of CCN. This overprediction occurs because measurements from the C-ToF-AMS are used to assign chemical compositions to the volume distribution measured by the DMA. If present, soot and ash will be measured by the DMA and assigned an incorrect composition based on the C-ToF-AMS measurements of the non-refractory aerosol. Because soot and ash tend to be less CCN active than mixed organic/sulfate particles, this leads to an overestimation of CCN number. Based on the PSAP measurements and the estimate based on fuel composition given in Table 5.3, soot and ash appear to be a relatively minor contributor to aerosol mass and their presence is not expected to be a major for the overestimation of CCN number concentration, though it may partially account for the slight overestimation of CCN calculated for this study.

5.6 Implications

The ship studied here, with a 2-stroke, slow-speed diesel engine, represents a very common class of vessel. Emission factors from this study and relevant literature

studies of ships burning heavy fuel oil are given in Table 5.5. All emission factors have been normalized to be in units of $(\text{kg fuel})^{-1}$ using the carbon dioxide balance method which was also used, in slightly varying forms, in all of the previous literature cited in Table 5.5. This method is based on the fact that CO_2 is the principal carbon emission from combustion of HFO (while carbon is also emitted as CO, methane, non-methane organic compounds (NMOC), and particulate mass, the mass contribution of these species is insignificant relative to CO_2). Assuming complete combustion to CO_2 and a hydrogen to carbon ratio of 1.8 for the fuel (53), 3.2 kg of CO_2 is formed per kg of fuel burned. Because CO_2 was measured in the stack, this conversion factor can be used to convert in-stack emission factors to a $(\text{kg fuel})^{-1}$ basis. Because neither CO_2 nor other gas-phase species were measured on the airborne platform, in-plume particulate measurements were scaled to in-stack CO_2 using particulate sulfate mass measurements (made on both the shipboard and airborne platforms) and assuming that perturbations in sulfate particulate mass above background atmospheric levels were caused solely by the ship exhaust. A potential source of error in this method is that the mass of particulate sulfate could change between the stack measurements and the atmosphere; however, further conversion is unlikely.

The SO_2 emission factors in Table 5.5 give some confidence that the heavy fuel oil being burned in these different studies was relatively similar, at least in terms of percent sulfur. The NO_x measured in the ship's stack during this study is significantly higher than any of the previous airborne measurements. While it is similar to the Petzold et al. study (11), their numbers were estimated based on fuel composition and knowledge of engine operating conditions. While the CN emission factor varies between studies, all

of the data show that the number of CN with diameters above 100 nm is roughly an order of magnitude less than the number of CN with diameters smaller than this. This study represents the second time that an emission factor for CCN has been calculated. The fraction of CN (> 10 nm in diameter) that activate into CCN at 0.3% supersaturation was found to be 0.24, similar to the 0.18 found by Sinha et al. (3). Finally, the airborne organic to sulfate mass ratio from this study (which is significantly higher than the in-stack measurement) agrees well with the most recent test-bed results of Petzold et al.(11); both of these estimates are significantly higher than the previous estimate from Petzold et al. (9) which was used by Eyring et al. (1) to estimate global emissions of 0.134 Tg OC per year; these results suggest that the global annual emissions of organic carbon may be significantly higher than previously estimated.

5.7 Acknowledgments

This work was supported by the Office of Naval Research. S.M and L. T. P. acknowledge support from the NASA Earth and Space Sciences Fellowship. A. N. acknowledges support from the NASA Radiation Science Program and an NSF CAREER. The authors gratefully acknowledge the NOAA Air Resources Laboratory (ARL) for the provision of the HYSPLIT transport and dispersion model. The authors are grateful to the ship crew and the shipping company, and the analytical support of Ms. Kathy Cocker, and Ms. Varalakshmi Jayaram.

5.8 Supporting Information

5.8.1 Shipboard Platform Test Methods

5.8.1.1 Measurement of Stack Gases

The concentrations of gases in the raw exhaust and the dilution tunnel were measured with a Horiba PG-250 portable multi-gas analyzer. For quality control, analyzer checks with calibration gases both before and after each test were made to check for drift. The SO₂ data presented here are calculated from the sulfur level in the fuel as suggested by the certification method in ISO 8178 (15).

5.8.1.2 Measurement of Particulate Matter (PM) mass and Ions

The mass concentrations of PM_{2.5} and ions were acquired by analysis of particulate matter collected on 47 mm diameter 2 µm pore Teflo filters (Pall Gelman, Ann Arbor, MI). The filters were measured for net gains using a Cahn C-35 (Madison, WI) microbalance following the weighing procedure guidelines of the Code of Federal Regulations (CFR) (16). Before and after collection, the filters were conditioned for 24 h in an environmentally-controlled room (RH = 40%, T = 25 °C) and weighed daily until two consecutive weight measurements were within 3 µg. Finally, the filters were extracted with HPLC grade water and isopropyl alcohol and analyzed for sulfate ions using a Dionex DX-120 ion chromatograph. Real time measurements of total particle mass were made by a Dekati Mass Monitor (DMM-230) with 1s time resolution (20).

5.8.1.3 Measurement of Particle-Phase Elemental and Organic Carbon

OC/EC analysis was performed on samples collected on 2500 QAT-UP Tissuquartz Pall (Ann Arbor, MI) 47 mm filters that were preconditioned at 600 °C for 5 h. A 1.5 cm² punch was cut out from the quartz filter and analyzed with a Sunset Laboratory (Forest Grove, OR) Thermal/Optical Carbon Aerosol Analyzer according to the NIOSH 5040 reference method (19).

5.8.1.4 Measurement of Size-Resolved Particulate Composition

A ten stage rotating Micro-Orifice Uniform Deposit Impactor (MOUDI) (MDI-110-R-366, MN) was used in order to obtain size resolved PM. The Model 110 provides cut-point diameters of 18, 10, 5.6, 3.2, 1.8, 1.0, 0.56, 0.32, 0.18, 0.1, and 0.056 µm. Aluminium (Al) filter substrates were used on all the upper stages and quartz filter substrate was used as after filter. The Al filters were measured for net PM gains using a Cahn C-35 (Madison, WI) microbalance. The quartz after filter (< 56nm) cannot be accurately weighed because of loss of quartz fibers during the sampling to the o-ring seal. The filters were subsequently analyzed for EC, OC, and sulfate following the standard procedures described in the previous section. This enabled the determination of the chemical composition of PM among various particle size bins.

5.8.1.5 Measurement of Carbonyls

Carbonyls were collected on 2,4-dinitrophenylhydrazine (DNPH) coated silica cartridges (Waters Corp., Milford, MA) behind the Teflon filter as shown in Figure 5.12

critical flow orifice was used to control the 1.0 liter per minute flow through the cartridge. Sampled cartridges were extracted using 5 mL of acetonitrile and injected into an Agilent 1100 series high performance liquid chromatograph (HPLC) equipped with a diode array detector. The column used was a 5 μm Deltabond AK resolution (200 cm x 4.6 mm ID) with upstream guard column. The HPLC sample injection and operating conditions followed the specifications in the SAE 930142HP protocol (18).

5.8.1.6 C₁₀ to C₃₀ Hydrocarbons, Including Naphthalene and PAHs

The diluted exhaust was collected through a quartz filter and into a column packed with polyurethane foam (PUF)/XAD-4 resin. A portion of the quartz filter was used to analyze for elemental and organic carbon, as described in the previous section. Both the PUF/XAD-4 cartridge and the remainder of the quartz filter were extracted with methylene chloride and analyzed using a modified method EPA TO13A protocol (GC-MS analysis) to determine total emission rates for PAHs and n-alkanes. Details on the analysis method are found in Shah et al. (17).

5.8.1.7 1,3 Butadiene; Benzene; Toluene; Ethylbenzene and Xylenes

Gaseous organics from C₄ (butadiene) through C₁₂ were collected and concentrated on a multi-bed adsorbent column, including molecular sieve, activated charcoal, and carbotrap resin. The most volatile compounds adsorb first; the remaining compounds adsorb sequentially in relation to their volatility. The GC sample injection,

column, and operating condition were set up according to the specifications of SAE 930142HP Method-2 for C4-C12 hydrocarbons.

5.8 Literature Cited

- (1) Eyring, V.; Kohler, H. W.; van Aardenne, J.; Lauer, A. Emissions from international shipping: 1. The last 50 years. *J. Geophys. Res.* **2005**, *110*, D17305, doi: 10.1029/2004JD005619.
- (2) Capaldo, K.; Corbett, J. J.; Kasibhatla, P.; Fischbeck, P.; Pandis, S. N. Effects of ship emissions on sulphur cycling and radiative climate forcing over the ocean. *Nature* **1999**, *400* (6746), 743-746.
- (3) Sinha, P.; Hobbs, P. V.; Yokelson, R. J.; Christian, T. J.; Kirchstetter, T. W.; Bruintjes, R. Emissions of trace gases and particles from two ships in the southern Atlantic Ocean. *Atmos. Environ.* **2003**, *37* (15), 2139-2148.
- (4) Corbett, J. J.; Winebrake, J. J.; Green, E. H.; Kasibhatla, P.; Eyring, V.; Lauer, A. Mortality from ship emissions: A global assessment. *Environ. Sci. Technol.* **2007**, *41*, 8512-8518.
- (5) Lauer, A.; Eyring, V.; Hendricks, J.; Jockel, P.; Lohmann, U. Global model simulations of the impact of ocean-going ships on aerosols, clouds, and the radiation budget. *Atmos. Chem. Phys.* **2007**, *7*, 5061-5079.
- (6) Corbett, J. J.; Koehler, H. W. Updated emissions from ocean shipping. *J. Geophys. Res.* **2003**, *108* (D20), doi: 10.1029/2003jd003751.
- (7) Hobbs, P. V.; Garrett, T. J.; Ferek, R. J.; Strader, S. R.; Hegg, D. A.; Frick, G. M.; Hoppel, W. A.; Gasparovic, R. F.; Russell, L. M.; Johnson, D. W.; O'Dowd, C.; Durkee, P. A.; Nielsen, K. E.; Innis, G. Emissions from ships with respect to their effects on clouds. *J. Atmos. Sci.* **2000**, *57* (16), 2570-2590.
- (8) Kasper, A.; Aufdenblatten, S.; Forss, A.; Mohr, M.; Burtscher, H. Particulate emissions from a low-speed marine diesel engine. *Aerosol Sci. Technol.* **2007**, *41* (1), 24-32.
- (9) Petzold, A.; Feldpausch, P.; Fritzsche, L.; Minikin, A.; Lauer, A.; Bauer, H. Particle emissions from ship engines, *Journal of Aerosol Science, Supplement 2*, *35*, S1095 - S1096, European Aerosol Conference, Budapest, **2004**.
- (10) Williams, E.; Lerner, B.; Quinn, P.; Bates, T. Measurements of gas and particle emissions from commercial marine vessels, AGU Fall Meeting Abstracts, **2005**.
- (11) Petzold, A.; Hasselbach, J.; Lauer, P.; Baumann, R.; Franke, K.; Gurk, C.; Schlager, H.; Weingartner, E. Experimental studies on particle emissions from cruising ship, their characteristic properties, transformation and atmospheric lifetime in the marine boundary layer. *Atmos. Chem. Phys.* **2008**, *8* (9), 2387-2403.

- (12) Agrawal, H.; Malloy, Q. G. J.; Welch, W. A.; Miller, J. W.; Cocker, D. R. In-use gaseous and particulate matter emissions from a modern ocean going container vessel. *Atmos. Environ.* **2008**, *42* (21), 5504-5510.
- (13) Agrawal, H., Welch, W.A., Miller, J.W., Cocker, D.R. Emission measurements from a crude oil tanker at sea. *Environ. Sci. Technol.* **2008**, *42* (19), 7098-7103.
- (14) Corbett, J. J. New directions: Designing ship emissions and impacts research to inform both science and policy. *Atmos. Environ.* **2003**, *37* (33), 4719-4721.
- (15) International Standards Organization, *ISO 8178-1 Reciprocating internal combustion engines - exhaust emission measurement -Part 1: Test-bed measurement of gaseous particulate exhaust emissions*; First edition, 1996 (8/15)
- (16) Code of federal regulations. *Protection of the environment*; 40 CFR 86.
- (17) Shah, S. D.; Ogunyoku, T. A.; Miller, J. W.; Cocker, D. R. On-road emission rates of PAH and n-alkane compounds from heavy-duty diesel vehicles *Environ. Sci. Technol.* **2004**, *39* (14), 5276-5284.
- (18) Siegl, W. O.; Richert, J. F. O.; Jensen, T. E.; Schuetzle, D.; Swarin, S. J.; Loo, J. F.; Probst, A.; Nagy, D.; Schlenker, A. M. Improved emissions speciation methodology for phase II of the auto/oil air quality improvement research programs hydrocarbons and oxygenates. SAE Tech. Pap. 1993, Ser., No. 930142, special publication sp-1000. **1993**.
- (19) National institute of occupational safety and health. *NIOSH manual of analytical methods*. NIOSH: Cincinnati, OH, 1996.
- (20) Dekati mass monitor (DMM). <http://www.dekati.com/cms/dmm>
- (21) Drewnick, F.; Hings, S. S.; DeCarlo, P.; Jayne, J. T.; Gonin, M.; Fuhrer, K.; Weimer, S.; Jimenez, J. L.; Demerjian, K. L.; Borrmann, S.; Worsnop, D. R. A new time-of-flight aerosol mass spectrometer (TOF-AMS) - instrument description and first field deployment. *Aerosol Sci. Technol.* **2005**, *39*, 637-658.
- (22) Bahreini, R.; Dunlea, E. J.; Matthew, B. M.; Simons, C.; Docherty, K. S.; DeCarlo, P. F.; Jimenez, J. L.; Brock, C. A.; Middlebrook, A. M. Design and operation of a pressure-controlled inlet for airborne sampling with an aerodynamic aerosol lens. *Aerosol Sci. Technol.* **2008**, *42* (6), 465-471.
- (23) Huffman, J. A.; Jayne, J. T.; Drewnick, F.; Aiken, A. C.; Onasch, T.; Worsnop, D. R.; Jimenez, J. L. Design, modeling, optimization, and experimental tests of a particle beam width probe for the aerodyne aerosol mass spectrometer. *Aerosol Sci. Technol.* **2005**, *39*, 1143-1163.
- (24) Canagaratna, M. R.; Jayne, J. T.; Jimenez, J. L.; Allan, J. D.; Alfarra, M. R.; Zhang, Q.; Onasch, T. B.; Drewnick, F.; Coe, H.; Middlebrook, A.; Delia, A.; Williams, L. R.; Trimborn, A. M.; Northway, M. J.; DeCarlo, P. F.; Kolb, C. E.; Davidovits, P.; Worsnop,

D. R. Chemical and microphysical characterization of ambient aerosols with the aerodyne aerosol mass spectrometer. *Mass Spectrom. Rev.* **2007**, *26* (2), 185-222.

(25) Sorooshian, A.; Brechtel, F. J.; Ma, Y. L.; Weber, R. J.; Corless, A.; Flagan, R. C.; Seinfeld, J. H. Modeling and characterization of a particle-into-liquid sampler (PILS). *Aerosol Sci. Technol.* **2006**, *40* (6), 396-409.

(26) Sorooshian, A.; Ng, N. L.; Chan, A. W. H.; Feingold, G.; Flagan, R. C.; Seinfeld, J. H. Particulate organic acids and overall water-soluble aerosol composition measurements from the 2006 Gulf of Mexico Atmospheric Composition and Climate Study (GoMACCS). *J. Geophys. Res.* **2007**, *112* (D13), D13201, doi:10.1029/2007JD008537.

(27) Virkkula, A.; Ahlquist, N. C.; Covert, D. S.; Arnott, W. P.; Sheridan, P. J.; Quinn, P. K.; Coffman, D. J. Modification, calibration and a field test of an instrument for measuring light absorption by particles. *Aerosol Sci. Technol.* **2005**, *39* (1), 68 - 83.

(28) Sorooshian, A.; Hersey, S.; Brechtel, F. J.; Corless, A.; Flagan, R. C.; Seinfeld, J. H. Rapid, size-resolved aerosol hygroscopic growth measurements: Differential aerosol sizing and hygroscopicity spectrometer probe (DASH-SP). *Aerosol Sci. Technol.* **2008**, *42* (6), 445 - 464.

(29) Roberts, G. C.; Nenes, A. A continuous-flow streamwise thermal-gradient CCN chamber for atmospheric measurements. *Aerosol Sci. Technol.* **2005**, *39* (3), 206-221.

(30) Lance, S.; Medina, J.; Smith, J. N.; Nenes, A. Mapping the operation of the DMT continuous flow CCN counter. *Aerosol Sci. Technol.* **2006**, *40* (4), 242-254.

(31) Aklilu, Y.; Mozurkewich, M.; Prenni, A. J.; Kreidenweis, S. M.; Alfarra, M. R.; Allan, J. D.; Anlauf, K.; Brook, J.; Leaitch, W. R.; Sharma, S.; Boudries, H.; Worsnop, D. R. Hygroscopicity of particles at two rural, urban influenced sites during pacific 2001: Comparison with estimates of water uptake from particle composition. *Atmos. Environ.* **2006**, *40*, 2650-2661.

(32) Gysel, M.; Crosier, J.; Topping, D. O.; Whitehead, J. D.; Bower, K. N.; Cubison, M. J.; Williams, P. I.; Flynn, M. J.; McFiggans, G. B.; Coe, H. Closure study between chemical composition and hygroscopic growth of aerosol particles during TORCH2. *Atmos. Chem. Phys.* **2007**, *7* (24), 6131-6144.

(33) Seinfeld, J. H.; Pandis, S. N., "Atmospheric chemistry and physics : From air pollution to climate change" 2nd ed.; Wiley-Interscience: Hoboken, N.J., 2006.

(34) Clegg, S. L.; Brimblecombe, P.; Wexler, A. S. Thermodynamic model of the system H⁺-NH₄⁺-Na⁺-SO₄²⁻--NO₃⁻--Cl⁻--H₂O at 298.15 K. *Journal of Physical Chemistry A* **1998**, *102* (12), 2155-2171.

(35) Wexler, A. S.; Clegg, S. L.; Brimblecombe, P. On-line aerosol inorganics model. <http://mae.ucdavis.edu/~sclegg/aim.html>

- (36) Medina, J.; Nenes, A.; Sotiropoulou, R. E. P.; Cottrell, L. D.; Ziemba, L. D.; Beckman, P. J.; Griffin, R. J. Cloud condensation nuclei closure during the International Consortium for Atmospheric Research on Transport and Transformation 2004 campaign: Effects of size-resolved composition. *J. Geophys. Res.* **2007**, D10S31, doi: 10.1029/2006jd007588.
- (37) Nenes, A.; Pandis, S. N.; Pilinis, C. Isorropia: A new thermodynamic equilibrium model for multiphase multicomponent inorganic aerosols. *Aquatic Geochemistry* **1998**, *4* (1), 123-152, <http://nenes.eas.gatech.edu/ISORROPIA>.
- (38) Brechtel, F. J.; Kreidenweis, S. M. Predicting particle critical supersaturation from hygroscopic growth measurements in the humidified TDMA. Part I: Theory and sensitivity studies. *J. Atmos. Sci.* **2000**, *57* (12), 1854-1871.
- (39) Brechtel, F. J.; Kreidenweis, S. M. Predicting particle critical supersaturation from hygroscopic growth measurements in the humidified TDMA. Part II: Laboratory and ambient studies. *J. Atmos. Sci.* **2000**, *57* (12), 1872-1887.
- (40) Rose, D.; Gunthe, S. S.; Mikhailov, E.; Frank, G. P.; Dusek, U.; Andreae, M. O.; Poschl, U. Calibration and measurement uncertainties of a continuous-flow cloud condensation nuclei counter (DMT-CCNC): CCN activation of ammonium sulfate and sodium chloride aerosol particles in theory and experiment. *Atmos. Chem. Phys.* **2008**, *8* (5), 1153-1179.
- (41) Draxler, R. R.; Rolph, G. D. Hysplit (hybrid single-particle lagrangian integrated trajectory) model access via NOAA ARL ready website. <http://www.arl.noaa.gov/ready/hysplit4.html>
- (42) Shah, S. D.; Cocker, D. R.; Miller, J. W.; Norbeck, J. M. Emission rates of particulate matter and elemental and organic carbon from in-use diesel engines. *Environ. Sci. Technol.* **2004**, *38* (9), 2544-2550.
- (43) DeCarlo, P. F.; Slowik, J. G.; Worsnop, D. R.; Davidovits, P.; Jimenez, J. L. Particle morphology and density characterization by combined mobility and aerodynamic diameter measurements. Part 1: Theory. *Aerosol Sci. Technol.* **2004**, *38* (12), 1185-1205.
- (44) Zhang, Q.; Alfarra, M. R.; Worsnop, D. R.; Allan, J. D.; Coe, H.; Canagaratna, M. R.; Jimenez, J. L. Deconvolution and quantification of hydrocarbon-like and oxygenated organic aerosols based on aerosol mass spectrometry. *Environ. Sci. Technol.* **2005**, *39*, 4938-4952.
- (45) Kondo, Y.; Miyazaki, Y.; Takegawa, N.; Miyakawa, T.; Weber, R. J.; Jimenez, J. L.; Zhang, Q.; Worsnop, D. R. Oxygenated and water-soluble organic aerosols in Tokyo. *J. Geophys. Res.* **2007**, *112*, doi: 10.1029/2006jd007056.
- (46) Takegawa, N.; Miyakawa, T.; Kawamura, K.; Kondo, Y. Contribution of selected dicarboxylic and omega-oxocarboxylic acids in ambient aerosol to the m/z 44 signal of an Aerodyne aerosol mass spectrometer. *Aerosol Sci. Technol.* **2007**, *41*, 418-437.

- (47) Aiken, A. C.; DeCarlo, P. F.; Kroll, J. H.; Worsnop, D. R.; Huffman, J. A.; Docherty, K.; Ulbrich, I. M.; Mohr, C.; Kimmel, J. R.; Sueper, D.; Zhang, Q.; Sun, Y.; Trimborn, A.; Northway, M.; Ziemann, P. J.; Canagaratna, M. R.; Onasch, T. B.; Alfarra, R.; Prevot, A. S. H.; Dommen, J.; Duplissy, J.; Metzger, A.; Baltensperger, U.; Jimenez, J. L. O/C and OM/OC ratios of primary, secondary, and ambient organic aerosols with high resolution time-of-flight aerosol mass spectrometry *Environ. Sci. Technol.* **2008**, *42* (12), 4478-4485.
- (48) Canagaratna, M. R.; Jayne, J. T.; Ghertner, D. A.; Herndon, S.; Shi, Q.; Jimenez, J. L.; Silva, P. J.; Williams, P.; Lanni, T.; Drewnick, F.; Demerjian, K. L.; Kolb, C. E.; Worsnop, D. R. Chase studies of particulate emissions from in-use New York City vehicles. *Aerosol Sci. Technol.* **2004**, *38* (6), 555-573.
- (49) Phinney, L.; Leaitch, W. R.; Lohmann, U.; Boudries, H.; Worsnop, D. R.; Jayne, J. T.; Toom-Sauntry, D.; Wadleigh, M.; Sharma, S.; Shantz, N. Characterization of the aerosol over the sub-arctic north east Pacific Ocean. *Deep-Sea Research Part Ii-Topical Studies in Oceanography* **2006**, *53* (20-22), 2410-2433.
- (50) McLafferty, F. W.; Turecek, F., "Interpretation of mass spectra " 4 ed.; University Science Books: Sausalito, CA, 1993; p 371.
- (51) Cocker, D. R.; Shah, S. D.; Johnson, K. C.; Zhu, X. N.; Miller, J. W.; Norbeck, J. M. Development and application of a mobile laboratory for measuring emissions from diesel engines. 2. Sampling for toxics and particulate matter. *Environ. Sci. Technol.* **2004**, *38* (24), 6809-6816.
- (52) Kaku, K. C.; Hegg, D. A.; Covert, D. S.; Santarpia, J. L.; Jonsson, H.; Buzorius, G.; Collins, D. R. Organics in the northeastern pacific and their impacts on aerosol hygroscopicity in the subsaturated and supersaturated regimes. *Atmos. Chem. Phys.* **2006**, *6*, 4101-4115.
- (53) Tuttle, K. L. *Combustion-generated emissions in marine propulsion systems*, Society of Naval Architects and Marine Engineers, Environmental Symp. Ship design and operation in harmony with the environment: Jersey City, NJ, 1995, 311-323.
- (54) Chen, G.; Huey, L. G.; Trainer, M.; Nicks, D.; Corbett, J.; Ryerson, T.; Parrish, D.; Neuman, J. A.; Nowak, J.; Tanner, D.; Holloway, J.; Brock, C.; Crawford, J.; Olson, J. R.; Sullivan, A.; Weber, R.; Schauffler, S.; Donnelly, S.; Atlas, E.; Roberts, J.; Flocke, F.; Hubler, G.; Fehsenfeld, F. An investigation of the chemistry of ship emission plumes during ITCT 2002. *J. Geophys. Res.* **2005**, *110* (D10).

Table 5.1: Selected Heavy Fuel Oil Properties

Product Grade	I.F.O. 380
Density @ 15°C	988.5 kg/m ³
Viscosity @ 50 °C	290.6 mm ² /s
Sulfur	3.01% m/m
Ash	0.05% m/m
Vanadium	75 mg/kg
Nickel	29 mg/kg

Table 5.2: Gaseous stack emission factors in g (kWhr)⁻¹ by chemical class. Emission factors for PAHs and Alkanes are for total (gas and particle phase) emissions.

Compound	Emissions Factor	Compound	Emissions Factor
NO _x (as NO ₂)	20.1 ± 0.1	PAHs*, Alkanes cont'd	
CO	0.29 ± 0.01	Tetradecane	(5.55 ± 0.26)E-04
CO ₂	638 ± 4	Hexadecane	(4.00 ± 1.32)E-04
Calc. SO ₂ ***	11.9 ± 0.1	Octadecane	(3.21 ± 1.13)E-04
BTEX**		Nonadecane	(2.00 ± 0.39)E-04
1,3 Butadiene	(1.3 ± 0.8)E-04	Fluorene	(2.50 ± 0.74)E-04
Benzene	(7.0 ± 0.4)E-04	Phenanthrene	(5.14 ± 2.15)E-04
Toluene	(4.4 ± 0.9)E-04	Anthracene	(1.22 ± 0.66)E-05
m&p Xylene	(3.3 ± 0.5)E-04	Fluoranthene	(7.48 ± 2.85)E-05
Ethyl Benzene	(1.1 ± 0.3)E-04	Eicosane	(2.49 ± 0.64)E-04
o-Xylene	(1.0 ± 0.05)E-04	Docosane	(6.84 ± 3.63)E-04
Carbonyls		Tetracosane	(9.55 ± 9.06)E-04
Formaldehyde	(8.32 ± 4.82)E-03	Hexacosane	(7.82 ± 7.96)E-04
Acetaldehyde	(5.21 ± 2.06)E-03	Octacosane	(7.37 ± 6.02)E-04
Acetone	(3.12 ± 2.15)E-03	Triacontane	(3.99 ± 2.41)E-04
Acrolein, Propionaldehyde, Crotonaldehyde, Methyl ethyl ketone, Methacrolein, Butyraldehyde, Benzaldehyde, n-Valeraldehyde, m- Tolualdehyde, Hexaldehyde	< 0.53E-03	Pyrene	(4.76 ± 1.48)E-05
PAHs* and Alkanes		Benz(a)anthracene	(8.19 ± 1.15)E-06
Naphthalene	(3.36 ± 1.06)E-02	Chrysene	(8.89 ± 0.84)E-06
Acenaphthylene	(2.35 ± 0.53)E-05	Benzo(b)fluoranthene	(6.35 ± 1.17)E-06
Acenaphthene	(1.16 ± 0.63)E-04	Benzo(k)fluoranthene	(4.73 ± 0.83)E-06
Dodecane	(2.34 ± 0.19)E-04	Benzo(a)pyrene	(1.62 ± 0.15)E-05
		Indeno(1,2,3-cd)pyrene	(4.86 ± 1.04)E-06
		Dibenzo(a,h)anthracene	(3.64 ± 1.02)E-06
		Benzo(ghi)perylene	(2.66 ± 1.02)E-05

*BTEX = Benzene, Toluene, Ethylbenzene, and Xylenes, **PAH = Polycyclic Aromatic Hydrocarbon

***SO₂ gas data is calculated from the sulfur level in the fuel as per ISO 8178 (15).

Table 5.3: Particulate Stack Emission Factors

Compound	Emissions Factor (g/kWhr)
Particulate Mass (PM)*	2.62 ± 0.03
Sulfate as $\text{H}_2\text{SO}_4 \bullet 6.5\text{H}_2\text{O}$	1.87 ± 0.24
Sulfate (dry)	0.84 ± 0.11
Organic Carbon (OC)	0.193 ± 0.004
Elemental Carbon (EC)	0.007 ± 0.001
Ash**	0.085

*Particulate mass measurements were made after filter equilibration at RH = 40% and T = 25 °C (see Section 5.8.1.2 of the Supporting Information for details)

** Ash emission factor estimated from the ash content in the fuel.

Table 5.4: Summary of absorption coefficient and non-refractory (n.r.) dry particulate composition in the ship exhaust plume at various plume ages.

Est. Plume Age (min)	0	24	62	<i>Out of Plume</i>
Altitude (m)	30	30	55	35-220
Sulfate (% n.r. dry mass)	68	67	70	73
Organic Mass (% n.r. dry mass)	31	31	28	18
Nitrate (% n.r. dry mass)	<1	<1	<1	1
<i>NH₄:SO₄</i> (mol ratio)	0.1	0.1	0.1	0.5
<i>m/z 57:Org</i> (% n.r. dry mass)	4	3	2	0.6
<i>m/z 44:Org</i> (% n.r. dry mass)	3	5	8	17
<i>Oxalate:Org</i> (% n.r. dry mass)	1	1	2	9
<i>Org Acids:Org</i> (% n.r. dry mass)	2	1	2	9
<i>CN:SO₄</i> (10^{15} g^{-1})	2.6	2.5	2.3	0.25
<i>B_{ABS}:SO₄</i> ($\text{Mm}^{-1} \text{ g}^{-1}$)^a	2.4E5	2.8E5	--	--

^a Measured at 532 nm by the PSAP

Table 5.5: Gas and particulate emission factors in g (kg fuel)⁻¹ from this and previous studies of emissions from ships burning heavy fuel oil.

	This Study	Petzold et al. 2008, 2004 (9, 11)	Chen et al. 2005 (54)	Sinha et al. 2003 (3)	Hobbs et al. 2000 (7)
NO_x (as NO*)	65.7 ± 0.3 ^b	112 ^a	30 ± 12 ^c	65.5 ± 3.3 ^c	23 ± 5 ^c
CO	1.5 ± 0.1 ^b	--	--	3.0 ± 0.2 ^c	--
SO₂	59.7 ± 0.5 ^a	51 ^a	27 ± 4 ^c	52.2 ± 3.7 ^c	62 ± 25 ^c
PM	12.9 ± 0.1 ^b	--	--	--	--
EC	0.04 ± 0.01 ^b	0.18 ± 0.02 ^d	--	--	--
OC	0.98 ± 0.03 ^b 1.3 ± 0.5 ^c	--	--	--	--
Sulfate	4.3 ± 0.5 ^b	--	--	--	--
CN 10¹⁶	1.3 ± 0.2 ^{c,e}	1.36 ± 0.24 ^{c,e} 3.43 ± 1.26 ^{d,e}	4.7 ± 1.3 ^c	6.2 ± 0.6 ^c	1.6 ± 0.5 ^c
CN 10¹⁵ (0.1-3 μm)	0.6 ± 0.1 ^c	2.3 ± 0.7 ^c	--	5.1 ± 0.5 ^c	--
CCN/CN (0.3% S)	0.24 ± 0.05 ^c	--	--	0.18 ± 0.07 ^c	--
OM:SO₄	0.42 ± 0.02 ^c	0.54 ^d , 0.17 ^{d**}	--	--	--

*Form of NO_x not specified in Petzold et al.

**OC:SO₄ ratio given in Petzold et al. (2004)

^aCalculated based on fuel composition

^bIn-stack measurement

^cAirborne plume measurement

^dTest-bed MAN B&W four-stroke marine diesel engine. **from Petzold et al. (2004)

^eCN emissions factor reported for CN > 10 nm (reported in the current study because the 3025 CPC gave suspect results in the emissions plume)



Figure 5.1: Photograph taken of the container ship from the cabin of the CIRPAS Twin Otter (the plane's wing tip is in the foreground) during the study. The exhaust plume is visible traveling with the mean wind at $\sim 10^\circ$ angle to the heading of the ship, which can be inferred by the visible wake.

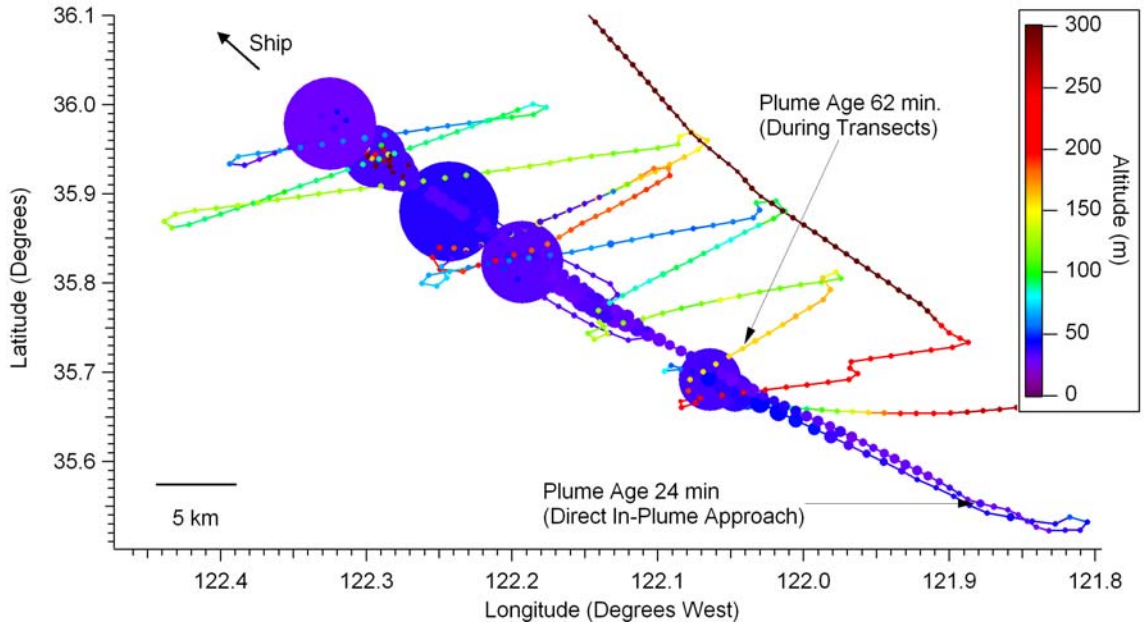


Figure 5.2: Flight track of the CIRPAS Twin Otter during the ship exhaust plume study on July 16, 2007. Marker size is proportional to the mass of sulfate in the particulate phase. The aircraft flew a series of 4 in-plume approaches to the ship. During the first approach, the estimated exhaust age at the point where the aircraft entered the plume was 24 min. This and each subsequent approach ended when the aircraft reached the stern of the ship, identifiable by the very large sulfate loadings observed there. After finishing the in-plume approaches, a series of 11 downwind transects were flown with the maximum plume age observed during the transects being 62 min. While the location of the 62 min transect may appear closer to the ship than the in-plume observations, it is important to remember that this transect was performed long after the in-plume approaches were finished when the ship had traveled beyond the area shown in the figure.

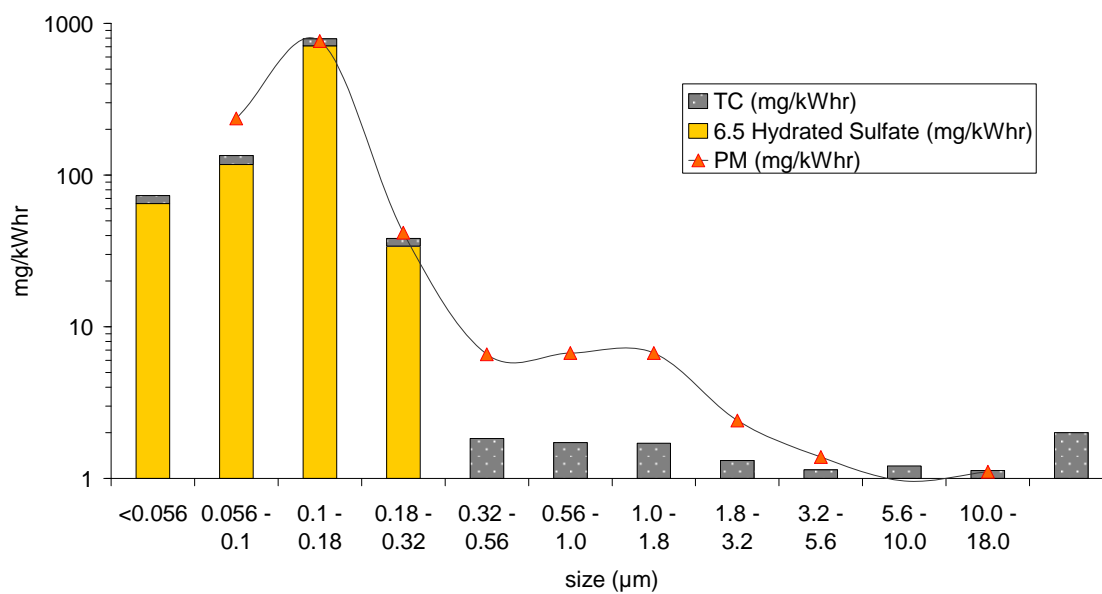


Figure 5.3: Size-resolved particulate chemical composition obtained through the MOUDI/filter setup in the ship's stack. The ratio of Total Carbon (TC) mass to hydrated sulfur ($\text{H}_2\text{SO}_4 \cdot 6.5\text{H}_2\text{O}$) mass remains relatively constant with size (12% < 0.056 μm , 14% 0.056-0.1 μm , 9% 0.1-0.18 μm , and 12% 0.18-0.32 μm).

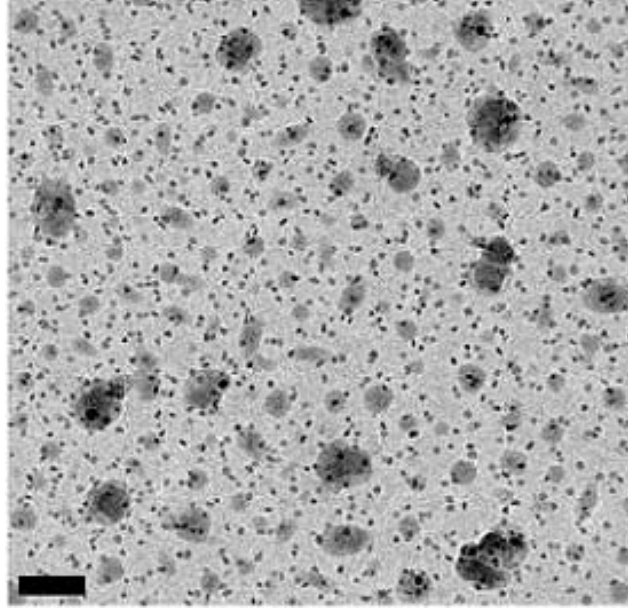


Figure 5.4: TEM image (scale bar in lower left corner = 100 nm) of particles collected with the in-stack thermophoretic sampler. Two classes of particles are observed: 1) nanoparticles in the size range of 5 to 8 nm, and 2) larger particles in a wide size ranges from 30 to over 100 nm. The nanoparticles outnumber the larger particles. EDS analysis showed distinctive peaks of sulfur and vanadium from both classes of particles.

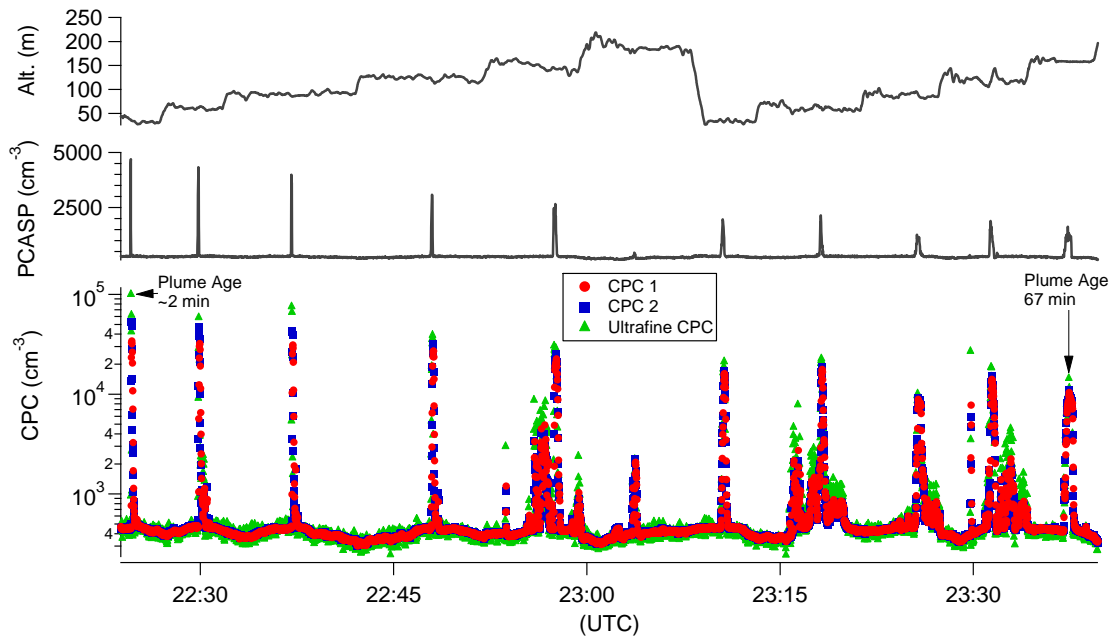


Figure 5.5: Time series of the aerosol number concentration measurements from the TSI 3010 and 3025 CPC's showing significant ultrafine particle concentrations at plume ages up to 1 h. The low PCASP concentrations indicate that the vast majority of particles in the ship exhaust plume are less than 100 nm in diameter. Plume passes were made at several different altitudes.

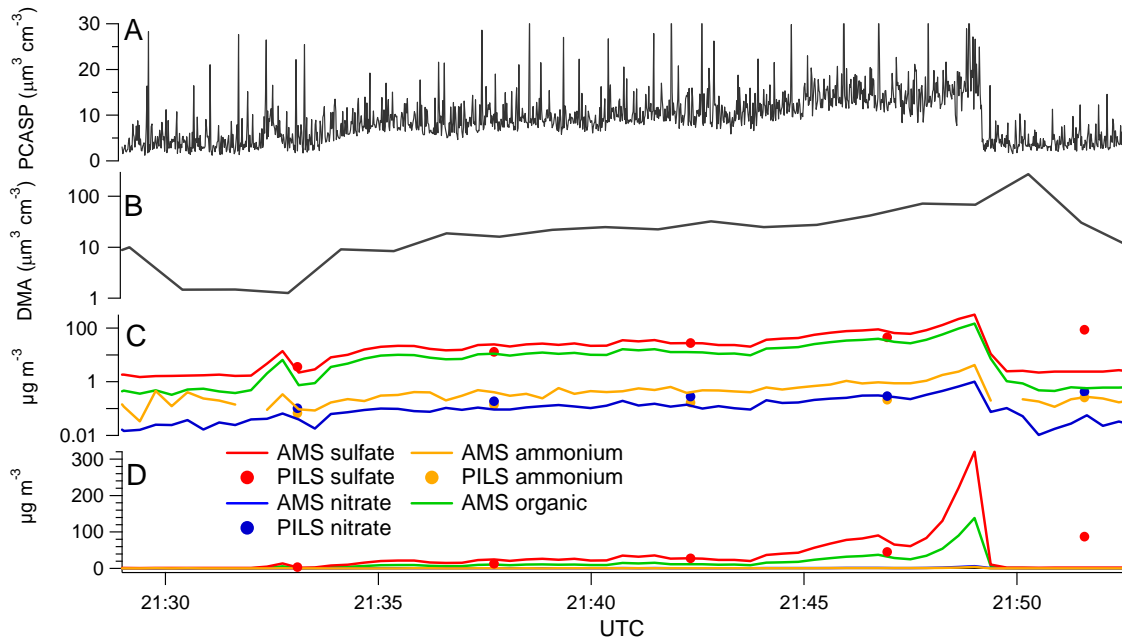


Figure 5.6: Time series of all instruments measuring aerosol mass or volume during the first in-plume approach to the ship. **(A)** PCASP particle volume. **(B)** DMA particle volume. **(C and D)** AMS and PILS measurements of particle chemistry shown on a log and linear axis respectively. The plane first enters the exhaust plume at 21:32 UTC, at which point the plume has aged for ~ 24 min since being emitted from the ship. The plane reaches the stern of the ship at 21:49, though the response of the DMA and the PILS is delayed because of averaging time within the instruments.

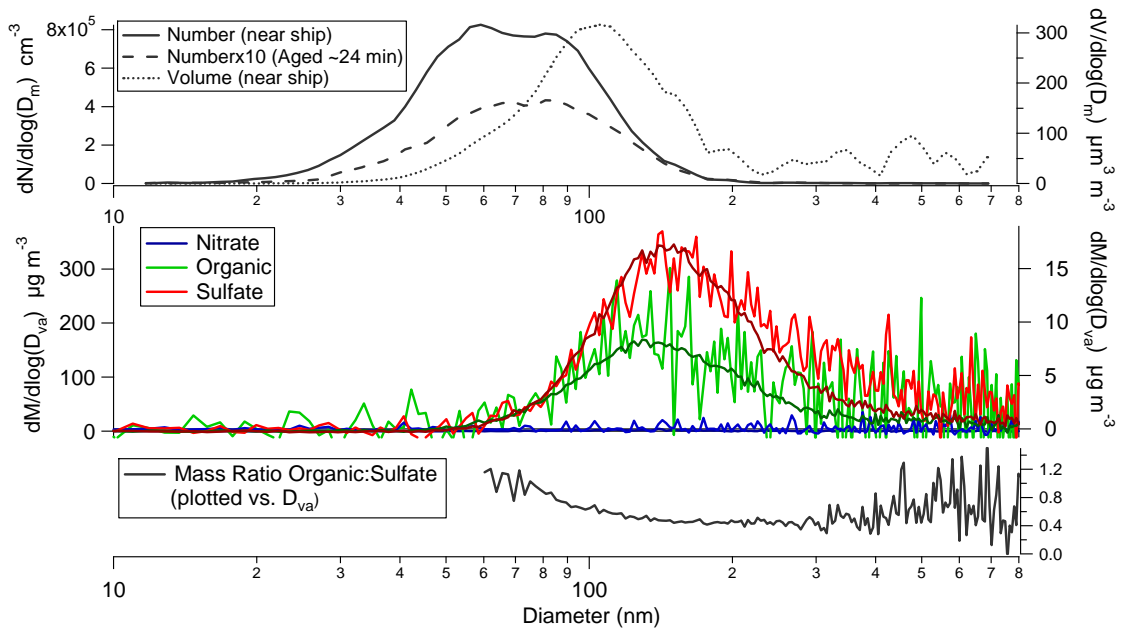


Figure 5.7: Top Panel: Particle number and volume distributions measured by the DMA (at $\sim 45\%$ RH) at different plume ages during the first in-plume approach to the ship. While there is a dramatic reduction in particle number as the plume is diluted, the peak position of the number distribution changes relatively little with plume age. **Middle Panel:** Chemically resolved mass distribution during the first in-plume approach to the ship. The noisy distributions (right axis) correspond to measurements made after the plume had aged for ~ 24 min while the much smoother distributions (left axis) were obtained in the fresh plume immediately behind the ship. Again, there is little change other than a decrease in particle mass. **Bottom Panel:** The organic:sulfate mass ratio measured by the C-ToF-AMS in the ship exhaust plume.

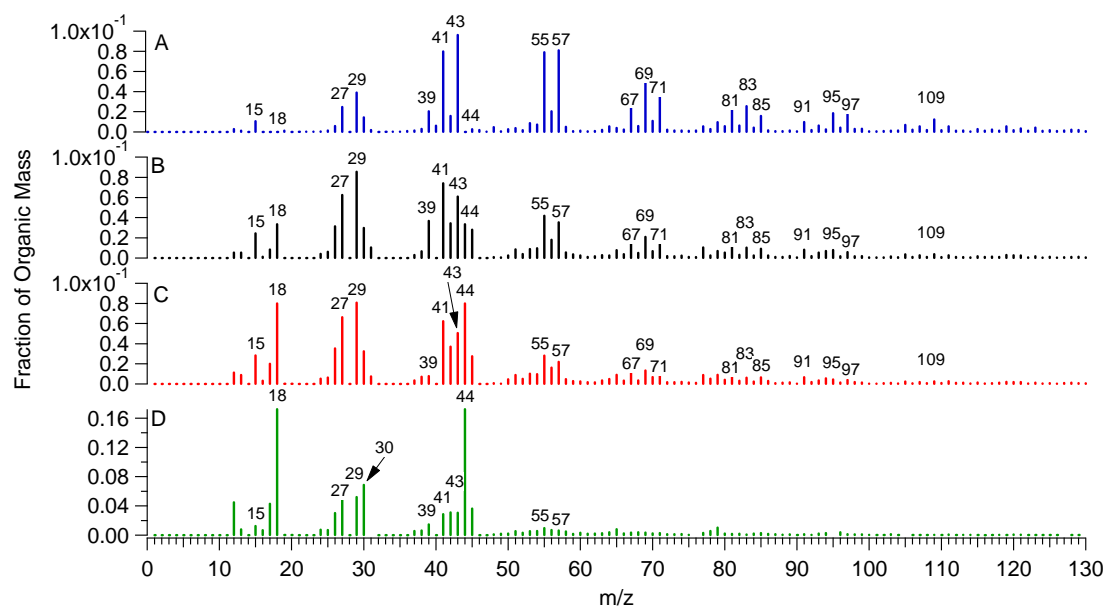


Figure 5.8: (A) Reference AMS organic mass spectrum from the diesel bus chase study of Canagaratna et al. (48). C-ToF-AMS organic mass spectra from (B) the ship exhaust plume a few hundred meters behind the stack, (C) the ship exhaust plume after it had aged for ~ 62 min, (D) background aerosol in the marine boundary layer outside of the ship exhaust plume. Signal at m/z 39 (typically indicative of potassium and not included in organic spectra) is shown because, based on peak location in the raw spectra (not shown), it does not appear to be potassium. Both spectra (A) and (B) strongly resemble the ship-exhaust organic AMS spectra observed by Phinney et al.(49).

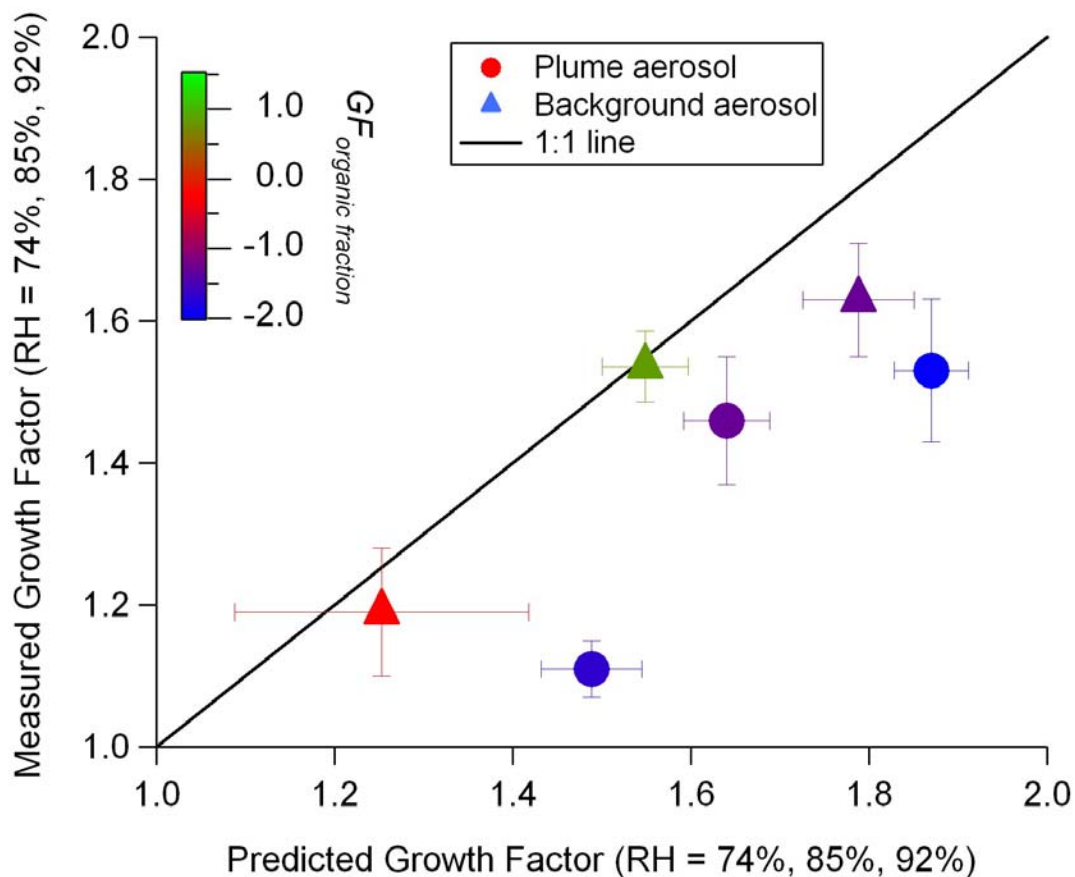


Figure 5.9: Hygroscopic growth factors for particles measured by the DASH-SP and predicted using the volume-weighted mixing rule using bulk chemical composition from the C-ToF-AMS and the assumption that organics have a growth factor of unity. Growth factors are smaller within the exhaust plume than in the background aerosol. Growth factors are suppressed relative to predictions in both the background and the plume aerosol, but the suppression is significantly more dramatic within the exhaust plume. The organic mass fraction is 0.28 ± 0.02 within the plume and 0.20 ± 0.15 outside of the plume. The color scale gives the growth factor that the organic fraction would be required to have to achieve closure between measurements and observations.

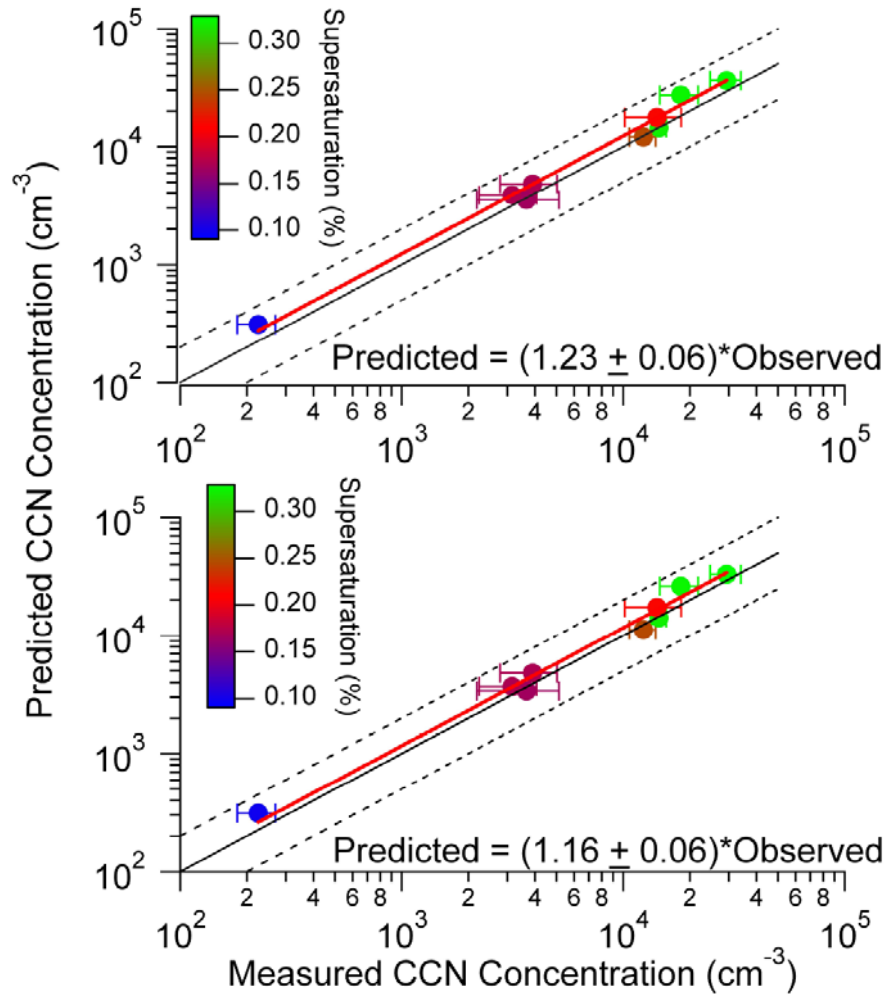


Figure 5.10: CCN droplet closure within the exhaust plume. **Top Panel:** Results obtained using bulk (size-averaged) chemistry. **Bottom Panel:** Results obtained when size-resolved chemistry is used in the calculations. Size-resolved chemistry slightly improves the closure. The color of the markers corresponds to the CCNc instrument operating supersaturation during the measurement. Dashed lines indicate values that are twice and one half of the 1:1 line, while the red lines indicate the least squares best fit. The slopes of the least squares fits are given in the predicted vs. observed equations at the bottom of each panel.

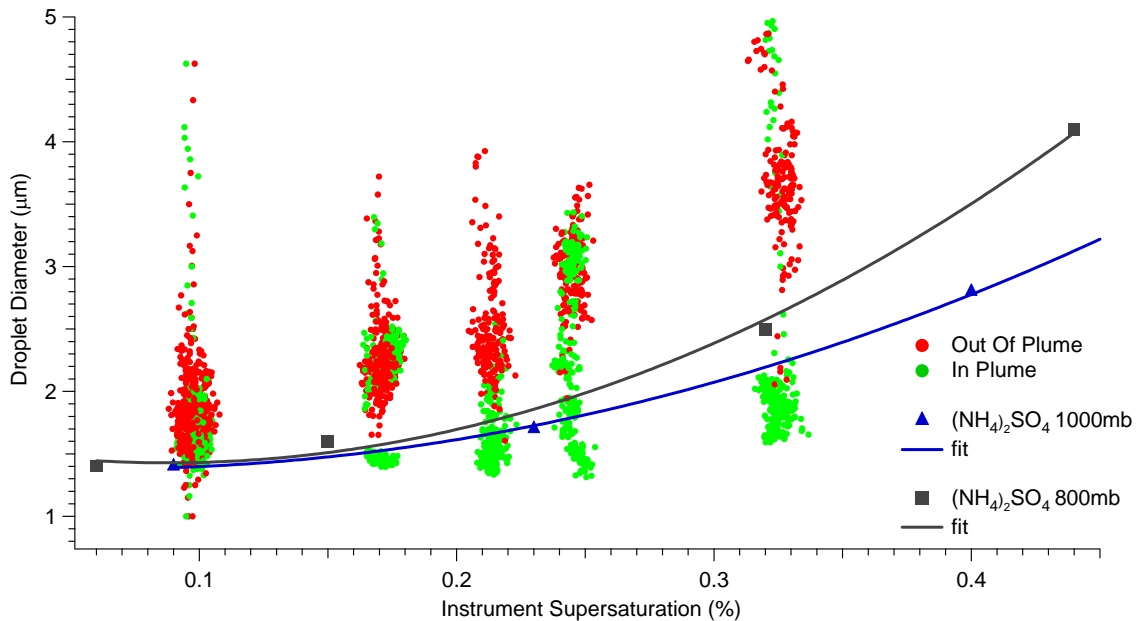


Figure 5.11: Growth kinetics plot for aerosol in and out of the ship exhaust plume. All measurements were made between 845 and 900 millibar, near the middle of the pressure range defined by the two ammonium sulfate calibrations shown in the figure. The calibration lines represent the final diameter achieved by ammonium sulfate particles with the minimum diameter required for activation at the given supersaturation. The vast majority of background particles grow to diameters greater than the minimum defined by the calibrations while the rate of growth of particles within the exhaust plume appears to be suppressed relative to that of ammonium sulfate.

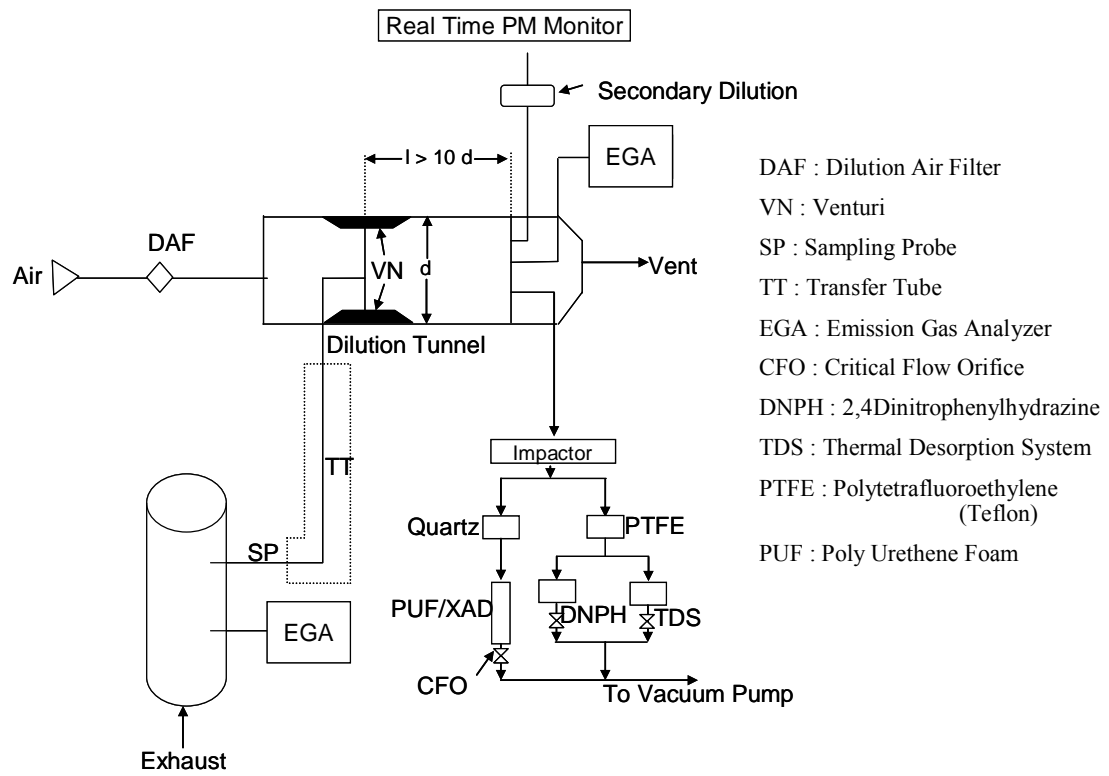


Figure 5.12: Flow Diagram of the Sampling System used on-board the container ship.

No transfer tube was used in this study.

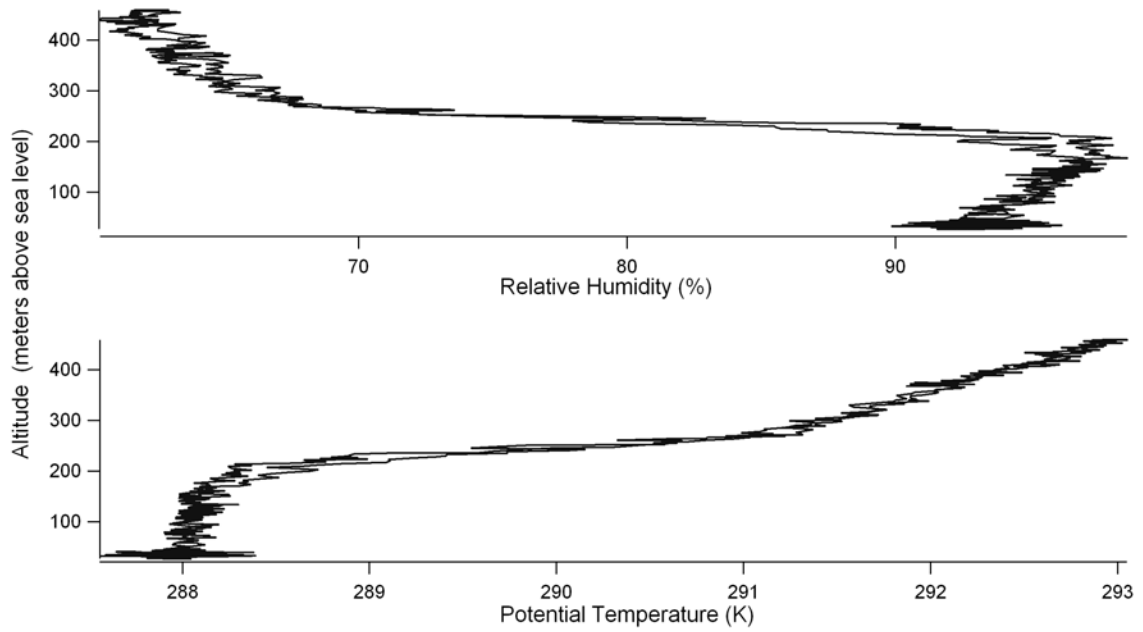


Figure 5.13: Vertical profiles of relative humidity and potential temperature during the study. Each plot has two traces, representing data from an ascent and a descent through the marine boundary layer.

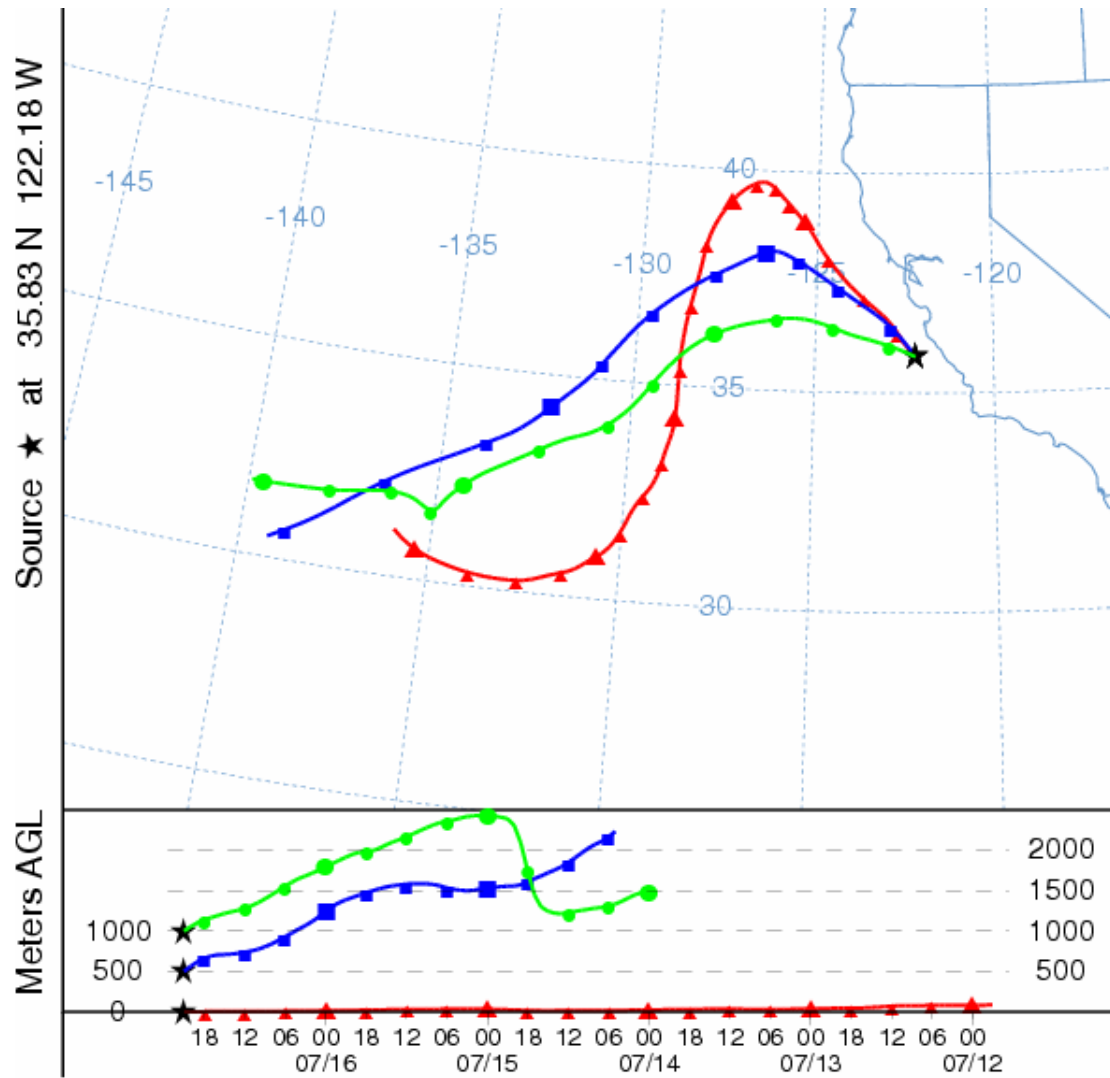


Figure 5.14: NOAA Hysplit three-day back trajectory for the air mass present during the study. At all altitudes, the air originates from the west and does not appear to be subject to recent continental influence.

Chapter 6

Conclusions and Future Studies

6.1 Conclusions

This thesis has focused on the composition of atmospherically relevant aerosols. Composition was shown to be a key tool in determining how aerosols are formed in both chamber experiments and airborne field studies. While many techniques were used to measure composition, special focus was given to mass spectrometry and online mass spectrometry in particular. The use of online mass spectrometry was critical for both the chamber experiments and the field experiments presented. In the chamber, while offline techniques based on extracting filters allow for detailed chemical identification of a fraction of the aerosol mass, online mass spectrometry allows for quantification of the entire aerosol mass. As shown in Chapter 2, the combination of online and offline mass spectrometric techniques is an important step to confirm that chemical products observed in using various offline techniques are not the result of the extensive extraction and preparation steps needed for those techniques. In the field, online mass spectrometry is the only method currently available with the speed and sensitivity necessary to make quantitative, size-resolved measurements of aerosol chemistry in narrow emission plumes near source regions. As discussed in Chapters 4 and 5, while the C-ToF-AMS online aerosol mass spectrometer is fast and sensitive, uncertainties in the collection efficiency make it necessary to compare the results from this instrument with as many other instruments as possible if quantitative results are desired (in this thesis comparisons were most frequently made with the PILS-IC and DMA). An area of great interest for the future is the incorporation of light scattering into the AMS to enable determination of the collection efficiency without the need for further instrumentation (Cross et al., 2008).

Chapters 2 and 3 presented chamber results for chemical compounds that had previously been largely overlooked in terms of aerosol production, isoprene and amines. While isoprene was known to have large gas-phase concentrations (emissions of ~ 500 Tg year⁻¹), it was not understood how its oxidation products could have low enough vapor pressures to form aerosol. Amines and their oxidation products were also thought to be much too volatile for aerosol production. While the aerosol yield from isoprene (see Appendix A for details) is modest (roughly 1-3 percent), its gas-phase emissions are so large that this small yield significantly impacts global secondary organic aerosol (SOA) burdens. On the other hand, because amines are strong bases and form extremely nonvolatile salts when reacted with acidic species, the aerosol yields from atmospheric reactions of amines can approach 100 percent under the right conditions. The potential for high aerosol yields and the fact that amines are the only atmospheric bases other than ammonia, mean that amines play a significant role in aerosol formation even though their emissions are relatively modest.

Chapter 2 described in detail the mechanism by which the oxidation products of isoprene can obtain low enough volatilities to enter the aerosol phase. Under high-NO_x conditions a key part of the answer is the formation of low volatility oligomers of 2-methylglyceric acid through esterification reactions; these oligomers account for ~ 22 – 34% of the aerosol mass. Confirmation of the existence and mass spectral properties of the oligomers using online mass spectrometry was crucial to confirm that the oligomers did not form on filters during aerosol collection or extraction. Under low-NO_x conditions a major fraction of the aerosol mass forms peroxides that are non-volatile enough to enter into the aerosol phase. In both low and high-NO_x photooxidation

experiments of isoprene, compounds were identified that have also been identified in ambient aerosol (C_5 alkene triols and 2-methyltetrols and 2-methylglyceric acid).

Identification of these compounds is a key finding because it confirms that the reactions occurring in the chamber are at least partially relevant to what occurs in the actual atmosphere.

During both the low- NO_x isoprene photooxidation experiments and the amine photooxidation experiments, aerosol mass formed and then decayed back to the gas-phase. In both cases, this is thought to be the result of equilibria shift as species are further reacted in either the gas or aerosol-phase. For isoprene oxidized in low- NO_x conditions, it appears that peroxides initially form aerosol and then are released back to the gas-phase. It is unclear whether the equilibrium shift of peroxides back to the gas-phase occurs because gas-phase peroxides are further reacted or because particle phase peroxides are reacted to form more volatile species. For amine photooxidations, aminium salts are formed at the beginning of photooxidation and return to the gas-phase as the experiment proceeds. In this case, the shift of the aminium salts back to the gas-phase could be caused by the further reaction of gas-phase amines, particle-phase amines, or the loss of nitric acid to the chamber walls. Independent of the exact mechanism of particulate mass loss, both the isoprene and amine experiments clearly show cases where the aerosol formed is semi-volatile and in a sensitive equilibrium with the gas-phase. For both the low- NO_x isoprene and amine photooxidations, aerosol-phase species which did not repartition back to the gas-phase as the reaction proceeded were also formed. In the case of isoprene, these non-volatile products appeared to consist largely of oligomers while for the amine system they were highly oxidized, non-salt, organics.

Aminium nitrates observed in the chamber reactions of Chapter 3 were quantified in ambient aerosol during the airborne study of a major bovine source described in Chapter 4. Both diethylamine (DEA) and ethylamine (EA) aerosol were observed during the study, though the mass of DEA was significantly higher and constituted up to 6 % of the observed total organic mass. The observation that diethylammonium nitrate was the most abundant aminium nitrate in the plume from the bovine source is consistent with it having the lowest theoretical dissociation constant of all amines considered in the thermodynamic calculations presented in Chapter 3. The ambient results of Chapter 4 show that amines are important atmospheric bases even in the presence of ammonia. Particulate amine concentrations are estimated to be 14–23% of that of ammonium in the aerosol plume from the bovine source. Emissions from the source were also shown to contain significant amounts of organics, ammonium, and nitrate with organics being the dominant chemical component constituting ~ 56–64% of the aerosol mass. This organic mass was found to suppress both the sub and supersaturated water uptake behavior of aerosols in the plume from the bovine source.

In Chapter 5, organics were found to constitute a larger fraction of the total aerosol mass emitted from container ships than previously estimated. For the ship studied, the mass ratio of particulate organic carbon to sulfate at the base of the stack was 0.23 ± 0.03 , increasing to 0.30 ± 0.01 in the airborne exhaust plume. This organic mass was found to be hydrophobic, significantly suppressing the subsaturated hygroscopic growth of particles in the ship-exhaust plume. The mass spectra of the organic aerosol in the exhaust plume strongly resembles hydrocarbon-like organic aerosol (HOA) from other diesel sources and there is no sign of oxidation or aging of the organic aerosol

within the first hour after emission. The organic aerosol mass is also not observed to repartition to the gas phase as the exhaust plume dilutes into the marine boundary layer. Organic mass was observed to be concentrated largely in particles below 100 nm in diameter, a significant finding given that these smaller diameters are where particles begin to be active as cloud condensation nuclei. A significant number of ultrafine particles were also observed during the study which could have implications for human health in coastal cities.

6.2 Future Studies

6.2.1 Tracing Organic Aerosol Production from Cloud Processing Reactions

A main focus of this thesis has been the formation of organic aerosol; the thesis described organic aerosol that was emitted as a primary emission, formed secondarily as the result of photooxidation or ozonolysis, and formed secondarily as the result of organic salt formation. A route that was not discussed, but is thought to be atmospherically important, is the formation of organic aerosol through liquid phase reactions in cloud droplets or high humidity aerosol.

Data that has been collected during the airborne field campaigns conducted for this thesis may have the potential to lend insight into this route of organic aerosol production. Preliminary analysis of data from field projects in Ohio, the Gulf of Mexico and Houston, and the Central California Coast indicate that the fraction of the total particulate organic mass composed of oxalate is significantly higher when an airmass has interacted with clouds. Additionally, the m/z 44 peak in the C-ToF-AMS (m/z 44 = CO_2^+ and is a marker peak for oxidized organics) appears to have much higher correlations

with oxalate mass when an airmass has been exposed to clouds or very high humidity. Determining the exact relationship between oxalate, total organic mass, and m/z 44 will be complicated by the fact that certain primary emissions, including ship and truck exhaust, contain oxalate. Nonetheless, this avenue of research is promising and may provide a tracer for when aerosols have been processed by clouds.

6.2.2 Determining the Chemical Characteristics of Ice Nuclei

In addition to focusing on the formation of organic aerosol, another focus of this thesis was the impact of organics on the hygroscopic growth and activity as cloud condensation nuclei of ambient aerosols. All of the research presented in the thesis focused on nucleation of liquid clouds. The Ice in Clouds Experiment-Layer Clouds (ICE-L) was conducted on the NCAR C-130 research aircraft from October 25th to December 16th, 2007, with the aim of quantifying the aerosol and microphysical conditions necessary for first ice formation in the troposphere. During the 3 test flights and 12 research flights conducted along the Front Range of the Rocky Mountains in Colorado and Wyoming, numerous ice-forming wave (or layer) clouds and several mixed-phase upslope cloud events were observed. The ICE-L mission was the first airborne campaign in which detailed aerosol chemistry and ice nuclei (IN) measurements were made outside of a cloud, followed by identical measurements of dried ice crystal residuals inside of the cloud. This strategy should enable assessment of the degree to which the chemical characteristics of aerosol entering a cloud determined the rate of ice formation within that cloud. In reality, this is a very complex issue because the water content, temperature and dynamical properties of each cloud must be accounted for before it is possible to determine if chemistry or dynamics played the central role in ice

formation. Nonetheless, the dataset collected during ICE-L, including data from the Caltech C-ToF-AMS, has already yielded insights into the role of aerosol chemistry in ice formation and, while analysis is ongoing, some preliminary results are given here.

Particle chemistry was measured during ICE-L primarily by two instruments: the Caltech Aerodyne Compact Time of Flight Aerosol Mass Spectrometer (C-ToF-AMS) and an Aerosol Time of Flight Mass Spectrometer (ATOFMS) from the Prather group at the University of California San Diego (UCSD). The rationale for deploying two mass spectrometers was that the C-ToF-AMS can provide quantitative mass measurements of non-refractory aerosol species and the ATOFMS, while not equally quantitative, can detect refractory species such as dust and unmodified soot that are thought to be important IN. IN themselves were measured by a Continuous Flow Diffusion Chamber (CFDC) from Colorado State University. When flying through a cloud, ice crystal residuals were fed to both mass spectrometers and the CFDC using a Counterflow Virtual Impactor (CVI) inlet operated by Cynthia Twohy of Oregon State University.

During several wave cloud flights, the chemistry of dried ice crystal residuals measured from the CVI inlet was very different from the chemistry of the out of cloud aerosol. Data from the C-ToF-AMS during Research Flight 3 is given in Figure 6.1. Higher amounts of chloride and organics are found in the ice and mixed cloud residuals than in the out of cloud aerosol. The increase in chloride mass is probably significantly more dramatic than shown because the C-ToF-AMS does not efficiently detect most chloride salts because they do not efficiently volatilize at the instrument's vaporizer temperature of $\sim 550^{\circ}\text{C}$. More ice crystals were formed in these clouds than would be predicted based on the number of heterogeneous IN measured by the CFDC at the

temperature of the flight level within the cloud, indicating that some of the ice measured may have been homogeneously frozen droplets falling from above. Nonetheless, the chemical results clearly show that certain chemical species, predominantly salts and organics, preferentially formed ice crystals. Currently analysis is underway to determine if this occurred because larger sized particles had higher salt and organic content or if chemistry alone was driving the process. While ice formation near homogeneous freezing temperatures was not the original focus of ICE-L, information on which particles freeze first in this temperature regime is very relevant to cirrus and other high tropospheric clouds, which are perhaps the most relevant ice clouds for climate.

6.3 References

- 1.) Cross, E. S., et al. (2008), Sources and Transformations of Organic Aerosol Particles Measured With a new Single Particle Technique During the MILAGRO 2006 Field Campaign in Mexico City, Eos Trans. *AGU*, 89(53), Fall Meet. Suppl., Abstract A22B-08

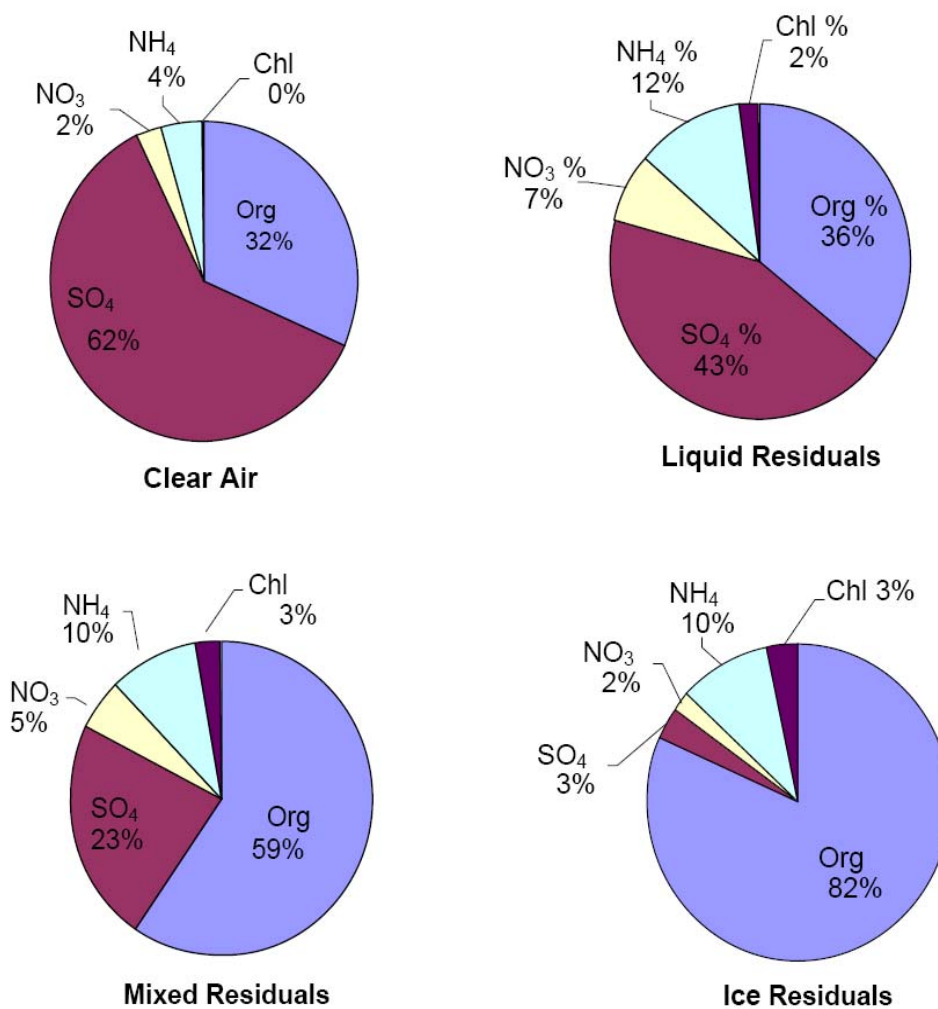


Figure 6.1: C-ToF-AMS data from Research Flight 3 of the ICE-L field campaign showing enhanced organic and chloride in mixed phase and ice clouds. Chemical measurements within cloud were made using a counterflow virtual impactor to measure the chemistry of evaporated cloud droplets and ice crystals.

Appendix

Appendix A

Secondary Organic Aerosol Formation from Isoprene Photooxidation*

*This chapter is reproduced by permission from “Secondary organic aerosol formation from isoprene photooxidation” by J. H. Kroll, N. L. Ng, S. M. Murphy, R. C. Flagan, J. H. Seinfeld, A. Lee., and A. H. Goldstein, *Environmental Science and Technology*, 40, 1869-1877, 2006. Copyright 2006. American Chemical Society.

Secondary Organic Aerosol Formation from Isoprene Photooxidation

JESSE H. KROLL, NGA L. NG,
SHANE M. MURPHY,
RICHARD C. FLAGAN, AND
JOHN H. SEINFELD*

*Departments of Environmental Science and Engineering and
Chemical Engineering, California Institute of Technology,
Pasadena, California 91125*

Recent work has shown that the atmospheric oxidation of isoprene (2-methyl-1,3-butadiene, C₅H₈) leads to the formation of secondary organic aerosol (SOA). In this study, the mechanism of SOA formation by isoprene photooxidation is comprehensively investigated, by measurements of SOA yields over a range of experimental conditions, namely isoprene and NO_x concentrations. Hydrogen peroxide is used as the radical precursor, substantially constraining the observed gas-phase chemistry; all oxidation is dominated by the OH radical, and organic peroxy radicals (RO₂) react only with HO₂ (formed in the OH + H₂O₂ reaction) or NO concentrations, including NO_x-free conditions. At high NO_x, yields are found to decrease substantially with increasing [NO_x], indicating the importance of RO₂ chemistry in SOA formation. Under low-NO_x conditions, SOA mass is observed to decay rapidly, a result of chemical reactions of semivolatile SOA components, most likely organic hydroperoxides.

Introduction

As a substantial fraction of tropospheric particulate matter (PM) is composed of organic material, a detailed understanding of the sources and sinks of condensed organic compounds in the atmosphere is necessary to understand the effects of PM on the earth's climate and human health. A major source of uncertainty is the formation of secondary organic aerosol (SOA), particulate matter that is not emitted into the troposphere directly but rather is formed by gas-to-particle conversion of the oxidation products of volatile organic compounds (VOC's). At present, the global formation of SOA is poorly constrained, with estimates from modeling studies ranging from 12 to 70 Tg/year (1). Such estimates rely critically on laboratory measurements of the amount of SOA produced by individual SOA precursors, typically carried out in large environmental (smog) chambers. From these yield measurements, coupled with atmospheric models, it is now understood that the dominant contributors to global SOA are biogenic hydrocarbons (terpenes and sesquiterpenes), which form SOA primarily by reaction with the hydroxyl radical (OH) and ozone (O₃) (2). Anthropogenic hydrocarbons (most notably aromatic compounds) are also

believed to make a minor contribution to SOA on a global scale (3).

The global emission of biogenic terpenes and anthropogenic hydrocarbons is far lower than that of isoprene (2-methyl-1,3-butadiene, C₅H₈), estimated at ~500 Tg/year (4). Despite this large flux, isoprene has generally not been considered to be an SOA precursor, owing to the high volatility of its known reaction products. First-generation reaction products of the OH-isoprene reaction (under high-NO_x conditions) are well-characterized, with a measured carbon balance approaching 100%; structures and yields are shown in Figure 1. These products are too volatile to partition appreciably into the aerosol phase, and on this basis, isoprene is not expected to form SOA. Pandis et al. (12) and Edney et al. (13), for example, observed no aerosol growth from the photooxidation of isoprene under high-NO_x conditions.

Recent work suggests that isoprene may contribute to organic aerosol formation via heterogeneous reactions. Claeys and co-workers (14–16) have recently measured tetrols with the same carbon backbone as isoprene (as well as related compounds) in a number of atmospheric samples. Such species are likely to be formed by heterogeneous reactions; formation of tetrols has been observed in the aqueous-phase oxidation of isoprene in the presence of acid and hydrogen peroxide (17), as well as in the gas-phase photooxidation of isoprene in the presence of NO_x, SO₂, and ammonium sulfate seed (13). In the latter study only ~6% of the SOA mass observed could be identified (as tetrols and related products), suggesting the formation of other low-volatility compounds. In fact, Limbeck et al. showed (18) that polymeric, humic-like substances are formed when isoprene is passed through filters impregnated with sulfuric acid. Czoschke et al. (19) reported that the (very small) SOA yields from the ozonolysis of isoprene were enhanced in the presence of acidic seed particles, suggesting the polymerization of gas-phase oxidation reaction products as well. Matsunaga et al. (20, 21) measured high concentrations of second-generation isoprene oxidation products (hydroxyacetone, methylglyoxal, and glycolaldehyde) in aerosol samples, which may also suggest heterogeneous reactions leading to enhanced uptake. Additionally, modeling studies (22, 23) predict that water-soluble isoprene oxidation products will be scavenged by clouds, where they may be oxidized to lower-volatility compounds that remain in the condensed phase after droplet evaporation. Thus, isoprene may contribute to SOA via a number of heterogeneous chemical reactions, involving either polymerization or oxidation of isoprene and its reaction products.

In a recent study (24), we provided laboratory evidence that the gas-phase oxidation of isoprene indeed forms SOA. Isoprene oxidation was initiated by the photolysis of nitrous acid (HONO) in the presence of NO_x and ammonium sulfate seed, with SOA (yields of 0.9–3.0%) detected from isoprene concentrations as low as 60 ppb. At smaller concentrations, SOA yields could not be determined, due to the loss of particles to the walls, so SOA formation from isoprene oxidation under tropospheric conditions could not be determined. The difference in these results from those of Pandis et al. (12) and Edney et al. (13) likely arose from lower temperatures (20 °C vs 30 °C) and differences in oxidative conditions. SOA was shown to be formed from the oxidation of first-generation reaction products, but details of the underlying chemistry remain unclear. Many factors that may play a role in SOA formation have yet to be examined, such as reactions by different oxidants (OH, O₃, and NO₃), heterogeneous reactions (such as those outlined above), and NO_x concentration.

* Corresponding author phone: (626) 395-4635; fax: (626) 796-2591; e-mail: seinfeld@caltech.edu.

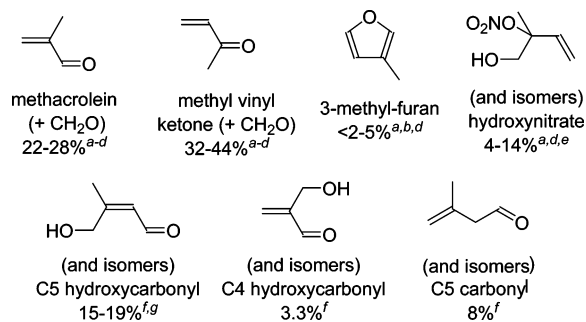


FIGURE 1. Structures and measured yields of first-generation products of the OH-initiated oxidation of isoprene under high-NO_x conditions. ^aTuazon and Atkinson (5). ^bPaulson et al. (6). ^cMiyoshi et al. (7). ^dSprengnether et al. (8). ^eChen et al. (9). ^fZhao et al. (10). ^gBaker et al. (11).

In the present study we examine SOA formation from isoprene in greater detail, to better understand the chemical mechanism of particle growth. The focus of this study is total SOA growth under varying reaction conditions (in particular NO_x and isoprene concentrations); the chemical composition of the SOA is beyond the scope of this work, and will be discussed in detail in a forthcoming paper. In these experiments, hydrogen peroxide (H₂O₂) is used as the radical precursor. H₂O₂ photolysis continually produces OH and HO₂ (from the OH + H₂O₂ reaction) over the course of the experiments, greatly simplifying the gas-phase chemistry. Gas-phase oxidation is dominated by reaction with OH (the primary oxidant of isoprene in the troposphere), with minimal interference by O₃ or NO₃. NO_x can be systematically varied over a wide range of concentrations by the addition of NO, and peroxy radical (RO₂) chemistry is relatively straightforward because any RO₂ formed will react only with HO₂ or NO. Additionally, here we use much lower seed particle loadings than in previous experiments, allowing for the precise measurement of small SOA volumes. From these measurements we are able to better constrain the chemical mechanism of SOA formation from isoprene oxidation, particularly the role of peroxy radicals.

Experimental Section

Experiments are carried out in Caltech's dual 28 m³ FEP Teflon chambers, described in detail elsewhere (25, 26). The chambers are surrounded by banks of blacklights (276 GE350BL) and aluminum sheets for maximum reflectivity. Numerous ports allow both for the introduction of clean air, gas-phase reagents, and inorganic seed, and for various gas-phase and particulate measurements. A differential mobility analyzer (DMA, TSI 3760) measures the size distribution and volume concentration of particles inside the chambers; settings are the same as described in Keywood et al. (26). In most experiments, an Aerodyne Time-of-Flight aerosol mass spectrometer (AMS, described in detail in ref. 27) is also used, for the measurement of mass distributions of particulate organics, sulfate, nitrate, and ammonium. A gas chromatograph coupled with flame ionization detection (GC-FID, HP 5890) allows for the measurement of gas-phase isoprene. GC-FID response is calibrated by sampling from a 60 L FEP Teflon bag into which known volumes of isoprene have been introduced. Temperature, relative humidity (RH), O₃, NO, and NO_x are all continually monitored. Experiments are run in each chamber on alternating days; the chamber that is not in use on a given day is repeatedly flushed with clean air and irradiated with UV light for cleaning.

The radical precursor used in the present experiments is hydrogen peroxide. H₂O₂ is introduced by bubbling 5 L/min of humidified room-temperature air for 2 1/2 hours through

a 50% H₂O₂ solution (Aldrich), through a particle filter to avoid the introduction of droplets, and finally into the chamber. The concentration of H₂O₂ is not measured directly, but from the rate of isoprene decay during irradiation, and literature values of $\sigma_{\text{H}_2\text{O}_2}$, $k_{\text{OH}+\text{isoprene}}$, and $k_{\text{OH}+\text{H}_2\text{O}_2}$ (28, 29), [H₂O₂] is estimated to be ~3–5 ppm; this may decrease somewhat over the course of the experiment due to wall loss, photolysis, and reaction with OH. To minimize potential uptake of H₂O₂ into the particle phase, all experiments are run under dry (RH < 10%) conditions. These conditions are substantially drier than those of the troposphere. The dependence of SOA growth on RH is beyond the scope of this work but warrants future investigation.

After introduction of H₂O₂, ammonium sulfate seed (if used) is introduced by atomization of a 0.015 M solution of (NH₄)₂SO₄ at 30 psi; initial volume concentrations are 4.6–7.1 μm³/cm³. For high-NO_x experiments, a known quantity of NO is then introduced from a 500 ppm gas cylinder (in N₂, Scott Specialty Gases). Typically, some fraction (20–40 ppb) is immediately converted to NO₂, likely from reactions with residual O₃ and NO₃/N₂O₅ in the chamber, and so the chamber is free of any oxidants when hydrocarbon is added. Isoprene (12–90 ppb) is introduced by sending air over a measured volume of the pure compound (Aldrich, 99.8%) and into the chamber.

When all components are well-mixed (measured values of isoprene, NO_x, and seed particle volume are constant), the blacklights are turned on, initiating photooxidation and the beginning of the experiment. Output from the lights in the ultraviolet is between 300 and 400 nm, with a maximum at 354 nm. The very weak absorption cross section of H₂O₂ in this range necessitates the use of more lights than in our prior study using HONO (24); half the available lights are used in the present experiments. Using measurements of photon flux inside the chamber enclosure and known absorption cross sections (28), we calculate J_{NO_2} and $J_{\text{H}_2\text{O}_2}$ to be 0.29 min⁻¹ and 0.00029 min⁻¹, respectively; hence, ppm concentrations of H₂O₂ are required. Heating from the lights leads to a temperature increase inside the chamber of approximately 5 °C over the course of the experiment. The DMA and AMS are both located outside the chamber enclosure and are at the temperature of the surrounding room (~20–22 °C). Thus, the air may cool slightly as it is sampled from the chamber and into the instruments, and the measured aerosol is likely to correspond to gas-particle partitioning at the temperature of the room rather than the temperature at which the gas-phase chemistry occurs. Such temperature differences (≤5 °C) are unlikely to affect results significantly.

Results

Blank Runs. To ensure that all SOA growth observed is indeed from isoprene photooxidation, blank runs are performed regularly over the course of the data collection. Minimal growth (<0.1 μg/m³) is observed from irradiation of mixtures of H₂O₂, NO_x, and/or inorganic seed (with no isoprene present). In addition, from the measured SOA yields and mass spectra, the particle growth observed cannot be the result of a small terpene impurity (~0.2%) in the isoprene. These results are described in detail in the Supporting Information.

Low-NO_x Experiments. Shown in Figure 2 is a typical low-NO_x experiment ([NO_x] < 1 ppb), in which 63.6 ppb isoprene is oxidized in the absence of inorganic seed. Particles are detected after ~40 min of irradiation; aerosol growth is measured using both the DMA and AMS and occurs mostly after all the isoprene has been reacted. AMS data confirm that the new particle mass is organic, with a typical mass spectrum shown in Figure 3. Ozone formation (not shown in Figure 2) of a few ppb is observed, possibly due to residual

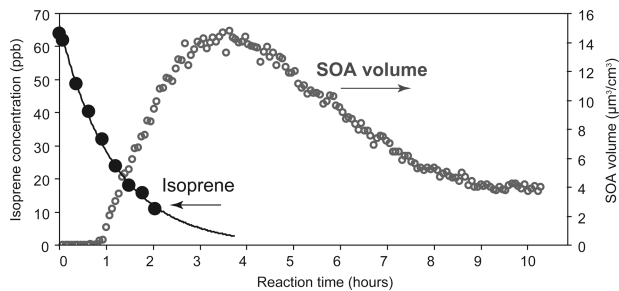


FIGURE 2. Reaction profile of a typical isoprene photooxidation experiment under NO_x -free conditions (Experiment 5).

NO_x emitted by the chamber walls. Such small O_3 concentrations are unlikely to have any appreciable effect on the gas-phase chemistry. After an initial period of aerosol growth, aerosol mass and volume are observed to decrease rapidly to lower final values. This is not a result of the loss of particles to the walls, as it is characterized by a shrinking of the aerosol size distribution rather than a decrease in number concentration. The loss of aerosol mass stops immediately when the lights are turned off, and resumes when the lights are turned back on, suggesting it is not caused by gradual changes in temperature or RH. Possible mechanisms are examined in the Discussion section.

Aerosol growth from isoprene photooxidation is also observed at lower isoprene concentrations (and, hence, smaller organic aerosol loadings). The DMA detects SOA from isoprene concentrations as low as 12.2 ppb; below that, the signal-to-noise is too poor for the detection of growth. Aerosol growth is detected at still lower isoprene concentrations (~ 8 ppb) by the AMS. The mass spectra of the SOA, at maximum growth and at the end of the experiment, are similar to those from the higher-concentration experiments, indicating that SOA formation is indeed significant, even at such low isoprene concentrations and particulate loadings.

Experimental conditions and results from all low- NO_x experiments are given in Table 1. For all these experiments, no inorganic seed is added; the small size of nucleated particles leads to good signal-to-noise of the DMA volume measurement so that very small growths ($< 1 \mu\text{m}^3/\text{cm}^3$) can be measured. Measured increases in aerosol volume are found to be largely insensitive to the presence of ammonium sulfate seed. Two values for the increase in aerosol volume are given in Table 1: “maximum growth” (before the rapid loss of SOA dominates) and “final growth” (once SOA volume and mass have leveled out). All volumes are corrected for losses to the chamber walls, by applying size-dependent first-order loss coefficients, estimated by running “seed-only” experiments in the absence of hydrocarbon (26). SOA yield,

TABLE 1. Experimental Conditions and Results for NO_x -free Experiments^a

expt. no.	isoprene reacted (ppb)	ΔM_0 (max) ($\mu\text{g}/\text{m}^3$) ^b	ΔM_0 (final) ($\mu\text{g}/\text{m}^3$) ^b	SOA yield (%) ^c	T_{max} ($^\circ\text{C}$)
1	90.0	27.0 ± 0.5	9.3 ± 0.4	3.6 ± 0.1	25.4
2	46.1	13.5 ± 0.6	3.8 ± 0.5	2.9 ± 0.3	25.6
3	23.0	2.3 ± 0.5	0.6 ± 0.3	0.9 ± 0.4	26.0
4	12.2	0.7 ± 0.1	0.3 ± 0.1	1.0 ± 0.3	25.7
5	63.6	17.8 ± 0.5	5.0 ± 0.5	2.8 ± 0.3	26.7
6	29.4	6.2 ± 0.8	2.2 ± 0.5	2.6 ± 0.6	28.7
7	47.8	11.1 ± 0.5	3.0 ± 0.4	2.2 ± 0.3	26.6
8	41.6	8.4 ± 0.4	2.4 ± 0.5	2.1 ± 0.5	26.4

^a Stated uncertainties (2σ) are from scatter in particle volume measurements. ^b Assuming an SOA density of $1.25 \text{ g}/\text{cm}^3$. ^c SOA yields from final growth only.

defined as the ratio of mass concentration of SOA formed to mass concentration of isoprene reacted, is given for the final growth only. This requires knowledge of the SOA density, determined by a comparison of aerosol volume (from the DMA) and aerosol mass (from the AMS), as described by Bahreini et al. (30). Density is determined to be $1.25 (\pm 0.1) \text{ g}/\text{cm}^3$ for SOA formed under low NO_x conditions. As is typical for SOA-forming reactions, yields are found to vary with the amount of hydrocarbon reacted (31, 32); the dependence of aerosol growth (both maximum and final growth) on the amount of isoprene reacted is illustrated in Figure 4.

High- NO_x Experiments. The addition of NO to the reaction mixture has a large effect on the gas-phase chemistry, as illustrated in Figure 5 for a typical experiment (42.7 ppb isoprene, 98 ppb NO, 31 ppb NO_2 , $6.4 \mu\text{m}^3/\text{m}^3$ seed). Isoprene decay is far faster than in the low- NO_x case, due to regeneration of OH from the $\text{HO}_2 + \text{NO}$ reaction. This reaction also rapidly converts NO to NO_2 . Ozone formation, from NO_2 photolysis, begins once $[\text{NO}]$ falls below ~ 50 ppb. When $[\text{NO}]$ approaches zero (concentrations of a few ppb), aerosol growth is observed. Aerosol mass and volume typically reach a maximum after ~ 4 h into the reaction; unlike in the low- NO_x case, no rapid loss of SOA is observed.

The mass spectrum of SOA formed from isoprene under typical high- NO_x conditions is shown in Figure 6. SOA composition is clearly different from that formed under NO_x -free conditions (Figure 3), with mass fragments displaying a more ordered, repetitive pattern. Aerosol growth is also observed from the oxidation of ~ 8 ppb isoprene (with 280 ppb NO); the mass spectrum is again the same as that from higher concentrations of isoprene (see Supporting Information).

Measurements of aerosol growth and SOA yield over a range of isoprene concentrations were not carried out for

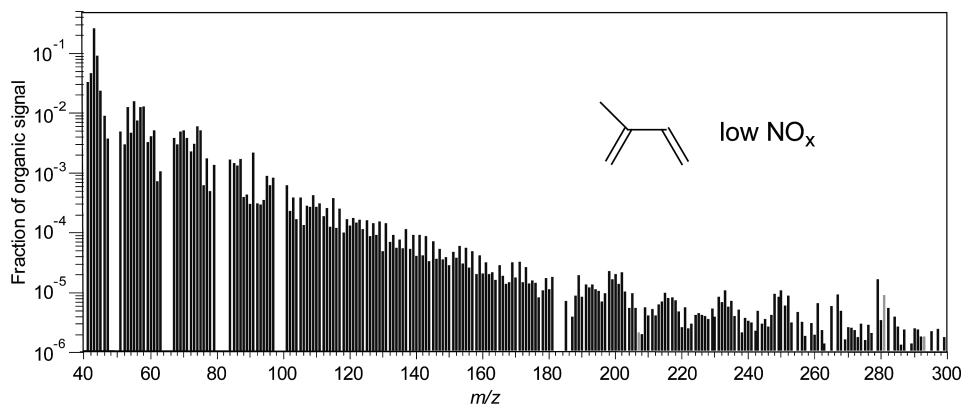


FIGURE 3. Typical AMS spectrum ($m/z \geq 40$) of SOA formed from isoprene photooxidation under low- NO_x conditions. For clarity, masses in which the organics overlap with peaks from sulfate (m/z 48–50, 64–66, 80–83, 98–100) and tungsten (from the filament; m/z 182, 184–186) have been omitted. Light gray bars correspond to negative values after data analysis.

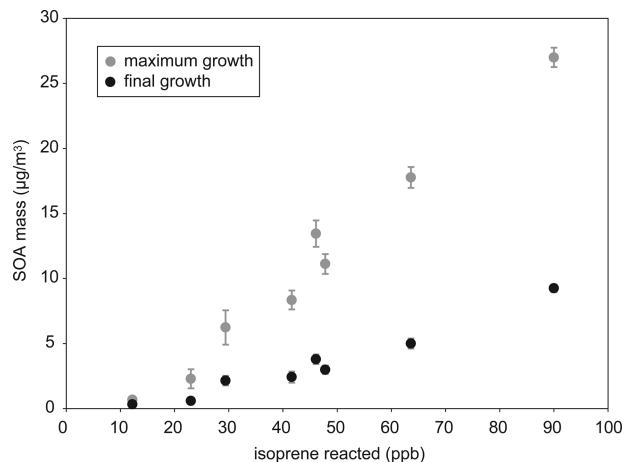


FIGURE 4. Measured SOA growth versus isoprene reacted (low- NO_x conditions). Gray circles: maximum growth; black circles: final growth, after photochemical loss of SOA (see text for details). Each pair of points (at a single value of isoprene reacted) corresponds to one experiment. Data are taken from Table 1; SOA mass is calculated using a density of 1.25 g/cm^3 .

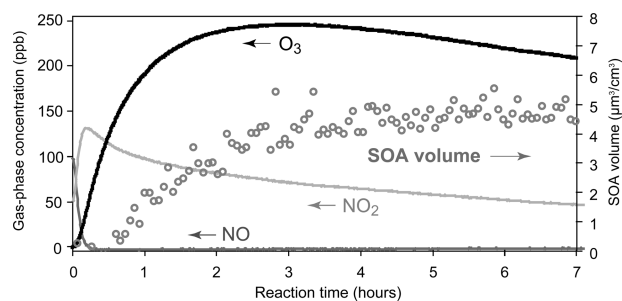


FIGURE 5. Reaction profile of a typical isoprene photooxidation experiment under high- NO_x conditions (Experiment 11). Decay of isoprene is rapid, with most consumed in the first 30 min of reaction, so it is omitted for clarity.

the high- NO_x case because we have presented such results previously (24). Instead, we focus on the dependence of SOA growth on NO_x concentration, in which initial isoprene concentrations are held essentially constant ($45 \pm 4 \text{ ppb}$). Shown in Table 2 are experimental conditions and results for the high- NO_x experiments. Ammonium sulfate seed is used in all cases to provide surface area onto which semivolatile products may condense. Running the reaction in the absence of seed leads to the formation of large number concentrations ($50\,000\text{--}150\,000 \text{ particles/cm}^3$) of very small particles, due to the fast rate of formation of condensable products. Such small particles are lost to the walls very quickly, precluding accurate (wall-loss-corrected) volume measurements, so seed particles are necessary. Under high- NO_x conditions, SOA density is determined to be $1.35 (\pm 0.05) \text{ g/cm}^3$. Shown in Figure 7 is SOA growth versus initial NO_x concentration. The SOA yields measured in these experiments are somewhat higher than those reported in our previous study (24); this may be a result of differences in gas-phase chemistry (such as initial $[\text{NO}_x]$, rate of change of $[\text{NO}_x]$, and the $[\text{NO}]:[\text{NO}_2]$ ratio), photolytic conditions, and/or RH. Understanding these possible effects requires further study. We note that in one previous photooxidation study (33), no RH-dependence of SOA yields was observed.

Isoprene Oxidation Products. Two additional studies are carried out in which methacrolein (500 ppb, Aldrich, 95%) and methyl vinyl ketone (500 ppb, Aldrich, 99%) are photooxidized under high- NO_x conditions (initial $[\text{NO}_x] = 860 \text{ ppb}$). While the oxidation of methyl vinyl ketone produces no SOA,

methacrolein oxidation produces substantial SOA ($170 \pm 1 \mu\text{m}^3/\text{cm}^3$), as reported previously in an experiment using HONO as the radical precursor (24). The AMS spectrum of SOA from methacrolein oxidation is shown in Figure 8.

Discussion

General Mechanism of SOA Growth. In both the low- and high- NO_x experiments, SOA growth does not begin until a significant fraction ($>50\%$) of the isoprene is consumed, and SOA growth continues even after the isoprene is fully consumed. This implies the existence of a rate-limiting step in SOA formation following the initial OH-isoprene reaction. As discussed in previous work (24), this step is likely the oxidation of first-generation reaction products; both double bonds of isoprene must be oxidized, resulting in the addition of up to four polar functional groups to the carbon skeleton. This conclusion is strongly supported by the observation of SOA production from the oxidation of methacrolein, a major first-generation isoprene oxidation product. The role of second-generation products in SOA formation (from the oxidation of isoprene and other biogenic hydrocarbons) is discussed in detail by Ng et al. (34).

Shown in Figure 9 is the simplified mechanism of the initial steps of the OH + isoprene reaction, leading to the formation of first-generation molecular products. The hydroxyl radical adds to one of the double bonds, primarily at the 1- or 4-position, and the subsequent addition of O_2 leads to the formation of six possible isoprene hydroxperoxy radicals (for simplicity, only one is shown in Figure 9). The fate of this radical depends on the level of ambient NO_x . At high NO_x ($[\text{NO}] \gg [\text{HO}_2] + [\text{RO}_2]$), peroxy radicals primarily react with NO. They may also react with NO_2 to form peroxy nitrates (RO_2NO_2), but these are thermally unstable, with lifetimes shorter than 1s, so they are generally unimportant under most conditions. Isoprene hydroxperoxy radicals plus NO forms either hydroxynitrates or hydroxyalkoxy radicals, the latter of which undergo decomposition, isomerization, or hydrogen abstraction by O_2 to form methacrolein, methyl vinyl ketone, and other first-generation isoprene oxidation products shown in Figure 1.

The rates and products of the oxidation reactions of many of these first-generation products are poorly constrained. The oxidation reactions of methacrolein and methyl vinyl ketone are well-studied, with known products accounting for $>90\%$ of the total reaction (35–37). Based on our observation of SOA production from methacrolein oxidation, it is clear that some products of the OH-methacrolein reaction (possibly minor, previously undetected species) are condensable. The similarity between the mass spectrum of SOA from methacrolein oxidation (Figure 8) and that of isoprene oxidation (Figure 6) strongly suggests that methacrolein is a principal intermediate in SOA formation from isoprene photooxidation under high- NO_x conditions. It is not straightforward to quantify the contribution of methacrolein oxidation products to SOA from isoprene oxidation, due to the dependence of gas-particle partitioning on available organic particulate matter (31, 34). Products of the oxidation of other first-generation products, accounting for 20–40% of the OH + isoprene reaction, have, for the most part, not been measured, but may also play a role in SOA formation.

The oxidation of isoprene under low- NO_x conditions has received far less study and so is more uncertain. When concentrations of peroxy radicals (HO_2 and RO_2) approach the concentration of NO, $\text{RO}_2 + \text{HO}_2$ and $\text{RO}_2 + \text{RO}_2$ reactions become competitive with $\text{RO}_2 + \text{NO}$, and a different product distribution is expected (lower half of Figure 9). The reaction of isoprene hydroxperoxy radicals with other RO_2 radicals is expected to lead to a mixture of hydroxycarbonyls, diols, and products from alkoxy radical reactions, such as methacrolein and methyl vinyl ketone, all of which have been

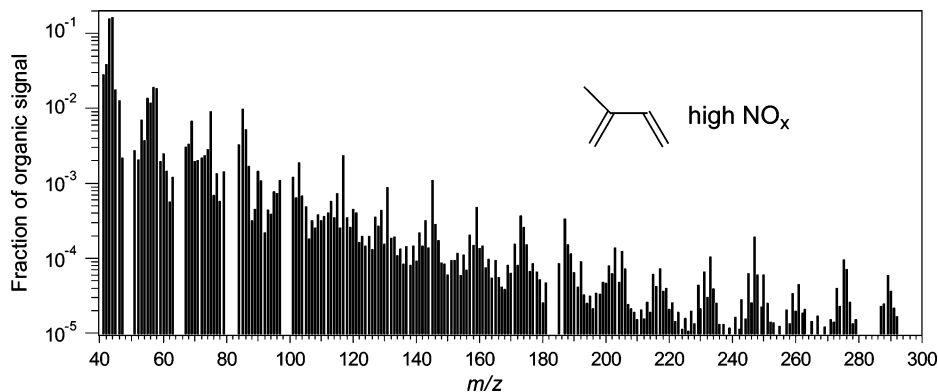


FIGURE 6. Typical AMS spectrum of SOA formed from isoprene photooxidation under high- NO_x conditions. See description of Figure 3 for details.

TABLE 2. Experimental Conditions and Results for High- NO_x Experiments^a

expt. no.	isoprene reacted (ppb)	initial [NO] (ppb)	Initial [NO _x] (ppb)	(NH ₄) ₂ SO ₄ volume (μm ³ /cm ³)	maximum [O ₃] (ppb)	ΔM ₀ (μg/m ³) ^b	SOA yield (%)	T _{max} (°C)
9	46.7	242	266	4.6 ± 0.2	342	6.3 ± 1.0	4.7 ± 0.7	28.3
10	43.5	496	526	7.1 ± 0.3	389	2.9 ± 1.2	2.3 ± 0.9	28.3
11	42.7	98	129	6.4 ± 0.7	245	6.7 ± 1.3	5.5 ± 1.0	28.1
12	49.1	51	78	6.5 ± 0.3	256	5.6 ± 1.3	4.0 ± 0.9	28.2
13	42.7	337	405	4.8 ± 0.2	508	4.6 ± 1.0	3.8 ± 0.8	28.3
14	42.0	708	745	4.7 ± 0.3	492	1.7 ± 1.1	1.4 ± 0.9	27.5

^a Stated uncertainties (2σ) are from scatter in particle volume measurements. ^b Assuming an SOA density of 1.35 g/cm³.

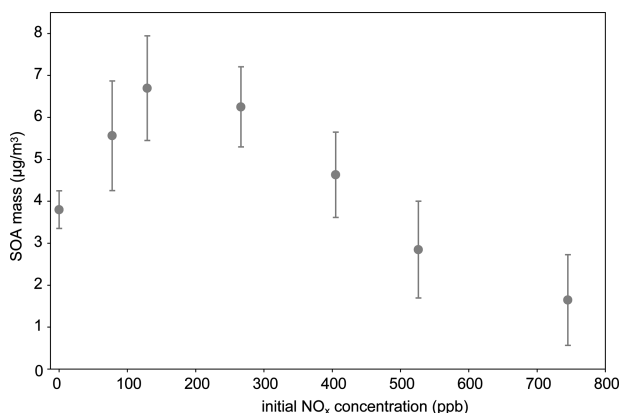


FIGURE 7. SOA growth as a function of initial NO_x concentration, for a fixed isoprene concentration (45 ± 4 ppb). Results shown are from Table 2; the NO_x -free point is final growth from Experiment 2, Table 1.

detected in the laboratory (7, 38–40); yields and carbon balance are not fully established. The hydroxyhydroperoxides expected from the reaction of HO_2 with isoprene RO_2 radicals have not been conclusively identified in the laboratory, though they have been tentatively identified in the troposphere (41). Miyoshi et al. (7) found that under conditions in which the $\text{HO}_2 + \text{RO}_2$ reaction dominates, organic hydroperoxides are formed in high concentrations with no other identifiable gas-phase products. The further reactions of these oxidation products have not been studied. In particular, the tropospheric fate of isoprene hydroxyhydroperoxides is highly uncertain, and the relative importance of photolysis and reaction with OH is largely unknown, as is the product distribution from each channel.

In summary, the lack of experimental data on the second-generation products (and, at low NO_x , even the first generation products) of isoprene oxidation makes it difficult to know the exact chemical mechanism of SOA formation. Under high- NO_x conditions, methacrolein is certainly an important

intermediate in the production of SOA. Numerous pathways may be put forth which lead to the formation of relatively nonvolatile second-generation oxidation products, with 4–5 carbon atoms and 3–4 polar functional (carbonyl, hydroxy, hydroperoxy, nitrate, or acid) groups. Further studies of the gas- and particle-phase products of isoprene oxidation would be useful for identifying the detailed chemistry of SOA formation.

In addition, particle-phase reactions of these products are likely to contribute to SOA formation. From the aerosol mass spectra (Figures 3, 6, and 8), it is clear that oligomers are formed. At both high- and low- NO_x , a significant fraction of the organic mass is from fragments of high molecular weight ($m/z > 200$), corresponding to species with more than five carbon atoms (C5 products will have masses ≤ 226 , the mass of the dihydroxy-dinitrate). An important role of such reactions in SOA formation may explain why methacrolein oxidation forms SOA but methyl vinyl ketone oxidation does not, as aldehydes are substantially more susceptible to nucleophilic attack (and hence oligomerization reactions) than are ketones (42). The chemical composition of the SOA will be discussed in detail in a forthcoming publication.

Role of NO_x . Despite uncertainties in the detailed chemical mechanism of isoprene oxidation, the dependence of SOA growth on NO_x level (Figure 7) provides some insight into the underlying chemistry of SOA formation. At high NO_x (>200 ppb), SOA yield is found to decrease with increasing NO_x ; similar decreases have been observed in a number of SOA yield measurements (12, 43–49). This dependence has been attributed to two effects: (1) relative levels of different oxidants (OH, NO_3 , and O_3) present in the reaction system (45), and (2) the chemistry of peroxy radicals (43, 46, 49). In the present study, OH is the dominant oxidant throughout the course of the experiment, due to the continual production of OH radicals from H_2O_2 photolysis. The O_3 and NO_3 produced in the high- NO_x experiments account for a negligible fraction of the isoprene reacted, because they are only formed once NO concentration is near zero, typically

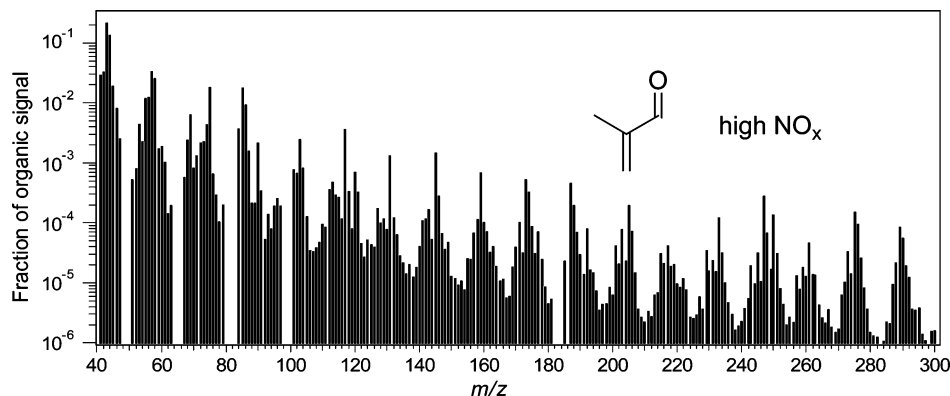


FIGURE 8. AMS spectrum of SOA formed from methacrolein photooxidation under high- NO_x conditions. See description of Figure 3 for details. The spectrum shown is similar to that of isoprene photooxidation (Figure 6), with the same major peaks, suggesting the importance of methacrolein as an intermediate in SOA formation from isoprene oxidation under high- NO_x conditions.

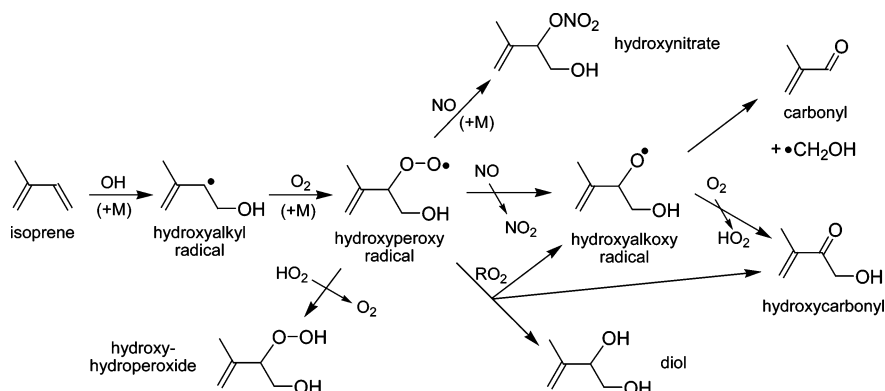


FIGURE 9. Reaction mechanism of isoprene oxidation, showing the formation of first-generation products. For clarity, only one of four possible alkyl radicals and one of six possible hydroperoxy radicals are shown. The first-generation reaction products are all unsaturated so they may be rapidly oxidized to second-generation products.

after all isoprene has been reacted away. Isoprene oxidation products may react with O_3 or NO_3 , but for major oxidation products, such reactions are slow (29) and are expected to be unimportant. There may, however, be exceptions (for example, 3-methyl-furan reacts rapidly with NO_3 (50)), and we cannot rule out the possibility that reactions of O_3 or NO_3 may be sinks for minor isoprene oxidation products.

Nonetheless, all of the oxidation of isoprene, and the oxidation of most of its reaction products, is initiated by the OH radical; the observed NO_x dependence of SOA yields is likely a result not of differences in OH, O_3 , and NO_3 reactions, but of rather differences in peroxy radical chemistry. In the present experiments, organic peroxy radicals will react with either HO_2 (formed in the OH + H_2O_2 reaction) or NO. RO_2 + RO_2 reactions are relatively unimportant because the concentration of H_2O_2 (which reacts with OH to form HO_2) is much higher than that of isoprene (which reacts with OH to form RO_2), and HO_2 + RO_2 reactions are significantly faster than RO_2 self-reactions (51). As mentioned above, peroxy-nitrate formed from RO_2 + NO_2 serves as only a short-lived reservoir of RO_2 . Thus the fate of RO_2 radicals depends on the relative concentrations of HO_2 and NO. At high [NO], alkoxy radicals and organic nitrates will be formed from the RO_2 + NO reaction; small alkoxy radicals are expected to fragment, and organic nitrates may be relatively volatile (49). On the other hand, at low [NO], RO_2 + HO_2 reactions form hydroperoxides, recently shown in both experimental (52) and modeling (46, 53, 54) studies to be important components of SOA. High concentrations of NO, therefore, appear to suppress the formation of SOA by suppressing hydroperoxide formation, consistent with the conclusions of other studies of the NO_x -dependence of SOA formation (43, 46, 49). This also explains our observations that SOA growth begins only

when NO concentrations approach zero, which appears to be a general feature of chamber measurements of SOA formation from hydrocarbon photooxidation (e.g., 45–47, 54). As discussed previously (24), in the studies of Pandis et al. (12) and Edney et al. (13), [NO] did not fall below ~30 ppb, and no SOA was produced. Thus the formation of hydroxyhydroperoxides is likely to play an important role in SOA formation from isoprene photooxidation. This is consistent with the results of Miyoshi et al. (7), who report the formation of both gas-phase hydroperoxides and particles from the OH + isoprene reaction at low NO_x and high HO_2 . In the particle phase, hydroperoxides may react further, oxidizing organics or reacting with aldehydes to form peroxyhemiacetals (55), oligomeric species which may account for some of the high-MW peaks seen in AMS spectra of SOA (Figure 6).

However, the suppression of SOA formation by NO does not fully explain the observed NO_x -dependence of aerosol yields from isoprene photooxidation, as yields increase with NO_x at low NO concentrations (Figure 7). Similar NO_x -dependences of aerosol yield have been observed in the photooxidation of α - and β -pinene (12, 44); however, those experiments were carried out under very different oxidative conditions than in the present study and so may not be directly comparable. The increase in SOA growth with NO_x may be the result of changes in reaction conditions over the course of the experiments; over time the [NO]/[HO_2] ratio decreases (as NO is converted to NO_2 , and the suppression of HO_2 by NO decreases), which may lead to a switch from high- NO_x to low- NO_x conditions. This could lead to a complex dependence of SOA formation on NO_x ; peroxy radicals formed in the first oxidation step (OH + isoprene) react with NO, whereas peroxy radicals formed by the oxidation of isoprene

reaction products react with HO₂. Such a change in NO_x conditions may be relevant in the troposphere during transport from a polluted to an unpolluted region, but it would be preferable to measure SOA yields under conditions in which the [NO]/[HO₂] ratio, and thus the fate of organic peroxy radicals, stays constant over the course of the entire experiment. More generally, to apply chamber results to atmospheric conditions, it is important that the [NO]/[HO₂] ratio be well-constrained; in our experiments, SOA is suppressed by 100s of ppb of NO, though in the atmosphere this is likely to occur at lower NO concentrations due to elevated HO₂ concentrations (estimated at 100s of ppt) in the chamber. Thus, reaction conditions need to be better controlled and characterized before parameterizations of SOA yields as a function of [NO_x] may be obtained.

It should be noted that the NO_x-dependence of SOA growth measured in this work may not apply generally to all SOA-forming reactions. For example, Edney et al. (13) showed that, in the presence of SO₂, isoprene oxidation forms SOA even in the presence of NO, suggesting that enhanced reactive uptake by acidic aerosol particles may counteract the reduced production of condensable species at high NO_x. Additionally, the reaction of NO with large peroxy radicals will form alkoxy radicals which isomerize rather than fragment. These will form large, multifunctional products, which may efficiently partition into the aerosol phase. Thus hydrocarbons substantially larger than isoprene are expected to form SOA even under high-NO_x conditions. Indeed, recently SOA formation from the OH-initiated oxidation of long-chain alkanes has been observed in the presence of several ppm of NO (56). In such cases, SOA yields may even be higher at high NO_x. Thus SOA formation may be a complex function of NO_x level, and future study is required.

Rapid Photochemical Loss of SOA. As noted earlier, under low-NO_x conditions ([NO_x] < 1 ppb), initial SOA growth from isoprene oxidation is large (sometimes reaching yields of > 10%), but is followed by a rapid decrease in aerosol volume as the reaction progresses (Figure 2). To our knowledge such an effect has not been reported in previous chamber studies of SOA formation. The decrease in SOA, characterized by a shrinking of particles rather than a reduction in particle number, is a photochemical effect, as it occurs only during chamber irradiation (when UV photons and OH radicals are present), ceasing immediately when the chamber lights are turned off. Therefore, this may be an example of photochemical "aging", or oxidative processing, of the SOA. We do not observe rapid loss of SOA formed in the low-NO_x photooxidation of β-pinene (140 ppb), indicating that it is not a general feature of the irradiation of all hydrocarbon/H₂O₂ mixtures.

The photochemical mechanism of volatilization is not clear at present. Recent experimental evidence shows that the reaction of gas-phase OH radicals with condensed organics may lead to efficient volatilization of organic compounds, thereby serving as a sink for SOA in the troposphere (57). However, such a mechanism probably cannot account for the fast rate of SOA loss observed, and we observe no obvious dependence of the rate of SOA loss on surface area, which would be expected for reactions of gas-phase oxidants with condensed-phase organics.

Instead, the SOA loss may be a result of gas-phase or particle-phase oxidation reactions continuing after particle formation. Once semivolatile compounds reach gas-particle equilibrium, any further gas-phase losses (by reaction with OH or photolysis) of those compounds may drive equilibrium away from the particle phase, leading to a decrease in SOA mass. If all losses are from such gas-phase reactions, and these reactions (rather than gas-particle partitioning) are the rate-limiting step, then the SOA loss (0.006–0.018 min⁻¹) is consistent with the reaction with OH (*k*_{OH} = 4.0 × 10⁻¹¹–1.2

× 10⁻¹⁰ cm³ molec⁻¹ s⁻¹ for [OH] = 2.5 × 10⁶/cm³), photolysis (*J* = 0.006–0.018 min⁻¹), or some combination of the two. Given that this effect is seen only at low NO_x, these reactive compounds are likely to be organic hydroperoxides. If loss is by photolysis, the inferred *J* value is significantly larger (by 1 or 2 orders of magnitude) than that of the simplest organic peroxide, CH₃OOH (29). The efficient photolysis of organic hydroperoxides has been put forth as an explanation for discrepancies between measured tropospheric ozone production and modeled HO_x chemistry (58), as well as for the observation that SOA yields from α-pinene ozonolysis are lower under UV irradiation than under dark conditions (59). In the latter case, the underlying chemistry (and inferred photolytic lifetime) is substantially different than in the present study, but it is clear that the photochemistry of structurally complex organic peroxides deserves further study.

However, gas-phase reaction is unlikely to account for all of the observed loss, as AMS results show that the chemical composition of the SOA changes over the course of the decrease; a number of high-MW organic fragments are observed to increase in intensity even during the rapid loss of organic aerosol mass. This may be a result of particle-phase reactions, such as the photolysis of condensed-phase hydroperoxides. Such reactions would form OH and alkoxy radicals within the aerosol, which would serve to rapidly oxidize other SOA components; products of such reactions may be quite volatile, leading to the loss of SOA mass, or oligomeric and highly nonvolatile. In a forthcoming publication, in which we focus on the chemical composition of SOA from isoprene oxidation, the chemistry of this photochemical aging process will be explored in greater detail.

Acknowledgments

This research was funded by the U.S. Environmental Protection Agency Science to Achieve Results (STAR) Program grant number RD-83107501-0, managed by EPA's Office of Research and Development (ORD), National Center for Environmental Research (NCER), and by the U.S. Department of Energy Biological and Environmental Research Program DE-FG03-01ER63099; this work has not been subjected to the EPA's required peer and policy review and, therefore, does not necessarily reflect the views of the Agency and no official endorsement should be inferred.

Supporting Information Available

Details of the blank runs, tests for the role of impurities, and low-concentration runs. This material is available free of charge via the Internet at <http://pubs.acs.org>.

Literature Cited

- (1) Kanakidou, M.; et al. Organic aerosol and global climate modelling: a review. *Atmos. Chem. Phys.* **2005**, *5*, 1053–1123.
- (2) Chung, S. H.; Seinfeld, J. H. Global distribution and climate forcing of carbonaceous aerosols. *J. Geophys. Res.* **2002**, *107*, 4407, doi:10.1029/2001JD001397.
- (3) Tsigaridis, K.; Kanakidou, M. Global modelling of secondary organic aerosol in the troposphere: a sensitivity analysis. *Atmos. Chem. Phys.* **2003**, *3*, 1849–1869.
- (4) Guenther, A.; et al. A global model of natural volatile organic compound emissions. *J. Geophys. Res.* **1995**, *100*, 8873–8892.
- (5) Tuazon, E. C.; Atkinson, R. Product study of the gas-phase reaction of isoprene with the OH radical in the presence of NO_x. *Int. J. Chem. Kinet.* **1990**, *22*, 1221–1236.
- (6) Paulson, S. E.; Flagan, R. C.; Seinfeld, J. H. Atmospheric photooxidation of isoprene, Part I: The hydroxyl radical and ground-state atomic oxygen reactions. *Int. J. Chem. Kinet.* **1992**, *24*, 79–101.

- (7) Miyoshi, A.; Hatakeyama, S.; Washida, N. OH radical-initiated photooxidation of isoprene: An estimate of global CO production. *J. Geophys. Res.* **1994**, *99*, 18,779–18,787.
- (8) Sprengnether, M.; Demerjian, K. L.; Donahue, N. M.; Anderson, J. G. Product analysis of the OH oxidation of isoprene and 1,3-butadiene. *J. Geophys. Res.* **2002**, *107*, D15, 4268, doi: 10.1029/2001JD000716.
- (9) Chen, X.; Hulbert, D.; Shepson, P. B. Measurement of the organic nitrate yield from OH reaction with isoprene. *J. Geophys. Res.* **1998**, *103*, 25,563–25,568.
- (10) Zhao, J.; Zhang, R.; Fortner, E. C.; North, S. W. Quantification of hydroxycarbonyls from OH-isoprene reactions. *J. Am. Chem. Soc.* **2004**, *126*, 2686–2687.
- (11) Baker, J.; Arey, J.; Atkinson, R. Formation and reaction of hydroxycarbonyls from the reaction of OH radicals with 1,3-butadiene and isoprene. *Environ. Sci. Technol.* **2005**, *39*, 4091–4099.
- (12) Pandis, S. N.; Paulson, S. E.; Seinfeld, J. H.; Flagan, R. C. Aerosol formation in the photooxidation of isoprene and β -pinene. *Atmos. Environ.* **1991**, *25A*, 997–1008.
- (13) Edney, E. O.; Kleindienst, T. E.; Jaoui, M.; Lewandowski, M.; Offenberg, J. H.; Wang, W.; Claeys, M. Formation of 2-methyl tetrols and 2-methylglyceric acid in secondary organic aerosol from laboratory irradiated isoprene/NO_x/SO₂/air mixtures and their detection in ambient PM_{2.5} samples collected in the eastern United States. *Atmos. Environ.* **2005**, *39*, 5281–5289.
- (14) Claeys, M.; et al. Formation of secondary organic aerosol through photooxidation of isoprene. *Science* **2004**, *303*, 1173–1176.
- (15) Ion, A. C.; Vermeylen, R.; Kourtchev, I.; Cafmeyer, J.; Chi, X.; Gelencsér, A.; Maenhaut, W.; Claeys, M. Polar organic compounds in rural PM_{2.5} aerosols from K-pusztá, Hungary, during a 2003 summer field campaign: sources and diel variations. *Atmos. Chem. Phys.* **2005**, *5*, 1805–1814.
- (16) Kourtchev, I.; Ruuskanen, T.; Maenhaut, W.; Kulmala, M.; Claeys, M. Observation of 2-methyltetrols and related photo-oxidation products of isoprene in boreal forest aerosols from Hyytiälä, Finland. *Atmos. Chem. Phys.* **2005**, *5*, 2761–2770.
- (17) Claeys, M.; Wang, W.; Ion, A. C.; Kourtchev, I.; Gelencsér, A.; Maenhaut, W. Formation of secondary organic aerosols from isoprene and gas-phase oxidation products through reaction with hydrogen peroxide. *Atmos. Environ.* **2004**, *38*, 4093–4098.
- (18) Limbeck, A.; Kulmala, M.; Puxbaum, H. Secondary organic aerosol formation in the atmosphere via heterogeneous reaction of gaseous isoprene on acidic particles. *Geophys. Res. Lett.* **2003**, *30*, 1996–1999.
- (19) Czoschke, N. M.; Jang, M.; Kamens, R. M. Effect of acidic seed on biogenic secondary organic aerosol growth. *Atmos. Environ.* **2003**, *37*, 4287–4299.
- (20) Matsunaga, S.; Mochida, M.; Kawamura, K. Growth of organic aerosols by biogenic semi-volatile carbonyls in the forestal atmosphere. *Atmos. Environ.* **2003**, *37*, 2045–2050.
- (21) Matsunaga, S.; Mochida, M.; Kawamura, K. Variation on the atmospheric concentrations of biogenic compounds and their removal processes in the northern forest at Moshiri, Hokkaido Island in Japan. *J. Geophys. Res.* **2004**, *109*, D04302, doi: 10.1029/2003JD004100.
- (22) Ervens, B.; Feingold, G.; Frost, G. J.; Kreidenweis, S. M. A modeling study of aqueous production of dicarboxylic acids: 1. Chemical pathways and speciated organic mass production. *J. Geophys. Res.* **2003**, *109*, D15205, doi: 10.1029/2003JD004387.
- (23) Lim, H.-J.; Carlton, A. G.; Turpin, B. J. Isoprene forms secondary organic aerosol through cloud processing: model simulations. *Environ. Sci. Technol.* **2005**, *39*, 4441–4446.
- (24) Kroll, J. H.; Ng, N. L.; Murphy, S. M.; Flagan, R. C.; Seinfeld, J. H. Secondary organic aerosol formation from isoprene photo-oxidation under high-NO_x conditions. *Geophys. Res. Lett.* **2005**, *32*, L18808, doi: 10.1029/2005GL023637.
- (25) Cocker, D. R., III; Flagan, R. C.; Seinfeld, J. H. State-of-the-art chamber facility for studying atmospheric aerosol chemistry. *Environ. Sci. Technol.* **2001**, *35*, 2594–2601.
- (26) Keywood, M. D.; Varutbangkul, V.; Bahreini, R.; Flagan, R. C.; Seinfeld, J. H. Secondary organic aerosol formation from the ozonolysis of cycloalkenes and related compounds. *Environ. Sci. Technol.* **2004**, *38*, 4157–4164.
- (27) Drewnick, F.; et al. A new time-of-flight aerosol mass spectrometer (TOF-AMS)—Instrument description and first field deployment. *Aerosol Sci. Technol.* **2005**, *39*, 637–658.
- (28) Atkinson, R.; et al. Evaluated kinetic and photochemical data for atmospheric chemistry: volume 1 – gas-phase reactions of O_x, HO_x, NO_x, and SO_x species. *Atmos. Chem. Phys.* **2004**, *4*, 1461–1738.
- (29) Atkinson, R.; et al. Evaluated kinetic and photochemical data for atmospheric chemistry: Supplement VII, Organic species, *J. Phys. Chem. Ref. Data* **1999**, *28*, 191–393.
- (30) Bahreini, R.; Keywood, M. D.; Ng, N. L.; Varutbangkul, V.; Gao, S.; Flagan, R. C.; Seinfeld, J. H. Measurements of secondary organic aerosol (SOA) from oxidation of cycloalkenes, terpenes, and *m*-xylene using an Aerodyne aerosol mass spectrometer. *Environ. Sci. Technol.* **2005**, *39*, 5674–5688.
- (31) Odum, J. R.; Hoffmann, T.; Bowman, F.; Collins, D.; Flagan, R. C.; Seinfeld, J. H. Gas/particle partitioning and secondary organic aerosol yields. *Environ. Sci. Technol.* **1996**, *30*, 2580–2585.
- (32) Kroll, J. H.; Seinfeld, J. H. Representation of secondary organic aerosol (SOA) laboratory chamber data or the interpretation of mechanisms of particle growth. *Environ. Sci. Technol.* **2005**, *39*, 4159–4165.
- (33) Cocker, D. R., III; Mader, B. T.; Kalberer, M.; Flagan, R. C.; Seinfeld, J. H. The effect of water on gas-particle partitioning of secondary organic aerosol: II. *m*-xylene and 1,3,5-trimethylbenzene photooxidation systems. *Atmos. Environ.* **2001**, *35*, 6073–6085.
- (34) Ng, N. L.; Kroll, J. H.; Keywood, M. D.; Bahreini, R.; Varutbangkul, V.; Flagan, R. C.; Seinfeld, J. H.; Lee, A.; Goldstein, A. H. Contribution of first- versus second-generation products to secondary organic aerosols formed in the oxidation of biogenic hydrocarbons. *Environ. Sci. Technol.* **2006**, in press.
- (35) Tuazon, E. C.; Atkinson, R. A product study of the gas-phase reaction of methyl vinyl ketone with the OH radical in the presence of NO_x. *Int. J. Chem. Kinet.* **1989**, *21*, 1141–1152.
- (36) Tuazon, E. C.; Atkinson, R. A product study of the gas-phase reaction of methacrolein with the OH radical in the presence of NO_x. *Int. J. Chem. Kinet.* **1990**, *22*, 591–602.
- (37) Orlando, J. J.; Tyndall, G. S.; Paulson, S. E. Mechanism of the OH-initiated oxidation of methacrolein. *Geophys. Res. Lett.* **1999**, *26*, 2191–2194.
- (38) Ruppert, L.; Becker, K. H. A product study of the OH radical-initiated oxidation of isoprene: formation of C₅-unsaturated diols. *Atmos. Environ.* **2000**, *34*, 1529–1542.
- (39) Benkelberg, H.-J.; Böge, O.; Seuwen, R.; Warneck, P. Product distributions from the OH radical-induced oxidation of but-1-ene, methyl-substituted but-1-enes and isoprene in NO_x-free air. *Phys. Chem. Chem. Phys.* **2000**, *2*, 4029–4039.
- (40) Lee, W.; Baasandorj, M.; Stevens, P. S.; Hites, R. A. Monitoring OH-initiated oxidation kinetics of isoprene and its products using online mass spectrometry. *Environ. Sci. Technol.* **2005**, *39*, 1030–1036.
- (41) Warneke, C.; et al. Isoprene and its oxidation products methyl vinyl ketone, methacrolein, and isoprene related peroxides measured online over the tropical rain forest of Surinam in March 1998. *J. Atmos. Chem.* **2001**, *38*, 167–185.
- (42) McMurry, J. *Organic Chemistry*, 4th ed.; Brooks/Cole: Pacific Grove, CA, 1995.
- (43) Hatakeyama, S.; Izumi, K.; Fukuyama, T.; Akimoto, H.; Washida, N. Reactions of OH with α -pinene and β -pinene in air: estimates of global CO production from the atmospheric oxidation of terpenes. *J. Geophys. Res.* **1991**, *96*, D1, 947–958.
- (44) Zhang, S.-H.; Shaw, M.; Seinfeld, J. H.; Flagan, R. C. Photochemical aerosol formation from α -pinene and β -pinene. *J. Geophys. Res.* **1992**, *92*, D18, 717–720, 729.
- (45) Hurley, M. D.; Sokolov, O.; Wallington, T. J.; Takekawa, H.; Karasawa, M.; Klotz, B.; Barnes, I.; Becker, K. H. Organic aerosol formation during the atmospheric degradation of toluene. *Environ. Sci. Technol.* **2001**, *35*, 1358–1366.
- (46) Johnson, D.; Jenkin, M. E.; Wirtz, K.; Martín-Reviejo, M. Simulating the formation of secondary organic aerosol from the photooxidation of toluene. *Environ. Chem.* **2004**, *1*, 150–165.
- (47) Martín-Reviejo, M.; Wirtz, K. Is benzene a precursor for secondary organic aerosol? *Environ. Sci. Technol.* **2005**, *39*, 1045–1054.
- (48) Song, C.; Na, K.; Cocker, D. R., III Impact of the hydrocarbon to NO_x ratio on secondary organic aerosol formation. *Environ. Sci. Technol.* **2005**, *39*, 3143–3149.
- (49) Presto, A. A.; Huff Hartz, K. E.; Donahue, N. M. Secondary organic aerosol production from ozonolysis: 2. Effect of NO_x concentration. *Environ. Sci. Technol.* **2005**, *39*, 7046.
- (50) Alvarado, A.; Atkinson, R.; Arey, J. Kinetics of the gas-phase reactions of NO₃ radicals and O₃ with 3-methylfuran and the OH radical yield from the O₃ reaction. *Int. J. Chem. Kinet.* **1996**, *28*, 905–909.

- (51) Jenkin, M. E.; Boyd, A. A.; Lesclaux, R. Peroxy radical kinetics resulting from the OH-initiated oxidation of 1,3-butadiene, 2,3-dimethyl-1,3-butadiene and isoprene. *J. Atmos. Chem.* **1998**, *29*, 267–298.
- (52) Docherty, K. S.; Wu, W.; Lim, Y. B.; Ziemann, P. J. Contributions of organic peroxides to secondary organic aerosol formed from reactions of monoterpenes with O₃. *Environ. Sci. Technol.* **2005**, *39*, 4049–4059.
- (53) Bonn, B.; von Kuhlmann, R.; Lawrence, M. G. High contribution of biogenic hydroperoxides to secondary organic aerosol formation. *Geophys. Res. Lett.* **2004**, *31*, L10108, doi: 10.1029/2003GL019172.
- (54) Johnson, D.; Jenkin, M. E.; Wirtz, K.; Martín-Reviejo, M. Simulating the formation of secondary organic aerosol from the photooxidation of aromatic hydrocarbons. *Environ. Chem.* **2005**, *2*, 35–48.
- (55) Tobias, H. J.; Ziemann, P. J. Thermal desorption mass spectrometric analysis of organic aerosol formed from reactions of 1-tetradecene and O₃ in the presence of alcohols and carboxylic acids. *Environ. Sci. Technol.* **2000**, *34*, 2105–2115.
- (56) Lim, Y. B.; Ziemann, P. J. Products and mechanism of secondary organic aerosol formation from reactions of *n*-alkanes with OH radicals in the presence of NO_x. *Environ. Sci. Technol.* **2005**, *39*, 9229–9236.
- (57) Molina, M. J.; Ivanov, A. V.; Trakhtenberg, S.; Molina, L. T. Atmospheric evolution of organic aerosol. *Geophys. Res. Lett.* **2004**, *31*, L22104, doi: 10.1029/2004GL020910.
- (58) Thornton, J. A.; et al. Ozone production rates as a function of NO_x abundances and HO_x production rates in the Nashville urban plume. *J. Geophys. Res.* **2002**, *107*, D12, doi: 10.1029/2001JD000932.
- (59) Presto, A. A.; Huff Hartz, K. E.; Donahue, N. M. Secondary organic aerosol production from terpene ozonolysis. 1. Effect of UV radiation. *Environ. Sci. Technol.* **2005**, *39*, 7036–7045.

Received for review December 3, 2005. Revised manuscript received January 13, 2006. Accepted January 18, 2006.

ES0524301

Appendix B

Apportionment of Primary and Secondary Organic Aerosols in Southern California during the 2005 Study of Organic Aerosols in Riverside (SOAR-1)*

*This chapter is reproduced by permission from. "Apportionment of primary and secondary organic aerosols in Southern California during the 2005 study of organic aerosols in Riverside (SOAR-1)." K.S. Docherty, E. A. Stone, I. M. Ulbrich, P. F. DeCarlo, D. C. Snyder, J. J. Schauer, R. E. Peltier, R. J. Weber, S. M. Murphy, J. H. Seinfeld, B. D. Grover, D. J. Eatough, J. L. Jimenez, *Environmental Science and Technology*, 42 (20), 7655-7662, 2008. Copyright 2008. American Chemical Society.

Apportionment of Primary and Secondary Organic Aerosols in Southern California during the 2005 Study of Organic Aerosols in Riverside (SOAR-1)

KENNETH S. DOCHERTY,^{†,‡}
ELIZABETH A. STONE,^{||}
INGRID M. ULBRICH,^{†,‡}
PETER F. DeCARLO,^{†,§,○}
DAVID C. SNYDER,^{||} JAMES J. SCHAUER,^{||}
RICHARD E. PELTIER,^{±,◆}
RODNEY J. WEBER,[±]
SHANE M. MURPHY,[#]
JOHN H. SEINFELD,[#]
BRETT D. GROVER,^{∇,¶}
DELBERT J. EATOUGH,[∇] AND
JOSE L. JIMENEZ^{*,†,‡}

Cooperative Institute for Research in Environmental Sciences and Department of Chemistry and Biochemistry, Department of Atmospheric and Oceanic Sciences, University of Colorado, Boulder, Colorado, Environmental Chemistry and Technology Program, University of Wisconsin, Madison, Wisconsin, School of Earth and Atmospheric Sciences, Georgia Institute of Technology, Atlanta, Georgia, Division of Chemistry and Chemical Engineering, California Institute of Technology, Pasadena, California, and Department of Chemistry and Biochemistry, Brigham Young University, Provo, Utah

Received March 21, 2008. Revised manuscript received July 30, 2008. Accepted July 31, 2008.

Ambient sampling was conducted in Riverside, California during the 2005 Study of Organic Aerosols in Riverside to characterize the composition and sources of organic aerosol using a variety of state-of-the-art instrumentation and source apportionment techniques. The secondary organic aerosol (SOA) mass is estimated by elemental carbon and carbon monoxide tracer methods, water soluble organic carbon content, chemical mass balance of organic molecular markers, and positive matrix factorization of high-resolution aerosol mass spectrometer data. Estimates obtained from each of these methods indicate that the organic fraction in ambient aerosol is overwhelmingly secondary in nature during a period of several weeks with moderate ozone concentrations and that SOA is

the single largest component of PM₁ aerosol in Riverside. Average SOA/OA contributions of 70–90% were observed during midday periods, whereas minimum SOA contributions of ~45% were observed during peak morning traffic periods. These results are contrary to previous estimates of SOA throughout the Los Angeles Basin which reported that, other than during severe photochemical smog episodes, SOA was lower than primary OA. Possible reasons for these differences are discussed.

Introduction

Aerosols are of interest due to their roles in several atmospheric processes including radiative forcing, heterogeneous reactions, and regional visibility degradation, as well as their negative impact on human health. The impact of particles on these and other atmospheric processes are dependent on particle size, the majority being strongly correlated with fine particles (PM_{2.5} or PM₁), and many also depend on chemical composition. In particular, the organic fraction (“organic aerosols”, OA), which typically constitutes a significant fraction of fine particle mass (*I*), is a poorly characterized aggregate of thousands of individual compounds either emitted directly in the particle-phase (“primary” OA, POA) or formed in the atmosphere from gas-to-particle conversion (“secondary” OA, SOA). Most of these compounds are not amenable to detection by currently available speciation techniques, which can identify only a small fraction of aerosol organics at the molecular level (2). The lack of molecular characterization of a large fraction of the mass is particularly important for SOA.

During the Study of Organic Aerosols in Riverside (SOAR-1), a variety of state-of-the-art instrumentation was assembled at the Air Pollution Research Center on the campus of the University of California-Riverside from July 18 through August 14, 2005 to investigate the chemical composition of ambient OA, representing, to our knowledge, the most complete set of OA field instruments at one location to date. Riverside is located ~80 km inland of the urban center of Los Angeles (LA). Due to its proximity to LA and the meteorology, topography, and intense emissions characteristic of the LA basin, Riverside and the surrounding areas are characterized by poor air quality, consistently rating as the worst in the United States for 24 h average fine particle concentrations both on short-term and annual bases (3).

Here, we estimate the fraction of SOA in fine particles using five methods including the elemental carbon (EC) and carbon monoxide (CO) tracer methods, water soluble organic carbon (WSOC) content, chemical mass balance (CMB) source apportionment of organic molecular markers (MMs), and positive matrix factorization (PMF) of high-resolution time-of-flight aerosol mass spectrometer (HR-ToF-AMS) organic mass spectra. Results obtained from each of these methods indicate that SOA contributes the majority of organic mass during a period that cannot be described as a “photochemical episode”. Estimates obtained from each of these methods are higher than previous SOA estimates in locations throughout the LA Basin including Riverside and surrounding areas.

Experimental Section

General. All measurements were conducted in Riverside, California at the Air Pollution Research Center on the campus of the University of California-Riverside (33°58'18.40"N, 117°19'21.41"W). During SOAR-1 (July 18 through August 14, 2005), the Riverside area was characterized by moderate

* Corresponding author e-mail: jose.jimenez@colorado.edu.
† Cooperative Institute for Research in Environmental Sciences.
‡ Department of Chemistry and Biochemistry, University of Colorado.
§ Department of Atmospheric and Oceanic Sciences, University of Colorado.
|| University of Wisconsin.
± Georgia Institute of Technology.
California Institute of Technology.
∇ Brigham Young University.
○ Currently at Paul Scherrer Institut, Switzerland.
◆ Currently at NYU School of Medicine, Department of Environmental Medicine, Tuxedo, New York.
¶ Currently at United States Environmental Protection Agency, National Exposure and Research Laboratory, Durham, North Carolina.

ozone concentrations (average peak daily ozone concentration in Riverside = 86 ppb; range 48–141 ppb). All times refer to Pacific Standard Time.

Sunset Semicontinuous EC/OC Measurements. PM_{2.5} organic carbon (OC) and elemental carbon (EC) concentrations were measured hourly using both standard (4) and dual-oven (5) Sunset semicontinuous carbon monitors (Sunset Laboratories, Tigard, OR).

Filter-Based Measurements. Filter samples were collected for source apportionment by CMB of solvent-extractable organic MMs (2). Details regarding particle collection, filter extraction, chemical analysis, and CMB procedures are similar to those presented in Stone et al. (6) with a few exceptions noted below.

Filter samples for CMB were collected daily according to the following schedule: 0400–0900; 0900–1400; 1400–1900; 1900–0400. Weekday samples collected on 7/26–7/28 and 8/2–8/4 and weekend samples collected on 7/30 and 8/6–8/7 were composited based on this schedule. For this analysis, weekday and weekend CMB source apportionment results were further composited to yield results irrespective of day of week. These samplers were not denuded. As a result, filter OC concentrations are likely inflated through adsorption of semivolatile gas-phase species. To obtain a conservative estimate of “other” OC, the results of CMB source apportionment were used in conjunction with coinciding standard Sunset OC concentrations (i.e., “other” OC = OC_{Sunset} – primary OC (POC)). If we were to instead use the CMB filter OC concentrations for this estimate, other OC increases by ~7% likely as a result of these adsorption artifacts.

Particle-Into-Liquid-Sampler (PILS) Organic Measurements. Water soluble OC (WSOC) and total OC were measured by a PILS-WSOC and PILS-OC, respectively (7). WSOC was measured continuously every 6 minutes from 7/18–7/27 and 7/30–8/15. The PILS-OC measured total OC continuously from 7/27–7/30 at the same rate. Further details are provided elsewhere (7).

HR-ToF-AMS Measurements. Nonrefractory PM₁ aerosols were measured by an Aerodyne HR-ToF-AMS from 7/14–8/10. Details regarding the HR-ToF-AMS are provided elsewhere (8).

Data Analysis. Conversion of carbon mass concentrations. Measured concentrations of OC, WSOC, and water insoluble organic carbon (WIOC) were converted to organic mass (OM) concentrations prior to calculating SOA fractions. POC and WIOC were converted using a factor of 1.2 μgOM/μgOC, whereas secondary OC (SOC) and WSOC were converted to secondary organic mass (SOM) using a factor of 1.8 μgOM/μgOC (9). In Supporting Information (SI) Table S-2, we explore the sensitivity of calculated SOA/OA ratios to the applied SOM/SOC conversion factor using additional conversion factors of 1.6 and 2.0 μgOM/μgOC. As this table shows, SOA/OA ratios vary only a few percent when these alternate conversion factors are used.

HR-ToF-AMS. Unit-resolution (UMR) ToF-AMS data were analyzed using established procedures for analysis of AMS data via customized data analysis software (Squirrel) (10). An AMS collection efficiency (CE) of 0.5 was used for all species, typical of aerosols measured in urban locations with similar composition (11, 12) and verified with intercomparisons with other collocated instruments. The AMS response may be slightly biased toward POA (13, 14), and these SOA/OA estimates should be considered lower limits. High-resolution (HR) ToF-AMS data were analyzed using a custom data analysis module (Pika) developed in our group (8) in Igor (Wavemetrics, Lake Oswego, OR).

PMF Analysis. AMS organic mass spectra were analyzed by PMF to identify the major components of PM₁ OA. PMF is a variant of factor analysis with nonnegative constraints on factor elements and has been described in detail elsewhere

(15). Its application to AMS spectra has been investigated in detail recently (16, 17). HR ($m/z \leq 100$ and UMR ($m/z > 100$) organic mass spectra were combined for PMF analysis. PMF2 (v4.2) was run in robust mode via a custom panel in Igor (16).

Lack of Important Biomass Burning (BB) Impact. Although the LA area is at times impacted by smoke from large wildfires that can increase PM₁₀ levels in the basin by 300–400% (18), fires throughout Southern California during SOAR-1 were small in size, short in duration, and not in the vicinity of the sampling location, according to the MODIS Active Fire Detections database (<http://maps.geog.umd.edu/firms/maps.asp>). This is supported by measurements by a collocated aerosol time-of-flight mass spectrometer that did not observe significant PM contributions from biomass burning/biofuel combustion sources (19). Moreover, m/z 60 (a BB tracer) in the AMS during the study (see SI Figure S1) as well as measured concentrations of the MM levoglucosan were low during SOAR-1 (see below).

Results and Discussion

EC-Tracer Method. This method assumes that EC results predominantly from combustion processes and can be used as a tracer for primary aerosol (20). POC is estimated by its proportionality with EC as

$$\text{POC} = [(\text{OC}/\text{EC})_p \times \text{EC}] + \text{NCPOC}, \quad (1)$$

where NCPOC is noncombustion POC, and SOC is determined by difference:

$$\text{SOC} = \text{OC} - \text{POC}. \quad (2)$$

The simple appearance of this method is belied by significant complexities associated with determining the coefficients $(\text{OC}/\text{EC})_p$ and NCPOC in eq 1, which are traditionally obtained by linear regression analysis of EC and OC data during periods that are deemed “not impacted by SOC.” NCPOC contributions (that are not correlated with EC due to similar source locations and/or activity patterns) are small relative to errors associated with the EC-tracer method (21). Therefore, they are lumped with SOC in the following EC-tracer calculations.

For ambient sampling, the correct $(\text{OC}/\text{EC})_p$ should be $\Sigma(\text{OC})/\Sigma(\text{EC})$ for all primary sources. Therefore, OC and EC data used in the regression analysis must be carefully selected to limit contributions from SOC, which would incorrectly inflate both $(\text{OC}/\text{EC})_p$ and POC. For areas like the LA Basin this is not trivial. Strader et al. (22) estimated $(\text{OC}/\text{EC})_p$ using regression analysis of data collected in California’s San Joaquin Valley and found that isolating a single period that was not impacted by photochemistry was “a dangerous proposition” due the long residence times of PM_{2.5}. Zhang et al. (23) showed that in Pittsburgh this method of estimating $(\text{OC}/\text{EC})_p$ led to a large overestimation of POA since SOA was always a significant fraction of the OA. This technique typically neglects variations in $(\text{OC}/\text{EC})_p$ throughout the day that can appear due to, e.g., variations in diesel and gasoline vehicle fractions, which may lead to some errors in the estimated diurnal profiles (24), as discussed below.

To explore the range of SOA contributions during SOAR-1, EC-tracer calculations were conducted using a range of $(\text{OC}/\text{EC})_p$ values estimated both using available emissions inventory data and from the literature. $(\text{OC}/\text{EC})_p$ ratios used to obtain SOA/OA estimates by the EC-tracer method, in addition to details regarding their determination, are presented in SI Table S1. $(\text{OC}/\text{EC})_p$ estimates were calculated using available vehicle emissions inventories for the South Coast Air Basin and emission factors determined in several recent tunnel studies in California. Due to the high concentration of primary emissions observed in tunnel studies which favor partitioning of semivolatile OC to the particle

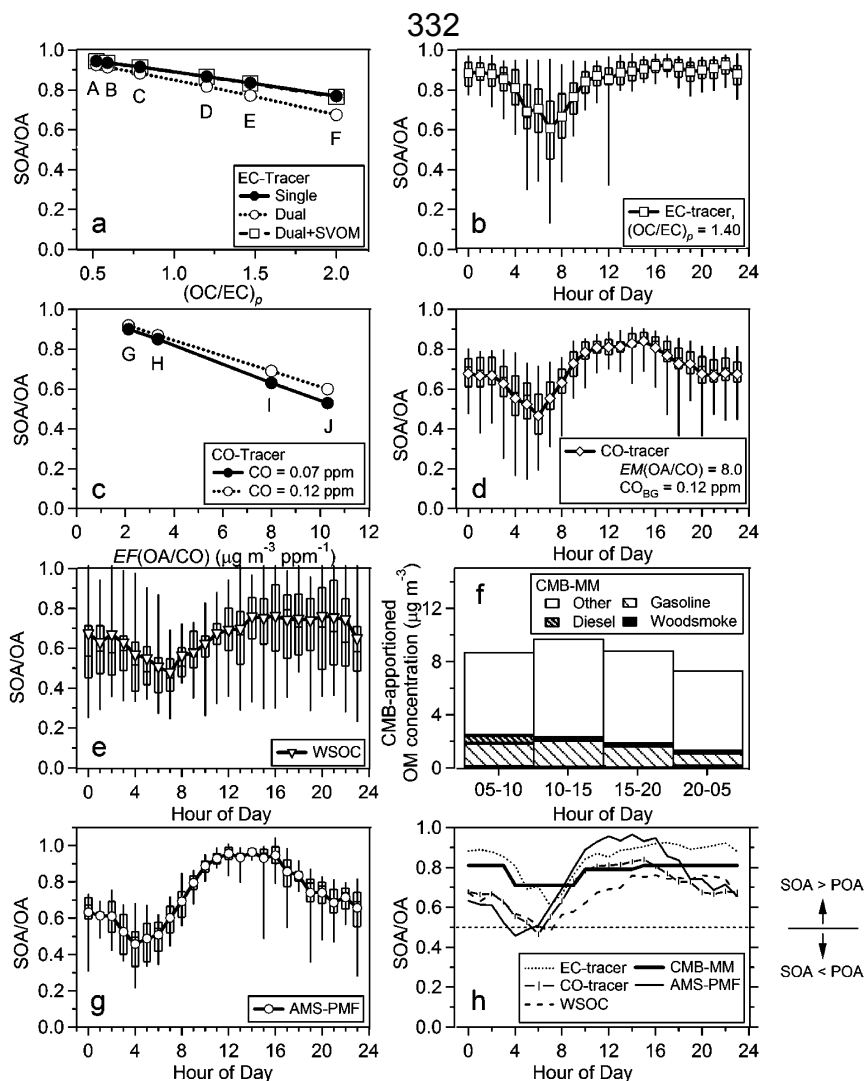


FIGURE 1. Estimated SOA/OA ratios and results of CMB OA apportionment during SOAR-1. Figure 1a shows campaign-average SOA fractions from the EC-tracer method as a function of $(OC/EC)_p$. Applied $(OC/EC)_p$ values for (A–C) were calculated using emissions ratios measured in several Caldecott Tunnel studies (26–28). Literature values for $(OC/EC)_p$ were obtained from (D) AMS spectral deconvolution (23), (E) radiocarbon determinations (30), and (F) traditional regression analysis of semicontinuous OC and EC data (29). Figure 1b shows the diurnal profile of SOA/OA ratios obtained from the EC-tracer method. Figures 1c and 1d show average SOA/OA ratios obtained from the CO-tracer method as a function of $EF(OA/CO)$ and the diurnal profile of SOA/OA ratios calculated using our central estimate ($EF(OA/CO)=8.0$ and $CO_{BG} = 0.12$ ppm), respectively. Figure 1e shows the diurnal profile of SOA/OA ratios obtained from the WSOC method. Figure 1f presents results of CMB OA apportionment while Figure 1g shows the diurnal profile of SOA/OA ratios obtained from PMF. Finally, Figure 1h compares SOA/OA estimates from all methods in the same plot to facilitate comparison.

phase, resulting emission factors should be considered as an upper bound to OC/EC for tunnel studies. $(OC/EC)_p$ was calculated from emissions data as follows:

$$(OC/EC)_p = \frac{[(OC_{diesel} + OC_{gasoline}) / (EC_{diesel} + EC_{gasoline})]}{[(EF_{OC,diesel} * DFU_{diesel}) + (EF_{OC,gas} * DFU_{gas})] / [(EF_{EC,diesel} * DFU_{diesel}) + (EF_{EC,gas} * DFU_{gas})]} \quad (3)$$

where DFU_{diesel} and DFU_{gas} are average daily fuel use ($kg \text{ day}^{-1}$) for diesel and gasoline, respectively, within the South Coast Air Basin for 2005 (25) and EF_x ($g \text{ OC kg}^{-1} \text{ fuel}$) are emission factors calculated from recent tunnel studies in California (26–28).

Estimates from the ambient linear regression method are likely to constitute an upper bound for $(OC/EC)_p$ due to the difficulty involved with eliminating SOC contributions (22). Recent studies in both Pittsburgh (29) and the Los Angeles basin (21) report $(OC/EC)_p \sim 2$. Somewhat lower $(OC/EC)_p$ estimates have been obtained by other methods including $^{14}C/^{12}C$ analysis of EC and OC samples (30) and by comparing the fraction of oxygenated OA resulting from AMS mass

spectral deconvolution with average SOA fractions calculated by the EC-tracer method (23). Due to the use of $^{14}C/^{12}C$ ratios in Szidat et al. (30), this estimate should have lower potential inflationary errors of incorporating SOC, although it applies to a European vehicle fleet which has some differences with that of California. In Zhang et al. (23), equivalent SOA fractions were obtained from both methods using an $(OC/EC)_p = 1.20$, which is equivalent to applying the regression method after subtracting the AMS-estimated SOA from the ambient OA during high POA periods. These latter literature estimates may be still higher than the tunnel studies due to the incorporation of POA from sources other than vehicle emissions, or some fast SOA formation from anthropogenic precursors (31).

Using each literature and emissions-based $(OC/EC)_p$ estimate, average POC and SOC concentrations were calculated using campaign-long average OC and EC concentrations measured by both Sunset instruments. Corresponding SOA estimates are shown in Figure 1a as a function of $(OC/EC)_p$. Two sets of results are shown for the dual-oven Sunset

instrument showing the impact of measured semivolatile organic mass (SVOM) concentrations (5). As Figure 1a shows, SOA contributes a majority of PM_{2.5} organic mass when averaged over the entire length of the sampling period. Conservative estimates of SOA fraction using $(OC/EC)_p = 2.0$ result in a SOA/POA ratio of $\geq 2:1$, whereas use of a more reasonable $(OC/EC)_p \sim 1.4$ gives corresponding ratios of $\geq 4:1$. Using $(OC/EC)_p$ ratios from tunnel studies results in a SOA/POA ratio $\geq 4.5:1$. The diurnal plot of SOA/OA ratios calculated from the EC-tracer method using EC/OC data from the standard Sunset instrument and an $(OC/EC)_p = 1.4$ is shown in Figure 1b. This calculation provides an overall average SOA/OA ratio $84 \pm 18\%$, with a minimum during the morning rush hour as expected.

CO-Tracer Method. The CO-tracer method is analogous to the EC-tracer method and has been used recently to estimate the fraction of SOA in PM₁ using collocated measurements of AMS organics and CO (32). Similar to the EC-tracer method, the CO-tracer method apportions POA mass using a tracer of primary emissions along with an estimated emissions ratio. However, due to different OA/CO and OA/EC emission ratios of different sources such as diesel and gasoline vehicles (24), the results of the CO-tracer method have some differences with those from the EC-tracer method. These differences are an indication of the uncertainty in the estimates for this type of simplified method. POA concentrations are calculated using

$$POA = (OA/CO)_p \times \Delta CO + NCPOC \quad (4)$$

where ΔCO is the CO enhancement above background (i.e., $CO_i - CO_{BG}$) and $(OA/CO)_p$ is the POA to CO emissions ratio. SOA concentrations are estimated as the difference between the measured OA and the summed POA similar to eq 2 above.

$(OA/CO)_p$, like $(OC/EC)_p$, needs to be estimated with similar methods, e.g., from regression analysis of "less processed" air (i.e., air masses where OA concentrations are thought to be dominated by primary combustion sources). This ratio has previously been estimated in a variety of locations including Pittsburgh (23), New England (33), and Tokyo (32) with values ranging from 4.3–14.4 $\mu g m^{-3} OA ppm^{-1} CO$. The minimum within this range was determined by Zhang et al. (23) based on regression of ambient CO and hydrocarbon-like aerosol obtained from deconvolution of AMS mass spectra and is higher than OA/CO emission ratios of 2.13 (26) and 3.33 $\mu g m^{-3} ppm^{-1}$ (28) obtained from California tunnel studies. The regression of total OA during high POA periods yields an $(OA/CO)_p = 10.3 \mu g m^{-3} ppm^{-1}$ during SOAR-1. As with the EC-tracer method, estimates based on total ambient OA are very likely biased high due to the presence of some SOA that also shows strong correlation with anthropogenic tracers (33) and should be considered upper limits. We use a ratio of 8.0 $\mu g m^{-3} ppm^{-1}$ and $CO_{BG} = 0.12 ppm$ (34) for our central estimate, and explore the sensitivity to the more conservative estimate obtained using a ratio of 10.3 and $CO_{BG} = 0.07 ppm$. We neglect changes in $(OA/CO)_p$ with time-of-day that can introduce some error in the diurnal profiles (24). CO produced through oxidation of volatile organic compounds is estimated to make a minimal contribution ($\sim 1\%$) to excess CO in the South Coast Air Basin (35).

Figure 1c shows SOA/OA ratios resulting from the CO-tracer method as a function of $(OA/CO)_p$ at background CO concentrations of 0.07 and 0.12 ppm. As this plots shows, the CO-tracer method again indicates that OA measured during SOAR-1 is dominated by SOA. The average SOA/OA ratio obtained from the central estimate is $69\% \pm 24\%$. This estimate decreases by $\sim 16\%$ when CO-tracer method calculations were repeated using the more conservative assumptions. Similarly, using the average ratio from tunnel studies and $CO_{BG} = 0.12$ increases the SOA/OA $\sim 20\%$

compared to the central estimate. The diurnal profile of SOA/OA ratios calculated using our central estimate of the CO-tracer method is presented in Figure 1d. Maximum SOA/OA ratios $> 80\%$ are observed during mid-day hours (1100–1600) and later steadily decline to a midnight value of $\sim 67\%$. As expected, minimum contributions from SOA were observed during the morning rush hour with an absolute minimum of $\sim 47\%$ at 0600.

SOA Estimate from WSOC Content. In polluted regions, compounds comprising WSOC are either mainly emitted from BB sources or formed via secondary atmospheric processes (36). SOA species are polar and typically highly oxygenated, leading to much higher water solubility than for reduced anthropogenic POA species. Due to the small fraction of BB OA during SOAR-1, most of the WSOC should be due to SOA species. In order to accurately use WSOC as a surrogate for SOC, measured WSOC concentrations must be adjusted to account for the water-insoluble fraction of oxygenated organic carbon (OOC). A conservative estimate of this fraction is obtained here from Kondo et al. (37) where it was estimated that 6–26% of summer OOC in Tokyo was water-insoluble based on direct comparisons between PILS-WSOC and Quadrupole AMS measurements. However, water-insoluble SOA fractions as large as 60% have recently been reported (38) which if applicable in CA would result in a low bias in our SOA estimates by this technique.

A WSOC/OC ratio of 0.56 ± 0.05 was obtained from PILS-WSOC and PILS-OC measurements during SOAR-1 (7). We estimate the SOA fraction using this ratio corrected for water-insoluble OOA content and converted to OM using factors discussed above. A conservative 24 h average SOA/OA estimate of $66 \pm 8\%$ is obtained using the 6% water-insoluble OOC correction, which increases by $\sim 9\%$ when the 26% water-insoluble OOC correction is instead applied. The diurnal profile of SOA/OA estimates from the WSOC method using the 6% water-insoluble OOC correction is shown in Figure 1e. A global minimum of 48% is obtained at 0700 with maximum values of $\sim 75\%$ occurring at mid-day. A final concern is the potential contribution of highly water soluble organics from BB to WSOC concentrations, which would artificially increase this SOA estimate. As discussed previously, the impact of BB throughout the LA basin during SOAR-1 was small. Using the results of CMB analysis (below) we estimate that the contribution of BB to WSOC and total OA is $\leq 1\%$ using a WSOC/OC emissions ratio of 0.71 (39). As a result, the estimate for SOA fraction obtained from this method would change little if the BB contribution were to be subtracted.

CMB of Organic Molecular Markers. CMB models are based on the mass conservation of individual organic species. The mass conservation equations are written as the matrix product of unknown time series of source contributions and known source profiles equaling the time series of known concentrations of a set of molecular marker species observed in ambient aerosol and are solved with the effective variance least-squares method. CMB models have been used to apportion source contributions to ambient PM_{2.5} in numerous locations including the LA Basin (e.g., refs 2, 6).

Here CMB is applied to selected OA tracer species that are solvent extractable and elutable from a gas chromatography (GC) column, which applies to only a limited amount of particle-associated organic compounds (2). However, this small subset is sufficient to act as tracers of major primary sources (2), including fossil fuel, coal, natural gas, and biomass combustion, vegetative detritus, and meat smoke. Hopanes and *n*-alkanes were included in the CMB model as markers for fossil fuel combustion (40). Markers for wood-smoke including levoglucosan (41) were also measured and included in the CMB model. Markers for coal, natural gas combustion, meat smoke, and vegetative detritus were either

not observed or negligible and were not included. The measured concentrations of selected PM_{2.5} organic marker species included in the CMB model are shown in SI Figure S2 by filter composite period. On average, the concentrations of all quantified organic species and CMB tracer species compose <5 and <0.5% of total OA, respectively.

Molecular markers for SOA, comprised of organic compounds formed in the atmosphere through condensation or gas-to-particle conversion, are difficult to quantify with GC analysis and are not typically apportioned by CMB models. An upper bound estimate of SOA, however, can be obtained by difference:

$$\text{SOA}_{\text{CMB}} = \text{OA} - \sum (\text{POA}_i) \quad (5)$$

where $\sum(\text{POA}_i)$ is the sum of the POA apportioned to all sources (2).

Results of CMB OA apportionment are shown in Figure 1f. For each composite period, CMB apportioned >95% of POC to fossil fuel emissions, with the majority (~64%) being attributed to emissions from gasoline vehicles. The small remainder (<5%) of the POC in each composite period was apportioned to BB (~0.1 $\mu\text{g m}^{-3}$ daily average). In each period, the total CMB-apportioned POA makes up a relatively small fraction of measured PM_{2.5} OA. In contrast, the "other" organics consistently contributes the largest amount of mass (77%; range 72–83%). Recent studies have indicated that the bulk of this fraction is SOA, which is also consistent with the estimates of the four other methods presented here. For example, CMB source apportionment of PM_{2.5} OA in six southeastern United States locations observed highest contributions of "other" organic in all locations during July, coinciding with peak photochemical activity (42). Additionally, strong correlations have been observed between this fraction and the sum of secondary inorganics (42) and ambient WSOC concentrations (6).

PMF Analysis of HR-ToF-AMS Data. In contrast to most of the methods discussed above that apportion SOA as the difference between measured OA and apportioned POA, PMF explicitly identifies individual OA components. PMF and similar advanced factor analysis models have previously used Quadrupole AMS data to determine OA sources in urban regions of Pittsburgh and Zurich, Switzerland (16, 17). The use of HR data results in greater differentiation between the spectra of the OA components, which has been shown to enhance AMS OA component separation using PMF (16).

The number of factors identified in the PMF solution was selected by examining both mathematical PMF diagnostics and interpretability of the identified factors based on similarity with AMS source spectra and time series of independent tracers (16, 17, 43). Reduced (hydrocarbon-like, HOA) components were classified as primary, OOA components were classified as secondary, and one small (~5% contribution to PM₁ OA mass) component was classified as "other" based on these comparisons (16, 17, 23, 44). Finally, the mass concentration of SOA was calculated as the sum of individual secondary factor mass concentrations. Some fresh SOA can have a reduced spectrum and may be incorrectly classified as POA by this method (45).

Over the entire sample period, the average SOA/OA ratio obtained from PMF analysis is $74 \pm 19\%$. The diurnal profile of SOA/OA ratios from PMF-AMS analysis is shown in Figure 1g. Minimum SOA/OA ratios ~45% are again observed during the morning rush hour period. Overall, this profile is very similar to that obtained with the CO-tracer method. However the EC-tracer method apportions SOA slightly differently throughout the evening/night, with higher SOA/OA ratios during those periods. This may result from higher $(\text{OC}/\text{EC})_p$ during the night due to reduced diesel traffic at that time (24).

In order to facilitate comparison, Figure 1h shows the diurnal profiles of SOA/OA estimated by all methods. Diurnal cycles of these ratios are similar with maximum SOA/OA ratios of 70–90% estimated by each method during the early afternoon. Minimum SOA/OA ratios obtained from each method do not fall below 45% during any 1 h period. The differences in the diurnal profiles are indicative of current uncertainties in the estimation of SOA from field measurements.

Dominant contributions of SOA to OA also do not appear to be limited to distant locations at the eastern part of the LA basin. AMS mass spectra from Riverside and Pasadena (14 km NNE of downtown LA) exhibit a high degree of similarity and suggest that Pasadena OA is also characterized by high SOA/OA ratios. SI Figure S3 compares Riverside UMR OA mass spectra averaged from 7/28 to 8/3 with that measured by a C-ToF-AMS at the California Institute of Technology (Caltech) in Pasadena over the same time period. The degree of OA oxidation, estimated using the ratio of m/z 44 (oxidized OA marker fragment) to total organics (46) is similar (even slightly higher in Pasadena), indicating a high degree of oxidation in OA observed in both locations, likely explained by rapid SOA formation (31). In support of this observation, we note that although estimates by Pandis et al. (47) are significantly lower than those obtained during SOAR-1, similar SOA contributions to total organics were calculated for Rubidoux and Burbank, which are located near Riverside and Pasadena, respectively. Back-trajectories shown in SI Figure S4 indicate that air masses arriving at each location at 1:00 p.m. were transported from the west through the Los Angeles urban area and spent several hours to a day over the urban area before their arrival at either measurement site.

Comparison with Previous Estimates of SOA in this Area.

Numerous studies have previously estimated the SOA in the LA Basin using a variety of methods including modeling (47–51), CMB-MM (2, 52), and the EC-tracer method (20, 21, 53). Figure 2 presents several previous estimates of SOA/OA in this region along with the five estimates from this study.

There is considerable variation in SOA estimates reported by previous studies much of which is likely due to differences in sampling season, location, and duration. Common to all these previous studies, however, is that POA contributes the majority of OA over extended periods. Unlike the current study, SOA/OA ratios >50% have previously been reported to occur only during severe photochemical smog events (SPSE), characterized by ozone concentrations in excess of ≥ 200 ppb. Schauer et al. (52) reported results of CMB source apportionment on filter samples collected throughout the LA basin during a two-day photochemical smog event in 1993. The eastern-most sampling location was Claremont, California, ~50 km inland of LA where CMB apportioned ~75% of measured OA as SOA. Similarly, Turpin et al. (20) observed several photochemical smog events in Claremont. During the events observed by Turpin et al., SOA/OA ratios were estimated to be greater than 50% for a few hours following the daily maximum ozone concentration. Both of these studies reported the predominance of SOA over short time periods with high photochemistry, which span between a few hours and two days. If we exclude these limited photochemical events, however, previous summer studies taken together indicate an average SOA fraction below 50% (20, 21, 47, 53). However, SOA fractions estimated during the multiweek SOAR-1 study are substantially higher (74% based on the average of the five methods) than estimated by these previous studies despite the fact that ozone concentrations in this part of the basin were not significantly elevated during SOAR-1.

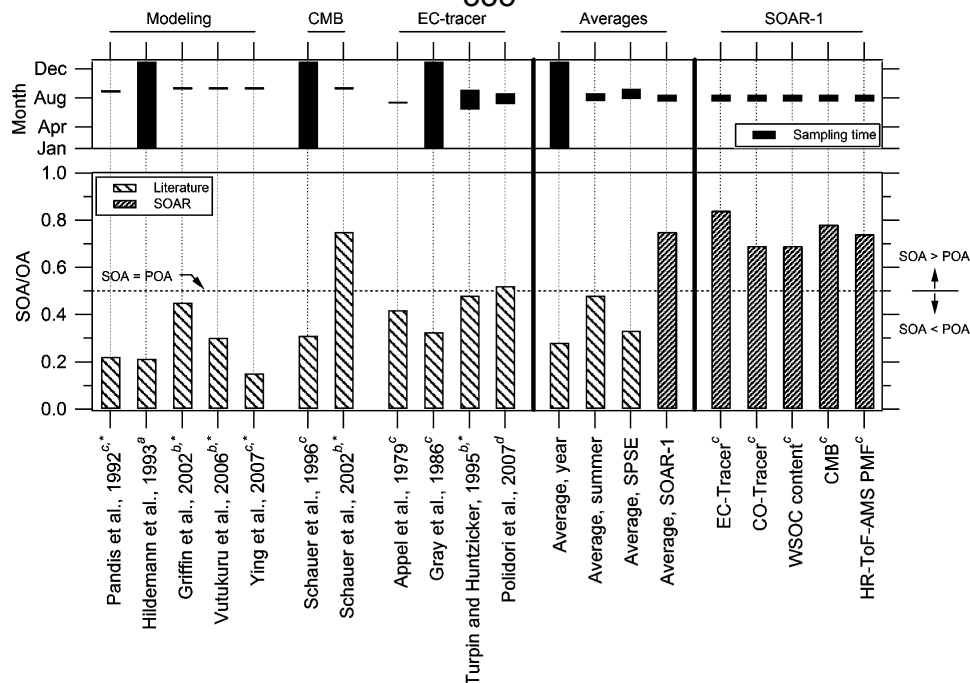


FIGURE 2. Comparison of SOA/OA ratios determined during SOAR-1 with previous measurements throughout the Eastern LA Basin using a range of analytical methods. The bottom shows the reported SOA fraction, whereas the top shows the time and duration of sampling corresponding to each estimate. Subscript letters indicate sampling location *a*) multiple locations; *b*) Claremont/Azusa; *c*) Riverside/Rubidoux; and *d*) undisclosed location (due to confidentiality) ~50 km east of LA, and * indicates an estimate obtained during a photochemical smog event.

Different SOA estimates between SOAR-1 and previous studies may have a number of underlying explanations including (1) atypical atmospheric conditions during the SOAR-1 campaign; (2) problems in methods used to obtain previous SOA estimates; and (3) genuine changes in organic aerosol sources. Differences are not likely due to anomalous conditions during SOAR-1. SI Figure S5 presents daily average $PM_{2.5}$, ozone, CO, and NO_x concentrations measured in Rubidoux (~10 km west of Riverside) along with total acres burned in fire events in Riverside and San Bernardino Counties for the period 7/15 to 8/15/2000–2006, whereas Figures S6 and S7 in the SI compare the meteorological conditions for these same periods. For 2005, ozone is very similar to previous years suggesting a likely similar contribution of SOA (54). While CO is lower, NO_x is very similar to previous years, indicating that the POA contribution was not drastically smaller than in 2000–2004. Since the main source of CO is gasoline vehicles, if we increase their CMB-estimated POA contribution proportional to the difference in CO, we would obtain a CO-corrected SOA estimate of 68% according to CMB, which should be treated as a lower limit since gasoline vehicles are also an important source of NO_x , and since the additional gasoline emissions would also increase SOA.

Some of this difference however can be explained by problems in the methods applied to obtain the previous estimates. For instance, large uncertainties in the Pandis et al. (47) SOA estimates were attributed to understated basin-wide emissions of gas-phase organics and discrepancies in experimentally determined SOA yields. Doubling the VOC emissions increased SOA fractions in Claremont by a factor of 2.3 and improved the correlation between projected and measured ozone concentrations. With regard to SOA yields, it has been shown that model predictions based on simulation chamber yields dramatically underestimate SOA formation in the polluted atmosphere (31). Recently determined SOA yields (e.g., ref 55) close the gap somewhat, but a significant discrepancy still remains. Scaling up the modeling SOA estimates (47–51) by the measurement/model discrepancies

summarized in ref 31 would produce SOA fractions of the order of those in this study. Additionally, estimates based on EC-tracer method calculations could be biased low due to difficulties estimating $(OC/EC)_p$ with the ambient regression method. Previous studies using the EC-tracer method in the LA basin have obtained $SOA/OA \leq 50\%$ using $(OC/EC)_p \geq 2$. As discussed earlier, this is likely an overestimate with more realistic values being ~1.4 or lower. Recalculating the results of Polidori et al. (21) using an $(OC/EC)_p = 1.4$ increases the SOA/OA to ~65%. Recalculating results from other studies which applied the EC-tracer method is not possible due to a lack of reported data.

Another possible reason for the observed differences is that the fraction of SOA in the LA basin may have increased with time via, e.g., more efficient POA emissions reduction (due to targeted policies such as vehicle emission controls), than reduction of SOA precursors (28). Although VOCs generally have been targeted by emission control policies with the main goal of reducing O_3 formation, the dominant precursors and pathways of SOA formation in urban areas are very unclear at present (31), so it is difficult to evaluate the impact of previous air quality improvement policies in SOA relative to POA.

Our estimates from SOAR-1 indicate that the composition of OA at the eastern part of the LA Basin is dominated by SOA by a wide margin, and that these results likely extend to the western part of the basin as well. Contributions from POA are significantly smaller and are similar to SOA only during the morning rush hour. These high contributions from SOA also occurred absent severe photochemical smog events. Source apportionment of OA is important to regulatory strategies involved with protecting air quality and human health. These efforts have put more emphasis on controlling direct POA emissions than emissions of SOA precursor gases. Our results strongly suggest that this strategy should be reconsidered due to the overwhelming contribution of SOA to OA during the summer in the LA basin.

Acknowledgments

We acknowledge funding provided by U.S. Environmental Protection Agency (EPA) STAR grants RD832161010 and R831080, National Science Foundation (NSF) grant ATM-0449815, and NSF/UCAR grant S05-39607. P.F.D. and I.M.U. were supported by EPA Fellowship FP-9165081 and NASA Fellowship NNG05GQ50H, respectively. We also thank Megan McKay and Allen Goldstein for the use of their CO measurements in the CO-tracer calculations, and the rest of the Jimenez group and Aerodyne Research for support in the field and helpful discussions. We would also like to thank Paul Ziemann and the Air Pollution Research Center for hosting the SOAR-1 study. The United States Environmental Protection Agency through its Office of Research and development collaborated in the research described here. It has been subjected to Agency review and approved for publication. Mention of trade names or commercial products does not constitute endorsement or recommendation for use.

Supporting Information Available

Figures S1–S7 and Tables S1 and S2. This material is available free of charge via the Internet at <http://pubs.acs.org>.

Literature Cited

- Zhang, Q.; et al. Ubiquity and dominance of oxygenated species in organic aerosols in anthropogenically-influenced Northern Hemisphere midlatitudes *Geophys. Res. Lett.* **2007**, *34*, L13801, doi: 10.1029/2007GL029979.
- Schauer, J. J.; et al. Source apportionment of airborne particulate matter using organic compounds as tracers. *Atmos. Environ.* **1996**, *30*, 3837–3855.
- American Lung Association's State of the Air, 2007, http://lungaction.org/reports/sota07_cities.html.
- Snyder, D. C.; Schauer, J. J. An inter-comparison of two black carbon aerosol instruments and a semi-continuous elemental carbon instrument in the urban environment. *Aerosol Sci. Technol.* **2007**, *41*, 463–474.
- Grover, B. D.; et al. Semi-continuous mass closure of the major components of fine particulate matter in Riverside, CA. *Atmos. Environ.* **2008**, *42*, 250–260.
- Stone, E. A.; et al. Source apportionment of fine organic aerosol in Mexico City during the MILAGRO Experiment 2006. *Atmos. Chem. Phys.* **2008**, *8*, 1249–1259.
- Peltier, R. E.; et al. Investigating a liquid-based method for online organic carbon detection in atmospheric particles. *Aerosol Sci. Technol.* **2007**, *41*, 1117–1127.
- DeCarlo, P. F.; et al. Field-deployable, high-resolution, time-of-flight aerosol mass spectrometer. *Anal. Chem.* **2006**, *78*, 8281–8289.
- Turpin, B. J.; Lim, H. J. Species contributions to PM_{2.5} mass concentrations: Revisiting common assumptions for estimating organic mass. *Aerosol Sci. Technol.* **2001**, *35*, 602–610.
- Sueper, D., ToF-AMS High Resolution Analysis Software—Squirrel, <http://cires.colorado.edu/jimenez-group/ToFAMSResources/ToFSoftware/SquirrelInfo/>.
- Salcedo, D.; et al. Characterization of ambient aerosols in Mexico City during the MCMA-2003 campaign with Aerosol Mass Spectrometry: results from the CENICA Supersite. *Atmos. Chem. Phys.* **2006**, *6*, 925–946.
- Canagaratna, M.; et al. Chemical and microphysical characterization of ambient aerosols with the Aerodyne Aerosol Mass Spectrometer. *Mass Spectrom. Rev.* **2007**, *26*, 185–222.
- Slowik, J. G.; et al. Particle morphology and density characterization by combined mobility and aerodynamic diameter measurements. Part 2: Application to combustion-generated soot aerosols as a function of fuel equivalence ratio. *Aerosol Sci. Technol.* **2004**, *38*, 1206–1222.
- Jimenez, J. L.; et al. Ambient aerosol sampling using the Aerodyne Aerosol Mass Spectrometer *J. Geophys. Res.-Atmos* **2003**, *108* 8425, doi: 10.1029/2001JD001213.
- Paatero, P.; Tapper, U. Positive matrix factorization—A nonnegative factor model with optimal utilization of error-estimates of data values. *Environmetrics* **1994**, *5*, 111–126.
- Ulbrich, I.; et al. Interpretation and of organic components from Positive Matrix Factorization of Aerosol Mass Spectrometric data. *Atmos. Phys. Chem. Discussions* **2008**, *8*, 6729–6791.
- Lanz, V. A.; et al. Source apportionment of submicron organic aerosols at an urban site by factor analytical modelling of aerosol mass spectra. *Atmos. Chem. Phys.* **2007**, *7*, 1503–1522.
- Phuleria, H. C.; et al. Air quality impacts of the October 2003 Southern California wildfires *J. Geophys. Res.-Atmos.* **2005**, *110*, D07S20, doi: 10.1029/2004JD004626.
- Prather, K. A. personal communication. **2007**.
- Turpin, B. J.; Huntzicker, J. J. Identification of secondary organic aerosol episodes and quantitation of primary and secondary organic aerosol concentrations during SCAQS. *Atmos. Environ.* **1995**, *29*, 3527–3544.
- Polidori, A.; et al. Indoor/outdoor relationships, trends, and carbonaceous content of fine particulate matter in retirement homes of the Los Angeles basin. *J. Air Waste Manage Assoc.* **2007**, *57*, 366–379.
- Strader, R.; et al. Evaluation of secondary organic aerosol formation in winter. *Atmos. Environ.* **1999**, *33*, 4849–4863.
- Zhang, Q.; et al. Hydrocarbon-like and oxygenated organic aerosols in Pittsburgh: insights into sources and processes of organic aerosols. *Atmos. Chem. Phys.* **2005**, *5*, 3289–3311.
- Harley, R. A.; et al. Changes in motor vehicle emissions on diurnal to decadal time scales and effects on atmospheric composition. *Environ. Sci. Technol.* **2005**, *39*, 5356–5362.
- CARB Emissions data for South Coast Air Basin, 2005, <http://www.arb.ca.gov/ei/emissiondata.html>.
- Kirchstetter, T. W.; et al. On-road measurement of fine particle and nitrogen oxide emissions from light- and heavy-duty motor vehicles. *Atmos. Environ.* **1999**, *33*, 2955–2968.
- Allen, J. O.; et al. Emissions of size-segregated aerosols from on-road vehicles in the Caldecott Tunnel. *Environ. Sci. Technol.* **2001**, *35*, 4189–4197.
- Ban-Weiss, G. A.; et al. Long-term changes in emissions of nitrogen oxides and particulate matter from on-road gasoline and diesel vehicles. *Atmos. Environ.* **2008**, *42*, 220–232.
- Cabada, J. C.; et al. Estimating the secondary organic aerosol contribution to PM_{2.5} using the EC tracer method. *Aerosol Sci. Technol.* **2004**, *38*, 140–155.
- Szidat, S.; et al. Contributions of fossil fuel, biomass-burning, and biogenic emissions to carbonaceous aerosols in Zurich as traced by C-14 *J. Geophys. Res., [Atmos]* **2006**, *111*, D07206, doi: 10.1029/2005JD006590.
- Volkamer, R.; et al. Secondary organic aerosol formation from anthropogenic air pollution: Rapid and higher than expected *Geophys. Res. Lett.* **2006**, *33*, 17, L17811, doi: 10.1029/2006GL026899.
- Takegawa, N.; et al. Seasonal and diurnal variations of submicron organic aerosol in Tokyo observed using the Aerodyne aerosol mass spectrometer *J. Geophys. Res., [Atmos]* **2006**, *111*, D11206, doi: 10.1029/2005JD006515.
- de Gouw, J. A.; et al. Budget of organic carbon in a polluted atmosphere: Results from the New England Air Quality Study in 2002 *J. Geophys. Res., [Atmos]* **2005**, *110*, D16305, doi: 10.1029/2004JD005623.
- Kleeman, M. J.; et al. Source contributions to the size and composition distribution of atmospheric particles: Southern California in September 1996. *Environ. Sci. Technol.* **1999**, *33*, 4331–4341.
- Griffin, R. J.; et al. Contribution of gas phase oxidation of volatile organic compounds to atmospheric carbon monoxide levels in two areas of the United States *J. Geophys. Res., [Atmos]* **2007**, *112*, D10S17, doi: 10.1029/2006JD007602.
- Weber, R. J.; et al. A study of secondary organic aerosol formation in the anthropogenic-influenced southeastern United States *J. Geophys. Res., [Atmos]* **2007**, *112*, D13302, doi: 10.1029/2007JD008408.
- Kondo, Y.; et al. Oxygenated and water-soluble organic aerosols in Tokyo *J. Geophys. Res., [Atmos]* **2007**, *112*, D01203, doi: 10.1029/2006JD007056.
- Favez, O.; et al. Significant formation of water-insoluble secondary organic aerosol in semi-arid urban environment *Geophys. Res. Lett.* **2008**, *35*, L15801, doi: 10.1029/2008GL034446.
- Sannigrahi, P.; et al. Characterization of water-soluble organic carbon in urban atmospheric aerosols using solid-state C-13 NMR spectroscopy. *Environ. Sci. Technol.* **2006**, *40*, 666–672.
- Rogge, W. F.; et al. Sources of fine organic aerosol 2. Noncatalyst and catalyst-equipped automobiles and heavy-duty diesel trucks. *Environ. Sci. Technol.* **1993**, *27*, 636–651.
- Simoneit, B. R. T.; et al. Levoglucosan, a tracer for cellulose in biomass burning and atmospheric particles. *Atmos. Environ.* **1999**, *33*, 173–182.
- Zheng, M.; et al. Source apportionment of PM_{2.5} in the southeastern United States using solvent-extractable organic

- compounds as tracers. *Environ. Sci. Technol.* **2002**, *36*, 2361–2371.
- (43) Reff, A.; et al. Receptor modeling of ambient particulate matter data using positive matrix factorization: Review of existing methods. *J. Air Waste Manage Assoc.* **2007**, *57*, 146–154.
- (44) Zhang, Q.; et al. Deconvolution and quantification of hydrocarbon-like and oxygenated organic aerosols based on aerosol mass spectrometry. *Environ. Sci. Technol.* **2005**, *39*, 4938–4952.
- (45) Kroll, J. H. Evolution of Diesel Exhaust Aerosol in an Urban Environment, EOS Transactions AGU, Fall Meeting Supp., paper A31E-02, 2007.
- (46) Aiken, A.; et al. O/C and OM/OC ratios of primary, secondary, and ambient organic aerosols with high resolution time-of-flight mass spectrometry. *Environ. Sci. Technol.* **2008**, *42*, 4478–4485.
- (47) Pandis, S. N.; et al. Secondary organic aerosol formation and transport. *Atmos. Environ. A* **1992**, *26*, 2269–2282.
- (48) Hildemann, L. M.; et al. Mathematical-modeling of urban organic aerosol—Properties measured by high-resolution gas-chromatography. *Environ. Sci. Technol.* **1993**, *27*, 2045–2055.
- (49) Griffin, R. J.; et al. Secondary organic aerosol - 3. Urban/regional scale model of size- and composition-resolved aerosols *J. Geophys. Res., [Atmos]* **2002**, *107*, 4334, doi: 10.1029/2001JD000544.
- (50) Vutukuru, S.; et al. Simulation and analysis of secondary organic aerosol dynamics in the South Coast Air Basin of California *J. Geophys. Res., [Atmos]* **2006**, *111*, 13, D10S12, doi: 10.1029/2005JD006139.
- (51) Ying, Q.; et al. Verification of a source oriented externally mixed air quality model during a severe photochemical smog episode. *Atmos. Environ.* **2007**, *41*, 1521–1538.
- (52) Schauer, J. J.; et al. Source reconciliation of atmospheric gas-phase and particle-phase pollutants during a severe photochemical smog episode. *Environ. Sci. Technol.* **2002**, *36*, 3806–3814.
- (53) Appel, B. R.; et al. Analysis of carbonaceous material in Southern California atmospheric aerosols. 2. *Environ. Sci. Technol.* **1979**, *13*, 98–104.
- (54) Herndon, S. C.; et al. The correlation of secondary organic aerosol with odd oxygen in a megacity outflow *Geophys. Res. Lett.* **2007**, *35*, L15804, doi: 10.1029/2008GL034058.
- (55) Ng, N. L.; et al. Secondary organic aerosol formation from *m*-xylene, toluene, and benzene. *Atmos. Chem. Phys.* **2007**, *7*, 3909–3922.

ES8008166

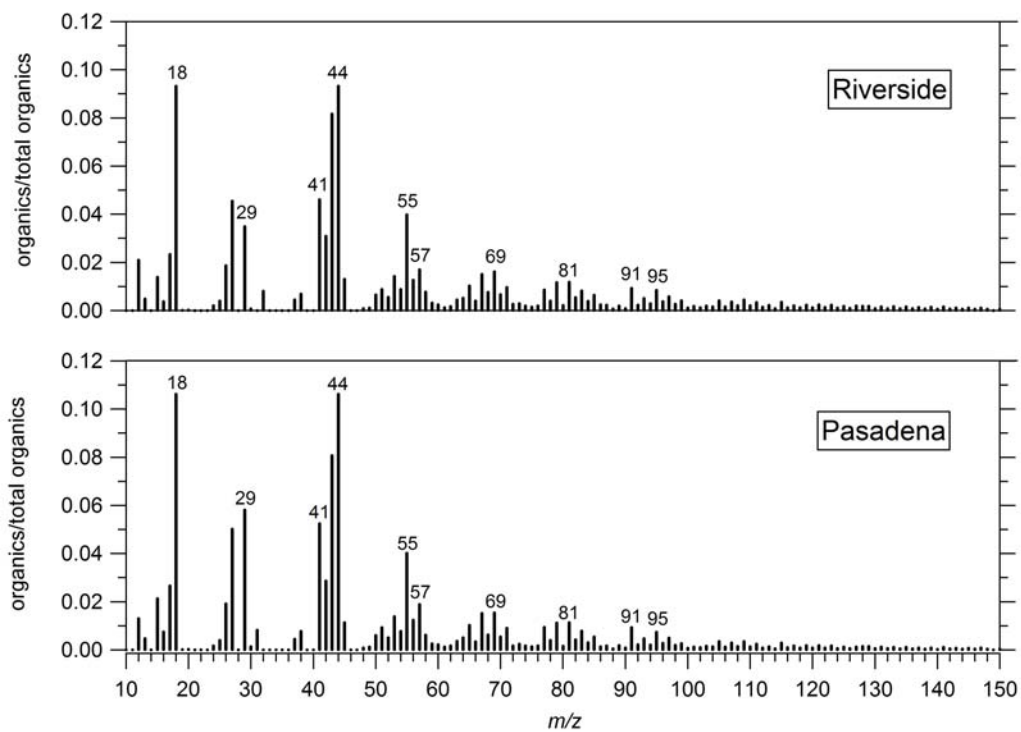


Figure S3. Comparison of Riverside and Pasadena (Caltech) AMS organic mass spectra (see text). Spectra are normalized to the total organics signal to facilitate comparison.

Appendix C

Aerosol Hygroscopicity in the Marine Atmosphere: A Closure Study Using High-Time Resolution, Multiple-RH DASH-SP and Size-Resolved C-ToF-AMS Data*

*This chapter is reproduced by permission from “Aerosol hygroscopicity in the marine atmosphere: A closure study using high-time-resolution, multiple-RH DASH-SP and size-resolved C-ToF-AMS data.” S. P. Hersey, A. Sorooshian, S. M. Murphy, R. C. Flagan, J. H. Seinfeld, *Atmospheric Chemistry and Physics*, 9 (7), 2543-2554, 2009. Copyright 2009 Authors. This work is licensed under a Creative Commons License.

Aerosol hygroscopicity in the marine atmosphere: a closure study using high-time-resolution, multiple-RH DASH-SP and size-resolved C-ToF-AMS data

S. P. Hersey, A. Sorooshian, S. M. Murphy, R. C. Flagan, and J. H. Seinfeld

Departments of Chemical Engineering and Environmental Science and Engineering, Caltech, Pasadena, CA 91125, USA

Received: 14 July 2008 – Published in Atmos. Chem. Phys. Discuss.: 4 September 2008

Revised: 17 November 2008 – Accepted: 24 March 2009 – Published: 7 April 2009

Abstract. We have conducted the first airborne hygroscopic growth closure study to utilize data from an Aerodyne compact Time-of-Flight Aerosol Mass Spectrometer (C-ToF-AMS) coupled with size-resolved, multiple-RH, high-time-resolution hygroscopic growth factor (GF) measurements from the differential aerosol sizing and hygroscopicity spectrometer probe (DASH-SP). These data were collected off the coast of Central California during seven of the 16 flights carried out during the MASE-II field campaign in July 2007. Two of the seven flights were conducted in airmasses characterized by continental origin. These flights exhibited elevated organic volume fractions ($VF_{\text{organic}}=0.56\pm 0.19$, as opposed to 0.39 ± 0.20 for all other flights), corresponding to significantly suppressed GFs at high RH (1.61 ± 0.14 at 92% RH, as compared with 1.91 ± 0.07 for all other flights), more moderate GF suppression at intermediate RH (1.53 ± 0.10 at 85%, compared with 1.58 ± 0.08 for all other flights), and no measurable GF suppression at low RH (1.31 ± 0.06 at 74%, compared with 1.31 ± 0.07 for all other flights). Organic loadings were slightly elevated in above-cloud aerosols, as compared with below-cloud aerosols, and corresponded to a similar trend of significantly suppressed GF at high RH, but more moderate impacts at lower values of RH. A hygroscopic closure based on a volume-weighted mixing rule provided good agreement with DASH-SP measurements ($R^2=0.78$). Minimization of root mean square error between observations and predictions indicated mission-averaged organic GFs of 1.22, 1.45, and 1.48 at 74, 85, and 92% RH, respectively. These values agree with previously reported values for water-soluble organics such as dicarboxylic and multifunctional acids, and correspond to a highly oxidized, presumably water-soluble,

organic fraction (mission-averaged O:C= 0.92 ± 0.33). Finally, a backward stepwise linear regression revealed that, other than RH, the most important predictor for GF is VF_{organic} , indicating that a simple empirical model relating GF, RH, and the relative abundance of organic material can provide accurate predictions ($R^2=0.77$) of hygroscopic growth for the California coast.

1 Introduction

Atmospheric aerosols change size with fluctuations in relative humidity, with a magnitude dictated by chemical composition. Because this hygroscopic response determines particle size, it influences direct climate forcing attributed to aerosols. Further, subsaturated hygroscopic growth factor ($D_{p, \text{wet}}/D_{p, \text{dry}}$) is strongly correlated with CCN activity (Prenni et al., 2001). Given the importance of aerosol water uptake on both the direct and indirect light scattering properties of aerosols, incomplete understanding of aerosol hygroscopicity has been identified as a major limitation in estimations of climate forcing (IPCC, 2007).

With a firm foundational understanding of hygroscopic properties of inorganic aerosol constituents, there has been a significant shift in focus toward organic hygroscopicity in the last decade, as a number of theoretical (e.g., Clegg and Seinfeld, 2006; Topping et al., 2005a,b), laboratory (Peng et al., 2001; Choi and Chan, 2002a,b; Peng and Chan, 2001; Sjogren et al., 2007; Virkkula et al., 1999; Cruz and Pandis, 2000; Prenni et al., 2001, 2007, 2003; Cocker et al., 2001a,b; Hameri et al., 2002; Saathoff et al., 2003; Petters et al., 2006; Varutbangkul et al., 2006; Sjogren et al., 2007; Moore and Raymond, 2008; Rood et al., 1985; Carrico et al., 1998, 2000; Dougle et al., 1998; Magi and Hobbs, 2003; Kim et al., 2006; Kreisberg et al., 2001; Hegg et al., 2006;



Correspondence to: J. H. Seinfeld
 (seinfeld@caltech.edu)

Massling et al., 2007), and chamber (e.g., Ansari and Pandis, 2000; Cocker et al., 2001a,b; Duplissy et al., 2008) studies have sought to address how the presence of organics affects the water uptake characteristics of atmospheric aerosol. Despite advances in understanding of hygroscopic characteristics of organic-containing particles, measurements of aerosol hygroscopicity in field campaigns have remained relatively sparse.

Closure studies, which attempt to reconcile simultaneously measured hygroscopic and chemical data, link laboratory studies of hygroscopicity, theoretical models for water uptake, and field measurements of aerosol-water interactions. The standard method for predicting hygroscopic growth from composition data is based on volume-weighted water uptake by the individual chemical constituents. While it is usually possible to predict water uptake for the inorganic fraction of atmospheric aerosols, the wealth of organic species in the atmosphere, combined with limited understanding of organic aerosol hygroscopicity, has led investigators to assign the water uptake of organics as the particle growth not explained by inorganic constituents (e.g., Malm et al., 2005).

An important approach in hygroscopicity closure is to combine ambient measurements of water uptake with simultaneous, detailed chemical measurements from the Aerodyne Aerosol Mass Spectrometer (AMS). One notable ground-based study in an urban atmosphere (Gysel et al., 2007) used chemical data from the AMS to make volume-weighted predictions of hygroscopic growth factor (GF), providing good agreement between predicted and measured hygroscopicity values. Their study represents an improvement in the hygroscopic treatment of organics over prior work, but is limited by both low time resolution and single-RH conditions inherent in HTDMA systems.

The current study presents data obtained during seven flights in the marine atmosphere off the coast of Central California during the second Marine Stratus/Stratocumulus Experiment (MASE-II). The dataset is the first to combine high-time-resolution, size-resolved AMS chemistry with high-time-resolution, size-resolved hygroscopic data at multiple RH values from the Differential Aerosol Sizing and Hygroscopicity Spectrometer Probe (DASH-SP). Hygroscopic studies have previously been carried out in the marine atmosphere (see Table 1), but none of those listed utilized either AMS chemical data or hygroscopic data as highly size-, time- and RH-resolved as those presented here.

2 Experimental

2.1 MASE-II Experiment

The data presented here were obtained during a series of seven cloud probing flights carried out as part of the second Marine Stratus/Stratocumulus Experiment (MASE-II) field campaign during July 2007. The MASE-II experiment was

the second of two airborne field campaigns directed toward measurement of aerosol-cloud relationships in marine stratocumulus in the Eastern Pacific Ocean. The Marine Stratus/Stratocumulus Experiment (MASE) was carried out in 2005 off the coast of Monterey, California (Lu et al., 2007), and MASE-II was undertaken in 2007 in the same region. Both experiments were carried out in the month of July, when marine stratocumulus are prevalent over the region, and utilized the CIRPAS Twin Otter aircraft. In each campaign, comprehensive airborne measurements were made of aerosol and cloud properties in areas both perturbed and unperturbed by continental emissions. Tables 2 and 3 list the flights carried out during MASE-II and the instrument payload onboard the Twin Otter, respectively. The present study addresses measurements of the hygroscopic properties of marine aerosols during MASE-II. Other flights probed emissions from a large bovine source and a large container ship, and these data are presented elsewhere (Sorooshian et al., 2008b; Murphy et al., 2009).

2.2 Aerosol composition measurements

Non-refractory aerosol chemical species were characterized by the Aerodyne compact Time-of-Flight Aerosol Mass Spectrometer (C-ToF-AMS) (Drewnick et al., 2004a,b). Particles with vacuum aerodynamic diameters (D_{va}) $50\text{ nm} \leq D_{va} \leq 800\text{ nm}$ are focused by an aerodynamic lens, pass through a 3.5% chopper, and are vaporized at 530–600°C. The chopper is operated in three modes, to detect background mass spectra, ensemble average mass spectra over all particle sizes, or size-resolved mass spectra. After particle vaporization, molecules are ionized via electron impact, and are pulsed into a time-of-flight mass spectrometer. MASE-II data were collected at unit mass resolution. AMS mass spectra are deconvolved into sulfate, nitrate, ammonium, and organic mass loadings (Allan et al., 2004). O:C ratios are determined by using mass concentration at m/z 44 and a parameterization presented in Aiken et al. (2008).

AMS measurements were averaged to match the time-resolution of hygroscopicity measurements, and particle density was calculated for each flight leg. Because the C-ToF-AMS measures particle vacuum aerodynamic diameter (D_{va}) and the DMA measures electrical mobility diameter (D_{em}), one can determine particle density by comparing the volume distribution from the DMA ($dV/d\log(D_{em})$) to the total mass distribution measured by the C-ToF-AMS ($dM/d\log(D_{va})$) (DeCarlo et al., 2004). If one assumes that the aerosol consists of an internal mixture of spherical particles, the relationship between the two diameters is $\rho_p = (D_{va}/D_{em})\rho_o$, where ρ_o is unit density (1 g/cm^3). Under these assumptions, the ratio of the D_{va} where the mass distribution peaks to the D_{em} where the volume distribution peaks is the density. Reference to the peak of each distribution is given for simplicity, though in practice the ratio that causes the entirety of the two distributions to best align is

Table 1. Previous marine aerosol hygroscopicity studies.

Investigators	Year	Study Area	Reported GFs
Hegg	1996	Eastern Pacific	1.4–2.0
Berg	1998	Pacific and Southern Oceans	1.56–1.78
Kotchenruther	1998	Mid-Atlantic	1.81–2.3*
Gasso	2000	Eastern Atlantic	$\gamma=0.51 - 0.75^{**}$
Swietlicki	2000	Northeastern Atlantic	1.6–1.8
Zhou	2001	Arctic Ocean	1.4–1.9
Hegg	2002	Eastern Pacific	$\gamma=0.2 - 0.7^{**}$
Vakeva	2002	Northeastern Atlantic	1.3–1.4***
Massling	2003	Atlantic and Indian Oceans	1.6–2.0
Hegg	2006	Eastern Pacific	1.3–1.5
Kaku	2006	Eastern Pacific	1.2–1.7
Tomlinson	2007	Southeastern Pacific	1.3–1.7****

* Ratio of light scattering coefficient at 80% RH to 30% RH.

** γ from the expression $b_{sp}(RH)/b_{sp}(RH_0) = ((1-RH/100)/(1-RH_0/100))^{-\gamma}$ (Kasten, 1969).

*** Aitken mode particles.

**** 85% RH.

the final calculated particle density. Organic density is then calculated by using the bulk chemistry from the C-ToF-AMS for a given time period and assuming the particles measured by the DMA are completely dry. The dry densities of all the inorganic components are known and, assuming volume additivity, the density of the organic component can then be estimated. If the inorganic component of the particles measured by the DMA is not completely dry, this procedure will result in an underestimate of the particle density because the D_{em} will be larger than it would have been for a dry particle. Particles entering the C-ToF-AMS are assumed to be dry, and even if they are not completely devoid of water, the presence of small amounts of water causes little change in the vacuum aerodynamic diameter. One important issue concerning C-ToF-AMS data is the collection efficiency of particles within the instrument (Huffman et al., 2005). In this study, C-ToF-AMS mass loadings were confirmed by comparison between the sulfate measurements from the C-ToF-AMS and the Particle Into Liquid Sampler – Ion Chromatograph (PILS-IC, Brechtel Mfg. Inc.) during periods when there were no rapid fluctuations in particulate mass loading. Composition data represent size-resolved AMS chemistry averaged over 10 nm size bins.

2.3 Hygroscopicity measurements

Hygroscopicity measurements were carried out with the Differential Aerosol Sizing and Hygroscopicity Spectrometer Probe (DASH-SP, Brechtel Mfg; Sorooshian et al., 2008a). Ambient particles pass through a nafion dryer before receiving a uniform charge distribution in a ^{210}Po neutralizer. A cylindrical, single-classification differential mobility analyzer (DMA) then size selects particles into narrow

Table 2. MASE-II flights.

Flight Number (RF)	Date (July 2007)	Type of Flight
1	10	Cloud/aerosol interactions
2	11	Cloud/aerosol interactions
3	12	Bovine source probe
4	14	Cloud/aerosol interactions
5	15	Cloud/aerosol interactions
6	16	Coordinated ship plume probe
7	21	Cloud/aerosol interactions
8	22	Cloud/aerosol interactions
9	23	Cloud/aerosol interactions
10	24	Cloud/aerosol interactions
11	25	Cloud/aerosol interactions
12	26	Cloud/aerosol interactions
13	28	Cloud/aerosol interactions
14	29	Cloud/aerosol interactions
15	30	Bovine source probe
16	31	Cloud/aerosol interactions

ranges of mobility-equivalent diameters (D_{em}) between 0.1 and 1.0 μm . The resulting monodisperse aerosol is split into five separate flows. One channel provides a redundant measurement of total particle concentration at the DMA-selected size with a water condensation particle counter (TSI Model 3831). The remaining four channels consist of parallel nafion humidification chambers (Perma Pure, LLP, Model MD-070-24FS-4), followed by correspondingly humidified custom optical particle counters (OPCs). In the OPC sample volume, particles pass through a focused

Table 3. MASE-II instrument payload.

Parameter	Instrument	Time Resolution	Detection Limit	Size Range
Particle Number Concentration	Condensation Particle Counter (TSI CPC 3010)	1 s	0–10 000 cm ⁻³	$D_p \geq 10$ nm
Particle Number Concentration (including ultrafine)	Condensation Particle Counter (TSI CPC 3025)	1 s	0–100 000 cm ⁻³	$D_p \geq 3$ nm
Aerosol Size Distribution	Scanning differential mobility analyzer (Dual Automated Classified Aerosol Detector, DACAD)	73 s	N/A	10–700 nm
Aerosol Size Distribution	Passive Cavity Aerosol Spectrometer Probe (PCASP)	1 s	N/A	0.1–2.6 μ m
Separation of Cloud Droplets From Interstitial Aerosol	Counterflow Virtual Impactor	N/A	N/A	N/A
Cloud Droplet Size Distribution	Phase Doppler Interferometer (PDI)	1 s	N/A	4–200 μ m
Cloud and Drizzle Drop Size Distribution	Forward Scattering Spectrometer Probe (FSSP)	1 s	N/A	1–46 μ m
Cloud Droplet Liquid Water Content	Light Diffraction (Gerber PVM-100 probe)	1 s	N/A	5–50 nm
Aerosol Bulk Ionic Composition and Soluble Organic Composition	Particle-Into-Liquid Sampler (PILS)	5 min	0.02–0.28 μ g/m ³	1 μ m
Aerosol Bulk Composition (non-refractory species)	Aerodyne compact Time-of-Flight Aerosol Mass Spectrometer (C-ToF-AMS)	1 s or 15 s	≤ 0.25 g/m ³	$40 \text{ nm} \leq D_{p, va} \leq 1 \mu\text{m}$
Aerosol Hygroscopicity	Differential Aerosol Sizing and Hygroscopicity Spectrometer Probe (DASH-SP)	15–100 s	N/A	$150 \text{ nm} \leq D_p \leq 1 \mu\text{m}$
Soot Absorption	Photoacoustic Absorption Spectrometer (PAS)	1 s	1 Mm ⁻¹	10 nm–5 μ m
Soot Absorption	Particle Soot Absorption Photometer (PSAP)	≥ 1 s	N/A	N/A

laser beam ($\lambda=532$ nm, World Star Technologies, Model TECGL-30) and scatter light in proportion to size (D_p) and refractive index (RI). Forward-scattered light is collected and focused on a photomultiplier tube, and the resulting electrical pulse is recorded by a high-speed data acquisition computer. An iterative data processing algorithm, based on laboratory calibrations with salts of known refractive indices, is used to determine the best fit on a solution surface relating electrical pulse height, size, and refractive index. The hygroscopic growth factor ($\text{GF} = D_{p, \text{wet}}/D_{p, \text{dry}}$) is corrected for the RI change caused by particulate liquid water at elevated RH. Temperature and pressure measurements are continually made at multiple locations in the instrument, and used to ensure that temperature and pressure variability do not impact hygroscopicity measurements.

In the current study, hygroscopicity was measured at dry sizes corresponding to D_{em} of 150, 175, and 200 nm. Multiple RH sensors in the nafion tubes and OPCs controlled RHs to dry ($\leq 8\%$), 74%, 85%, and 92%, with RH uncertainty of 1.5%. Low particle loadings inherent in the marine atmosphere required increased on-line collection times at each DMA size step, but usually ≤ 1 min was sufficient to overcome counting statistic limitations. Overall uncertainty in GF calculations is 4.5%.

Assuming particles to be uniform, non-light-absorbing spheres allows the assumption that the intensity of scattered light is a function of only RI and D_p . This assumption also allows calculation of dry, “effective” RI from the known DMA-selected D_p and measured scattered light intensity.

2.4 Hygroscopic closure

A volume-weighted mixing rule was used to perform a hygroscopic closure using AMS and DASH-SP data, under the assumption of independent and additive water uptake by individual constituents in each particle:

$$\text{GF}_{\text{mixed}}(a_w) = \left(\sum_i \epsilon_i \text{GF}_i(a_w)^3 \right)^{1/3} \quad (1)$$

where GF_{mixed} is the overall particle GF, a_w is the water activity, GF_i is the hygroscopic growth factor for pure species i , and ϵ_i is the volume fraction of species i . At equilibrium, $a_w = \text{RH}$ (Seinfeld and Pandis, 2006). Values for ϵ_i were calculated for the following species, using AMS masses of ammonium (NH_4^+), nitrate (NO_3^-), sulfate (SO_4^{2-}), and total organic: ammonium nitrate (NH_4NO_3), ammonium sulfate ($(\text{NH}_4)_2\text{SO}_4$), ammonium bisulfate (NH_4HSO_4), sulfuric acid (H_2SO_4), and organic. Partitioning between sulfate

species was determined on the basis of the ammonium to sulfate molar ratio ($SR=[\text{NH}_4^+]/\text{SO}_4^{2-}$). When $SR \leq 1$, the sulfate was assumed to be a mixture of H_2SO_4 and NH_4HSO_4 ; when $1 < SR < 2$, sulfate was assumed to be a mixture of NH_4HSO_4 and $(\text{NH}_4)_2\text{SO}_4$; when $SR \geq 2$, sulfate was assumed to be solely $(\text{NH}_4)_2\text{SO}_4$. During MASE-II, sulfate was predominantly found to exist as NH_4HSO_4 . $(\text{NH}_4)_2\text{SO}_4$ is assumed to have a GF of unity at RH equal to 74% since particles are exposed to RH well below its efflorescence point before subsequent rehumidification. The organic fraction was assumed to be hydrophilic, based on evidence of a high degree of organic oxygenation from AMS mass spectra (see Sect. 3.3). Values of GF_i for the organic fraction were calculated as those necessary to minimize the root mean square error in comparing predictions with measured hygroscopicity.

3 Results

GF values for seven flights are presented (RF 7, 10, 11, 12, 13, 14, and 16 in Table 2). Table 4 presents measured GFs at each RH and each $D_{em, dry}$. Typically, multiple measurements were made on each leg, at each size, for each flight. The error reported is \pm one standard deviation in these multiple measurements. When only one measurement was made at a given size in a given leg, it is reported without error. Ship plumes were encountered on flights 10 and 16, as evidenced by brief, significantly elevated particle number concentration. Analysis of GF measurements in these presumptive plumes is not presented in the present work. Aerosol densities were calculated for each leg and used in the analysis below. Mission-averaged densities (averaged over all flight legs) were found to be 1.53 ± 0.19 , 1.56 ± 0.20 , and $1.47 \pm 0.15 \text{ g/cm}^3$ for below-cloud, above-cloud, and free troposphere legs, respectively. Mission-averaged organic densities were calculated to be 1.20 ± 0.76 , 1.34 ± 0.46 , and 1.30 ± 0.24 for below-cloud, above-cloud, and free troposphere legs, respectively.

3.1 Airmass origin

Relative to the other flights, RF 12 and 16 exhibited significantly suppressed water uptake at high RH for all dry sizes. During these two flights, 92% GF values for 200 nm $D_{em, dry}$ particles averaged 1.61 ± 0.14 , as compared with 1.91 ± 0.07 for all other flights. These low-GF flights corresponded to significantly elevated total organic, as measured by the AMS. Mass concentration averaged $1.97 \pm 1.71 \mu\text{g/m}^3$ organic (as opposed to $0.58 \pm 0.63 \mu\text{g/m}^3$ for all other flights), corresponding to volume fraction organic ($VF_{organic}$) of 0.56 ± 0.19 (as opposed to 0.39 ± 0.20 for all other flights).

Back-trajectory analysis suggests that the MASE-II flights can be categorized by airmass origin as either polluted/continental (flights 12, 16), or non-continentially influenced (flights 7, 10, 11, 13, 14). Figure 1 shows

92% GF measurements for 200 nm $D_{em, dry}$ particles, with corresponding 48-h HYSPLIT (available at: <http://www.arl.noaa.gov/ready/hysplit4.html>) back-trajectories identifying airmass origin. Note that the low GFs and high $VF_{organic}$ measured on flights 12 and 16 correspond with airmass origins over the continental United States, while higher GFs and lower $VF_{organic}$ measured on other flights correspond to airmass origins over the clean marine environment. It is interesting to note that trajectories at sea level have marine origins for all flights (including low-GF flights 12 and 16), and that there is a general trend of descending air from aloft over the course of the trajectories. This suggests that mixing of air from aloft is a significant factor in determining aerosol characteristics in the marine boundary layer. It is also noteworthy that GF values at low RH were not significantly suppressed, with values of 1.31 ± 0.06 at 74% (compared with 1.31 ± 0.07 for all other flights). GF values at intermediate RH were moderately suppressed in the continental airmasses, measuring 1.53 ± 0.10 at 85% (compared with 1.58 ± 0.08 for all other flights). In other words, the effect of the high- $VF_{organic}$, continental airmass was to significantly suppress GF at high RH, while having no measurable effect on aerosol water uptake at low RH and a moderate impact at intermediate RH. These results, while suggestive of continental airmass influence, should be interpreted in light of the relatively coarse grid resolution of the HYSPLIT model. In this analysis, small shifts in back-trajectories toward continental origin correlate with significantly suppressed high-RH GFs.

3.2 Hygroscopicity trends

No size-dependent hygroscopicity was observed over the range of measured $D_{em, dry}$, and in addition, no significant size-dependent trends in $VF_{organic}$ were observed. Further, organic-to-sulfate ratios from the AMS showed no significant variation over the size range measured by the DASH-SP. This suggests an internally-mixed aerosol between dry sizes of 150 and 200 nm.

Figure 2 shows below- and corresponding above-cloud 92% GF values for all flights. There exists a ubiquitous trend of higher below-cloud aerosol GF values at high RH when compared with top of cloud hygroscopicity values (1.88 ± 0.14 below cloud, versus 1.78 ± 0.18 above cloud). Marker sizes, proportional to $VF_{organic}$, suggest a trend of higher organic loading above cloud in several flights (0.36 ± 0.15 below cloud, versus 0.43 ± 0.22 above cloud). While variability is rather large in these measurements, the trend of elevated $VF_{organic}$ above-cloud does correspond to suppressed GF at high RH. There is a trend of more moderate GF suppression at intermediate RH in the higher $VF_{organic}$ above-cloud layer (1.53 ± 0.06 above cloud, as compared with 1.58 ± 0.07 below cloud). Unlike the continental-influenced flights, there is evidence of greater suppression of low-RH GFs in above-cloud legs, with 74% GF values of

1.31 ± 0.05 above cloud, compared with 1.36 ± 0.05 below. It appears, then, that the elevated organic loadings typical of above-cloud legs are correlated with GF suppression at high RH, and more moderate GF suppression at lower RHs.

3.3 Hygroscopic closure

A hygroscopic closure was performed, using volume-weighted hygroscopic contributions from each chemical constituent identified by the AMS. O:C ratios for the flights presented were very similar for below-cloud (0.93 ± 0.32), above-cloud (0.91 ± 0.26), and free troposphere (0.92 ± 0.25) legs in both continentally- (0.94 ± 0.30) and marine-influenced (0.91 ± 0.25) flights. This result indicates that the organic component was consistently highly oxidized. With this evidence, the organic fraction was treated as a bulk, water-soluble constituent and was not divided into soluble and insoluble fractions based on AMS organic mass spectra (Kondo et al., 2007). As described in Sect. 2.4, GF values were calculated for the organic component of the aerosol by minimizing root mean square error when comparing measured GFs with volume-weighted closure predictions. Mission-averaged organic GFs were determined to be 1.22, 1.45, and 1.48 at 74, 85, and 92% RH, respectively. Agreement at 74 and 92% RH is within 2%, compared with the hydrophilic multifunctional and dicarboxylic acids parameterized in Peng et al. 2001, though the 85% organic GF is overpredicted here by 7%. Closure results are presented in Fig. 3. Markers in Fig. 3 are color-coded according to relative humidity, and marker size is proportional to VF_{organic} . The volume-weighted hygroscopic closure utilizing size-resolved AMS chemistry achieves good agreement with the 675 DASH-SP GF measurements, with an R^2 of 0.78. Agreement is better at lower values of RH, owing to smaller GF magnitudes and less overall GF variability.

Aside from the obvious RH dependence of GF values, the clearest trend in Fig. 3 is that of larger markers (higher VF_{organic}) at low GF transitioning to smaller markers (lower VF_{organic}) at high values of GF for the same RH. The clarity and regularity of this trend reveal the importance of the organic fraction in determining GF values.

3.4 Simplified parameterization

To further investigate the relative importance of each parameter in quantifying aerosol water uptake, and to determine the simplest empirical model still capable of accurately predicting GF, a backward stepwise linear regression was performed. The process, which eliminates predictors one-by-one to generate increasingly simplified linear representations of data, started with over 60 predictors, ranging from PILS and AMS chemical parameters to atmospheric data. The result is a two-parameter model that predicts GF as a function of RH and VF_{organic} :

$$GF = -0.312 + 0.0233(RH) - 0.282(VF_{\text{organic}}) \quad (2)$$

Figure 4 demonstrates the accuracy with which this model predicts DASH-SP GF values over the measured range of RH and VF_{organic} . It is noteworthy that the R^2 for this model is 0.77, indicating that the simple, two-parameter model explains only 1% less variability than the full volume-weighted chemical closure, which contains significantly more information (i.e. multiple inorganic chemical species and their individual GFs, in addition to organic fraction with its associated GF). It appears as though accurate predictions of particle water uptake in this region can be made simply on the basis of relative humidity and the relative abundance of organics in the aerosol, given a relatively uniform, highly-oxidized organic component internally mixed with predominantly ammonium bisulfate. While this model accurately predicts GF over the range of RH and VF_{organic} , and for the O:C ratios measured during MASE-II, it should not be used when RH is outside the range $74\% \leq RH \leq 92\%$, or where VF_{organic} is less than 0.1 or greater than 0.9.

4 Discussion

Comparing mixed organic-inorganic particles with those comprised entirely of inorganic salts, there is a strong RH-dependence in the effect of organics on hygroscopicity (Peng et al., 2001). During the MASE-II field campaign, GF values at 74% RH averaged ~ 1.3 . Organic GFs were calculated to be 1.22 at 74% RH, suggesting that they contributed significantly to overall aerosol water uptake at low RH. GF values at 85% RH averaged ~ 1.6 during the campaign, and so the organic GF of 1.45 calculated for 85% RH suggests that organics played a less significant role, but still influenced water uptake at intermediate RH. An organic GF value of 1.48 was calculated for 92% RH, with DASH-SP 92% GF measurements of ~ 1.8 indicating that organics make little contribution to overall water uptake at high RH.

Inorganic salts exhibit deliquescent behavior as RH is increased. Many organics do not deliquesce or crystallize when RH is increased or decreased, respectively, but instead retain water at RH values well below the RH of deliquescence (RHD) of the inorganic salts with which they often co-exist in ambient particles. As a result, at RH values below the salt RHD, the presence of organics enhances water uptake. Thus, the effect of organics is to contribute significantly to overall water uptake at low values of RH in mixed organic-inorganic particles. At high RH, on the other hand, organics tend to take up significantly less water than the inorganic constituents with which they co-exist in ambient particles. Therefore, at RH values above the inorganic RHD, organics appear to suppress water uptake relative to that which a pure inorganic particle would exhibit.

Figure 5 shows simplified behavior of a pure ammonium sulfate (AS) particle, pure organic acid (OA) particle (as described by Peng et al., 2001), and a mixed organic acid and ammonium sulfate (OA/AS) particle over the range

Table 4. GF results for below, above, free troposphere (FT), and ship plume measurements.

Flight	150 nm											
	Below			Above			FT			Ship Plume		
	74%	85%	92%	74%	85%	92%	74%	85%	92%	74%	85%	92%
7	1.40±0.04	1.57±0.03	1.82±0.05	1.26±0.06	1.55±0.04	1.78±0.01	1.40±0.03	1.55±0.03	1.84±0.04			
10	1.42±0.04	1.60±0.06	1.80±0.04	1.37±0.10	1.57±0.04	1.71±0.11	1.42±0.03	1.56±0.04	1.70±0.07	1.42±0.04	1.62±0.03	1.78±0.04
11	1.44±0.05	1.61±0.06	1.80±0.07	1.40±0.07	1.51±0.02	1.64±0.05	1.38±0.07	1.52±0.06	1.65±0.10			
12	1.38±0.03	1.58±0.03	1.63±0.04	1.34±0.04	1.51±0.03	1.55±0.01	1.38±0.02	1.60±0.01	1.63±0.01			
13	1.39±0.01	1.61±0.05	1.82±0.02	1.35±0.01	1.61±0.03	1.75±0.05	1.27±0.05	1.49±0.07	1.61±0.08			
14	1.36±0.05	1.65±0.21	1.82±0.14	1.39±0.02	1.62±0.01	1.87±0.09	1.37±0.03	1.60±0.03	1.77±0.06			
16	1.41±0.02	1.58±0.05	1.64±0.08	1.33±0.03	1.52±0.03	1.54±0.03	1.29±0.04	1.49±0.07	1.52±0.06	1.38±0.02	1.59±0.02	1.61±0.04
Flight	175 nm											
	Below			Above			FT			Ship Plume		
	74%	85%	92%	74%	85%	92%	74%	85%	92%	74%	85%	92%
7	1.36±0.06	1.54±0.02	1.95±0.03	1.28±0.04	1.53±0.03	1.91±0.06	1.24±0.08	1.52±0.03	1.87±0.10			
10	1.41±0.06	1.59±0.05	1.93±0.02	1.34±0.05	1.51±0.01	1.83±0.06	1.33±0.02	1.60±0.03	1.89±0.05	1.34±0.02	1.55±0.05	1.88±0.06
11	1.31±0.08	1.48±0.07	1.82±0.09	1.31±0.03	1.44±0.09	1.77±0.03	1.33±0.04	1.53±0.12	1.77±0.23			
12	1.33±0.02	1.55±0.04	1.63±0.08	1.26±0.06	1.48±0.08	1.51±0.07	1.35±0.02	1.57±0.01	1.60±0.01			
13	1.34±0.03	1.58±0.04	2.00±0.05	1.3	1.55	1.78	1.24±0.05	1.44±0.06	1.63±0.10			
14	1.34±0.01	1.63±0.02	2.03±0.01	1.32±0.02	1.58±0.02	1.91±0.05	1.33±0.02	1.50±0.08	1.79±0.22			
16	1.35±0.04	1.54±0.03	1.62±0.06	1.28±0.02	1.43±0.04	1.45±0.04	1.24±0.04	1.38±0.06	1.40±0.10	1.33±0.03	1.52±0.04	1.55±0.03
Flight	200 nm											
	Below			Above			FT			Ship Plume		
	74%	85%	92%	74%	85%	92%	74%	85%	92%	74%	85%	92%
7	1.37±0.04	1.57±0.03	1.98±0.03	1.22±0.06	1.56±0.05	1.92±0.01	1.21±0.01	1.54±0.08	1.91±0.04			
10	1.41±0.09	1.72±0.09	2.01±0.05	1.33±0.02	1.57±0.07	1.87±0.04	1.35±0.01	1.63±0.06	1.93±0.06	1.33±0.04	1.66±0.06	1.95±0.05
11	1.25±0.11	1.45±0.17	1.86±0.07	1.26	1.47	1.83	1.36±0.16	1.56±0.15	1.89±0.20			
12	1.33±0.03	1.64±0.03	1.73±0.05	1.29±0.03	1.48±0.10	1.55±0.12	1.37±0.05	1.64±0.05	1.69±0.04			
13	1.36±0.05	1.68±0.05	2.01±0.04	1.3	1.61	1.85	1.21±0.08	1.45±0.07	1.78±0.12			
14	1.42±0.11	1.65±0.05	1.98±0.10	1.31±0.05	1.60±0.03	1.96±0.01	1.35±0.09	1.59±0.10	1.89±0.11			
16	1.35±0.02	1.59±0.05	1.77±0.08	1.26±0.02	1.45±0.08	1.53±0.10	1.23±0.06	1.40±0.10	1.40±0.11	1.33±0.03	1.62±0.04	1.66±0.06

50% ≤ RH ≤ 94%. Note that the mixed OA/AS particle shows smooth growth with RH, as opposed to the deliquescent behavior exhibited by the pure AS particle. The tendency of organics to retain water at low RH causes water uptake behavior for the OA/AS particle to follow that of the descending (i.e. efflorescence) branch of the pure AS growth curve. Since pure OA takes up less water at high RH than does pure AS, the growth curve for the OA/AS particle is suppressed, compared with that of pure AS. The overall result, as predicted by thermodynamic theory, is that the presence of OA leads to enhanced water uptake at low RH and suppressed GF at high RH.

Virkkula et al. (1999) concluded that the most important factor contributing to GF suppression at high RH was the volume fraction of organic present in an aerosol. Others have suggested that the exact chemical identity of the organic constituents is not especially important, and that for an organic component classified as either oxidized or hydrocarbon-like, its relative abundance determines its effect on GF values (McFiggans et al., 2005; Moore and Raymond, 2008). The aerosol measured during MASE-II was comprised of an internally-mixed combination of highly-oxidized organics with predominantly ammonium bisulfate in the size

range 150–200 nm. Results presented here from a stepwise linear regression on GF data from the marine atmosphere suggest that the single most important factor in predicting GF (aside from RH) is, indeed, VF_{organic} . This suggests that an aerosol containing a uniform, highly-oxidized organic component may be sufficiently characterized in global models by a size distribution, RH, and a bulk estimate of the relative abundance of organics.

A brief sensitivity study was undertaken, in order to determine the importance of the VF_{organic} term in predicting water uptake for the marine aerosol encountered during this study. Predictions of hygroscopic GF based on the assumption of an entirely inorganic aerosol yielded poorer agreement ($R^2=0.68$) than the simple parameterization presented in this paper ($R^2=0.77$). This suggests that accurate predictions of organic volume fraction are important to predict water uptake for a marine aerosol with a uniformly oxidized organic component.

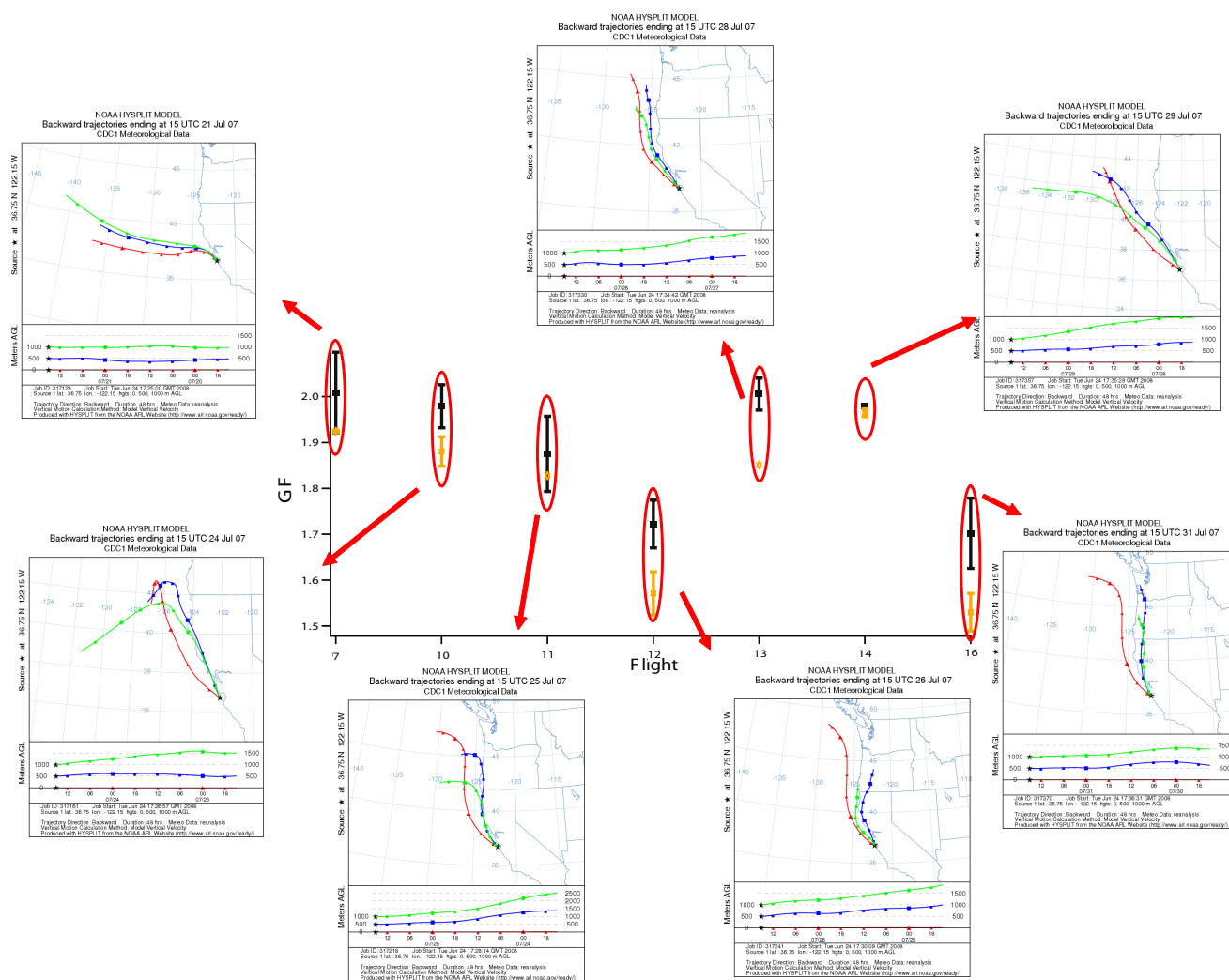


Fig. 1. 92% GF values for $D_{em, dry}=200$ nm particles are shown for below (black) and above (yellow) cloud flight legs. 48-h HYSPLIT back-trajectories show air mass origin for each flight. Flights 12 and 16 show both suppressed GF values and continental, polluted air mass origin.

In most instruments that measure aerosol hygroscopicity, residence times for humidification are on the order of seconds; much longer than the equilibration time for most inorganics with water vapor. Sjogren et al. (2007) noted, however, that particles with high volume fraction organic material may require as long as 40 s to achieve equilibrium with water vapor. If such long times are necessary to achieve equilibrium, hygroscopic measurement methods suitable for the field will tend to overpredict GF at low RH (water vapor does not evaporate completely from the particle during the drying process), while underpredicting GF at high RH (insufficient humidification time is provided for the organic fraction to achieve thermodynamic equilibrium with water vapor). In electrodynamic balance (EDB, Cohen et al., 1987a,b,c) studies, suspended particles are subjected to extended exposure to water vapor (minutes to hours), establishing equilibrium.

Some organics exhibit extremely high deliquescence relative humidities (DRH) (e.g., oxalic acid), while others exhibit gradual hygroscopic growth at low RH and substantial growth at high RH (e.g., malonic acid) (Peng et al., 2001). It is possible, given the wide range of organic species in the atmosphere and correspondingly wide range of hygroscopic properties associated with those species, and the relatively short humidification times in the DASH-SP and other similar instruments, that the effects attributed to organics may reflect some kinetic instrumental limitations.

Additionally, while particles entering the DASH-SP are dried to well below relative humidity of efflorescence (RHE) for the inorganic salts encountered in the marine atmosphere, it is possible that the presence of organics causes some particles to remain in a supersaturated (with respect to efflorescence) state after drying. The inorganic fraction of such

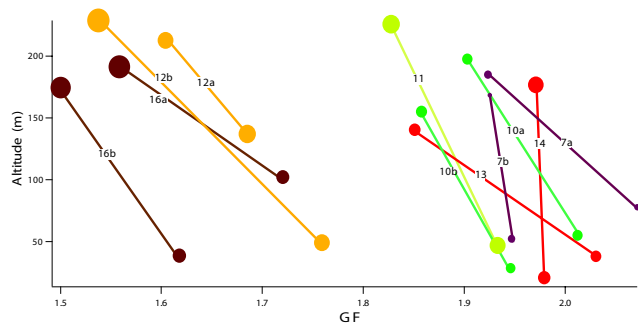


Fig. 2. Below- and above-cloud 92% GF values for D_{em} , dry 200nm particles as a function of altitude, with lines connecting measurements made on the same ‘trip’ from bottom to top of cloud. Marker size is proportional to $VF_{organic}$, and ranges from 0.10 to 0.90. ‘a’ and ‘b’ designate separate ‘trips’ during the same flight.

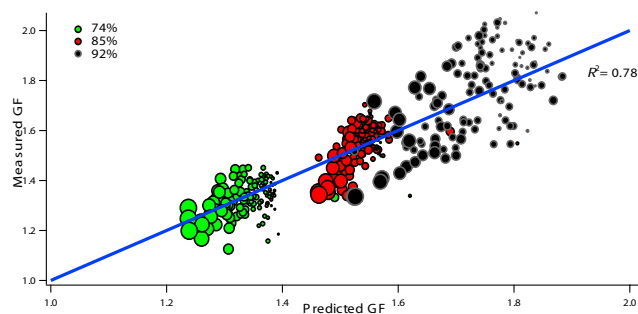


Fig. 3. Measured GF values versus volume-weighted predictions. Markers are color-coded with RH, and marker size is proportional to $VF_{organic}$ (ranging from 0.10 to 0.90). The blue line represents 1:1.

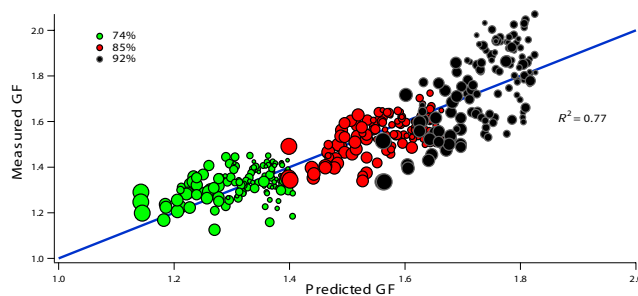


Fig. 4. Predictions of GF from the simplified parameterization. Markers are color-coded with RH, and marker size is proportional to $VF_{organic}$ (ranging from 0.10 to 0.90). The blue line represents 1:1.

a supersaturated particle would exhibit gradual water uptake with increased relative humidity, even at RH lower than the RHD for the inorganic salt. Assuming deliquescent behavior of the inorganic salt (i.e. the inorganic fraction is crystalline at RH RHE), this enhanced water uptake at low RH would be attributed to solely the organic fraction, thereby leading to a potential overestimation in the organic GF.

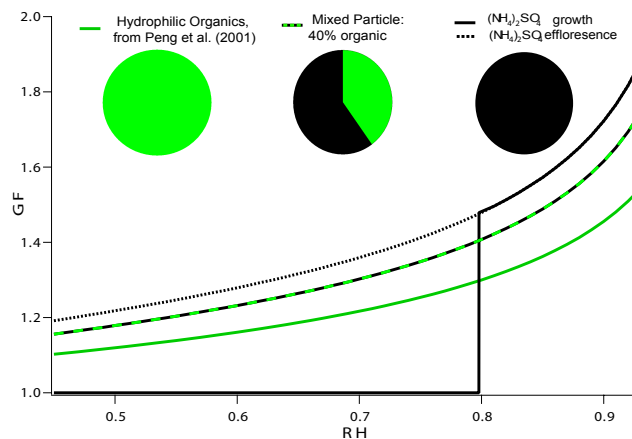


Fig. 5. Comparison of growth curves for pure ammonium sulfate, pure hydrophilic organic, and mixed organic/inorganic particles. Ammonium sulfate curves calculated from AIM (Clegg et al., 1998).

5 Conclusions

We report a hygroscopic closure study for the coastal California aerosol, using size-resolved C-ToF-AMS chemical data coupled with highly time-resolved, multiple-RH hygroscopicity measurements from the DASH-SP.

Airmasses originating from continental locations showed elevated organic loading, and correspond to significant GF suppression at high RH. More moderate GF suppression was measured at intermediate RH and no impact was observed at low RH. A comparison of above-cloud with below-cloud aerosol indicated that a slightly organic-enriched layer above cloud corresponded with suppressed GFs at high RH. A volume-weighted hygroscopic closure provided excellent agreement with measured GFs, and mission-averaged organic GFs at 74, 85, and 92% were calculated to be 1.22, 1.45, and 1.48, respectively. These GF values are relatively high when compared with many previous estimations of organic GF, but agree well with values reported for dicarboxylic and multifunctional acids. These high organic GFs are indicative of the highly oxidized state of the aged organic fraction. A simplified parameterization for predicting GF was developed using a stepwise linear regression method. This parameterization is a function of only RH and $VF_{organic}$, and explains only 1% less variability than does the volume-weighted chemical closure. These results may be more broadly applicable to similar coastal conditions, where some aged organics are present in an otherwise marine-influenced atmosphere.

The richness of this hygroscopic/chemical data set underlies the significance of coupling the DASH-SP instrument with the AMS. The improved time resolution available with the DASH-SP eliminates much of the time-averaging of AMS composition data that is otherwise necessary with less highly time-resolved HTDMA hygroscopicity measure-

ments. The importance of simultaneous GF measurements at multiple RH values is demonstrated by a simplified parameterization for predicting GF as a function of RH and VF_{organic} ; a result potentially important for efficiently representing aerosol-water interactions in global models.

Acknowledgements. This work was supported by the Office of Naval Research grant N00014-04-1-0118. We acknowledge the committed, meticulous work of the CIRPAS Twin Otter crew, especially pilot Mike Hubbell and copilot Chris McGuire.

Edited by: A. Nenes

References

- Aiken, A. C., DeCarlo, P. F., Kroll, J., Worsnop, D., J.A., H., Docherty, K., Ulbrich, I., Mohr, C., Kimmel, J., Sueper, D., Sun, Y., Zhang, Q., Trimborn, A., Northway, M., Ziemann, P., Canagaratna, M., Onasch, T., Alfarra, M., Prevot, A., Dommen, J., Duplissy, J., Metzger, A., Baltensperger, U., and Jimenez, J. L.: O/C and OM/OC Ratios of Primary, Secondary, and Ambient Organic Aerosols with High-Resolution Time-of-Flight Aerosol Mass Spectrometry, *Environ. Sci. Technol.*, 42, 4478–4485, 2008.
- Allan, J., Bower, K., Alfarra, M., Delia, A., Jimenez, J., Middlebrook, A., Drewnick, F., Onasch, T., Canagaratna, M., Jayne, J., and Worsnop, D.: Technical note: Extraction of Chemically Resolved Mass Spectra from Aerodyne Aerosol Mass Spectrometer Data, *J. Aerosol Sci.*, 35, 909–922, 2004.
- Ansari, A. S. and Pandis, S. N.: Water absorption by secondary organic aerosol and its effect on inorganic aerosol behavior, *Environ. Sci. Technol.*, 34, 71–77, 2000.
- Berg, O. H., Swietlicki, E., and Krejci, R.: Hygroscopic growth of aerosol particles in the marine boundary layer over the Pacific and Southern Oceans during the First Aerosol Characterization Experiment (ACE 1), *J. Geophys. Res.*, 103, 16 535–16 545, 1998.
- Carrico, C. M., Rood, M. J., and Ogren, J. A.: Aerosol light scattering properties at Cape Grim, Tasmania, during the First Aerosol Characterization Experiment (ACE 1), *J. Geophys. Res.*, 103, 16 565–16 574, 1998.
- Carrico, C. M., Rood, M. J., Ogren, J. A., Neususs, C., Wiedensohler, A., and Heintzenberg, J.: Aerosol optical properties at Sagres, Portugal during ACE-2, *Tellus B*, 52, 694–715, 2000.
- Choi, M. Y. and Chan, C. K.: Continuous measurements of the water activities of aqueous droplets of water-soluble organic compounds, *J. Phys. Chem. A*, 106, 4566–4572, 2002a.
- Choi, M. Y. and Chan, C. K.: The effects of organic species on the hygroscopic behaviors of inorganic aerosols, *Environ. Sci. Technol.*, 36, 2422–2428, 2002b.
- Clegg, S. L. and Seinfeld, J. H.: Thermodynamic models of aqueous solutions containing inorganic electrolytes and dicarboxylic acids at 298.15 K. 2. Systems including dissociation equilibria, *J. Phys. Chem. A*, 110, 5718–5734, 2006.
- Clegg, S. L., Brimblecombe, P., and Wexler, A. S.: Thermodynamic model of the system $\text{H}^+ - \text{NH}_4^+ - \text{SO}_4^{2-} - \text{NO}_3^- - \text{H}_2\text{O}$ at tropospheric temperatures, *J. Phys. Chem. A*, 102(12), 2137–2154, 1998.
- Cocker, D. R., Clegg, S. L., Flagan, R. C., and Seinfeld, J. H.: The effect of water on gas-particle partitioning of secondary organic aerosol. Part I: alpha-pinene/ozone system, *Atmos. Environ.*, 35, 6049–6072, 2001a.
- Cocker, D. R., Mader, B. T., Kalberer, M., Flagan, R. C., and Seinfeld, J. H.: The effect of water on gas-particle partitioning of secondary organic aerosol: II. m-xylene and 1,3,5-trimethylbenzene photooxidation systems, *Atmos. Environ.*, 35, 6073–6085, 2001b.
- Cohen, M. D., Flagan, R. C., and Seinfeld, J. H.: Studies of concentrated electrolyte-solutions using the electrodynamic balance. 1. Water activities for single-electrolyte solutions, *J. Phys. Chem.*, 91, 4563–4574, 1987a.
- Cohen, M. D., Flagan, R. C., and Seinfeld, J. H.: Studies of concentrated electrolyte-solutions using the electrodynamic balance. 2. Water activities for mixed-electrolyte solutions, *J. Phys. Chem.*, 91, 4575–4582, 1987b.
- Cohen, M. D., Flagan, R. C., and Seinfeld, J. H.: Studies of concentrated electrolyte-solutions using the electrodynamic balance. 3. Solute nucleation, *J. Phys. Chem.*, 91, 4583–4590, 1987c.
- Cruz, C. N. and Pandis, S. N.: Deliquescence and hygroscopic growth of mixed inorganic-organic atmospheric aerosol, *Environ. Sci. Technol.*, 34, 4313–4319, 2000.
- DeCarlo, P., Slowik, J., Worsnop, D., Davidovits, P., and Jimenez, J.: Particle Morphology and Density Characterization by Combined Mobility and Aerodynamic Diameter Measurements. Part 1: Theory, *Aerosol. Sci. Tech.*, 39, 1185–1205, 2004.
- Dougle, P. G., Veefkind, J. P., and ten Brink, H. M.: Crystallisation of mixtures of ammonium nitrate, ammonium sulphate and soot, *J. Aerosol Sci.*, 29, 375–386, 1998.
- Drewnick, F., Jayne, J. T., Canagaratna, M., Worsnop, D. R., and Demerjian, K. L.: Measurement of ambient aerosol composition during the PMTACS-NY 2001 using an aerosol mass spectrometer. Part II: Chemically speciated mass distributions, *Aerosol. Sci. Tech.*, 38, 104–117, suppl. 1, 2004a.
- Drewnick, F., Schwab, J. J., Jayne, J. T., Canagaratna, M., Worsnop, D. R., and Demerjian, K. L.: Measurement of ambient aerosol composition during the PMTACS-NY 2001 using an aerosol mass spectrometer. Part I: Mass concentrations, *Aerosol. Sci. Tech.*, 38, 92–103, suppl. 1, 2004b.
- Duplissy, J., Gysel, M., Alfarra, M. R., Dommen, J., Metzger, A., Prevot, A. S. H., Weingartner, E., Laaksonen, A., Raatikainen, T., Good, N., Turner, S. F., McFiggans, G., and Baltensperger, U.: Cloud forming potential of secondary organic aerosol under near atmospheric conditions, *Geophys. Res. Lett.*, 35, L03818, doi:10.1029/2007GL031075, 2008.
- Gasso, S., Hegg, D. A., Covert, D. S., Collins, D., Noone, K. J., Ostrom, E., Schmid, B., Russell, P. B., Livingston, J. M., Durkee, P. A., and Jonsson, H.: Influence of humidity on the aerosol scattering coefficient and its effect on the upwelling radiance during ACE-2, *Tellus B*, 52(2), 546–567, 2000.
- Gysel, M., Crosier, J., Topping, D. O., Whitehead, J. D., Bower, K. N., Cubison, M. J., Williams, P. I., Flynn, M. J., McFiggans, G. B., and Coe, H.: Closure study between chemical composition and hygroscopic growth of aerosol particles during TORCH2, *Atmos. Chem. Phys.*, 7, 6131–6144, 2007, <http://www.atmos-chem-phys.net/7/6131/2007/>.
- Hameri, K., Charlson, R., and Hansson, H. C.: Hygroscopic properties of mixed ammonium sulfate and carboxylic acids particles,

- AICChE J., 48, 1309–1316, 2002.
- Hegg, D. A., Covert, D. S., Rood, M. J., and Hobbs, P. V.: Measurements of aerosol optical properties in marine air, *J. Geophys. Res.*, 101, 12 893–12 903, 1996.
- Hegg, D. A., Covert, D. S., Crahan, K., and Jonssen, H.: The dependence of aerosol light-scattering on RH over the Pacific Ocean, *Geophys. Res. Lett.*, 29, 60–4, 2002.
- Hegg, D. A., Covert, D. S., Crahan, K. K., Jonsson, H. H., and Liu, Y.: Measurements of aerosol size-resolved hygroscopicity at sub and supermicron sizes, *Geophys. Res. Lett.*, 33, L21808, doi:10.1029/2006GL026747, 2006.
- Huffman, J., Jayne, J., Drewnick, F., Aiken, A., Onasch, T., Worsnop, D., and Jimenez, J.: Design, modeling, optimization, and experimental tests of a particle beam width probe for the aerodyne aerosol mass spectrometer, *J. Aerosol Sci.*, 38, 1143–1163, 2005.
- IPCC: Climate Change 2007: The Physical Science Basis. Contribution of Working Group I to the Fourth Assessment Report of the Intergovernmental Panel on Climate Change, Cambridge University Press, Cambridge, United Kingdom and New York, NY, USA, 153–180, 2007.
- Kaku, K. C., Hegg, D. A., Covert, D. S., Santarpia, J. L., Jonsson, H., Buzorius, G., and Collins, D. R.: Organics in the Northeastern Pacific and their impacts on aerosol hygroscopicity in the subsaturated and supersaturated regimes, *Atmos. Chem. Phys.*, 6, 4101–4115, 2006, <http://www.atmos-chem-phys.net/6/4101/2006/>.
- Kasten, F.: Visibility forecast in phase of pre-condensation, *Tellus*, 21(5), 631–635, 1969.
- Kim, J., Yoon, S. C., Jefferson, A., and Kim, S. W.: Aerosol hygroscopic properties during Asian dust, pollution, and biomass burning episodes at Gosan, Korea in April 2001, *Atmos. Environ.*, 40, 1550–1560, 2006.
- Kondo, Y., Miyazaki, Y., Takegawa, N., Miyakawa, T., Weber, R. J., Jimenez, J. L., Zhang, Q., and Worsnop, D. R.: Oxygenated and water-soluble organic aerosols in Tokyo, *J. Geophys. Res.*, 112, D01203, doi:10.1029/2006JD007056, 2007.
- Kreisberg, N. M., Stolzenburg, M. R., Hering, S. V., Dick, W. D., and McMurry, P. H.: A new method for measuring the dependence of particle size distributions on relative humidity, with application to the Southeastern Aerosol and Visibility Study, *J. Geophys. Res.*, 106, 14 935–14 949, 2001.
- Lu, M. L., Conant, W. C., Jonsson, H. H., Varutbangkul, V., Flagan, R. C., and Seinfeld, J. H.: The Marine Stratus/Stratocumulus Experiment (MASE): Aerosol-cloud relationships in marine stratocumulus, *J. Geophys. Res.*, 112, D10209, doi:10.1029/2006JD007985, 2007.
- Magi, B. I. and Hobbs, P. V.: Effects of humidity on aerosols in southern Africa during the biomass burning season, *J. Geophys. Res.*, 108, 8495, doi:10.1029/2002JD002144, 2003.
- Malm, W. C., Day, D. E., Kreidenweis, S. M., Collett, J. L., Carrico, C., McMeeking, G., and Lee, T.: Hygroscopic properties of an organic-laden aerosol, *Atmos. Environ.*, 39, 4969–4982, 2005.
- Massling, A., Leinert, S., Wiedensohler, A., and Covert, D.: Hygroscopic growth of sub-micrometer and one-micrometer aerosol particles measured during ACE-Asia, *Atmos. Chem. Phys.*, 7, 3249–3259, 2007, <http://www.atmos-chem-phys.net/7/3249/2007/>.
- Massling, A., Wiedensohler, A., Busch, B., Neusüß, C., Quinn, P., Bates, T., and Covert, D.: Hygroscopic properties of different aerosol types over the Atlantic and Indian Oceans, *Atmos. Chem. Phys.*, 3, 1377–1397, 2003, <http://www.atmos-chem-phys.net/3/1377/2003/>.
- McFiggans, G., Alfarra, M. R., Allan, J., Bower, K., Coe, H., Cubison, M., Topping, D., Williams, P., Decesari, S., Facchini, C., and Fuzzi, S.: Simplification of the representation of the organic component of atmospheric particulates, *Faraday Discuss.*, 130, 341–362, 2005.
- Moore, R. H. and Raymond, T. M.: HTDMA analysis of multicomponent dicarboxylic acid aerosols with comparison to UNIFAC and ZSR, *J. Geophys. Res.*, 113, D04206, doi:10.1029/2007JD008660, 2008.
- Murphy, S., Agrawal, H., Sorooshian, A., Padaro, L., Gates, H., Hersey, S., Welch, W., Jung, H., Miller, J., Cocker, D., Nenes, A., Jonsson, H., Flagan, R., and Seinfeld, J.: Comprehensive Simultaneous Shipboard and Airborne Characterization of Exhaust from a Modern Container Ship at Sea, *Environmen. Sci. Technol.*, doi:10.1021/es802413j, published online: <http://pubs.acs.org/doi/abs/10.1021/es802413j>, 2009.
- Peng, C., Chan, M. N., and Chan, C. K.: The hygroscopic properties of dicarboxylic and multifunctional acids: Measurements and UNIFAC predictions, *Environ. Sci. Technol.*, 35, 4495–4501, 2001.
- Peng, C. G. and Chan, C. K.: The water cycles of water-soluble organic salts of atmospheric importance, *Atmos. Environ.*, 35, 1183–1192, 2001.
- Petters, M. D., Kreidenweis, S. M., Snider, J. R., Koehler, K. A., Wang, Q., Prenni, A. J., and Demott, P. J.: Cloud droplet activation of polymerized organic aerosol, *Tellus B*, 58, 196–205, 2006.
- Prenni, A. J., DeMott, P. J., Kreidenweis, S. M., Sherman, D. E., Russell, L. M., and Ming, Y.: The effects of low molecular weight dicarboxylic acids on cloud formation, *J. Phys. Chem. A*, 105, 11 240–11 248, 2001.
- Prenni, A. J., De Mott, P. J., and Kreidenweis, S. M.: Water uptake of internally mixed particles containing ammonium sulfate and dicarboxylic acids, *Atmos. Environ.*, 37, 4243–4251, 2003.
- Prenni, A. J., Petters, M. D., Kreidenweis, S. M., DeMott, P. J., and Ziemann, P. J.: Cloud droplet activation of secondary organic aerosol, *J. Geophys. Res.*, 112, D10223, doi:10.1029/2006JD007963, 2007.
- Rood, M. J., Larson, T. V., Covert, D. S., and Ahlquist, N. C.: Measurement of laboratory and ambient aerosols with temperature and humidity controlled nephelometry, *Atmos. Environ.*, 19, 1181–1190, 1985.
- Saathoff, H., Naumann, K. H., Schnaiter, M., Schock, W., Mohler, O., Schurath, U., Weingartner, E., Gysel, M., and Baltensperger, U.: Coating of soot and (NH₄)₂SO₄ particles by ozonolysis products of alpha-pinene, *J. Aerosol Sci.*, 34, 1297–1321, 2003.
- Seinfeld, J. and Pandis, S.: *Atmospheric Chemistry and Physics*, Wiley-Interscience, New York, NY, USA, 2nd edn., 2006.
- Sjogren, S., Gysel, M., Weingartner, E., Baltensperger, U., Cubison, M. J., Coe, H., Zardini, A. A., Marcolli, C., Krieger, U. K., and Peter, T.: Hygroscopic growth and water uptake kinetics of two-phase aerosol particles consisting of ammonium sulfate, adipic and humic acid mixtures, *J. Aerosol Sci.*, 38, 157–171, 2007.

- Sorooshian, A., Hersey, S., Brechtel, F., Corless, A., Flagan, R., and Seinfeld, J.: Rapid, Size-Resolved Aerosol Hygroscopic Growth Measurements: Differential Aerosol Sizing and Hygroscopicity Spectrometer Probe (DASH-SP), *Aerosol. Sci. Tech.*, 42, 445–464, 2008a.
- Sorooshian, A., Murphy, S. M., Hersey, S., Gates, H., Padro, L. T., Nenes, A., Brechtel, F. J., Jonsson, H., Flagan, R. C., and Seinfeld, J. H.: Comprehensive airborne characterization of aerosol from a major bovine source, *Atmos. Chem. Phys.*, 8, 5489–5520, 2008b.
- Swietlicki, E., Zhou, J. C., Covert, D. S., Hameri, K., Busch, B., Vakeva, M., Dusek, U., Berg, O. H., Wiedensohler, A., Aalto, P., Makela, J., Martinsson, B. G., Papaspiropoulos, G., Mentes, B., Frank, G., and Stratmann, F.: Hygroscopic properties of aerosol particles in the northeastern Atlantic during ACE-2, *Tellus B*, 52, 201–227, 2000.
- Tomlinson, J. M., Li, R. J., and Collins, D. R.: Physical and chemical properties of the aerosol within the southeastern Pacific marine boundary layer, *J. Geophys. Res.*, 112, 1–13, 2007.
- Topping, D. O., McFiggans, G. B., and Coe, H.: A curved multi-component aerosol hygroscopicity model framework: Part 1 - Inorganic compounds, *Atmos. Chem. Phys.*, 5, 1205–1222, 2005a.
- Topping, D. O., McFiggans, G. B., and Coe, H.: A curved multi-component aerosol hygroscopicity model framework: Part 2 - Including organic compounds, *Atmos. Chem. Phys.*, 5, 1223–1242, 2005b.
- Vakeva, M., Hameri, K., and Aalto, P. P.: Hygroscopic properties of nucleation mode and Aitken mode particles during nucleation bursts and in background air, *J. Geophys. Res.*, 107(D19), PAR9-1-11, 2002.
- Varutbangkul, V., Brechtel, F. J., Bahreini, R., Ng, N. L., Keywood, M. D., Kroll, J. H., Flagan, R. C., Seinfeld, J. H., Lee, A., and Goldstein, A. H.: Hygroscopicity of secondary organic aerosols formed by oxidation of cycloalkenes, monoterpenes, sesquiterpenes, and related compounds, *Atmos. Chem. Phys.*, 6, 2367–2388, 2006, <http://www.atmos-chem-phys.net/6/2367/2006/>.
- Virkkula, A., Van Dingenen, R., Raes, F., and Hjorth, J.: Hygroscopic properties of aerosol formed by oxidation of limonene, alpha-pinene, and beta-pinene, *J. Geophys. Res.*, 104, 3569–3579, 1999.
- Zhou, J. C., Swietlicki, E., Berg, O. H., Aalto, P. P., Hameri, K., Nilsson, E. D., and Leck, C.: Hygroscopic properties of aerosol particles over the central Arctic Ocean during summer, *J. Geophys. Res.*, 106, 32 111–32 123, 2001.